

PROCEEDINGS OF SPIE



SPIE—The International Society for Optical Engineering

Optical Sensing, Imaging, and Manipulation for Biological and Biomedical Applications

Robert R. Alfano
Ping-Pei Ho
Arthur E. T. Chiou
Chairs/Editors

26–28 July 2000
Taipei, Taiwan

Sponsored by
SPIE—The International Society for Optical Engineering
National Science Council (Taiwan)
PIDA—Photonics Industry Development Association



Volume 4082

200101221941



PROCEEDINGS OF SPIE
SPIE—The International Society for Optical Engineering

Optical Sensing, Imaging, and Manipulation for Biological and Biomedical Applications

Robert R. Alfano
Ping-Pei Ho
Arthur E. T. Chiou
Chairs/Editors

26–28 July 2000
Taipei, Taiwan

Sponsored by
SPIE—The International Society for Optical Engineering
National Science Council (Taiwan)
PIDA—Photonics Industry Development Association

Published by
SPIE—The International Society for Optical Engineering



20011130 081

Volume 4082

SPIE is an international technical society dedicated to advancing engineering and scientific applications of optical, photonic, imaging, electronic, and optoelectronic technologies.

AQ F02-02-0302



The papers appearing in this book compose the proceedings of the technical conference cited on the cover and title page of this volume. They reflect the authors' opinions and are published as presented, in the interests of timely dissemination. Their inclusion in this publication does not necessarily constitute endorsement by the editors or by SPIE. Papers were selected by the conference program committee to be presented in oral or poster format, and were subject to review by volume editors or program committees.

Please use the following format to cite material from this book:

Author(s), "Title of paper," in *Optical Sensing, Imaging, and Manipulation for Biological and Biomedical Applications*, Robert R. Alfano, Ping-Pei Ho, Arthur E. T. Chiou, Editors, Proceedings of SPIE Vol. 4082, page numbers (2000).

ISSN 0277-786X
ISBN 0-8194-3721-2

Published by
SPIE—The International Society for Optical Engineering
P.O. Box 10, Bellingham, Washington 98227-0010 USA
Telephone 1 360/676-3290 (Pacific Time) • Fax 1 360/647-1445
<http://www.spie.org/>

Copyright ©2000, The Society of Photo-Optical Instrumentation Engineers.

Copying of material in this book for internal or personal use, or for the internal or personal use of specific clients, beyond the fair use provisions granted by the U.S. Copyright Law is authorized by SPIE subject to payment of copying fees. The Transactional Reporting Service base fee for this volume is \$15.00 per article (or portion thereof), which should be paid directly to the Copyright Clearance Center (CCC), 222 Rosewood Drive, Danvers, MA 01923 USA. Payment may also be made electronically through CCC Online at <http://www.directory.net/copyright/>. Other copying for republication, resale, advertising or promotion, or any form of systematic or multiple reproduction of any material in this book is prohibited except with permission in writing from the publisher. The CCC fee code is 0277-786X/00/\$15.00.

Printed in the United States of America.

REPORT DOCUMENTATION PAGE

Form Approved OMB No. 0704-0188

Public reporting burden for this collection of information is estimated to average 1 hour per response, including the time for reviewing instructions, searching existing data sources, gathering and maintaining the data needed, and completing and reviewing the collection of information. Send comments regarding this burden estimate or any other aspect of this collection of information, including suggestions for reducing this burden to Washington Headquarters Services, Directorate for Information Operations and Reports, 1215 Jefferson Davis Highway, Suite 1204, Arlington, VA 22202-4302, and to the Office of Management and Budget, Paperwork Reduction Project (0704-0188), Washington, DC 20503.

1. AGENCY USE ONLY (Leave blank)		2. REPORT DATE July 2000	3. REPORT TYPE AND DATES COVERED 26-27 July 2001 Conference Proceedings - Final Report	
4. TITLE AND SUBTITLE Optical Sensing, Imaging and Manipulation for Biological and Biomedical Applications Held in Taipei, Taiwan on 26-27 July 2000. Proceedings.			5. FUNDING NUMBERS	
6. AUTHOR(S) Robert R. Alfano, Ping-Pei Ho, and Arthur E.T. Chiou, Editors				
7. PERFORMING ORGANIZATION NAME(S) AND ADDRESS(ES) Industrial Technology Research Institute Taipei, Taiwan			8. PERFORMING ORGANIZATION REPORT NUMBER ISSN 0277-786X	
9. SPONSORING/MONITORING AGENCY NAME(S) AND ADDRESS(ES) US Department of the Air Force Asian Office of Aerospace Research and Development (AOARD) Unit 45002 APO AP 96337-5002			10. SPONSORING/MONITORING AGENCY REPORT NUMBER	
11. SUPPLEMENTARY NOTES Proceedings of SPIE, Vol. 4082. Published by: SPIE-The International Society for Optical Engineering, P.O. Box 10, Bellingham, Washington 98227-0010. This work relates to Department of the Air Force grant issued by the Asian Aerospace Office of Research and Development. The United States has a royalty free license throughout the world in all copyrightable material contained herein.				
12a. DISTRIBUTION/AVAILABILITY STATEMENT Approved for Public Release. U.S. Government Rights License. All other rights reserved by the copyright holder. (Code 1, 20)			12b. DISTRIBUTION CODE A	
12. ABSTRACT (Maximum 200 words) This conference on Optical Sensing, Imaging and Manipulation for Biological and Biomedical Applications was part of the International Optoelectronics Symposium Held in Taipei, Taiwan on 26-28 July 2000 in conjunction with Photonics Taiwan 2000 (See http://www.spie.org/web/meetings/programs/pt00/pt00_home.html). This conference brings together the state-of-the art biomedical photonics technologies from three continents for future product advancement. The main goal of photonics is aiming high-speed and high-volume communication and computation. Telemedicine and fiber endoscopies can improve the screening of diseases in GI tracts, GYN tracts, dermatology and otorhinolaryngology areas. Minature optical sources, filters, detectors, spectrometers, optical fibers, and time-resolved devices are needed. The conference papers discuss work in the areas of biomedical imaging, microscopy, spectroscopy, fluorescence, multiphoton microscopy, fiber optics, biochips, and biosensors.				
13. SUBJECT TERMS AOARD, Foreign reports, Photonics, Optics, Biomedicine, Imaging			15. NUMBER OF PAGES	
			16. PRICE CODE	
17. SECURITY CLASSIFICATION OF REPORT UNCLASSIFIED	18. SECURITY CLASSIFICATION OF THIS PAGE UNCLASSIFIED	19. SECURITY CLASSIFICATION OF ABSTRACT UNCLASSIFIED	20. LIMITATION OF ABSTRACT UL	

NSN 7540-01-280-5500

Standard Form 298 (Rev. 2-89)
Prescribed by ANSI Std. Z39-18
298-102

Contents

- ix *Conference Committee*
- xi *Introduction*

KEYNOTE PAPER

- 2 **Photonic technologies in the 21st century: creation of new industries [4082-201]**
T. Hiruma, Hamamatsu Photonics K.K. (Japan)

SESSION 1 ADVANCES IN BIOMEDICAL IMAGING I

- 8 **Early light imaging for biomedical applications (Invited Paper) [4082-01]**
P.-P. Ho, R. R. Alfano, CUNY/City College (USA)
- 14 **Optical imaging of objects in turbid medium with ultrashort pulses [4082-02]**
C.-Y. Wang, I-Shou Univ. (Taiwan) and National Taiwan Univ.; C.-W. Sun, C. C. Yang,
Y.-W. Kiang, C.-W. Lin, National Taiwan Univ.

SESSION 2 ADVANCES IN BIOMEDICAL IMAGING II

- 24 **Development and application of noninvasive optical topography (Invited Paper) [4082-03]**
T. Yamamoto, A. Maki, Y. Yamashita, Hitachi, Ltd. (Japan); H. Yoshizawa, M. Iwata, Tokyo
Women's Medical Univ. (Japan); E. Watanabe, Tokyo Metropolitan Police Hospital (Japan);
Y. Tanikawa, Y. Yamada, Mechanical Engineering Lab. (Japan); H. Koizumi, Hitachi,
Ltd. (Japan)
- 34 **Application of near-infrared spectroscopy to investigate brain activity: clinical research
(Invited Paper) [4082-04]**
W. Lichty, K. Sakatania, Tsinghua Univ. (China) and Sino-Japanese Friendship Hospital (China);
Y. Xie, H. Zou, Sino-Japanese Friendship Hospital (China)
- 40 **Optical computed tomography for imaging the breast: first look (Invited Paper) [4082-05]**
R. J. Grable, S. L. Ponder, N. A. Gkanatsios, W. Dieckmann, P. Olivier, R. H. Wake, Y. Zeng,
Imaging Diagnostic Systems, Inc. (USA)

SESSION 3 ADVANCES IN MICROSCOPIC AND SPECTROSCOPIC IMAGING

- 48 **Development of 200-channel mapping system for tissue oxygenation measured by
near-infrared spectroscopy (Invited Paper) [4082-08]**
M. Niwayama, D. Kohata, J. Shao, N. Kudo, Hokkaido Univ. (Japan); T. Hamaoka,
T. Katsumura, Tokyo Medical College (Japan); K. Yamamoto, Hokkaido Univ. (Japan)
- 57 **Low-coherence interference microscopy at high numerical apertures (Invited Paper) [4082-09]**
C. J. R. Sheppard, M. Roy, Univ. of Sydney (Australia); P. Svahn, Univ. of Sydney (Australia)
and Royal Institute of Technology (Sweden)

- 61 **Difference-of-Gaussian annular pupil for extended depth of focus three-dimensional imaging** [4082-10]
T.-C. Poon, A. Kourakos, Virginia Polytechnic Institute and State Univ. (USA)
- 71 **DNA and protein change in human breast tissues by diffuse reflectance spectrum** [4082-11]
Y. Yang, CUNY/City College (USA); E. J. Celmer, St. Vincent's Medical Ctr. of Richmond (USA); J. A. Koutcher, Memorial Sloan-Kettering Cancer Ctr. (USA); P.-P. Ho, R. R. Alfano, CUNY/City College (USA)

SESSION 4 FLUORESCENCE AND MULTIPHOTON MICROSCOPY AND SPECTROSCOPY I

- 76 **Determination of a quantitative algorithm for the measurement of muscle oxygenation using cw near-infrared spectroscopy: mean optical pathlength without the influence of the adipose tissue** [4082-17]
J. Shao, Hokkaido Univ. (Japan); L. Lin, Tianjin Univ. (China); M. Niwayama, N. Kudo, K. Yamamoto, Hokkaido Univ. (Japan)
- 87 **Multiphoton fluorescence spectroscopy of fluorescent bioprobes and biomolecules** [4082-18]
P. Cheng, SUNY/Buffalo (USA); B.-L. Lin, Institute of Molecular Biology (Taiwan); F.-J. Kao, National Sun Yat-sen Univ. (Taiwan); C.-K. Sun, National Taiwan Univ.; Y.-S. Wang, National Sun Yat-sen Univ. (Taiwan); T.-M. Liu, National Taiwan Univ.; Y. Wang, J. Chen, M.-K. Huang, National Sun Yat-sen Univ. (Taiwan); I. Johnson, Molecular Probes Inc. (USA)
- 92 **Two-photon optical-beam-induced current microscopy of indium gallium nitride light-emitting diodes** [4082-19]
F.-J. Kao, M.-K. Huang, Y.-S. Wang, S.-L. Huang, M.-K. Lee, National Sun Yat-sen Univ. (Taiwan); C.-K. Sun, National Taiwan Univ.; P. Cheng, SUNY/Buffalo (USA)

SESSION 5 FLUORESCENCE AND MULTIPHOTON MICROSCOPY AND SPECTROSCOPY II

- 100 **Multiphoton microspectroscopy of biological specimens (Invited Paper)** [4082-20]
B.-L. Lin, Institute of Molecular Biology (Taiwan); F.-J. Kao, National Sun Yat-sen Univ. (Taiwan); P. Cheng, SUNY/Buffalo (USA); C.-K. Sun, National Taiwan Univ.; R.-W. Chen, Institute of Molecular Biology (Taiwan); Y. Wang, J. Chen, Y.-S. Wang, National Sun Yat-sen Univ. (Taiwan); T.-M. Liu, National Taiwan Univ.; M.-K. Huang, National Sun Yat-sen Univ. (Taiwan)
- 105 **Applications of two-photon fluorescence microscopy in deep-tissue imaging** [4082-21]
C. Y. Dong, B. Yu, L. Hsu, Massachusetts Institute of Technology (USA); P. D. Kaplan, Univerlever Edgewater Lab. (USA); D. Blankschtein, R. Langer, P. T. C. So, Massachusetts Institute of Technology (USA)
- 115 **Simultaneous multichannel nonlinear imaging: combined two-photon excited fluorescence and second-harmonic generation microscopy** [4082-22]
R. Gauderon, P. B. Lukins, C. J. R. Sheppard, Univ. of Sydney (Australia)
- 119 **Second-harmonic generation microscopy of tooth** [4082-23]
F.-J. Kao, Y.-S. Wang, M.-K. Huang, S.-L. Huang, National Sun Yat-sen Univ. (Taiwan); P. Cheng, SUNY/Buffalo (USA)

- 125 **Using differential confocal microscopy to detect the phase transition of the membrane of giant unilamellar liposomes** [4082-24]
C.-H. Lee, W.-J. Lin, Institute of Applied Science and Engineering Research (Taiwan); J. Wang, Institute of Atomic and Molecular Sciences (Taiwan) and National Taiwan Univ.
- 134 **Multiphoton fluorescence microscopy: behavior of biological specimens under high-intensity illumination** [4082-25]
P. Cheng, SUNY/Buffalo (USA); B.-L. Lin, Institute of Molecular Biology (Taiwan); F.-J. Kao, National Sun Yat-sen Univ. (Taiwan); C.-K. Sun, National Taiwan Univ.

SESSION 6 FIBER OPTICAL SENSORS

- 140 **Optic fiber needle to probe inside the body using fluorescence ratio method** [4082-26]
G. C. Tang, A. Katz, Y. Budansky, R. R. Alfano, CUNY/City College (USA)
- 144 **Fabrication of deuterium-loaded fiber Bragg grating and its spectral characteristics in thermal annealing** [4082-30]
M. C. Shih, C. C. Wang, C. T. Yu, National Taiwan Ocean Univ.; T. J. Chuang, Institute of Atomic and Molecular Sciences (Taiwan)
- 151 **Temperature performance of Raman scattering in a data fiber and its application in a distributed temperature fiber optic sensor** [4082-31]
D. Liu, J. M. Wang, S. Liu, Huazhong Univ. of Science and Technology (China)
- 157 **Novel fiber grating sensing technique based on the torsion beam** [4082-32]
W. Zhang, D. Feng, L. Ding, Y. Zhang, X. Dong, C. Zhao, X. Dong, Nankai Univ. (China)

SESSION 7 BIOCHIP AND BIOSENSOR TECHNOLOGY

- 162 **Research and development of biochip technologies in Taiwan (Invited Paper)** [4082-33]
S. J. Y. Ting, Tunghai Univ. (Taiwan); A. E. T. Chiou, National Dong Hwa Univ. (Taiwan)
- 173 **Novel CMOS photosensor with a gate-body tied NMOSFET structure** [4082-34]
Y.-J. Kook, J.-H. Jeong, Y.-J. Park, H.-S. Min, Seoul National Univ. (Korea)
- 181 **Electro-optically modulated biomolecular interaction analysis sensor** [4082-36]
Y. Cheng, Synchrotron Radiation Research Ctr. (Taiwan); Y. Chang, National Chiao-Tung Univ. (Taiwan); C. Lin, Synchrotron Radiation Research Ctr. (Taiwan); L. Hsu, National Chiao-Tung Univ. (Taiwan); M. K. Chyu, Univ. of Pittsburgh (USA)
- 192 **In-vivo noninvasive glucose monitoring with optical heterodyne polarimetry in a range of 50 mg/dl to 100 mg/dl** [4082-37]
W.-H. Wang, C.-Y. Han, P.-C. Tu, C. Chou, National Yang-Ming Univ. (Taiwan)
- 198 **Design and development of laser Doppler velocimetry based on DSP technique for blood flow measurement** [4082-38]
Y.-H. Lin, Y.-Y. Chen, Y. Ho, Y.-L. Li, G.-J. Jan, National Taiwan Univ.

SESSION 8 OPTICAL MANIPULATION

- 210 **Particle-trapped near-field scanning optical microscopy: scattering and depolarization (Invited Paper) [4082-39]**
M. Gu, Swinburne Univ. of Technology (Australia)
- 213 **Applications of optical tweezers and an integrated force measurement module for biomedical research [4082-40]**
J.-W. Tsai, National Yang-Ming Univ. (Taiwan); B.-Y. Liao, Institute of Information Science (Taiwan); C.-C. Huang, National Dong Hwa Univ. (Taiwan); W.-L. Hwang, D.-W. Wang, Institute of Information Science (Taiwan); A. E. T. Chiou, National Dong Hwa Univ. (Taiwan); C.-H. Lin, National Yang-Ming Univ. (Taiwan)
- 222 **Quantitative comparison of single-beam gradient-force optical traps and dual-beam optical traps [4082-41]**
Z. H. Huang, D. S. Mehta, H. C. Huang, C. F. Wang, A. E. T. Chiou, National Dong Hwa Univ. (Taiwan)
- 232 **Automation of optical tweezers [4082-42]**
T.-M. Hsieh, B.-J. Chang, L. Hsu, National Chiao-Tung Univ. (Taiwan)
- 241 **Application of phase contrast microscopy to the study of marine microbiota [4082-43]**
M. C. Shih, C. T. Lian, C. S. Hwang, National Taiwan Ocean Univ.

POSTER SESSION

- 248 **Characteristics of acoustic wave propagation in dermis for the diagnosis of the superficial tissue damage in radiation therapy [4082-44]**
C.-W. Lyu, National Yang-Ming Univ. (Taiwan); H.-J. Wang, Ministry of National Defense (Taiwan); L.-C. Peng, C. Chou, National Yang-Ming Univ. (Taiwan)
- 255 **Analysis system for PET detector [4082-45]**
H.-C. Liu, H.-C. Liang, Institute of Nuclear Energy Research (Taiwan)
- 261 **Detection of objects hidden in highly scattering media using time-gated imaging methods [4082-46]**
L. M. Wang, X. Liang, P. A. Galland, P.-P. Ho, R. R. Alfano, CUNY/City College (USA)
- 265 **Tightly bending loss measurement for 1.3- μ m and 1.5- μ m broadband wavelength division multiplexing fiber sensor systems [4082-52]**
S.-L. Tsao, W.-M. Cheng, Yuan Ze Univ. (Taiwan)
- 275 **Experimental study on fiber Bragg grating electric current sensor [4082-53]**
D. Feng, G. Kai, L. Ding, H. Liu, X. Dong, Nankai Univ. (China)
- 278 **Characteristics analysis of SOI waveguide Michelson interferometers for developing biomedical fiber temperature-sensing head [4082-54]**
S.-L. Tsao, S.-G. Lee, Yuan Ze Univ. (Taiwan)
- 286 **Implementation of a 1280- to 1380-nm light source for reflective spectrum measurement of biomedical fiber sensors [4082-55]**
S.-L. Tsao, S.-C. Chiou, Yuan Ze Univ. (Taiwan)

- 298 **Electro-optical measurement of highly intense electric field with high frequency [4082-57]**
X. Zeng, H. Chen, Huazhong Univ. of Science and Technology (China)
- 305 **Channel-switching add/drop multiplexer with tunable fiber Bragg grating based on the cantilever beam [4082-58]**
D. Feng, H. Liu, W. Zhang, C. Ge, G. Kai, X. Dong, Nankai Univ. (China)
- 310 **Novel interferometer for measuring small distances [4082-59]**
Z. Wu, Yanshan Univ. (China); Z. Li, Harbin Institute of Technology (China); K. Tong, Yanshan Univ. (China); X. Qiang, Harbin Institute of Technology (China)
- 315 **Grating angular displacement transducer using a Fabry-Perot structure [4082-60]**
Z. Li, X. Qiang, Harbin Institute of Technology (China); Z. Wu, L. Fan, Yanshan Univ. (China)
- 321 **Numerical analysis of near-field optical trapping using tapered fiber probe [4082-61]**
G. Zhang, Z. Zhu, Y. Li, G. Xia, Q. Lin, Central China Normal Univ.
- 329 *Author Index*

Conference Committee

Conference Chairs

Robert R. Alfano, CUNY/City College (USA)
Ping-Pei Ho, CUNY/City College (USA)
Arthur E. T. Chiou, National Dong Hwa University (Taiwan)

Program Committee

Chien Chou, National Yang-Ming University (Taiwan)
Min Gu, Swinburne University of Technology (Australia)
Gwo-Jen Jan, National Taiwan University
Fu-Jen Kao, National Sun Yat-sen University (Taiwan)
Ting-Chung Poon, Virginia Polytechnic Institute and State University (USA)
Colin J. R. Sheppard, University of Sydney (Australia)
Chih Chung Yang, National Taiwan University

Session Chairs

- 1 Advances in Biomedical Imaging I
Arthur E. T. Chiou, National Dong Hwa University (Taiwan)
- 2 Advances in Biomedical Imaging II
Ping-Pei Ho, CUNY/City College (USA)
- 3 Advances in Microscopic and Spectroscopic Imaging
Min Gu, Swinburne University of Technology (Australia)
- 4 Fluorescence and Multiphoton Microscopy and Spectroscopy I
Ping-chin Cheng, SUNY/Buffalo (USA)
- 5 Fluorescence and Multiphoton Microscopy and Spectroscopy II
Ting-Chung Poon, Virginia Polytechnic Institute and State University (USA)
- 6 Fiber Optical Sensors
Chih Chung Yang, National Taiwan University
- 7 Biochip and Biosensor Technology
Chien Chou, National Yang-Ming University (Taiwan)
- 8 Optical Manipulation
Fu-Jen Kao, National Sun Yat-sen University (Taiwan)

Introduction

Optical biopsy, the use of light to diagnose disease, began at the City College of New York (CCNY) in the early 1980s when Michelle Alfano, a Riverdale County high school student, was searching for a project to commence her research for the Westinghouse Talent Research Award (now called the Intel Science Competition). Since she was interested in a career in medicine (she is now a successful architect in New York City), she came to the Institute for Ultrafast Spectroscopy and Lasers (IUSL) of CCNY to start her research under the direction of her father, Robert R. Alfano. Her proposal to use light to find cancers started the biomedical photonics research effort at IUSL. During the past 15 years, with some private funding from Hamamatsu Photonics K.K. and Mediscience Technology Corp. and government grants from the Ballistic Missile Defense Initiative (BMDO), Center for Advanced Technology under the New York State Science & Technology Foundation, and the Institution Research Award of NASA, researchers at IUSL have published over 100 papers in refereed journals and over 100 conference proceeding papers, and have been awarded over 30 patents in biomedical photonics. During this period, biomedical photonics grew in the United States, where SPIE and OSA have organized more than 100 topical conferences.

During the past 10 years, the economics of Taiwan have made a significant change in terms of semiconductor foundry and OEM computers. Over the past two years, Taiwan's photonics industry has expanded and now supplies approximately 80% of the computer CD-ROM drives in the world. This effort is attributed in part to Taiwan's Photonics Industry Development Association (PIDA) and the Electro-Optics Science and Technology Committee of National Science Council (NSC). With advance planning and aggressive implementation, they have used their limited resources to invest in certain well-defined target areas to make a significant impact. The biochip technology is one example. This technology was first revealed to the public in 1998. Within two years, 47 projects have been funded by NSC.

This conference brings together the state-of-the-art biomedical photonics technologies from three continents for future product advancement. The fusion of two main thrusts, photonics and biomedicine, will advance the future technology and have major economic impact for the 21st century. The main goal of photonics is aiming for high-speed and high-volume communication and computation. Telemedicine and fiber endoscopies can improve the screening of diseases in GI tracts, GYN tracts, dermatology, and otorhinolaryngology areas. Miniature optical sources, filters, detectors, spectrometers, optical fibers, and time-resolved devices are needed as components to construct compact biomedical photonic devices and instruments.

In this conference, 52 papers by renown scientists from around the world (specifically, the U.S., China, Japan, Australia, Korea, Sweden, and Taiwan) will present their work in the areas of biomedical imaging, microscopy, spectroscopy, fluorescence, multiphoton microscopy, fiber optics, biochips, and biosensors. Some of these

technologies have the potential for immediate clinical applications, such as optical biopsy. Other technologies may provide an impact in future biomedical applications, such as biochips, fiber sensors, and wavelength demultiplexing for compact spectroscopic screening instruments.

We are grateful to SPIE, NSC, and PIDA, for sponsoring this conference and for providing the necessary financial and technical assistance. We wish to thank all of the contributors for their efforts to make this conference a success.

Ping-Pei Ho
Arthur E. T. Chiou
Robert R. Alfano

Keynote Paper

Photonic Technologies in the 21st Century : Creation of New Industries *

Teruo Hiruma
Hamamatsu Photonics KK
Hamamatsu, Japan

ABSTRACT

As we approach the new millennium, the ongoing aim of human society is not only for promoting scientific technology but also creating new industries. To achieve this goal, each person in industry must recognize anew that the real meaning of science is to explore the absolute truth. It is also important that people recognize that there are unlimited matters which we humans do now yet know.

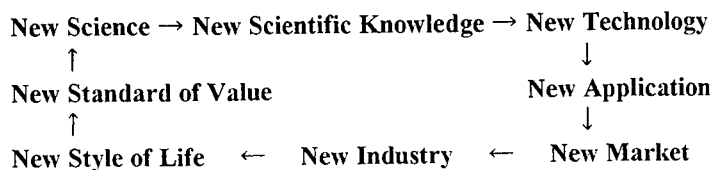
1. INTRODUCTION

The 20th century was one that witnessed many great discoveries and our knowledge increased many times during the last one hundred years. Yet even with such an explosion of knowledge and information there is much more that we do not yet understand. Our present knowledge represents only a fraction of what there is to know. For example, there have been major breakthroughs in understanding cell structure by studying individual components or systems such as the role of calcium ions in signal transduction. However very little is known about how all of these components work in concert. It is very much like trying to understand an orchestra by studying the individual instruments. In the future we will develop methods to study the function of the entire cell not just individual systems. On the molecular level we are just beginning to study the details of molecular dynamics during a chemical reaction. The work of this year's Nobel Prize winner in chemistry, Dr Zewail shows how it is possible to use photonics to study the intimate detail of a chemical reaction. Once we gain such detailed information about more complex systems it will be possible to more efficiently produce the chemicals we need and to destroy those that we no longer require.

At Hamamatsu Photonics it is our corporate mission to provide photonics technology that will help us to gain new knowledge of the world we live in. Photonic technologies are very unique in that they let us observe the parts of the world that are very far away (thousands of light years), very small (nanometers) or happen very quickly (in femtoseconds). The roots of our company can be found in the pioneering spirit of Professor Kenjiro Takayanagi who independently developed the technology of television despite the fact those around believed it could not be done because it had never been done. Professor Takayanagi hoped to develop a new way for people to experience the world. We inherited his spirit and continue this idea by using photonics to gain knowledge as well as improve the quality of life for all people.

In the twenty first century it will be possible that we could make all of mankind healthy. Not just in a physical sense but in the definition of the World Health Organization where "Health is a state of complete physical, mental and social well-being and not merely the absence of disease or infirmity." Photonics has the potential for creating the knowledge and industry that could make this possible. It is our hope that this new century sees the beginning of a new economic cycle shown in Figure 1. While industry is designed to generate profit, the purpose of industrialization is for all of mankind to share a common understanding of the New Life Style and to benefit from the New Standard of value, namely Health as defined above.

Figure 1:



*Also published in Proceedings of SPIE Volumes 4078, 4079, 4080, and 4081

Through the application of photonics we are now beginning to develop the New Science that will lead to the cycle illustrated in Figure 1. In this cycle, mankind is constantly improving its status by using new technologies to discover new knowledge. The application of this new knowledge leads first to new industries and then to a change in the social fabric of society. We understand that this is a very long-term goal. But mankind needs to dream in order to progress. Only by trying to see over the horizon can we discover something that will radically improve all of our lives. Thus while Hamamatsu Photonics' short-term goal is to generate profits, these profits are to be used in the quest for new knowledge which is our long-term target.

2. TECHNOLOGIES

This paper will discuss several technologies that are key to the development of new knowledge which will eventually produce new industries. Application of these technologies will be also discussed.

A. The Ultimate Laser Photon (Photon Factory)

The light emitted by a laser is unique in that it is monochromatic, coherent and directional. These properties have made laser-generated photons vital to all types of research ranging from biology to high-energy physics. We need to obtain a better understanding of exactly what is a photon and how it interacts with the world. By better understanding the photon on a fundamental level we will be able to use it more effectively. Phenomena such as the particle wave duality and teleportation must be better understood through a study of the photon.

The development of very small terawatt and pedawatt laser systems give many researchers access to inexpensive ultra high power. New physical phenomena are being discovered when such intense laser beams interact with matter because these lasers create electric fields much greater than those seen in any other experiment do.

B. Ultra Fast Measurement Technology

By continuing to push the speed at which we make measurements we will discover greater detail of how our world operates. We now have lasers that are capable of measuring the individual motion of atoms in molecules. Newer and faster methods will help get even greater detail of how molecules react. Even faster methods will allow us to follow the motion of electrons during important chemical reactions such as photosynthesis or vision.

C. Optical Correlation Technology

Even though we have discovered only a small fraction of our knowledge, we are severely limited in using it because even this limited amount of knowledge is too great to process with conventional computer systems. We must learn how to process information in parallel with optical processors such as spatial light modulators. Ultimately our goal is to process information in 3 or more dimensions using technology that must still be invented.

D. Forecast Simulators

With time not only has our information become too complex, but also the questions we need to answer become more difficult. As our planet's population increases and our technology becomes more complex, the risk of answering a question incorrectly grows exponentially. For example, the consequences of incorrectly predicting the outcome of global warming will be severe if we either under estimate or over estimate the significance of burning fossil fuels. Premature curtailing of fossil fuels will severely curtail the growth of developing countries leading to unnecessary pain and suffering. Failure to prevent global

warming will have even worse consequences. We need better methods to simulate events or conditions so we can better guide environmental, economic, technical, political, and military decisions.

Ultimately nations will never again fight a war on the battlefield but instead will use simulations to replace them. The simulations will simultaneously decide the output as well as convince the parties that physical conflict is too costly.

E. High Power Lasers

Photons are capable of doing many important things such as curing cancer, printing this manuscript or repairing an integrated circuit. At very high photon densities there are many new things that photons can do. At present, it is expensive to generate a lot of photons because the photon sources are expensive. Semiconductor laser diodes hold the promise of being able to reliably and inexpensively generate photons for many new and exciting applications. Just like the replacement of the vacuum tube with the transistor and then to the integrated circuit, so too will the semiconductor laser evolve and result in important technologies and new industries that we cannot even imagine today.

F. New Photochemistry

Much of our planet's energy is wasted in creating chemicals that we need to live or to improve our lives. Lasers are capable of creating specific excited states. Finding ways to selectively excite molecules so that they can be moved along specific reaction pathways will lead to huge savings in cost, energy and pollution. New knowledge on how to perform pathway specific photochemistry is vital to the goal of making everyone healthy according to the World Health Organization's definition of health.

3. APPLICATIONS

We can only speculate on what the full effect of such new photonic technologies will have in the long term. However over a short period of time we can easily imagine some of the benefits we might enjoy from these as well as other photonic technologies. Some of these benefits are discussed below.

A. Measurement of Physiological Functions

The pulse oximeter has already found an important role in guaranteeing that the oxygen concentration of the blood is maintained at as close to optimum as possible. Countless lives have been saved and others have had severe injury prevented by this simple optical device. Not very far away are devices that will permit rapid and painless screening for diabetes. Noninvasive cancer diagnosis is already being tested in clinical trials.

Ultimately a device will be available that checks your body's functions on a daily basis. It screens for potential problems before they cause disease. Adjustments to exercise, diet or even administration of drugs can be performed before the individual is aware of a problem. Such an advanced detection system would save costs, pain and anxiety. It would go as long way to attaining the goal of making people truly healthy.

B. Optical Medicine

In the past few years, photodynamic therapy has been shown to be a valuable treatment for some forms of cancer. In some cases it is far more useful than other techniques such as surgery because it leaves the effected organ in tact. Therefore for young women, cancer of the cervix no longer means that it is the end of their dream to have a family. For older people suffering from the wet form of macula degeneration, photodynamic therapy will soon be used to prevent the blindness caused by this disease.

New chemicals are being developed that are absorbed faster by the cancer cells and discharged more rapidly by the body. This will make treatment simpler and more effective. Patients may not even need to stay overnight in a hospital. Presently PDT can only be used on cancers that are found on a surface. Techniques are being developed that will be used in the treatment of cancers that are deep inside an organ.

Cosmetic uses of photons for hair removal, port wine stain removal or tattoo removal make it easier for a person to be accepted by society. These applications are far from superficial since they greatly improve the quality of life for those that need them.

Other applications of photonics to medical practice will certainly emerge in the near future for things such as the treatment of stroke, heart disease, healing of wounds and reducing or relieving pain.

C. Early Detection of Disease

Cancer screening using Positron Emission Tomography (PET) holds the promise of early detection and cure of this terrible affliction. Injection of fluorodeoxyglucose into the blood stream is current used to uncover cells that are metabolizing at rates faster than those of their neighbors. These cells are then analyzed to determine if they are malignant. Such a screening method could in the near future make an entire city cancer death free.

Light CT uses nonionizing infrared photons to take a three dimensional image of the body. Work is under way in many places around the world to use light CT as a method for detecting breast cancer. This technique could be less expensive than x-ray methods and used safely on all individuals including pregnant women. Other uses of the light CT would be to quickly determine if a stroke is caused by ischemia or a hematoma. Such information is vital in determining the correct treatment. Rapid treatment of stroke can greatly reduce the damage to the brain resulting in a patient that can lead a normal life even after such a severe trauma.

In the future we hope to quantify the health of a person, not just the presence of disease.

D. Fiberless Optical Communication

Information is the most important commodity in our society. We are constructing very large and expensive infrastructures to move information from one location to the other. Fiber optics is one of the key technologies for information transport because of the very high capacity available due to wavelength division multiplexing. This technique suffers from the fact that fibers must be placed between locations. At Hamamatsu Photonics we have developed a series of fiberless optical communications systems. These operate by transmitting the optical signals through air. They have the capability to send data, or video without the need for government licenses or owning a right of way. One such a fiberless system is used at sporting events such as golf tournaments to transmit the video camera output to the broadcaster's trailer or even back to a studio. Such a system was used at the Atlanta Olympics and is now being tested in Hamamatsu City. In our hometown it is being used to connect elementary schools with the city hall. It could also be used to connect remote clinics with the medical school for telemedicine.

E. Health Industry for Successful Aging

Many countries will soon suffer from an increase in their average age. In the past such an increase in age would greatly burden society in terms of medical expenses and the cost of financially supporting an aging population. We believe that it is possible to completely eliminate the impact of a graying population by finding ways to reduce the pace and effect of the aging process. At Hamamatsu Photonics we are using photonic technology to understand how locomotion is effected as a person ages. We hope to develop exercises that will prevent the loss of mobility and greatly reduce the probability of an older person falling. While just a small step, it will have a big impact on the quality of life of our seniors.

F. Disposal of Industrial Waste

High power lasers and controlled photochemistry hold the promise of being able to safely dispose of dangerous waste products. It will do this by selective destruction of the dangerous ingredients into less danger or even harmless smaller molecules. These smaller molecules can then be recycled into new products.

G. Search for New Energy Sources

Perhaps the biggest impact that photonics can have on mankind is the development of clean and inexpensive energy. For once this is available; the quality of life of the entire world can be improved without damaging the planet. We must continue our search for a way to harness laser fusion and solar energy for they are needed to make the world a better place to live for all of us.

Photonics holds the promise of creating New Science and New Technology which will lead to New Industrial and of course to a world population that is truly healthy.

SESSION 1

Advances in Biomedical Imaging I

Early Light Imaging for Biomedical Applications

P. P. Ho¹ and R. R. Alfano

Institute for Ultrafast Spectroscopy and Lasers
Departments of Electrical Engineering and Physics
The City College of The City University of New York, NY, NY 10031

ABSTRACT

Objects located in highly scattering biomedical media can be imaged with sub-millimeter spatial resolution using the early light selected by time, spatial, and polarization gates. Spectroscopic fingerprints can provide diagnostic potentials for medical screening by utilizing fluorescence, excitation, absorption, and Raman approaches.

1. INTRODUCTION

Current tools used by the medical professionals to diagnose diseases rely heavily on X-rays, nuclear radiation, magnetic resonance, chemical analysis, positron emission, and ultrasound. Video and computer imaging have enhanced some of these modalities to detect pathological changes caused by disease. To increase the sensitivity of existing screening techniques (e.g., 75% of women whose mammograms were identified to be positive turned out to be benign after a biopsy) and to reduce possible side effects of X-rays and isotope radiation, new techniques are needed.

Over the past fifteen years, various optical detection and imaging methods have appeared on the scene to measure objects hidden in turbid and biomedical media. Ultrafast lasers and spectroscopy techniques with computer-assisted optical tomography can improve the accuracy of diagnosis. Using an optical Kerr gate¹, the early light was selected to generate clear images¹ of a 0.1-mm width test bar hidden behind a 3.5-mm thick human breast tissue. Using a time gated streak camera method² and high repetition rate 100-fs laser pulse illumination to scan and collect the transmitted signals, the image of a ~ piece of chicken fat of ~ 2.5-mm thickness embedded in a 40-mm thick chicken breast tissue was obtained.

Optical spectroscopy offers a mean for the characterization of physical and chemical changes that occur in diseased tissues. Adding spectral information obtained from fluorescence, absorption, excitation, and scattering in spatial domains with early light imaging optical approaches offer advantages in the minimal invasive approach to identify hidden objects such as cancers in their earliest stage of growth. This presentation focuses on the principle and methods of ultrafast early gating techniques.

2. HISTORY OF EARLY LIGHT IMAGING

When photons travel through a turbid medium, three signal components¹⁻⁴ can be defined: ballistic, snake, and diffusive. A schematic diagram of these three components is shown in Fig.1. Ballistic photons take the shortest path through the medium, while the diffusive scattered light of the incident photons travels over a much larger distance in turbid samples. The snake component arises from those photons scattering within a small forward angular cone which arrives on the onset of the diffusive component. In a thick highly turbid inhomogeneous medium, such as human tissues, the contribution to the ballistic component becomes exceedingly small and is buried and merged into the snake/diffusive component. The early light (ballistic and snake photons) preserves some direct image information.

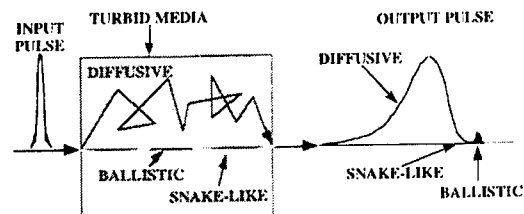


Fig.1 Schematic of ballistic, snake, and diffusive signal of an ultrashort laser pulse propagating through a turbid medium. Ballistic: coherently forward scattered

Several schemes have evolved over the years to sort out the image-bearing ballistic and snake photons from the multiple-scattered diffuse photons. Beside the use of an ultrafast time shutter, these schemes exploit one or more of the changes that scattering induces on the characteristics such as directionality, polarization, coherence and temporal duration of the incident light. Since, the image-bearing photons change the least, the idea is to devise a *gate* that will let the photons with a specific initial property through but block others. One such scheme is a *space gate* that exploits the fact that the ballistic and snake photons come out of the tissue in the incident direction, while the multiple-scattered light emerges in all directions. A small aperture centered on the direction of incidence and placed after the sample will collect the on-line-transmitted light and effectively discriminate against a significant fraction of the scattered light. Similarly, a *time gate* capitalizes on the fact that image-bearing photons emerge from

¹ Correspondence: Email: ho@photonicsmail.sci.ccnyc.cuny.edu Telephone: 212 650 6808; Fax: 212 650 5530

the sample sooner than the diffusive photons. For early light imaging, one then needs a shutter that will open for a short duration, typically a few picoseconds, to let the early photons through and then close in time to leave out the delayed scattered photons. Similar gating schemes based on polarization and coherence of light have also been devised. Often a single gate may not be discriminating enough. A space gate cannot filter out the photons that have first been scattered out of the incident direction and then back into it. A time gate employed after the space gate can cut out such "on-line" scattered photons, since the scattering makes them travel longer distances and emerge out of the sample later than the ballistic photons that propagate straight through.

Several other groups have pioneered in early light imaging techniques. A photon counting based delayed coincidence detection technique⁵ was developed to detect the internal structures inside turbid media. Using ps diode lasers⁶ and a 120-ps early light time-gating, a large tumor embedded in a thick breast tissue was identified. Reintjes et al used the nonlinear gain from stimulated Raman scattering⁷ to enhance the quality of optical images in scattering media. Chance et al⁸⁻¹¹ has demonstrated an optical imaging system using the streak camera technology to study the deoxyhemoglobin in brain with a simulation system. Coherent imaging (time-resolved holography) was measured^{12,13} using the principle of the pulse holographic interference technique. A holographic image is formed from the coherent (ballistic) part and is separated out from the incoherent (diffusive) part which takes a longer path and contributes a uniform noise background. Diffusive optical tomography using second harmonic nonlinear correlation detection has also been demonstrated¹⁴⁻¹⁶. An e^{-32} factor attenuation of femtosecond input signals through turbid media has been observed. Imaging quality can be improved by reducing the diffusive component using absorption and fluorescence-absorption techniques^{17,18}. Results based on the ps time-of-flight and absorption change,¹⁸ the image of the internal structure of rats in vivo was obtained.

3. TIME GATES

An ideal ultrafast shutter for early light imaging desires the \sim ps or fs time resolution, fast (\sim ps) triggering response time and jitter, low gate temporal fluctuation ($< 1\%$), high (\sim GHz) repetition rate, large dynamic range ($> 10^{10}$), wideband (200-nm to 5,000-nm) spectral sensitivity, large acceptance angle, low operation power, small geometrical dimension, good environmental stability, easy operation, and low cost.

3.A Electronic Controlled Time Gates

Gated Image Intensifier: The image intensifier is an electro-optical device which can detect and intensify 2D optical images from the near uv to the near IR wavelength regions. A microchannel plate (MCP) image intensifier uses an MCP to convert incident photons into electrons with $\sim 10,000$ times gain. An MCP consists of arrays of millions of glass capillary coated with second-electron-emission materials to amplify the electron signal current produce from an image sensor (photocathode). For a gated image intensifier, the time gated function is added by introducing an electronic gate voltage pulse to the amplification photocathode. A gated image intensifier¹⁹ is used as an ultrafast time shutter with an opening time (FWHM) of ~ 80 -ps.

Streak Camera: In this method, signal photons are focused onto a photocathode through a thin slit. After the emitted photoelectrons from the cathode are accelerated through an anode, these electrons are deflected by an applied voltage ramp which increases with time and streaks the electrons onto a phosphor screen to be displayed. These electrons which are released at different times and arrived the phosphor screen at different spatial locations with a phosphorescent track can be recorded by a CCD camera. Only one-dimensional signals can be imaged. The minimum time resolution of a streak camera is ~ 1 -ps.

3.B Nonlinear Optical Time Gates

Optical Kerr Gate (OKG): OKG is based on the third order (χ^3) nonlinear optical process and has similar design parameters as a regular camera shutter and can also be used to gate incoherent optical signals. All other three types of nonlinear optical gates listed below require the phase matching condition and are limited to coherent signals only. Two optical beams are needed in an OKG. One beam is used as the gating beam and the other is used as the probing beam. The intensity of the probing pulse should be kept to be small in compared to the gating pulse. A Kerr medium is situated between a pair of crossed polarizers. The gating pulse induces a transient birefringence in a Kerr medium and causes the polarization change of the probing beam. To prevent the "coherent artifact" in an OKG, the wavelength of the probing beam should be different from the gating beam. To avoid the saturation effect²⁰ and the nonlinear absorption²¹ in a Kerr medium, the gating pulse intensity at the Kerr cell should be set to be < 1 GW/cm² for a 1-cm long CS₂ Kerr medium. The time delay between the gating and probing pulse is controlled by a stepping-motor with a minimum temporal resolution to be \sim fs. The minimum temporal resolution of an OKG is ~ 100 -fs which is limited by the gating pulse duration (~ 100 -fs) and the response time of the gating material (< 10 -fs for glass).

Optical Parametric Amplified Gate (OPAG): OPAG²² is based on the second order nonlinear optical process (χ^2). When an intense gating laser pulse at frequency ω_1 and a weak signal beam at ω_2 ($\omega_2 < \omega_1$) co-propagate in a χ^2 material, the output signal under the phase matching condition can be gated and amplified. The intensity of the output idle signal is proportion to a function of $\sinh^2 [\frac{1}{2} GL]$, where L is the interaction length of the χ^2 material and G is a gain parameter ($\sim I_{\text{gate}} \times \chi^2$). Using a 22-mm long KTP gating material and a 10-mJ 532-nm 30-pJ gating pulse, a time-gated signal at 1064-nm with a $> 1,000$ gain factor can be obtained (see SPIE #4082-46).

Up-Conversion Gate (UCG) and Second-Harmonic Auto-Correlation Gate (SHAG): The up-conversion uses a χ^2 NLO process.

The major difference between UCG and OPAG is the output signal frequency used in UCG, ω_s , is equal to the sum of the gating frequency and incident signal frequency ($= \omega_1 + \omega_2$). While in OPAG, the output frequency, ω_s , is equal to the difference of the gating frequency and incident signal frequency ($= \omega_1 - \omega_2$). SHAG is a special case of UCG where both the gating frequency and incident signal frequency are equal ($\omega_1 = \omega_2 = \omega$). The output signal frequency $\omega_s = 2\omega$. The minimum temporal resolution from both UCG and SHAG is in the fs region which is limited by the time convolution of the gating pulse and the signal pulse. Based on the output frequency is increased (up) or decreased (down), the output signal from UCG or OPAG will be either a function of $\sim \sin^2[\frac{1}{2}GL]$ or $\sinh^2[\frac{1}{2}GL]$. The maximum possible output signal from a UCG is always less or equal to the incident signal. While from the PAG, the output signal can be exponentially grown to the limitation \sim the gating pulse energy. The advantage of a UCG is that when the incident frequency ω_2 is in the infrared region where the detector sensitivity is poor, using a proper gating frequency, the output signal frequency ω_s can be shifted to the visible region with improved sensitivity and S/N.

Four-Wave-Mixing Coherence Gating: Optical coherent imaging (OCI),^{14,15} holographic methods,^{12,13} four-wave mixing (FWM) gate,²³ and coherent anti-Stokes Raman scattering (CARS) gate⁷ are different four-wave mixed gating techniques. In all of these gating methods, phase matching or coherence conditions are required. The advantages of these methods are good temporal resolution and the flexibility of optics from the combination of four-waves. However, all these methods are suffered to the lower sensitivity. The interference between image-bearing photons and a reference beam derived from the same initial pulse of light forms the mechanism for selective detection in coherence techniques. Photons that are coherent with the reference pulse give rise to a gated signal, while diffusive light does not. The coherence time of the reference pulse determines the duration of the gate. OCI systems are based on interferometry with low-coherence light. In an interferometer, a beam of light is split into two parts and are recombined after they travel two different paths. The two beams form an interference pattern only when they are coherent that is the phase difference between the two remains fixed. If one of the beams interacts with a scattering medium only the ballistic photons will retain their original phase and interfere with the reference beam. Diffusive component loses its original phase and cannot interfere. Interference thus filters out image-bearing ballistic photons and a fraction of snake photons. Light retro-reflected from different depths within the sample are measured by scanning the axial position of the reference mirror and simultaneously recording the interferometric signal amplitude. The two beams interfere only when the two arm path lengths match within the source coherence length. A broadband light source such as super-luminescence diodes with short coherence length, typically $\sim 10 \mu\text{m}$, is used in OCT systems. The longitudinal position of the image can be determined with high-resolution. By scanning the sample beam along the transverse dimensions and performing a longitudinal scan at each position, a two-dimensional image can be obtained.

3.C Equivalent Time Gates: Space, Polarization, and Absorption

Based on spatial arrangements and polarization properties, image information with an equivalent time gated properties can be obtained. These gates can be coupled with an ultrafast time shutter either as described in sections 3A and 3B to achieve higher S/N for a sophisticated imaging instrument or sometimes be used alone for a compact low-cost early light screening tool.

Space Gating Collimator imaging²⁵ and Fourier spatial filtering^{26,27} are two commonly used space gating techniques. In confocal imaging, an optical fiber collimator shines light on the sample and an on-line receiving fiber collimator that faces the transmitter collects the light that passes straight through. Since, the diameter of the collecting fiber is small, it only accepts ballistic light and rejects off-axis scattered light. A two-dimensional image can be formed point by point by scanning the illuminator and collector fibers synchronously across the object while keeping them precisely aligned.

In a Fourier gate, a collimated beam shines the object and a lens of focal length F placed at a distance F focuses the photons that retain their collimation at a distance of $2F$ from the object. The angular spatial frequencies of scattered light will be forward Fourier transformed to the Fourier spectral plane²⁷. The central pattern arising from the collimated portion of the transmitted light represents the zero frequency (DC) component. The intensity of the region spread around the central part represents higher spatial frequencies. Higher angular frequencies are of larger radii. The earlier and the later diffusive signals can be spatially filtered and separated out. A small aperture placed at the focus of the lens transmits the image-bearing light and rejects most of the diffusive component. For example, a hidden object with dimensions of ~ 0.1 to 1-cm embedded in a turbid medium consisting of scattering particles with dimensions ~ 1 to $10\text{-}\mu\text{m}$. The Fourier spatial frequency ($\sim 1/\text{object size}$) of the object is much smaller than that from the surrounding small random particles to be separated.

Kerr-Fourier Time-Space Gate

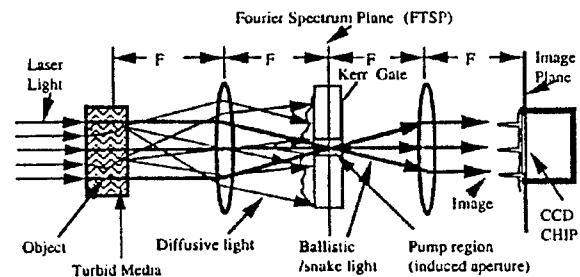


Fig.2 Schematic diagram of early light Kerr-Fourier gated imaging.

Mode-locked laser is used for the gating and probing source. The probing beam is used to illuminate the sample. The gating beam is used to open the Kerr gate. The Kerr cell is set at the back focal plane of the Fourier transform lens and is situated between a pair of crossed polarizers (not shown here). For the Fourier imaging measurement of the object, the second lens L_2 is located at one focal length away from the FTSP and the CCD camera was located at one focal length from L_2 as the $4F$ imaging system.

For most biomedical imaging applications, a large dynamic range of $\geq 10^{10}$ is needed to obtain image information of an object embedded in thick turbid media, such as tumors in breast tissues. A simple time-gating approach may not achieve the required dynamic range. A Fourier spatial filtering technique²⁷ coupled with ultrafast time gating has the capability to improve the dynamic range and S/N. A schematic diagram of early light Kerr-Fourier gated (KFG) imaging is shown in Fig.2. The spatial dimension of the gating laser pulse radial profile can induce a spatial aperture of a given diameter at the Kerr cell to effectively remove the higher spatial frequencies. In this manner, information from the surrounding random small particles can be removed while the lower spatial frequency from the object is transformed. This KFG imaging can detect phantoms in a 70-mm thick 2% intralipid solution with better than 1-mm resolution. The feasibility of constructing a three-dimensional tomographic image was demonstrated by combining two-dimensional shadowgrams formed with a KFG using a back-projection algorithm on a personal computer.²⁸

Polarization Gating The polarization gate makes use of the fact that scattering events depolarize an incident beam of linearly polarized light so that ballistic photons retain their polarization state while the multiple-scattered photons are depolarized. In practice a polarization gate is implemented by shining the object through a linear polarizer and collecting the emerging light through a second linear polarizer. The degree of polarization, defined as $(I_p - I_s)/(I_p + I_s)$ where I_p and I_s are transmitted intensities with the axis of the second polarizer parallel and perpendicular to that of the first respectively, of the transmitted light is used to select the image-bearing component since it is ideally expected to be unity for ballistic light and zero for completely depolarized light. Time-dependent²⁹ polarization status of an optical pulse propagating through a scattering medium is shown in Fig.3. The depolarization coefficient (D) of an ultrashort polarized laser pulse at 532-nm propagating through a suspension of 200-nm diameter polystyrene micro-spheres in water was measured by a streak camera. The suspension was placed in a 50-mm thickness water cell and the scattering length is 4-mm. The measured D values of the ballistic component and the later arrived diffusive component were ~ 1 and 0, respectively.

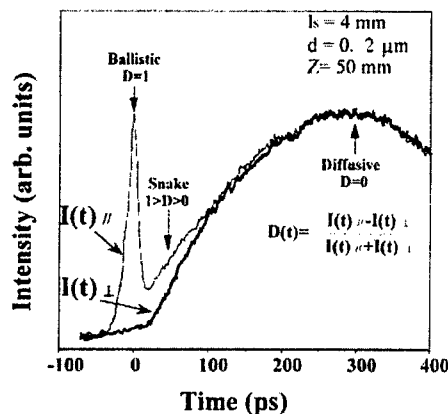


Fig.3 Time-dependent polarization status of optical pulse propagating in scattering media.

Absorption Gating For the fluorescence imaging of an object embedded in a host turbid medium, absorption can reduce the amount of multiple scattered diffusive photons by shortening the optical path of the signal light propagating through the host.¹⁷ The image quality of an object could be improved when it is viewed in the overlapping spectral region between the luminescence spectrum of the object and the absorption spectrum of the surrounding medium.

4. EARLY LIGHT SPECTROSCOPY IMAGING

Optical spectroscopies³¹ can be employed to show the spectral differences caused by the change of the concentration, biological and ionic characters, chemical composition of bonds, organic materials and biological samples.

Diagnosis of Cancer Tissues: The visible fluorescence spectra and relaxation time from cancerous and normal rat kidney, bladder, and prostate tissues show different spectra characteristics. The line of research using fluorescence and excitation spectra was extended to human lung and breast normal and cancerous tissues³². The fluorescence spectral profiles from normal human tissues were found to peak at about 520 nm, often with complex structures. For breast tissues, cancerous fluorescence profiles were smoother and the peak was shifted. The natural fluorophor responsible for the main signature appears to be flavin. It is believed that the absorption from oxy-hemoglobin may be the marker responsible for the spectral structure using visible excitation. Using uv sources, basic molecules, such as NADH, elastin, and collagen in tissues can be excited and used as fingerprints of materials.

Atherosclerosis Diagnosis: Atherosclerosis is a major medical problem for the middle-aged and elderly, and X-ray visualization of arteries following an injection of radio opaque material via a catheter is the common method of diagnosis. Thus, optical spectroscopy offers a means to determine whether a given arterial wall is diseased. Once the plaque is located by spectroscopy, an intense laser can ablate the plaque. Too much plaque or tissue removal can produce perforated arteries. Normal and diseased samples exhibit two peaks near 550 and 600 nm. The intensity of the 600 nm peak was smaller than the 550 nm peak in the diseased samples. The valley between the peaks at 580 nm was used to normalize the spectra from the tissue. The ratio of intensity at 600 nm to 580 nm for a normal artery was 2 and for a diseased artery was unity.³³

Raman Spectroscopy: The molecular components of human tissues are principally composed of proteins, nucleic acids, and lipids. These molecules have characteristic vibrations which can be accurately characterized by Raman spectroscopy. The number of Raman active mode will most likely be altered when the molecular structures change from normal to abnormal states. Raman spectroscopy can be used to analyze these changes on a molecular scale. Visible Raman and fluorescence spectra from 500 nm to 700 nm of human cancerous and normal breast tissues excited at 488 nm have shown noticeable spectral differences. These differences most likely arise from the presence of hemoglobin. A significant difference between the two spectra is the presence of narrow spike-like bands atop the broad band in normal tissue spectra which are absent in cancer. These narrow

spike-like bands arise from Raman scattering spectral lines which was confirmed by changing the excitation wavelengths from 488 nm to 514.5 nm. By comparing the locations in wave numbers of the narrow spike-like bands of the normal breast tissue spectra, we conclude that these narrow bands arise from Raman scattering. The Raman lines are shifted by about 1036, 1242, 1584, 2745, and 2944 cm^{-1} from the laser lines. The normal breast tissue spectrum had two subsidiary maxima located at 556 nm and 592 nm, while no additional maxima were recorded in cancerous breast tissue.

In most biological tissues a large fluorescence emission inhibits the observation of Raman spectral lines. To eliminate the fluorescence background, one must excite and measure Raman spectra in the IR spectral region where fluorescence is much weaker than that in visible spectral region³⁴. NIR Raman scattering spectra of benign breast tissue, benign tumor and malignant tumor breast tissues were measured. From the vibrational modes of the CH_2 , amide, and protein bonds, intense Raman lines were located at ~ 1078 , 1300, 1445 and 1651 cm^{-1} for benign breast tissues; ~ 1240 , 1445 and 1659 cm^{-1} for a benign tumor; and ~ 1445 and 1651 cm^{-1} for a malignant tumor. There were differences in both the number of Raman lines and the intensity ratio among different Raman lines.

A combined Fourier space and polarization gated spectral imaging to sort out early arrived imaging bearing photons of biomedical samples was demonstrated. 2D transillumination spectroscopy images¹⁹ of in-vitro human breast tissue specimens were recorded by an InGaAs NIR camera using 1225-1300 nm light from a forsterite laser. Near-resonant images of a 28mmx12mmx10-mm human breast tissue sample comprising adipose and fibrous tissues were measured with 1225-nm laser and non-resonant images of the same sample were obtained using a 1285-nm laser. These results demonstrate that an appreciable spectroscopic difference may significantly enhance the contrast between different types of early light images from breast tissues.

For the spectral polarization imaging, light from an appropriate white light or low-power laser sources can be used to illuminate the sample. The illumination wavelength is selected by band pass filters located on a multiple filter wheel which can be rotated to the desired filter position by computer control to select the appropriate NIR wavelength. Images can be recorded for the implementation of the scattering (the illuminating and detecting wavelengths are the same) and emission (the detecting wavelengths are different from the illuminating wavelength), respectively. Since the scattering and emission properties of the tissues and tumors are different, both scattered and emitted NIR light images can be used to identify tumors. For polarization difference imaging, the analyzer is kept in a direction while polarizer for illumination is alternatively placed in the parallel and perpendicular polarization directions in respect to the analyzer. Two polarization images will be obtained when the polarization direction of the analyzer is parallel or perpendicular to that of polarizer. The parallel and perpendicular images are used to investigate the surface and inter structures of tumors, respectively. The polarization difference image is obtained by subtracting the perpendicular image from the parallel image. For excitation difference imaging, at least two different wavelengths are used for illumination while a same detection wavelength or wavelength region is used for recording the fluorescence images. Two or more fluorescence images will be obtained with different excitation wavelengths. The excitation difference image can be obtained by subtracting one image from another. For emission difference imaging³⁵, at least two different detection wavelengths are used for recording the fluorescence images while a same excitation wavelength is used for illuminating. Two fluorescence images of a luminous object (1-mm diameter chicken breast tissue stained by Cardio Green) located 31-mm underneath the surface of a host chicken breast tissue illuminated by a 630-nm mode-locked ps laser source was measured at 790-nm and 830-nm as shown in Fig.4a and 4b, respectively. The emission difference image of Fig.4c was obtained by subtracting Fig.4a image from Fig.4b. The image visibility enhancement from the difference imaging can be attributed from the reduction of host tissue emission and diffusion processes.

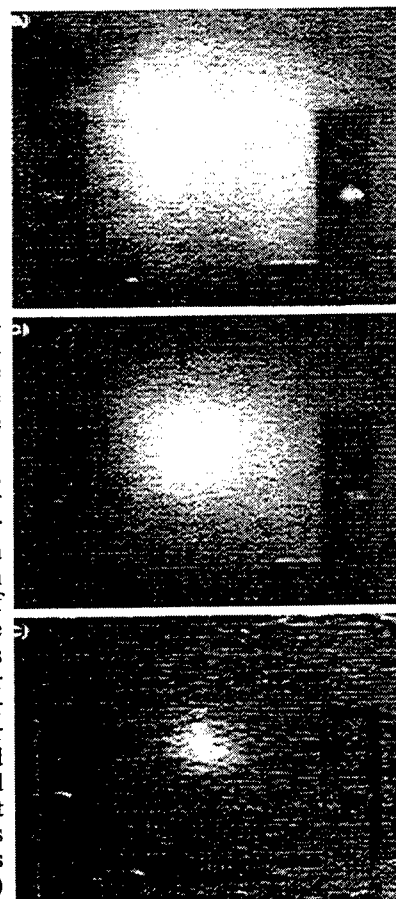


Fig.4 Difference fluorescence imaging of a small piece stained tissue inside a 6cmx5cmx4cm chicken breast tissue. Black U-image is the sample holder.

5. SUMMARY

Photonics can play an important role in today's and tomorrow's biomedical technology for screening and surgical applications. Imaging through a thick highly scattering biomedical sample remains to be a challenge problem. Pico and femtosecond laser sources which are the key element for the early light imaging technique are becoming reliable and compact in size. Early light imaging can be implemented in a number of clinical applications for screening such as prostate cancer, breast cancer, cervical cancer, glaucoma, macular degeneration, macular edema, and atherosclerosis plaques. Understanding of the spectroscopic information from the photonic technology will be the key factor toward the success of disease diagnosis.

ACKNOWLEDGMENT

This research is supported in part by grants from NASA/IRA, NASA/FAR, DoE Center for Excellence in Laser Medicine, U.S. ARMY Medical Research Acquisition Activity, CUNY/CAT NY State Science & Technology Foundation.

REFERENCES

1. L. Wang, P. Ho, C. Liu, G. Zhang, R.R. Alfano, "Ballistic 2-D imaging through scattering walls using an ultrafast Kerr gate", *Science*, **253**, 769-771 (1991)
2. B. Das, K. Yoo, R. Alfano, "Ultrafast time gated imaging in thick tissues", *Optics Letters* **18**, 1002-4 (1993)
3. K. Yoo and R. R. Alfano, "Time-resolved coherent and incoherent components of forward light scattering in random media", *Opt. Lett.* **15**, 320-322, (1990)
4. R. R. Alfano, X. Liang, L. Wang, P. Ho, "Time-resolved imaging of translucent drops in highly scattering medium", *Science* **264** 1913-5 (1994)
5. S. Anderson-Engels, R. Berg, S. Svanberg, O. Jarlman, "Time-resolved transillumination for medical diagnosis", *Opt. Lett.* **15**, 1178-1180 (1990); "Effects of optical constants on time-gated transillumination", *J. Photochem. Photobiol.* **B16**, 155-167 (1992)
6. R. Berg, O. Jarlman, S. Svanberg, "Medical transillumination using short-pulse diode lasers", *Applied Optics*, **32** (1993)
7. M. Duncan, R. Mahon, L. Tankersley, J. Reintjes, "Spectral and temporal characteristics of spontaneous Raman scattering in the transient regime", *Opt. Lett.* **16** 1868-1670 (1991)
8. B. Chance, J. Leigh, J. Miyake, D. Smith, S. Nioka, R. Greenfield, M. Finander, K. Kaufmann, W. Levy, M. Young, P. Cohen, H. Yoshioka, R. Boretsky, "Comparison of time-resolved and un-resolved measurements of deoxyhemoglobin in brain", *Proc. Nat. Acad. Sci.* **5**, 4971-4975 (1988)
9. B. Chance ed. "Photon Migration in Tissues", Plenum Press, NY (1990)
10. E. Sevick, N. Wang, B. Chance "Time dependent photon migration imaging", *SPIE*, **1599** 274-283 (1992)
11. "Photon migration and imaging in random media and tissues", B. Chance, R. Alfano, ed. *SPIE*, **1888** (1993)
12. K.G. Spears, J. Serafin, N.H. Abramson, "Chron-Coherent Imaging for Medicine", *IEEE Trans. Biomed. Eng.* **36** 1210-1221 (1989)
13. H. Chen, Y. Chen, D. Dillworth, E. Leith, J. Lopez, J. Valdmann, "Two-dimensional imaging through diffusing media using 150-fs gated electronic holography techniques", *Opt. Lett.*, **16** 487-489 (1991)
14. J. Fujimoto, W. Drexler, U. Morgner, F. Kartner, E. Ippen, "Optical coherence tomography", *Optics & Photonics News*, pp25-31, Jan. (2000)
15. J. Fujimoto, S. De Silversti, E. Ippen, R. Margolis, A. Oseroff, "Femtosecond optical ranging in biological system" *Opt. Lett.* **11**, 150-152 (1986); *Science*, "Optical coherence tomography" **254**, 1178-1182 (1991).
16. K. Yoo, Q. Xing, R. Alfano, "Imaging objects hidden in highly scattering media using femtosecond second-harmonic-generation cross-correlation time gating", *Opt. Lett.*, **16** 1019-1021 (1991)
17. K. Yoo, Z. Zang, S. Ahmed, R. Alfano, "Imaging objects hidden in scattering media using a fluorescence-absorption technique", *Opt. Lett.*, **16** 1252-1254 (1991)
18. D. Benaron, D. Stevenson "Optical time-of-flight absorbance imaging of biomedical media" *Science*, **259** 1463-1466 (1993)
19. S. K. Gayen and R. R. Alfano "Sensing lesion in tissues with light", *Optics Express* **4** 475-480 (1999)
20. P. Ho and R. Alfano, "Oscillatory optical induced Kerr kinetics in nitrobenzene", *Opt. Comm.* **30** 428-430 (1979)
21. P. Ho, P. Lu, R. Alfano, "Time-dependent multi-photon absorption in liquids", *J. Chem. Phys.* **74** 1605-9 (1980)
22. J. Watson, P. Georges, t. Lepine, B. Alonzi, A. Brun, "Imaging in diffuse media with UPAG", *Opt. Lett.*, **20** 231-233 (1995)
23. A. D. Sappey, "Optical Imaging through turbid media with a degenerate four wave mixing correlation time gate", *Appl. Opt.* **33** 8346-8353 (1994)
24. M. A. O Leary et al., "Experimental images of heterogeneous turbid media by frequency-domain diffusing-photon tomography," *Opt. Lett.* **20** 426-428 (1995)
25. P. French, "The light fantastic medical show," *New Scientist*, March 11, 25-29 (1995)
26. B. E. A. Saleh and M. C. Teich, *Fundamentals of Photonics*, John Wiley and Sons, Inc., NY, pp136-139 (1991)
27. L. Wang, P. Ho, R. Alfano, "Time-resolved Fourier Spectrum and Imaging in Highly Scattering Media", *Applied Optics*, **32** 5043-8 (1993).
28. L. Wang, P. Ho, X. Liang, R. Alfano, "Fourier-Kerr Imaging in Thick Turbid Media", *Optics Letters*, **18** 241-243 (1993).
29. L. Kalpaxis, L. Wang, X. Liang, P. Galland, P. Ho, R. Alfano, "3D temporal image reconstruction", *Opt. Lett.* **18** 1691-3 (1993)
30. S. G. Demos and R. R. Alfano, "Temporal gating in highly scattering media by the degree of optical polarization," *Opt. Lett.* **21** 161-3 (1996)
31. R. R. Alfano ed. "Optical Biopsy III" *SPIE Vol.3917* (2000)
32. R. R. Alfano, G. C. Tang, Asima Pradhan, W. Lam, D. S. J. Choy, E. Opher, "Fluorescence spectra from cancerous and normal human breast and lung tissues," *IEEE J. Quantum Electron.* **QE-23**, 1806 (1987).
33. C. Kittrel et al., *Applied Optics*, **24**, 2280 (1985).
34. C. H. Liu, W. L. Sha, H. R. Zhu, D. L. Akins, L. Deckelbaum, M. Stetz, K. O'Brien, J. Scott and R. Alfano, "NIR Fourier transform Raman spectroscopy of normal and atherosclerotic human aorta", *Laser in Life Sci.*, **4** 257-261 (1992)
35. W. B. Wang, S. G. Demos, J. Ali, G. Zhang, and R. R. Alfano, "Visibility enhancement of fluorescent objects hidden in animal tissues using spectral fluorescence difference method," *Opt. Comm.* **147** 11-15 (1998)

Optical imaging of objects in turbid medium with ultrashort pulses

Chih-Yu Wang^{a,b}, Chia-Wei Sun^b,
C. C. Yang^{* b,c}, Yean-Woei Kiang^c, Chii-Wann Lin^d

^aDepartment of Biomedical Engineering, I-Shou University, Kaoushung, Taiwan, R.O.C.

^bGraduate Institute of Electro-Optical Engineering, National Taiwan University, Taipei, Taiwan, R.O.C.

^cDepartment of Electric Engineering, National Taiwan University Taipei, Taiwan, R.O.C.

^dGraduate Institute of Biomedical Engineering, National Taiwan University Taipei, Taiwan, R.O.C.

ABSTRACT

Photons are seriously scattered when entering turbid medium; thus the images of objects hidden in turbid medium can not be obtained by just collecting the transmitted photons. Early-arriving photons, which are also called ballistic or snake photons, are much less scattered when passing through turbid medium, and contains more image information than the late-arriving ones. Therefore, objects embedded in turbid medium can be imaged by gathering the ballistic and snake photons. In the present research, we try to recover images of objects in turbid medium by simultaneously “time-gate” and “polarization-gate” to obtain the snake photons. An Argon-pumped Ti-Sapphire laser with 100fs pulses was employed as light source. A streak camera with 2ps temporal resolution was used to extract the ballistic and snake photons. Two pieces of lean swine meat, measured 4mm×3mm and 5mm×4mm, respectively, were placed in a 10cm×10cm×3cm acrylic tank, which was full of diluted milk. A pair of a polarizer and an analyzer was used to extract the light that keeps polarization unchanged. The combination of time gating and polarization gating resulted in good images of objects hidden in turbid medium.

1. INTRODUCTION

1.1 Recent development of near-infrared light imaging

Recently, optical imaging through highly scattering medium with near-infrared light has received much attention [1-8]. Because of its noninvasive nature, researchers have regarded near-infrared light as a safe alternative to ionizing radiation such as x-ray or positron emission tomography. However, near-infrared light can penetrate into biological tissues only a limited depth because of strong scatter. Therefore, advanced optical techniques are required for such imaging application.

It was shown that near-infrared light is only weakly absorbed by most biological tissues, and light propagating in biological tissues is mainly attenuated through scattering [9-11]. Based on this fact, two approaches were commonly adopted for

* Correspondence: Email: ccy@cc.ee.ntu.edu.tw; Telephone: 886-2-23657624; Fax: 886-2-23652637

imaging with near-infrared light: 1) capturing snake photons for direct imaging [2,8,12,13], and 2) collecting diffusive photons and reconstructing the image with the theory of diffuse photon density wave [1,5,10,11]. The second approach costs less than that of the first one; however, its spatial resolution is usually unsatisfied. Due to multiple scattering, the image information of the embedded objects for the diffusive light are almost lost. In fact, the spatial resolution of reconstructed images by using diffusive photons is limited by many factors, including optical properties of the turbid medium, the thickness of the samples, the wavelength of the probe light, etc. Therefore, the reconstruction of high-resolution images is not a cakewalk [14]. On the other hand, the collection of ballistic or snake photons can provide high-resolution image, but the amount of these photons are very small and not easily captured. Furthermore, these photons exist in a very short time period (200ps~300ps), dependent on the optical property of the measured tissues. In recent years, due to the development of high speed detector, such as electronic gated CCD and streak camera, the research on imaging techniques with ultrashort pulses has gradually become popular [13,15].

1.2 polarization gating and time gating for snake photons

Since snake photons encounter little scattering and are along shorter path when transmitting the measured sample, they arrive at the detector earlier than diffuse photons. By gating those early arriving photons, we are able to obtain the images of the embedded objects. However, usually it is not easy to determine the time interval of snake photons. Another property of the snake photons is that their polarization almost keeps unchanged during propagation. In other words, if the incident pulse is polarized, the output snake photons bear the same polarization [16]. Therefore, combining time gating and polarization gating is useful for extracting snake-photons and get clear images.

2. EXPERIMENTAL PROCEDURES

2.1 Samples—turbid medium and targets

In the experiment, diluted milk (the milk was made up by milk power branded “Kolin”), was used to simulate turbid medium. The milk was contained in an transparent acrylic tank, with 10cm×10cm×3cm in dimensions. Two pieces of lean swine meat, measured 4 mm×3 mm and 5 mm×4 mm, respectively, hanged in the center of the tank and separated by about 3 mm, were embedded in the milk as objects to be imaged. The thickness of the both meat was about 1 mm. The total attenuation coefficient (μ_t) of the objects and the background medium are 13.6cm^{-1} and 10cm^{-1} , respectively. The tank was then placed on a motor-controlled two-dimensional translation stage for measurement.

2.2 Measurement instruments

The experimental setup is shown in Fig. 1. An Argon-pumped Ti-Sapphire laser (Spectra Physics, USA), which emits 100fs short pulses, was employed as the light source. The streak camera was operated in the synchronous scan mode, which would accumulate the light intensity of many pulses, to obtain a high signal to noise ratio. One of the split light from the first beam splitter (BS₁) was incident on a PIN diode to generate a trigger signal. The other part of light was separated into two paths by the second beam splitter (BS₂). One is then incident on the samples for imaging, while the other was sent to the streak

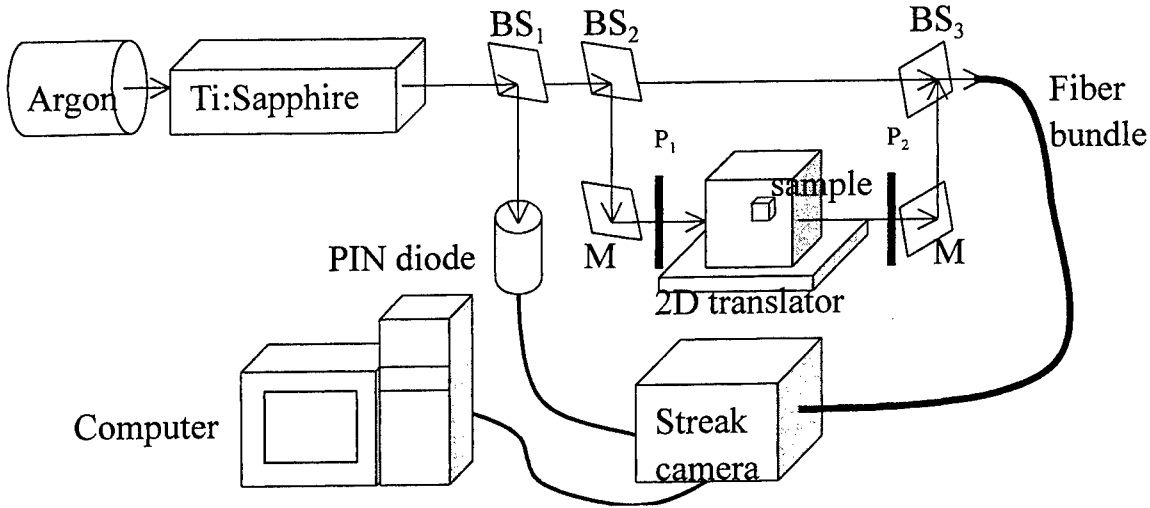


Fig.1 Experimental setup.

camera (Hamamatsu, K.K., Japan) directly as the reference signal. During measurement, the incident light and the detector were fixed and aligned with each other, while the tank was moved with a two-dimensional motor-controlled translation stage. The measurement area was $2\text{cm} \times 2\text{cm}$ in dimensions. The temporal profiles of pulses, which were broadened (diffused) to become about 1.1 ns in width after transmitting the turbid medium, were collected point by point. Two polarizers P_1 and P_2 , placed before and after sample, were used to gating the output photons whose polarization remained unchanged. This will help the streak camera extracting the early-arriving photons, whose polarization was supposed to be unchanged.

2.3 Instrument control and data acquisition

The instrument control and data acquisition were implemented by using software named LabVIEW (National Instruments Inc., USA). The movement of the two-dimensional translation stage, including the moving speed, step, displacement, axis, etc, can be controlled by the self-developed software. The timing for sample moving was pre-determined to match time required for getting profiles by the streak camera. The acquired temporal profile was stored and translated into a text-format file. The data processing, including intensity normalization, temporal calibration, etc, was completed with an analysis program written in LabVIEW. After calculation, the data were stored in the hard disk, and the image was displayed on the screen.

3. IMAGING RESULTS

3.1 Temporal profile

Temporal profiles of output pulses can be obtained by integrating the streak image for each measuring point of the sample. The reference beam, which did not pass through the turbid medium and always arrived at the detector periodically with fixed intensity, was used for time and intensity calibration. Figure 2 shows a typical temporal profile. Occasionally jitters occur due to the instability of the pulse repetition rate and laser intensity. To remove such undesired effects we normalize the intensity of the signals based on that of the reference. Also, the temporal positions of the profile were adjusted according to the center of reference. Figure 3 shows a typical calibrated temporal profile. In this chart, all data points were shifted such that the peak of the reference signal was positioned at zero time ($t = 0$).

3.2 Measurement with polarizers

To further reject the diffusive photons for improving the imaging results, two polarizers were placed before and behind the sample (see Fig. 1). The first polarizer (P_1), which was placed before the sample, was used to generate a linearly polarized incident light. The second one (P_2), which was placed behind the sample, was used as a polarization analyzer. During the measurement, the analyzer (P_2) was first rotated to have the same orientation of P_1 , and the measured signal was denoted as L_p (parallel polarization). Next, it was rotated to become perpendicular to P_1 , and the measured signal was denoted as L_c (cross polarization). It is supposed that ballistic and snake photons, which are almost not scattered while propagating in the turbid medium, maintain the original polarization. However, the diffusive photons, which has been seriously scattered, have lost the original polarization information after transmitting through the scattering medium, and the orientations of polarization for such photons were random. About 50% of the diffusive light passes the parallel- and cross-polarization analyzer, respectively. Hence, the summation of L_p and L_c represents the total output light. Only those photons keeping their original polarization left in the profile of L_p-L_c . Figure 4 shows the results for summation and subtraction of L_p and L_c . In this figure, we saw that the diffusive light (the late-arriving photons) still exists in L_p+L_c , while only the ballistic and snake photons (close to the leading edge of the curve) left in the curve L_p-L_c . Therefore, we conclude that with two polarizers and a streak camera, we can extract the light keeping the original polarization, which bears abundant information for imaging.

To evaluate the possibility for optical imaging with the described method, we scanned a $2\text{cm} \times 2\text{cm}$ area for images. The depth of the tank was about 3cm. For each measuring point, the parallel polarized light (L_p) and cross polarized light (L_c) were both measured. Figure 5 shows the image that was obtained from L_p+L_c , the total light passing the turbid medium. Since the signal contains diffusive photons, we can hardly recognize the shape of the targets.

On the other hand, Fig. 6 shows the image of obtained from the profile L_p-L_c . As the inset shows, only the early arriving photons (near the leading edge of the profile) are used. Further calculation shows that the contrast (defined as the image minus background to the background ratio) of the image in Fig. 6 are about 2.5 times of that in Fig. 5. In other words, in Fig. 6 the embedded objects can be identified more clearly than in Fig. 5. The white square boxes indicate the actual positions of the two pieces of meat.

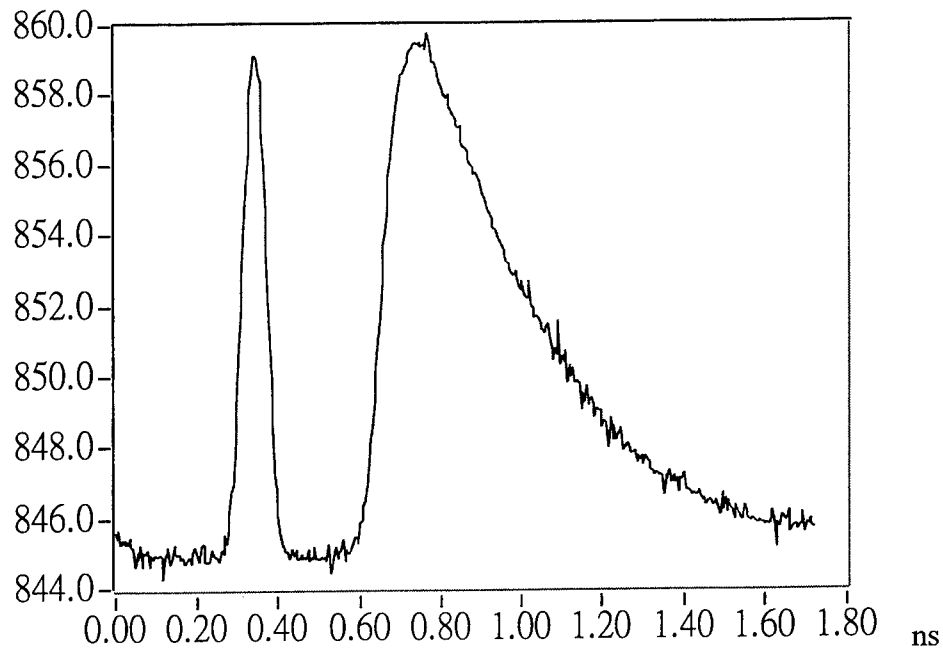


Fig. 2 Original temporal profile obtained from the streak camera at a measuring point. The first peak represents the reference beam.

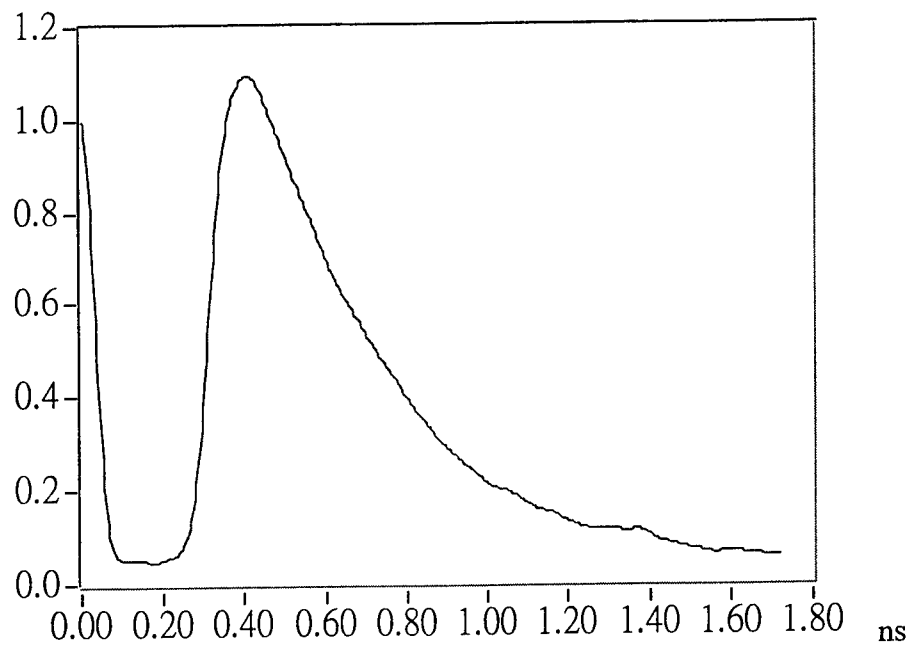


Fig.3 Temporal-position-adjusted and intensity-normalized profile. This temporal profile has been made smooth by using a low pass filter.

4. DISCUSSION AND CONCLUSION

In Fig. 6, the left image is much clearer than the right one. In fact, the right one contains more fat than the left one. Since the color of fat is almost white at room temperature, the scattering effect of this piece of meat was much severe than regular lean meat. Therefore, the image of the right one became blurrier than the left one.

In this research, by combining time gating and polarization gating, we obtained the images of biological tissues embedded in turbid medium (diluted milk). It was shown that polarization gating was an efficient approach that could help extracting ballistic and snake photons. Therefore, clearer image can be obtained. Furthermore, the addition of polarization gating provides a useful criterion for judging the interval of “snake photons”, which would be very useful for the study of optical properties of tissues to be measured.

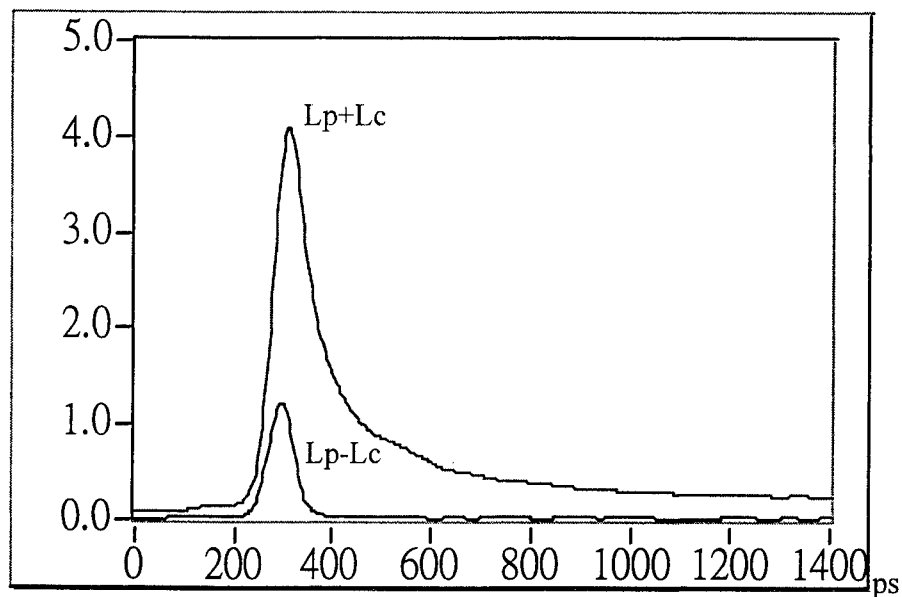


Fig. 4 Temporal profiles for the summation of parallel- and cross-polarization light ($Lp+Lc$, which represents the photons passing through the sample and analyzer without considering the polarization), and the subtraction of parallel- and cross-polarization light ($Lp-Lc$, which represents the photons without changing their polarization after passing through the sample).

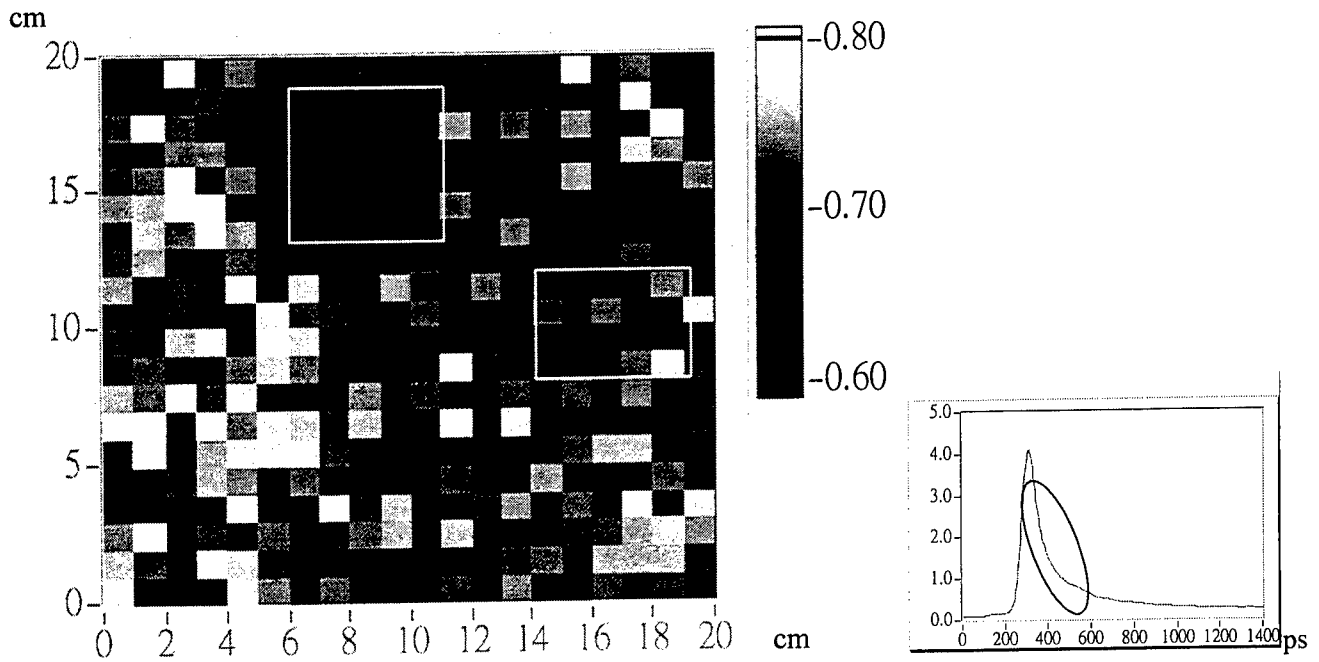


Fig. 5 Image of objects with diffusive photons. The inset shows the resulted profile of L_p+L_c , and the interval used for calculation.

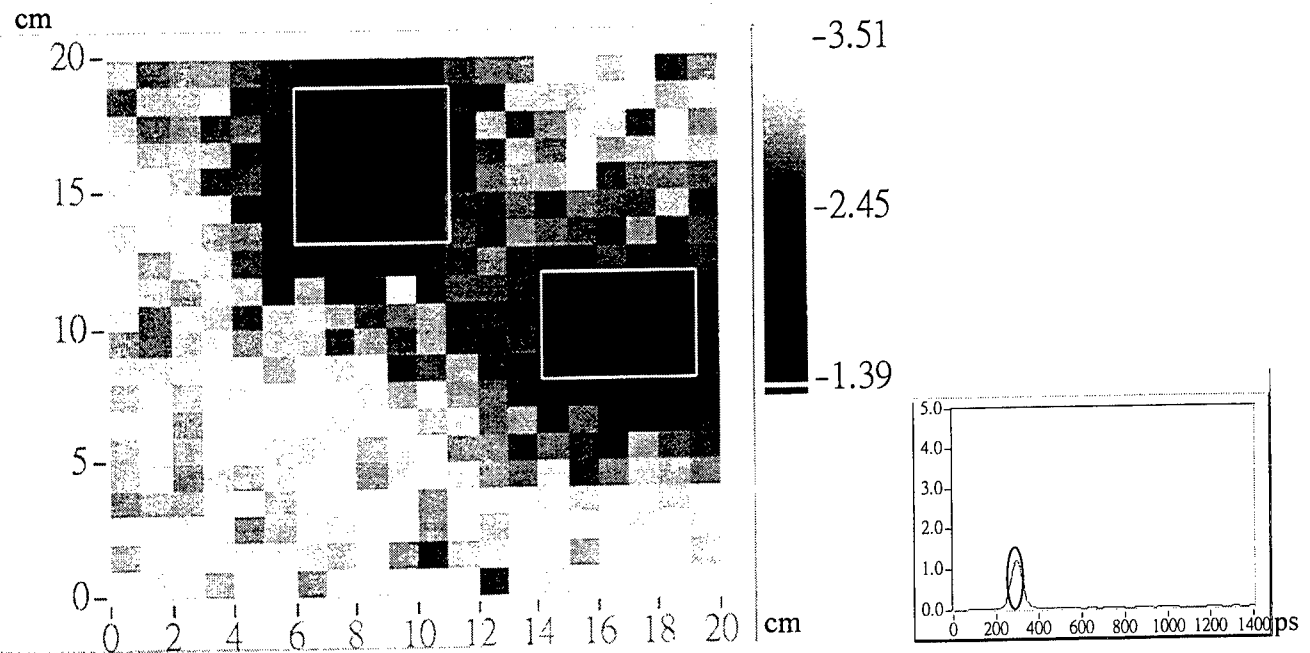


Fig. 6 Image of objects with snake photons, which was extracted form from diffusive light with their polarization nature. The inset shows the resulted profile of L_p-L_c , and the interval used for calculation.

REFERENCES

1. A. Ishimaru, "Diffusion of light in turbid material," *Appl. Opt.* **28**, 2210-2215, 1989.
2. L. Wang, P.P. Ho, C. Liu, G. Zhang, and R.R. Alfano, "Ballistic 2-D imaging through scattering walls using an ultrafast optical Kerr gate," *Science*. **253**, 769-771, 1991.
3. B.C. Wilson, E.M. Sevick, M.S. Patterson, and B. Chance, "Time-dependent optical spectroscopy and imaging for biomedical applications," *Proc. IEEE*. **80**, 918-930, 1992.
4. H. Jiang, K.D. Paulsen, U.L. Osterberg, B.W. Pogue, and M.S. Patterson, "Simultaneous reconstruction of absorption and scattering profiles in turbid media from near-infrared frequency-domain data," *Opt. Lett.* **20**, 2128-2130, 1995.
5. H. Jiang, K.D. Paulsen, and U.L. Osterberg, "Optical image reconstruction using DC data: simulations and experiments," *Phys. Med. Biol.* **41**, 1483-1498, 1996.
6. H. Hajime, K. Eiji, and Y. Takeaki, "Simultaneous measurements of three-dimensional reflectivity distribution in scattering medium based in optical frequency-domain reflectometry," *Opt. Lett.* **23(18)**, 1420-1422, 1998.
7. C. K. Hitzenberger and A.F. Fercher, "Differential phase contrast in optical coherence tomography," *Opt. Lett.* **24(9)**, 622-624, 1999.
8. J.C. Hebden, F.E.W. Schmidt, M.E. Fry, M. Schweiger, E. M.C. Hillman, and D.T. Depledge, "Simultaneous reconstruction of absorption and scattering images by multichannel measurement of purely temporal data," *Opt. Lett.* **24(8)** 534-536, 1999.
9. R.R. Anderson and J.A. Parrish, "The optics of skin," *J. Invest. Dermatol.* **77**, 13-19, 1981.
10. S.A. Walker, S. Fantini, and E. Gratton, "Image reconstruction by backprojection from frequency-domain optical measurements in highly scattering media," *Appl. Opt.* **36(1)**, 170-179, 1997.
11. X.D. Li, T. Durduran, A.G. Yodanis, B. Chance, and D.N. Pattanayak, "Diffraction tomography for biochemical imaging with diffuse-photon density waves," *Opt. Lett.* **22(8)**, 573-575, 1997.
12. J.C. Heden, and S.R. Arridge, "Time-resolved imaging of solid tissue phantoms using a perturbation model," *OSA TOPS on Advances in Optical Imaging and Photon Migration*. (Edited by R.R. Alfano and J.G. Fujimoto), **2**, 353-356. Optical Society of America, Washington DC, USA, 1996.
13. M.E. Zevallos, S.K. Gayen, B.B. Das, M. Alrubaiie, and R.R. Alfano, "Picosecond electronic time-gated imaging of bones in tissues," *IEEE J. Sel. Top. Quantum. Electron.* **5(4)**, 916-922, 1999.
14. J.A. Moon, R. Mahon, M.D. Duncan, and J. Reintjes, "Resolution limits for imaging through turbid media with diffuse light," *Opt. Lett.* **18(19)**, 1591-1593, 1993.
15. D. Grosenick, H. Wabnitz, H.H. Rinneberg, K.T. Moesta, and P.M. Schlag, "Development of a time-domain optical mammography and first in vivo application," *Appl. Opt.* **38(13)**, 2927-2943, 1999.
16. V. Sankaran, K. Schonenerger, J.T. Walsh Jr., and D.J. Maitland, "Polarization discrimination of coherently propagated light in turbid media," *Appl. Opt.* **38(19)**, 1999.

SESSION 2

Advances in Biomedical Imaging II

Development and application of noninvasive optical topography

Tsuyoshi Yamamoto[1]¹, Atsushi Maki[1], Yuichi Yamashita[1], Hiroshi Yoshizawa[2],
Makoto Iwata[2], Eiju Watanabe[3], Yukari Tanikawa[4], Yukio Yamada[4],
and Hideaki Koizumi[1]

[1] Advanced Research Laboratory, Hatoyama, Saitama 350-0395, Japan

[2] Tokyo Women's Medical University, 8-1 Kawada, Shinjuku, Tokyo, 162-8666, Japan

[3] Tokyo Metropolitan Police Hospital, 2-10-41, Fujimi, Chiyoda, Tokyo, 102-8161, Japan

[4] Mechanical Engineering Laboratory, 1-2 Namiki, Tsukuba, Ibaraki 305-8564, Japan

ABSTRACT

Optical topography (OT) is a method for visualizing brain functions noninvasively. In an OT measurement system, near-infrared light, to which living tissue is highly permeable, is irradiated from the scalp of the subject, and the scattered light reflected from the cerebral cortex is detected elsewhere on the scalp. The spatio-temporal blood volume change in the cortex is visualized based on the signal detected using two-dimensionally arranged optodes. The measurement imposes few constraints on the subject, either physically or mentally, thus the subject is in a natural and relaxed condition during measurement. Here, we describe our OT system, then report on an experiment to evaluate the system using a phantom. We found that OT can accurately locate the activated region in the cortex. Also, as an example of a clinical application of OT, we used our system to measure the language function, demonstrating the system's ability to measure the activity of Broca's area.

Key Words: optical topography, brain function, blood-volume, phantom, and language function

1. INTRODUCTION

The systematic clarification of human brain functions will lead to wide application in fields such as psychology, information engineering, and educational engineering, as well as in the field of clinical medicine. For this reason, various measurement systems have been developed. The electroencephalogram which Berger invented in 1929 measures the electric current induced by the activity of nerve cells in the brain [1]. This method, known as EEG, is used in clinical medicine and in clarifying brain functions. Other than EEG, several noninvasive measurement systems - MEG (magnetoencephalography), PET (positron emission computed tomography), and fMRI (functional magnetic resonance imaging) - have been proposed [2-4]. In these measurement systems, the subject is highly restrained. The subject is kept with in a narrow space and cannot move during the examination, thus it is difficult for the subject to relax.

The measurement of brain functions using near-infrared spectroscopy (NIRS) imposes little restraint on the subject. In this method, near-infrared light, to which living tissue is highly permeable, is irradiated from the scalp of the subject and the light scattered in the cerebral cortex is detected on the scalp [5-7]. This method measures the change in the blood-volume associated with brain activation. When brain nerve cells are activated, blood-volume increases to supply more oxygen to these cells, and this increase is detected through the change in absorption of the light due to the increased hemoglobin (Hb) content.

Based on the NIRS method, the authors developed optical topography (OT), a method in which blood-volume changes are measured at multiple points on the scalp for a subject. In OT, the signals are detected by two-dimensionally arranged optodes, and the spatio-temporal activity of the brain is visualized from these signals [8-11].

In this paper, we explain the principles of measuring brain functions by NIRS and describe the 24-

¹ Correspondence: TEL:+81-492-96-6111, E-mail:tymt@harl.hitachi.co.jp, <http://hatoyama.hitachi.co.jp>.

channel OT measurement system developed by our group. After that, we report on our evaluation of the location accuracy of OT, which was done using a phantom. It is difficult to directly evaluate with high accuracy the position inside the actual brain where the blood volume changes. The phantom was used to simulate the light scattering characteristics of living tissue and the blood-volume change associated with the brain activation. Finally, a clinical application of OT is described. The brain activity associated with the language function was measured with our OT system, and it was clearly shown that the blood-volume increased in Broca's area.

2. METHODS

2-1 Principle of OT

Figure 1 shows the method used to measure blood-volume change in the cortex. The near-infrared light enables high optical permeability through the various types of tissue, but it is strongly scattered by these tissues. Thus, only part of the light is transmitted through the skull and reflected from the cerebral cortex at about 15 mm below the scalp. The reflected light reaches the scalp again at a distance of about 30 mm from the illuminated point. The Hb in the blood absorbs the near-infrared light. If the blood-volume, and thus the absorption coefficient, increases in the cortex because of brain activation during the stimulation period, the intensity of the reflected light decreases. Therefore, the difference between reflected-light intensities R and R^s , obtained before and after the stimulation, respectively (Fig. 1), provides information on the blood-volume change in the cortex.

In the actual measurement (Fig. 2), two 0.5-mW-output continuous wave (CW) lasers with a wavelength of 780 nm or 830 nm are used as light sources to measure the change in the concentration of the oxy-Hb and deoxy-Hb. The oscillators operate at different frequencies on the order of 1 kHz to modulate the diode output power. The outputs from the diodes are mixed by an optical fiber coupler, and illuminated onto the scalp. After the reflected light passes through the human tissue it is picked up by an optical fiber. The photodiode then converts the reflected light into an electrical signal and sends the signal to two lock-in amplifiers. Each lock-in amplifier, which refers to the modulation frequency of each light source, separates the reflected light into one of the two original wavelengths (780 nm or 830 nm). The reflected intensity $R(\lambda, t)$ for the wavelength λ (780 nm or 830 nm), and measurement time t is obtained and sent to the analog/digital (A/D) converter. A personal computer analyzes the reflected intensity.

When the subject is at rest (before brain activation), $R(\lambda, t)$ satisfies

$$-\ln[R(\lambda, t)] = \epsilon_{\text{oxy}}(\lambda) C_{\text{oxy}}(t) d + \epsilon_{\text{deoxy}}(\lambda) C_{\text{deoxy}}(t) d + sc(\lambda), \quad (1)$$

where $\epsilon_{\text{oxy}}(\lambda)$ and $\epsilon_{\text{deoxy}}(\lambda)$ are the molar absorption coefficients of oxy- and deoxy-Hb, respectively. C_{oxy} and C_{deoxy} are the concentrations of oxy- and deoxy- Hb, d is the effective path length in the tissue, and $sc(\lambda)$ is the attenuation due to the scattering in the tissue. In the same way, when the subject is activated by the stimulation, the reflected intensity $R^s(\lambda, t)$ satisfies

$$-\ln[R^s(\lambda, t)] = \epsilon_{\text{oxy}}(\lambda) C_{\text{oxy}}^s(t) d + \epsilon_{\text{deoxy}}(\lambda) C_{\text{deoxy}}^s(t) d + sc(\lambda), \quad (2)$$

where the superscript "s" denotes stimulation. By subtracting equation (1) from equation (2), we obtain

$$-\ln[R^s(\lambda, t) / R(\lambda, t)] = \epsilon_{\text{oxy}}(\lambda) [C_{\text{oxy}}^s(t) - C_{\text{oxy}}(t)] d + \epsilon_{\text{deoxy}}(\lambda) [C_{\text{deoxy}}^s(t) - C_{\text{deoxy}}(t)] d. \quad (3)$$

We rewrite the right-hand side of equation (3) as

$$-\ln[R^s(\lambda, t) / R(\lambda, t)] = \epsilon_{\text{oxy}}(\lambda) \Delta C_{\text{oxy}}^s(t) + \epsilon_{\text{deoxy}}(\lambda) \Delta C_{\text{deoxy}}^s(t), \quad (4)$$

where

$$\Delta C_{\text{oxy}}^s(t) = [C_{\text{oxy}}^s(t) - C_{\text{oxy}}(t)] d, \quad (5)$$

$$\Delta C_{\text{deoxy}}^s(t) = [C_{\text{deoxy}}^s(t) - C_{\text{deoxy}}(t)]d, \quad (6)$$

respectively, because the value of d in the tissue is difficult to obtain at present. The ratio of the reflected intensities in the left-hand side of equation (4) is measured at each wavelength (780 nm and 830 nm), and the concentration changes of the oxy-Hb and deoxy-Hb are obtained. The concentration change of the total-Hb is the sum of these.

To obtain a topographic image of the blood-volume change, an array of optodes that act as light sources (incident positions) and optodes that act as detectors (detection positions) are placed on the subject's scalp. Figure 3 shows the 24-channel measurement system. 16 light sources (eight sources for each wavelength of 780 nm and 830 nm) and eight avalanche photodiodes (Hamamatsu C5460-01) are employed. For the light illumination on the scalp and to pick up the transmitted light, optical fibers with a 1-mm cladding diameter are attached to the scalp to eliminate interference from hair. These optodes that make up each source-detector pair are separated by 30 mm. The sensitivity to the blood-volume change is highest at the middle point of each optode pair, so the middle points are used as measurement points [12]. In the Fig. 3, there are 24 measurement points at the middle of the optode pairs. The minimum distance between measurement points is 21 mm, and the octagonal measurement area, surrounded by these measurement points, is 90×90 mm. The blood-volume changes at these 24 measurement points are estimated, then a topographic image of the changes is obtained by spline interpolation.

2-2 Phantom for OT

Here, we have developed a phantom that can be used to simulate the brain activation measured by OT. For clinical application of the OT, location accuracy of the topographic image is critical, but the location of the blood-volume change inside the cerebral cortex is difficult to detect accurately. The blood-volume increase in the cortex is analogous to an increase in the absorption coefficient within a scattering medium. Our phantom simulates the light scattering characteristics of the living tissue.

The phantom is made of epoxy resin (Buehler Corp.) containing the powdered titanium-oxide (TiO_2 , KA30-K: Titan Kogyo Corp.) [13], and it consists of the body and inserts (Fig. 4). The size of the body is $200 \times 200 \times 40$ mm to model the adult head size. The surface area of the body is five times the measurement area of the 24-channel system in Fig. 3 to avoid the effects of light reflection at the boundary. The height of the body is more than double the depth from the scalp to the cortex (15 mm). The scattering and absorption coefficients of this phantom, estimated by the time-resolved measurement method [14], were respectively 0.5 mm^{-1} and 0.0 mm^{-1} at the 830-nm wavelength.

To simulate brain activation, the absorption coefficient inside the phantom should be variable. A 10-mm-diameter hole was drilled in the center of the phantom, and inserts to be placed inside of the phantom were prepared. The structure of the inserts (A) and (B) in Fig. 4 are homogeneous and heterogeneous, respectively. The optical properties of insert (A) and sections (I) and (III) of insert (B) are the same as those of the body. On the other hand, section (II) of insert (B) contains a greenish brown light absorber. This light absorber has absorption in the NIR region and its absorption coefficient is 0.025 mm^{-1} . In Figs. 5(a) and (b), inserts (A) and (B), respectively, are placed inside the body of the phantom. The absorber is located near the center of the phantom and simulated the blood-volume (absorption coefficient) change in the cerebral cortex.

The measurement system we used to evaluate our phantom is shown in Fig. 6. The optodes were arranged on the phantom. Eight laser light sources (wavelength: 830 nm) were modulated at different frequencies (1 to 10 kHz), and were coupled to the eight optodes used for illumination. Eight optodes to detect the transmitted light were connected to avalanche photodiodes. The outputs from the photodiodes were sent to lock-in-amplifiers that separated the transmitted light intensity into the 24 measurement points. The data were processed with a computer.

To obtain a topographic image of the absorber in the phantom, the absorbance change ΔA at each of the 24 measurements point is given as,

$$\Delta A = -\ln(R^s/R) \quad (7),$$

where, R^s and R denote the reflected intensities with the light absorber and without the absorber in the phantom, respectively. The distribution of ΔA inside the measurement area was estimated and a topographic image of the absorber in the phantom was obtained.

2-3 Language function measurement

The language function is a brain function peculiar to humans. There is powerful need for a method of measuring the language function for both basic research and clinical medicine purpose. In our language function measurement, the subject was shown a picture of an object to activate the language function. The subject wrote the word for the object and an inspector objectively checked and evaluated the activation of the subject's language function. Measurement with a conventional brain function measuring system is difficult, because the head of the subject moved during the test and this movement caused signal noise.

Since the optical fibers used to irradiate and detect reflected light in OT are attached to the subject's scalp, there is little noise during the measurement even if the subject moves a little. Thus, the subject is likely to feel more natural and relaxed, compared, for example, to when being examined by MRI during which immobility and an uncomfortable posture is required. For realistic language-function measurement, an OT system may therefore be indispensable.

In this experiment, language functions were activated by a writing task rather than a speaking task because the load is generally considered to be higher for a writing task[15]. There are two language function areas in the cortex: Broca's area in the frontal lobe, and Wernicke's area in the temporal lobe. The subject was a 27-year-old right-handed healthy male volunteer. Almost all (99 %) right-handed people have language function territory fields on the left hemisphere sinceput, so the measurement area was arranged on the subject's left hemisphere sinceput. Informed consent was obtained from the subject before the investigation. The subject was awake and sitting relaxed in a chair. No special room was required for this experiment, which would not be the case for PET or fMRI. The location of the subject's language function area was estimated by anatomic MRI and with the neuronavigator [16]. The task sequence for this experiment is shown in Fig. 7. The subject was shown a card with a picture of an object for 3 seconds(In Fig. 7, a picture of a knife is shown). During the 3 seconds, the subject wrote down the name of the object in Japanese "kana" which is a phonetic syllabary. The task was repeated 30 times so the total stimulation period was 90 seconds. As a control task, the subject was shown a figure with no meaning, which he was required to draw. The shape vaguely resembled Japanese "kana", and would require a similar drawing motion for 3 seconds. Sample figures for this experiment are shown on both sides of the picture of the knife in Fig. 7. During the writing and control tasks, the motor area located in the frontal lobe was activated, because the subject moved his arm and hand when writing letters and drawing figures. Therefore, the activation of the motor area was eliminated by subtracting the signal intensities during the control task from the signal intensities during the writing task. In the same way, the signal from the visual cortex could be removed. The control task was performed as pre-stimulation for a total of 60 seconds and as post-stimulation for a total of 70 seconds. The subject rested for 30 seconds between post-stimulation and pre-stimulation for the next series of the task.

3. RESULTS AND DISCUSSION

3-1 Location accuracy

Figure 8 shows topographic images of ΔA and the relative locations of the optodes on the phantom and the absorbers in the phantom. In Fig. 8(a), the absorber was set midway between two optodes, where ΔA sensitivity was the highest. On the other hand, in Figs. 8(b) and (c), the absorbers were placed below an optode and at the center of four optodes, respectively. These figures show that the location of the absorber on the topographic image was consistent with the actual location inside the phantom within a 3-mm margin of error. This value is less than the interval between the measurement points (21 mm). This value is also lower than the size of the visual cortex (more than 20×20 mm) and of the motor area (more than 10×10 mm) [17]. Therefore, these results demonstrate that the OT system can be used to identify the area of brain activation.

However, the full width at half maximum of each ΔA distribution was more than 20 mm. This is more than twice the diameter of the absorber inside the phantom. Thus, the spatial resolution of the topographic image needs to be improved.

3-2 Language function measurement

Figure 9 shows a spatial map of the change in total-Hb obtained during the writing task and MRI of the subject. To obtain this static topographic image, we averaged the change in Hb-concentration during the writing task, compared to before and after at each channel position. Furthermore, the z-value of the total-Hb concentration change at each measurement point was obtained. Among the 24 measurement points, the z-value at channel 9 was the largest, and this channel corresponded to the Broca's area of the subject as indicated by the MRI. Figure 10 shows the temporal change in the oxy-Hb, deoxy-Hb, and total-Hb concentrations for channels 9 and 1. A hemodynamic response was observed approximately 30 seconds after the writing task started and the peak response occurred at about 60 seconds after the start. In the region showing the highest activity there was an increase in oxy-Hb and total-Hb with a decrease in deoxy-Hb. This is consistent with increased metabolic demand. On the other hand, in the outer region of Broca's area, for example at the measuring point of channel 1, the oxy-Hb concentration and the total-Hb concentration decreased 30 seconds after the writing task started.

4. CONCLUSION

Optical topography offers clear advantages for noninvasive brain function measurement compared to other methods, we have developed a 24-channel OT system. To evaluate the topographic imaging of our system, we created a phantom to simulate light scattering by the live tissue and the blood volume change in the cortex. The topographic images identified the position of the light absorber in the phantom with an accuracy of 3 mm. A potential application of optical topography is language function measurement, and in doing this we observed increased blood-volume in Broca's area during a writing task.

REFERENCES

1. H. Berger, "Über das Electrenkephalogramm des Menschen". *Archiv für Psychiatrie* **87**, 527-570(1929).
2. D. Cohen, "Magnetic field around the torso: Production by electrical activity of the human torso". *Science* **156**, 652-654(1967).
3. M. E. Raichle, "Measurement of local cerebral blood flow and metabolism in man with positron emission tomography". *Fed. Proc.* **40**, 2331-2334(1981).
4. S. Ogawa, T. -M. Lee, A.S. Nayak and P. Glynn, "Oxygenation-sensitivity contrast in magnetic resonance image of rodent brain at high magnetic fields". *Magn. Reson. Med.* **14**, 68-78(1990).
5. F. F. Jöbsis, "Non-invasive infrared monitoring of cerebral and myocardial oxygen sufficiency and circulatory parameters". *Science* **198**, 1264-1267(1977).
6. M. Cope and D. T. Delpy, "A system for long term measurement of cerebral blood and tissue oxygenation in new born infants by near-infrared spectroscopy". *Med. Biol. Engl. Comp.* **32**, 1457-1467(1988).
7. T. Kato, A. Kameim S. Takashima and T. Ozaki, "Human visual cortical function during photic stimulation monitoring by means of near-infrared spectroscopy". *J. Cereb. Blood Flow Metab.* **13**, 516-520(1993).
8. A. Maki, Y. Yamashita, Y. Ito, E. Watanabe and H. Koizumi, "Spatial and temporal analysis of human motor activity using noninvasive NIR topography". *Med. Phys.* **22**, 1997-2005(1995).
9. Y. Yamashita, A. Maki, Y. Ito, E. Watanabe, Y. Mayanagi and H. Koizumi, "Noninvasive near-infrared topography of human brain activity using intensity modulation spectroscopy". *Opt. Eng.* **35**, 1046-1049(1996).
10. E. Watanabe, Y. Yamashita, A. Maki, Y. Ito and H. Koizumi, "Non-invasive functional mapping with multi-channel near-infrared spectroscopic topography in humans". *Neurosci. Lett.* **205**, 41-44(1996).
11. H. Koizumi, Y. Yamashita, A. Maki, T. Yamamoto, Y. Ito H. Itagaki and R. Kennan, "Higher-order brain function analysis by trans-cranial dynamic near-infrared spectroscopy imaging". *J. of Biomed.*

- Opt. 4, 403-413(1999).
12. P. W. McCormich, M. Stewart, G. Lewis, M. Dujovny and J. I. Ausman: "Intracerebral penetration of infrared light", J. Neurosurg., 76, 315-318(1992).
 13. M. Firbank, M. Hiraoka and D. T. Delpy: "Development of a stable and reproducible tissue equivalent phantom for use in infrared spectroscopy and imaging", Proceeding of SPIE, 1888, 264-270(1993).
 14. G. Zaccanti, P. Bruscaglioni, A. Ismaelli, L. Carraresi, M. Gurioli and Q. Wei: "Transmission of a pulsed thin light beam through thick turbid media: experimental results", Appl. Opt., 31, 2141-2147(1992).
 15. T. Yamamoto, Y. Yamashita, H. Yoshizawa, A. Maki, M. Iwata, E. Watanabe and H. Koizumi, "Non-invasive measurement of language function by using optical topography", Proc. of SPIE 3597, 250-237(1999).
 16. E. Watanabe, T. Watanabe, S. Manaka, Y. Mayanagi and K. Takakura, "Three-dimensional digitizer (neuronavigator): New equipment for computed tomography-guided stereotaxic surgery", Surg. Neurol. 27, 543-547(1987).
 17. J. Talairach, P. Tournoux, "Co-planar stereotactic atlas of the human brain", Thieme Press, New York (1988).

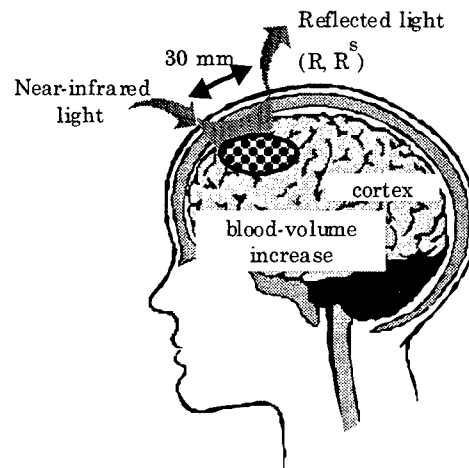


Figure 1 Method used to measure the blood-volume change in the cortex.

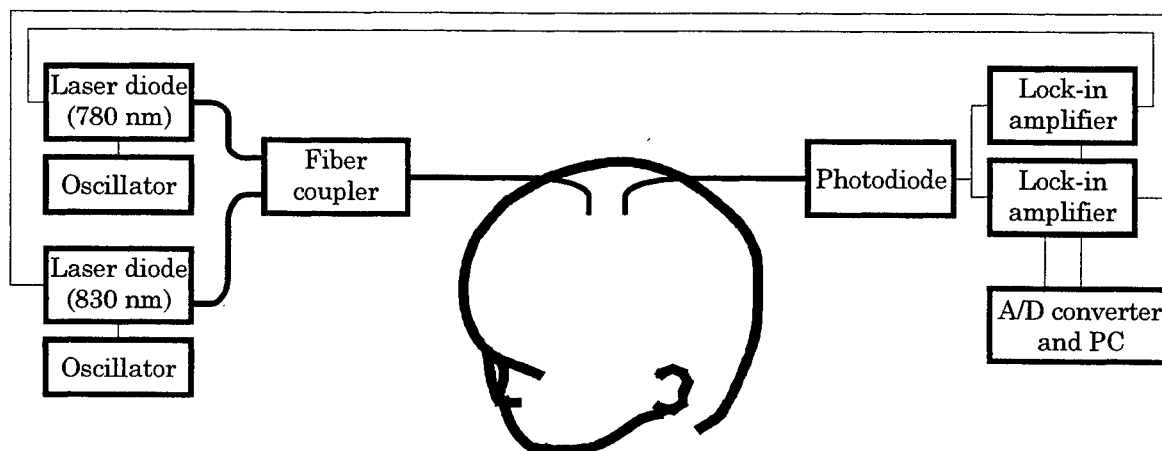


Figure 2 Method used to measure the change in concentration of the oxy-Hb and deoxy-Hb by NIR spectroscopy.

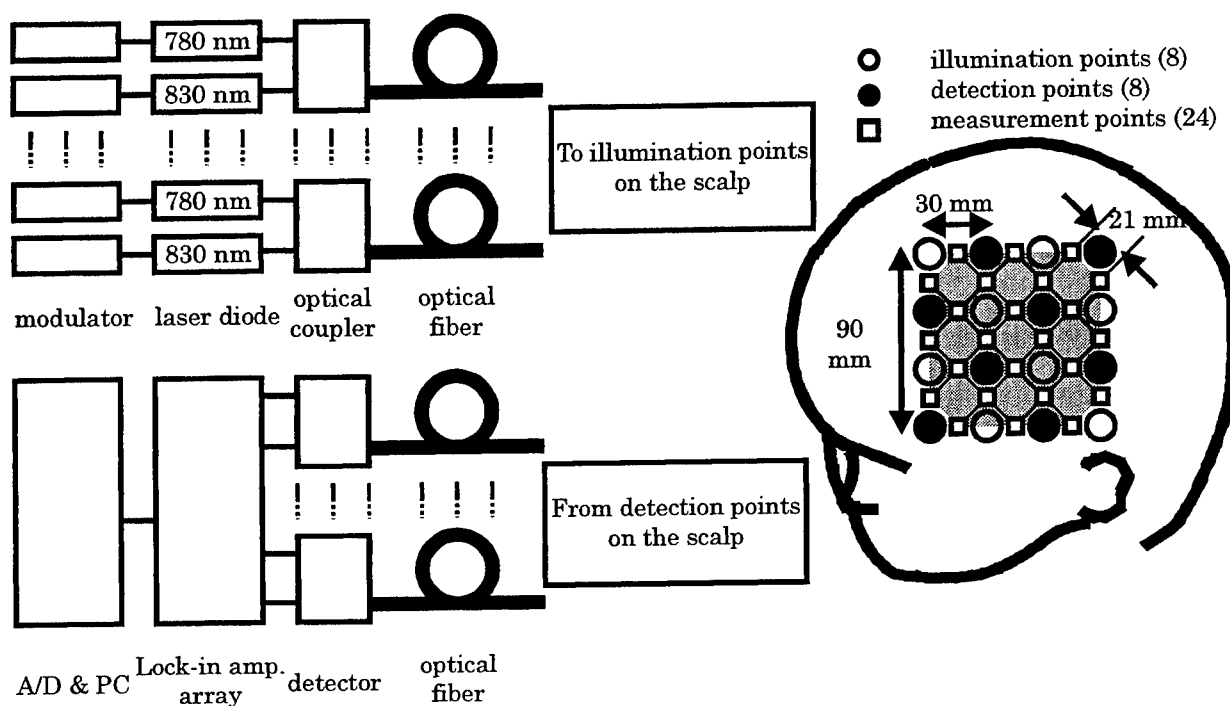


Figure 3 The 24-channel measurement OT system.

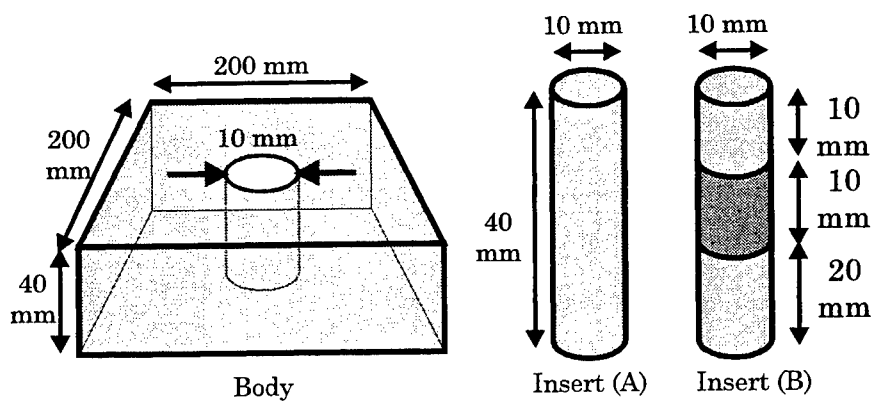


Figure 4 Structure of the phantom for OT.

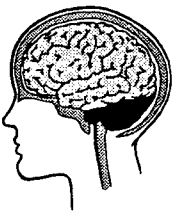
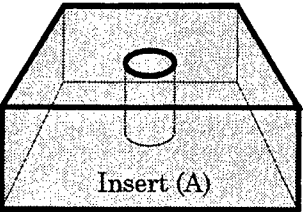

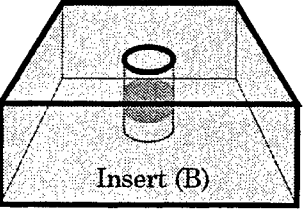
	Actual living body	Simulation with the phantom
Before brain activation		
After brain activation		

Figure 5 Simulation method of the brain activation in the cortex by the phantom.

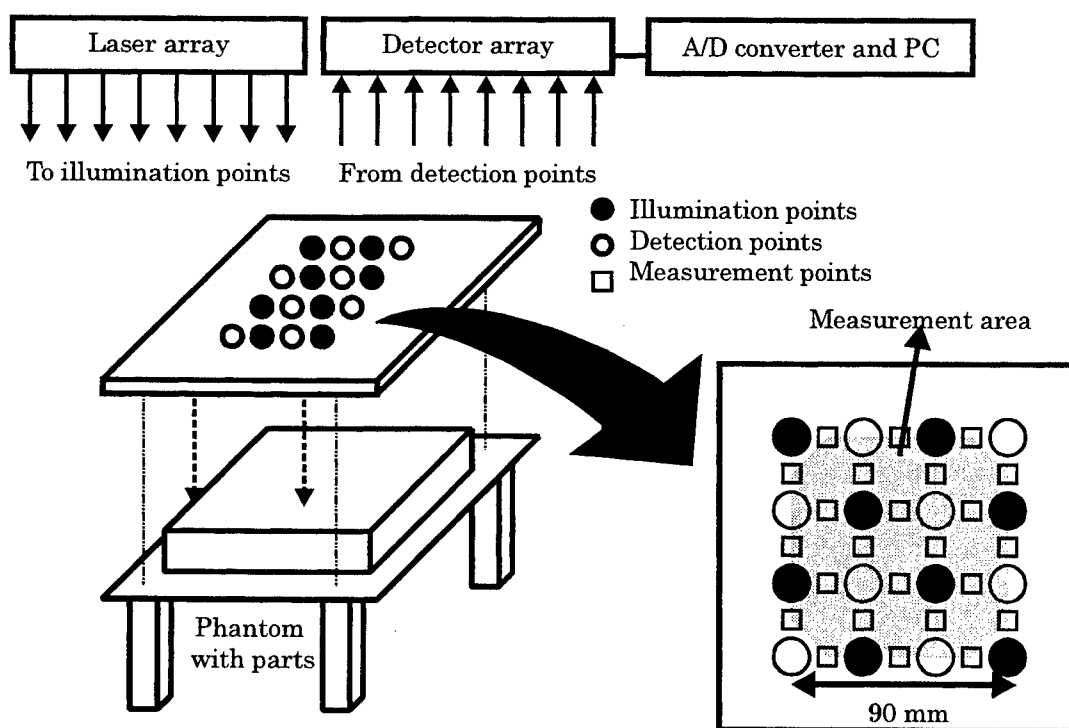


Figure 6 Measurement system to obtain a topographic image of the absorber in the phantom.

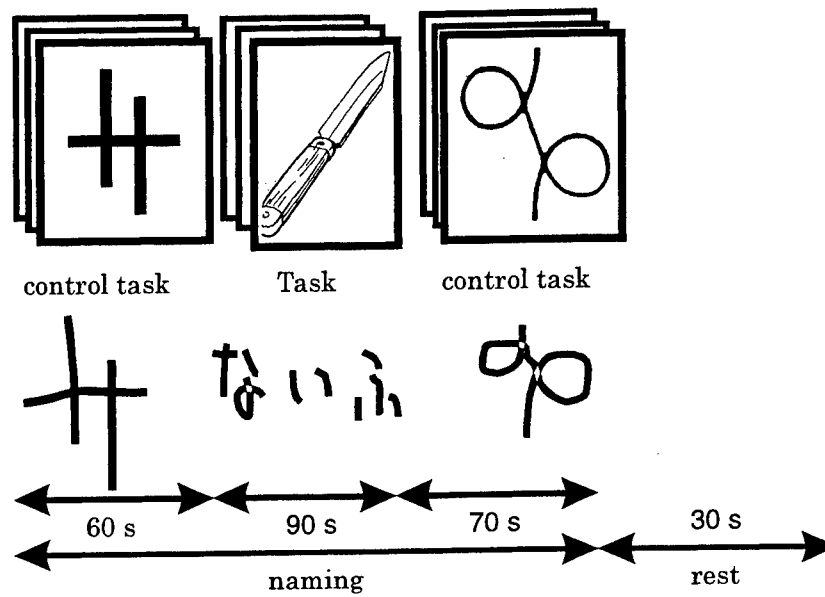


Figure 7 Task sequence for the language function measurement

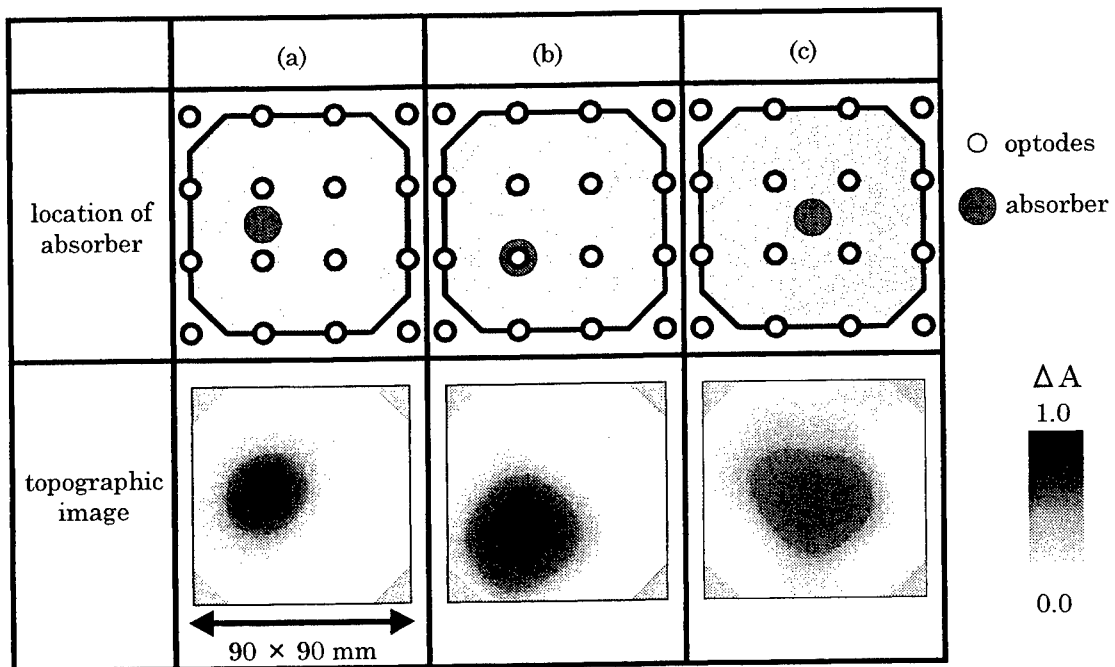


Figure 8 Topographic images of the absorber in the phantom.

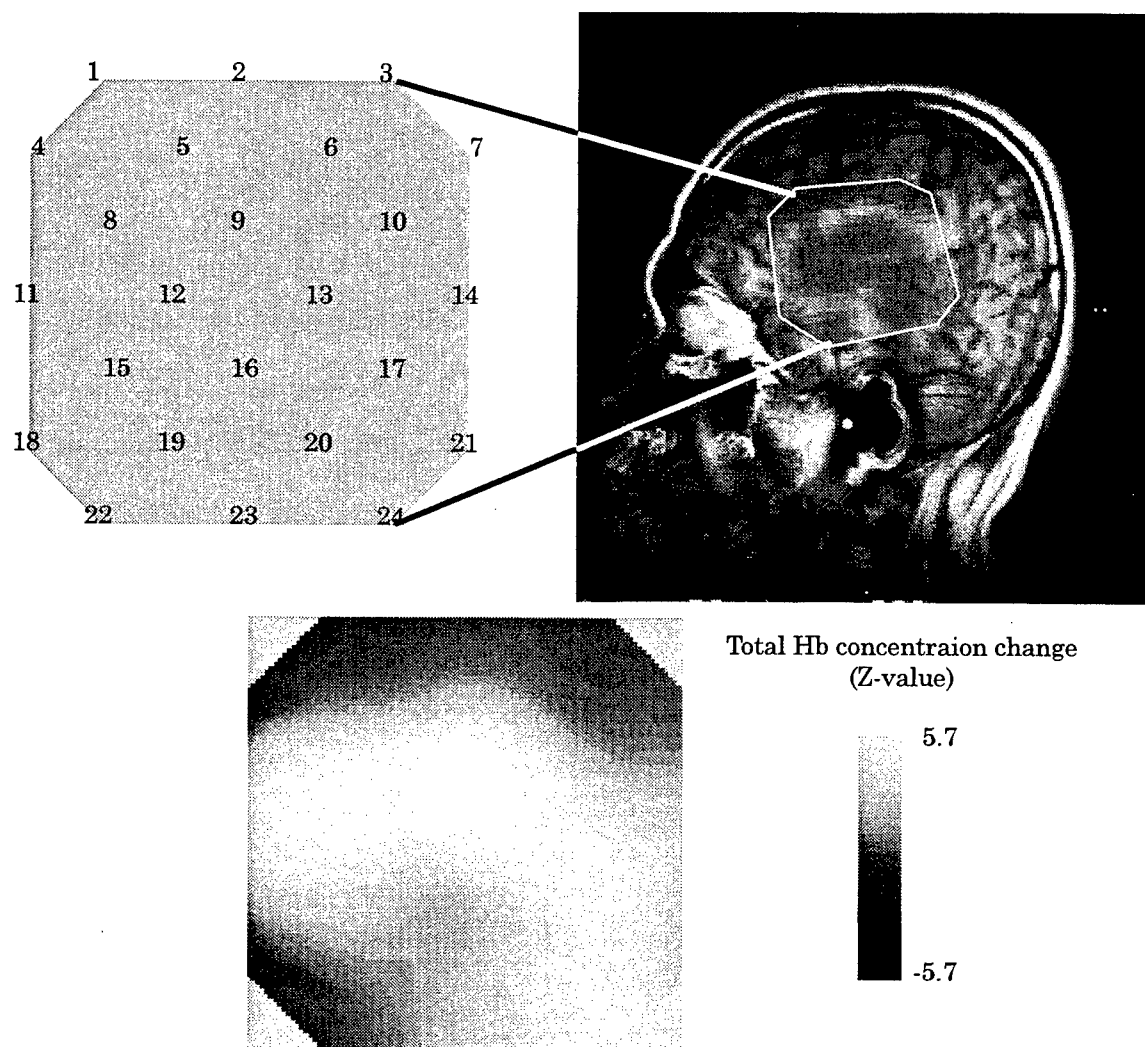


Figure 9 Topographic image (total-Hb concentration change) of the language function and anatomic MRI.

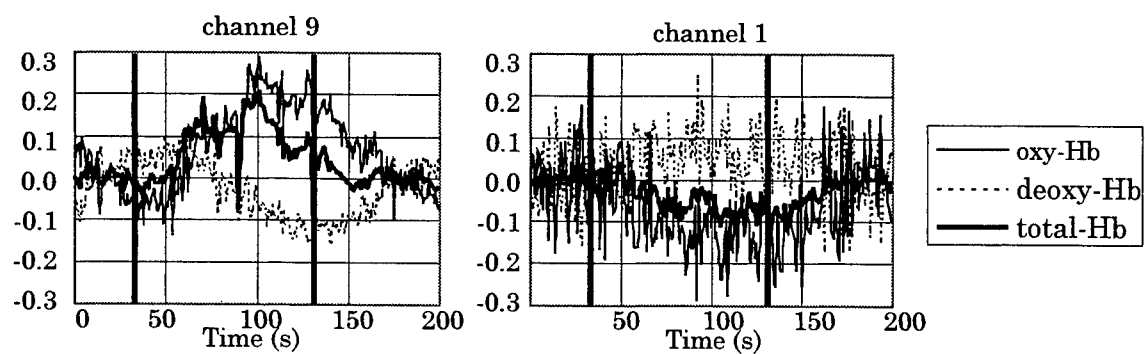


Figure 10 Time responses of the concentration changes (oxy-Hb, deoxy-Hb, and total Hb) for channels 1 and 9 in Fig. 9. The two thick vertical lines in these figures denote the start and the end of the writing task.

Application of Near-Infrared Spectroscopy to Investigate Brain Activity: Clinical Research

Wemara Lichty^{*a}, Kaoru Sakatania^{ab} Yuxiao Xie^b, Huangcong Zuo^b

^a Tsinghua University/Sino-Japanese Friendship Hospital Medical Sciences Institute, Beijing, CHINA

^b Dept of Neurosurgery (KS,HZ), Rehabilitation (YX), Sino-Japanese Friendship Hospital, Beijing

ABSTRACT

Near infrared spectroscopy has recently been used to measure changes of optical parameters (i.e., light absorption or scattering) of brain tissue. The fact that the equipment is generally compact, portable, noninvasive, and reasonably priced makes it ideal for clinical and nonclinical evaluation and monitoring of brain function. Clinical and nonclinical studies evaluating changes related to light absorption are discussed, with an emphasis on cerebral blood oxygenation (CBO) changes and hemodynamic responses while performing cognitive tasks. With respect to the clinical studies, the focus is on variations in patterns of oxygenated hemoglobin (Oxy-Hb), deoxygenated hemoglobin (Deoxy-Hb) and Total-Hb (sum of Oxy-Hb and Deoxy-Hb). The studies about clinical applications includes research we have conducted with older adults and aphasics. Implications regarding the use of NIRS for clinical purposes are considered.

KEYWORDS: Near-infrared spectroscopy, brain activation, cognition, language, cerebral blood flow,

1. INTRODUCTION

NIRS is an optical method to measure concentration changes of Oxy-Hb and Deoxy-Hb in cerebral vessels by means of the characteristic absorption spectra of hemoglobin in the near-infrared range. Changes in Total-Hb indicate blood volume changes and correlate with rCBF. Simultaneous measurements made with NIRS and PET demonstrated that neuronal activation during mental tasks results in changes in cerebral oxygenation and hemodynamics measured by NIRS that were consistent with PET results¹

NIRS has been applied to the evaluation of cerebral blood oxygenation and hemodynamic changes in a variety of brain activation studies¹⁻⁵. In general, brain activation is related to an increase in Oxy-Hb, no change or a slight decrease in Deoxy-Hb, and an increase in Total-Hb. However, some research has suggested that in clinical subjects "typical" response may be less prevalent and other types of responses may be more common or typical of the clinical condition⁶. The studies discussed here address this issue as well as basic research related to cognitive activation.

2. NEAR-INFRARED SPECTROSCOPY EQUIPMENT

We measured cerebral blood oxygenation and hemodynamics with a NIRO-500 (Hamamatsu Photonics). Near-infrared light from laser diodes, wavelengths 775, 825, 850, and 904 nm) was directed at the head through a fiberoptic bundle ("optode"), and reflected light was collected in the receiving fiberoptic bundle and transmitted to a photomultiplier tube. With the use of an algorithm developed by Cope et al⁷, absolute concentration changes of Oxy-Hb, Deoxy-Hb, and Total-Hb were continuously analyzed by means of a computer interfaced with the apparatus. NIRS data are expressed in arbitrary units. If the differential pathlength factor of the adult head is assumed to be 5.9, which was determined by time-of-flight measurement of a picosecond-length optical pulse through the tissues, 1 arbitrary unit equals 1 $\mu\text{mol/L}$. The optical distance was 3 to 4 cm. With an optode distance of 4 cm, correlations of Oxy-Hb and Total-Hb measured by NIRS and rCBF measured by PET suggested that the reliable penetration depth of near-infrared light into brain tissue is about 1.3 cm⁸

*email address: lw823@public2.east.net.cn or wemara@hotmail.com

3. AGING STUDY

Brain activation studies using positron-emission tomography (PET) have shown a variety of age-related alterations in neuronal activity that may suggest connectivity changes or variations in activation patterns⁹. In this study, NIRS was used to evaluate age-related alterations in CBO changes during the performance of various cognitive tasks¹⁰. An additional objective was to determine if CBO response patterns varied in relation to type of cognitive task. Although our aging study concerns normal adults, we consider aging a clinical topic because of the nature of brain changes that occur with aging.

3.1. Methods

Twenty-six normal adults participants performed cognitive tasks to evaluate changes between the young group (13; mean age \pm SD, 28.8 ± 4.4) and the older group (13; 50.7 ± 8.0). The groups were equivalent in education, $P > 0.10$). Six different cognitive tasks requiring oral language were performed with each task varying in the types of cognitive ability being tested. Tasks included semantic verbal fluency, confrontational naming, forward digit span, backward digit span, counting, and reading. The evaluation included a rest period (5-10 minutes), followed by the cognitive performance.

Optodes were placed on the left forehead so that the center was at the Fp2 position of the international EEG 10-20 system, thus the NIRS measured CBO changes in the left prefrontal cortex, an area of the brain involved in language, executive function, and complex problem solving. Participants were seated and their eyes were open during the entire experiment.

3.2. Results

In many NIRS studies on neuronal activation with the use of NIRO-500, the values of NIRS parameters were compared among different individuals; however, in the present study, qualitative pattern analyses were performed rather than quantitative analyses to avoid possible problems related to changes of the pathlength factor during aging. Skull thickness, skin absorption, and scattering properties of underlying brain structures such as subarachnoid space through which light passes, may change during aging, and the anatomical changes might alter the pathlength factor.

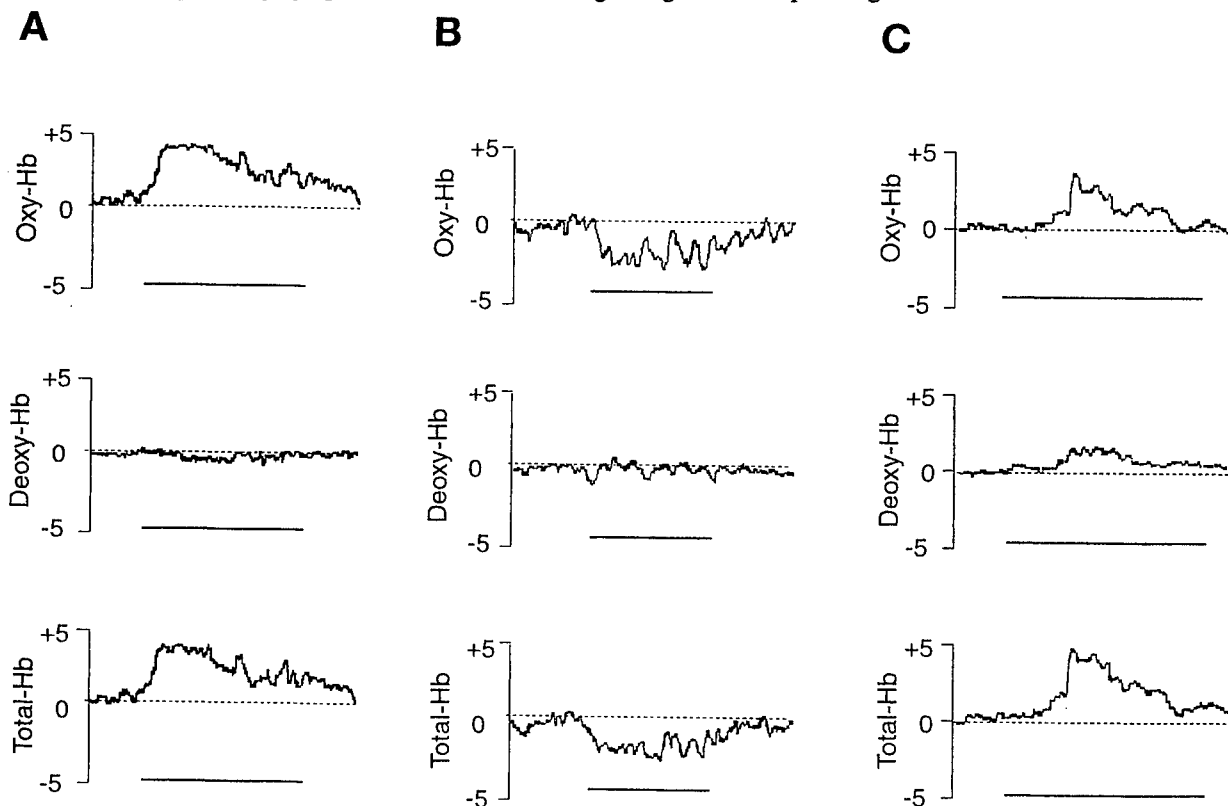


Figure 1. Examples of the three patterns: (A) the most common pattern, (B) the second most common pattern, and (C) the third most common pattern.

The qualitative analyses consisted of determining the pattern of decrease and/or increase of the three NIRS parameters (Oxy-Hb, Deoxy-Hb, and Total-Hb), based on the maximum value from the preactivation baseline.

Each subject performed 6 cognitive tasks, making a total of 156 cognitive events. For the analyses, data from 3 subjects were deleted for the reading task and from 3 subjects for the counting tasks because of movement artifacts; therefore, a total of 150 events were evaluated.

The cognitive tasks altered CBO in the left prefrontal cortex of both young and older adults. To determine the types of response patterns, data for young and older subjects were combined. Most of the CBO changes could be classified into 3 patterns (Fig 1): Pattern A--Oxy-Hb and Total-Hb increased, Deoxy-Hb showed a little or no decrease; Pattern B--Oxy-Hb and Total-Hb increased, Deoxy-Hb shows little or no change; Pattern C--all three parameters increased.

Comparisons of the young and older group showed striking differences in the occurrence of the NIRS response patterns, as shown in Table 1. Although Pattern A was the most prevalent pattern in both groups, it occurred less often in the older group, $P < 0.01$. In contrast, Pattern B, occurred more often in the older subjects than the young subjects, $P < 0.0001$. Pattern C showed no age-related difference.

Table 1. Patterns of NIRS Parameter Changes Induced by Cognitive Tasks Performed by Young and Older Subjects

Pattern	Oxy, Deoxy, Tot	Young Group	Older Group
A "typical"	+, ~0, +	68.1%	46.2%
B	-, ~0 ~+, +	6.9%	34.6%
C	+, +, +	9.7%	12.8%

Regarding specific tasks, age differences were evident verbal fluency and reading with the other tasks yielding no differences. Fig 2 shows the occurrence of the Patterns A and B induced by the tasks. In both tasks, Pattern A was more common for young subjects compared with the older subjects, and B was more common for the older subjects compared with the younger subjects. In the reading task, Pattern A occurred in 70% of the younger subjects; whereas, Pattern B was evident in 77% of the older subjects.

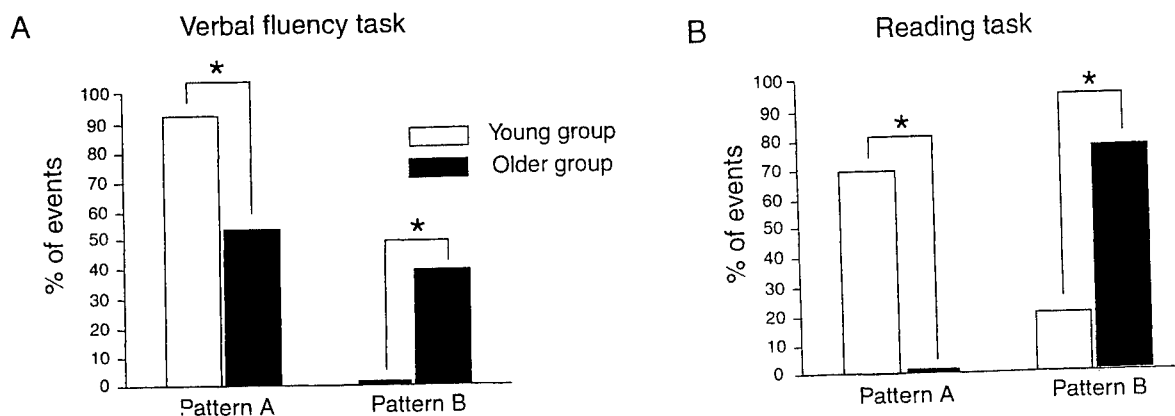


Figure 2. Comparison of the occurrence of the NIRS response patterns induced by the verbal fluency (A) and reading (B) tasks in the young and older groups.

3.3. Discussion

The study showed that cognitive tasks related to the frontal lobe caused various patterns of CBO responses in the left prefrontal cortex. The patterns of CBO responses were age-dependent and task-dependent. In both the young and older groups, the "typical" response of increases of Oxy-Hb and Total-Hb accompanied by a slight decrease or no change in

Deoxy-Hb was the most common pattern of NIRS parameter changes during the cognitive tasks (Pattern A). The NIRS parameter changes of Pattern A reflect an increase in rCBF at the measurement areas (6,8). The second most common pattern (Pattern B) has been observed in normal adults during cognitive tasks.

Although the "typical" pattern was most common for both young and older adults, it was less prevalent in the older group, and was evident in less than half the events. In the verbal fluency task, Pattern B was observed more in the older group than the young group. The results of the reading task are particularly intriguing in that almost all the older adults showed Pattern B, suggesting that for some types of tasks, rCBF response may change from an increasing response to a decreasing response during aging.

The results may reflect a possible functional reorganization during aging. Neuronal activities near the NIRS recording site may steal the blood flow at the NIRS measurement area, resulting in decreased rCBF. Other mechanism may also be involved, and further studies are necessary to clarify the physiological mechanism and roles of the rCBF decrease during neuronal activity.

This study demonstrates that NIRS can detect age-related changes in CBO and hemodynamics related to cognitive performance. NIRS has some advantages over PET and fMRI for brain activation studies, particularly related to aging. (1) PET images integrate CBO changes during task performance; in contrast, NIRS can monitor real-time (0.5 s) CBO changes during the tasks. Therefore, NIRS may be able to detect the neuronal activation that PET cannot image. (2) Compared with blood oxygenation level dependent (BOLD) ;contrast function MRI (fMRI), NIRS can measure changes of not only Deoxy-Hb but also Oxy-Hb and Total-Hb, which reflect CBF changes; whereas, BOLD fMRI detects only Deoxy-Hb changes. (3) The portability of the system makes investigations of the general population feasible.

It should be emphasized that the relatively small differences in age among subjects caused the age-related difference in CBO changes detected by NIRS, indicating that the age of subjects should be in narrow bands in NIRS cognitive studies.

4. NONFLUENT (BROCA'S) APHASIA STUDY

Aphasia is a disorder of language function that is one of the major symptoms caused by cerebrovascular disorder (CVD). We studied changes of cerebral blood oxygenation and hemodynamics induced by language activities in order to determine differences among nonfluent (Broca's) aphasic patients, normal subjects, and poststroke non-aphasic patients¹¹.

4.1. Methods

Three groups of age-matched subjects participated: nonfluent aphasics (n=10, mean age=56.9y), poststroke nonaphasic patients (n=6, mean age=52.5y), and normal controls (n=13, mean age=50.7y) performed a confrontational naming task, which is commonly included in aphasia test batteries. Methods were the same as those in the aging study.

4.2. Results

Analyses of the data are similar to the aging study, and as in the aging study, Patterns A, B, and C shown in Fig. 1 were the main patterns.

A summary of the occurrence of patterns appears in Table 2. Of note is the finding that the non-aphasic CVD patients and normal controls showed similar patterns; whereas, for the aphasic patients, Pattern C occurred most often. This pattern was evident in the normal and non-aphasic groups, but it was not as prevalent as it was in the aphasic patients.

Table 2 Patterns of NIRS Parameter Changes Induced by Naming Task in Age-Matched Normal Adults, Non-Aphasic CVD Patients, and Aphasic Patients.

Pattern	Oxy, Deoxy, Tot	Age-matched Controls	Non-aphasic CVD Patients	Aphasic Patients
A "typical"	+, ~ 0, +	39%	50%	30%
B	-, ~ 0, -	31%	33%	0%
C	+, +, +	23%	17%	50%

Table 3 summarizes the mean changes of the NIRS parameters. Results of a one-way ANOVA comparing the performance of the 3 groups in the naming task demonstrated a significant effect for Deoxy-Hb, $F(2,27)=4.47$, $P < 0.05$, with aphasic patients differing significantly from normal subjects and nonaphasic CVD patients, while the 2 nonaphasic groups did not differ from each other. In contrast, there were no significant differences in Oxy-Hb or Total-Hb among the groups ($P > 0.05$).

Table 3. Mean \pm SEM Changes of Oxy-Hb, Deoxy-Hb, and Total-Hb in Age-Matched Control Subjects, Nonaphasic CVD Patients, and Aphasic Patients

Parameter	Age-Matched Controls	Nonaphasic CVD Patients	Aphasic Patients	p
Oxy-Hb	0.43 \pm 0.54	0.58 \pm 0.64	1.41 \pm 0.39	0.36
Deoxy-Hb	0.06 \pm 0.16 ^a	-0.18 \pm 0.22 ^a	0.78 \pm 0.29 ^b	0.02
Total-Hb	0.48 \pm 0.58	0.39 \pm 0.71	2.19 \pm 0.40	0.08

NOTE: groups with similar letters did not differ

4.3. Discussion

In the aphasic patients with an increase of Deoxy-Hb, the rCBF in the left prefrontal cortex must be increased by the language task since both Oxy-Hb and Total-Hb were increased by the task, indicating the presence of coupling between rCBF and neuronal activity. However, the mean increase of Total-Hb in the aphasic patients was larger than that seen in normal subjects and nonaphasic CVD patients, suggesting that a larger increase of rCBF was induced by the language task in the aphasic patients. On the other hand, the increase of Deoxy-Hb indicates that the increase of oxygen consumption in the left prefrontal cortex of the aphasic patients was greater than that of nonaphasic patients. These observations suggest that the left prefrontal cortex, in most of the aphasic patients, is more activated during language processing, resulting in more oxygen delivery and oxygen utilization compared with the nonaphasic patient group.

The advantages of NIRS with respect to PET and fMRI were discussed earlier in the Aging section. This study of aphasia confirms the need to consider oxygenation and deoxygenation when conducting clinical studies. In addition, the results of the quantitative one-way ANOVA highlights the value of doing qualitative analysis of NIRS parameter patterns as well as quantitative analyses. Although our analyses supported the finding about patterns, that all three parameters increased for the aphasic patients, it did not account for the fact that 50% of the aphasic patients had patterns that were not of this nature. The pattern of increases in all parameters is the most common pattern for the aphasics, but the sheer size of the response overrode the influence of other patterns. This should serve as a caveat, both for clinical researchers who focus only on quantitative data and to a tendency in some fields to assume that the nontypical response is artifactual or that subjects with nontypical responses should not be included in a study.

Because NIRS is portable and easy to use, it might be used to study recovery of function and CBO response after a stroke. For example patients who see the doctor could routinely be evaluated for CBO response induced by brain activation. The difficulties would relate to placement of the optodes and finding tasks that be given repeatedly without reduction in activation.

5. SUMMARY

To summarize, NIRS has shown that although normal adults show a "typical" pattern of increases in Oxy-Hb and Total-Hb, accompanied by a small or no decrease in Deoxy-Hb, there are a number of other patterns which should be considered and which may relate to neuronal loss or changes.

Regarding aging, older adults did not show the typical pattern as often as young adults. In addition, they tended to show a pattern of decreasing Oxy-Hb and Total-Hb with little or no change in Deoxy-Hb more often than young people. Concerning aphasics, the most common pattern was an increase in all three parameters which suggests excess oxygen utilization.

These issues call into question the use of pooled data for clinical groups without consideration of individual activation patterns. In addition, the fact that a person does not respond in the "typical" way does not mean the person is should be considered an outlier.

In spite of the low spatial resolution of contemporary NIRS equipment, it can be an important compliment to other brain activation research and diagnostic tools such as PET and fMRI. The temporal resolution surpasses PET, and the fact that oxygenation and deoxygenation changes means that NIRS offers information that cannot be obtained using fMRI. In addition, the portability and ease of use could make it a valuable tool in clinics, and perhaps for intensive care monitoring

REFERENCES

- ¹ Hoshi, Y, Onoe H, Watanabe Y, Anderson J, Bergstam M, Lilja A, Langstrom B, Tamura M. Non-synchronous behavior of neuronal activity, oxidative metabolism and blood supply during mental tasks in man. *Neurosci Lett*, **172**, pp:129-133, 1994.
- ² Hoshi Y, Tamura M. Dynamic multichannel near-infrared optical imaging of human brain activity. *J Appl Physiol*, **75**, pp 1842-1846, 1993.
- ³ Hoshi Y, Tamura M. Dynamic multichannel near-infrared optical imaging of human brain activity. *Neurosci Lett*, **150**, pp 5-8, 1993.
- ⁴ Kato T, Kamei A, Takashim S, et al. Human visual cortical function during photic stimulation monitoring by means of near-infrared spectroscopy. *J Cereb Blood Flow Metab*, **13**, pp 516-520, 1993.
- ⁵ Kleinschmidt A, Obrig H, Requardt M et al. Simultaneous recording of cerebral blood oxygenation changes during human brain activation by magnetic resonance imaging and near-infrared a spectroscopy. *J Cereb Blood Flow Metab*, **16**, pp 817-826, 1996.
- ⁶ Hock C, Muller-Spahn F, Schuh-Hofer S, et al. Age dependency of changes in cerebral hemoglobin oxygenaton during brain activaon: A near-infrared spectroscopy study. *J Cereb Blood Flow Metab*, **15**, pp 1103-1108, 1995.,
- ⁷ Cope M, Delpy DT, Reynolds EO, Wray S, Tyatte J, Van der Zee P. Methods of quantitating cerebral near-infrared spectroscopy data. *Adv Exp Med Biol*, **222** pp 183-189, 1988.
- ⁸ Hock C, Villringer K, Muller-Spahn F, et al. Decrease in parietal cerebral hemoglobin oxygenation during performance of a verbal fluency task in patients with Alzheimer's disease monitored by means of near-infrared spectroscopy (NIRS)-correlation with simultaneous rCBF-PET measurements. *Brain Res* **755**, pp 203-303, 1997.
- ⁹ Cabeza R, McIntosh AR, Tulving E, et al. Age-related differences in effective neural connectivity during encoding and recall. *Neuroreport*, **8**, pp 3470-3483., 1997.
- ¹⁰ Sakatani, K, Lichty, W, Xie Y, Li S, Zuo H. Effects of aging on Inaguage-activated cerbral blood oxygenation changs of the left prefrontal cortex: Near infrared spectroscopy study. *J of Stroke & Cerebrov Diseases*, **8**, pp 398-403, 1999.
- ¹¹ Sakatani K, Xie Y, Lichty W et al. Language-activated cerebral blood oxygenation and hemodynamic changes of the left prefrontal cortex in poststroke aphasic patients: A near-infrared spectroscopy study. *Stroke*, **29**, pp 1299-1304, 1998.

Optical computed tomography for imaging the breast: First look

Richard J. Grable*, Steven L. Ponder, Nikolaos A. Gkanatsios, William Dieckmann, Patrick Olivier,
Robert H. Wake, Yueping Zeng

Imaging Diagnostic Systems, Inc., Plantation Florida, U.S.A.

ABSTRACT

The purpose of the study is to compare computed tomography optical imaging with traditional breast imaging techniques. Images produced by a computed tomography laser mammography (CTLM™) scanner are compared with images obtained from mammography, and in some cases ultrasound and/or magnetic resonance imaging (MRI). During the CTLM procedure, a near infrared laser irradiates the breast and an array of photodiodes detectors records light scattered through the breast tissue. The laser and detectors rotate synchronously around the breast to acquire a series of slice data along the coronal plane. The procedure is performed without any breast compression or optical matching fluid. Cross-sectional slices of the breast are produced using a reconstruction algorithm. Reconstruction based on the diffusion theory is used to produce cross-sectional slices of the breast. Multiple slice images are combined to produce a three-dimensional volumetric array of the imaged breast. This array is used to derive axial and sagittal images of the breast corresponding to cranio-caudal and medio-lateral images used in mammography. Over 200 women and 3 men have been scanned in clinical trials. The most obvious features seen in images produced by the optical tomography scanner are vascularization and significant lesions. Breast features caused by fibrocystic changes and cysts are less obvious. Breast density does not appear to be a significant factor in the quality of the image. We see correlation of the optical image structure with that seen with traditional breast imaging techniques. Further testing is being conducted to explore the sensitivity and specificity of optical tomography of the breast.

Keywords: breast imaging, optical tomography, transillumination, laser mammography, optical imaging, image reconstruction

1. INTRODUCTION

1.1 Early optical breast-imaging experience

Optical imaging techniques for imaging the breast have been evaluated beginning with Dr. M. Cutler's article in 1929 describing a simple breast transillumination system.¹ A cooled light source was used to transilluminate the breast in a darkened room, and the unaided eye viewed the breast. In 1980, Ohlsson reported on his experiences with a more sophisticated form of breast transillumination called diaphanography.² This technique employed a 35mm camera that used near infrared sensitive film to photograph the breast transilluminated by a high-intensity strobe lamp contained within the light source. In 1984, Isard reported on his experience with this system.^{3,4} The technology continued to advance with different approaches used to transilluminate the breast. Carlsen reported on a breast transilluminator that used a dual-wavelength (red, 698nm, and near infrared, 861nm) pulsed light source in a digital spectroscopy technique to evaluate the optical transmission characteristics of the breast.⁵ Lafreniere reported on his experiences using a continuous wave light source and an analog infrared video transillumination system.⁶

The breast transillumination evaluations of the 1980's-era generally concluded that the dual-wavelength, digital spectroscopy technique's use was unwarranted because it provided a marginal contribution over mammography and had an undesirable number of false positives.^{7,8,9} In 1991, the U.S. Food and Drug Administration (FDA) Obstetrics and Gynecology Devices Panel recommended that breast transilluminators be classified as Class III devices and that a Pre-Market Approval (PMA) would be required to allow the distribution and use of breast transilluminators in the United States.¹⁰ In 1994, the FDA classified breast transilluminators as Class III devices, thus mandating that a PMA be submitted and approved prior to commercial distribution of this device.

* Correspondence: Email: grable@imds.com; Telephone: 954 581 9800; Fax: 954 581 0555

1.2 Next-generation optical breast-imaging devices

In the late 1990's, several groups explored the use of computed tomography (CT) techniques to image the breast. Jackson used a quartz halogen lamp and photomultiplier tube in a first generation CT traverse-and-rotate scanning configuration.¹¹ In 1989, my group exhibited a first generation CT traverse-and-rotate scanning configuration using a laser diode and photodiode detectors at the 74th annual meeting of the Radiological Society of North America (RSNA).¹² This configuration used a Intel™ 386, 33 MHz computer, acquired one slice of data in 3 ½ minutes, reconstructed one slice-plane image in 10 minutes, and could resolve a 1cm lesion. In 1989, these capabilities did not offer any competition to x-ray mammography.

In 1991, Wang reported on the use of a Nd:glass laser and optical Kerr gate to perform 2-dimensional imaging.¹³ In 1994, our group designed and constructed a computed tomography laser breast imaging using a stationary collimated circular array of 600 avalanche photodiodes and a laser fan-beam produced by a rotating polygon mirror and a Argon-pumped mode-locked Ti:Sapphire (Coherent Laser, Mountain View, CA) laser. This device was exhibited at the 79th RSNA annual meeting as a work-in-progress system. Data was simultaneously acquired from groups of 150 detectors at 4,000 points in the orbit of the laser around the breast. This design did not have adequate detector collimation and the fan-beam laser did not have an adequate number of photons to allow imaging of a breast with 17-cm cross-section.

Development of optical breast imaging devices continued throughout the 1990's. By the end of this period several groups had developed different scanning configurations. van de Mark reported on use of continuous wave (CW) laser diodes at multi-wavelengths (679nm, 779nm, and 867nm) in an optical computed tomography 3-dimension breast imaging device developed by Philips Research Laboratories of the Netherlands.¹⁴ Over 300 woman have been scanned with this device in European clinical trials. The woman is prone on the scanning table, with one breast at a time immersed in a 13cm diameter container filled with optical matching fluid. 255 source-detector pairs are used to reconstruct the images. The CW optical tomography device yields the oxygen saturation level and bloodvolume data and suggests that characterization of tumors is possible. Data acquisition is completed in about 9 minutes, and image reconstruction requires several hours.

Heffer reported on the results obtained from studying 130 women with a 70 MHz frequency-domain multi-wavelength scanner.¹⁵ The breast is compressed between two clear plastic plates and immersed in an optical matching fluid. Cranio-caudal and medio-lateral oblique views of each breast are acquired. A planar-tandem scan is performed and amplitude and phase information is obtained and is used to create a two-dimensional projection image of each breast. The differences in the spectral properties of malignancies and benign tumors are being studied and results are reported to be encouraging. Culver reported on a similar CW, compression plate, CCD imaging system that used Intralipid® (Pharmacia AB) as an optical coupling matching fluid.¹⁷ A total of 32 source positions were used and 10,000 measurements are made in about 30 seconds. The field of view is approximately 2.6cm by 2.6cm, with a typical breast compressed thickness of 6cm-7cm. An Algebraic Reconstruction Technique (ART) is used for image reconstruction. Three-dimensional reconstruction of a tissue phantom demonstrates resolution of about 5mm.

Paulsen reported on the results obtained from a pilot study of 15 women using a frequency domain scanner using 16 sources and 16 detectors.¹⁶ The patient is prone on a scanning table with one breast pendant through an opening. The imaging system sensors can be radially translated to form a variable diameter opening ranging from 7-10cm. Illumination at several wavelengths is used in order to convert the multispectral absorption coefficient images into functional parameters such as hemoglobin concentration. Preliminary clinical experience has been positive. In vivo quantitative estimates of the hemoglobin concentration can be made.

In all of these scanner configurations, the breast is either immersed in an optical matching fluid or is contacted by the source and detector optics. Only the system reported by van de Mark is capable of performing a computed tomography reconstruction. The other systems employ a sophisticated form of breast transillumination, i.e., the breast is positioned between the source(s) and detector(s) and single projection images are obtained.

2. Optical Computed Tomography Design

2.1 Scanner Configuration

The optical computed tomography scanners that we have tested, with one exception, did not contact the breast. The one exception used a source fiber that was placed in light contact with the breast through use of a pivoted arm. Safety and

sanitary considerations arising from having the scanner's source in physical contact with the breast convinced us to abandon this approach.

The design of the scanner places the patient prone on a scanning table, with one breast at a time extending through the tabletop into the scanning area. Interchangeable rings are provided to accommodate the range of breast sizes, up to 20cm, normally encountered, and to generally center the breast in the scanning chamber. There is no breast contact, i.e., the breast is not compressed, and no optical matching fluid is used.

The current design uses two rows of 84 silicon photo-diodes arranged in a circular arc around the breast. One row of detectors is fitted with optical filters to remove the laser excitation wavelength when fluorescence imaging is used. Each detector is fitted with an optical collimator to define its field of view. The laser source and the detector array are rotated 360° around the breast. Measurements are made at about 200 points in the orbit to provide over 16,000 measurements. A single slice of data is acquired in about 30 seconds.

In order to obtain multiple slices, the laser source and the detector array are moved vertically between acquisitions, usually downward, in increments of a few millimeters (typically 4mm). The direction of the orbit is reversed from clock-wise to counter-clock-wise for each data acquisition to prevent excessive twisting of the electronic cables. Depending on the breast size as many as 50 slice-planes of data are acquired to cover a maximum vertical distance of 20cm. A bilateral breast examination requires about 15 minutes.

2.2 Image Reconstruction

After the raw data has been processed to compensate for hardware-induced variations, a data reconstruction algorithm is applied to create the slice-plane image. We are currently working with two reconstruction schemes. One is a variation on the classic filtered back projection technique in which the effects of optical absorption and scattering are taken into account. The other is an iterative scheme that takes advantage of finite-element modeling as well as standard algebraic reconstruction methods. The modified back projection reconstruction technique reconstructs a single slice of data in typically 75 seconds using a 700 MHz CPU. Due to its computational intensity, the iterative reconstruction scheme may take from several minutes to several hours to reconstruct a slice, depending upon which reconstruction options are selected. Both techniques may be extended to include three-dimensional data and effects at the expense of increased reconstruction times.

2.3 Image Display

The individual slice-plane images can be directly displayed as individual coronal views of the breast. A volumetric reconstruction technique is applied to the array of slice-plane images to allow simultaneous display of axial and sagittal optical images, i.e., equivalent to cranio-caudal (CC) and medio-lateral (ML) projections routinely seen with mammography. However, instead of a single axial and sagittal projections, a series of sequential axial and sagittal projections are provided. These projections are used to examine the features seen in the mammography films by positioning the axial and sagittal views to better visualize the suspect area.

A bilateral axial and sagittal display is also provided. This features emulates the common practice of placing left and right CC and ML mammography films on a film display box.

The displayed optical coronal, axial, and sagittal views are available for printing on an external printer.

3.0 Clinical Images

Over 200 women and 3 men have been scanned with the computed tomography laser mammography (CTLMTM) scanner. In the clinical trial series, CTLM images are compared with x-ray mammography and, where appropriate, ultrasound and magnetic resonance imaging (MRI).

Figure 1 is a cranio-caudal and Figure 2 is a medio-lateral mammogram that reveals grouped or clustered, heterogeneous or pleomorphic calcifications (granular) in the 7 o'clock position, posterior third of the breast. This is a new finding when compared to the previous examination and is suspicious for abnormality. The radiologist classified the lesion as a BIRADS (BIRADS = Breast Imaging Reporting And Data System) category 4. The lesion is suspected solely on the basis of the calcifications. No mass is associated with the lesion.

Figure 3 illustrates Computed Tomography Laser Mammography™ coronal, axial and sagittal views for the same breast. The optical signature of the lesion is clearly seen.

Pathological results demonstrated infiltrated ductal carcinoma of grade III out of III. There was also ductal carcinoma in situ of solid type and high grade. It was difficult pathologically to determine how much of the lesion represented invasive carcinoma versus ductal carcinoma in situ, although at least minimal invasion was thought present.



Figure 1, Cranio-Caudal View



Figure 2, Medio-lateral Oblique View

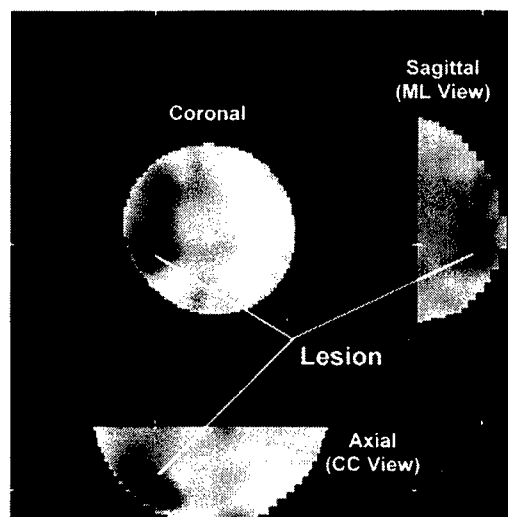


Figure 3, Computed Tomography Coronal, Axial, & Sagittal Views

Figure 4 is a cranio-caudal and Figure 5 is a medio-lateral mammogram that reveals two irregular, speculated masses measuring 3.5cm and 2.5cm in the upper inner portion of the left breast at the nine-thirty position. Spicules link the two masses suspicious for satellite, bridging, and multifocal carcinoma. The radiologist classified the lesion as a BIRADS category 5. A multifocal malignancy was diagnosed following biopsy.

Figure 6 illustrates Computed Tomography Laser Mammography™ coronal, axial and sagittal views for the same breast. The optical signature of the lesion is clearly seen.

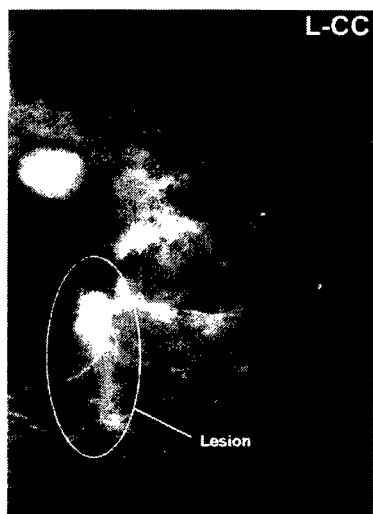


Figure 4, Cranio-Caudal View

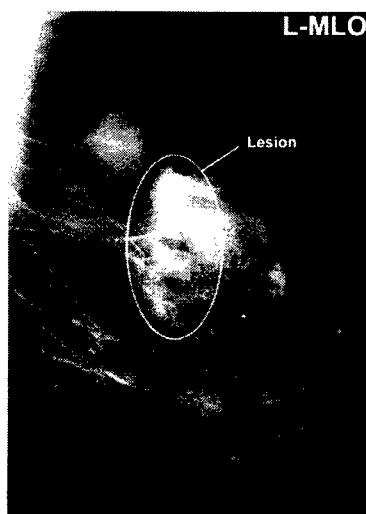


Figure 5, Medio-lateral Oblique View

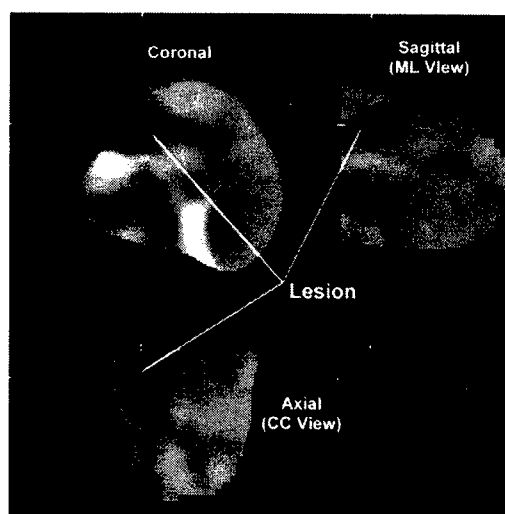


Figure 6, Computed Tomography Coronal, Axial, & Sagittal Views

Figure 7 is a cranio-caudal and Figure 8 is a medio-lateral mammogram that reveals a 27mm, round, high-density mass with speculated margins in the two-o'clock position, posterior third of the left breast. The mass is associated with grouped or clustered fine, linear (casting) calcifications. Pathology reported invasive ductal carcinoma, grade II or III. Ductal carcinoma in situ (DCIS), high grade, with comedonecrosis.

Figure 9 illustrates Computed Tomography Laser Mammography™ coronal, axial and sagittal views for the same breast. The optical signature of the lesion is clearly seen.

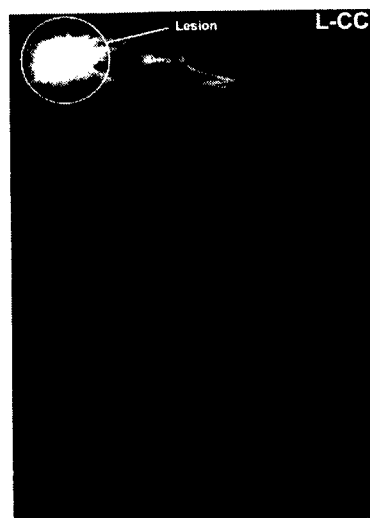


Figure 7, Cranio-Caudal View

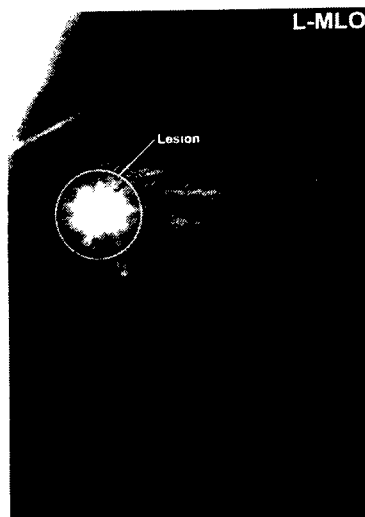


Figure 8, Medio-lateral Oblique View

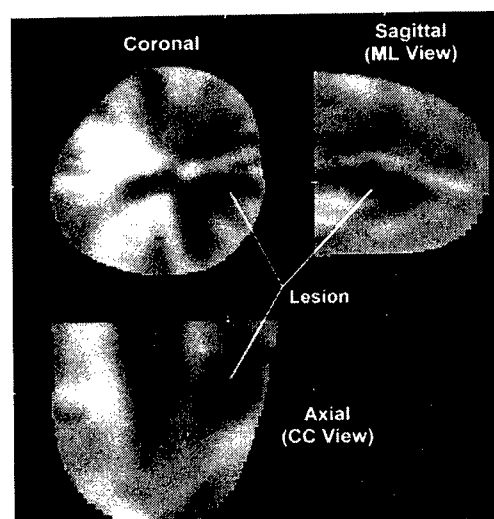


Figure 9, Computed Tomography Coronal, Axial, & Sagittal Views

4.0 Summary

Clinical testing has confirmed the ability of the CTLM to detect and display breast cancer that has been confirmed by biopsy and that was seen in the respective mammograms. Preliminary results with this scanner configuration are encouraging, and clinical testing is ongoing to properly assess the capabilities of this device.

REFERENCES

1. Cutler M., "Transillumination as an aid in the diagnosis of breast lesions", *Surg Gynecol Obstet*; 48:721-9, 1929
2. Olhsson B, Gunderson J, Nilsson DM. Diaphanography: A method for evaluation of the female breast. *World J Surg* 1980; 4:701-7
3. Isard HJ. Diaphanography: Transillumination of the breast revisited. Schwartz GF, Marchant DJ, ed. *Breast Disease: Diagnosis and Treatment*, New York: Elsevier North Holland, 1981; 67-71
4. Isard HJ. Other imaging techniques. *Cancer*; 53:658-664, 1984
5. Carlsen EN, Transillumination light scanning. *Diag Imag*; 3:28-33, 1982
6. Lafreniere R, Ashkar FS, Ketcham AS. Infrared light scanning of the breast, *Amer Surg*; 52(3):123-8
7. Monsees B, Destouet JM, Totty WG. Light scanning verses mammography in breast cancer detection. *Radiology*; 163:463-5, 1987
8. Monsees B, Destouet JM, Gresell D. Light Scan evaluation of non palpable breast lesions. *Radiology*; 163:467-70, 1987
9. Alveryd A, Andersson I, Aspegren K, et al. Lightscanning verses mammography for the detection of breast cancer in screening and clinical practice. *Cancer*; 4:1671-7, 1990
10. Summary Minutes of the 45th Meeting of the Obstetrics and Gynecology Devices Panel, Food and Drug Administration, U.S. Public Health Service, January 11, 1991
11. Jackson PC, Stevens PH, Smith JH, Kear D, Key H, Wells PNT. The development of a system for transillumination computed tomography. *Br. J. Radiol.*;60:375-80, 1987
12. Personal papers

13. Wang L, Ho PP, Liu C, Zhang G, Alfano RR, Ballistic 2-D imaging through scattering walls using an ultrafast optical Kerr gate. *Science*; 253: 769-771, 1991
14. van der Mark MB, Hooft GW, Wachters AJH, de Vries UH, Janssen JP, Masser MNJM. Clinical study of the female breast using spectroscopic diffuse optical tomography, Paper presented at Optical Society of America Biomedical Topical Meeting, April 2000
15. Heffer E, Franceschini MA, Schutz O, Siebold H, Heywang-Kobrunner S, Gotz G, Heinig A, Fantini S. Analysis of frequency domain optical mammograms using spectral information. , Paper presented at Optical Society of America Biomedical Topical Meeting, April 2000
16. Paulsen KD, Osterman KS, Kerner TF, Hartov A, Pogue BW, McBride TO, Osteberg UL, Poplack SP. Model-based image reconstruction: A general framework for multi-modality imaging of the breast. Paper presented at Optical Society of America Biomedical Topical Meeting, April 2000
17. Culver JP, Ntziachristos V, Zubkov L, Durduran T, Pattanayak DN, Yodh AG, Data size set and image quality in diffuse optical mammography: Evolution of a clinical prototype. . Paper presented at Optical Society of America Biomedical Topical Meeting, April 2000

SESSION 3

Advances in Microscopic and Spectroscopic Imaging

Development of 200-channel mapping system for tissue oxygenation measured by near-infrared spectroscopy

Masatsugu Niwayama^{*}, Daisuke Kohata, Jun Shao, Nobuki Kudo, Takafumi Hamaoka^a,
Toshihito Katsumura^a, and Katsuyuki Yamamoto

Division of Biomedical Systems Engineering, Graduate School of Engineering,
Hokkaido Univ., Sapporo 060-8628, Japan

^a Tokyo Medical College, Shinjuku 6-1-1, Tokyo 160-8402, Japan

ABSTRACT

Near-infrared spectroscopy (NIRS) is a very useful technique for noninvasive measurement of tissue oxygenation. Among various methods of NIRS, continuous wave near-infrared spectroscopy (CW-NIRS) is especially suitable for real-time measurement and for practical use. CW-NIRS has recently been applied to *in vivo* reflectance imaging of muscle oxygenation and brain activity. However, conventional mapping systems do not have a sufficient mapping area at present. Moreover, they do not enable quantitative measurement of tissue oxygenation because conventional NIRS is based on the inappropriate assumption that tissue is homogeneous. In this study, we developed a 200-channel mapping system that enables measurement of changes in oxygenation and blood volume and that covers a wider area (30 cm x 20 cm) than do conventional systems. The spatial resolution (source-detector separation) of this system is 15 mm. As for the effects of tissue inhomogeneity on muscle oxygenation measurement, subcutaneous adipose tissue greatly reduces measurement sensitivity. Therefore, we also used a correction method for the influence of the subcutaneous fat layer so that we could obtain quantitative changes in concentrations of oxy- and deoxy-hemoglobin. We conducted exercise tests and measured the changes in hemoglobin concentration in the thigh using the new system. The working muscles in the exercises could be imaged, and the heterogeneity of the muscles was shown. These results demonstrated the new 200-channel mapping system enables observation of the distribution of muscle metabolism and localization of muscle function.

Keywords: near-infrared spectroscopy, tissue oxygenation, skeletal muscle, functional imaging

1. INTRODUCTION

Near-infrared spectroscopy (NIRS) has been applied to clinical measurements as a very useful technique for noninvasive measurement of tissue oxygenation. Tissue oxygenation is closely related to metabolic activity or the presence of disease. Chance¹ and co-workers first applied NIRS to imaging of metabolic activity of the brain. Maki *et al.*² developed optical topography, based on continuous wave spectroscopy (CW-NIRS) as a practical imaging method for observing brain activity. Cerebral oxygenation imaging using NIRS has recently been clinically applied to investigations of brain function^{3,4}. Several studies on muscle oxygenation imaging have also been carried out. Maris *et al.*⁵ obtained images of the forearm muscle using a mechanical scanning system consisting of several optical probes based on intensity modulated spectroscopy. Niioka *et al.*⁶ examined the function of lower extremity muscles (gastrocnemius in the calf muscle and two muscles in the quadriceps muscle group) during exercise using CW-NIRS. They showed the feasibility of optical imaging for studying muscle function. However, conventional imaging systems do not have a sufficient mapping area; a measurement area of about 10 cm x 10 cm is not sufficient for measurement in the thigh. Moreover, it should be noted that quantitative measurement of tissue oxygenation has not been possible because conventional NIRS is based on the inappropriate assumption that tissues are homogeneous. In muscle oxygenation measurement, the subcutaneous fat layer greatly affects measurement sensitivity⁷⁻¹⁰.

In this study, we developed a 200-channel mapping system for muscle oxygenation that can cover a wide area (30 cm x 20

^{*} Correspondence: E mail: niwa@bme.eng.hokudai.ac.jp; Telephone: +81-11-706-6777; Fax: +81-11-706-7196

cm). This system was applied to measurements of changes in muscle oxygenation in almost the entire region of the thigh during exercise. Furthermore, we applied our correction method^{8,10} for the influence of the fat layer to this mapping system in order to quantitatively image muscle oxygenation.

2. METHODS

2.1. Instrumentation

The developed system has 200 channels and can receive signals from 40 probes, each of which contain 5 channels. As shown in Fig. 1, a probe is composed of a light source, five photo diodes (Hamamatsu Photonics, S2386-18K, 45K), and a current-to-voltage (I-V) converter. A light-emitting diode (OPTRANS, 95010), including two diode-elements of 830- and 770-nm peak wave lengths, was used for the light source. The photo diodes were located at 3 and 15 mm from the light source. A photo diode of 3-mm separation was used to examine the effects of blood within the skin. The photo-diode current was converted to a voltage signal by the I-V converter, which was buried within each probe in order to reduce external noise. In measurement in muscle, an optical probe should appropriately be in contact with the skin surface even when it deforms due to contraction of the muscle. Therefore, the probe was made of silicone so as to fit the skin surface and so that there would be little change in source-detector separation.

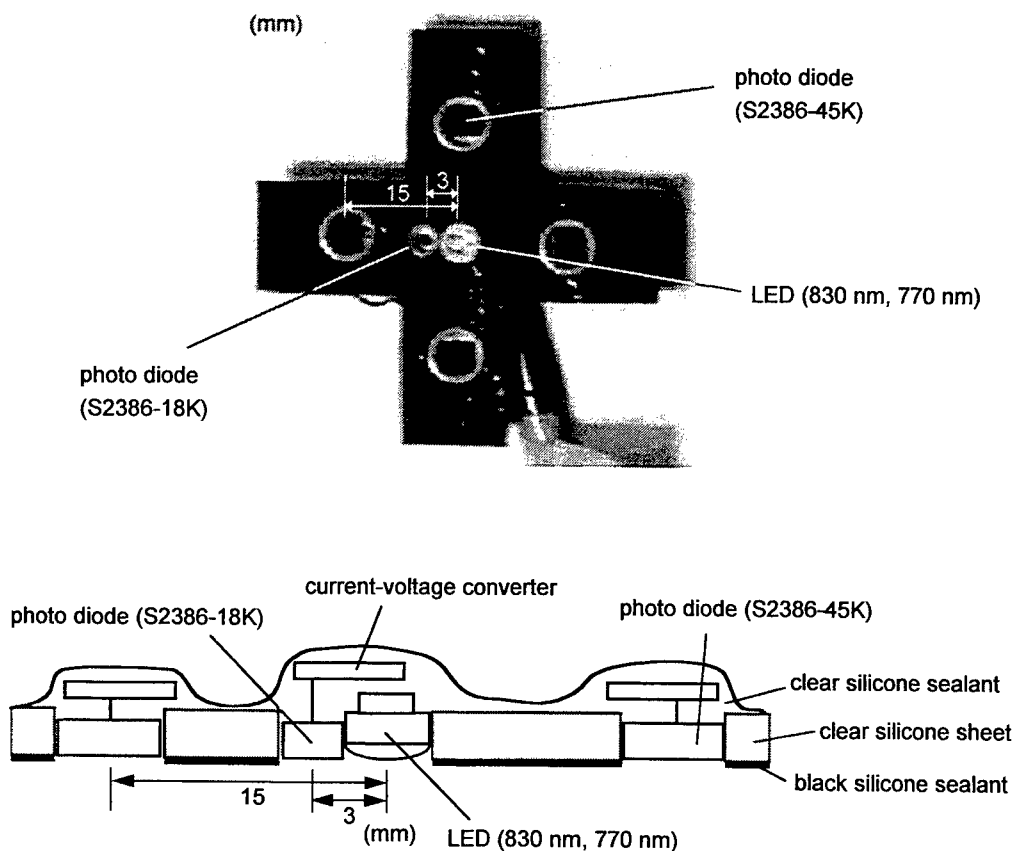


Fig. 1. An optical probe used in the mapping system.

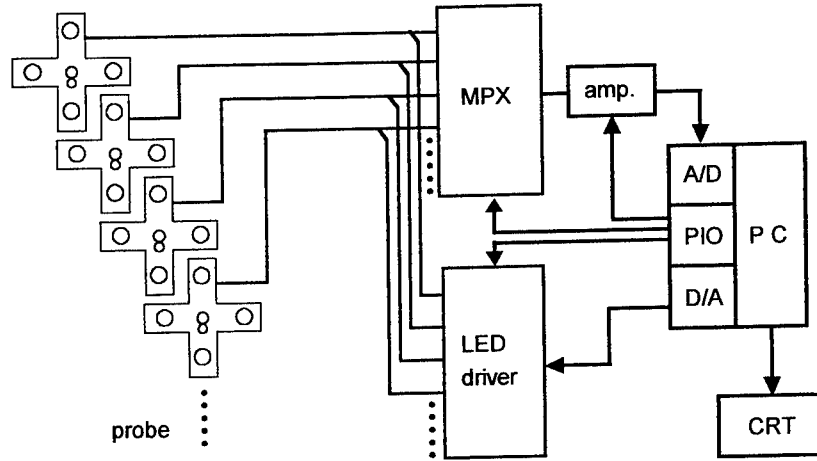


Fig. 2. Block diagram of the mapping system.

A block diagram of the mapping system is shown in Fig. 2. The basic construction is the same as that of oximeters previously reported⁷⁻¹⁰. Voltage outputs from the I-V converter were multiplexed and amplified by 2 to 100 times. The outputs from the amplifier were fed into a personal computer via an A/D converter. The gain of the amplifier and light intensity of the LED were automatically adjusted by the computer in order to obtain an appropriate signal level of detected light at the start of measurement. The data acquisition of 200 channels and calculation of oxygenation were completed within 1.2 s, and traces were displayed on a CRT in real time.

We employed the following equations to determine the change in concentrations of HbO₂, Hb and total Hb.

$$\Delta[\text{HbO}_2] = \frac{1}{\rho \text{DPF}} \frac{\epsilon_{\lambda_2}^{\text{Hb}} \Delta OD_{\lambda_1} - \epsilon_{\lambda_1}^{\text{Hb}} \Delta OD_{\lambda_2}}{\epsilon_{\lambda_1}^{\text{HbO}_2} \epsilon_{\lambda_2}^{\text{Hb}} - \epsilon_{\lambda_2}^{\text{HbO}_2} \epsilon_{\lambda_1}^{\text{Hb}}}, \quad (1)$$

$$\Delta[\text{Hb}] = -\frac{1}{\rho \text{DPF}} \frac{\epsilon_{\lambda_2}^{\text{HbO}_2} \Delta OD_{\lambda_1} - \epsilon_{\lambda_1}^{\text{HbO}_2} \Delta OD_{\lambda_2}}{\epsilon_{\lambda_1}^{\text{HbO}_2} \epsilon_{\lambda_2}^{\text{Hb}} - \epsilon_{\lambda_2}^{\text{HbO}_2} \epsilon_{\lambda_1}^{\text{Hb}}}, \quad (2)$$

$$\Delta[\text{total Hb}] = \Delta[\text{HbO}_2] + \Delta[\text{Hb}], \quad (3)$$

where $\Delta[\text{HbO}_2]$, $\Delta[\text{Hb}]$, and $\Delta[\text{total Hb}]$ are changes in concentrations of HbO₂, Hb, and total Hb, respectively; $\epsilon_{\lambda_{1,2}}^{\text{Hb}}$ and $\epsilon_{\lambda_{1,2}}^{\text{HbO}_2}$ are molar extinction coefficients¹¹ of Hb and HbO₂, respectively, at wavelengths λ_1 and λ_2 ; ρ is source-detector distance; and DPF is a differential pathlength factor¹² based on the assumption that tissue is homogeneous. In this study, DPF was determined by the diffusion theory, the validity of which had been confirmed by our phantom experiments⁹. At a source-detector separation of 15 mm, DPF was 3.1. The changes in concentrations of HbO₂, Hb, and total Hb are expressed as mM.

2.2. Correction of the influence of a fat layer

In order to eliminate the influence of subcutaneous fat layer, we used the correction curve shown in Fig. 3. This curve was obtained from the results of Monte Carlo simulation and the results of two groups of *in vivo* experiments¹⁰. The relationship between normalized measurement sensitivity S and fat layer thickness h was expressed by the following equation:

$$S = \exp\left\{-\left(\frac{h}{A_1}\right)^2\right\} - A_2 G(\alpha, \beta), \quad (4)$$

where $G(\alpha, \beta)$ is a gamma distribution. The constants A_1 , A_2 , α , and β at a source-detector separation of 15 mm were 6.9, 1.15, 7.86 and 0.80, respectively. These constants are dependent on the optical properties of tissues to some extent, but the dependence on the properties is much less than that on fat layer thickness. Thus, the value of S was determined in practice only by h , and then corrected measurements were obtained by dividing the measurements calculated from equations (1)–(3) by S .

Fat thicknesses were measured by a diagnostic ultrasound apparatus (Toshiba, SSA-320A, 7.5-MHz center frequency). The fat layer can readily be distinguished from a muscle layer, because the muscle layer is easily identified by contraction of the muscle. Fat layer thickness was determined by reading the thicknesses on a hard copy of the ultrasound image, as shown in Fig. 4.

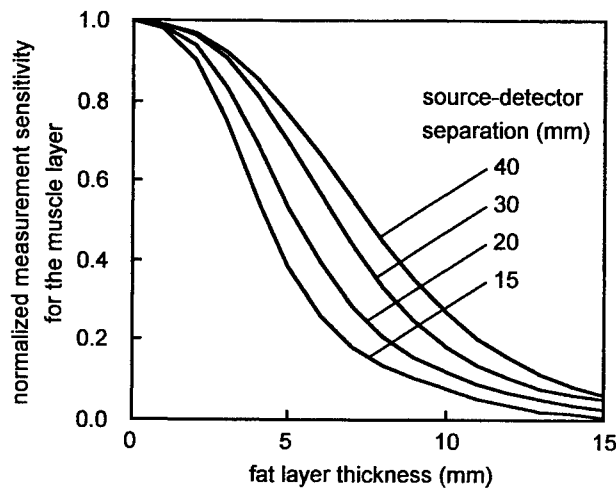


Fig. 3. A curve for correction of the influence of a fat layer: normalized measurement sensitivity for the muscle at each source-detector separation.

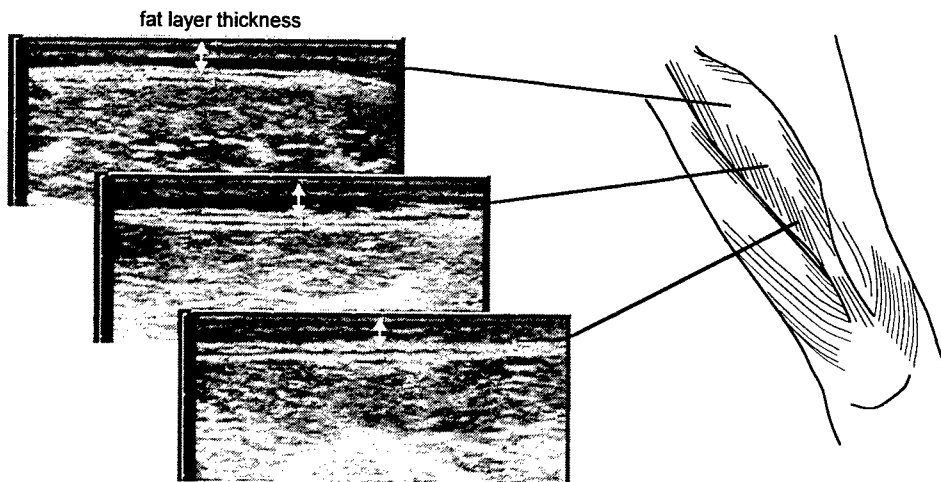


Fig. 4. Thickness of a fat layer measured from an ultrasound image.

2.3. In vivo tests

A healthy male (27 years of age and 53 kg in weight) participated in exercise tests. Changes in muscle oxygenation and blood volume were measured in the thigh muscles: vastus lateralis (VL), rectus femoris (RF), vastus medialis (VM), and biceps femoris (BF). The measurement region was 8-23 cm proximal to the center of the patella. We used 28 probes (112 detectors of 15-mm separation and 28 detectors of 3-mm separation) to cover the right thigh. The probes were fixed on the skin surface with surgical tape (3M Health Care, Transpore) at intervals of 5 and 7 cm in circumferential and longitudinal directions, respectively, as shown in Fig. 5. The subject repeated contractions of the maximal isometric knee flexor or extensor for 60 seconds with a 2-minute recovery between the two exercises. Mapping images of 45 cm x 15 cm were obtained.

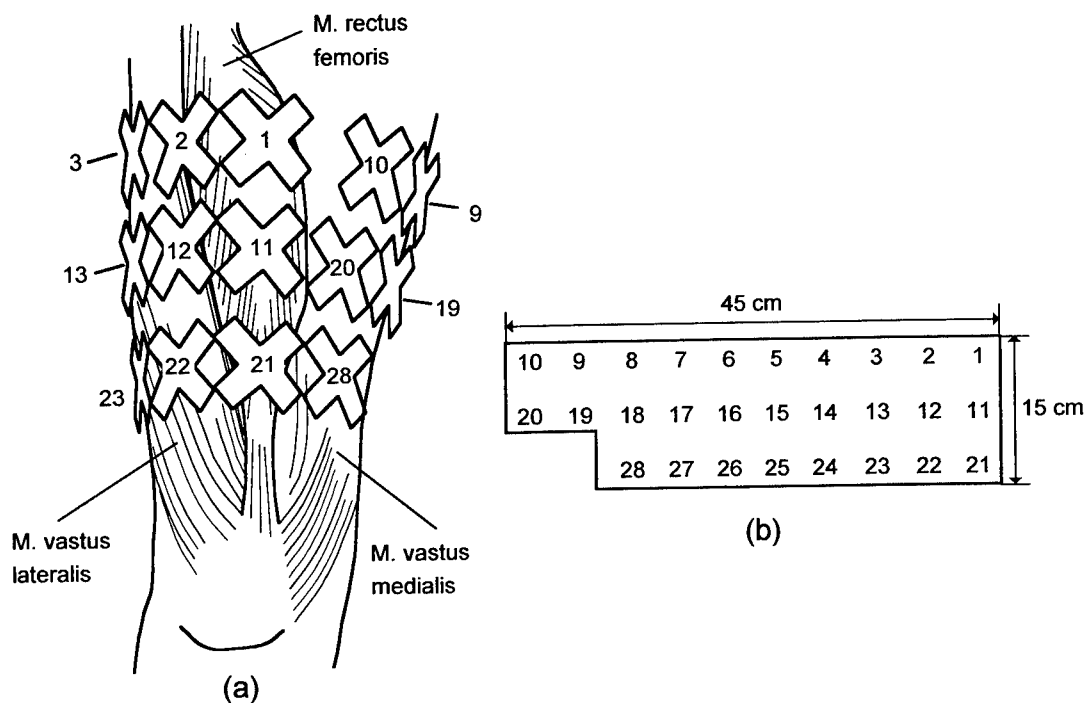


Fig. 5. Arrangement of the parts of the optical probe (a) and arrangement in a mapping image (b).

3. RESULTS AND DISCUSSION

3.1. Mapping of muscle oxygenation

Figure 6 shows an example of traces in each muscle in the exercise test at a source-detector separation of 15 mm. Mapping images were obtained, as shown in Fig. 7. Reduction in blood volume and deoxygenation occurred in the BF muscle during the knee flexion exercise. During recovery, a large hyperemic response was concomitantly found in the medial part of the BF muscle. During knee extension exercise, a marked reduction in blood volume and deoxygenation occurred in the RF and VM muscles. In comparison with these muscles, the VL muscle responded less to the exercise. Thus, the working muscles in the exercises could be imaged, and the heterogeneity of the muscles was successfully shown.

Although the optical probe was designed to be flexible and in contact with the skin surface, signals from some probes placed on a recessed portion were saturated, probably due to direct incidence of light from a source. A more reliable method for fixing optical probes must be used; e.g., light pressure by a flexible cuff wrapped around an array of the probes.

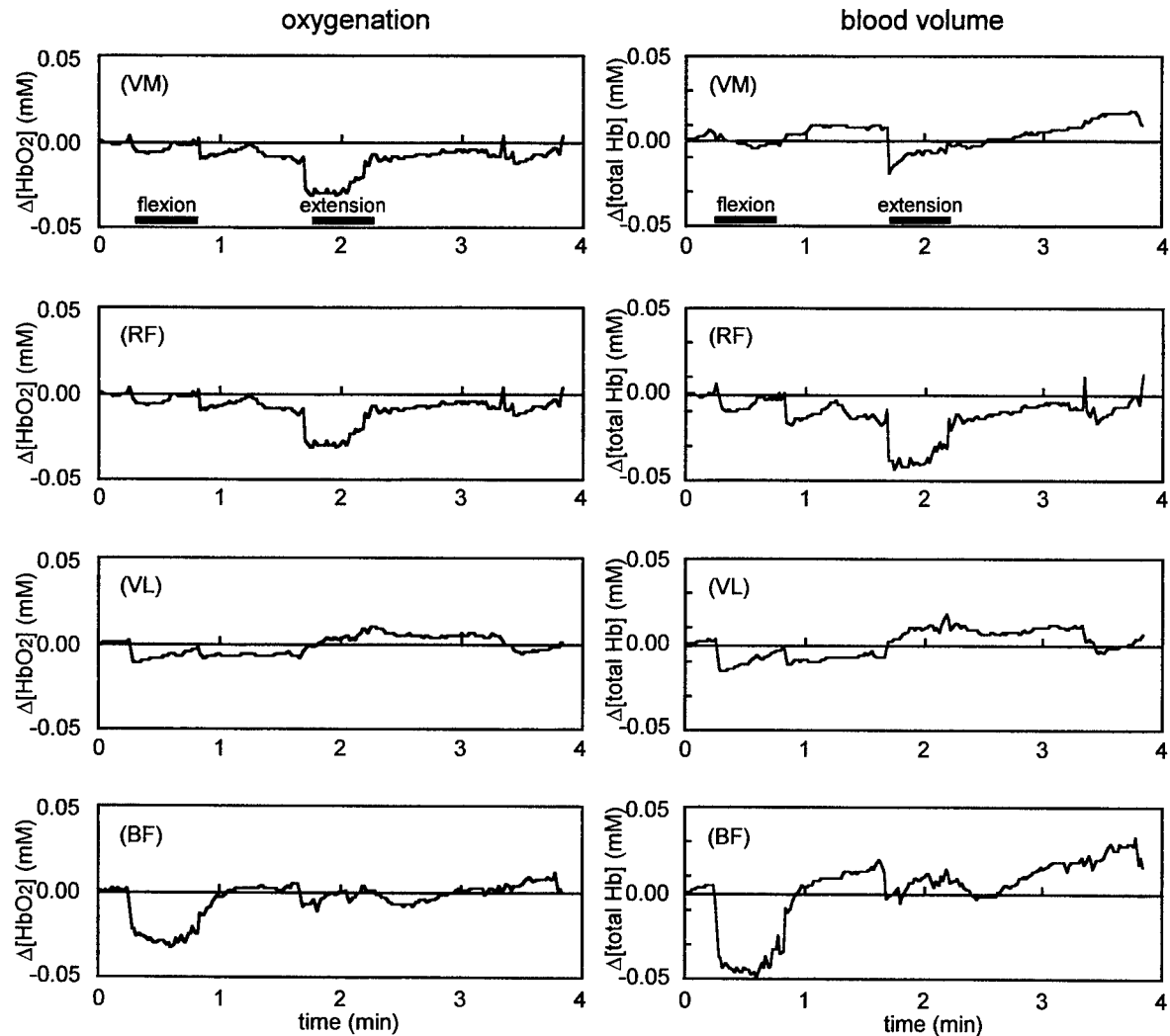


Fig. 6. Typical traces of changes in the concentrations of HbO_2 and total Hb in the thigh muscles: vastus medialis (VM), rectus femoris (RF), vastus lateralis (VL), and biceps femoris (BF). Source-detector separation was 15 mm.

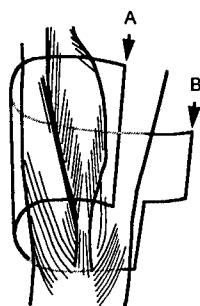
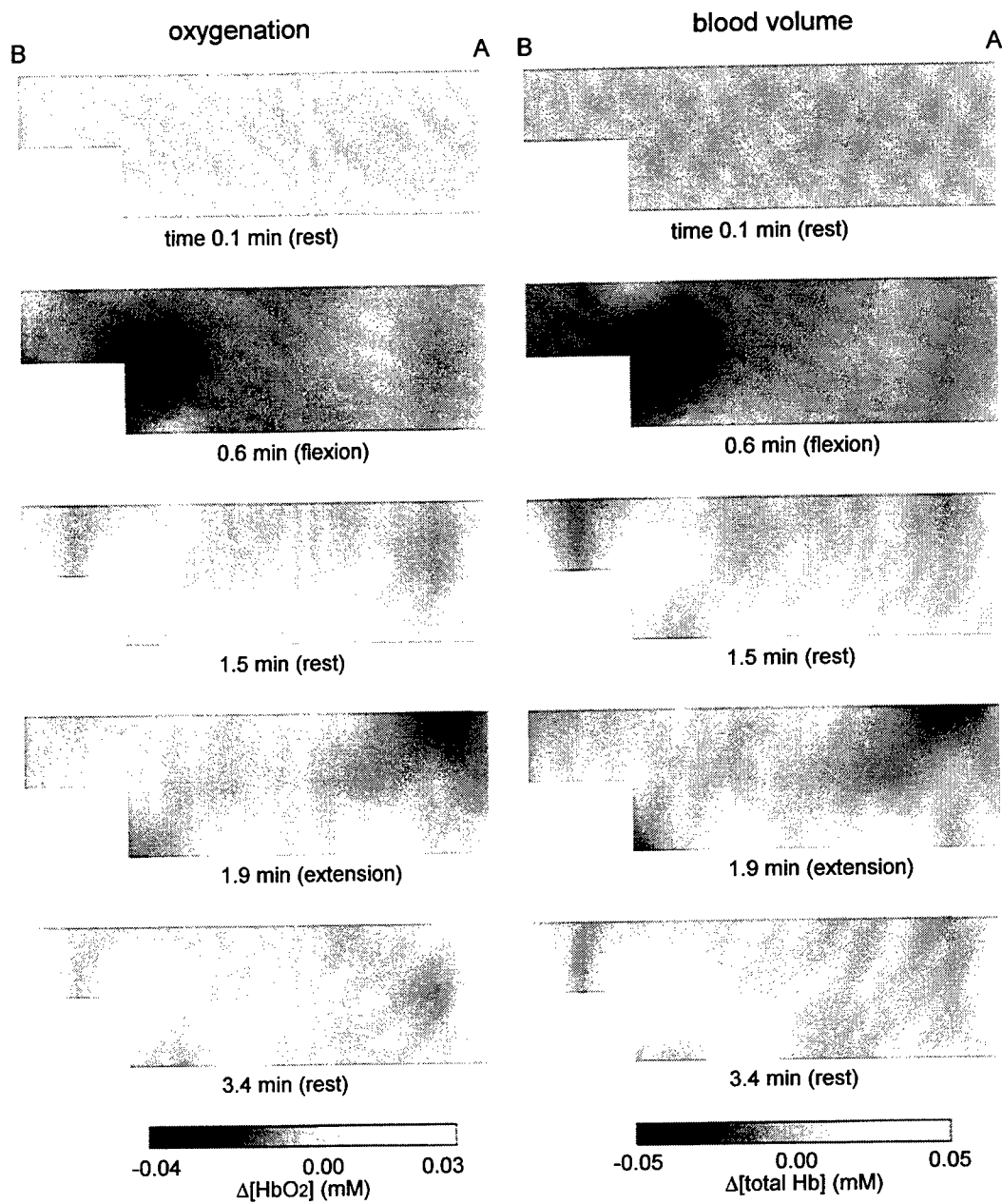


Fig. 7. Mapping images of changes in the concentrations of HbO_2 and total Hb in the thigh.

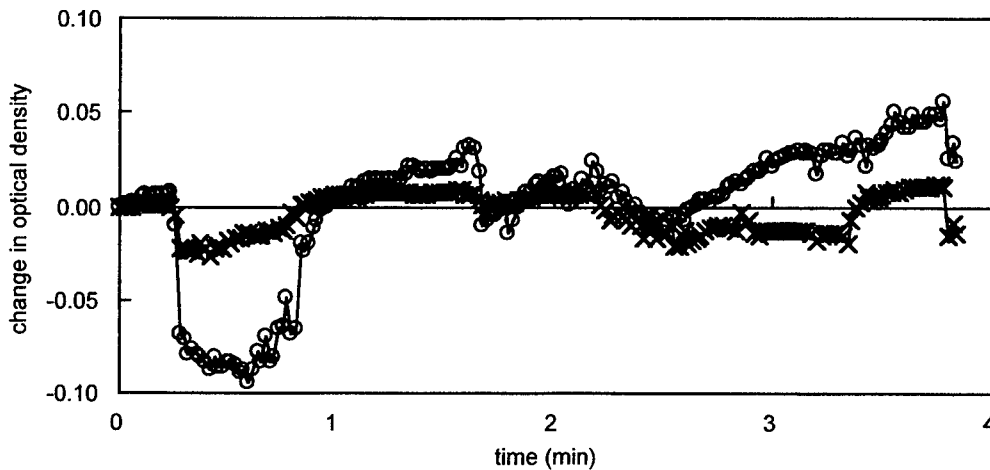


Fig. 8. Changes in optical density at 830 nm obtained at 3-mm (×) and 15-mm separations (○) in the vastus medialis muscle.

3.2. Influence of skin blood flow

The influence of skin blood flow on muscle oxygenation measurement was examined using a detector located at a 3-mm separation from a light source. Figure 8 shows changes in optical density (ΔOD) obtained at source-detector separations of 3 and 15 mm in the VM muscle at a wavelength of 830 nm. The change in optical density of 3-mm separation varied by about 20% of ΔOD of 15-mm separation. This result suggests that there is a significant influence of skin blood flow. This influence could be eliminated by subtracting ΔOD of 3-mm separation from that of 15-mm separation, if measurement sensitivity of 3-mm separation for the muscle can be ignored compared to that of 15-mm separation.

In the experiments, we measured fat layer thicknesses by placing an ultrasound probe on many different portions of the thigh. From a practical point of view, this inefficient procedure should be improved. We have proposed a method for correcting the influence of a fat layer using detected light intensity at rest⁸. This correction method is based on the fact that detected light intensity increases with fat layer thickness due to the much lower absorption of light in a fat layer than in a muscle layer. This relationship can be easily incorporated in a calculation algorithm of an oximeter, although the accuracy of this correction method is not as good as that of the method in the present study, which uses a known measured thickness. Each probe used in the present mapping system also has a near-by detector besides a source for correcting the effects of skin blood flow, as mentioned above. This system enables elimination of both the influences of a fat layer and skin blood flow, and therefore more quantitative and simple measurements can be performed using this system without the need of any additional equipment.

5. CONCLUSIONS

We have developed a 200-channel mapping system using continuous wave near-infrared spectroscopy that covers a wide area and that enables measurement of quantitative changes in oxygenation and blood volume. Mapping images of the entire of the right thigh were able to be obtained using this system, and temporal and spatial heterogeneity of muscle oxygenation during exercise was successfully detected. These results show that the newly developed 200-channel mapping system enables observation of the distribution of muscle metabolism and localization of muscle function.

ACKNOWLEDGMENT

This research was supported in part by Grant-in-Aid for Scientific Research from the Ministry of Education, Science and Culture of Japan.

REFERENCES

1. B. Chance, A. Villringer, V. Dirnagl, and K. M. Einhaupl, "Optical imaging of brain function and metabolism," *J. Neurology*, **239**, pp. 359-360, 1992.
2. A. Maki, Y. Yamashita, Y. Ito, E. Watanabe, Y. Mayanagi, and H. Koizumi, "Spatial and temporal analysis of human motor activity using noninvasive NIR topography," *Med. Phys.*, **22**, pp. 1997-2005, 1995.
3. J. R. Mansfield, M. G. Sowa, and H. Mantsch : "Near-infrared spectroscopic reflectance imaging : methods for functional imaging and in vivo monitoring," *Proc. SPIE*, **3597**, 270-280, 1999.
4. Y. Chen, S. Zhou, S. Nioka, and B. Chance, "A Novel Portable System for Neonatal Brain Imaging," *Proc. SPIE*, **3597**, 262-269, 1999.
5. M. Maris, E. Gratton, J. Maier, W. Mantulin, and B. Chance, "Functional near-infrared imaging of deoxygenated hemoglobin during exercise of the finger extensor muscles using the frequency-domain technique," *Bioimaging*, **2**, pp. 174-183, 1994.
6. S. Nioka, H. Miura, H. Long, A. Perry, D. Moser, and B. Chance: "Functional muscle imaging in elite and untrained subjects", *Proc. SPIE*, **3597**, 282-290, 1999.
7. K. Yamamoto, M. Niwayama, T. Shiga, L. Lin, N. Kudo, and M. Takahashi, "Accurate NIRS measurement of muscle oxygenation by correcting the influence of a subcutaneous fat layer," *Proc. SPIE*, **3194**, pp. 166-173 1998.
8. K. Yamamoto, M. Niwayama, T. Shiga, L. Lin, N. Kudo, and M. Takahashi, "A near-infrared muscle oximeter that can correct the influence of a subcutaneous fat layer," *Proc. SPIE*, **3257**, pp. 145-155, 1998.
9. L. Lin, M. Niwayama, T. Shiga, N. Kudo, M. Takahashi, and K. Yamamoto, "Two-layered phantom experiments for characterizing the influence of a fat layer on measurement of muscle oxygenation using NIRS," *Proc. SPIE*, **3257**, pp. 156-166, 1998.
10. M. Niwayama, L. Lin, J. Shao, T. Shiga, N. Kudo, and K. Yamamoto, "Quantitative measurement of muscle oxygenation by NIRS: Analysis of the influences of a subcutaneous fat layer and skin," *Proc. SPIE*, **3597**, pp. 291-299, 1999.
11. S. J. Matcher, C. E. Elwell, C. E. Cooper, M. Cope, and D. T. Delpy, "Performance comparison of several published tissue near-infrared spectroscopy algorithms," *Analytical Biochemistry*, **227**, pp. 54-68, 1995.
12. D. T. Delpy, M. Cope, P. van der Zee, S. Arridge, S. Wray, and J. Wyatt, "Estimation of optical pathlength through tissue from direct time of flight measurement," *Phys. Med. Biol.*, **33**, pp. 1433-1442 (1988).

Low-coherence interference microscopy at high numerical apertures

C. J. R. Sheppard^{a,b}, M. Roy^a and P. Svahn^{a,c}

^aDepartment of Physical Optics, School of Physics A28,
University of Sydney, NSW 2006, Australia

^bAustralian Key Centre for Microscopy and Microanalysis,
University of Sydney, NSW 2006, Australia

^cDepartment of Physics II, Royal Institute of Technology, Stockholm, Sweden

ABSTRACT

A white-light Linnik interference microscope using high numerical aperture optics has been constructed. The system uses a tungsten halogen source and Köhler illumination with separate control over field and aperture stops, so that experiments can be conducted with a range of different operating conditions. Infinity tube length objectives are used in the two arms. Images are recorded with a CCD camera. Different algorithms have been investigated for extraction of information from the image data. These are based on phase stepping, which is achieved based on the principle of the geometric phase, using a polarizing beam splitter, a quarter wave plate and a rotating polarizer. Image information extracted from the visibility of the fringes and also from the phase of the interference fringes has been investigated.

Keywords: Low-coherence interferometry, optical coherence tomography, coherence-probe microscope, white-light interferometry, phase-shifting, geometric phase, surface profiling.

1 INTRODUCTION

Recently white-light interferometry (WLI) has grown in importance in a variety of applications documented by various authors. These include 3-D imaging for medical diagnostics using optical coherence tomography (OCT),^{1,2} in optical fibre sensors³⁻⁵ and in a surface profiling techniques using coherence probe microscopy (CPM).⁶⁻¹¹ It has many advantages over the conventional (monochromatic) interferometric techniques. The most promising property of WLI is that it can overcome the ambiguity problems, inherent to monochromatic interferometric systems. WLI systems have a virtually unlimited unambiguous range, so that surfaces can be measured without using phase unwrapping techniques. Another important characteristic of WLI is its optical sectioning property. This is due to the short coherence length of the source, so that the interference term is appreciable only for a short range of depths, and hence an optical section is extracted which allows three-dimensional images to be formed.

In this technique the images are produced by scanning the object in depth and calculating the degree of coherence (visibility peak) between corresponding pixels in the object and reference image planes. In OCT this is done using heterodyning techniques. A single point is observed and an image built up by scanning. In our work, as in CPM, a complete two-dimensional image is observed using a CCD detector. While various digital filtering techniques have been used to recover the fringe visibility curve, they tend to be numerically intensive. The use of conventional phase-shifting technique to simplify the processing is complicated by the fact that the phase shift introduced by changing the optical path is wavelength dependent, leading to systemic errors in the fringe visibility. An alternative way to achieve phase shifting is by means of the geometric phase (Pancharatnam phase).^{12,13} This is the phase shift experienced by a light beam as a result of a cyclic change in its state of polarization. Because the geometric phase is a topological phenomenon, it is, in principle, independent of the wavelength.

2 EXPERIMENTAL SET-UP

A schematic diagram of the white-light interference microscope is depicted in Fig. 1. A tungsten halogen lamp (12V, 100W) is used as a source. The linearly polarized beam transmitted by the polariser is divided at the polarising beam splitter into two orthogonally polarised beams which are focused on to a reference mirror and a specimen by two identical infinity tube-length 40X microscope objectives with numerical aperture 0.75. After reflection at the reference mirror and object these beams return along their original paths to a second beam-splitter which sends them through a second polarizer to the CCD camera.

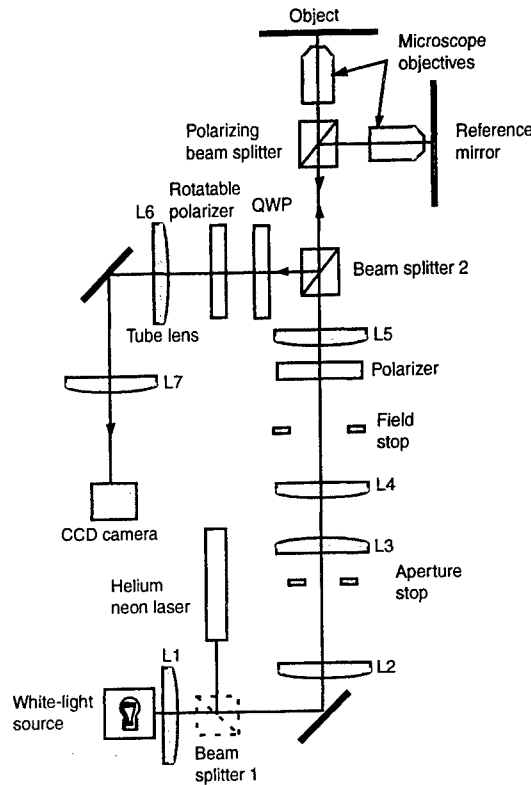


Fig.1. The white-light interferometric microscope

The phase difference between the beams was varied by a Geometric Phase-Shifter (GPS) consisting of a quarter-wave plate (QWP) with its axis fixed at an azimuth of 45° , and a polarizer which can be rotated by known amounts. In this case, if the polarizer is set with its axis at an angle θ to the axis of the QWP, the linearly polarized beam reflected from the reference mirror acquires a geometric phase shift equal to 2θ . The orthogonally polarized beam from the specimen acquires a geometric phase shift equal to -2θ , so that the additional phase difference introduced between the two beams is 4θ . This additional phase difference is very nearly independent of the wavelength.

A 3mW He-Ne laser is also provided. Since the coherence length of the laser is much longer than that of the white-light source, the laser is used for finding the interference fringes.

The operation of the achromatic phase shifter was verified by observation of the fringe system obtained by tilting the reference mirror slightly and by using a mirror as a test surface. With monochromatic illumination, rotation of the polarizer resulted in a continuous movement of the interference fringes across the field of view. When the direction of rotation of the polarizer was reversed, the fringes moved continuously in the opposite direction.

To illuminate the object uniformly, a Koehler illumination system is used, consisting of lenses L1-L4 together with a microscope objective. This system allows separate control of both the illumination aperture stop and the field stop. Stopping down the illumination aperture allows the system to be operated as a conventional interference microscope.

Reducing the field of view keeps the scattered light collected by the detector to a minimum and keeps specimen heating to a minimum. Field of view of the system is $25\mu\text{m} \times 43\mu\text{m}$.

The object is scanned along the z axis by means of a piezoelectric transducer (PZT) over a range of $5\mu\text{m}$ centred approximately on the zero-order white light fringe. At each step, three, four or five measurements were made of the intensity, depending on which phase-shifting algorithm was used. We obtained best results with the five-step algorithm. Since the additional phase differences introduced by the GPS are the same for all wavelengths, the visibility of the interference fringes at any given point in the field can be extracted. The visibility falls off as a result of both the coherence length of the source and the correlation effect,⁸ which give similar sectioning to that in confocal microscopy.

When observing a surface structure, for example an integrated circuit, as specimen, the surface height can be extracted by finding for each pixel the peak of the visibility variation. This can be done by various algorithms. We found a good algorithm was to fit a parabola through three points. Surface height can also be determined from observation of the phase of the interference fringes.

3. DISCUSSION

We have shown the successful use of GPS for white-light interferometric surface profiling on a microscopic scale. The range of surface height that can be profiled with this technique is limited only by the characteristics of the PZT used to translate the specimen along the z axis and the available computer memory. However, since the steps between height settings at which data have to be taken can correspond to changes in the optical path difference of the order of a wavelength or more, a much smaller number of steps are required to cover a large range of depths than for conventional WLISP.

Phase shifting at each step can be carried out rapidly in an actual contouring system, by replacing the rotating HWP plate in the phase shifter with a pair of Ferro-electric Liquid Crystal (FLC) devices. With these devices, it is possible to implement the phase shift at each step within a few milliseconds making this only a small time penalty compared to the 40ms video frame period. Eventually, this will allow acquisition of the intensity data much more rapidly than any scheme using PZT phase stepping alone.

4. ACKNOWLEDGMENTS

Support from the Australian Research Council and the Science Foundation for Physics within the University of Sydney is acknowledged.

REFERENCES

1. D. Huang, E. A. Swanson, C. P. Lin, J. S. Schuman, W. G. Stinson, W. Chang, M. R. Lee, T. Flotte, K. Gregory, C. A. Puliafito and J.G. Fujimoto, Optical Coherence Tomography, *Science*, **254**, pp.1178-1181, 1991.
2. J. M. Schmitt, A. Knüttel and R. F. Bonner, Measurement of optical properties of biological tissue by low coherence reflectometry, *Appl. Opt.*, **32**, pp. 6032-6042, 1993.
3. S. Chen, A. W. Palmer, K. T. V. Grattan and B. T. Meggitt, Digital signal-processing techniques for electronically scanned optical-fiber white-light interferometry, *Appl. Opt.*, **31**, pp. 6003-6010, 1992.
4. Y. J. Rao, Y. N. Ning and D. A. Jackson, Synthesized source for white-light sensing systems, *Opt. Lett.*, **18**, pp. 462-464, 1993.
5. M. V. Plissi, A. L. Rogers, D. J. Brassington and M. G. F. Wilson, Low-coherence interferometric system utilizing an integrated optical configuration, *Appl. Opt.*, **34**, pp. 4735- 4739, 1995.
6. M. Davidson, K. Kaufman, I. Mazar and F. Cohen, An application of interference microscopy to integrated circuit inspection and metrology, *Proc. SPIE*, **775**, pp.233-247, 1987.
7. B. L. Danielson and C. Y. Boisrobert, Absolute optical ranging using low coherence interferometry, *Appl. Opt.*, **30**, pp. 2975-2979, 1991.
8. S. S. C. Chim and G. S. Kino, Correlation microscope, *Opt. Lett.*, **15**, pp. 579-581, 1990.
9. T. Dresel, G. Häusler and H. Venzke, Three dimensional sensing of rough surfaces by coherence radar, *Appl. Opt.*, **31**, pp. 919-925, 1992.
10. L. Deck and P. d. Groot, High-speed noncontact profiler based on scanning white-light interferometry, *Appl. Opt.*, **33**, pp. 7334-7338, 1994.
11. P. Sandoz, An algorithm for profilometry by white-light phase-shifting interferometry, *J. Mod. Opt.*, **43**, pp.

- 1545-1554, 1996.
12. M.V. Berry, The adiabatic phase and Pancharatnam's phase for polarized light, *J. Mod. Opt.*, **34**, pp. 1401-1407, 1987.
 13. P. Hariharan and M. Roy, A geometric-phase interferometer, *J. Mod. Opt.*, **39**, pp. 1811-1815, 1992.

Difference-of-Gaussian Annular Pupil for Extended Depth-of-Focus Three-Dimensional Imaging

Ting-Chung (T.-C.) Poon and Alexander Kourakos

Optical Image Processing (OIP) Laboratory
Bradley Department of Electrical and Computer Engineering
Virginia Polytechnic Institute and State University (Virginia Tech)
Blacksburg, Virginia 24061, USA

ABSTRACT

We propose a technique for 3-D microscopic imaging with extended depth-of-focus using a novel illumination scheme in a laser scanning optical microscope. The novel illumination scheme creates an effective annular pupil, called the difference-of-Gaussian annular pupil, without the critical drawback of stopping and wasting the light. Two laser beams of different Gaussian pupils with different temporal frequencies are first generated. The laser beams are then combined spatially and used to scan the specimen. The scattered light from the object is picked up by a photodetector whose output consists of a DC and an AC current (due to the optical heterodyning of the two optical beams). The DC signal is no difference from the DC output of a conventional laser scanning microscope with the processing pupil as a Gaussian function, whereas the AC signal is derived from the mixing of the two Gaussian beams and would be given by effectively a Gaussian pupil with a different size than that generated by the DC signal. The AC and the DC signals are then subtracted by electronics and hence the effective pupil function would be given by the difference of the two Gaussian pupil functions. By properly choosing the size of the two Gaussian laser beams, we could realize the difference of the two Gaussian pupils which becomes a new type of annular pupil called the difference-of-Gaussian annular pupil.

I. INTRODUCTION

Three-dimensional (3D) imaging is a formidable task in optical microscopy. It is well known that by using a higher numerical aperture (NA) of the objective lens in the microscope, one can achieve a high lateral resolution in the image. However, the improvement of the resolving power results in a depth-of-focus (DOF) reduction [1]. This trade-off problem between the resolving power and the DOF is common to optical microscopes. When the thickness of the specimen exceeds the depth of focus, only a fraction of the total information content of the specimen is imaged in focus or sharply. The result is a low resolution and contrast within the image. Hence improvement in the depth-of-focus has been of great interest in all areas of imaging, especially in high-resolution microscopy [2-5]. 3-D imaging in microscopy therefore aims to develop techniques that could provide high lateral resolution and at the same time with a large depth of field so that a thick specimen could be observed conveniently.

Current practical 3-D imaging techniques include optical sectioning microscopy (OSM) and confocal scanning microscopy (CSM). In OSM [6], 3-D information is collected by recording a series of 2-D images at various focal planes throughout the 3-D specimen. Since each 2-D image contains the in-focus as well as the out-of-focus information, reconstruction of the 3-D information, i.e., extraction of the in-focus information from these 2-D images, is required. Many reconstruction algorithms exist [6]. The difficulty of optical sectioning lies in the fact that during the recording stage it is important that exact focal spacing between adjacent 2-D images be accurately controlled. During the reconstruction, it is also critical to precisely align the 2-D images before processing. Recognizing these problems, a radically new microscope design, the scanning confocal microscope (SCM), has emerged [7]. In SCM, a doubly focused objectives lens system and a pin-hole aperture in front of a photomultiplier are used to image only a single point within the 3-D specimen. Three-dimensional information is then gathered by scanning the specimen

in three dimensions while collecting the light transmitted through the specimen with the photomultiplier. The main difficulty of SCM is that the instrumental tolerances required to achieve high-resolution imaging are very difficult to obtain. Also, 3-D scanning is time-consuming which precludes, for example, the possibility of monitoring interactions taking place within the living cell. In addition, considerably more photobleaching using confocal microscopy will occur if the microscope operates in a fluorescent mode as it requires a time-consuming 3-D scan [6]. This may be critically important in the analysis of living cells. Therefore, confocal microscopy with a scanning laser approach is too slow to do three-dimensional for a dynamic intracellular applications.

Indeed, the major drawback of the two practical 3-D imaging techniques is the required depth- or z-scanning. In this paper, we propose a novel technique in that inspection of 3-D space is required by a single 2-D scan of the thick specimen. The proposed system employs a novel annular-illumination so that a large depth of focus can be achieved in the microscope and yet the system will not waste or stop any light as in conventional system using annular pupils. In what follows, in Section II) we first review a standard laser scanning imaging system. In Section III), we discuss three-dimensional imaging and optical transfer functions. Section IV) describes an annular pupil and its long depth-of-focus capability. Finally, in section V) we describe a novel idea to create a new type of annular pupil, called the difference-of-Gaussians annular pupil, which does not waste or stop the light when implemented in the proposed scanning imaging system. Implementation of the idea is presented at the end of the section.

II. CONVENTIONAL LASER SCANNING SYSTEM

Fig. 1 shows an idealized version of a conventional laser scanning system. $p(x,y)$ is the pupil function. The pupil function forms a point spread function (PSF), $h(x,y)$, onto the object $I_o(x,y)$. The PSF is then two-dimensionally scanned the object to give an output $I_i(x,y)$ displayed on the 2-D display. Mathematically, we have

$$I_i(x,y) = \iint I_o(x',y')h(x-x',y-y')dx'dy' = I_o(x,y)*h(x,y), \quad (1)$$

where $*$ denotes the 2-D convolution, and the PSF, $h(x,y)$, is given by the absolute squared of the Fourier transform of the pupil function $p(x,y)$, i.e.,

$$h(x,y) = |F\{p(x,y)\}|^2 = |P(\frac{x}{\lambda f}, \frac{y}{\lambda f})|^2, \quad (2)$$

where F denotes the Fourier transform of and we denote that $F\{p\} = P$, i.e., the upper case function P is the Fourier transform of the lower case function p . λ is the wavelength of the scanning laser light and f is the focal length of the lens as shown in fig. 1. In this context, the optical transfer function (OTF) is defined by taking the Fourier transform of $h(x,y)$, or

$$OTF(X,Y) = F\{h(x,y)\}, \quad (3)$$

where X and Y are the spatial frequencies along the x and y direction, respectively.

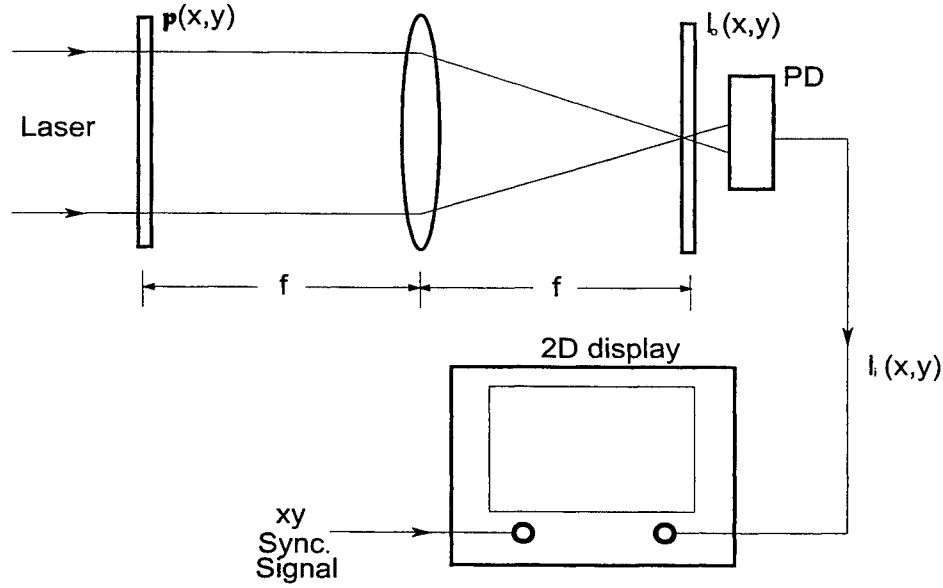


Fig. 1 Conventional laser scanning imaging system

III. THREE-DIMENSIONAL IMAGING AND OPTICAL TRANSFER

For 3-D imaging, we are interested in the defocused PSF, $h(x,y,z)$, which can be calculated by modifying eq.(2) as follows:

$$\begin{aligned}
 h(x,y,z) &= |F\{p(x,y)\} * \frac{1}{-j\lambda z} \exp(-j2\pi z / \lambda) \exp(-\frac{\pi}{\lambda z}(x^2 + y^2))|^2 \\
 &= |P(\frac{x}{\lambda f}, \frac{y}{\lambda f}) * \frac{1}{-j\lambda z} \exp(-j2\pi z / \lambda) \exp(-\frac{\pi}{\lambda z}(x^2 + y^2))|^2,
 \end{aligned} \quad (4)$$

where the quantity inside the absolute value represents the diffraction pattern of the function $P(\frac{x}{\lambda f}, \frac{y}{\lambda f})$ propagating at a distance z away from the focal plane of the lens. The 3-D OTF can be calculated, similar to eq.(3), by taking the 3-D Fourier transform of $h(x,y,z)$ and that gives

$$OTF(X,Y,Z) = F\{h(x,y,z)\}, \quad (5)$$

and Z is the spatial frequency along the z direction.

IV. ANNULAR PUPIL AND ITS LONG DEPT-OF-FOCUS

It has been known that annular pupil can increase the depth-of-focus and lateral resolution simultaneously as compared with a circular pupil [8,9]. An annular pupil is defined as a clear circular pupil with a central obstruction as shown in fig. 2.

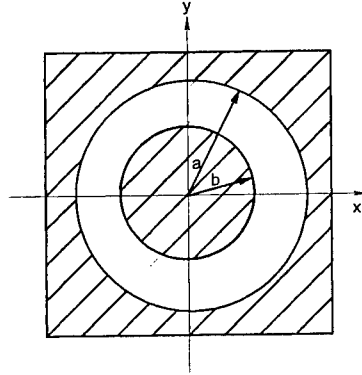


Fig. 2 Annular pupil

If the pupil is an annulus with outer radius a and inner radius b , we can define a central obscuration ratio of $\varepsilon = b/a$ [9]. The depth-of-focus δz_{annu} of an annular pupil has recently been derived by using the Heisenberg's uncertainty principle [9]:

$$\delta z_{ann} \approx \frac{1}{1 - \varepsilon^2} \delta z_{cir}, \quad (6)$$

where $\delta z_{cir} = \lambda / NA^2$ is the depth-of-focus when using a circular pupil and NA is the numerical aperture of the objective lens. For the lateral resolution, it is $\delta x_{annu} = c(\varepsilon) \times \delta x_{cir}$, where $\delta x_{cir} = \lambda / 2NA$ is the resolution of the optical system when a circular pupil with its radius equal to the outer radius, a , of the annulus is used. Note that $c(\varepsilon)$ depends on ε and is smaller than 1. Hence we see that annular pupil provides a better resolution and at the same time a longer depth-of-focus as compared with the circular pupil.

Let us now pay some attention to the depth-of-focus of the annulus. By inspecting Table 1, it is clear that for small ε , the effect of long-depth-of-focus is minimal. However, for $\varepsilon = 0.95$, the depth-of-focus of the annulus is more than a factor of 10 than that of a circular pupil with the radius of the circular aperture equal to the outer radius of the annulus. At $\varepsilon = 0.99$, a factor of more than 50 is achieved. As an example, for $NA = 0.3$ and at illumination wavelength $\lambda = 0.6 \mu m$, $\delta x_{cir} = 1 \mu m$ and $\delta z_{cir} = 6.67 \mu m$, whereas $\delta x_{ann} \approx 1 \mu m$ and $\delta z_{ann} = 50.25 \times \delta z_{cir} = 50.25 \times 6.67 \approx 335 \mu m$ for $\varepsilon = 0.99$. Hence, any thick specimens of thickness less than $300 \mu m$ would be able to be imaged sharply by this annular pupil without any z-scanning and at the same time without any out-of-focus contamination. Indeed, the 3-D OTF has been calculated for a laser-scan fluorescence microscope [11]. An annular illumination microscope has also been constructed and investigated recently [12]. However, due to the low value of ε being used, the gain in depth-of-focus was not significant enough and depth scanning was required for 3-D inspection [12].

ε	$\frac{1}{1 - \varepsilon^2} \delta z_{cir}$
0.99	$50.25 \delta z_{cir}$
0.95	$10.25 \delta z_{cir}$
0.9	$5.26 \delta z_{cir}$
0.8	$2.78 \delta z_{cir}$

Table 1: Depth-of-focus of annular pupils in terms of the depth-of-focus of circular pupils when ε varies

However, the use of an annular aperture for $\varepsilon \approx 1$ has a major drawback in that it stops and wastes a large amount of light and, therefore, in particular, it has not been used effectively for fluorescence microscopes for the purpose of achieving larger depth of focus for 3-D microscopic imaging.

V. PROPOSED NOVEL ILLUMINATION

We develop a technique for 3-D microscopic imaging with extended depth-of-focus using a novel illumination scheme in a laser scanning optical microscope. The novel illumination scheme creates an effective annular pupil, called the difference-of-Gaussian annular pupil, without the critical drawback of stopping and wasting the light. Two laser beams of different Gaussian pupils with different temporal frequencies are first generated. The laser beams are then combined spatially and used to scan the specimen. The scattered light from the object is picked up by a photodetector whose output consists of a DC and an AC current (due to the optical heterodyning or mixing of the two optical beams). The DC signal is no difference from the DC output of a conventional laser scanning microscope with the processing pupil as a Gaussian function, whereas the AC signal is derived from the mixing of the two Gaussian beams and would be given by effectively a Gaussian pupil with a different size than that generated by the DC signal. The AC and the DC signals are then subtracted by electronics and hence the effective pupil function would be given by the difference of the two Gaussian pupil functions. By properly choosing the size of the two Gaussian laser beams, we could realize the difference of the two Gaussian pupils which becomes a new type of annular pupil called the difference-of-Gaussian annular pupil. Since no stopping of the light is used to create the novel annular aperture, the proposed system could prove to be more robust and practical than currently available methods in 3-D imaging when extended depth- of- focus is required. In addition, the proposed system does not require depth- or z-scanning for 3-D imaging which is important for many practical applications.

i) Design Idea

The novel pupil we want to synthesize is of the form of difference-of-Gaussians. The idea is as follows. Let the pupil function, $p(x)$, of the form of the difference of two Gaussian function:

$$p(x) = g_1(x) - g_2(x) \quad , \quad (7)$$

where we denote that $g_1(x)$ and $g_2(x)$ are two Gaussian functions of different size. The corresponding PSF is then given by, according to (2),

$$h(x) = |F\{p(x)\}|^2 = |F\{g_1(x) - g_2(x)\}|^2 = |G_1(\frac{x}{\lambda f}) - G_2(\frac{x}{\lambda f})|^2, \quad (8)$$

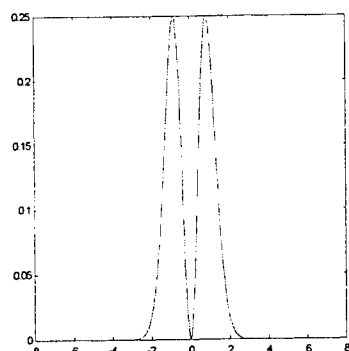
where G_1 and G_2 are Fourier transforms of g_1 and g_2 , respectively, and they are also Gaussian functions as the Fourier transform of a Gaussian function is also a Gaussian function. In fact, Gaussian functions are the so-called self-Fourier transform functions [13]. Expanding eq.(8), the PSF now becomes

$$h(x) = G_1^2 + G_2^2 - 2G_1G_2. \quad (9)$$

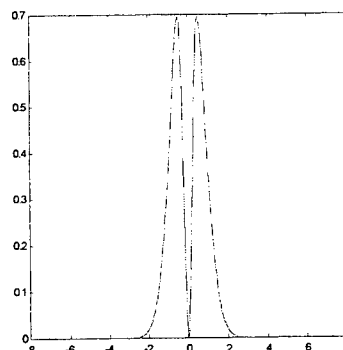
The form of the PSF given in (9) is the effective PSF expression that we are looking for to be implemented. Before we discuss how to implement the PSF shown in eq.(9), let us first discuss briefly the difference-of-Gaussians annular pupil of the form given by (7). Fig. 3) shows two examples of the difference-of-

Gaussians function. For the Gaussian function given by the expression e^{-wx^2} , we define w as the width of the Gaussian. Fig. 3a) shows the difference of two Gaussians with width=1.0 and 2.0, and fig. 3b) with the widths =1.0 and 10.0. Fig. 3 shows only a 1-D plot of the pupil function. We can recover a full 2-D pupil

function by changing x^2 to $x^2 + y^2$ in the Gaussian function. Note that the spatial extent of the graphs in fig. 3 is from -3 to +3 and the separation of the two peaks of the graph in fig. 3b) is closer than that of fig 3a). Hence by choosing different widths of the two Gaussians, one could synthesize the difference-of-Gaussian annular pupil with different obscuration ratio.



$\exp(-1.0 \cdot x.^2) - \exp(-2.0 \cdot x.^2)$
Fig. 3a) Difference-of-Gaussians annular pupil
(w =1 and 2)



$\exp(-1.0 \cdot x.^2) - \exp(-10. \cdot x.^2)$
Fig. 3b) Difference-of-Gaussians annular pupil
(w=1 and 10)

ii) Implementation method:

In the novel illumination scheme, two laser beams with different temporal frequencies are first generated. The optical beams are then combined spatially and used to scan the specimen. The scattered light or the transmitted light from the object is then picked up by a photodetector. The photodetector has two outputs, one is a DC current and the other is an AC current. The two currents represent the two scanned and processed version of the original object and can be sent to a monitor for real-time display or to a digital storage device for possible further processing. Let us now discuss an optical implementation of the idea. Referring to Fig. 4, a spatial filter (SF) cleans up the laser beam to give a clean Gaussian beam. The Gaussian beam is then collimated by lens L. The two beamsplitters (BS) and the two mirrors (M) then form an interferometer. u and v represents two pupil functions along the two paths of the interferometer. However, the temporal frequency of the laser beam along the path where the pupil v is located has been shifted to the amount equal to $\omega_0 + \Omega$, where ω_0 is the frequency of the laser, and Ω is the frequency shift provided by an acousto-optic frequency shifter (AOFM) [14]. The AOFM is a device, which accept the incident laser beam at frequency ω_0 and give out a laser beam at frequency $\omega_0 + \Omega$ [14]. Now, the two pupils u and v are combined by beamsplitter BS2 to give an effective overall PSF of the form, at the focal plane of lens L1,

$$h(x, y) = |F\{u\}e^{j\omega_0 t} + F\{v\}e^{j(\omega_0 + \Omega)t}|^2 = |Ue^{j\omega_0 t} + Ve^{j(\omega_0 + \Omega)t}|^2 \quad (10)$$

Lenses L2 and L3 just form an optical relay system such that the PSF formed at the focal plane of lens L1 is projected and focused onto the specimen.

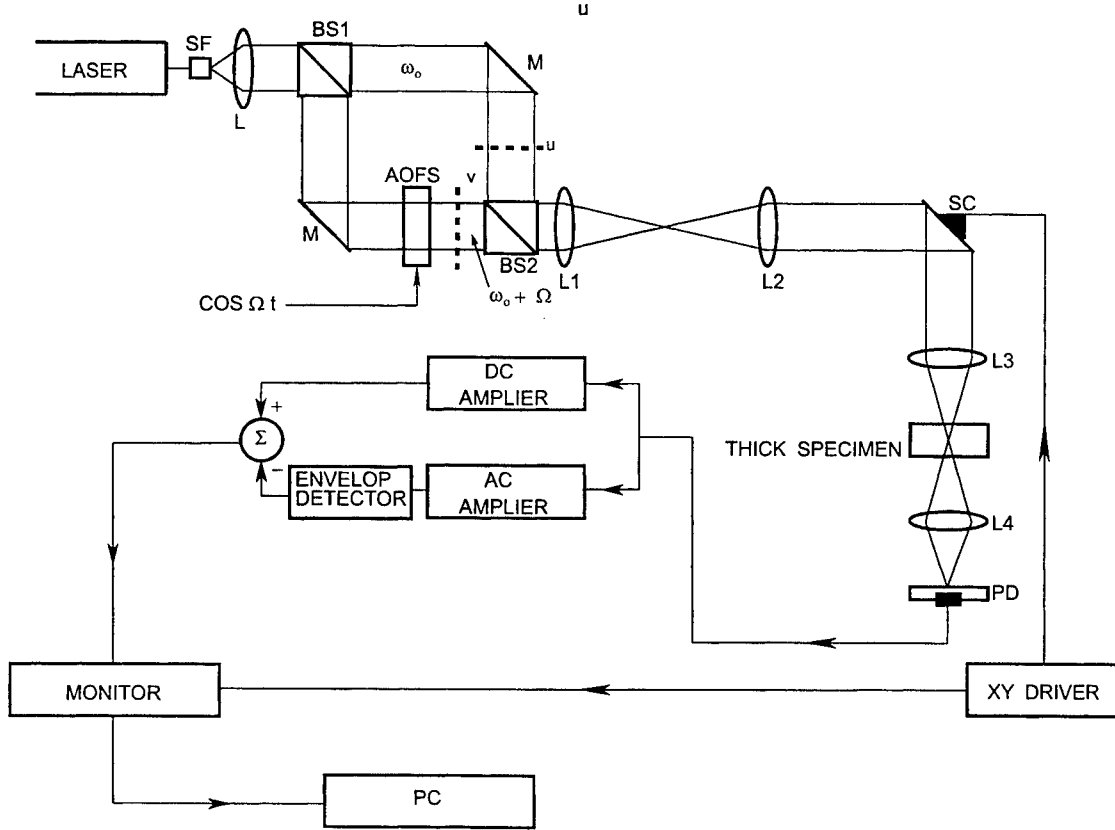


Fig. 4 : Proposed system for implementing difference-of-Gaussians annular aperture The AC amplifier has a gain of β . Σ is an electronic summer. u and v are the two Gaussian pupils

Note that by comparing to the conventional PSF of the laser scanning system [see equation (2)], the PSF in the proposed system has two terms contributing to the effective PSF. In addition, the two terms are carried by two different frequencies. As we can see that, by expanding (10), we have

$$\begin{aligned}
 h(x, y) &= |U|^2 + |V|^2 + U^* V e^{j\Omega t} + U V^* e^{-j\Omega t} \\
 &= |U|^2 + |V|^2 + 2|UV| \cos[\Omega t + \arg(V) + \arg(U)] \\
 &= h_{dc}(x, y) + h_{ac}(x, y) |\cos[\Omega t + \arg(V) + \arg(U)]|,
 \end{aligned} \tag{11}$$

where U and V are Fourier transforms of u and v and $\arg(\cdot)$ stands for the argument of. We now clearly see that the effective PSF consists of a DC term and an AC term at frequency Ω due to the mixing (or heterodyning) of U and V as indicated in (10). Now, by substituting (11) into (1), we have

$$\begin{aligned}
 I_i(x, y) &= I_0(x, y) * h(x, y) \\
 &= I_0(x, y) * [|U|^2 + |V|^2 + 2|UV| \cos[\Omega t + \arg(V) + \arg(U)]] \\
 &= I_0(x, y) * (|U|^2 + |V|^2) + I_0(x, y) * 2|UV| \cos[\Omega t + \arg(V) + \arg(U)].
 \end{aligned} \tag{12}$$

We see that the photodetector's output consists of a DC and an AC signal. Both of the signals contain the scanned and processed version of the object, $I_o(x, y)$, and can be separated by a lowpass filter and a bandpass filter tuned at frequency Ω , giving outputs as

$$(I_i(x, y))_{dc} = I_o(x, y) * (|U|^2 + |V|^2) \quad ; \quad (13a)$$

$$(I_i(x, y))_{\Omega} = I_o(x, y) * 2|UV| \cos[\Omega t + \arg(V) + \arg(U)], \quad (13b)$$

respectively. Note that $(I_i(x, y))_{\Omega}$ is an amplitude modulated signal with temporal frequency at Ω . To demodulate the signal, one can use an envelope detector. The demodulated signal then carries the processed version of $I_o(x, y)$ at the AC channel and is now given by

$$(I_i(x, y))_{ac} = I_o(x, y) * 2|UV| \quad (14)$$

Now, by performing subtraction of the two outputs $(I_i(x, y))_{dc}$ and $(I_i(x, y))_{ac}$ as shown in fig. 4 by an electronic summer, we can construct or synthesize a final processed output $I_i(x, y)$ of the proposed system as, using (13),

$$\begin{aligned} I_i(x, y) &= (I_i(x, y))_{dc} - \beta (I_i(x, y))_{ac} \\ &= I_o(x, y) * (|U|^2 + |V|^2) - \beta I_o(x, y) * 2|UV| \\ &= I_o(x, y) * PSF_{novel} \quad , \end{aligned} \quad (15)$$

where $PSF_{novel} = (|U|^2 + |V|^2) - 2\beta |UV|$ is the novel point spread function of the proposed system, and β is the gain of the AC amplifier. Note that this synthesized novel PSF has the same functional form of the desired PSF given by (9) when U and V are Gaussians. Indeed, when we employ a laser beam. The laser beam shape has a Gaussian profile and that means the two pupils u and v are Gaussians and hence U and V are Gaussians, as again $F\{u\} = U$ and $F\{v\} = V$.

iii) Computer Post-Processing

The PSF proposed in (15) should allow us to synthesize an obscuration ratio associated with the novel annular aperture such that a long depth-of-focus can be achieved and yet at the same time without the drawback of stopping or wasting light. However, the use of annular-type pupils has the effect of lowering the contrast in the obtained image. Fig. 5 shows the OTF associated with the conventional annular aperture of outer radius equal to a . In the figure, f is the focal length of the objective lens. The solid line represents the OTF corresponding to the annular aperture, whereas the dotted line represents the OTF corresponding to a circular lens with a as the radius. Note that, for the annular pupil, high frequency content of the information of the object has been attenuated as compared to the use of a circular lens. Hence the proposed annular aperture will also lead to low contrast images. Fortunately, the loss in contrast can be restored by using a computer effectively. Indeed an inverse filter operation can be performed on the computer. To investigate 3-D filtering of the imaging system, we need to find the 3-D OTF of the proposed system, and this can be done in general by using (4) and (5) where $p(x, y)$ is given by (7) when (7) is written in x and y coordinates. Since the pupil function given by (7) involves the difference of two Gaussians, the OTF therefore can be calculated analytically quite easily. To restore contrast, we use $1/OTF$, an exact inverse filter.

However, since the use of this novel annular aperture leads to a longer depth-of-focus, I speculate that the use of in-focus PSF would serve the purpose of restoring contrast as the OTF would not change appreciably during de-focus. This needs to be investigated for this type of novel pupil. If this turns out to be true, OTF can be calculated simply by taking the Fourier transform of the in-focus PSF_{novel} given in (15) and that would save a lot of computation time when restoring contrast.

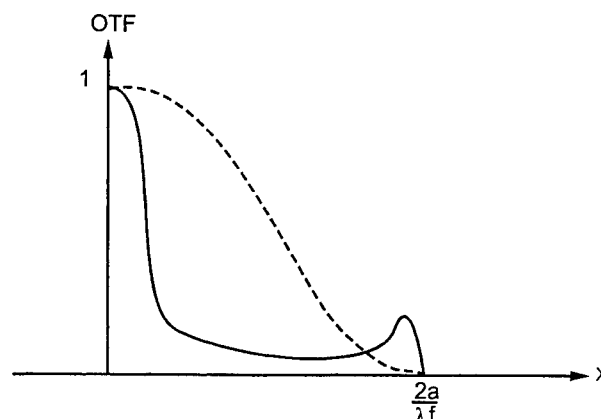


Fig. 5 : OTFs of conventional annular lens and the circular lens.
Solid line: annulus, Dotted line: circular lens
X is the spatial frequency along the x-direction.

ACKNOWLEDGMENT

We acknowledge the support of the National Institutes of Health (James A. Shannon Director's Award).

REFERENCES

- [1] G. Hausler, "A method to increase the depth of focus by two step image processing," *Optics Communications* 6, pp.38-42, 1972.
- [2] R.J. Pieper and A. Korpel, "Image processing for extended depth of field," *Applied Optics* 22, pp. 1449-1453, 1983.
- [3] S. Sugimoto and Y. Ichioka, "Digital composition of images with increased depth of focus considering depth information," *Applied Optics* 24, pp. 2076-2080, 1985.
- [4] G. Indebetouw and H. Bai, "Imaging with Fresnel Zone Pupil mask: extended depth of field," *Applied Optics* 23, 4299, 1985.
- [5] E. Dowski and T. Cathey, "Extended depth of field through wave-front coding," *Applied Optics* 10, pp.1859-1866, 1995.
- [6] D.A. Agard, "Optical sectioning microscopy: cellular architecture in three dimensions," *Ann. Rev. Biophys. Bioeng.* 13, pp.191-219 (1984).
- [7] T. Wilson, Ed., *Confocal microscopy*, Academic Press, London, 1990.
- [8] E. H. Linfoot and E. Wolf, *Proc. Phys. Soc. B* 66, 1953.
- [9] C. W. McCutchen, *Journal of Optical Society of America*. 54, pp. 240-244, 1964.
- [10] T.-C. Poon and M. Motamedi, "Optical/digital incoherent image processing for extended depth of field," *Applied Optics* 26, pp. 4612-4615 (1987)
- [11] S. Kawata et al., "Three-dimensional optical-transfer-function analysis for a laser-scan fluorescence microscope with an extended detector," *Applied Optics* 8, pp. 171-175, 1991.
- [12] T. Noda et al., "Three-dimensional phase contrast imaging by an annular illumination microscope," *Applied Optics* 29, pp. 3810-3815, 1990.

- [13] P.P. Banerjee and T.-C. Poon, "Self-Fourier objects and other self-transform objects: comments," *Journal of the Optical Society of America A* 12, pp.425-426, 1995.
- [14] A. Korpel, *Acousto-Optics*, Marcel Dekker, NY, 1988.

DNA and protein change in human breast tissues by diffuse reflectance spectrum

Yuanlong Yang*, Edward J. Celmer (MD)**, Jason A Koutcher (MD)*** P. P. Ho* and R. R. Alfano*

* Institute for Ultrafast Spectroscopy and Lasers. New York State Center for Advanced Technology for Ultrafast Photonic Materials and Applications. The City College, and Graduate School of the City University of New York. NY 10031.

**St. Vincent's Medical Center of Richmond, Department of Pathology, Staten Island, NY 10310-1699

***Memorial Sloan-Kettering Cancer Center, New York, N.Y.10021

ABSTRACT

Breast tissues were investigated using diffuse reflectance spectroscopy to yield the absorption spectrum from Kubelka-Munk Function (KMF). A specified spectral feature measured in adipose tissue was assigned to β -carotene, which can be used to separate fat from other molecular components in breast tissues. The peaks of (KMF) at 260nm and 280nm were attributed to DNA and proteins

Keywords: *Diffuse reflectance spectroscopy, Breast Cancer Diagnose, Optical biopsy DNA, proteins,*

1. INTRODUCTION

In our past work, the fluorescence, excitation and Raman spectra from native human breast tissues have been studied as a potential clinical tool for cancer diagnostic purposes. The critical parameters of certain intensity ratios at definite wavelengths in the fluorescence and excitation spectra have been used to separate malignant from benign tissue (1-4). Due to multiple photon scattering, direct measurement of absorption spectra of tissues by conventional transmission means is not easily done. The diffuse reflectance spectrum offers a way to obtain a measure of the absorption spectrum (5).

In this paper, the diffuse reflectance spectrum was measured from breast tissues. The Kubelka-Munk function was calculated to give information about the absorption spectrum. The spectral features of the Kubelka-Munk function of breast tissue were attributed to hemoglobin (oxygenated and deoxygenated hemoglobin), collagen, and β -carotene (it exists in adipose tissue), proteins and nucleic acid components.

2. MATERIALS

Excised benign, adipose, fibroadenoma and malignant breast tissue samples were obtained from St. Vincent Hospital, Memorial Sloan Kettering Cancer Center, and National Disease Research Interchange (NDRI). Specimens were neither chemically treated nor frozen prior to spectroscopic measurements. Samples of random shapes were mounted in a 1cm \times 1cm \times 5cm commercial quartz cuvette and closely attached to its inner surface for measurement of spectra. Usually, the spectra were measured at up to 3 different location of the sample. The malignant breast tissue specimens were classified into carcinoma *in situ*, infiltrating or invasive carcinoma, and mixed *in situ* and invasive (part *in situ* and part invasive) according to the pathology report. In this paper, 25 invasive carcinoma, 22 mixed *in situ* and invasive, 14 fibroadenoma, 44 benign, and 31 adipose specimens have been studied.

The diffuse reflectance, fluorescence, and excitation spectra were performed from same spot of the sample, using an automated dual lamp-based spectrophotometer (Mediscience Technology Corp. CD scanner.). The measurements of diffuse reflectance spectra were selected using synchronized scan mode, in which the emission and excitation monochromators were scanning on the same wavelengths synchronously. The diffuse reflectance spectrum was scanned from 250nm to 650nm.

As a reference standard, β -carotene crystal was obtained commercially from Sigma Co. The concentration of the carotene solution was 0.8 mg/ml. The small particles of Ti_2O_3 (0.2 μ) were added into carotene solution to enhance the scattering signal during diffuse reflectance measurements.

3. MODEL

Kubelka and Munk function was obtained from diffuse reflectance R_∞ is (6,7)

$$f \equiv (1-R_\infty)^2/2R_\infty = k/s, \quad (1)$$

The function f is the ratio of absorption to scattering coefficients.

Plotting $\log f$ against the wavelength for a particular sample, the curve obtained corresponds to the absorption spectrum of the compound with intercept displacement given by $-\log s$ in the ordinate axis.

4. RESULTS

The K-M function of typical malignant, fibroadenoma adipose and benign breast tissue displayed in Fig. 1. Some features can be found in the K-M curves of these tissues as shown in Fig. 1(b). No carotene peak at 480nm in K-M function of benign or malignant breast tissues is observed. The feature of β -carotene peak definitely appeared in adipose tissue. The peak near 280nm appeared for all kinds of tissue, but the amplitude was different. The amplitude of malignant was higher than fibroadenoma and benign tissue. This peak is corresponding to the absorption of proteins. The another peak near 265nm only appeared for malignant tissue. This peak is corresponding to the absorption of DNA. To prove this, the absorption spectra of

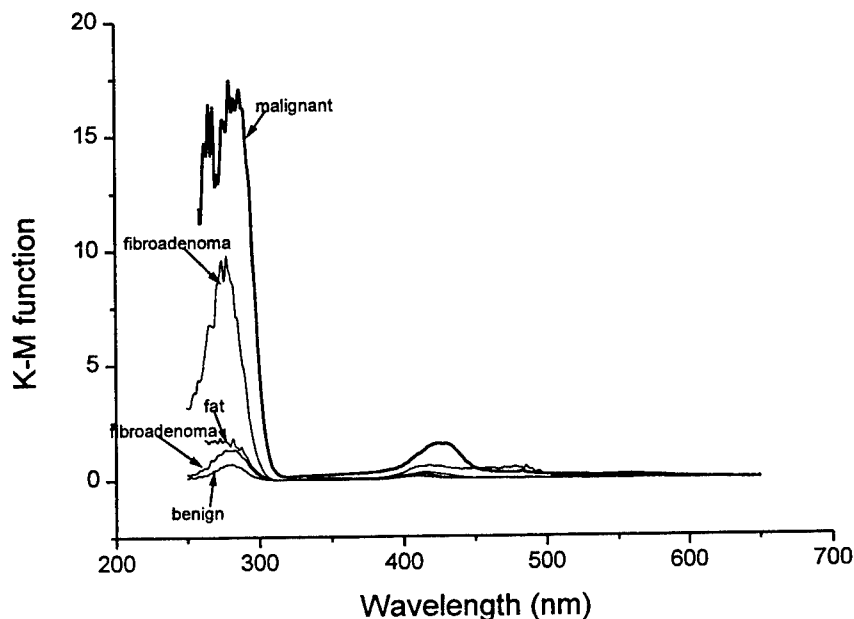


Figure 1: The Kubelka-Munk function of typical benign, malignant, fibroadenoma and adipose breast tissue.

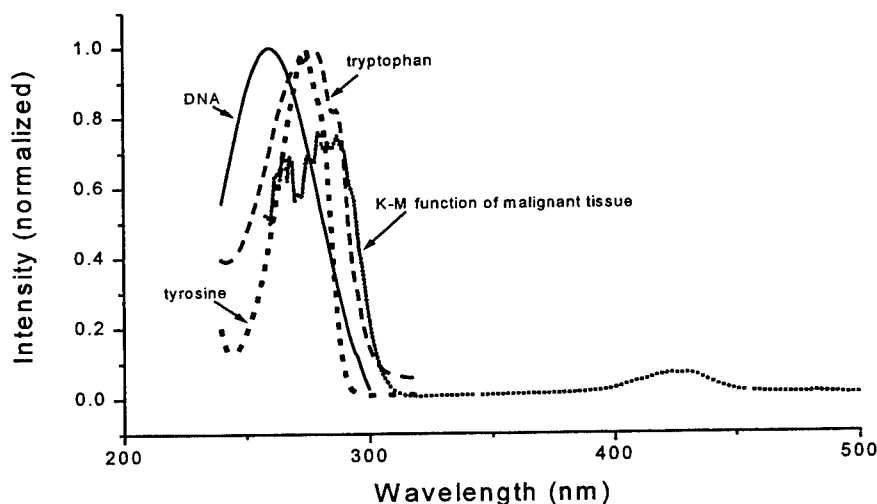


Figure 2: The absorption spectra of DNA, amino acid of tryptophan, tyrosine and K-M function of malignant breast tissue.

DNA, amino acids tryptophan and tyrosine were displayed in fig. 2. The K-M function of malignant tissue was also displayed in Fig. 2. It is clear that two peaks of malignant are overlap with the absorption peak of DNA and amino acids. For fibroadenoma, the peak of K-M curve near 280nm is uncertain. Some specimen was higher some was lower but less 265nm peak was existed as compared to malignant tissue.

Table 1: The averaged value of K-M function $f(r_\infty)$ and logarithm K-M function ($\log f(r_\infty)$) at 275nm–285nm and 255nm–265nm for different kinds of breast tissues.

Type of specimens	Averaged at 275nm to 285nm		Averaged at 255nm to 265nm	
	$f(r_\infty)$	$\log f(r_\infty)$	$f(r_\infty)$	$\log f(r_\infty)$
Invasive carcinoma	13.11±10.39	0.98±0.39	19.05±18.70	1.06±0.52
Mixed invasive and <i>in situ</i>	5.23±4.16	0.58±0.36	8.78±13.30	0.65±0.50
Benign	0.88±0.69	-0.15±0.29	0.66±0.70	-0.36±0.39
Fibroadenoma	5.23±5.69	0.48±0.46	3.62±4.41	0.24±0.56

Fibroadenomas are usually found in young women. It is a tumor composed of epithelial and stromal elements that originates from the terminal duct lobular unit. It is important to distinguish fibroadenoma from malignancy. From Table 1, it was found the averaged amplitude of $f(r_\infty)_{255\text{nm}-265\text{nm}}$ was higher than $f(r_\infty)_{275\text{nm}-285\text{nm}}$ for malignant tissue and lower for benign and fibroadenoma tissue. The another ratio parameter $A = [f(r_\infty)_{275\text{nm}-285\text{nm}}] \div [f(r_\infty)_{255\text{nm}-265\text{nm}}]$ was selected. The statistical averaged values, standard deviations and peak position of Gaussian fit curve of parameter A were given in Table 2.

Table 2. The averaged value of parameter $A = [f(r_\infty)_{275\text{nm}-285\text{nm}}] \div [f(r_\infty)_{255\text{nm}-265\text{nm}}]$ for different kinds breast tissues.

Type of specimens	$A = [f(r_\infty)_{275\text{nm}-285\text{nm}}] \div [f(r_\infty)_{255\text{nm}-265\text{nm}}]$	
	Statistical mean value and standard deviation	Gauss fit center and width
Invasive carcinoma	0.93±0.52	0.85±0.35
Mixed invasive and <i>in situ</i>	0.89±0.36	0.85±0.31
Benign	1.97±1.42	1.49±0.84
Fibroadenoma	1.82±0.56	1.64±0.48

5. CONCLUSION:

KMF function in UV spectral range was used to determine the absorption peak at 265nm and 285nm. The proteins and DNA absorption peak was observed in malignant tissues. For benign tissues, the absorption of proteins was lower and there was less DNA absorption. Furthermore, for fibroadenoma tissue, while protein absorption was sometimes in the range of malignant samples, but relative weaker DNA absorption was found. The KMF function gives information of DNA and proteins content in tissues.

6. ACKNOWLEDGEMENT:

We thank Dr. N. N. Zhadin, Dr. S. Gayen, and Mr. Wei Cai, and Mr. Guang Zhang for helpful discussions. Organized Research of CUNY, and DOE for support of this research, and Mediscience Technology Corp. help for the use of instrument.

7. REFERENCES:

1. R. R. Alfano, Das Bidyut B., Joseph Cleary, Romulo Prudente, Edward J. Celmer. "Light sheds light on cancer-distinguishing malignant tumor from benign tissue and tumors The Bulletin of the New York Academy of Medicine (1991). 67 143,
2. Yuanlong Yang, A. Katz, Edward J. Celmer, Margaret Zarawska-Szczepaniak, and R. R. Alfano. "Optical Spectroscopy of Benign and Malignant Breast Tissue." Lasers in the Life Sciences (1996) 7(2): 115-127

3. Yuanlong Yang, A. Katz, Edward J. Celmer, Magaret Zarawska-Szczepaniak, and R. R. Alfano. "Fundamental Differences of Excitation Spectrum between Malignant and Benign Breast Tissues" *Photochemistry and Photobiology* (1997) **66**(4): 518-522
4. Yuanlong Yang, Edward J. Celmer, Magaret Zarawska-Szczepaniak, and R. R. Alfano. "Excitation spectrum of malignant and benign breast tissues: A potential optical biopsy approach" *Lasers in the Life Sciences* (1997) **7**(4): 249-265
5. N. Zhadin, Y. Yang, S. Ganesan, N. Ockman, and R. R. Alfano. "Enhancement of the Fluorescence Cancer Diagnostic Method of Tissues Using Diffuse Reflectance and the Analysis of Oxygenation State." *SPIE Proceeding* (1996) **2697**: 142-148
6. Wesley, WM. Wendlandt and Harry G. Hecht, "Reflectance Spectroscopy" p. 55-65, Interscience Publishers (1966)
7. Kubelka P. "New contribution to the optics of intensely light-scattering materials. Part I" *J. of the Opt. Soc. Am.* **38**(5), 448-457, (1948)
8. P. Kubelka, and F. Munk. "Ein beitrage zur optik der farbanstriche" *Z. Tech. Phys* **12**, 593-604, (1931)

SESSION 4

Fluorescence and Multiphoton Microscopy and Spectroscopy I

Determination of a quantitative algorithm for the measurement of muscle oxygenation using CW near-infrared spectroscopy—Mean optical pathlength without the influence of adipose tissue—

Jun Shao^a, Ling Lin^b, Masatsugu Niwayama^a,
Nobuki Kudo^a, and Katsuyuki Yamamoto^{*a}

^aDivision of Biomedical Systems Engineering, Graduate School of Engineering,
Hokkaido Univ., North 13 West 8, Sapporo 060-8628, Japan

^bCollege of Precision Instruments and Optoelectronics Engineering,
Tianjin University, Tianjin 300072, P. R. China

ABSTRACT

Near-infrared spectroscopy (NIRS) is a useful technique for noninvasive measurement of oxygenation of the brain and muscle. However, no accurate, quantitative algorithms for continuous wave NIRS (CW-NIRS) have yet been presented due to the following two problems. The first is that inhomogeneous tissue structure greatly affects measurement sensitivity. We previously reported on the influence of a fat layer on muscle oxygenation measurement and proposed a method for correcting the sensitivity. The second problem is that almost all algorithms for CW-NIRS have been experimentally determined, although an algorithm can be theoretically determined on the basis of diffusion theory if the mean optical pathlength in muscle in an *in vivo* state is known. In this study, we derived basic equations for a CW-NIRS algorithm based on diffusion theory, and we determined linear and nonlinear algorithms from mean optical pathlengths and validated them by results obtained from phantom experiments. For the determination of pathlength, the absorption and scattering coefficients of the muscle must be obtained *by taking into account the influence of a fat layer*. Laser pulses of 752 and 871 nm were applied to the forearms of subjects, and the temporal point spread function (TPSF) was obtained by using a streak camera. The absorption and scattering coefficients of the muscle were determined by fitting the measured TPSF with that obtained by a Monte Carlo model consisting of skin, fat and muscle layers. From these coefficients, the mean optical pathlengths at two wavelengths were obtained and the algorithms were determined.

Keywords: NIRS, tissue oximeter, muscle, hemoglobin concentration, mean optical pathlength, time resolved spectroscopy

1. INTRODUCTION

In recent years, near-infrared spectroscopy (NIRS) has been used clinically as a noninvasive method for measuring tissue oxygenation. Among various techniques for NIRS, continuous wave (CW) NIRS is the simplest technique and it can be easily be applied to real-time monitoring, including a mapping system of tissue oxygenation. However, CW-NIRS only enables measurement of the relative change in oxygenation from an initial level. There have been many efforts to determine the absolute value of oxygenation using time-resolved spectroscopy, spatially resolved spectroscopy, and intensity modulated spectroscopy. However, even if these techniques are used to measure tissue oxygenation, quantitative measurement is difficult because of the inaccurate assumption that tissue is homogeneous.

Overlying tissues such as the skull and subcutaneous adipose tissue greatly affect the measurement sensitivity of NIRS. Therefore, changes in oxygenation, even from the initial level, can not be compared among subjects. As for muscle oxygenation measurement, Homma *et al.*¹ showed the influence of a fat layer by *in vivo* experiments using CW-NIRS. We²⁻⁵ have also verified from the results of *in vivo* measurements and Monte Carlo simulation that a strong correlation exists between fat layer thickness and measurement sensitivity. Based on the results of analyses of the influence of a fat layer, we have developed correction methods for measurement sensitivity using a detected light intensity or correction curves. After correcting the measurement sensitivity, we are able to obtain the change in absorption using an algorithm that assumes homogeneity of tissue.

*Correspondence: E-mail: yamamoto@bme.eng.hokudai.ac.jp; Phone: +81-11-706-6763; Fax: +81-11-706-7802

Most algorithms used for CW-NIRS are based on the modified Beer-Lambert law⁶, which assumes that the change in optical density is proportional to the change in absorption and that the proportional constant, mean optical pathlength, does not greatly vary when the change in absorption is small. Delpy and his group obtained a theoretical equation for determining this pathlength from a temporal point spread function (TPFS)⁶. However, an analytical solution, based on CW theory, for the determinations of the mean optical pathlength and the coefficients of an algorithm is not available. Furthermore, different algorithms that are experimentally determined are used at present and therefore these algorithms result in inconsistent measurements as pointed out by Matcher⁷.

In the present study, we theoretically derived algorithms, based on diffusion theory, for continuous wave (CW) spectroscopy to determine the change in tissue oxygenation and the algorithms were validated by the results of phantom experiments. The relationship between change in optical density and change in absorption is essentially nonlinear; therefore, algorithms with and without consideration of the nonlinear relationship were derived. Since the optical properties of muscle must be determined for obtaining the algorithms, we also measured absorption and scattering coefficients of muscle from a TPSF *by taking into account the influence of an overlying fat layer*.

2. THEORETICAL DERIVATION OF THE ALGORITHMS

2.1. Tissue oximetry with CW light

In NIRS, back-scattered light is detected at a distance from a light source, and tissue oxygenation is determined from the change in absorption coefficients of a tissue using a basic equation of conventional oximetry. Assuming that the change in absorption is mostly due to the change in blood oxygenation or volume, changes in the concentrations of oxy-hemoglobin ΔHbO_2 and deoxy-hemoglobin ΔHb can be determined as follows.

Change in the absorption coefficient of a tissue $\Delta\mu_a$ is expressed as

$$\Delta\mu_a = \varepsilon_{\lambda}^{HbO_2} \Delta HbO_2 + \varepsilon_{\lambda}^{Hb} \Delta Hb, \quad (1)$$

where $\varepsilon_{\lambda}^{HbO_2}$ and $\varepsilon_{\lambda}^{Hb}$ are molar extinction coefficients of HbO_2 and Hb at a wavelength of λ , respectively. The two unknowns, ΔHbO_2 and ΔHb , can be determined by solving simultaneous equations, which are obtained from measurements at two wavelengths.

$$\Delta HbO_2 = \frac{1}{k} (\varepsilon_2^{Hb} \Delta\mu_{a1} - \varepsilon_1^{Hb} \Delta\mu_{a2}), \quad (2)$$

$$\Delta Hb = \frac{-1}{k} (\varepsilon_2^{HbO_2} \Delta\mu_{a1} - \varepsilon_1^{HbO_2} \Delta\mu_{a2}), \quad (3)$$

$$k = \varepsilon_1^{HbO_2} \varepsilon_2^{Hb} - \varepsilon_1^{Hb} \varepsilon_2^{HbO_2}, \quad (4)$$

where the subscripts 1 and 2 indicate the wavelengths. The change in absorption $\Delta\mu_a$ is determined by various NIRS techniques; i.e., CW, spatially resolved, intensity-modulated and time-resolved spectroscopy. The CW method, which is the simplest, only enables determination of the change in absorption, whereas corresponding optical properties of absolute values can be obtained by using the other techniques. However, it is difficult to eliminate the effects of absorption other than that of hemoglobin, such as absorption of myoglobin. Therefore, only $\Delta\mu_a$ is usually measured in NIRS, assuming that the change in optical properties is only due to blood.

In CW-NIRS, change in optical density defined by $\Delta OD = \ln(R_0/R)$, where R_0 and R are intensities of back-scattered light at a reference state (usually taken at the start of measurement) and during the measurement, respectively, is measured. Assuming that the scattering coefficient does not change during the measurement, we can determine $\Delta\mu_a$ using the modified Beer-Lambert law⁶.

$$\Delta OD = \Delta \mu_a d, \quad (5)$$

where d is $d = \partial OD / \partial \mu_a$, which is defined as the differential pathlength and is equal to the mean optical pathlength⁶. In the next section, we will present a theoretical equation for determining d , based on CW theory.

2.2. Derivation of an algorithm based on linear approximation

Intensity of back-scattered light $R(\rho)$ at a distance ρ from a CW light source in a semi-infinite medium is given by the following solution⁸, which is obtained from the optical diffusion equation.

$$R(\rho) = \frac{1}{a\mu'_t} \left(\mu_{eff} + \frac{1}{\rho} \right) \frac{e^{-\mu_{eff}\rho}}{\rho^2}, \quad (6)$$

$$\mu'_t = \mu_a + \mu'_s, \quad (7)$$

$$\mu_{eff} = \sqrt{3\mu_a(\mu_a + \mu'_s)}, \quad (8)$$

where a is a constant. From equation (6), the change in optical density (base e) is given by

$$\Delta OD = \ln \frac{R_0(\rho)}{R(\rho)} = \rho(\mu_{eff} - \mu_{eff}^0) - \left\{ \ln(1 + \rho\mu_{eff}) - \ln(1 + \rho\mu_{eff}^0) \right\}, \quad (9)$$

where $R_0(\rho)$ and μ_{eff}^0 are $R(\rho)$ and μ_{eff} in a reference state, respectively. Since it holds in tissues that $\mu_a \ll \mu'_s$, μ_{eff} can be approximated by

$$\mu_{eff} = \sqrt{3\mu_a(\mu_a + \mu'_s)} \approx \sqrt{3\mu_a\mu'_s}. \quad (10)$$

From the definition of a differential pathlength and equations (9) and (10), mean optical pathlength d is derived as follows.

$$d = \frac{\partial \Delta OD}{\partial \mu_a} = \frac{\partial \Delta OD}{\partial \mu_{eff}} \frac{\partial \mu_{eff}}{\partial \mu_a} = \frac{\rho^2 \mu_{eff}}{1 + \rho\mu_{eff}} \frac{3\mu'_s}{2\sqrt{3\mu_a\mu'_s}} = \rho' \frac{3\mu'_s}{2\mu_{eff}} = \rho' \frac{\mu_{eff}}{2\mu_a}, \quad (11)$$

$$\rho' = \frac{\rho^2 \mu_{eff}}{1 + \rho\mu_{eff}}. \quad (12)$$

According to equation (11), d depends on the optical properties of a tissue. In actual measurement, μ'_s can be regarded as a constant, but μ_a changes. Thus, equation (5) does not strictly hold but is linearly approximated around an operating point on the assumption that the change in μ_a is small. When the linear approximation is valid, we can obtain the following theoretical algorithm for the determination of ΔHbO_2 and ΔHb from equations (2) to (5).

$$\Delta HbO_2 = \frac{1}{k} \left(\frac{\varepsilon_2^{Hb} \Delta OD_1}{d_1} - \frac{\varepsilon_1^{Hb} \Delta OD_2}{d_2} \right), \quad (13)$$

$$\Delta Hb = \frac{-1}{k} \left(\frac{\varepsilon_2^{HbO_2} \Delta OD_1}{d_1} - \frac{\varepsilon_1^{HbO_2} \Delta OD_2}{d_2} \right), \quad (14)$$

where d_1 and d_2 are mean optical pathlengths determined by equation (11) at wavelengths 1 and 2, respectively. These equations are similar to conventional ones used for two-wavelength transmission spectroscopy, in which $d=d_1=d_2$, but this does not hold in a reflection method. Moreover, d_1 and d_2 should be determined with consideration to the absorption of

tissue other than that of blood. In other words, the mean optical properties of measured tissue around an operating point (in a reference state) are necessary for the determination of d_1 and d_2 . If these pathlengths are known, coefficients of the algorithm can be determined.

2.3. Nonlinear algorithm

The calculation error of the linear approximation can not be ignored when $\Delta\mu_a$ is large. In this section, we derive theoretical equations that take into account the nonlinear relationship between optical density and absorption. The equation that we need is a function of ΔOD that gives $\Delta\mu_a$. Since equation (9) is an implicit function of μ_{eff} , which is a function of μ_a , some approximation is needed in order to derive the algorithm. Taylor expansion gives the following relationship when we ignore the high-order terms above the second derivative; the second-derivative term was less than 2% of the first-derivative one, as confirmed by substituting typical values into each term, assuming that μ_{eff} increases by 50%.

$$\begin{aligned}\Delta OD &\approx \Delta OD(\mu_{eff}^0) + \frac{\partial \Delta OD}{\partial \mu_{eff}} \Delta \mu_{eff} \\ &= \rho \Delta \mu_{eff} - \frac{\rho \Delta \mu_{eff}}{1 + \rho \mu_{eff}^0} \\ &= \frac{\rho^2 \mu_{eff}^0}{1 + \rho \mu_{eff}^0} \Delta \mu_{eff} \\ &= \rho' \Delta \mu_{eff}\end{aligned}\quad (15)$$

This equation means that ΔOD is not proportional to $\Delta\mu_a$ but simply proportional to $\Delta\mu_{eff}$. Substituting $\mu_{eff} = \mu_{eff}^0 + \Delta\mu_{eff}$ and $\mu_a = \mu_a^0 + \Delta\mu_a$ into equation (10), $\Delta\mu_a$ can be expressed by the second-order equation of $\Delta\mu_{eff}$:

$$1 + \frac{\Delta \mu_{eff}}{\mu_{eff}^0} = \sqrt{1 + \frac{\Delta \mu_a}{\mu_a^0}}, \quad (16)$$

$$\Delta \mu_a = \left\{ 2 \frac{\Delta \mu_{eff}}{\mu_{eff}^0} + \left(\frac{\Delta \mu_{eff}}{\mu_{eff}^0} \right)^2 \right\} \mu_a^0. \quad (17)$$

From equations (15) and (17), we obtain

$$\Delta \mu_a = \left(1 + \frac{1}{4\mu_a} \frac{\Delta OD}{d} \right) \frac{\Delta OD}{d}. \quad (18)$$

The first term of this equation is equivalent to equation (5), and the second term represents the nonlinear relationship. The equation for determining ΔHbO_2 and ΔHb can be obtained by substituting the above equation into equations (2) and (3).

$$\Delta HbO_2 = \frac{1}{k} \left(\varepsilon_2^{Hb} \left(1 + \frac{1}{4\mu_{a1}} \frac{\Delta OD_1}{d_1} \right) \frac{\Delta OD_1}{d_1} - \varepsilon_1^{Hb} \left(1 + \frac{1}{4\mu_{a2}} \frac{\Delta OD_2}{d_2} \right) \frac{\Delta OD_2}{d_2} \right), \quad (19)$$

$$\Delta Hb = \frac{-1}{k} \left(\varepsilon_2^{HbO_2} \left(1 + \frac{1}{4\mu_{a1}} \frac{\Delta OD_1}{d_1} \right) \frac{\Delta OD_1}{d_1} - \varepsilon_1^{HbO_2} \left(1 + \frac{1}{4\mu_{a2}} \frac{\Delta OD_2}{d_2} \right) \frac{\Delta OD_2}{d_2} \right). \quad (20)$$

3. PHANTOM EXPERIMENTS

3.1. Materials and methods

In order to validate the theoretically derived algorithms, we performed phantom experiments using the apparatus shown in Fig. 1. The apparatus consisted of a phantom, a driver and a light source, a detector and an amplifier, and a computer. The construction of this apparatus is only described simply below since it is almost the same as that of a previously reported one⁴.

As the light source, a two-wavelength light-emitting diode (LED, 840 and 760 nm) was used. Back-scattered light was detected by a photodiode (Hamamatsu Photonics, S2386-45K) at a distance of 30 mm from the LED. The phantom consisted of 1% Intralipid solution suspended in phosphate-buffered saline (PBS), into which bovine hemoglobin solution was gradually added. The reduced scattering coefficient of the Intralipid suspension was determined by TPSF, which was measured by a pulsed laser (Hamamatsu Photonics, PLP-02, 752 nm) and a streak camera (Hamamatsu Photonics, C4334): $\mu'_s = 0.85 \text{ mm}^{-1}$. The size of the tank for the phantom was $15 \times 14 \times 12.5 \text{ cm}^3$, and the volume of solution used in the experiments was about 1500 ml. Three experiments were conducted under the following conditions.

Experiment 1: The relationship between changes in OD and concentrations of fully oxygenated hemoglobin was obtained. Concentration of hemoglobin solution of the phantom was varied from 0 to 0.1 mM by adding this solution to the phantom in steps of 0.008 mM using a micropipette. Oxygen gas was bubbled into the phantom to ensure full oxygenation, which was confirmed by using a blood gas analyzer (Ciba-Corning, Model 170); the calculated oxygen saturation of hemoglobin was more than 99%.

Experiment 2: The same experiment as that of above was conducted under the condition of a fully deoxygenated state. Five grams of yeast, suspended in the phantom, was used to make a fully deoxygenated state. When the hemoglobin solution was added, the phantom solution was sufficiently stirred to ensure complete oxygen consumption by the yeast. The blood gas analyzer was also used to confirm that a fully deoxygenated state had been achieved.

Experiment 3: Oxygen saturation was varied while the hemoglobin concentration was fixed at 0.054 mM (1% of corresponding hematocrit). The phantom was first bubbled with oxygen gas and then bubbled with nitrogen gas to vary the oxygen saturation of hemoglobin, which was also measured by the blood gas analyzer.

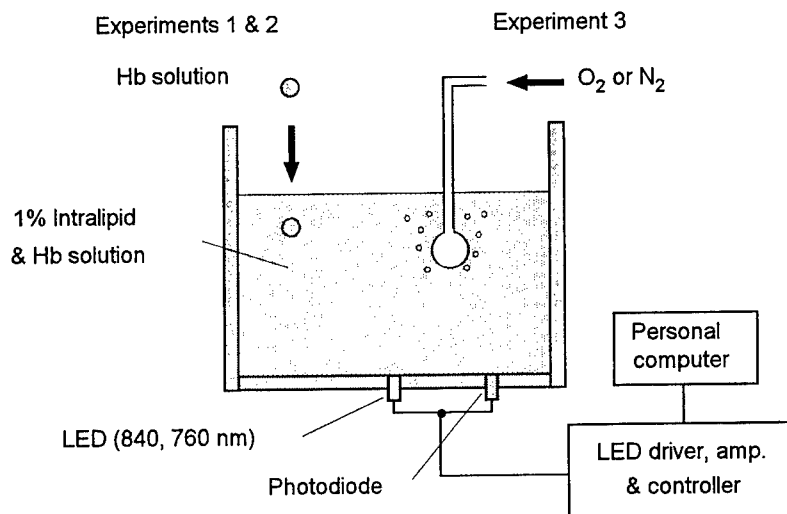


Fig. 1 Experimental apparatus using a tissue-mimic phantom. Changes in optical density with addition of hemoglobin solution were measured under fully oxygenated and deoxygenated states in experiments 1 and 2, respectively. In experiments 3, oxygen saturation was varied while the hemoglobin concentration was fixed.

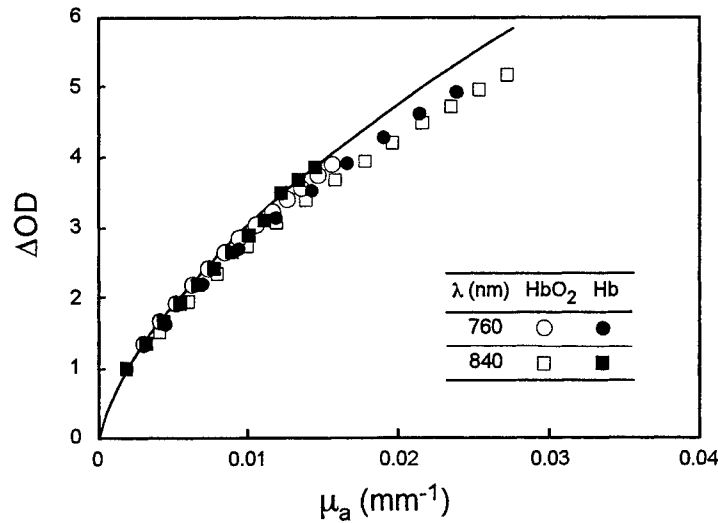


Fig. 2 Relationship between change in optical density and absorption coefficient of the phantom. Results of experiments 1 and 2, denoted by HbO₂ and Hb, respectively, were plotted.

3.2. Experimental results

In order to compare the experimental results with the theoretical values, all of the results of experiments 1 and 2 were plotted against the absorption coefficient, which was calculated from the molar extinction coefficient of hemoglobin⁷ and its concentration (Fig. 2). Absorption of water (0.003 mm⁻¹) was also taken into account, and the reference state of the change in optical density was set to be theoretically zero in absorption; therefore, the experimental results were shifted upward so that the first point of the plotted results of each experiment before addition of the hemoglobin solution was consistent with the theoretical curve, which is indicated by a solid line. As shown in Fig. 2, the experimental results agreed well with the theoretical curve, which was obtained from equation (9).

3.3 Evaluations of theoretical CW-NIRS algorithms

The algorithms for obtaining ΔHbO_2 and ΔHb , equations (13) and (14) and equations (19) and (20), were evaluated by comparing calculated concentrations with those set in the experiments. When calculating the concentrations, we need the mean optical pathlengths d_1 and d_2 at an operating point in order to determine the coefficients of the algorithm. In the evaluation using the results of experiments 1 and 2, we set the operating point on 0.054 mM of hemoglobin concentration, assuming that equivalent hematocrit of a muscle tissue is 1%. In experiment 3, in which oxygen saturation was varied, we chose 70% saturation as the operating point. The corresponding optical pathlengths for each experiment were thus determined from equations (11) and (12) using absorption and scattering coefficients of the phantom.

Figure 3 shows the results obtained by equations (13) and (14) that were based on linear approximation. The abscissa is the hemoglobin concentration, which was set in experiments 1 and 2 or calculated from oxygen saturation measured in experiment 3. The straight line in each figure is a line of identity. The calculated concentrations agree well with those obtained from the experiments around the operating points. However, in regions far from these points (change in hemoglobin concentration > about 0.02 mM in experiments 1 and 2), significant deviations occurred due to the linear approximation. Compared to this, the calculated concentrations using equations (19) and (20) agreed well with those obtained from the experiments even when there was a large change in absorption, as shown in Fig. 4.

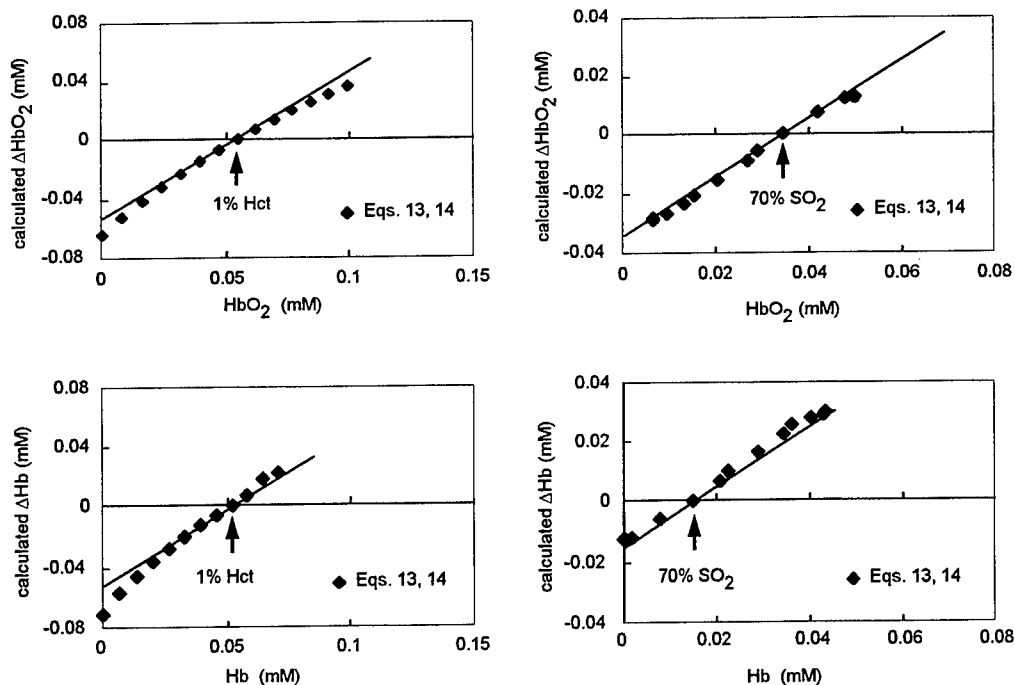


Fig. 3 Changes in hemoglobin concentration calculated from equations 13 and 14. The abscissa is hemoglobin concentration set in the experiments. The straight line in each figure is a line of identity. Upper left: experiment 1; lower left: experiment 2; right: experiment 3. Arrows indicate operating points chosen for the calculation.

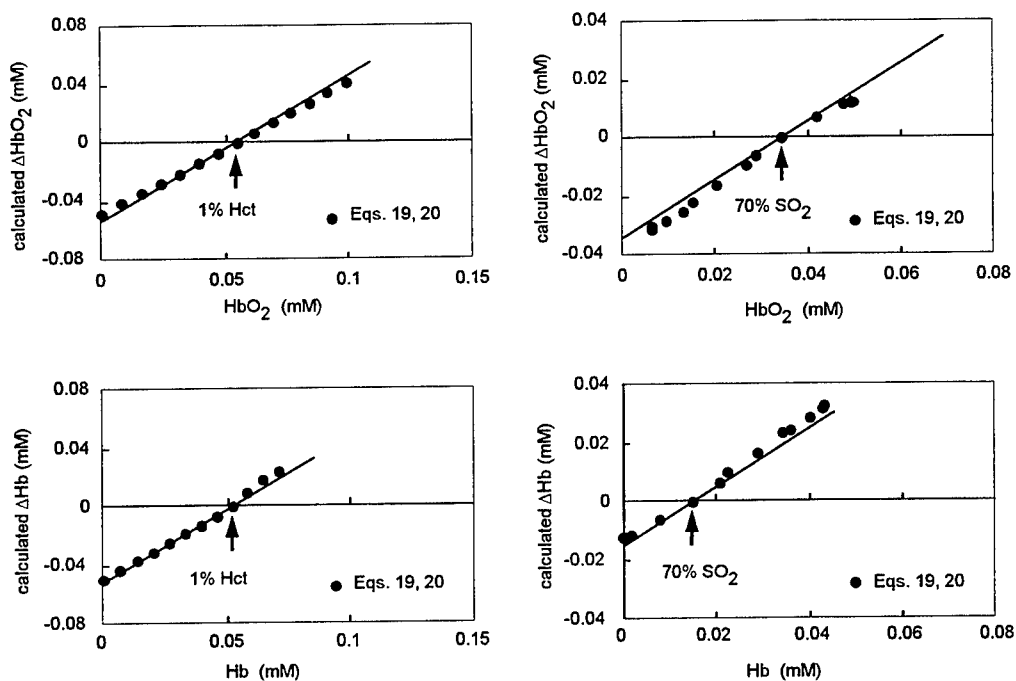


Fig. 4 Changes in hemoglobin concentration calculated from equations 19 and 20. The abscissa is the hemoglobin concentration set in the experiments. The straight line in each figure is a line of identity. Upper left: experiment 1; lower left: experiment 2; right: experiment 3. Arrows indicate operating points chosen for the calculation.

4. DETERMINATIONS OF *IN VIVO* OPTICAL PROPERTIES OF MUSCLE AND CW-NIRS ALGORITHM

Our final goal was to determine the coefficients of algorithms that can be applied to *in vivo* measurements. If the absorption coefficient of the muscle does not greatly vary during measurements and among subjects, we can determine coefficients of the algorithms. For accurate determination of pathlength, the optical properties of muscle must be obtained by eliminating the influence of a fat layer. However, there have only been a few studies⁹ on these properties.

4.1. Materials and methods

4.1.1. Instrumentation

Pico-second pulsed lasers (Hamamatsu Photonics, PLP-02, 50-ps FWHM, wavelengths of 752 and 871 nm) and a streak camera (Hamamatsu Photonics, C4334) were used to measure the TPSF of back-scattered light from tissues (Fig.5). The optical arrangement is shown in Fig. 4. An optical fiber of 200 μm in core diameter was coupled to the laser, and light pulses were guided to a skin surface. The photons back-scattered from the tissues were collected by an optical fiber bundle of 1.6 mm in diameter and fed into the streak camera. Fibers were arrayed in line at the end of the bundle that was connected to the streak camera; thus, the signal-to-noise ratio was substantially improved. Photons were counted while the pulsed light was emitted at a repetition rate of 1 MHz, and temporal profile data were stored in a computer.

The separation between the source fiber and the detector fiber was 15 mm for adipose measurements on the abdomen and 25 mm for muscle measurements on the forearm. The instrument function was measured after each measurement by placing the source and detector fibers close to each other. To reduce light intensity, an attenuator was placed between both fiber ends. The obtained instrument function was used to deconvolute the measured TPSFs yielding the corrected reflectance.

4.1.2. *In vivo* measurements and data analysis

Measurements on the abdomen were performed to obtain μ_a and μ_s' of adipose tissue in three males, whose fat layer thicknesses of the abdomen were about 20 mm. The fibers were fixed longitudinally with respect to the abdominal wall. A separation of 15 mm of the source-detector fibers was chosen so as to be less than the thickness of the fat layer. Measurements on the forearms of four males and one female were also carried out to determine μ_a and μ_s' of the muscle. The fibers were in contact with the extensor site of the right forearm placed on a desk. The separation of the source and

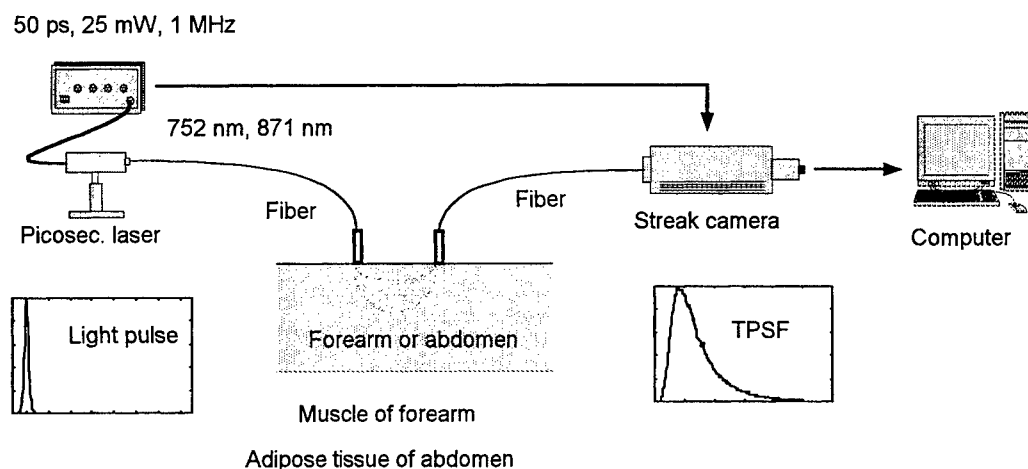


Fig. 5 Experimental setup for the measurement of TPSF.

detector fibers was 25 mm.

Absorption and reduced scattering coefficients were determined by fitting the measured TPSFs with those obtained by Monte Carlo simulation, which consisted of the skin, fat and muscle layers. The thickness of the fat layer of the model was set to be the same as that measured on each subject using ultrasonography. Coefficients μ_a and μ_s' of the skin were taken from the literatures^{9,10}. First, the coefficients of the adipose tissue were determined using the TPSFs measured on the abdomens. After updating the optical properties of a fat layer of the model, μ_a and μ_s' of the muscle layer in each subject were determined by repeating the simulation.

4.2. Results

4.2.1. Optical properties of adipose and muscle tissues

Figure 6 (a) shows an example of the TPSF measured on the abdomen of one of the subjects at 752 nm. The TPSF obtained from the Monte Carlo simulation is also depicted by a solid line in this figure. The values of μ_a determined for the adipose tissue were 0.003–0.004 mm⁻¹ at both wavelengths, and those of μ_s' were 1.1–1.15 mm⁻¹ at 752 nm and 0.98–1.1 mm⁻¹ at 871 nm. From these values, we chose the following values and used them in the simulation for determining the optical properties of muscle: μ_a =0.003 mm⁻¹ and μ_s' =1.1 mm⁻¹ at 752 nm, and μ_a =0.004 mm⁻¹ and μ_s' =1.0 mm⁻¹ at 871 nm.

Figure 6 (b) shows an example of the TPSF obtained from the forearm at 752nm. Table 1 shows μ_a and μ_s' of the forearm determined from the TPSF of each subject. As summarized in Table 1, μ_a and μ_s' of muscle determined in this study show only a small variation regardless of the thickness of the fat layer. These results indicate that the optical properties of muscle without the influence of a fat layer can be determined using by our method, although the uniqueness of a combination of μ_a and μ_s' must be quantitatively examined in further studies.

4.2.2. CW-NIRS algorithm

Using the mean values of μ_a and μ_s' shown in Table 1, we obtained the mean optical pathlengths of 110 and 98 mm at 752 and 871 nm, respectively. Substituting these pathlengths and the absorption coefficients into equations (19) and (20), the nonlinear algorithm is readily obtained. Before applying this algorithm to measured ΔOD , it must be corrected by the thickness of the fat layer. The corrected ΔOD is thus equivalent to ΔOD , which is observed in a homogeneous muscle tissue.

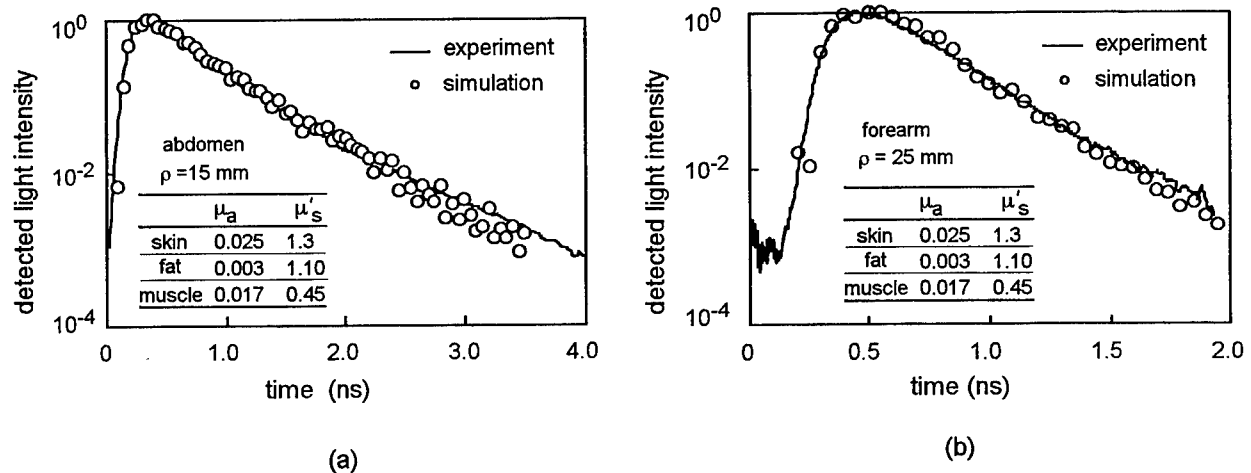


Fig. 6 Profiles of the TPSF measured on the abdomen (a) and forearm (b) of one of the subjects at 752 nm. Solid lines indicate fitting curves obtained from Monte Carlo simulation, in which absorption and scattering coefficients listed in tables were used.

Table 1 Optical properties of muscles obtained from *in vivo* measurements on the forearms of 5 subjects.

subject	h_f (mm)	μ_a (mm ⁻¹)		μ_s' (mm ⁻¹)	
		752 nm	871 nm	752 nm	871 nm
1	3.2	0.017	0.019	0.45	0.40
2	5.1	0.019	0.021	0.46	0.42
3	4.2	0.019	0.021	0.46	0.41
4	2.3	0.017	0.020	0.44	0.40
5*	2.8	0.015	0.017	0.45	0.42
mean \pm	3.5 \pm	0.017 \pm	0.020 \pm	0.45 \pm	0.41 \pm
SD	1.1	0.001	0.002	0.008	0.01

*female

Therefore, an algorithm based on tissue homogeneity can be applied to corrected ΔOD , and the quantitative change in oxygenation can be obtained.

However, there are some limitations to CW-NIRS. The optical properties around an operating point must be known in advance. If these are known, ΔHbO_2 and ΔHb can be accurately estimated by using the nonlinear algorithm, as was verified by the results of the phantom experiments, but the values known before measurement are average values of different subjects. Lin et al.¹¹ estimated that the error of linear approximation is less than 10% when the operating point of μ_a is inappropriately set by ± 0.005 mm⁻¹ from a true value and that this error is much less than that resulting from the influence of fat layer. The error, when using the nonlinear algorithm, is much smaller than that of linear approximation, only if an adequate operating point is obtained. If not, the error might not be substantially improved even by the nonlinear algorithm.

One of the most practical solutions to the above-mentioned problem is to introduce spatially resolved (SR) NIRS, which gives the absolute value of μ_a if μ_s' is known. CW-NIRS and SR-NIRS are much more simplified and definitely less costly than intensity-modulated or time-resolved spectroscopy, although these sophisticated techniques enable the determination of both μ_a and μ_s' . In addition, real-time monitoring is possible only by using CW-NIRS or SR-NIRS, as inferred from the actual tedious procedures for obtaining μ_a and μ_s' described in the previous section. Complementary *in vivo* studies on the optical properties of tissues under various conditions using these different techniques should lead to realization of more quantitative measurement of tissue oxygenation using NIRS.

5. CONCLUSIONS

Equations for CW-NIRS algorithms using linear approximation and taking into account the nonlinear relationship between change in optical density and change in absorption coefficient were derived using the theoretical mean optical pathlength. The validity of these theoretical algorithms was examined on the basis of results obtained by phantom experiments. It was verified that the nonlinear algorithm is applicable to a wider range of absorption coefficients than is the linear algorithm if the initial operating point is appropriately given. To determine coefficients of the algorithms, the optical properties of muscle were measured using time-resolved spectroscopy by taking into account the influence of an overlying fat layer. In spite of the preliminary nature of our study, absorption and scattering coefficients were successfully obtained regardless of different thicknesses of the fat layer, and the coefficients of the algorithms were determined.

ACKNOWLEDGMENT

This research was supported in part by Grant-in-Aid for Scientific Research from the Ministry of Education, Science and Culture of Japan.

REFERENCES

1. S. Homma, T. Fukunaga, and A. Kagaya, "Influence of adipose tissue thickness on near infrared spectroscopic signal in the measurement of human muscle," *J. Biomedical Optics.*, **1**, pp. 418-424, 1996.
2. K. Yamamoto, M. Niwayama, T. Shiga, L. Lin, N. Kudo, and M. Takahashi, "Accurate NIRS measurement of muscle oxygenation by correcting the influence of a subcutaneous fat layer," *Proc. SPIE*, **3194**, pp. 166-173 1998.
3. K. Yamamoto, M. Niwayama, T. Shiga, L. Lin, N. Kudo, and M. Takahashi, "A near-infrared muscle oximeter that can correct the influence of a subcutaneous fat layer," *Proc. SPIE*, **3257**, pp. 145-155, 1998.
4. L. Lin, M. Niwayama, T. Shiga, N. Kudo, M. Takahashi, and K. Yamamoto, "Two-layered phantom experiments for characterizing the influence of a fat layer on measurement of muscle oxygenation using NIRS," *Proc. SPIE*, **3257**, pp. 156-166, 1998.
5. M. Niwayama, L. Lin, J. Shao, T. Shiga, N. Kudo, and K. Yamamoto, "Quantitative measurement of muscle oxygenation by NIRS: Analysis of the influences of a subcutaneous fat layer and skin," *Proc. SPIE*, **3597**, pp. 291-299, 1999.
6. D. T. Delpy, M. Cope, P. Zee, S. Arridge, S. Wray, and J. Wyatt, "Estimation of optical pathlength through tissue from direct time of flight measurement," *Phys. Med. Biol.*, **33**: 1433/1442 (1988)
7. S. J. Matcher, C. E. Elwell, C. E. Cooper, M. Cope, and D. T. Delpy, "Performance comparison of several published tissue near-infrared spectroscopy algorithms," *Analytical Biochemistry*, **227**, pp. 54-68, 1995.
8. H. Liu, D. A. Boas, Y. Zhang, A. G. Yohd and B. Chanc, "Determination of optical properties and blood oxygenation in tissue using continuous NIRS light," *Phys. Med. Biol.*, **40**, 1983/1993 (1995)
9. A. Kienle, L. Lilge, M. S. Patterson, B. C. Wilson, R. Hibst and R. Steiner, "Investigation of Multi-Layered Tissue with *In-vivo* Reflectance Measurements," *Proc. SPIE*, **2326**, pp. 212-221, 1994.
10. C. R. Simpson, M. Kohl, M. Essenpreis and M. Cope, "Near-infrared optical properties of *ex vivo* human skin and subcutaneous tissues measured using the Monte Carlo inversion technique," *Phys. Med. Biol.* **43**: 2465-2478, 1998.
11. L. Lin, M. Niwayama, T. Shiga, N. Kudo, M. Takahashi and K. Yamamoto, "Influence of a fat layer on muscle oxygenation measurement using near-IR spectroscopy: quantitative analysis based on two-layered phantom experiments and Monte Carlo simulation," *Frontiers Med. Biol. Engng.*, **10** (in press).

Multi-photon fluorescence spectroscopy of fluorescent bio-probes and bio-molecules

Ping-chin Cheng¹, Bai-Ling Lin^{2*}, Fu-Jen Kao^{3,6*}, Chi-Kuang Sun^{4*}, Yung-Sheng Wang³, Tzu-Ming Liu⁴, Yi-min Wang³, Jian-cheng Chen³, Mao-Kuo Huang³, I. Johnson^{5*}

¹AMIL, Department of Electrical Engineering, State University of New York, Buffalo, NY 14260 USA

²Institute of Molecular Biology, Academia Sinica, Taipei, Taiwan, Rep. of China

³Department of Physics, National Sun Yat-sen University, Kaohsiung, Taiwan, Rep. of China

⁴Department of Electrical Engineering, National Taiwan University, Taipei, Taiwan, Rep. of China

⁵Molecular Probes Inc., Eugene, OR, 97402, USA

⁶Center for Neuroscience, National Sun Yat-sen University, Kaohsiung 80424, Taiwan, Rep. of China

ABSTRACT

Multi-photon fluorescence spectra of a number of commonly used biological probes were measured in this study. Significant spectral variation has been detected between single and multi-photon excitation. The result is important for the proper selection of spectral setting/ dichroic beam splitter in the set-up of a multi-photon fluorescence microscope. The information can also be useful in the detection of multi-photon fluorescence in bio-chip technology. In addition, we have investigated a few highly fluorescent bio-molecules commonly found in plant cells.

Keywords: Multi-photon fluorescence spectroscopy, two-photon, three-photon, fluorescence probes, biological probes, auto-fluorescence, bio-chip

1. INTRODUCTION

Fluorescent probes are commonly used in biological fluorescence microscopy for tracking specific structures and subcellular compartments, for measuring cellular ionic conditions and for indication of cell survival. For instance, FITC is routinely used to tag antibodies to localize specific antigen; Indo-1 is used to measure the Ca^{++} concentration within a cell and Calcein is used as an indicator for the integrity of the cell membrane. Recent development in multi-photon fluorescence microscopy has greatly expanded the usage of these fluorescent probes in biomedical research. Considering its non-linear nature, two-photon excitation may generate very different fluorescence spectral response in the sample when compared with single photon excitation¹⁻⁴. It is thus necessary to measure the two-photon spectra of various fluorescent probes, so that two-photon fluorescence microscopy may be performed effectively and the images properly interpreted. Knowledge on the fluorescent properties of these dyes is also required for bio-chip technology. This report represents the third installment of a continued effort in characterizing the multi-photon fluorescence spectra of some commonly used bio-probes^{3,6}. In addition, the auto-fluorescence in biological specimen frequently contributes to background noise in fluorescence microscopy and in bio-chip signal detection, thus characterization of the two-photon fluorescence properties of bio-molecules is necessary.

2. MATERIALS AND METHODS

1. Optical set-up

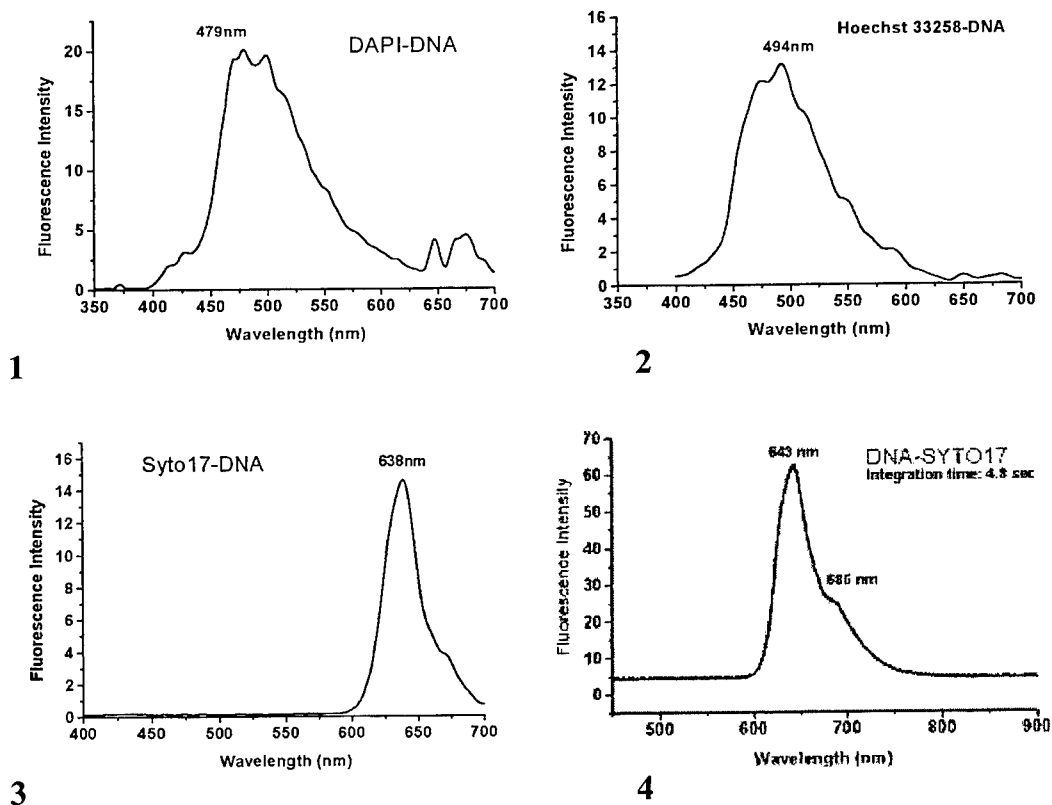
Two-photon fluorescence spectra excited with near infrared at 780nm were obtained with a SpectraPro-500 spectrophotometer (Acton Research) equipped with a TE-cooled PMT and coupled to a Spectra-Physics Tsunami Ti:sapphire laser pumped by a Coherent Verdi solid-state laser operated at 82MHz, 100fs pulse. The 1240nm infrared (IR) excitation was obtained from a Spectra-Physics Millennia IR (1064nm) pumped Chromium-doped Forsterite laser (built by CKS)⁷ operated at 120MHz, 130fs pulse. A cooled CCD array spectrophotometer (Acton Research) was used for spectral detection. An

* Corresponding authors: B. L. Lin (biology), F. J. Kao and C. K. Sun (optics)

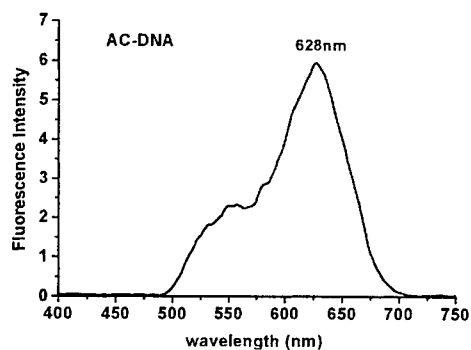
Olympus BX microscope trinocular head and an epi-fluorescence beam-splitter housing were modified for the measurements. A 740nm dichroic beam splitter was used for separating the excitation beam and the fluorescence emission. In addition, two IR cut-off filters (Edmond Scientific, Cat. K53-710) were installed in front of the entrance slit of the monochromator to reject scattered IR from the sample. A 4x microscope objective was used to focus the pump beam into a 0.3ml microfuge tube. For DNA probes, 2 μ M dye in the presence of 160 μ g/ml fragmented salmon sperm DNA in TE buffer (10mM Tris, 1mM EDTA, pH7.4)Fluorescence samples were prepared for spectral analysis. Methanol was used as solvent for MitoTracker and LysoTracker. Aqueous solutions of riboflavin, NADH and NADPH and acetone solution of chlorophyll a and chlorophyll b were used in this study.

3. RESULT AND DISCUSSION

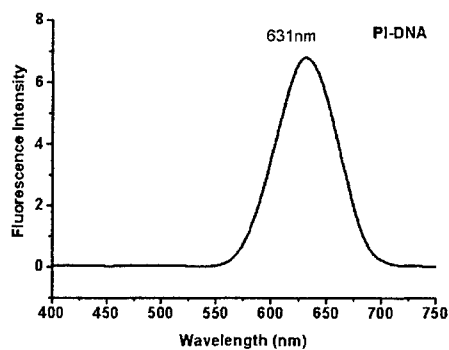
Figures 1- 12 show two-photon pumped fluorescence spectra of seven commonly used DNA-probes. Measurements of DAPI (Fig. 1), Hoechst 3258 (Fig. 2), Syto 17 [Fig. 3 (Ex=780nm) and Fig. 4 (Ex=1240nm)], Acridine Orange (Figure 5), Propidium Iodide (Figure 6), and Ethidium bromide (Figure 7) were performed with 2 μ M dye in the presence of 160 μ g/ml fragmented salmon sperm DNA in TE buffer (10mM Tris, 1mM EDTA, pH7.4). This concentration approximates 50 base pairs of DNA per dye molecule. In addition, methanol solutions of MitoTracker® (Molecular Probe M-7512; Fig. 8 and LysoTracker Red® (Molecular Probe L-7528; Fig. 9) were used in the measurement. Spectra in Figures 8 and 9 were excited with IR at 1240nm, therefore, the MitoTracker emission is the result of three-photon excitation, while the spectrum of LysoTracker is a mixed result of two and three-photon excitation. Table1 summarize the emission maximum of the above mentioned dyes and compare with single-photon emission maximum published by Molecular Probes Inc. Figure 10-12 show two-photon excited fluorescence spectra of riboflavin (Fig. 10), NADH (Fig. 11) and NADPH (Fig. 12). Table 2 summarize the emission maximum of riboflavin, NADH, NADPH, chlorophyll a and chlorophyll b..



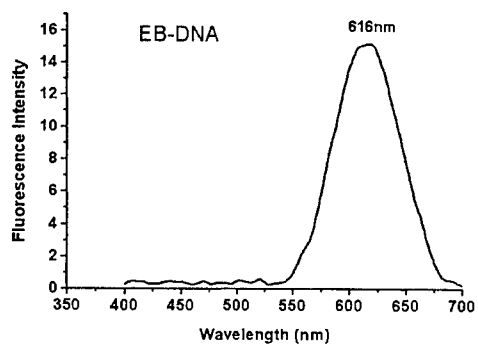
Figures 1-4. Two-photon pumped fluorescence spectra of DAPI [Figure 1 (Ex=780nm)], Hoechst 33258 [Figure 2 (Ex=780nm)], SYTO 17 [Figure 3 (Ex=780nm), Figure 4 (Ex=1240nm)].



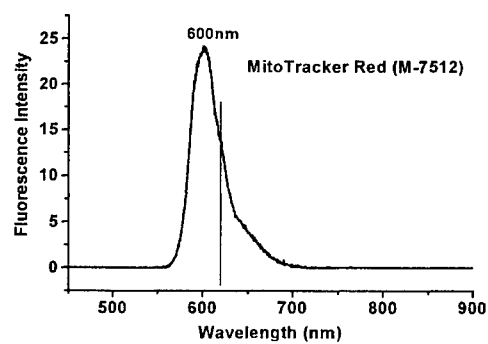
5



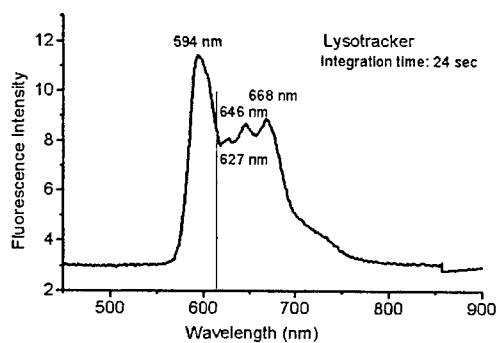
6



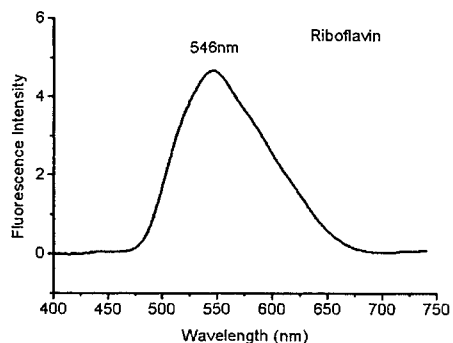
7



8

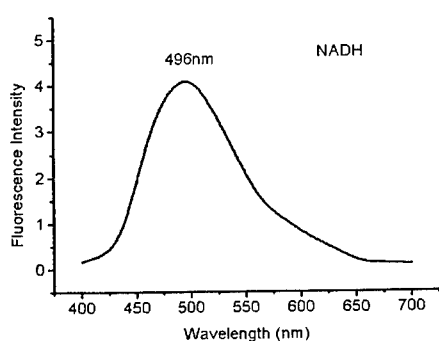


9

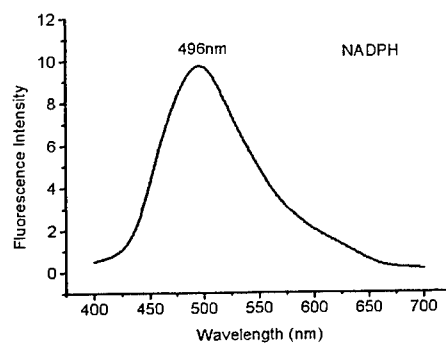


10

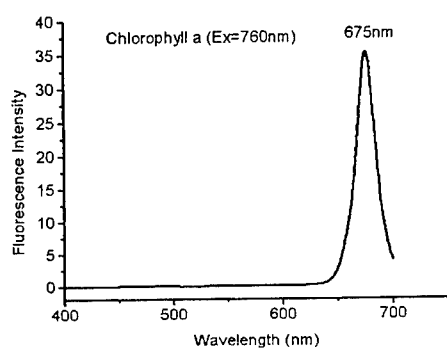
Figure 5-10. Acridine orange [Figure 5 (Ex=780nm)], Propidium Iodide [Figure 6 (Ex=780nm)], ethidium bromide [Figure 7 (Ex=780nm)], Mitotracker®M-7512 [Figure 8 (Ex=1240nm)], Lysotracker®L-7528 [Figure 9 (Ex=1240nm)], Riboflavin [Figure 10 (Ex=780nm)]. The vertical line in Figure 8 and 9 indicates the $1/2\lambda$ of the excitation wavelength.



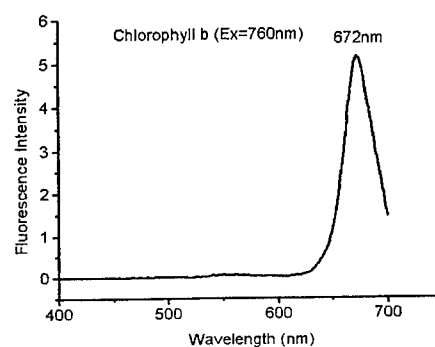
10



12



13



14

Figure 11-14. Two-photon excited fluorescence spectra of NADH [Figure 11 (Ex=780nm)], NADPH [Figure 12 (Ex=780nm)], chlorophyll a [Figure 13 (Ex=760nm)] and chlorophyll b [Figure 14 (Ex=760nm)].

	1P (Em)*	2P Em (Ex=780nm)	2P Em (Ex=1234nm)
DAPI - DNA	461nm	479nm	-
Hoechst 33258 - DNA	461nm	494nm	-
Syto 17 -DNA	640nm	638nm	643nm
Acridine orange -DNA	626nm	628nm	-
Propidium Iodide -DNA	617nm	631nm	-
Ethidium bromide - DNA	605nm	616nm	-
Mitotracker®Red M-7512	599nm	-	600nm (2P and 3P)
Lysotracker r®Red L-7528	592nm	-	594nm (3P), 646nm (2P), 668nm (2P)

Table 1. Single-photon (1P) and two-photon (2P) excited fluorescence emission maximum of various DNA dyes. 3P: three-photon excited fluorescence. Ex: excitation wavelength, Em: emission maximum. *Data adopted from Molecular Probes Catalog (1999).

	2P
Riboflavin	546nm (Ex=780nm)
NADH	496nm (Ex=780nm)
NADPH	496nm (Ex=780nm)
Chlorophyll a	675nm (Ex=760nm)
Chlorophyll b	672nm (Ex=760nm)

Table 2. Two-photon (2P) excited fluorescence emission maximum of five bio-molecules. Ex: excitation wavelength.

ACKNOWLEDGEMENTS

This project was support by Academia Sinica (BLL), the National Science Council [NSC-88-2811-B-001-0023 (PCC), NSC-89-2311-B-001-032(BLL), NSC89-2112-M-110-016, NSC89-2216-E-110-003 (FJK), NSC89-2215-E-002-004 (CKS)], Academic Excellence Program of the Ministry of Education (89-B-FA08-1-4), Republic of China and Mr. and Mrs. Jin-Mu Huang of Aurum Belle Investment Co. (on behalf of the Ge-An Charity) to PCC. Fluorescent probes were provided by Molecular Probes, Inc. Eugene, OR, USA.

REFERENCES

1. Cheng, P. C., S. J. Pan, A. Shih, K.-S. Kim, W. S. Liou and M. S. Park, "Highly efficient upconverters for multiphoton fluorescence microscopy," *J. Microscopy* 189 pp. 199-212, 1997.
2. P. C. Cheng, B. L. Lin, F. J. Kao, M. Gu, M. G. Xu, X.-s. Gan, M. K. Huang and Y. S. Wang, "Multi-photon fluorescence microscopy—the response of plant cells to high intensity illumination," *Micron* (in press) 2000.
3. F. J. Kao, B. L. Lin and P. C. Cheng, "Multi-photon fluorescence micro-spectroscopy," *Proceedings of SPIE*, 3919, (in press), 2000.
4. F. J. Kao, B. L. Lin and P. C. Cheng, "Multi-photon fluorescence micro-spectroscopy of plant tissues," *Microsc Microanal*, 6, Proceedings issue (in press), 2000.
5. P. C. Cheng, B. L. Lin, F. J. Kao, C. K. Sun and I. Johnson, "Multi-photon Excited Fluorescence Spectrum of Common Nucleic Acid probes," *Microsc Microanal*, 6, Proceedings issue (in press) 2000.
6. P. C. Cheng, F. J. Kao, C. K. Sun, B. L. Lin, T. M. Liu, Y. S. Wang, M. K. Huang, Y.-m. Wang, J. -c. Chen, I. Johnson, "Multi-photon excited fluorescence spectra of common bio-probes," *Scanning* 22, No. 3 (in press), 2000.
7. C. K. Sun, S. W. Chu, T. M. Liu, P. C. Cheng, "High intensity scanning microscopy with a femtosecond Cr:Forsterite laser," *Scanning*, 22, pp. 95-96, 2000.

Two-photon optical-beam-induced current microscopy of indium gallium nitride light emitting diodes

Fu-Jen Kao^{*a,b}, Mao-Kuo Huang^a, Yung-Shun Wang^a, Sheng-Lung Huang^c, Ming-Kwei Lee^d, Chi-Kuang Sun^e, Ping-chin Cheng^f

^aDepartment of Physics, National Sun Yat-sen University, Kaohsiung 80424, Taiwan;

^bCenter for Neuroscience, National Sun Yat-sen University, Kaohsiung 80424, Taiwan;

^cInstitute of Electro-Optical Engineering, National Sun Yat-sen University, Kaohsiung 80424, Taiwan;

^dDepartment of Electrical Engineering, National Sun Yat-sen University, Kaohsiung 80424, Taiwan;

^eInstitute of Electro-Optical Engineering, National Taiwan University, Taipei 106, Taiwan

^fAMIL, Department of Electrical Engineering, State University of New York, Buffalo, NY, 14260 USA

ABSTRACT

In this study, epilayers of packaged indium gallium nitride light emitting diodes (LED's) are characterized by optical beam induced current (OBIC) and photoluminescence laser scanning microscopy through two-photon excitation. OBIC reveals spatial and electrical characteristics of LED's which can not be distinguished by photoluminescence. When compared with single-photon OBIC, two-photon OBIC imaging not only exhibits superior image quality but also reveals more clearly the characteristics of the epilayers that are being focused on. The uniformity of these LED's OBIC images can also be related to their light emitting efficiency.

Keywords: Indium gallium nitride, two-photon excitation, optical beam induced current, confocal microscopy, blue LED

1. INTRODUCTION

Optical beam induced current (OBIC) imaging is widely applied in the characterization of semiconductor based devices and integrated circuits, for instance, in failure analysis¹⁻³. Conventionally, OBIC is performed through carrier generation by single-photon absorption. It has been shown that the effective point spread function (PSF) needs to be modified to account for the exponentially decaying optical field inside the material as a result of strong absorption^{4,5}. When compared with photoluminescence imaging, OBIC imaging has the advantages of observing features that are more directly related to the electrical characteristics of semiconductor devices. The OBIC imaging of semiconductor devices has to meet the seemingly contradictory conditions in that (a) the substrate or overlayers do not absorb or scatter the illuminating light strongly and (b) the photo-excited carriers are efficiently generated in the active layer. These requirements can be met if OBIC is performed with two-photon excitation⁶ that employs wavelengths that are less than the bandgap photon energy, as demonstrated by Xu and Denk⁷. In this way absorption and scattering in the overlayers and substrate can be greatly reduced while carriers are effectively generated in the active layer.

In this report, we apply the two-photon OBIC technique to investigate indium gallium nitride (InGaN) based light emitting diodes (LED's) that have found wide spread applications in optoelectronics⁸. InGaN is considered to be the most important compound semiconductor among III-V nitride compounds because the InGaN enables light emitting through efficient carrier recombination⁹. One can obtain strong band-to-band emission from the green to the UV by varying the In content of InGaN. InGaN based LED's exhibit high external quantum efficiency and brightness and are the most viable blue LED's currently in use. It has been proposed that the emission is related to the presence of deep localized energy states that may originate from the In-rich regions which act as quantum dots¹⁰⁻¹⁴. However, the intensity distribution of LED's can exhibit poor spatial uniformity in active region, as can be seen under a microscope when LED's are forward biased. This poor spatial uniformity is associated with the fluctuation in In concentration and with the localized defects such as deficiency of nitrogen atoms in the lattice and threading dislocations. Imperfection in the electrodes would also affect the spatial uniformity of LED's.

We have found that two-photon excitation is effective in penetrating the packaging as well as the overlayers, such as *p*-doped GaN layers, or an *n*-doped GaN layer and sapphire substrate, if the laser beam is incident from the substrate side. The loss in two-photon excitation that is due to absorption and scattering is greatly reduced when compared with the loss in single-photon excitation. Absorption correction to the optical field inside the material is then not necessary^{4,5}. In addition,

the effect of spherical aberration when laser beam penetrates LED's plastic packaging is also reduced as a result of employing a longer wavelength. Therefore, two-photon OBIC imaging not only exhibits superior image quality but also reveals more clearly the characteristics of the epilayers focused on.

2. EXPERIMENTAL SETUP

2.1 Two-photon laser scanning microscopy

An inverted microscope and a galvano-mirror-based scanning system (Fluoview-IX70, Olympus) form the imaging platform. A mode-locked Ti:sapphire pulse laser (Tsunami, Spectra-Physics) pumped by a frequency doubled solid state laser (Millennia, Spectra-Physics) provides laser pulses of approximately 150 fs at 760 nm and 82 MHz for two-photon excitation, which is equivalent to 380 nm in excitation energy. A 740nm dichroic beam splitter is installed in the excitation path of the scanning unit to accommodate the coupling of the ultrafast laser pulses into the confocal microscope. The 488 nm line of a Kr-Ar laser is employed when single photon excitation is performed.

To avoid exceeding the response speed (10 KHz) of the current amplifier, the samples are scanned at a very slow rate of 157 sec/frame (150 μ s dwell time/pixel) at 1024x1024 pixels. A 40X (numerical aperture, 0.65) long working distance objective is employed for image acquisition. At focal point, the average power measured was 10 mW, therefore, the average energy exerted on the specimen for each pixel is approximately 1.5 μ J (obtained by 150 μ s X 10 mW). On the other hand, considering the laser operating at 82 MHz with 150 fs pulse, when a NA=0.65 objective lens was used, the average and peak power densities at the focal point approximate 5×10^5 W/cm² and 4×10^{10} W/cm², respectively. We employ a very sensitive current amplifier (EG&G, model 181) of transimpedance as high as 10^9 V/A for photocurrent (PC) detection.

The total irradiated area is approximately 300 μ m x 300 μ m. The detected signal would correspond to photocurrent of a few nano-amperes. The two input channels in the scanning system detect the photoluminescence (PL) and the PC concurrently. The images are then reconstructed from the signals as a function of beam position. A schematic of this setup is shown in Fig. 1.

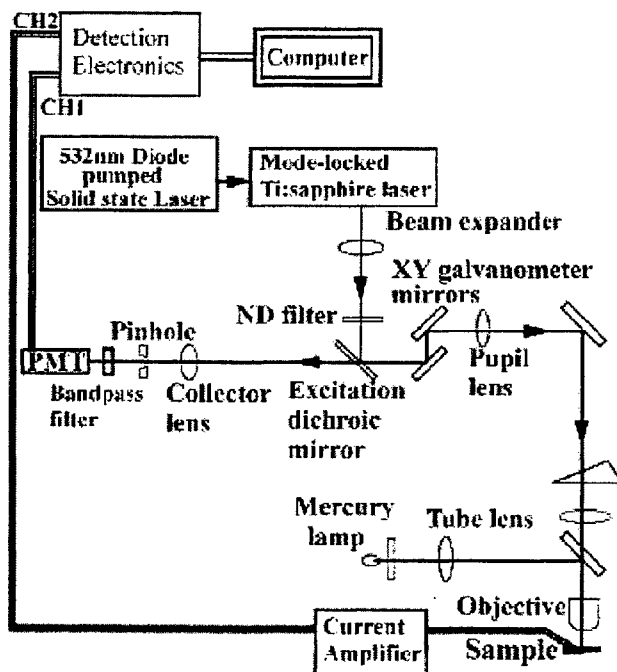


Figure 1. Schematics of the two-photon optical beam induced current and photoluminescence imaging system. The two input channels allow simultaneous acquisition of photocurrent and photoluminescence images.

2.2 InGaN LED's

The epilayers of GaN and InGaN are grown on top of a sapphire substrate. Since sapphire substrate is non-conducting, the two electrodes must be attached in the front side. There are two different brands of blue InGaN LED's being investigated in this study. One (Fig.2, LED A) has higher efficiency than the other (Fig. 2, LED B), as shown in their corresponding electro-luminescence spectra. Under the same driving current (0.5 mA), diode A emits brighter electro-luminescence than diode B. The diode samples observed are commercially available and have electro-luminescence that peaked around 475 nm with full width at half maximum (FWHM) bandwidth 35 nm, as shown in Fig. 2. Thinning, grinding, and polishing the packaging of the diodes allow direct observation and excitation under a microscope. We employ bandpass filters to select specific spectral bands for luminescence imaging.

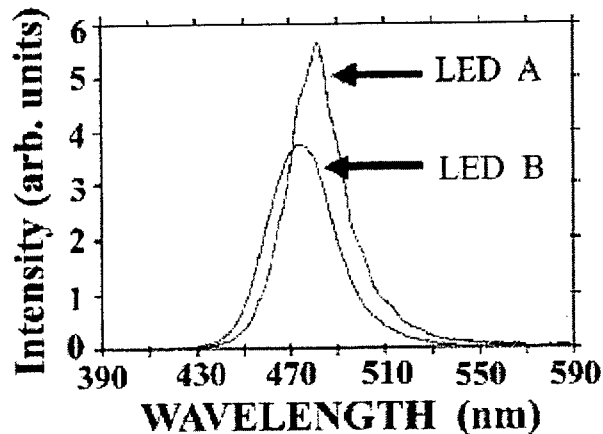


Figure 2. Electro-luminescence spectra of two different InGaN LED's.

3. RESULTS

Figures 3(a) and 3(b) show the power dependence of the PC signals from diode A and B, respectively. As expected for two-photon excitation, the slope values of 2.12 and 1.9 indicates the square dependence of such a nonlinear process.

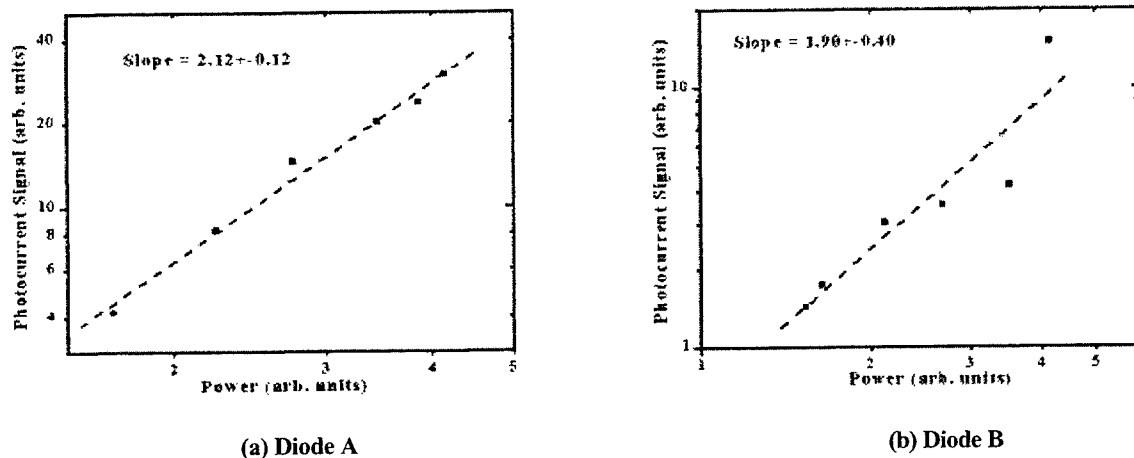


Figure 3. Photocurrent magnitude as a function of incident laser power for diode A(a) and B (b), respectively. The slope values are closed to 2, indicating two-photon excitation process is involved.

Two-photon PC and PL images of diode A are presented in Figs. 4(a) and 4(b), respectively. For comparison, the two-photon PC and PL images of diode B are presented in Figs. 4(c) and 4(d). The two electrodes are clearly shown in the PC images as one circular and one square dark region. They appear dark since there is no carrier generated underneath. The thin metallization layer is identified as the darker gray area that covers most of the active region shown in the PC image, whereas the bright strip in the edge shows the active region without thin metallization. In confocal PL imaging, fluorescence from the

epilayers cannot be discriminated against that from the sapphire substrate spatially since the epilayers are thinner than the width of PSF in z-axis. In contrast, PC imaging would only detect a signal as a result of photocarrier generation. When compared with PL imaging, PC imaging has the advantages of being more specific and related to the diodes' electrical properties.

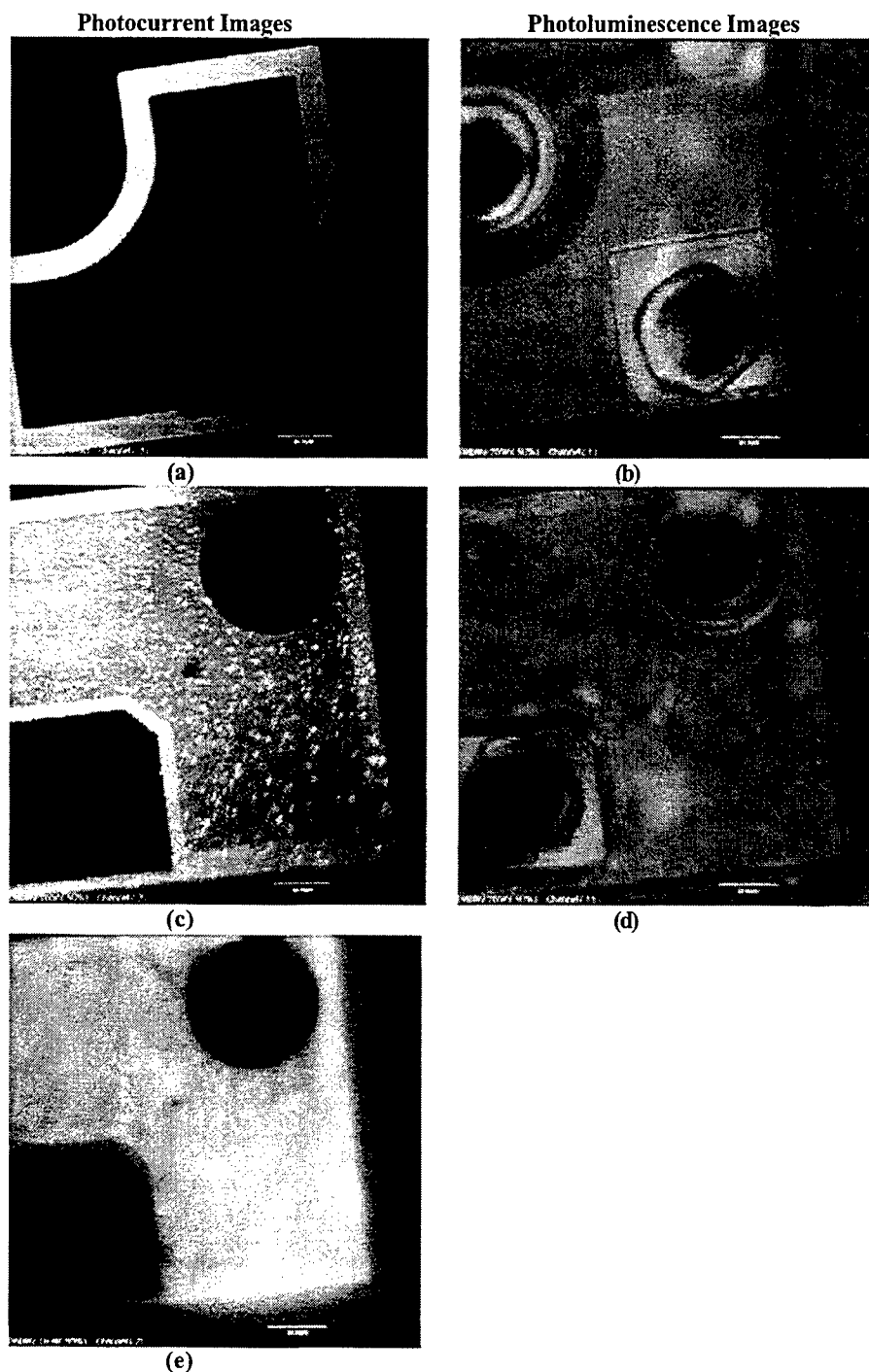


Figure 4. PC and PL images from diode A and diode B. (a) and (b) are two-photon PC and PL images from diode A, respectively. (c) and (d) are two-photon PC and PL images from diode B, respectively. In both (b) and (d) a bandpass filter

centered at 450 nm with 50 nm bandwidth is used in acquiring PL images. For comparison, one-photon PC image of diode B is shown in (e).

The most pronounced features in the PC image are the bright spots spread over the LED's in Fig. 4(c), which are a result of local variation in carrier transportation or generation efficiency. These spots have sizes ranging from 5 μm to less than the resolution of the objective used in our optical system, which is approximately 1.3 μm . The spots are similar to what have been observed in micro-spectroscopy of cathodoluminescence in InGaN quantum well devices¹². Spots can also be found in the PL image, Fig. 4(d), which is acquired with a band pass filter of central wavelength 450 nm and bandwidth 50 nm. These spots do overlap with those found in the PC image, indicating that PC and PL have similar origin. However, the contrast in the PL image is less pronounced. According to Nakamura and co-workers¹⁰⁻¹⁴, fluctuation in the In concentration will generate localized deep levels that greatly facilitate carrier recombination, and possibly carrier generation. Therefore PC may be a more sensitive indicator than PL in detecting local variation in the active region. For comparison, Diode A did not exhibit the spots as in Diode B, as shown in Figure 4 (a) and 4 (b). The advantage of two-photon excitation is further clarified by comparing the PC image obtained through single photon excitation shown in Fig. 4(e). The 488 nm line of an argon-krypton mixed gas laser is employed for single photon excitation. The image appears blurred with reduced contrast and no detailed features can be observed.

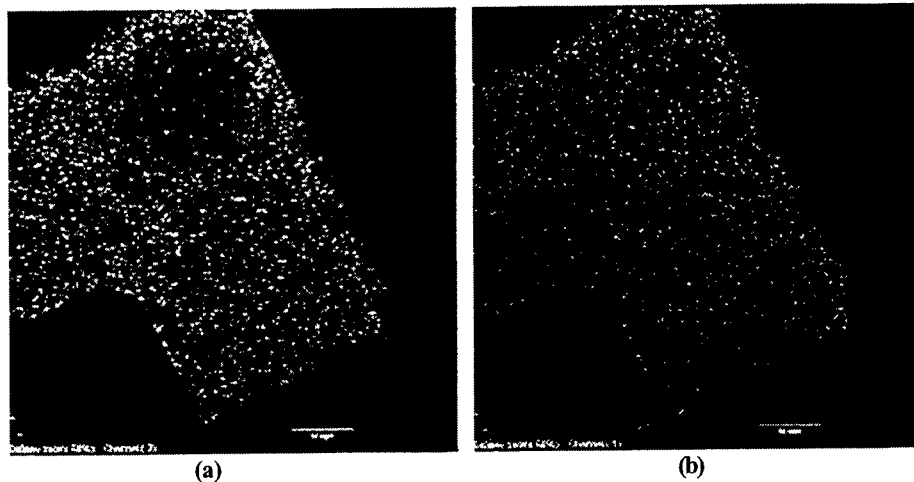


Figure 5. PC (a) and PL (b) images from an unpackaged diode with heavy indium doping.

To observe the effects of heavy indium doping, the PC and PL images of an unpackaged InGaN diode are shown in Fig. 5(a) and (b), respectively. The color of electro-luminescence from this diode is green. In contrast with PC images shown in Fig. 4, there is PC signal coming out of one of the electrodes, as shown in Fig. 5(a). Unlike a packaged diode in which scanning beam must irradiate from the side of electrodes, in this case the scanning laser beam can penetrate the sapphire substrate during imaging. The weaker magnitude of PC signal within the circular electrode indicates that there is an insulation layer under the electrode to homogenize the current distribution over the diode. High indium concentration was expected to generate greater inhomogeneity within the active layer and this inhomogeneity is manifested in Fig. 5.

4. DISCUSSION

4.1 Two-photon excitation

Optically the advantages of two-photon OBIC over single-photon OBIC can be summarized as (1) deeper penetration, (2) less distortion to field distribution or PSF, and (3) less spherical aberration¹⁵. Absorption in the top epilayer can be minimized by using a excitation wavelength that is below bandgap photon energy. Deeper penetration would then result because of reduced absorption. Regarding the image formation of OBIC, detailed model for 1-photon OBIC has been developed by Wilson *et al.*^{4,5}, in which a semi-infinite piece of semiconductor is considered. Within the model, a specific PSF that takes into account substrate absorption is introduced. It is found that the resolution is not limited by the carrier diffusion length and the optimum focus position in terms of the maximum number of carriers generated is a few optical units below the surface. In the case of single-photon OBIC, it would then be more difficult to perform conventional deconvolution calculation to improve image quality since the PSF is distorted as a result of absorption. In contrast, two-

photon OBIC would open the possibility for image deconvolution. The reduction of spherical aberration is expected since the magnitude of it is proportional to the path length difference in the optical imaging system and inversely proportional to wavelength, i.e. $\Delta\phi \propto \frac{\Delta L}{\lambda}$. Employing a longer wavelength would naturally result in smaller spherical aberration.

However, two-photon OBIC may present the following problems. Most significantly, at high excitation intensity, multi-photon effects may damage the LED's.

4.2 InGaN LED's

Efficient light emission of a blue LED is related to deep localized energy states formed in the In-rich regions acting as quantum dots in the InGaN layer. These states may also be the origin of photocurrent. Since the direct band gap (~3.4 eV) of intrinsic GaN is much higher than that of InGaN, it is less probable that the wavelength we used would excite carriers over GaN's band gap. According to Nakamura and Fasol⁸, though the PL spectra of p-doped GaN and InGaN overlap each other, the PL intensity from InGaN is higher by more than an order of magnitude. It is likely that most photo-generated carriers are generated in the InGaN layer. In OBIC, the detected signal can be regarded as the convolution of carrier generation and transportation to the electrodes. Owing to the LED's planar structure and the relatively low resistance in the p-dope and n-doped layers, the overall carrier transportation efficiency should present little variation over the LED's plane. Therefore, the spots observed in Fig. 4(a) may reflect local variation of carrier generation efficiency in the active layer. This variation may also be caused by changes in indium compositions. The higher contrast in the PC image than the PL image indicates that PC is more sensitive to local variation in carrier generation. For the two InGaN light emitting diodes. Their light emitting quality and efficiency are reflected in the PC images. In particular, as indium concentration increases, the inhomogeneity observed in the active layer also increases.

5. CONCLUSIONS

In conclusion, we have demonstrated the characterization of the InGaN based LED's through two-photon OBIC laser scanning microscopy¹⁶. However, one needs to be careful about damages induced by nonlinear optical excitation. Compared with single-photon excitation, two-photon excitation clearly exhibits better spatial resolution and reveals some interesting features not found before. Optoelectronic devices are of multilayered heterostructure with active layers buried in the middle. Two-photon excitation is more effective than one-photon excitation in reaching the active layers of these devices. Specifically, PC is more sensitive and specific than PL in showing their characteristics.

ACKNOWLEDGEMENT

We gratefully acknowledge support of this research by the National Science Council of Taiwan under Grant NSC89-2112-M-110-016 and NSC-89-2216-E-110-003 and by the Academic Excellence Program of the Ministry of Education (89-B-FA08-1-4). We are also indebted to Yuan-Li Optical Co. for strong technical supports in providing numerous optical components.

REFERENCES

1. T. Wilson and C.J.R. Sheppard, *Theory and Practice of Scanning Optical Microscopy*, Academic, New York, (1984).
2. B.P. Richards and P.K. Footner, *The Role of Microscopy in Semiconductor Failure Analysis*, Oxford University Press, New York, 1992.
3. H. Komoda and K. Shimizu, "Optical beam induced current techniques for failure analysis of very large scale integrated circuits devices", *Jpn. J. Appl. Phys.* **33**, pp. 3393-3401, 1994.
4. T. Wilson and E.M. McCabe, "Distribution of charge carriers generated in a semiconductor by a focused convergent light beam", *J. Appl. Phys.* **59**, pp. 2638-2642, 1986.
5. T. Wilson and E.M. McCabe, "Theory of optical beam induced current images of defects in semiconductor", *J. Appl. Phys.* **61**, pp. 191-195, 1987.
6. W. Denk, J.H. Strickler, and W.W. Webb, "Two-Photon Laser Scanning Fluorescence Microscopy", *Science* **248**, pp. 73-76, 1990.
7. C. Xu and W. Denk, "Two-photon optical beam induced current imaging through the backside of integrated circuits", *Appl. Phys. Lett.* **71**, pp. 2578-2580, 1997.
8. S. Nakamura and G. Fasol, *The Blue Laser Diode*, Springer-Verlag, Berlin, 1997.

9. S. Nakamura, "The Roles of Structural Imperfections in InGaN-Based Blue Light-Emitting Diodes and Laser Diodes", *Science* **281**, pp. 956-961, 1998.
10. S. Chichibu, T. Azuhata, T. Sota, and S. Nakamura, "Spontaneous emission of localized excitons in InGaN single and multi-quantum well structures", *Appl. Phys. Lett.* **69**, pp. 4188-4190, 1997.
11. S. Chichibu, T. Azuhata, T. Sota, and S. Nakamura, "Luminescence from localized states in InGaN epilayers", *Appl. Phys. Lett.* **70**, pp. 2822-2824, 1997.
12. S. Chichibu, K. Wada, and S. Nakamura, "Spatially resolved cathodoluminescence spectra of InGaN quantum wells", *Appl. Phys. Lett.* **71**, pp. 2346-2348, 1997.
13. Y. Narukawa, Y. Kawakami, M. Funato, Sz. Fujita, Sg. Fujita, and S. Nakamura, "Role of self-formed InGaN quantum dots for exciton localization in the purple laser diode emitting at 420nm", *Appl. Phys. Lett.* **70**, pp. 981-983, 1997.
14. Y. Narukawa, Y. Kawakami, Sz. Fujita, Sg. Fujita, and S. Nakamura, "Recombination dynamics of localized excitons in $\text{In}_{0.20}\text{Ga}_{0.80}\text{N}$ - $\text{In}_{0.05}\text{Ga}_{0.95}\text{N}$ multiple quantum wells", *Phys. Rev. B* **55**, pp. R1938-R1941, 1997.
15. M. Gu, *Three dimensional confocal microscopy*, World Scientific, Singapore, 1996.
16. F. Kao *et al.*, "Two-photon optical beam induced current imaging of indium gallium nitride light emitting diodes", *Opt. Lett.*, **24**, pp. 1407-1409, 1999.

SESSION 5

Fluorescence and Multiphoton Microscopy and Spectroscopy II

Multi-photon micro-spectroscopy of biological specimens

Bai-Ling Lin^{1*}, Fu-Jen. Kao^{2,5*}, Ping-chin Cheng^{3*}, Chi-Kuang Sun^{4*}, Rang-Wu Chen¹, Yi-min Wang², Jian-cheng Chen², Yung-Shun Wang², Tzu-Ming Liu⁴ and Mao-Kuo Huang²

¹Institute of Molecular Biology, Academia Sinica, Taipei 11529, Taiwan, ROC

²Department of Physics, National Sun Yat-sen University, Kaohsiung 80424, Taiwan, ROC

³AMIL, Department of Electrical Engineering, State University of New York, Buffalo, NY 14260, USA

⁴Department of Electrical Engineering, National Taiwan University, Taipei 10617, Taiwan, ROC

⁵Center for Neuroscience, National Sun Yat-sen University, Kaohsiung 80424, Taiwan, ROC

ABSTRACT

The non-linear nature of multi-photon fluorescence excitation restricts the fluorescing volume to the vicinity of the focal point. As a result, the technology has the capacity for micro-spectroscopy of biological specimen at high spatial resolution. Mesophyll protoplasts of *Arabidopsis thaliana* and maize stem sections were used to demonstrate the feasibility of multi-photon fluorescence micro-spectroscopy at subcellular compartments. Time-lapse spectral recording provides a means for studying the response of cell organelles to high intensity illumination.

Keywords: Micro-spectroscopy, multi-photon fluorescence spectroscopy, second harmonic generation, plant tissues, stem, chloroplast, protoplast, maize, *Arabidopsis*

1. INTRODUCTION

Due to its non-linear nature, two-photon excitation may generate very different spectral response when compared with single photon excitation. It is thus necessary to measure the two-photon spectra of samples under study, so that the two-photon fluorescence microscopic images may be properly interpreted^{1,2}. However, fluorescence spectra obtained from bulk specimen may not provide appropriate information for microscopy. For instance, when the spectrum of a generally fluorescing specimen as a whole is obtained, a small number of fluorescent particles may escape from detection due to the relatively small contribution to the total fluorescence. In addition, signals resulted from second harmonic generation (SHG) may be mixed with low level broad band background autofluorescence which is commonly found in biological specimen. Therefore, measuring fluorescence spectrum from a micro-focused volume is essential to properly interpret multi-photon fluorescence microscopic images. Under two-photon excitation, the background noise may be greatly reduced due to the naturally limited excitation volume of the focused laser beam. In this study, leaf protoplasts of *Arabidopsis thaliana* and stem slices of maize (*Zea mays*) were used as samples to address these issues in a set-up for micro-spectroscopy.

2. MATERIALS AND METHODS

Protoplasts of *Arabidopsis thaliana* were isolated from leaves through enzyme digestion of the cell wall, and suspended in culture medium according to the methods of Huang and Chen³. For microscopic observation, the protoplast suspension was placed in a chambered coverglass (Lab-Tek, Illinois, USA). Unstained and Calcofluor White-stained stem slices of maize were also used.

Two-photon induced fluorescence spectra were measured with two sets of spectrometers. For static spectra, a SpectraPro-500 spectrometer (Acton Research) equipped with a TE-cooled PMT is used to achieve higher spectral precision. Whereas for time-lapse spectra, a 1/8m spectrometer (Oriel, #77250) equipped with a liquid-nitrogen-cooled CCD camera is used for high speed spectrum acquisition. The excitation laser beam is derived from a Spectra Physics Tsunami Ti:sapphire laser pumped

* Corresponding authors. Fu-Jen Kao and Ping-chin Cheng (optics), Chi-Kuang Sun (Cr:Forsterite laser).

by a Coherent Verdi solid-state laser at 532nm. The Ti:sapphire laser is mode-locked at 780nm and has a repetition rate of 82 MHz with a pulse width of approximately 100fs. A ChromaTech dichroic beam splitter (650DCSP) was used to achieve epi-illumination and on-axis fluorescence detection in a modified Olympus BX microscope. In addition, two IR cut-off filters (Edmond Scientific, Cat. K53-710) were installed in front of the entrance slit of the monochromator to reject scattered IR from the sample. Using this set-up, site-specific spectral information was obtained from the samples⁴. Excitation intensity as high as 10^{12} W/cm² was reached at the focal point. A second set-up using a Spectra-Physics Millennia IR (1064nm) pumped Chromium-doped Forsterite laser (built by CKS), operated at 120MHz and 130fs pulse, was used for 1234nm infrared (IR) excitation. Figure 1 is a diagrammatic representation of our micro-spectroscopy set-up.

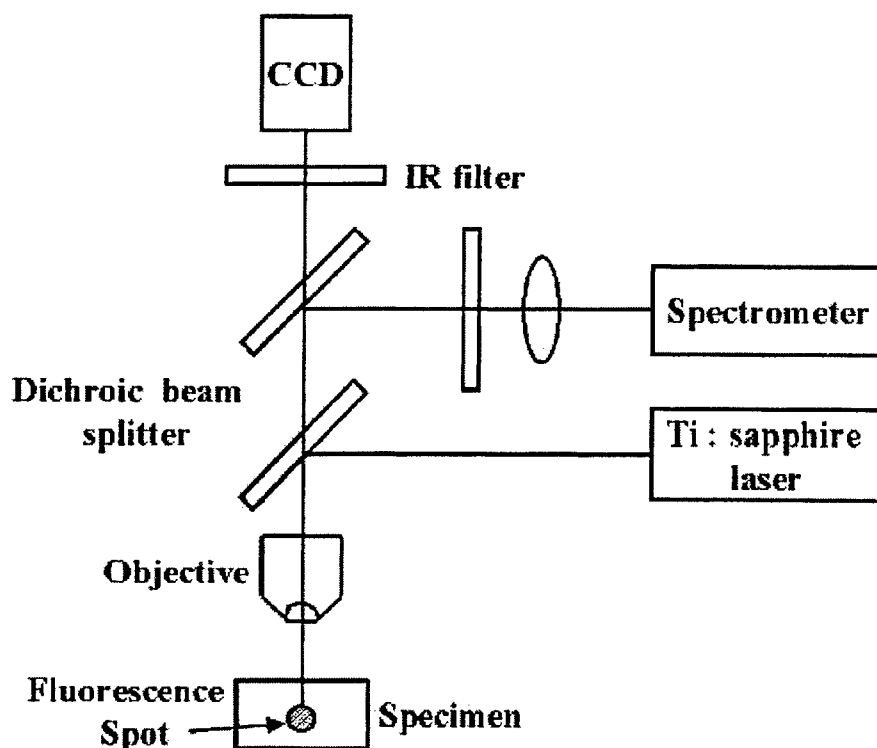


Figure 1. Diagrammatic representation of micro-spectroscopy set-up.

3. RESULTS AND DISCUSSION

Figure 2a is a transmission image of a maize stem showing cortical parenchyma cells and a vascular bundle. An IR beam was tightly focused on a region of a cell in the vascular bundle and generated a fluorescence spot. Two-photon excited spectrum taken from this spot shows a broad band fluorescence peaked approximately at 500nm (Figure 2b). When stained with Calcofluor White, a fluorescent dye staining cellulose, the cortical parenchyma cell wall shows two-photon fluorescence (Figure 3a), while the emission spectrum has the characteristics of Calcofluor White (Figure 3b). These results demonstrate the potential of micro-spectroscopy in studying fluorescence emission properties of subcellular compartments. Because of the non-linear properties of the two-photon fluorescence excitation, this technique provides superb spatial resolution in 3D.

Figures 4a and 4b are two-photon fluorescence micrographs of *Arabidopsis thaliana* mesophyll protoplasts. In these micrographs, the center region received a single 3.3sec/frame scan ($8.4\mu\text{s}$ dwell time/pixel) at 768×512 pixels. The total irradiated area is $180\mu\text{m} \times 120\mu\text{m}$. At focal point, the average power measured was 6.4 mW, therefore, the average energy exerted on the specimen for each pixel is approximately 54nJ (obtained by $8.4\mu\text{s} \times 6.4\text{mW}$). On the other hand, considering the laser operating at 82 MHz with 100fs pulse, when a $\text{NA}=1.2$ objective lens was used, the average and peak power densities at the focal point approximate $3 \times 10^6 \text{W/cm}^2$ and $3.9 \times 10^{11} \text{W/cm}^2$, respectively. After the first scan, it was noted that a significant reduction in red fluorescence occurred, as evident when using different filters (comparing Figure 4a with 4b). The images were taken at a lower magnification to show the scanned area. Figures 4c and 4d show fluorescence images

obtained from the 1st and 3rd scan. Though the fluorescence intensity is seen to reduce after several scans, the images do not provide detailed information on the possible spectral variation.

Figure 5b shows a three-dimensional plot of spectra against time indicating the spectral and intensity changes of the green autofluorescence from a chloroplast under intense NIR illumination (Figure 5a). In addition to the broad band green fluorescence emission, peaked at 532nm/550nm (Figure 5b), a prominent red fluorescence peak with emission maximum at 663nm has been observed in a previous study². The 663nm emission is the result of chlorophyll fluorescence while the origin of the 532/550nm emission is yet to be determined². These results demonstrate that the set-up for micro-spectroscopy allows time-lapse recording in subcellular organelles, and thus will be useful for detailed spectral analysis of possible cellular damages or photochemical reactions under multi-photon excitation.

Micro-spectroscopy also provides insights into the origin of signals detected in a multi-photon microscopic imaging system. For instance, Figure 6 shows an emission spectrum obtained from the cortex of a maize stem. When excited with 1234nm IR, a red fluorescence peak at 682nm and a small peak at 617nm were observed. The red peak originates from the autofluorescence of chlorophyll. The smaller peak is likely the result of second harmonic generation (SHG) in the plant cell wall. In this case, micro-spectroscopy provides a means of verification that, indeed, SHG occurs in plant samples⁵.

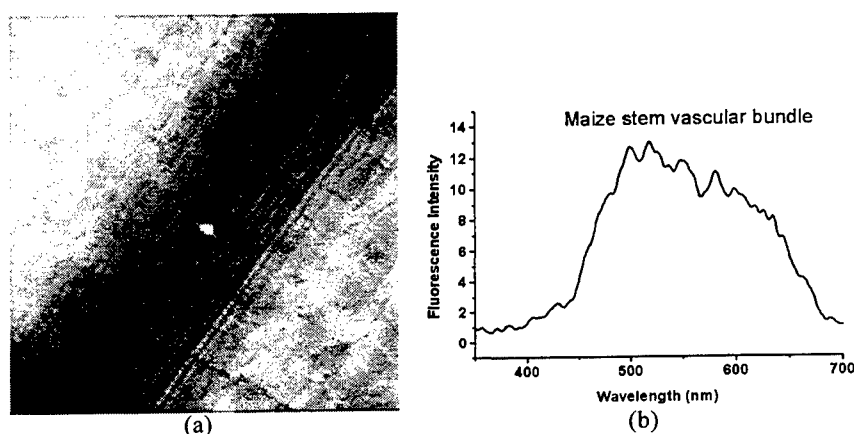


Figure 2 (a) Transmission micrograph of a longitudinal section of maize stem. The bright spot in the center of the micrograph indicates two-photon excited fluorescence emission generated by a tightly focused IR beam. (b) The fluorescence spectrum obtained from the spot shown in (a).

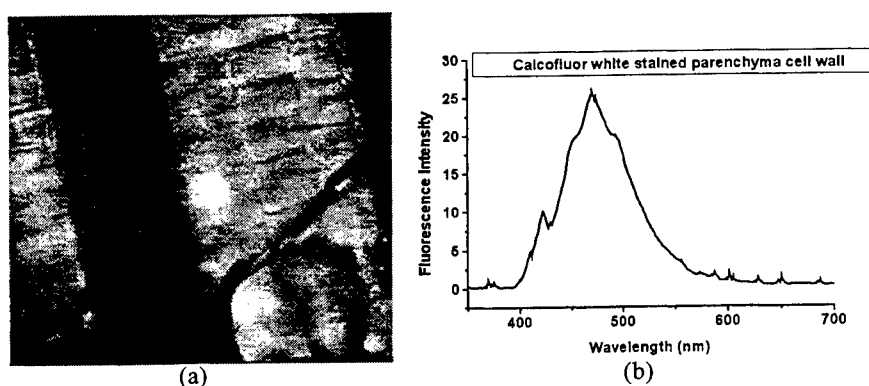


Figure 3. (a) Transmission micrograph of a longitudinal section of Calcofluor White-stained maize stem. The large bright spot in the center of the micrograph is two-photon excited fluorescence emission generated by intense IR beam. (b) The fluorescence spectrum obtained from the spot shown in (a).

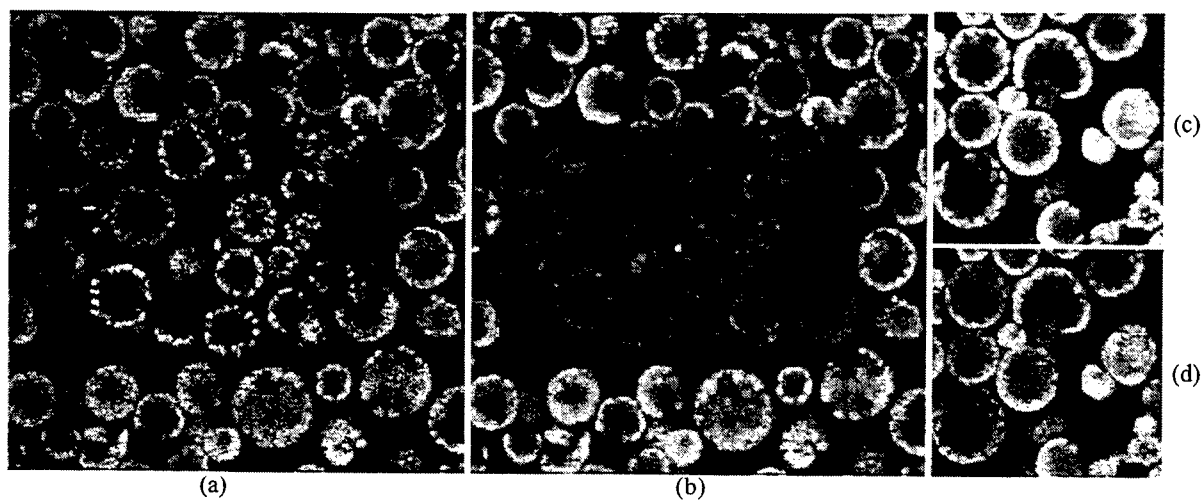


Figure 4. (a) and (b) two-photon fluorescence images showing a previously scanned area in the center. In (a), obtained with a green filter, the scanned area is brighter, whereas in (b), obtained with a red filter, the scanned area is dimmer. The contrast in fluorescence intensity is induced by a single imaging scan. (c) and (d) sequential images obtained from the 1st and 3rd scan, respectively. In (c) and (d), both green and red fluorescence images are superimposed.

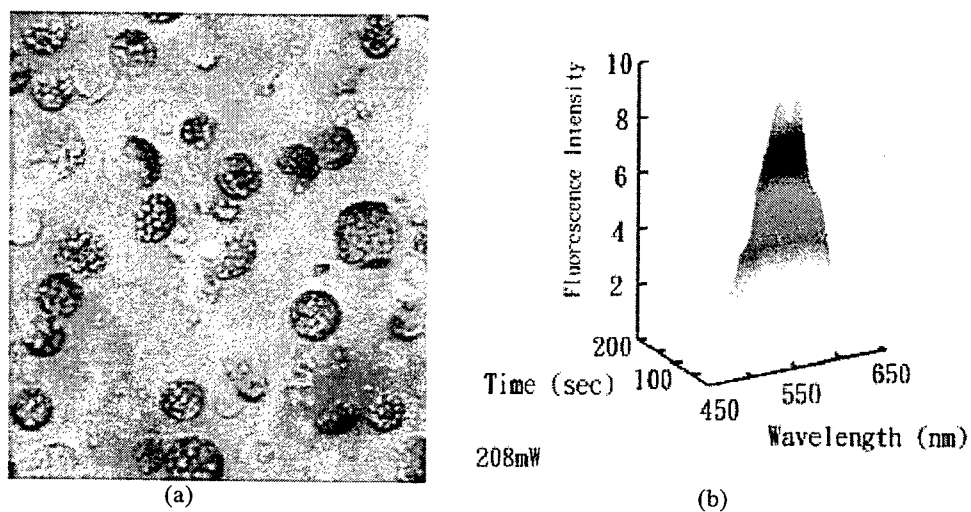


Figure 5. (a) Transmission micrograph of *Arabidopsis thaliana* protoplasts. The bright spot in the center is the fluorescence emission generated by a tightly focused NIR beam. (b) Three-dimensional plot of fluorescence emission spectra vs. time showing changes in spectrum and intensity of fluorescence from within a protoplast of *Arabidopsis thaliana* as shown in (a).

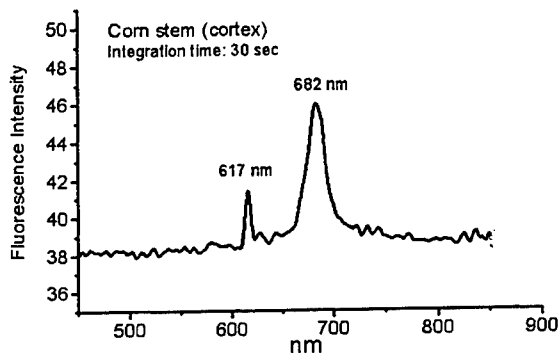


Figure 6. Spectrum obtained from the cortex in maize stem cross-section excited by 1234nm IR. Note the red fluorescence at 682nm and SHG at 617nm.

ACKNOWLEDGEMENTS

Supported by Academia Sinica (BLL), National Science Council, [NSC-89-2311-B-001-032 (BLL), NSC-89-2112-M-110-016 and NSC89-2216-E-110-003 (FJK), NSC89-2215-E-002-004 (CKS), NSC-88-2811-B-001-0023 (PCC)], Academic Excellence Program of the Ministry of Education (89-B-FA08-1-4), Republic of China, and Mr. Jin -Mu Huang and Mrs. Li-Ling Huang of Aurum Belle Investment Co. (on behalf of the Ge-An Charity, for PCC).

REFERENCES

1. P. C. Cheng, S. J. Pan, A. Shih, K.-S. Kim, W. S. Liou and M. S. Park, "Highly efficient upconverters for multiphoton fluorescence microscopy," *J. Microscopy* **189**, pp. 199-212, 1997.
2. P. C. Cheng, B. L. Lin, F. J. Kao, M. Gu, M. G. Xu, X-s. Gan, M. K. Huang and Y. S. Wang, "Multi-photon fluorescence microscopy -the response of plant cells to high intensity illumination," *Micron* (in press) 2000.
3. H.-C. Huang and C. -C Chen, "Genome multiplication in cultured protoplasts of two *Nicotiana* species," *J. Heredity* **79**, pp. 28-32, 1998.
4. F. J. Kao, B. L. Lin and P. C. Cheng, "Two-photon micro-spectroscopy of chloroplasts from *Arabidopsis thaliana*," *SCANNING* **22**, pp. 91-92, 2000.
5. C. K. Sun, S. W. Chu, T. M. Liu, and P. C. Cheng, "High intensity scanning microscopy with a femtosecond Cr:Forsterite laser," *SCANNING* **22**, pp. 95-96, 2000.

Applications of Two-Photon Fluorescence Microscopy in Deep Tissue Imaging

C. Y. Dong^a, B. Yu^b, L. Hsu^a, P. Kaplan^c, D. Blankschtein^b, R. Langer^b, and P. T. C. So^a

^aDepartment of Mechanical Engineering, Massachusetts Institute of Technology, Cambridge, MA

^bDepartment of Chemical Engineering, Massachusetts Institute of Technology, Cambridge, MA

^cUniverlever Edgewater Laboratory, Edgewater, NJ

ABSTRACT

Based on non-linear excitation of fluorescence molecules, two-photon fluorescence microscopy has become a significant new tool for biological imaging. The point-like excitation characteristic of this technique enhances image quality by the virtual elimination of off-focal fluorescence. Furthermore, sample photodamage is greatly reduced because fluorescence excitation is limited to the focal region. For deep tissue imaging, two-photon microscopy has the additional benefit in the greatly improved imaging depth penetration. Since the near-infrared laser sources used in two-photon microscopy scatter less than their UV/blue-green counterparts, in-depth imaging of highly scattering specimen can be greatly improved. In this work, we will present data characterizing both the imaging characteristics (point-spread-functions) and tissue samples (skin) images using this novel technology. In particular, we will demonstrate how blind deconvolution can be used further improve two-photon image quality and how this technique can be used to study mechanisms of chemically-enhanced, transdermal drug delivery.

Keywords: Two-photon, fluorescence, microscopy, deep-tissue, imaging

1. INTRODUCTION

In two-photon fluorescence microscopy, molecular excitation of fluorescent molecules is caused by the absorption of two near-infrared (IR) photons. Popularized in 1990 by the Webb group, the technique has become a powerful tool in examining biological specimen¹. As a novel microscopic imaging technique, two-photon fluorescence microscopy has several significant advantages compared to conventional technology. Since two-photon excitation requires the interaction of two near-IR photons with the fluorescent molecule, high incident photon flux is required for efficient two-photon excitation. As a result, two-photon absorption is only likely to occur near the focal volume of a microscopic objective where the excitation photons are confined spatially to induce molecular absorption. Therefore, fluorescence imaging using this technology results in much superior image contrast since off-focal fluorescence is virtually eliminated. The point-like excitation volume of two-photon (or higher order excitation) fluorescence microscopy also confine excitation-induced photodamage to near the focal volume. Furthermore, since Rayleigh scattering probability is inversely proportional to the fourth power of the wavelength², the redder photons used for two-photon excitation can penetrate deeper into multiply scattering samples such as the tissue than the UV, blue, or green photons used for one-photon microscopy. It has been demonstrated, for example, that multiphoton imaging can penetrate biological specimen at least twice deeper than confocal imaging³. Finally, since the near-IR light source used for two-photon excitation is well separated spectrally from the fluorescence emission, the entire fluorescence spectrum can be well studied using two-photon excitation.

In this paper, we present two-photon data characterizing the PSF, blind deconvolved skin images, and monitoring of transdermal drug delivery. Our results show that two-photon fluorescence microscopy is

a powerful technique for studying both the physiological structure and transport characteristics of tissue. With further development, two-photon fluorescence microscopy potentially can be developed into an effective medical instrument at the cellular level for non-invasive, in vivo diagnosis of diseases such as skin cancer.

1.1 Two-Photon Excitation of Fluorescent Molecules

One-photon and two-photon excitation processes have different mathematical forms and physical interpretation. The two processes are demonstrated in Fig. 1⁴.

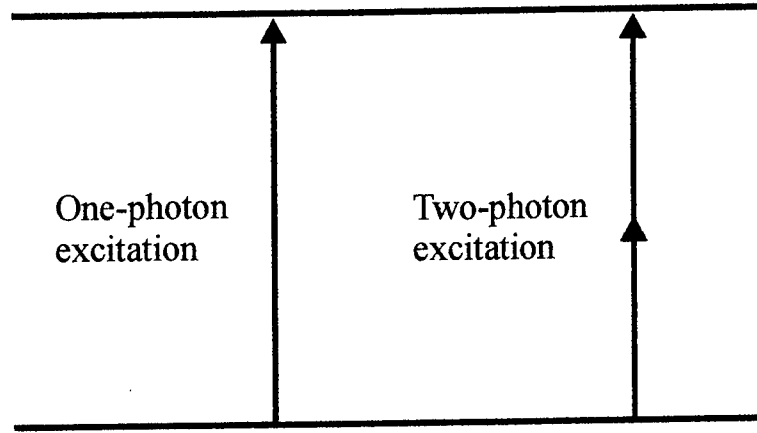


Fig. 1: One- and Two-photon excitation

In one-photon absorption, a molecule absorbs one photon whose energy matches the transition energy between the molecule's ground and excited states. The transition probability is

$$P_{1\gamma} \sim I |e \cdot \langle f | r | i \rangle|^2 \quad (1)$$

where r is the position operator, e is the electromagnetic polarization vector, I is the excitation intensity, i and f represent the initial and final states, respectively.

The two-photon absorption process is mathematically represented by

$$P_{2\gamma} \sim I^2 \left| \sum_m \frac{e \cdot \langle f | r | m \rangle \langle m | r | i \rangle \cdot e}{E_{mi} - E} \right|^2 \quad (2)$$

where m represents the intermediate state, E is the energy of the photon, and E_{mi} is the transition energy between the intermediate and initial states. In this mode of interaction, the molecule is interpreted to absorb the two red photons in sequential steps. One such photon is absorbed and the molecule is taken from the initial state i to the intermediate state m . At almost the same time, the molecule absorbs the second red photon and reaches the final state f from m . Since two photons are involved in the absorption process, the excitation probability is proportional to the square of excitation intensity, the origin of the non-linear nature of this process. As to the detection of the intermediate state m , one can estimate its lifetime using the uncertainty principle relating the lifetime τ to the energy spread ΔE by

$$\Delta E \tau \sim \hbar \quad (3)$$

where \hbar is Planck's constant. Assuming an uncertainty in the intermediate state energy to be approximately that of a typical fluorescent photon 500 nm in wavelength, the intermediate state only has a lifetime of approximately 0.3 fs, a time too short for realistic detection^{5,6}.

1.2 Skin as a Deep Tissue Sample

Skin is a tissue sample which two-photon fluorescence microscopy has been applied in studying. The structure of the skin is shown in Fig. 2. In short, the surface of the skin is composed of the epithelium. The basal layer represents the germinating layer from which the epithelial cells are generated. Cells from the basal layers divide and as they divide, the cells migrate toward the skin surface. Structurally, these migrating cells flatten as they approach the skin surface. The outer most layer of the epithelium is the stratum corneum, a layer of structure which forms the protective layer against the environment. Beneath the epithelium layer is the dermis, composed of filamentous structure⁷.

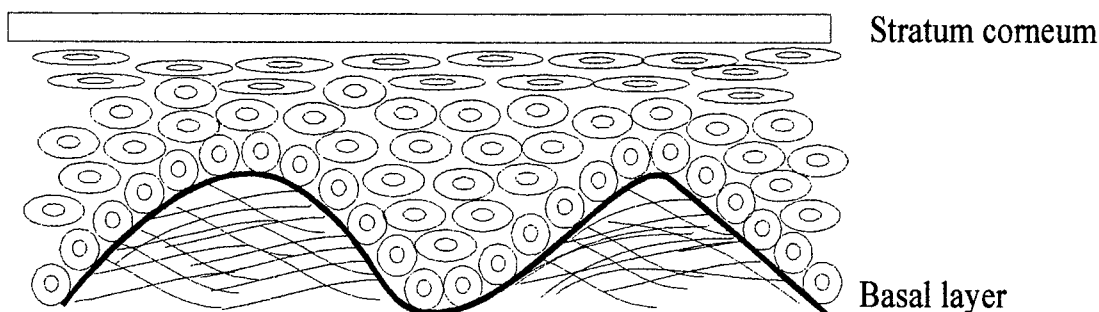


Fig. 2: Structure of the skin

2. EXPERIMENTAL APPARATUS

2.1 Laser Sources for Two-Photon Excitation

For efficient two-photon excitation, photons need to arrive at the sample within a narrow time window. Therefore, lasers with short pulse widths are natural choices for two-photon microscopy. In the commercial market, the titanium-sapphire (ti-sa) laser with pulse duration around 100 fs satisfies this temporal requirement. The titanium-sapphire systems can be pumped by an argon-ion laser (488/514nm) or frequency-doubled, diode pumped Nd-doped crystals (532 nm). These femtosecond sources can generate pulse trains at approximately 80 MHz. In addition, the high lasing bandwidth (700-1000 nm) of the ti-sapphire lasers make them versatile light sources for two-photon microscopy. In addition to the ti-sa lasers, other femtosecond sources such as the Cr:LiSAF and Nd-YLF (pulse compressed) lasers can be used for two-photon excitation^{8,9}.

In addition, picosecond and continuous-wave (cw) lasers can also be used for two-photon excitation. Mode-locked Nd-YAG with pulse width of 100 ps, dye lasers with pulse duration of around 1 ps, and picosecond ti-sa lasers are possible excitation sources. The 647 nm output of a cw ArKr laser has been used to image DAPI and bisbenzimidazole Hoechst 33342 labeled nuclei¹⁰. The commonly available 1064 nm output of the cw Nd-YAG laser can also be used for non-linear excitation of fluorescent samples.

2.2 Experimental Set-up of a Two-Photon Fluorescence Microscope

The experimental arrangement for a typical two-photon fluorescence microscope is shown in Fig. 3. A femtosecond ti-sa laser is shown to be the excitation source but other excitation sources discussed in the previous section can also be used for sample excitation.

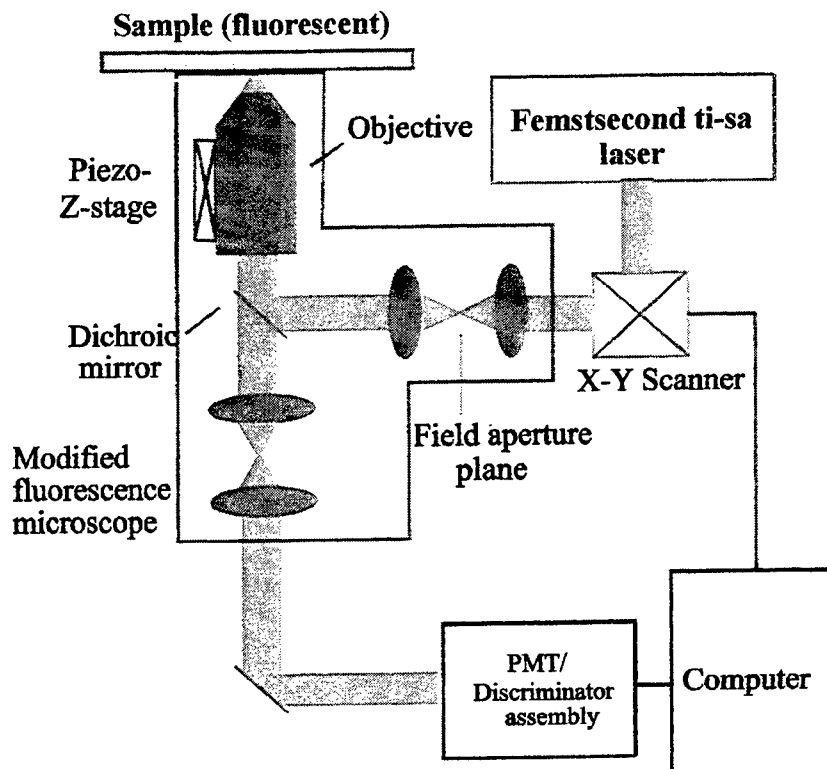


Fig 3: A two-photon fluorescence microscope

The output of the ti-sa laser passes through an x-y scanner prior to entering the modified fluorescence microscope. In our experience, 780 nm output of the ti-sa is sufficient to excite a wide range of fluorophores and is a very useful wavelength. The laser beam then passes a pair of beam expanding lenses where the beam diameter is enlarged to ensure overfilling of the microscope objective's back aperture. To ensure high image resolution, microscope objectives with high numerical aperture (NA) are frequently used. An example is the Zeiss Fluor 40x objective with NA of 1.25. A dichroic reflects the excitation laser into the microscope objective. The angular deviations of the scanning mirrors translate into linear positioning of the focused laser spot on the fluorescent sample. A typical x-y scan is composed of 256x256 pixels. In depth positioning of the focused laser spot on the specimen is achieved by a piezo-driven objective positioner. The fluorescence generated from the two-photon spot is collected by the same microscope objective, passes through the dichroic, and then onto the photomultiplier detector and detection electronics. A commonly used detection scheme involves the use of a discriminator for single photon counting analysis. A computer controls the movement of the laser spot at the sample and also records the incoming fluorescent photons for image analysis.

3. RESULTS

3.1 Two-Photon Point-Spread Functions (PSF)

The spatial resolution in the point-scanning mode of two-photon fluorescence microscopy is determined by the point-spread-function (PSF). Shown in Fig. 4 are the radial and axial PSF's acquired using 0.1 μm fluorescent spheres. The objective used for the PSF measurements was the oil immersion Zeiss 63x Plan Neofluar (NA 1.25). These fluorescent spheres are imbedded in 2% agarose gel and the two-photon microscope is used to acquire a 3-D scan of the spheres.

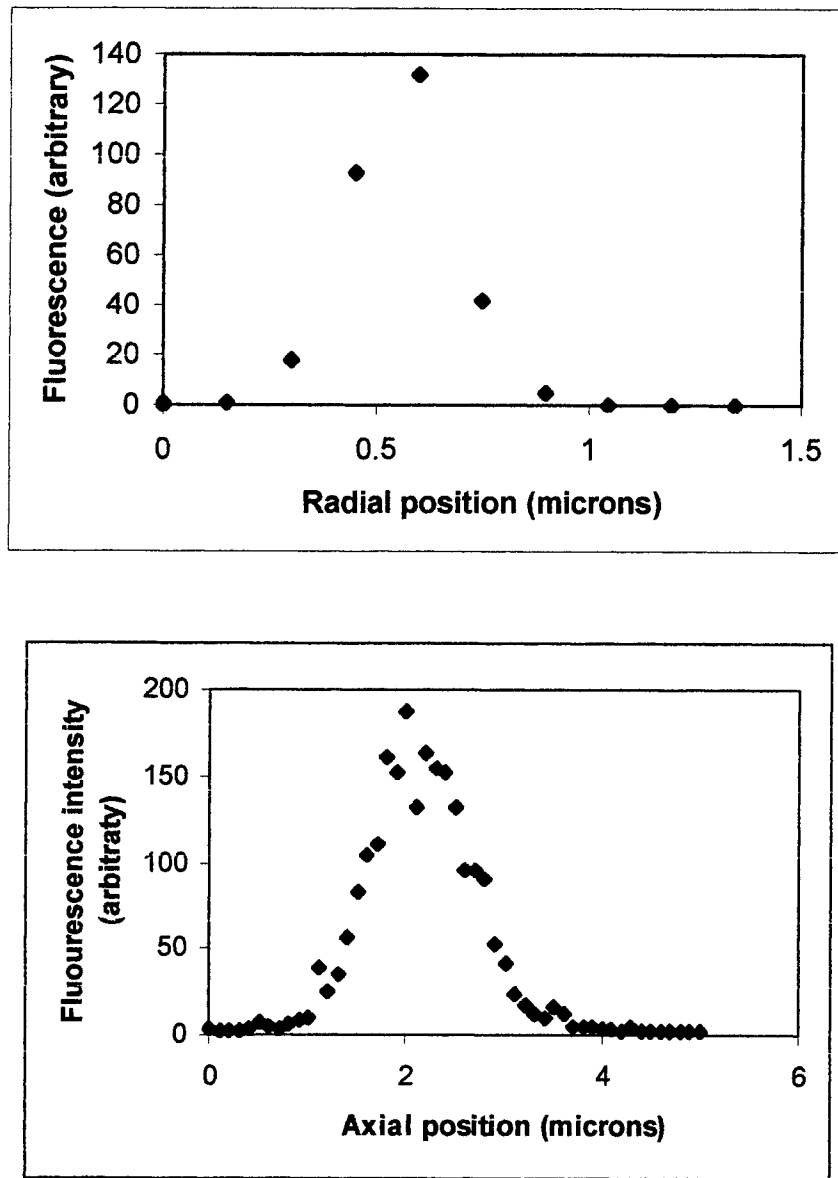


Fig. 4: Radial (top) and axial (bottom) PSF's near the focal plane of the two-photon focal spot, as determined from measuring the intensity of 0.1 micron fluorescent spheres.

From Fig. 4, one can estimate the full width at half maximum (FWHM) of the PSF along the radial and axial coordinates and they turn out to be about 0.3 and 1.2 microns, respectively. Compared to the theoretical results of 0.23 and 1.6 microns, our results compare favorably¹¹.

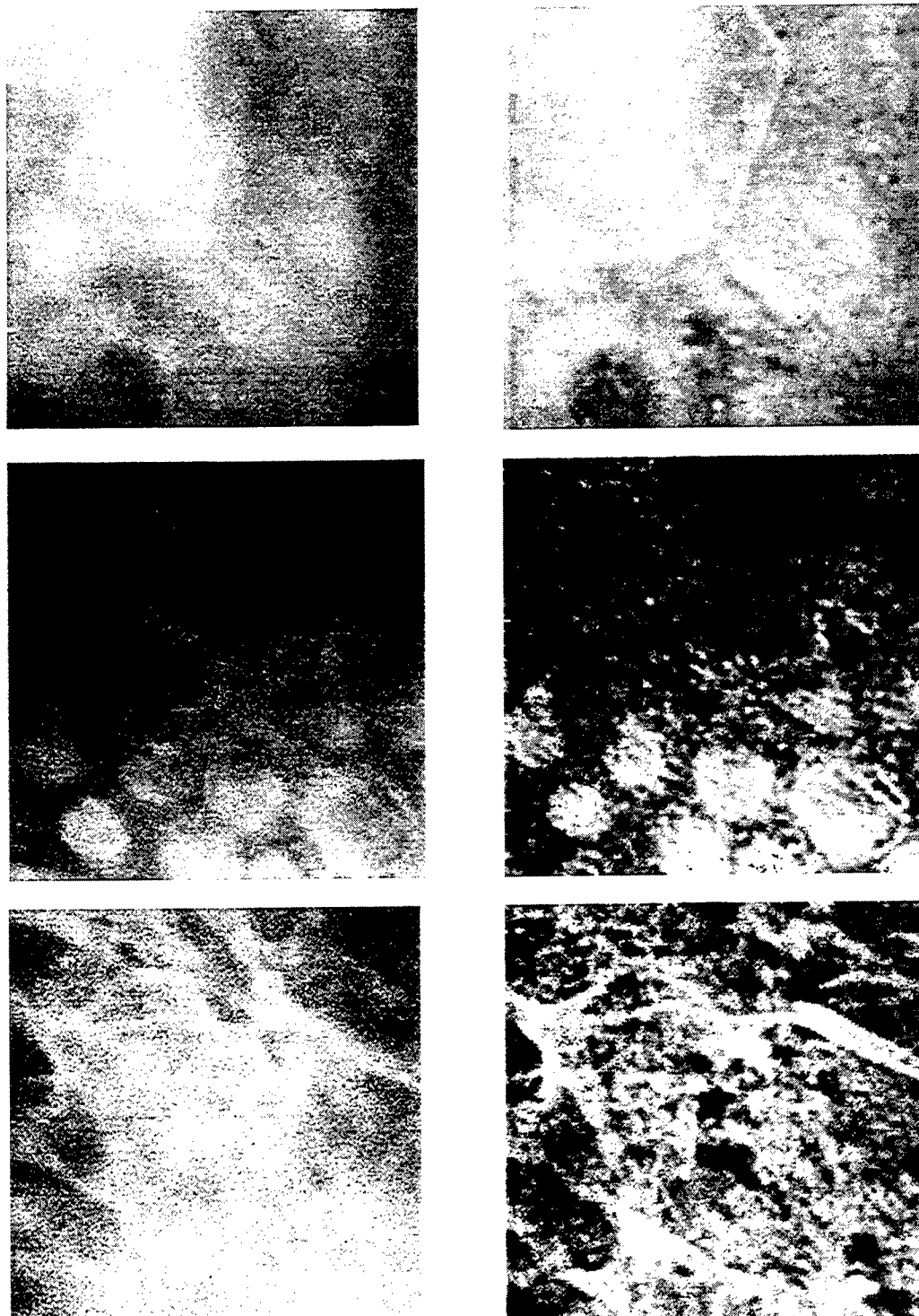


Fig. 5: Raw (left) and post blind deconvolution (right) images of three skin (human) layers. Top: stratum corneum, middle: basal layer, bottom: dermal fiber.

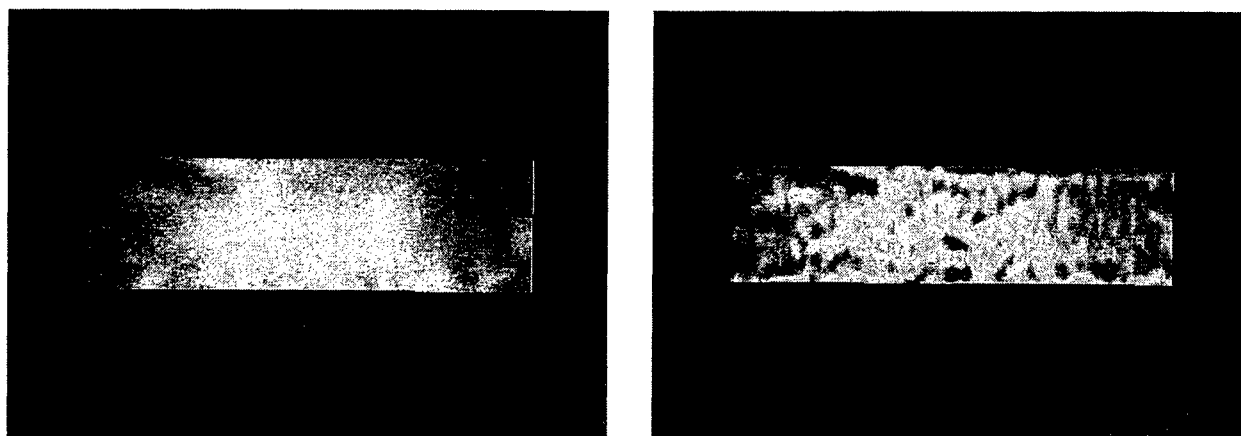


Fig. 6 Raw (left) and blind deconvoluted (right) axial images of the skin (human).

3.2 Skin Image Enhancement by Blind Deconvolution

A common technique used in our lab is to apply blind deconvolution algorithm for further improvement in image resolution. We use the software AutoDeblur™ (AutoQuant, Watervliet, NY) for such image processing. This deconvolution algorithm is based on maximum likelihood approach¹². Fig. 5 shows both the raw image and deconvoluted images of three different axial planes inside the human skin sample. The surface stratum corneum, the basal layer, and the dermal fibers were all imaged and deconvoluted. In all three cases, the deconvoluted images were sharper and showed finer details than the raw images. For the stratum corneum and the basal layers, the granular nature in the structure is much more apparent. And in fibrous layer, the boundaries of individual fibers were much more apparent. Fig. 6 shows an axial section of the raw and blind deconvoluted results. Once again, structures that were fuzzy in the raw data set show up much sharper after deconvolution.

3.3 Modeling of Transdermal Drug Delivery

Due to the non-invasive nature of two-photon imaging, the technique is ideal for studying the process of transdermal drug delivery. In particular, two-photon microscopy can help to elucidate the method by which the transport pathways are altered under different chemical delivery conditions. To model drugs with different chemical properties delivered through the skin (human), fluorescent dyes with different chemical properties can be used. For example, 1,1'-dioctadecyl-5,5'-diphenyl-3,3',3'-tetramethyl indocarbocyanine chloride can be used as a lipophilic model drug under different chemical delivery environment. Fig. 7 shows the delivery of the lipophilic drug, in the presence and absence of the chemical enhancer oleic acid. The model drug delivery solution is kept in contact with the skin until equilibrium is reached. When the delivery medium is composed of PBS (buffer) and ethanol, there is low fluorescence counts at the skin surface and the fluorescence gradient across the skin is small. However, when the delivery medium contains 5% oleic acid, the fluorescence counts at the surface is much higher (by about at least 5 times) and fluorescence through the skin depth examined is greater. Furthermore, the fluorescence gradient increased by about at least 3 times near the skin surface (within about 10 μm). Two facts are indicated by these results. First, the generally higher fluorescence throughout the skin treated with oleic acid indicate that oleic acid most likely increased the membrane fluidity of the skin and that permits the dye to get through the skin easier. Secondly, the larger fluorescence gradient, in the presence of oleic acid, indicates that the flux across the skin is higher, and more of the model drug is delivered across the skin. For hydrophilic molecules, the transport mechanism is quite different. Fig. 8 shows the results for a hydrophilic probe sulfonerrhodamine bis-(PEG 2000). In this case, the surface fluorescence intensity didn't change much with and without oleic acid but the intensity gradient is much more significant in the presence of oleic acid. This indicates that oleic acid affects the transport pathway and not the fluidization of membrane and it is the enhanced gradient that is responsible for molecular transport.

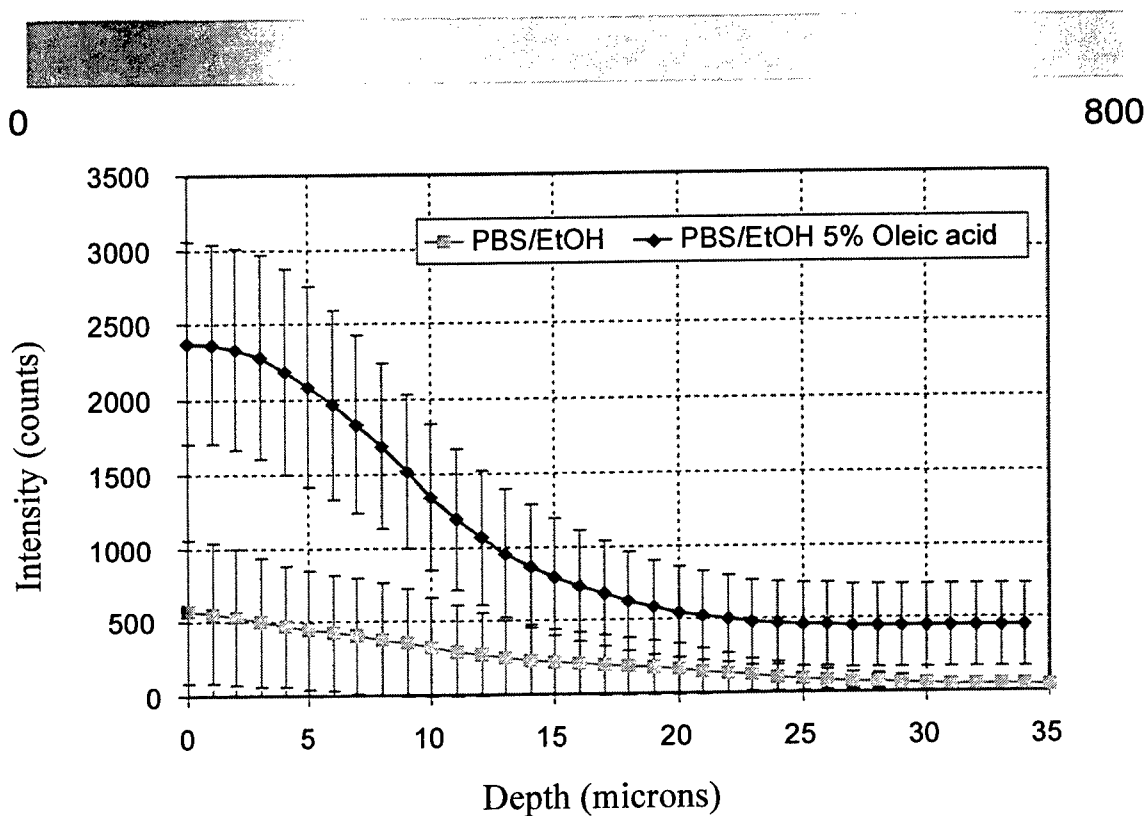
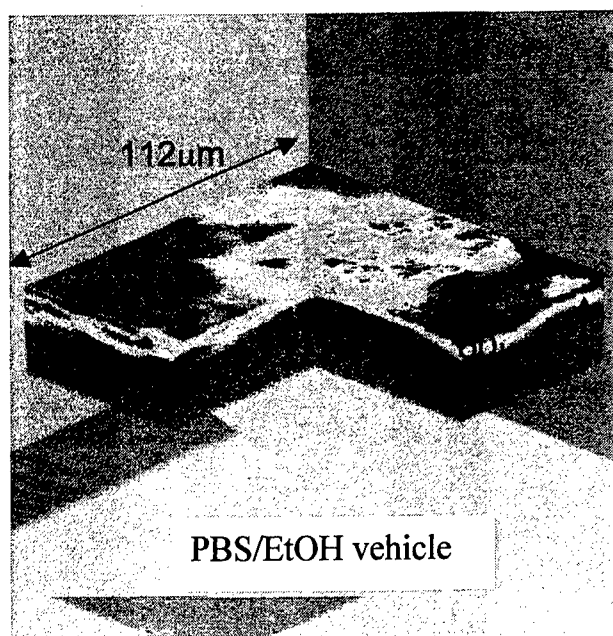


Fig. 7: Effect of chemical enhancer (oleic acid) on the penetration of lipophilic model drug (1,1'-dioctadecyl-5,5'-diphenyl-3,3,3',3'-tetramethyl Indocarbocyanine chloride) across skin (human).

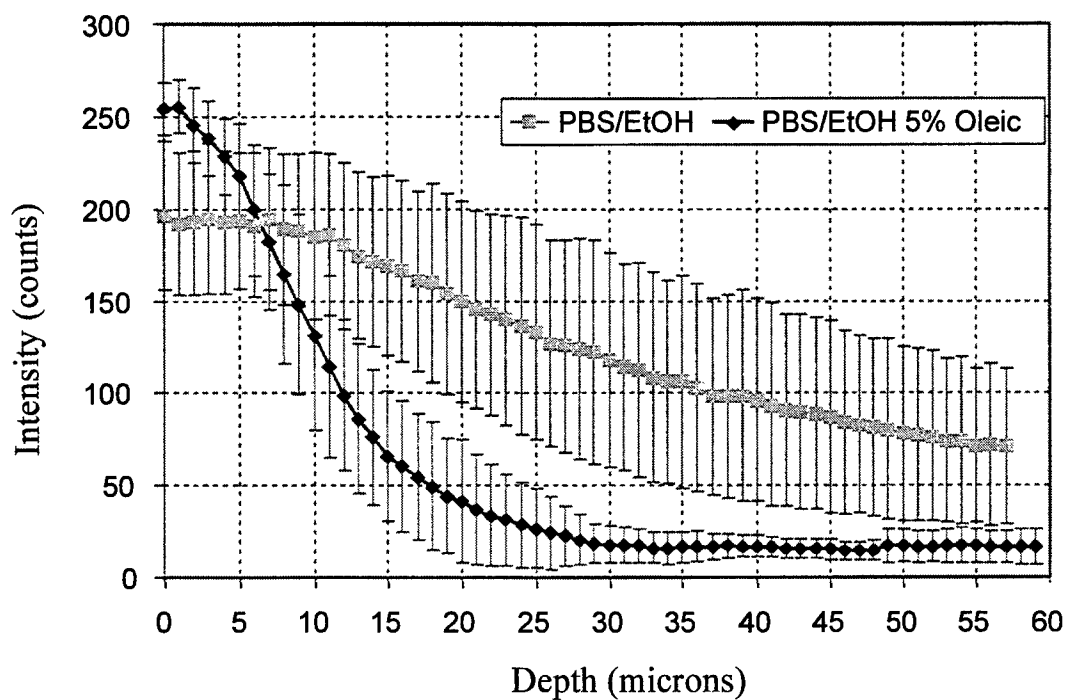
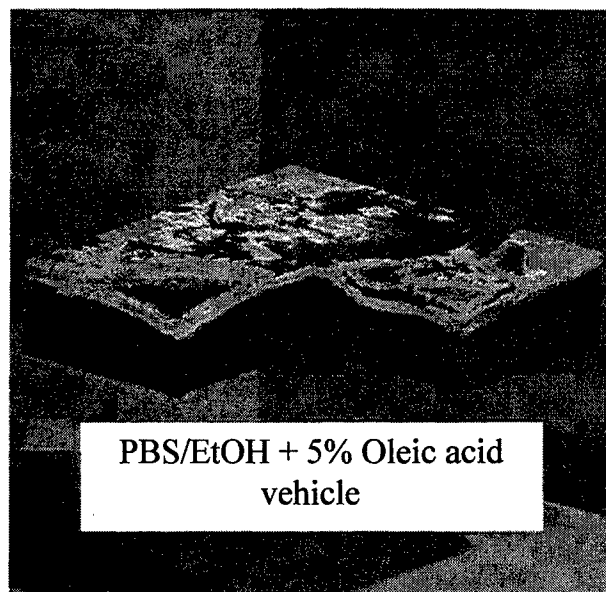
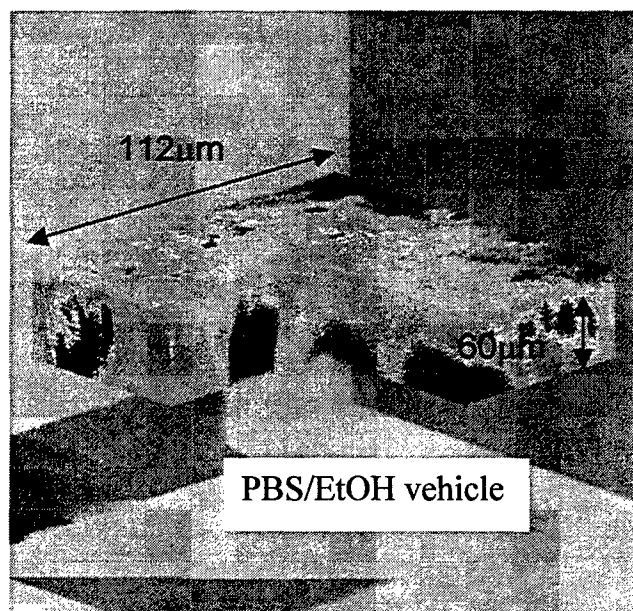


Fig. 8: Effect of chemical enhancer (oleic acid) on the penetration of hydrophilic model drug sulfonerhodamine bis-(PEG 2000) across skin (human).

4. CONCLUSION

In this work, we have demonstrated how two-photon fluorescence microscopy can be used as a powerful experimental tool. Point-like excitation and reduced scattering of excitation light source makes this technique ideal for deep tissue imaging. We have shown that the two-photon PSF obtained experimentally compares favorably with the theoretical predictions. Furthermore, it has been shown that blind deconvolution can be used to furthermore improve image quality of skin at the stratum corneum, basal layer, and fiber level. Finer details in the skin structure boundary separation are revealed after the raw images have been post-processed under blind deconvolution. In addition, two-photon fluorescence microscopy is useful in revealing the effects of chemical enhancer on model drug delivery across the skin. In the presence of oleic acid, both the lipophilic and hydrophilic model drug's gradients across the skin are greater.

Fluorescence microscopy based on two-photon excitation is a useful technique for studying deep tissue process non-invasively. With further development, this technology can become a major diagnostic tool for clinical applications.

5. REFERENCES

1. W. Denk, J. H. Strickler, and W. W. Webb. "Two-photon laser scanning fluorescence microscopy," *Science*, **248**, pp. 73-76, 1990.
2. J. D. Jackson. *Classical Electrodynamics*. John Wiley & Sons, New York, 1975.
3. V. E. Centonze and J. G. White. "Multiphoton excitation provides optical sections from deeper within scattering specimens than confocal imaging," *Biophysical Journal*, **75**, pp. 2015-2024, 1998.
4. J. R. Lakowicz. *Principles of Fluorescence Spectroscopy*. Kluwer Academic/Plenum Publishers, New York, 1999.
5. W. M. McClain and R. A. Harris. "Two-photon spectroscopy in liquids and gases," in *Excited States 3*, E. C. Lim, ed., pp. 1-56, Academic Press, New York, 1977.
6. C. Xu and W. W. Webb. "Multiphoton excitation of molecular fluorophores and nonlinear laser microscopy," in *Topics in Fluorescence Spectroscopy Vol. 5*, J. R. Lakowicz ed., pp. 471-540, Plenum Press, New York, 1997.
7. K. H. Kim, P. T. C. So, I. E. Kochevar, B. R. Maters, and E. Gratton. "Two-photon fluorescence and confocal reflected light imaging of thick tissue structures," *SPIE Proceedings*, **3260**, pp. 46-57, 1998.
8. D. L. Wokosin, V. E. Centonze, and J. G. White. "Multi-photon Excitation Imaging with an All-Solid-State Laser," *SPIE Proceedings* **2678**, pp. 38-49, 1996.
9. D. L. Wokosin, V. E. Centonze, J. G. White, D. Armstrong, G. Robertson, and A. I. Ferguson. "All-solid-state ultrafast lasers facilitate laser multiphoton excitation fluorescence imaging," *IEEE Journal of Selected Topics in Quantum Electronics*, **2** (4), pp. 1051-1065, 1996.
10. S. W. Hell, M. Booth, and S. Wilms. "Two-Photon Near- and Far-Field Fluorescence Microscopy with Continuous-Wave Excitation," *Optics Letters*, **23**(25), pp. 1238-1240, 1998.
11. C. Y. Dong, P. T. C. So, C. Buehler, and E. Gratton. "Spatial resolution in pump-probe microscopy," *Optik*, **106**, pp. 7-14, 1997.
12. T. Holmes. "Blind deconvolution of quantum-limited incoherent imagery: maximum-likelihood approach," *J. Opt. Soc. Am. A*, **9** (7), pp. 1052-1061, 1992.

Simultaneous multichannel nonlinear imaging: combined two-photon excited fluorescence and second-harmonic generation microscopy

R. Gauderon^a, P. B. Lukins^a and C. J. R. Sheppard^{a,b}

^aDepartment of Physical Optics, School of Physics A28,
University of Sydney, NSW 2006, Australia

^bAustralian Key Centre for Microscopy and Microanalysis
University of Sydney, NSW 2006, Australia

ABSTRACT

Simultaneous two-photon excited fluorescence (TPF) and second-harmonic generation (SHG) imaging is demonstrated using a single femtosecond laser and a scanning microscope. This composite nonlinear microscopic technique was applied to imaging DNA and chromosomes, and it was shown that the two different interaction mechanisms provide complementary information on the structure and nonlinear properties of these biological materials beyond that achievable using either TPF or SHG imaging alone. The use of separate modes of detection, in reflection and transmission respectively, and the simultaneous nature of the acquisition of the two images allows pure TPF and SHG images in precise registration to be obtained.

Key words: nonlinear imaging, two-photon microscopy, fluorescence, second-harmonic generation

1. INTRODUCTION

Confocal fluorescence laser scanning microscopy has been widely used for three-dimensional high-resolution optical imaging of biological specimens. More recently, several nonlinear optical microscopies have been developed including those based on two-photon excited fluorescence,^{1,2} three-photon excited fluorescence,³ second-harmonic generation^{4,5} and third-harmonic generation.^{6,7} These nonlinear microscopies have been shown, to various extents, to be valuable techniques for biomedical imaging^{2,8,9} and their use is likely to become more wide-spread particularly with the increasing availability of turn-key solid-state femtosecond laser sources. These microscopies are based on the interaction between the high peak power density that exists at the laser focus and the nonlinear optical properties of the specimen in the focus region. The spatial variation of this interaction in the focus region gives a "soft-aperture" effect which leads to an inherent optical sectioning capability without the need for a confocal pinhole. For example, in two-photon imaging, the intensity of the signal produced is proportional to the square of the fundamental incident intensity leading to a reduction in the size of the effective point-spread-function by a factor of $\sqrt{2}$.^{10,11} The interest in these techniques stems partly from the greater penetration and hence imaging depth possible with the longer (usually near-infrared) wavelengths used, the reasonably high interaction efficiency especially for two-photon excited fluorescence, and the improved optical detection efficiency arising from the fact that a confocal pinhole is not required. While two-photon excited fluorescence (TPF) and second-harmonic generation (SHG) microscopies have been demonstrated using CW^{4,12} and long-pulse¹³ lasers, femtosecond sources are generally more desirable because the effect due to a given pulse varies inversely with the square of the laser pulse-width for pulsed excitation.

Although TPF and SHG imaging systems are optically similar, the nature of the interactions and the contrast-generating mechanisms are very different. TPF is a resonant process involving simultaneous absorption of two low energy photons to cause molecular electronic excitation followed by fluorescent emission with an angular distribution determined by the molecular configuration (symmetry and orientation) and a fluorescence decay time determined by the electronic upper-state lifetime. On the other hand, SHG is a non-resonant virtually instantaneous process giving rise to harmonic radiation in the forward direction. Therefore, TPF is incoherent whereas SHG is coherent. Obviously, TPF can be detected over the emission bandwidth of the fluorophore whereas SHG radiation occurs only at the second harmonic of the excitation laser frequency.

So far, all of the 3D optical imaging techniques, whether they involve single-photon or multiphoton excitation, have been applied as single microscopic techniques. Even when more than one two-photon technique is used in a study,¹⁴ this has involved two separate single-channel measurements made at different times with different experimental parameters. However, there is also the possibility of imaging a specimen using two or more imaging modes (or channels) simultaneously in time. Such a multichannel imaging approach may be particularly attractive for nonlinear microscopy where the laser pulse may interact with several nonlinear optical properties of the specimen and the resulting optical signals may be detected separately to form simultaneous composite nonlinear optical images of the specimen. Furthermore, a simultaneous imaging capability would be useful for time-series studies and in cases where photodamage must be minimised or where specimen changes or drift occur during the scan period. In this paper, we demonstrate high-resolution TPF and SHG imaging performed simultaneously in time using a two-channel synchronized detection method. The approach is illustrated by imaging DNA and chromosomes using a modified commercial confocal microscope. We also show that the combination of TPF and SHG imaging provides information about the specimen that is beyond that provided by either TPF or SHG imaging alone.

2. MATERIALS AND METHODS

Two-photon microscopy was carried out using a modified inverted Leica TCS NT confocal microscope coupled to a Coherent Mira 900 femtosecond Ti:sapphire laser (~150 fs pulse-width, 720-860 nm) pumped by a Coherent 5W Verdi solid-state laser.¹⁵ For this laser pulse-width, an adjustable group velocity dispersion (GVD) precompensation arrangement was not necessary.¹⁵ This microscope is of the beam-scanning type with an acquisition rate of up to 4 images (512 x 512 pixels) per second. All images were taken with a x40/0.75NA air objective. An important capability of this system is that it can operate simultaneously in both transmission and reflection modes. Fig. 1 shows a schematic of the system for simultaneous TPF/SHG

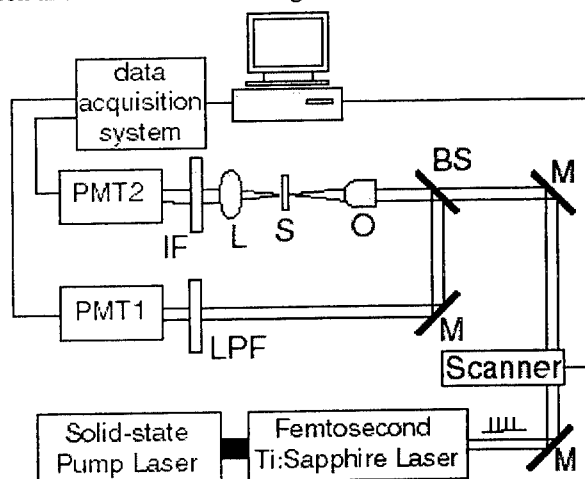


Fig. 1. Experimental arrangement for simultaneous TPF/SHG imaging. BS, beamsplitter; IF, 400 nm interference filter; L, lens; LPF, long-pass filter; M, mirror; O, objective; S, specimen.

imaging in which fluorescence was detected in reflection and second-harmonic light was detected in transmission. For the fluorescence channel, a broadband dichroic was used and the fluorescence detection bandwidth determined by a long-pass filter with a cutoff wavelength ~450 nm. For the SHG channel, the 800 nm fundamental beam was excluded from the detector using a 400 nm interference filter with a bandwidth of 20 nm FWHM and a rejection ratio at 800 nm of $>10^5$. In order to maximise the sensitivity, particularly for the unstained specimens, no confocal pinhole was used.

The observed resolution for both TPF and SHG modes was ~0.5 μm , which is close to the theoretical value of $0.61 \lambda / \text{NA}\sqrt{2} = 0.46 \mu\text{m}$. We emphasise that in the simultaneous TPF/SHG mode, the TPF and SHG images are acquired essentially simultaneously with synchronization to within the aperture time (~2 μs) of the sample-and-hold circuitry. The time registration is therefore better than the pixel dwell time.

3.RESULTS AND DISCUSSION

In order to demonstrate multichannel TPF/SHG imaging, we chose biological specimens that are well-defined and well-known, for example DAPI-stained cultured onion root cells in various stages of mitosis, TPF and SHG images of which are shown elsewhere.¹⁶ These cells do not give strong natural fluorescence and so are best imaged using a fluorescent labelling dye such as DAPI. Although this enables straightforward TPF imaging, SHG imaging of specimens labelled with DAPI is complicated by the fact that the second-harmonic wavelength (~400 nm) is within the fluorescence emission band of DAPI (~390 - 600 nm) and so may be overwhelmed by DAPI fluorescence.

Biological materials are attractive specimens for SHG imaging because biomolecules typically have large molecular anisotropy and second-order nonlinearity. Apart from the obvious interest in DNA, this biomolecular system is of particular interest here since SHG may be enhanced by pseudo-phaseshmatching resulting from the extended double-helix structure. This can then give a relatively strong contrast mechanism in SHG imaging and the prospect of obtaining microscopic nonlinear information about DNA without the complications associated with additives such as fluorescent labels. Another sample which has been used is herring sperm DNA.¹⁶

In order to achieve simultaneous TPF/SHG imaging, it is desirable to use an unstained specimen which can yield a suitable level of natural fluorescence. We produced reflection TPF and transmission SHG images obtained simultaneously on precisely the same area and at the same depth for a specimen comprising *B. Tyroni* fruit fly polytene chromosomes. In these there are some features, which are in almost perfect registration, that appear common to each image and others that are clearly unique to one image or the other. Nevertheless, the fluorescence and harmonic images are clearly both qualitatively and quantitatively distinct, and the two images represent essentially pure fluorescence and harmonic images. Therefore, the simultaneous acquisition of TPF and SHG images clearly provides a means of obtaining new and complementary information about this specimen.

Although we used a non-confocal detection method for both TPF and SHG imaging in order to maximise sensitivity, improved resolution can be obtained by using a confocal pinhole albeit at the expense of signal level.^{17, 18} The approach used here could also be extended by using multiple detectors and the unsharp masking technique.¹⁹ Since the 3D OTF for TPF shows negative values for large pinhole sizes,²⁰ the resolution can be further improved by subtracting the image formed with an open pinhole from that formed with a small pinhole. Therefore, an example of a simple layout for multichannel two-photon microscopy with enhanced spatial resolution might consist of two independent fluorescence detection channels (with and without pinholes) in either a reflection configuration, as used here, or in a transmission mode using dichroics to separate the fluorescence signals from harmonic signals which are best detected in transmission in this case. In this arrangement, differential processing of the separate images from the multiple detectors should yield a useful resolution enhancement. We also note that Klar and Hell²¹ have recently demonstrated resolution beyond the diffraction limit by using a UV pulse to create a confined region of excited molecules in a specimen and a spatially different infrared pulse to quench fluorescence from the outer part of the focus region through stimulated emission.

3.CONCLUSIONS

We have demonstrated TPF and SHG imaging both separately and simultaneously. Furthermore, this has been achieved using a commercial femtosecond laser and a commercial confocal microscope together with only a few additional components. We believe that the simultaneous use of two or more multiphoton microscopic techniques will develop as an important new direction in 3D optical microscopy particularly in biomedical and materials applications where the use of several multiphoton interactions can provide greater insight into the physico-chemical properties of the sample. We envisage that in the future, microscopists may use a single flexible pulsed-laser scanning microscope which can be suitably reconfigured to study specimens using simultaneous detection of two or more multiphoton interactions with either confocal or non-confocal detection. Such a multichannel or multifunction optical microscope would be particularly useful for applications involving specimens with complex structure and subtle physico-chemical properties.

ACKNOWLEDGMENTS

The authors would like to thank Leica Microsystems, Coherent Scientific Pty Ltd, the Australian Key Centre for Microscopy, Dr G. Cox, Mrs. E. Kable and Dr Jing-Ting Zhao. Financial support from the Australian Research Council is gratefully acknowledged.

REFERENCES

1. C. J. R. Sheppard and R. Kompfner, Resonant scanning optical microscope. *Appl. Opt.*, **17**, pp. 2879-2882, 1978.
2. W. Denk., J. H. Strickler and W. W. Webb, Two-photon laser scanning fluorescence microscopy. *Science*, **248**, pp. 73-76, 1990.
3. S. W. Hell, K. Bahlmann, M. Schrader and M. Soini, Three-photon excitation in fluorescence microscopy. *J. Biomed. Opt.*, **1**, pp. 71-74, 1996.
4. J. N. Gannaway and C. J. R. Sheppard, Second-harmonic imaging in the scanning optical microscope. *Opt. and Quantum Elect.*, **10**, pp. 435-439, 1978.
5. R. Gauderon, P. B. Lukins and C. J. R. Sheppard, Three-dimensional second-harmonic generation imaging with femtosecond laser pulses. *Opt. Lett.*, **23**, pp. 1209-1211, 1998.
6. M. Mueller, J. A. Squier, K. R. Wilson and G. J. Brakenhoff, 3D microscopy of transparent objects using third-harmonic generation. *J. Microsc.*, **191**, pp. 266-274, 1998.
7. J. A. Squier, M. Mueller, G. J. Brakenhoff and K. R. Wilson, Third-harmonic generation microscopy. *Optics Express*, **3**, pp. 315-324, 1998.
8. Y. Guo, P. P. Ho, H. Savage, D. Harris, P. Sacks, S. Schantz., F. Liu, N. Zhadin and R. R. Alfano, Second-harmonic tomography of tissues. *Opt. Lett.*, **22**, pp. 1323-1325, 1997.
9. P. J. Campagnola, M. Wei, A. Lewis and L. M. Loew, High-resolution nonlinear optical imaging of live cells by second-harmonic generation. *Biophys. J.*, **77**, pp. 3341-3349, 1999.
10. M. Gu and C. J. R. Sheppard, Comparison of three-dimensional imaging properties between two-photon and single-photon fluorescence microscopy. *J. Microsc.*, **177**, pp. 128-137, 1995.
11. M. Gu and X. S. Gan, Effect of the detector size and the fluorescence wavelength on the resolution of three- and two-photon confocal microscopy. *Bioimaging*, **4**, pp. 129-137, 1996.
12. M. J. Booth and S. W. Hell, Continuous-wave excitation two-photon fluorescence microscopy exemplified with the 647 nm ArKr line. *J. Microsc.*, **190**, pp. 298-304, 1998.
13. J. Vydra and M. Eich, Mapping of the lateral polar orientation distribution in second-order nonlinear films by scanning second-harmonic microscopy. *Appl. Phys. Lett.*, **72**, pp. 275-277, 1998.
14. G. Peleg, A. Lewis, M. Linial and L. M. Loew, Nonlinear optical measurement of membrane potential around single molecules at selected cellular sites. *Proc. Natl. Acad. Sci. USA*, **96**, pp. 6700-6704, 1999.
15. R. L. Fork, O. E. Martinez and J. P. Gordon, Negative dispersion using pairs of prisms. *Opt. Lett.*, **9**, pp. 150-152, 1984.
16. R. Gauderon, P. B. Lukins and C. J. R. Sheppard, Simultaneous multichannel nonlinear imaging: combined two-photon excited fluorescence and second harmonic generation microscopy, submitted to *Micron*.
17. E. H. K. Stelzer, S. W. Hell, S. Lindek, R. Stricker, R. Pick, C. Storz, G. Ritter and N. Salmon (1994) Nonlinear absorption extends confocal fluorescence microscopy into the ultra-violet region and confines the illumination volume. *Opt. Commun.*, **104**, pp. 223-228, 1994.
18. R. Gauderon, P. B. Lukins and C. J. R. Sheppard, Effect of a confocal pinhole in two-photon microscopy. *Microsc. Res. & Tech.*, **47**, pp. 210-214, 1999.
19. C. J. R. Sheppard and C. J. Cogswell (1990) Confocal microscopy with detector arrays. *J. Mod. Opt.*, **37**, pp. 267-279, 1990.

Second-harmonic Generation Microscopy of Tooth

Fu-Jen Kao^{*a,b}, Yung-Shun Wang^a, Mao-Kuo Huang^a, Sheng-Lung Huang^c, Ping-Chin Cheng^d

^aDepartment of Physics, National Sun Yat-sen University, Kaohsiung 80424, Taiwan, ROC

^bCenter for Neuroscience, National Sun Yat-sen University, Kaohsiung 80424, Taiwan, ROC

^cInstitute of Electro-Optical Engineering, National Sun Yat-sen University, Kaohsiung 80424, Taiwan, ROC

^dDepartment of Electrical Engineering, University at Buffalo, Buffalo, NY 14260, USA

ABSTRACT

In this study, we have developed a high performance microscopic system to perform second-harmonic (SH) imaging on a tooth. The high sensitivity of the system allows acquisition rate of 300 seconds/frame with resolution at 512x512 pixels. The surface SH signal generated from the tooth is also carefully verified through micro-spectroscopy, polarization rotation, and wavelength tuning. In this way, we can ensure the authenticity of the signal. The enamel that encapsulates the dentine is known to possess highly ordered structures. The anisotropy of the structure is revealed in the microscopic SH images of the tooth sample.

Keywords: Second-harmonic generation, confocal microscopy, micro-spectroscopy, tooth, enamel

1. INTRODUCTION

Second-harmonic generation (SHG) is a highly coherent nonlinear optical process. It is often used in extending coherent light sources to shorter wavelengths¹ and to probe anisotropy of various structures in a specimen.^{2,3} In combination with scanning optical microscopy, SHG can be used to image samples of highly ordered structure without resorting to dyes. Microscopic imaging employing SHG was first reported by Gannaway and Sheppard⁴ in 1978. SHG mapping of nonlinear crystals, tissues, and polycrystalline molecular films has been reported.⁵⁻⁸ However, the nonlinear susceptibility of different materials varies a lot. SHG signal from nonlinear crystals or crystalline structures is relatively strong and easy to detect. Whereas SHG from less ordered structure is much weaker and requires very sensitive detecting scheme for image mapping. In this study, we have employed a confocal microscope, a mode-locked Ti:sapphire laser, and a liquid-nitrogen-cooled back-illuminated CCD camera to form a very sensitive SHG scanning microscopic imaging system. The peak light intensity at the focal point is estimated to be greater than 1×10^{10} W/cm². At this intensity, generation of surface SHG is feasible.

The second-harmonic signal exhibits the characteristic square power dependence on incident power. However, the cross section for generating second-harmonic signal is very small. Given the high instantaneous intensity of the pumping beam, it is likely that other nonlinear processes may also take place, such as two-photon fluorescence⁹, which also possesses square dependence on incident power. It is thus necessary to verify the measured signal to ensure the authenticity of image contrast as a result of SHG. We have employed the following techniques in the verification of measured signals, which include micro-spectroscopy, polarization rotation, and wavelength tuning.

2. EXPERIMENTAL SETUP

2.1 Scanning Confocal Microscope for SHG image acquisition

A mode-locked Ti:sapphire laser (Tsunami, Spectra-Physics) pumped by a frequency-doubled all-solid-state laser (Verdi, Coherent) provides ultrafast laser pulses centered at 780 nm with pulse width approximately 100 femtoseconds. The repetition rate of the laser is 82 MHz. For the acquisition of SHG microscopic images, a beam scanning confocal microscope (Fluoview, Olympus) and a liquid nitrogen cooled CCD camera with a back-illuminated chip of 512x512 pixels (Orbis II, SpectraSource) are carefully integrated as shown in Fig. 1. The galvo-mirror set of the confocal microscope scans the laser beam over a designated area of the sample. A dichroic mirror reflects the scanned images toward the CCD. A relay lens is used to image this scanned area to the CCD chip. In between the dichroic and the CCD imaging chip, band pass and interference filters are used to ensure that only the SH signal is passed.

*correspondence: Email: fjk@mail.nsysu.edu.tw; Telephone: +886-7-5253720; Fax: +886-7-5253709

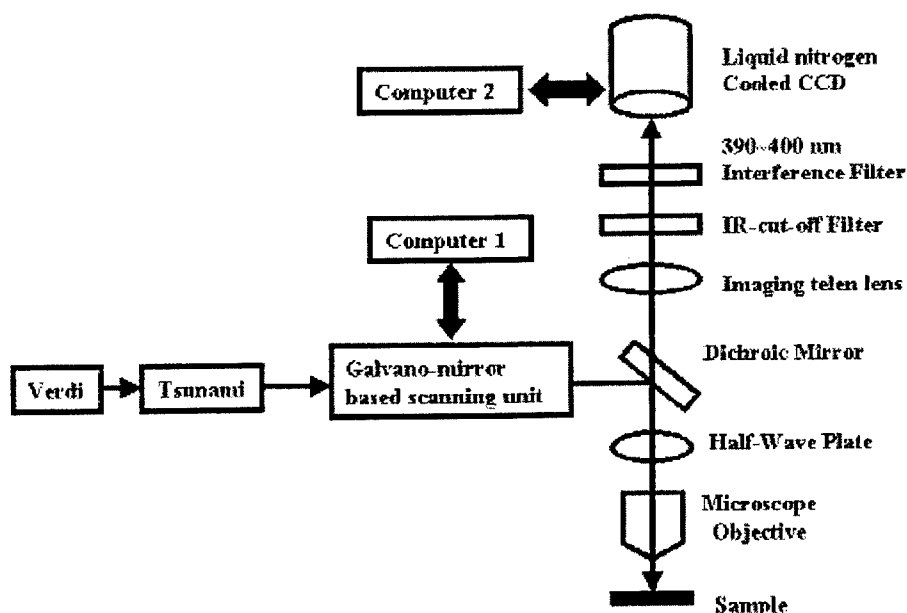


Figure 1. Schematics of the scanning microscope for SHG imaging. The mode-locked ti:sapphire laser provides ultrashort laser pulses for SHG excitation. The scanned area on the sample is imaged to the cooled CCD camera. The combination of IR cut-off filter and interference filter are used to reject non-SHG signal.

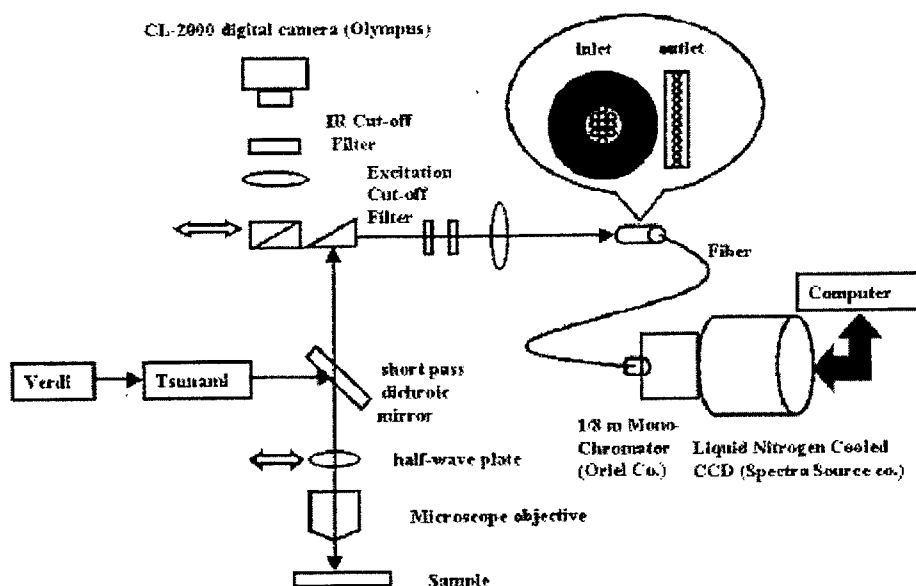


Figure 2. Schematic of the micro-spectroscopy. A specialized fiber bundle as shown in the figure is used to effectively couple the fluorescence collected from the microscope to the spectrometer. The outlet of the fiber bundle is vertically aligned to form a slit. The spectra acquired would form a band-like image on the CCD. The spectral range covered in a single frame depends on the grating installed in the monochromator. With a 600-groove grating, a spectral range of 150 nm can be contained in an image frame.

Using cooled CCD camera to integrate the very weak SHG signal is necessary, since the photomultiplier tubes that come with the confocal microscope are not sensitive enough. For a photo-multiplier to work, one would have to resort to pulse counting to integrate the signal and to reach sufficient signal-to-noise ratio. Pulse counting would nonetheless greatly

complicate the setup and subject the system to greater electronic noise. The use of a liquid nitrogen cooled CCD camera is very effective in this setup. Its very high quantum efficiency and natural ability to integrate signal enable efficient acquisition of SH images.

2.2 Micro-spectroscopy

A micro-spectroscopic setup is also employed to verify the nature of the signal thus obtained, as shown in Fig. 2. The laser beam is coupled into a modified fluorescence microscope (BX50, Olympus) through a dichroic mirror. The optical signal reflected from the sample is then guided to the spectrometer (77250, Oriel) through fiber coupling. The same liquid nitrogen cooled CCD camera described above is attached to the spectrometer for spectrum acquisition. Normally, a 10X objective of NA0.25 is employed for beam focusing. After loss in the optical path, a maximum power of 200mW is measured under the objective, which would correspond to intensity as high as 10^{10} W/cm^2 . Neutral density filters are used for power level adjustment. A half-wave plate is placed right next to the focusing objective. The half-wave plate is used to rotate the polarization of the incident beam so that the anisotropy of the sample can be detected.

The effectiveness of the above setup is tested with an unpolished KTP crystal. A fall-out primary tooth from a six year-old girl is used as the sample.

3. RESULTS

For SHG in the reflected direction, the intensity can be expressed as

$$I(2\omega) = \frac{32\pi^3 \omega^2 \sec^2 \theta_{2\omega}}{c^3 \epsilon_1(\omega) \epsilon_1^{\frac{1}{2}}(2\omega)} |e_{2\omega} \cdot \chi^{(2)} : e_{\omega} e_{\omega}|^2 I^2(\omega) \quad (1)$$

According to the above equation, it is estimated that assuming $|\chi^{(2)}| \sim 10^{-15} \text{ esu}$, a SH output of 10^5 photons/second can be obtained. With a liquid nitrogen cooled CCD camera, such signal is readily detectable and is able to form clear images. The contribution to SHG contains both the surface layer and the bulk. The bulk contribution comes essentially from a layer of $\lambda/2\pi$ thick near the surface. It has been pointed out that if the structure of surface $\chi^{(2)}$ is sufficiently different from that of volume $\chi^{(2)}$, the relative intensity of $\chi^{(2)}_{\text{surf}}$ can be enhanced by polarization selection.

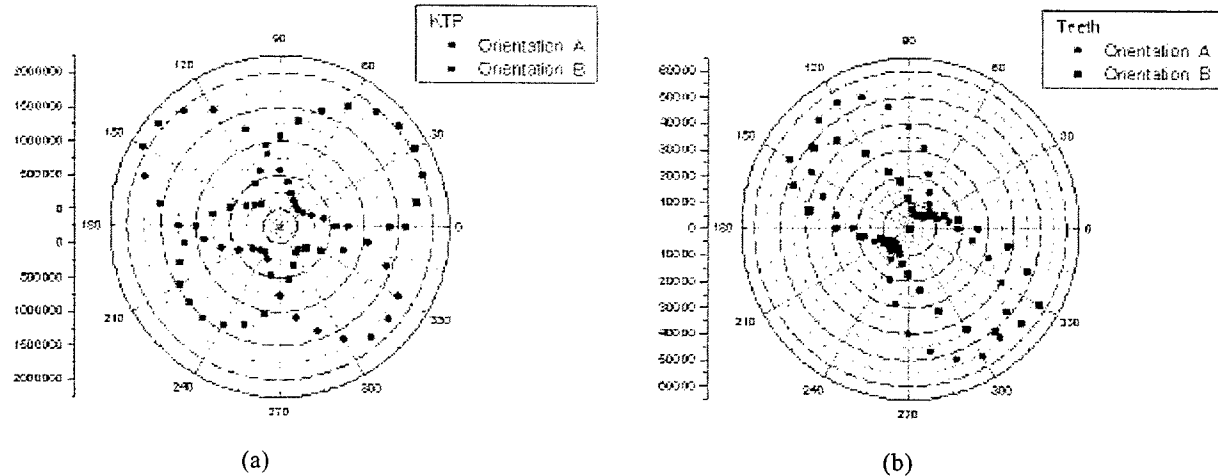


Figure 3. Polar plots of SHG intensity as a function of polarization orientation from (a) a KTP crystal and (b) the primary tooth sample, respectively. The orientation of the samples is rotated to ensure that the anisotropy of the SHG distribution is resulted from the samples instead of the optical elements within the imaging microscope.

The surface SHG signal is usually very weak. It is thus necessary to discriminate the signal against other nonlinear backgrounds, such as two-photon fluorescence that has much higher cross section. In our measurements, methods of micro-spectroscopy and polarization rotation were employed to ensure the authenticity of the signal. Figure 3 shows the polar dependence of SHG intensity on incident beam polarization. The polarization of the incident beam is selected by the half-

wave plate placed next to the imaging objective. The dumb-bell shape of the plots clearly indicates the anisotropy of the sample.

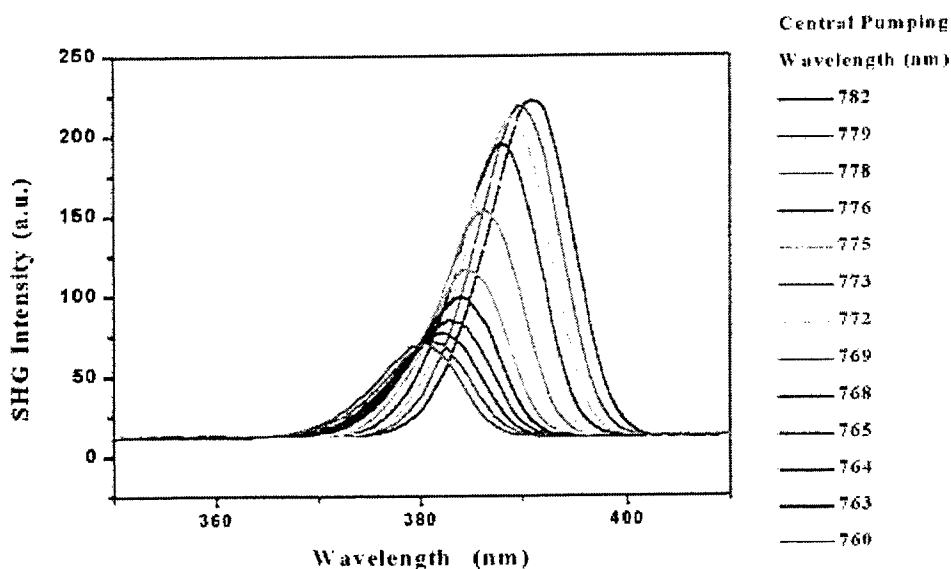


Figure 4. SHG Spectra as a function of pumping wavelength. The peak position of the detected spectra shifts accordingly as the wavelength of the excitation beam changes, clearly indicating the signal being SHG. The intensity of the SHG decreases as the central wavelength becomes shorter. This decrement reflects that the laser cavity is optimized to operate around 780 nm.

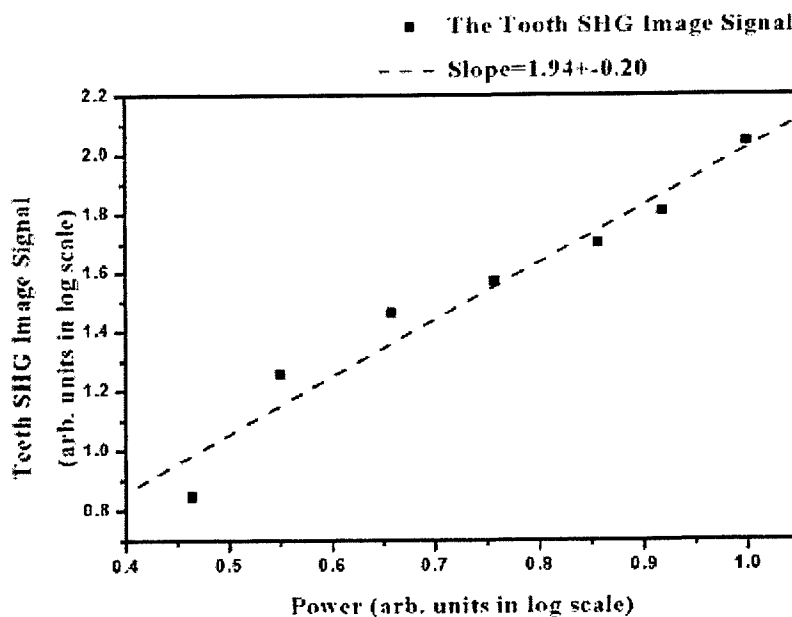


Figure 5. The SHG signal from the tooth as a function of incident power. The slope of 1.94 indicates the square power dependence of SHG.

Signal verification through micro-spectroscopy is shown in Fig. 4, where the SHG spectra as a function of pumping beam wavelength are plotted. The peak wavelength of the SHG shifts accordingly as the central wavelength of the pumping beam

is adjusted. This correlation in wavelength tuning strongly suggests that the signal is indeed SHG. In addition, the SHG signal as a function of incident power is shown in Fig. 5. The square power dependence indicates the two-photon nature of the excitation process. The microscopic reflection and SH images are shown in Fig. 6. The reflective images shown are somewhat obscured by scattering resulted from surface roughness and back-reflection from lens within the microscope system. The contrast from reflective images is not sensitive to polarization orientation. For comparison, the SHG images exhibit clear contrast and structural anisotropy.

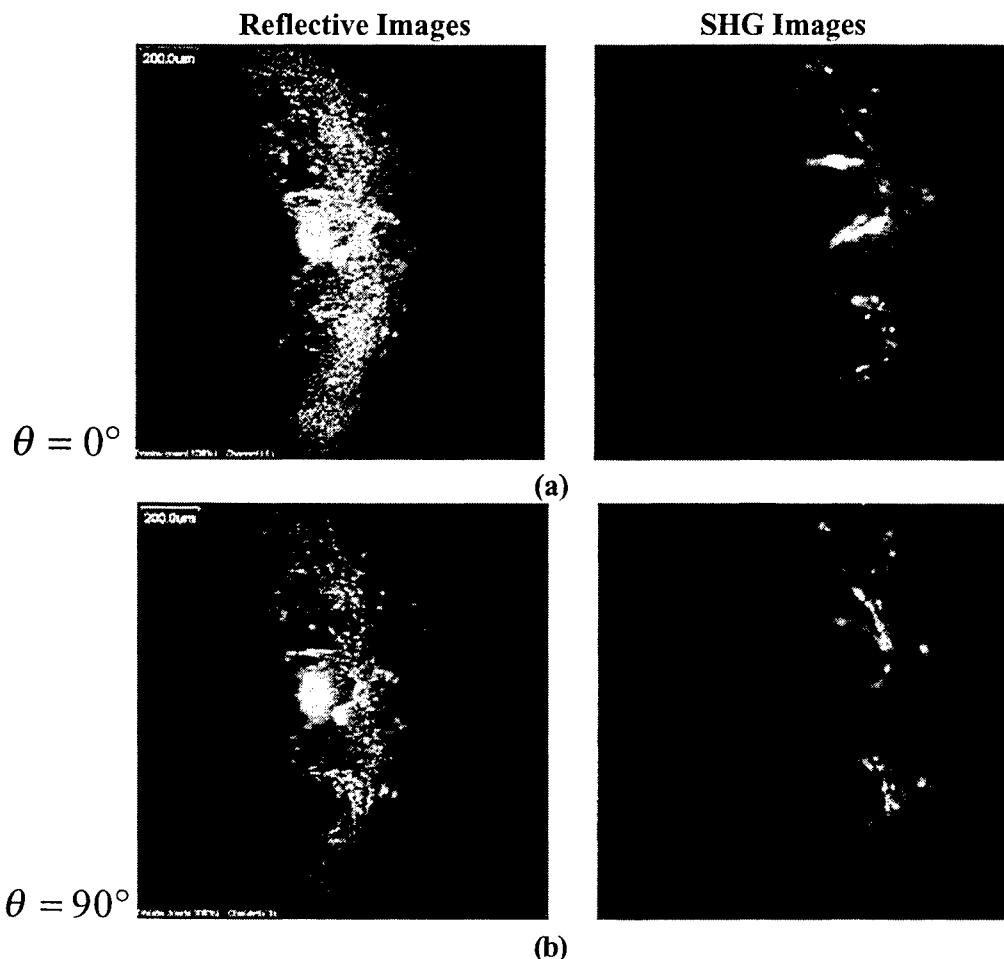


Figure 6. Reflective and SHG images acquired at two different polarization orientations that are perpendicular to each other. The reflective images obtained at the two polarization orientations are basically the same. The big bright spot in the center of reflective images is characteristics to such images, which results from back reflection from lens in the scanning laser beam path. For comparison, the SHG images show very clear contrast. In addition, the different pattern obtained at the two polarization orientations indicates that the tooth is highly anisotropic.

4. DISCUSSION

The theory of surface SHG has been well developed. The physical origin of surface SHG can be attributed to structural discontinuity and field discontinuity at the interface. It was believed that the effect of structural discontinuity dominates a semiconductor surface with dangling bonds. On the other hand, field discontinuity may dominate a liquid or glass surface, where the surface structure is not very different from that in the bulk.^{2,3} A surface modification should certainly be distinguishable by surface SHG even in the presence of bulk contribution. Many experiments have shown that surface SHG can reach sub-monolayer sensitivity.¹⁰ From the discussion in the above section, signal intensity in the order of 10^5 photons/sec is attainable, which is sufficient for forming a SHG microscopic image within reasonable time scale. When compared with SHG generated in the bulk that satisfies phase matching conditions, the surface SHG is relatively weak. It is

thus necessary to employ highly sensitive detecting schemes as described above for image acquisition. The maximum SHG intensity available is limited by the onset of surface damages that may result from multi-photon ionization or free electron acceleration heating.

5. CONCLUSIONS

In summary, we have developed a high performance microscopic system for SHG imaging. Using the above system, we have successfully acquired microscopic second-harmonic images of a tooth. Methods of polarization rotation, micro-spectroscopy, and wavelength tuning were also employed to verify the authenticity of the SHG signal. The signal that forms the image contrast is likely the surface SHG from the enamel layer that encapsulating the dentine.

The spatial resolution should be comparable with other two-photon techniques, such as two-photon fluorescence microscopy.⁹ We expect that the technique thus developed will find further applications in microscopic inspection of many other systems, such as mineral samples, semiconductor surfaces or interfaces, biological systems, ..etc. The highly sensitive SHG imaging system described above also has the advantage of being relatively fast in image acquisition. It allows frame rate at 300 seconds/frame with resolution at 512x512 pixels. If a sample is raster-scanned with a 2D translation stage at the same resolution and a PMT is used for signal detection, the frame rate could well exceed hours. Sensitivity and speed will be determining factors for practical applications of the SHG microscopic systems.

ACKNOWLEDGEMENT

We gratefully acknowledge support of this research by the National Science Council of Taiwan under Grant NSC89-2112-M-110-016 and NSC-89-2216-E-110-003 and by the Academic Excellence Program of the Ministry of Education (89-B-FA08-1-4).

REFERENCES

1. A Yariv, *Quantum Electronics 3rd edition*, John Wiley & Sons, New York, 1989.
2. R. Shen, *The Principles of Nonlinear Optics*, John Wiley & Sons, New York, 1984.
3. Y.R. Shen, "Surface properties probed by second-harmonic and sum-frequency generation", *Nature* **337**, pp. 519-525, 1989.
4. J.N. Gannaway and C.J.R. Sheppard, "Second-harmonic imaging in the scanning optical microscope", *Opt. Quantum Electron.* **10**, pp. 435-439, 1978.
5. J. Vydra and M. Eich, "Mapping of the lateral polar orientational distribution in second-order nonlinear thin films by scanning second-harmonic microspectroscopy", *Appl. Phys. Lett.* **72**, pp. 275-277, 1998.
6. R. Gauderon, P.B. Lukins, and C.J.R. Sheppard, "Three-dimensional second-harmonic generation imaging with femtosecond laser pulses", *Opt. Lett.* **23**, pp. 1209-1211, 1998.
7. Y. Guo *et al*, "Optical harmonic generation from animal tissues by the use of picosecond and femtosecond laser pulses", *Appl. Opt.* **35**, pp. 6810-6813, 1996.
8. Y. Guo *et al*, "Second-harmonic tomography of tissues", *Opt. Lett.* **22**, pp. 1323-1325, 1997.
9. W. Denk, J.H. Strickler, and W.W. Webb, "Two-Photon Laser Scanning Fluorescence Microscopy", *Science* **248**, pp. 73-76, 1990.
10. T.F. Heinz *et al*, "Spectroscopy of molecular monolayers by resonant second-harmonic generation", *Phys. Rev. Lett.* **48**, pp. 478-481, 1982.

Using differential confocal microscopy to detect the phase transition of the membrane of giant unilamellar liposomes

Chau-Hwang Lee^{*a}, Wan-Jen Lin^a, Jyhpyng Wang^{b,c,d}

^aInstitute of Applied Science and Engineering Research, Academia Sinica

^bInstitute of Atomic and Molecular Sciences, Academia Sinica

^cGraduate Institute of Electro-Optics, National Taiwan University

^dDepartment of Electrical Engineering, National Taiwan University

ABSTRACT

Giant unilamellar liposomes (diameter > 10 μm) are important for cell-membrane research and controlled drug-delivery. Mechanical properties of unilamellar liposomes in different physiological conditions are crucial for their applications. For example, liquid-gel phase transition of the bilayer membrane under different temperatures determines the stability and activity of liposomes. Bending rigidity is the most closely related mechanical property to phase transition. Owing to the flexible nature of bilayer membranes, accurate measurements of the bending rigidity of membranes are difficult. Here we report an all-optical technique to directly measure the bending modulus of unilamellar liposomes. We use differential confocal microscopy, a far-field optical profilometry with 2-nm depth resolution, to monitor the thermal fluctuations and the deformation of unilamellar liposomes. From the amplitude changes of thermal fluctuations along with temperature we can directly determine the phase-transition temperature of the membrane structure. We then employ optical force to induce sub-micrometer deformation of the unilamellar liposomes. From the deformation we obtain their bending rigidity with simple calculation. We find the bending modulus decreases from 8–11 pico-erg to 0.5–0.9 pico-erg as the liposomes are heated across the phase-transition temperature. All the measurements are done without contacting the samples, and the shapes of liposomes remain the same after the experiments.

Keywords: differential confocal microscopy, unilamellar liposome, bending rigidity, phase transition

1. INTRODUCTION

Soft materials, such as colloids, lipid membranes, liquid crystals, polymers, and the micro- or nano-structures they form, are among the important bases of modern applied sciences and biomedical engineering. For example, unilamellar liposomes are not only important model systems for cell-membrane research but also useful in controlled drug-delivery by encapsulating therapeutic components and transporting them into cells.¹ The mechanical properties of soft materials are important for the engineers and researchers to produce, manipulate, and understand these microstructures. Owing to the “softness,” however, the measurement of mechanical properties is usually accompanied by intrusion, even unrecoverable damage, especially for the bilayer lipid membrane (BLM) structures. Because the surfaces of BLM specimens consist of only two layers of lipid molecules, it is difficult to directly apply stress on them and measure the mechanical properties. The main technical challenges are: (1) The measurement should be non-intrusive to avoid artifacts. Previous studies using atomic force microscopy on cellular membranes has the advantage of high spatial resolution, but it was found that the contact of the probe can penetrate the membrane.² (2) The stress-induced deformation should be sufficiently small to keep the corresponding strain in a linear reversible region, so that the mechanical properties can be analyzed with linear mechanical models. For ordinary unilamellar liposomes, this means nanometer deformation, hence nanometer resolution is required in measurement. (3) The measurement speed should be fast enough to track dynamic mechanical response, e.g., the thermal fluctuations of membranes. To date, micropipette aspiration is the most common method used for the measurement of the mechanical properties of BLM's, liposomes, polymersomes, etc.^{3–5} However, micropipette aspiration can only perform static measurement, and it deforms the sample so large that a complicated mathematical model is required to analyze the data. In addition, when working with membranes composed of lipid mixtures, the high curvature in the area sucked into the pipette can cause changes in lipid composition.⁴

* Correspondence: Email: clee@gate.sinica.edu.tw; WWW: http://lml.iam.s.sinica.edu.tw/laboratory/members/Chau-Hwang_Lee.html; Telephone: 886-2-2782-6670 ext 18; Fax: 886-2-2782-6680

In this paper we report an all-optical approach to detect the phase transition of unilamellar liposomes and to measure their bending rigidity under different temperatures. The key technique used in these measurements is differential confocal microscopy, a far-field optical profilometric technique with 2-nm depth resolution and 0.3- μm lateral resolution.⁶ Because the probe of differential confocal microscopy is a microscope objective lens of which the working distance is on the order of 1 mm, the soft sample surface can be kept from being damaged. The measurement speed of differential confocal microscopy can be as fast as the response of optical detectors, therefore we can easily track the thermal fluctuations of liposome membranes. The high depth resolution of differential confocal microscopy enables us to detect the small deformation caused by femtonewton optical force. Since the deformation is less than 5% the diameters of liposomes, the data can be analyzed with simple analytical geometry, and the sample can always return to its natural shape after the experiments. With these unique features, it was pointed out that differential confocal microscopy is very suitable in the study of mechanical properties of BLM structures.⁷

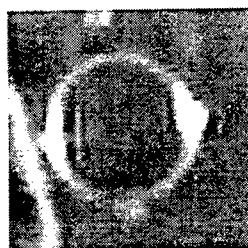
In Section 2 we describe the sample preparation and the experimental setup. We will also explain the working principle of differential confocal microscopy. We show the experimental data and discuss the methods to deduce the bending modulus in Section 3. The measurements on the same liposome at different temperatures clearly shows the phase transition behavior, and the measured bending modulus is consistent with that obtained with x-ray scattering.

2. MATERIALS AND METHODS

2.1 Preparation of liposomes

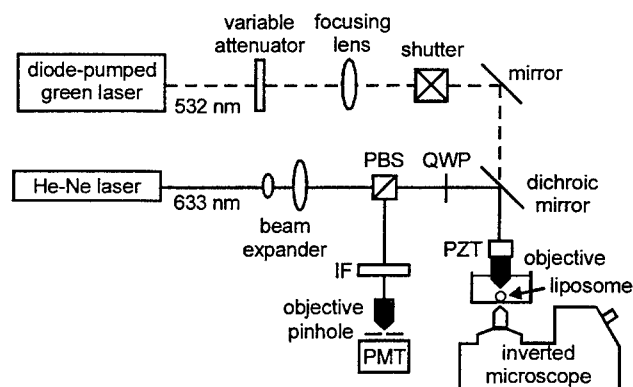
Giant unilamellar liposomes made of dipalmitoyl phosphatidylcholine (DPPC) were prepared with the following procedures:⁸ DPPC and charged phosphatidylserine were mixed at 9:1 by weight in chloroform:methanol (2:1 by volume) to make a 10 mg/ml lipid solution. About 0.1 ml solution was dried to form a lipid film on a culture dish, which was blown with dry nitrogen for 24 hours to remove the solvent in the lipid film. The lipid film was then prehydrated at 45° C with water-saturated nitrogen for 45–60 minutes. Next we added an aqueous solution containing 0.1-M sucrose and 0.1-M KCl into the culture dish. This solution would then be enclosed in the liposomes, therefore we termed it as the “inner solution.” The culture dish was then sealed under dry nitrogen and incubated at 37° C for 24 hours. During the incubation the lipid film gradually stripped off the bottom surface of the culture dish and formed a “white cloud” floating in the solution, which contained the liposomes. Liposomes made with the above procedures could be stable in the culture dish for 2–3 days.

We then moved a drop of the liposome “white cloud” into another culture dish containing a 0.1-M glucose and 0.1-M KCl aqueous solution. This dish was then placed on an inverted optical microscope. Because the density of this outer solution was less than that of the inner solution, the liposomes stayed at the dish bottom after we kept the dish rest for one hour. Figure 1 shows an image of one liposome viewed through the inverted microscope. Through the experiments the liposomes were kept in the outer solution.

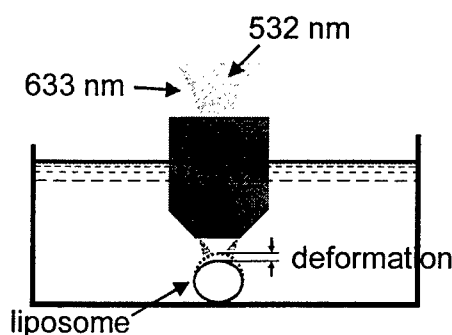


10 μm

Fig. 1. Image of a DPPC liposome viewed by an inverted optical microscope. In order to enhance the contrast of the membrane, we raked the illuminating light source such that light can be reflected from the membrane into the objective lens of the microscope.



(a)



(b)

Fig. 2. (a) Experimental setup. IF, interference filter; PBS, polarization beam splitter; PMT, photo-multiplier tube; PZT, piezo-electric transducer; QWP, quarter wave plate. (b) The arrangement of beam sizes on the liposome. The 532-nm beam, used to exert optical force, was pre-focused such that its beam diameter was $14\text{ }\mu\text{m}$ on the liposome. The 633-nm beam was expanded to fill the whole input aperture of the objective lens, so that it probed the deformation only at the center of the 532-nm beam, where the deformation was uniform. The spot size of the 633-nm beam on the liposome was about $1\text{ }\mu\text{m}$ in diameter.

2.2 Optical setup

The experimental setup is shown in Fig. 2(a). Our set-up bore close resemblance to a conventional confocal microscope, where the probe light (the 633-nm beam), reflected from the liposome membrane and filtered by a $5\text{-}\mu\text{m}$ diameter pinhole at the conjugate focal point, formed the confocal signal.⁹ For the operation of differential confocal microscopy, the focal plane was intentionally placed slightly away from the liposome surface, such that the position of the membrane was on a steep slope of the confocal axial response curve. This made the signal light that entered the confocal aperture extremely sensitive to the position of the membrane.⁶ Owing to the low reflectivity of BLM's (10^{-3} – 10^{-4}) in the surrounding solution,¹⁰ the reflected signal light was measured with a photo-multiplier tube.

Two light sources of different wavelengths were used in the experiment. The 532-nm beam of 45 mW (measured after the water-immersion objective lens) was used to exert optical force on a single liposome, giving rise to a press force of 56 femtonewtons. The force f was calculated directly from the momentum conservation law: $f = 2Rnp/c$, where R is the reflectivity, n the index of refraction of the surrounding medium, p the optical power incident on the membrane, and c the speed of light in vacuum. The 633-nm beam of $70\text{ }\mu\text{W}$ was used as the probe beam to measure the deformation. These two beams were co-linearly focused by a $40\times$ water-immersion objective lens with 0.75 numerical aperture (ICS Achroplan, Carl Zeiss, Oberkochen, Germany). The objective lens was mounted on a piezoelectric-transducer (PZT) driven objective

holder (PIFOC, Physik Instrumente, Waldbronn, Germany). Locations of the light spots on the liposome were monitored with an inverted optical microscope. The probe beam was expanded before entering the objective lens, such that it could be focused to a 1- μm diameter at the center of the 532-nm beam. To generate a uniform optical force, the 532-nm beam was pre-focused on the back focal plane of the objective lens, such that its spot size was as large as 14 μm in diameter on the focal plane (see Fig. 2(b)). The optical pressure produced by the 532-nm beam was practically constant in the beam center where measurements were made, and the beam-size variation was negligible within a few micrometers of distance along the optical axis. This arrangement ensured that the spatial distribution of the optical force was uniform.

2.3 Working principle of differential confocal microscopy

The axial response function of conventional confocal microscopy (see Fig. 3) is $I(z) = I(0)\sin^2(az)/(az)^2$, where I is the optical power of the signal, z the distance between the focal plane and the sample surface, and $a = 4\pi\sin^2(\alpha/2)/\lambda$ with $\sin(\alpha)$ the numerical aperture of the objective lens and λ the wavelength of the probe light.⁹ Differential confocal microscopy takes advantage of the steep slope of the axial response function to obtain high depth resolution. The normalized slope of the axial response can be expressed as:

$$S(z) = \frac{1}{I(0)} \left| \frac{dI(z)}{dz} \right|. \quad (1)$$

In the linear slope region (shown as the black segments in Fig. 3) of the axial response curve, $S(z)$ is practically constant. Therefore the differential change of confocal signal is proportional to the displacement of the reflective surface. The proportional constants S and $I(0)$ are obtained before the measurement by scanning the focal plane through the sample surface with a high-accuracy transducer, such as the PZT-driven objective holder used in our experiment. In our setup $S \approx 1.0/\mu\text{m}$ in the linear slope region; hence a change of membrane position as small as 10 nm caused a readily detectable 1% change of the confocal signal. Such a sensitivity enabled us to measure liposome deformation down to a few nanometers.

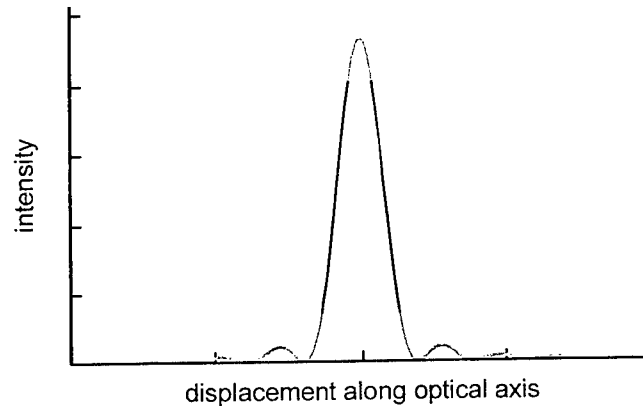


Fig. 3. Axial response curve of confocal microscopy. Black segments indicate the working region of differential confocal microscopy.

The depth resolution of our system was 2 nm, limited by the 0.2% power fluctuation of the power-stabilized He-Ne laser. As to the temporal resolution, since differential confocal microscopy relies on neither feedback control nor phase-locking mechanisms, the measurement can be as fast as the response of the photo-multiplier. However, in practice one has to set the detection time constant large enough in order to make the shot noise smaller than the power fluctuation. This is of importance for the conditions with weak optical signal.

2.4 Procedures of measurement

By observing the laser spots and the liposomes through the inverted microscope, we overlapped the laser beams and a single liposome laterally. Then we descended the objective lens along the optical axis and monitored the change of confocal signal of the 633 nm beam. When the confocal signal reached the first maximum after the objective lens was immersed into the outer solution, we were sure that the focal plane was right on the liposome surface. At this position we obtained $I(0)$. Then we raised the objective lens for a few hundreds of nanometers to place the liposome surface at the linear slope region of the confocal axial response curve. In the linear slope region we used a triangular high-voltage waveform to modulate the PZT objective holder and recorded the optical signal. From the displacement of the objective holder and the change of optical signal we determined the slope S . With $I(0)$ and S , from Eq. (1) we can determine Δz from ΔI . To match the requirements for high signal-to-noise ratio in different conditions of experiments, the signal amplification and the detection time constant were controlled by the biasing voltage of the photo-multiplier tube and a current amplifier. The amplified data were analyzed on-line with a fast Fourier transform spectrum analyzer, and stored in a personal computer through a 16-bit analog-to-digital converter.

We monitored the thermal fluctuations of the membrane before applying optical force to induce the deformation. In order to obtain sufficient signal-to-noise ratio and to cover the bandwidth of these fluctuations, here we set the measurement time constant to be 5 ms. It is well known that the thermal fluctuations of BLM reflect the mechanical properties. However, because of the low signal-to-noise ratio of previous measurements, complicated mathematical models were required to interpret the data.¹¹ Based on the high resolution of differential confocal microscopy we would directly observe the amplitudes of thermal fluctuations of BLM along with the temperature changes. Across the phase transition temperature the fluctuation behaviors had to be different, then we could determine the phase transition temperature of the membrane molecular structures.

Next we applied optical force on the liposome membrane by turning on the 532-nm beam, and measured the deformation of liposome along the optical axis (the z -axis). This experiment was to determine the bending modulus of the liposome membrane. To reduce the influence of thermal fluctuations, we fixed the power of 532-nm beam to be 45 mW and set the time constant of measurement to be 50 ms. For the calculation of bending modulus, the original diameter of the liposome was measured from the image obtained with the inverted microscope.

3. RESULTS AND DISCUSSIONS

3.1 Thermal fluctuations of membranes

The fluctuations of the shape of liposomes come from the Brownian motion of their membranes. From the models established in early studies on the flickering of erythrocytes, there exists a simple relation between the mean squared value of the change in diameters of such spherical vesicles and the temperature:

$$\langle |\Delta d|^2 \rangle \propto \frac{kT}{\kappa}, \quad (2)$$

where Δd is the change in diameter, k the Boltzmann's constant, T the absolute temperature, and κ the bending modulus of the membrane.¹¹ Therefore if we plot the squared values of fluctuation amplitudes as a function of temperature, we should obtain a straight line. When the temperature is changed across the phase-transition temperature, the slope of this straight line must be different according to the change of κ . This measurement can determine the phase transition temperature for further investigation.

Figure 4 shows the thermal fluctuations of a DPPC liposome measured with differential confocal microscopy. Because the liposomes were stable in the solution, we repeated the measurement on the same liposome at a temperature for four times, then changed the temperature. Each measurement lasted for 20 seconds. Since the amplitudes were very distributed even at a fixed temperature, we drew the histogram of the squared values of amplitudes in each measurement, and calculated their centroid as $|\Delta d|^2$:

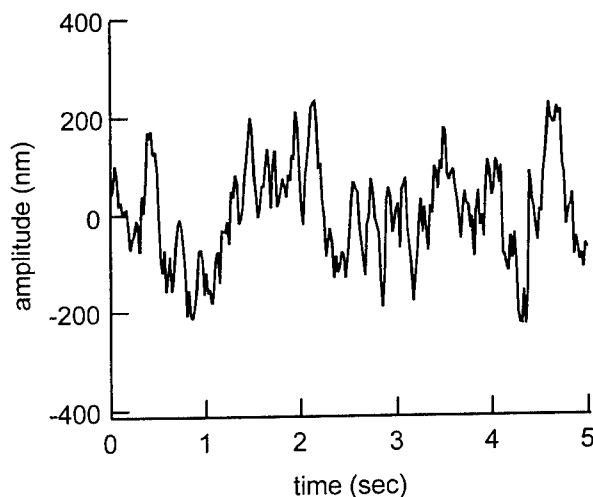


Fig. 4. Measured thermal fluctuations of a DPPC liposome at 45.5° C.

$$|\Delta d|^2 = \frac{\sum_i a_i^2 n_i}{\sum_i n_i}, \quad (3)$$

where a_i is the amplitude of the i -th interval of the histogram, and n_i is the number of amplitudes falling in the i -th interval. The amplitude range of each interval was set to be 20 nm. We calculated the average $|\Delta d|^2$ at each temperature, then plotted them as a function of temperature. The results are shown in Fig. 5. As we increased the temperature from 25.5° C to 51.5° C, we clearly observed the change of the slope of the fitting straight lines, caused by the change of bending modulus. In Fig. 5 the two lines intersect at 44° C, which approximates the phase-transition temperature ($T_c \approx 41^\circ \text{C}$) of DPPC in water.¹ The difference results from the difficulty to obtain reliable data near T_c . In experiments we found the reflectivity of DPPC membrane decreased dramatically as we increased the temperature to $\sim 40^\circ \text{C}$. The reflectivity was so low that we could not record any data. Nevertheless, when we continued increasing the temperature to $\sim 44^\circ \text{C}$, the reflectivity recovered to be

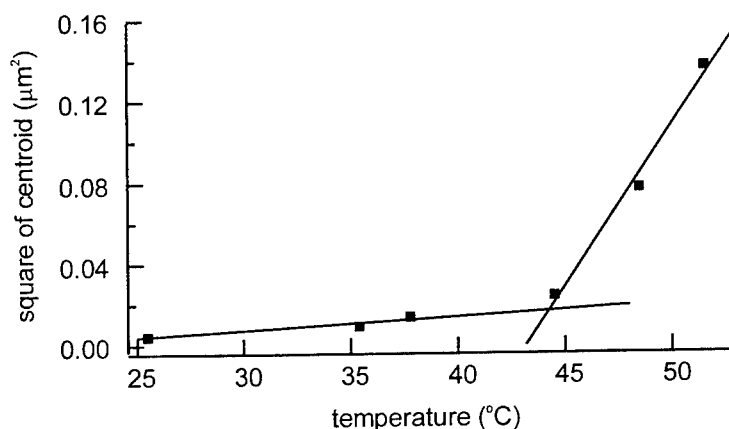


Fig. 5. Squared values of the centroid of measured amplitudes as a function of temperature. From the intersection of the two fitting straight lines we can approximately determine the phase-transition temperature.

about the same as in low temperatures. We found the same behavior of reflectivity as we decreased the temperature from 51.5° C to 25.5° C. This phenomenon indicates that the structure of molecules in BLM does not switch directly between the gel and the liquid phases. However, the discussions of the dynamical reconstruction of lipid molecules near the phase-transition temperature are beyond the scope of this study.

3.2 Bending rigidity of membranes

The second experiment was conducted to determine the bending rigidity of liposome membranes. We would first explain how we calculated the bending modulus from the diameter of a liposome and the sub-micrometer deformation caused by optical force.

Considering a liposome surface Ω , the free energy E can be expressed as follows:

$$E = \frac{\kappa}{2} \int_{\Omega} (c_1 + c_2)^2 dA + \gamma \int_{\Omega} c_1 c_2 dA, \quad (4)$$

where c_1 and c_2 are the two principal curvatures, dA is the surface element, and γ is the Gaussian (or saddle) rigidity. For continuous perturbations of a closed surface, the term $\int_{\Omega} c_1 c_2 dA$ reduces to a constant.¹¹ In this case the changes in free energy can result only from the term of bending modulus κ . When the liposome is deformed by optical force, from energy conservation, the change in free energy is equal to the work W done by optical force. Since the optical force is known from the measured reflectivity, by measuring the changes in diameter of the liposome along the optical axis with differential confocal microscopy, we can determine W .

In order to obtain κ , the change in $\int_{\Omega} (c_1 + c_2)^2 dA$ has to be determined independently. Because there is no inner supporting structure inside a liposome, surface tension makes the liposome surface a perfect sphere. Thus without the optical force, $c_1 = c_2 = 1/r$, where r is the radius of the liposome, and $E = 8\pi\kappa + \gamma \int_{\Omega} c_1 c_2 dA$. When the liposome is deformed along the optical axis, its shape becomes an ellipsoid. Since the optical force is applied vertically, there is only one axis shorter than the other two. Therefore the principal curvature along the meridian can be calculated as

$$c_1 = - \frac{\left[2 \left(\frac{dr}{d\theta} \right)^2 - r \frac{d^2 r}{d\theta^2} \right] + r^2}{\left[\left(\frac{dr}{d\theta} \right)^2 + r^2 \right]^{3/2}}, \quad (5)$$

where θ is the azimuthal angle of the surface element from the short axis, and $r = \left[a^2 b^2 / (a^2 \sin^2 \theta + b^2 \cos^2 \theta) \right]^{1/2}$ with a the length of the short axis and b the length of the two long axes.¹² We applied the constant-surface-area constraint on the liposome surface Ω . Therefore, with the measured deformation along the optical axis we obtained both a and b . The other principal curvature is calculated by projecting the radius of curvature along the parallel onto the normal direction, i.e., $c_2 = -r \cos(\alpha)/b^2$, where the cosine value of the angle α between the radius of curvature along the parallel and the normal direction is

$$\cos \alpha = \frac{2r}{\sqrt{4r^2 + \left(\frac{1}{r} \frac{dr^2}{d\theta} \right)^2}}. \quad (6)$$

Therefore the change in free energy is

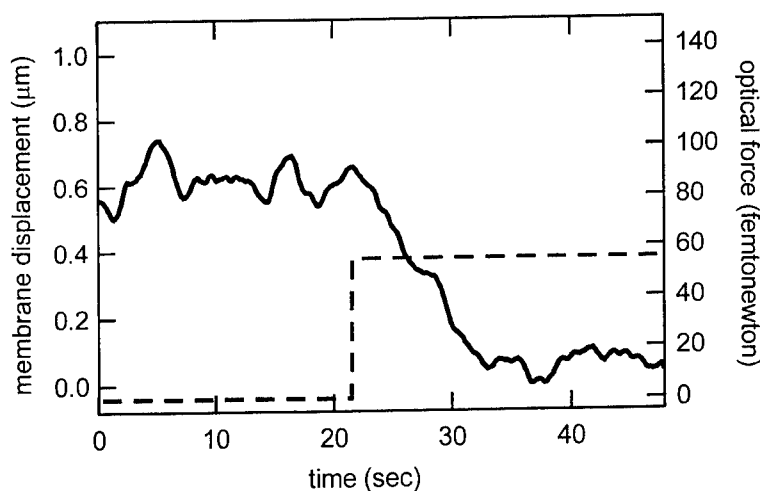


Fig. 6. DPPC liposome deformation along the optical axis under 56-femtonewton optical force at 27° C. Solid line, membrane displacement; dashed line, optical force.

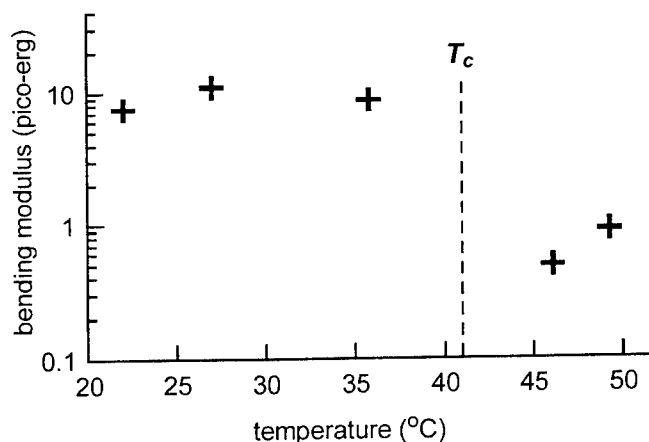


Fig. 7. Measured bending modulus of a DPPC liposome as a function of temperature. Across the phase-transition temperature T_c , the bending modulus decreases for an order of magnitude.

$$\Delta E = W = \frac{\kappa}{2} \int_{\Omega} (c_1 + c_2)^2 dA - 8\pi\kappa. \quad (7)$$

Figure 6 shows the liposome deformation under 56-femtonewton optical force at 27° C. The liposome was found to be deformed by ~ 600 nm. The corresponding work done by the optical force was thus 0.34 pico-erg. From the image obtained by the inverted optical microscope, the original diameter of this liposome was measured to be $14 \pm 1 \mu\text{m}$. With these data, from Eq. (7) we obtained $\kappa = 11$ pico-erg. Since this temperature was far below T_c , this κ value should be the bending modulus of the DPPC bilayer membrane in gel phase. With the same optical force, we found that the bending modulus remained almost the same for the temperature range of 22–36° C, as shown in Fig. 7. But when the temperature approached T_c , the low reflectivity again prevented us from taking reliable data. After the temperature was raised above T_c , we measured

κ values of 0.5–0.9 pico-erg. This was the bending modulus of DPPC membranes in liquid phase, which agreed with the recently published data obtained with x-ray scattering.¹³ The sharp decrease of bending modulus in Fig. 7 clearly indicates the phase transition of the BLM structure. The results in Fig. 7 demonstrates both the correctness and the accuracy of our method to determine the bending rigidity of unilamellar liposomes in solution.

4. CONCLUSION

In this paper we describe an all-optical method to detect the structural phase transition and to determine the bending rigidity of unilamellar liposomes. We used differential confocal microscopy to monitor the thermal fluctuations of a DPPC liposome as the temperature changed, and observed the phase transition through the change of the linear relation between the squared amplitudes and the temperatures. Although an accurate measurement of the phase-transition temperature T_c was prevented by the low reflectivity of the BLM near T_c , we could obtain an approximate value with an error < 8% of other published values.

Using femtonewton optical force to deform the liposome, we measured the sub-micrometer deformation and calculated its bending modulus. Since the deformation was smaller than 5% of the diameter of liposome, only simple analytical geometry was required to calculate the bending modulus. The liposome returned to its original shape after each deformation, therefore we could repeat the measurement on the same sample for different temperatures. We found the bending moduli decreased for an order of magnitude when the temperature was increased across the phase-transition temperature. This macroscopic result clearly revealed the microscopic gel-to-liquid structural transition.

The technique presented in this paper is very convenient for biophysical experimentalists. The same measurement procedures are suitable to characterize kinds of molecular structures, such as BLM's, polymersomes, lipid tubules, etc. Thanks to the high resolution and long working distance of differential confocal microscopy, the samples can be measured *in situ*, and the data require only simple linear theoretical models to interpret. We believe differential confocal microscopy can serve as a daily tool for the studies related to membranes or other soft matters.

ACKNOWLEDGMENTS

We thank the fruitful discussions with Prof. Chi-Ming Chen in Department of Physics, National Taiwan Normal University.

REFERENCES

1. M. N. Jones and D. Chapman, *Micelles, monolayers, and biomembranes*, Wiley-Liss, New York, 1995.
2. M. Radmacher, R. W. Tillmann, M. Fritz, and H. E. Gaub, "From molecules to cells: imaging soft samples with the atomic force microscope," *Science* **257**, pp. 1900–1905, 1992.
3. E. Evans and W. Rawicz, "Entropy-driven tension and bending elasticity in condensed-fluid membranes," *Phys. Rev. Lett.* **64**, pp. 2094–2097, 1990.
4. D. V. Zhelev, D. Needham, and R. M. Hochmuth, "A novel micropipet method for measuring the bending modulus of vesicle membranes," *Biophys. J.* **67**, pp. 720–727, 1994.
5. B. M. Discher, Y.-Y. Won, D. S. Ege, J. C.-M. Lee, F. S. Bates, D. E. Discher, and D. A. Hammer, "Polymersomes: tough vesicles made from diblock copolymers," *Science* **284**, pp. 1143–1146, 1999.
6. C.-H. Lee and J. Wang, "Noninterferometric differential confocal microscopy with 2-nm depth resolution," *Opt. Commun.* **135**, pp. 233–237, 1997.
7. C.-M. Chen, "Theory for bending anisotropy of lipid membranes and tubule formation," *Phys. Rev. E* **59**, pp. 6192–6195, 1999.
8. K. Akashi, H. Miyata, H. Itoh, and K. Kinoshita, Jr., "Preparation of giant liposomes in physiological conditions and their characterization under an optical microscope," *Biophys. J.* **71**, pp. 3242–3250, 1996.
9. T. Wilson, in *Confocal Microscopy*, edited by T. Wilson, Chap. 1, Academic Press, London, 1990.
10. H. Ti Tien, *Bilayer lipid membranes (BLM): theory and practice*, M. Dekker, New York, 1974.
11. M. D. Mitov, J. F. Faucon, P. Meleard, and P. Bothorel, "Thermal fluctuations of membranes," *Advances in Supramolecular Chemistry* **2**, pp. 93–139, 1992.
12. M. P. Do Carmo, *Differential Geometry of Curves and Surfaces*, p. 25, Prentice-Hall, New Jersey, 1976.
13. H. I. Petrache, N. Gouliarov, S. Tristram-Nagle, R. Zhang, R. M. Suter, and J. F. Nagle, "Interbilayer interactions from high-resolution x-ray scattering," *Phys. Rev. E* **57**, pp. 7014–7024, 1998.

Multi-photon fluorescence microscopy: behavior of biological specimens under high intensity illumination

Ping-chin Cheng¹, Bai-Ling Lin^{2*}, Fu-Jen Kao^{3,5*}, Chi-Kuang Sun^{4*}

¹Department of Electrical Engineering, State University of New York, Buffalo, NY 14260 USA

²Institute of Molecular Biology, Academia Sinica, Taipei, Taiwan, Rep. of China

³Department of Physics, National Sun Yat-sen University, Kaohsiung, Taiwan, Rep. of China

⁴Department of Electrical Engineering, National Taiwan University, Taipei, Taiwan, Rep. of China

⁵Center for Neuroscience, National Sun Yat-sen University, Kaohsiung 80424, Taiwan, Rep. of China

ABSTRACT

Recent development in multi-photon fluorescence microscopy, second and third harmonic generation microscopy (SHG and THG) and CARS open new dimensions in biological studies. Not only the technologies allow probing biological specimen both functionally and structurally with increasing spatial and temporal resolution, but also raise the interest in how biological specimens respond to high intensity illumination commonly used in these types of microscopy. We have used maize leaf protoplast as a model system to evaluate the photo-induced response of living sample under high intensity illumination. It was found that cells can be seriously damaged by high intensity NIR irradiation even the linear absorption coefficient is low in these wavelengths. Micro-spectroscopy of single chloroplast also allows us to gain insight on the possible photo-damage mechanism. In addition to fluorescence emission, second harmonic generation was observed in the maize protoplasts.

Keywords: Multi-photon fluorescence microscopy, photon damage, cell damage, high intensity illumination, maize

1. INTRODUCTION

Multi-photon fluorescence microscopy has been cited for its advantage in the intrinsic axial resolution and in increased depth penetration due to low linear absorption coefficient of biological specimen and many organic polymers in the near infrared (NIR) range^{1,2}. Using a pulsed laser, it is possible to efficiently excite two-photon fluorescence with a high peak power while keeping the average power low to minimize thermal and photochemical damages to the specimen. Currently, mode-locked Ti:sapphire and Cr:Forsterite lasers³ that generate sub-picosecond pulses are used as light source for multi-photon fluorescence microscopy. Because of the need of high peak power for efficiently exciting two-photon fluorescence, the relationship between cell damage and peak power has become an interesting and much debated topic in the applications of multi-photon fluorescence microscopy⁴⁻⁷. It is conceivable that at high illumination intensity, non-linear photochemical processes have impacts on cell physiology and viability in ways much different from low illumination in the linear domain. Therefore, it has become a frequently asked question whether there is an optimal peak intensity and pulse width for biological and material multi-photon fluorescence microscopy.

2. MATERIALS AND METHODS

1. Biological specimen preparation

Leaf protoplasts of maize (*Zea mays* L., var. Ohio 43) were isolated from growth chamber-grown seedlings at 4th leaf emerging. Huang and Chen's⁸ protocol was followed in the protoplast isolation. The protoplast culture of maize consists of a mixture of mesophyll, epidermal and bundle sheath cells. For microscopic observation, the protoplast was placed in a chambered coverglass (Lab-Tek, Illinois, USA). To evaluate cell survival under high intensity illumination, protoplasts were loaded with 2mM Calcein AM (Molecular Probe s, OR) for 15min prior to NIR irradiation.

* Corresponding authors: B. L. Lin (biology), F. J. Kao and C. K. Sun (optics)

2. Optical set-up

Two-photon fluorescence microscopy was performed on a modified Olympus Fluoview confocal microscope equipped with a Coherent Verdi pumped Spectra-Physics Tsunami mode-locked Ti:sapphire laser operated at 780nm with 100fs pulse at 82MHz. An Olympus water immersion objective (UPLANapo 60x W-PSF, NA=1.2) was used in this experiment. A 650nm short-pass dichroic beam splitter (Chroma Technology, 650DCSP) was used in the illumination beam. The average and peak power densities at the focal point approximate $3 \times 10^6 \text{ W/cm}^2$ and $3.9 \times 10^{11} \text{ W/cm}^2$, respectively.

Two-photon induced fluorescence spectra were measured with a SpectraPro-500 spectrometer (Acton Research) equipped with a TE-cooled PMT. The excitation laser beam is derived from a Spectra Physics Tsunami Ti:sapphire laser pumped by a Coherent Verdi solid-state laser at 532nm. The Ti:sapphire laser is mode-locked at 780nm and has a repetition rate of 82 MHz with a pulse width approximately 100fs. A ChromaTech dichroic beam splitter (650DCSP) was used to achieve epillumination and on-axis fluorescence detection in a modified Olympus BX microscope. In addition, two IR cut-off filters (Edmond Scientific, Cat. K53-710) were installed in front of the entrance slit of the monochromator to reject scattered IR from the sample. Using this set-up, site-specific spectral information was obtained from the samples⁹. Excitation intensity as high as 10^{12} W/cm^2 was reached at the focal point. A second set-up using a Spectra-Physics Millennia IR (1064nm) pumped Chromiumdoped Forsterite laser (built by CKS), operated at 120MHz and 130fs pulse, was used for 1234nm infrared (IR) excitation.

3. RESULT AND DISCUSSION

The intrinsic optical sectioning capability of two-photon excitation is demonstrated in Fig. 1. Under a microscope objective lens, the fluorescing volume in a dye solution appears only in the vicinity of the focal spot. In addition, the use of NIR and IR as excitation source in two-photon excitation opens the entire visible spectrum for fluorescence detection. Figure 2 shows simultaneous excitation of four fluorescence dyes by 780nm NIR.

Maize protoplasts exhibit a strong red fluorescence peaked at 663nm and a green fluorescence peak at 570nm¹⁰. The 663nm emission is the result of chlorophyll fluorescence while the origin of the 570nm emission is as yet unidentified. Upon high intensity near infrared (NIR, 780nm) irradiation, maize protoplast shows an initial increase in both green and red autofluorescence followed by a rapid decrease in red and green fluorescence (Figure 5). The green fluorescence intensity has a higher rate of increase initially, resulting in a green-shift of the fluorescence image when visualized (i.e. the protoplasts initially fluorescing in red, then rapidly shifted to yellow and finally green). If the ratio of red and green fluorescence intensity is plotted against NIR irradiation, an exponential decay function is evident (Figure 6). When correlated with Calcein dye retention (as a live cell indicator), cell survival can be identified by measuring the red/green fluorescence ratio. Figure 3 shows a sequence of NIR irradiation to Calcein AM loaded maize protoplasts. Micro-spectroscopy study of single chloroplast (C) from maize protoplast (Figure 4a) reveals detailed information on spectral changes as photo-damage proceeds. Figure 4b and 4c shows time-lapse study of the red fluorescence spectrum as a function of irradiation dose. Since we have recently characterized the linear absorption and multi-photon fluorescence properties, maize protoplasts can be used as a model system in the study of cell response to high intensity illumination.

Figure 7 shows emission spectrum of the cortex of a maize stem under high intensity IR (1234nm) illumination. In addition to the 682nm red fluorescence resulting from chlorophylls¹¹, a small 617nm peak is evident. The 617nm peak is the result of second harmonic generation from maize tissue.

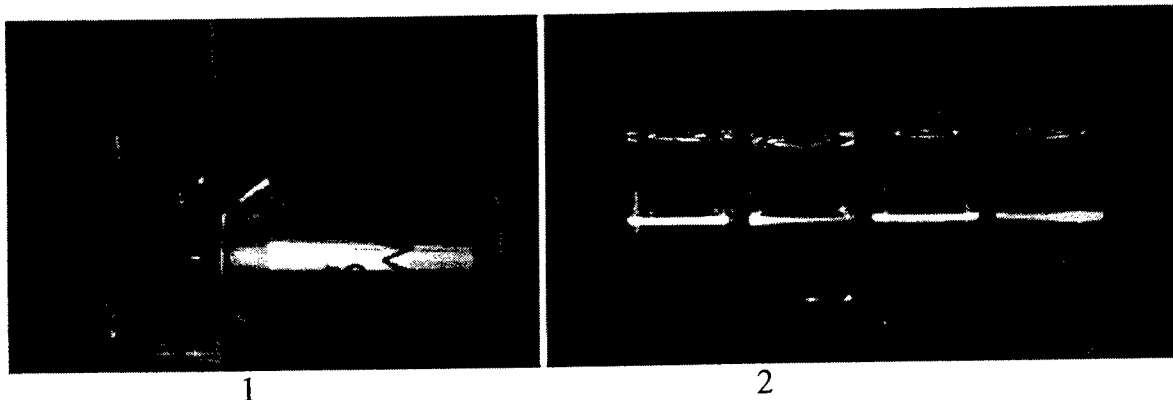


Figure 1. Two-photon excited fluorescence spot in a dye solution. Note the fluorescence generation is restricted to the vicinity of the focal spot, hence provides intrinsic optical sectioning capability. The dye solution was APSS¹ in EtOH. Excitation wavelength was 780nm from a mode-locked Ti:sapphire laser.

Figure 2. Two-photon excited fluorescence in a series of four vials containing dye-solution. The unfocused NIR (780nm) beam enters from the left. From left to right: Calcofluor White, BBTDOT¹, APSS¹ and Rhodamine 6G.

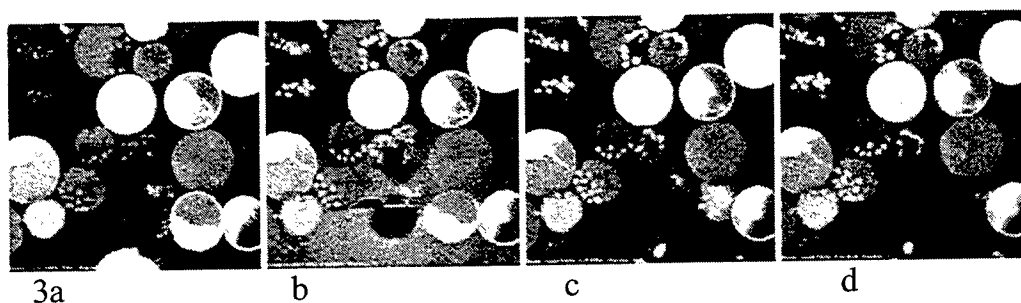


Figure 3. Sequence of NIR exposure to Calcein AM loaded protoplasts. 3a represents the first exposure similar to the dose indicated in Fig 5, 3b: the 3rd exposure, 3c: the 5th exposure, 3d: 7th exposure. Note cell #1 in Fig. 3a expelled its Calcein dye in the 3rd scan, and cell #2 in Fig. 3b busted in the 5th scan.

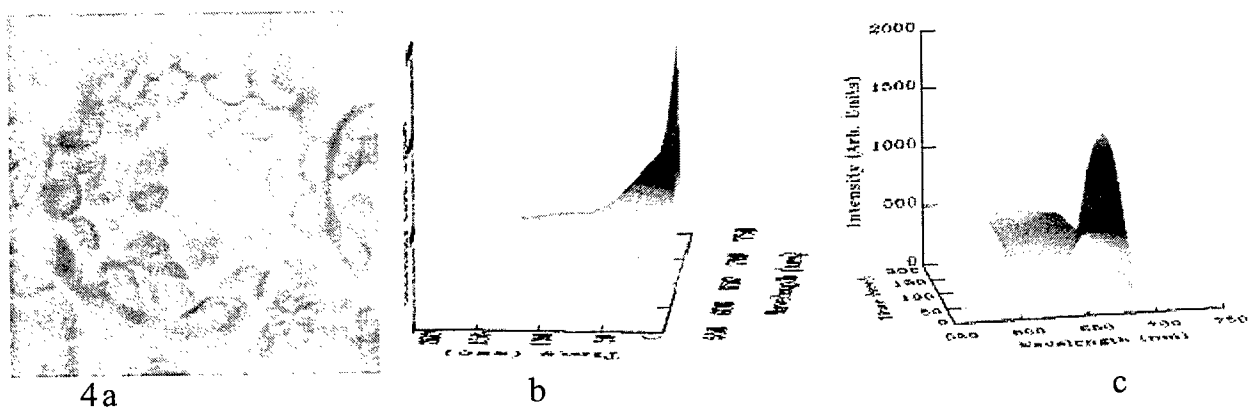
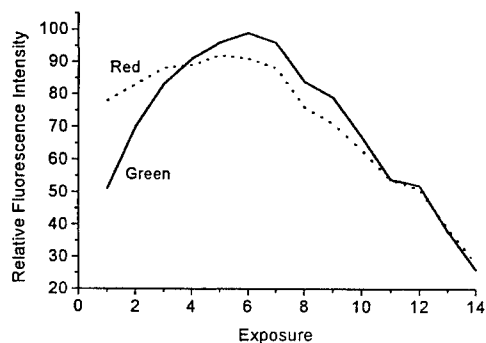
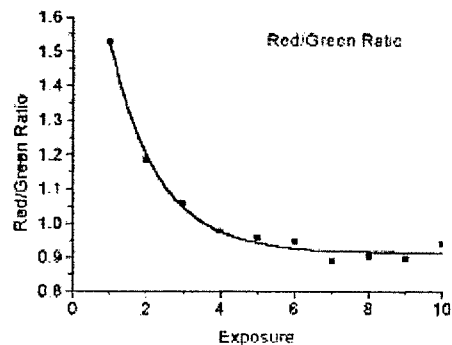


Figure 4. (a) maize protoplast showing numerous chloroplast (c). (b) and (c) different perspective of a 3D plot of two-photon excited red fluorescent spectrum against NIR irradiation dose. The data was obtained from a single chloroplast.



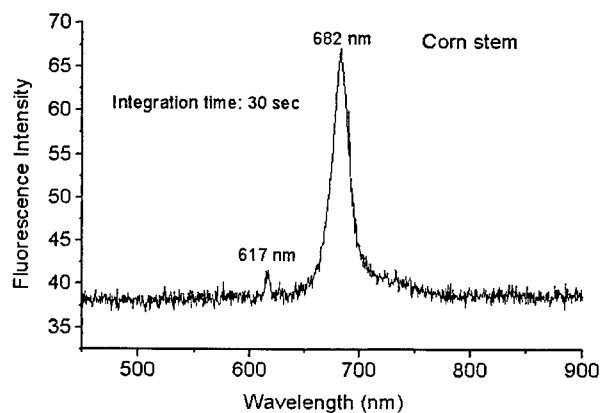
5



6

Figure 5. Normalized auto-fluorescence intensity plot against NIR exposure. The total energy exert on each pixel is 54nJ x number of exposures.

Figure 6. Fluorescence intensity ratio (red/green) plot against NIR exposure showing an exponential decay function.



7

Figure 7. Emission spectrum of the cortex region of a maize stem showing red fluorescence (682nm) and second harmonic generation signal at 617nm. The illumination wavelength is 1234nm from a Chromiumdoped Forsterite laser, operated at 120MHz and 130fs pulse.

ACKNOWLEDGEMENTS

Supported by Academia Sinica (BLL), National Science Council, Republic of China [NSC-88-2311-B-001-087 (BLL), NSC-89-2112-M-110-016, NSC89-2216-E-110-003 (FJK), NSC-88-2811-B-001-0023 (PCC)], the Academic Excellence Program of the Ministry of Education (89-B-FA08-1-4), and Mr. Jin-Mu Huang and Mrs. Li-Ling Huang of Aurum Belle Investment Co., (on behalf of the Ge-An Charity).

REFERENCES

1. P. C. Cheng, S. J. Pan, A. Shih, K.-S. Kim, W. S. Liou and M. S. Park, "Highly efficient upconverters for multiphoton fluorescence microscopy," *J. Microscopy* 189, pp. 199-212, 1997.
2. P. C. Cheng, B. L. Lin, F. J. Kao, M. Gu, M. G. Xu, X.-s. Gan, M. K. Huang and Y. S. Wang, "Multi-photon fluorescence microscopy—the response of plant cells to high intensity illumination," *Micron* (in press) 2000.
3. C. K. Sun, S. W. Chu, T. M. Liu, P. C. Cheng, "High intensity scanning microscopy with a femtosecond Cr:Forsterite laser," *Scanning*, 22, pp. 95-96, 2000.
4. K. Konig, H. Liang, M. W. Berns and B. J. Tromberg, "Cell damage by near-IR microbeams," *Nature* 377 pp. 20-21, 1995.
5. K. Konig, H. Liang, M. W. Berns and B. J. Tromberg, "Cell damage in near-infrared multimode optical traps as a result of multi-photon absorption," *Optics Lett.* 21: pp. 1090-1092, 1996.
6. B. L. Lin, F. J. Kao, P. C. Cheng, W. Y. Cheng, "The Response of maize protoplasts to high intensity illumination in multi-photon fluorescence microscopy," *Micro. Microanal* 6, Proceeding issue, (in press) 2000.
7. B. L. Lin, F. J. Kao, P. C. Cheng, R. W. Chen, M. K. Huang, Y. S. Wang, J.-c. Chen, Y.-m. Wang, W. Y. Cheng, "The response of maize protoplasts in multi-photon fluorescence microscopy," *Scanning* 22(3), (in press) 2000.
8. H.-C. Huang and C. -C Chen, "Genome multiplication in cultured protoplasts of two *Nicotiana* species," *J. Heredity* 79, pp. 28-32, 1998.
9. F. J. Kao, B. L. Lin and P. C. Cheng, "Two-photon micro-spectroscopy of chloroplasts from *Arabidopsis thaliana*," *Scanning* 22, pp. 91-92, 2000.
10. Kao, F. J., B. L. Lin and P. C. Cheng, "Multi-photon fluorescence micro-spectroscopy," *SPIE* 3919 (in press) 2000.
11. P. C. Cheng, B. L. Lin, F. J. Kao, C. K. Sun, Y. S. Wang, T. M. Liu, Y.-m. Wang, J.-c. Chen, M. K. Huang, I. Johnson, "Multi-photon fluorescence spectroscopy of fluorescent bio-probes and bio-molecules," this volume, 2000.

SESSION 6

Fiber Optical Sensors

Optical Fiber Needle to Probe Inside the Body Using Fluorescence Ratio Method

G.C.Tang, A.Katz, Y.Budansky, and R.R.Alfano

Institute for Ultrafast Spectroscopy and Lasers

The City University of New York /The City College

New York, NY 10031

ABSTRACT

An optical fiber needle probe was developed that can be inserted into a hollow metallic needle for tumor diagnosis using fluorescence at key wavelengths for breast, kidney, liver, and brain. The optical fiber needle probe is based on fluorescence ratio method which will allow to detect tumor *in vivo* for a real time evaluation. This method will be coupled with other current modalities such as X-ray, ultrasound and MRI.

Keywords: Spectroscopy, Optical Fiber, Breast Tumor, Diagnosis, Biopsy.

1. INTRODUCTION

Native fluorescence spectroscopy offers new techniques for detection and characterization of the physical and chemical changes that occur in diseased tissue, for either *in vivo* or *in vitro* applications. Tissue systems are made up of proteins, nucleic acids, lipids, and water with fluorescing and non-fluorescing chromophors. There are a number of natural fluorophores in cells and tissues fluorescing in the UV and visible region ^{1,2} such as flavins, tryptophan, tyrosine, nicotinamide adenine dinucleotide (NADH), collagen, and elastin. Native Fluorescence spectroscopy has been applied to study human tissues of different organs including breast ³⁻⁹, gynecological ^{10,11}, colon ¹²⁻¹⁴, and esophageal tissues ¹⁵. Differences in the fluorescence spectral profile and intensity from cancerous and normal tissues were identified, and attributed to either differences in the molecular environment, differences in structure, or differences in concentration of fluorophores in the different types of tissue specimens. There are several intrinsic fluorophores in tissues responsible for these fingerprints. The 340 nm emission, with 290 nm excitation is attributed most likely to the emission from tryptophan, the 380 nm emission band, with 340 nm excitation is from elastin and collagen, and the 460 nm emission band is from NADH.

Fluorescence emission and excitation spectroscopy of breast tissues has been studied for many years. It was found that when tissues are excited with UV or visible light, the native fluorescence spectra are significant difference among cancerous, benign or normal tissue ^{3,4,5,7,8}. When breast tissue is excited at 300 nm and the emission is observed in the region from 320 to 580 nm, differences between cancerous and normal tissue are clearly observed ^{7,9}. It is important to note that the spectrum from benign tumor appears similar to normal tissue rather than appearing malignant. As a result the fluorescence spectroscopy techniques have been developed to effectively distinguish malignant tumor from benign tissue.

Based on an analysis of spectral profile and relative intensities, it has been determined that the intensity ratios at certain crucial wavelengths is a highly accurate criterion for predicting the presence of malignancy ⁷. The existence of these key wavelengths makes it possible to optically detect tumor, using a small set of optical filters to measure emission at the key wavelengths rather than measuring the entire spectrum.

In this paper, we will describe an optical fiber fluorescence ratiometer instrument which measures the fluorescence intensity ratios at key wavelengths. We have developed a suitable optical fiber needle probe that can be inserted freely into a hollow stereotactic needle system and probe tissues to deep to be interrogated by surface probes. The optical fiber needle based ratiometer technique allows for real time tissue evaluation and tumor detection *in vivo*. This technique will help target tissues for fine needle aspiration biopsy and reduce the number of false positive biopsies.

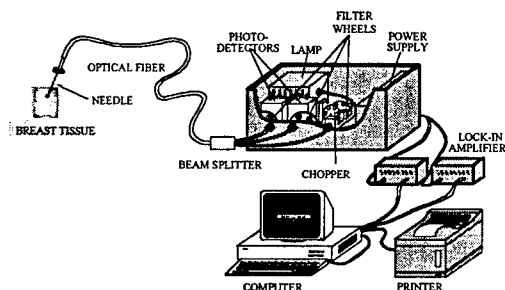
2. TECHNIQUES AND METHODS

The fluorescence spectroscopic ratiometer with an optical fiber needle is shown in Fig.1. The main components of the ratiometer are: (1) broadband xenon excitation lamp, (2) computer controlled filter wheels for selection of excitation and detection wavelengths, (3) UV transmitting optical fibers and collimators to deliver the excitation light to the tissue, and collect the emitted fluorescence, (4) photo multiplier tubes with dual channel phase sensitive detection, and (5) personnel computer to control instrumentation and analyze data.

The optical fiber needle probe consists of a 270 μm core fiber terminated with a 30 cm rigid metal jacket length for easy insertion into a hollow stereotactic needle. The front surface of the probe terminates with a normal fiber surface for directing excitation light and collecting fluorescence. The power density was about $0.13\mu\text{W}/\text{cm}^2$.

The two fibers are directed to the two emission filter wheels. The light exiting the fibers is collimated and passes through the filter wheels. The transmitted and selected wavelengths are incident on two photo multiplier tubes. Stepping motors rotate the filter wheels to the correct filter position. Each stepping motor is independently computer controlled by the ratiometer software.

The two photo multiplier tubes convert the optical signal to the electrical signal, with the current being proportional to the optical signal intensity. The electrical signals are directed to the two lock-in amplifiers. A lock-in amplifier is a phase sensitive detector at a specific frequency, while rejecting all other signals. A personal computer is used to control the instrumentation, to process the amplified signals, and to display and store the ratio data.



3. EXPERIMENTAL RESULTS

3.1. Simulation with layered tissue

A simulation of the ability to detect tumor tissue imbedded in normal tissue, such as a small tumor inside a human breast, was performed to investigate problems which may arise during an in vivo examination. Some potential problem areas include deformation of the needle probe or deposition of body fluids on the probe surface. It may also be important to understand how the interface between tissue types could effect measurements. This simulation was created by "sandwiching" a cancer sample between two normal tissues, as displayed in Fig. 2. The optical fiber needle was mounted on a three-axis translation stage with 10 μm resolution. The holder is shown in Fig. 3. The fluorescence intensity ratios of 340 nm to 440 nm, with 300 nm excitation, were measured as a function of penetration depth. The total sample thickness was about 12 mm. Measurements were taken at 0.2 mm intervals. The intensity ratios are plotted as a function of penetration depth in Fig. 4. The sharp transition between the normal and malignant tissue regions is clearly evident in Fig 4. The average value of the I_{340}/I_{440} ratio for the three tissue layers is shown in Fig. 5. From Figs. 4 and 5, one can clearly distinguish the cancerous and normal breast tissue layers. These results demonstrate the potential ability of the fluorescence ratiometer with an optical fiber needle probe to distinguish between normal and abnormal tissues in the human body.

3.2. Differentiating fat from tumor with multiple wavelength ratios

It was observed that adipose tissue also exhibited a high I_{340}/I_{440} ratio leading to the possibility that adipose tissue may falsely be classified as malignant. This issue has been investigated by Yang et. al.^{8,9} in which multiple intensity ratios were used to correctly distinguish among normal, adipose and malignant tissue. In this study, spectral differences were distinguish adipose from malignant tissue. The first algorithm was based on the 340 nm emission intensity with 289 nm and 271 nm excitation and the second was based on the 460 and 520 nm emission intensities with 340 nm excitation.

The application of these algorithms for use with the ratiometer was tested by measuring the 340 nm emission for 271 and 289 nm excitation, and the 460 nm and 520 nm emission for 340 nm excitation at 18 different locations on the adipose sample, malignant, and normal sample. For the normal tissue, the average values of I_{289}/I_{271} and I_{460}/I_{520} were 0.509 ± 0.021 , and 1.055 ± 0.025 , respectively. For the fat sample, the corresponding average ratio values were 0.872 ± 0.097 and 1.314 ± 0.036 ;

and for the cancer samples, the average ratio values were 0.445 ± 0.051 and 1.655 ± 0.024 . The I_{460}/I_{520} ratio from the cancer sample was significantly higher than the ratios from either normal or fat tissue while the I_{289}/I_{271} ratio from fat tissue was higher than the corresponding ratios from the normal and cancer tissues. For the normal specimens, the fluctuations in the ratio were less than 5%. For the cancer and fat samples, the fluctuations were less than 12%. These results are summarized in Table 1. These measurements indicate that the I_{289}/I_{271} and I_{460}/I_{520} ratios could effectively distinguish cancerous tissue from fat tissue.

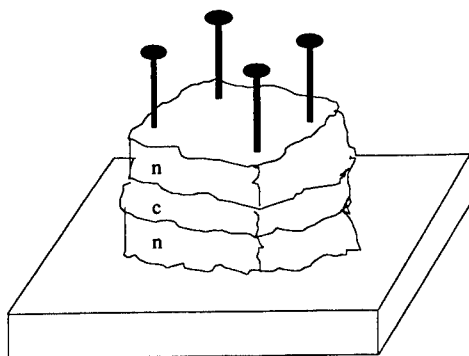


Fig. 2 Simulated tissue layer structure formed by "sandwiching" cancer tissue between two normal tissues.

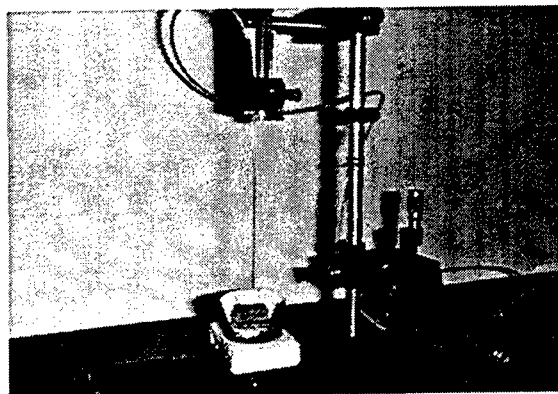


Fig. 3 Fluorescence ratios at wavelengths 340 and 440 nm for depth measurements of tissues.

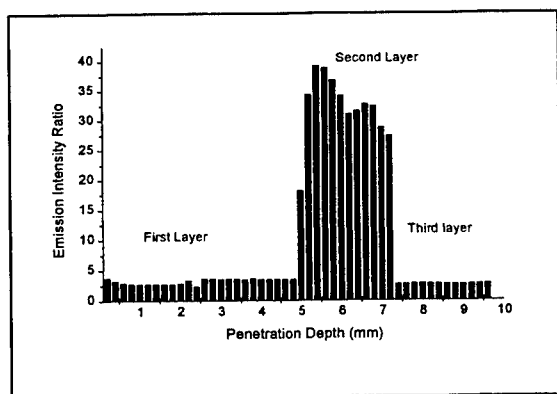


Fig. 4 Fluorescence ratios at wavelengths 340 and 440 nm for depth measurements of tissues.

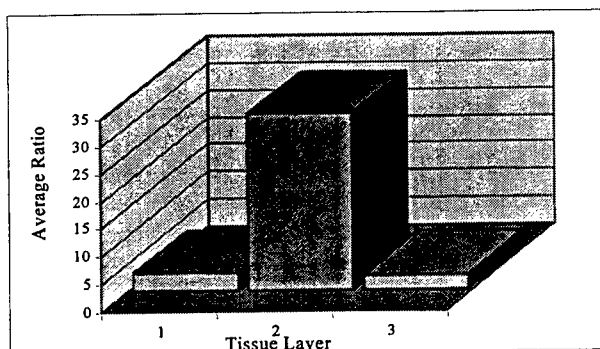


Fig. 5 Average value of 340/440 ratios for the three layers in the normal-cancer-normal sample.

Table 1 Summary of the 289/271 excitation ratio (emission at 340 nm) and the 460/520 emission ratio (excitation at 340 nm)

	289/271	460/520
Normal	0.509 ± 0.021	1.055 ± 0.025
Fat	0.872 ± 0.097	1.314 ± 0.036
cancer	0.445 ± 0.051	1.655 ± 0.024

4. DISCUSSION

Since diameter of the optical fiber is relatively small, the interrogated area was small and therefore the measured ratios were subjected to local variations in tissue state. The interrogated area was on the order of 300 to 500 μm . The variation in ratio

measurements may be related to the concentration of cancer cells, with higher ratios coming from locations with a higher concentration of malignant cells.

The fluorescence intensity ratio of 340 nm to 440 nm was a criterion to identify malignancy from benign and normal tissues. A multiple wavelength detection method has been introduced into the ratiometer to increase the identification capability of cancer from the benign and normal, specifically to separate cancer from fat. The ratiometer not only can distinguish between cancer and the normal, but also can identify cancer from fat.

In conclusion, there is a need to develop methods to probe deep into organs, such as a tumor inside breast, for a real time evaluation and diagnosis of tumor *in vivo*. An optical fiber needle based ratiometer, which is based on native spectroscopic differences between diseased and normal tissues, has been designed, assembled, and tested. A key point of the research project is using an optical fiber needle as a probe to delivery excitation light on tumor and collect the fluorescence from that tumor region, with a small diameter of about 300 μm , which can go through the organ and arrive at the inside tumor. Cancerous, benign/normal breast tissues have been measured and distinguished by the ratiometer *in vitro*. The simulation measurements of a tumor inside breast were performed using layering samples. Multiple wavelengths have been introduced to the optical fiber needle based ratiometer for increasing the capabilities to separate fat from cancer. The measurement results have indicated that the ratiometer can identify different tissue types reading fluorescence intensity ratio at two specified wavelengths. This research demonstrates the technological and commercial potentials of the optical fiber needle based ratiometer and *in situ* spectroscopy to reduce or replace breast biopsy and to obtain information from other in assemble body organ locations without surgical biopsy.

We thank DOE and Mediscience Technology Corp.

REFERENCES

1. S. Undenfriend, Fluorescence Assay in Biology and Medicine, Vol.I, New York, Academic Press, (1962).
2. M.Brenboim, A. N. Domanskii, K. K. Turoverov, Luminescence of biopolymers and cells, Plenum, New York, (1969).
3. R. R. Alfano, G. C. Tang, A. Prachan, W. Lam, D. S. J. Choy, Fluorescence Spectra from Cancerous and Normal Human Breast and Lung Tissues IEEE J.Quantum Electron. QE-23, 1806-1811 (1987).
4. R. R. Alfano, A. Pradhan, G. C. Tang, S. J. Wahl, Optical spectroscopic diagnosis of cancer and normal breast tissues, J.Opt.Soc. Am. B 6, 101 (1989).
5. G. C. Tang, A. Pradhan, and R. R. Alfano, Spectroscopic Differences between Human Cancer and Normal Lung and Breast Tissues, Lasers in Surgery and Medicine 9, 290-29 (1989).
6. G. C. Tang, Asima Pradhan, W. Sha, J. Chen, C. H. Liu, S. J. Wahl, and R. R. Alfano, Pulse and CW Laser Fluorescence Spectroscopy from Cancer and Chemically Treated Normal and Lung Tissues, Applied Opticals 6, 2337-2342 (1989).
7. R. R. Alfano, B. Das, J. Cleary, R. Prudente, and B. J. Celmer, Light sheds light on cancer, distinguishing malignant tumor from benign tissue and tumors, Bull. N. Acad. Med., second series 67(2), 143 (1991).
8. Yuanlong Yang, E. J. Celmer, Margaret Zurawka-Szczepaniak, and R. R. Alfano, Excitation spectrum of malignant and benign breast tissues: A potential optical biopsy approach, Lasers in the Life Sciences 7(4), 249-265 (1996).
9. Yuanlong Yang, A. Katz, E. J. Celmer, Margaret Zurawka-Szczepaniak, and R. R. Alfano, Fundamental differences of excitation spectrum between malignant and benign breast tissues, Photochemistry and Photobiology 66(4), 516-622 (1997).
10. W. Sha Glassman, C. H. Liu, G. C. Tang, S. Lubicz, and R. R. Alfano, Ultraviolet Excited Fluorescence Spectra from Non-malignant and "Malignant Tissues of Gynecological Tract," Lasers in Life Science, 5(12), 49-58, (1992).
11. N. Ramanujam, M.F. Mitchell, A. Mahadevan, S. Thomsen, E. Silva, and R.R. Rechards-Kortum, In Vivo diagnosis of cervical intraepithelial neoplasia (CIN) using 337 nm laser induced fluorescence, Proc. Nat. Acad. Sci. U.S.A. 91, 10193-10197 (1994).
12. Yuanlong Yang, G. C. Tang, M. Bessler, and R. R. Alfano, Fluorescence Spectroscopy as a photonic Pathology Method for Detecting Colon cancer, Lasers in the Life Science 6 (4), 259-276 (1995).
13. C. R. Kapadia, F. W. Cutruzzola, K. M. O'Brien, M. L. Stetz, R. Enriquez, L. I. Deckelbaum, Detection of adenomatous transformation of colonic mucosa by fiberoptical laser-induced fluorescence (LIF) spectroscopy, Gastroenterology 99, 150 (1990).
14. R. M. Cothren, M. V. Sivak, J. Van Dam, R. E. Petras, M. Fitzmaurice, J. Crawford, J. Wu, J. F. Brennan, R. P. Rava, R. Manohara, M. S. Feld, Detection of dysplasia at colonoscopy using laser-induced fluorescence: Ablinded study, Gastrointestinal Endoscopy 44, 168-176 (1996).
15. J. Hung, S. Lam, J.C. LeRiche, and B. Palcic, Autofluorescence of normal and malignant bronchial tissue, Lasers in Surgery and Medicine 11, 99-105 (1991).

The Fabrication of Deuterium Loaded Fiber Bragg Grating and Its Spectral Characteristics in Thermal Annealing

M. C. Shih^a, C. C. Wang^a, C. T. Yu^a, and T.J. Chuang^b

^a *Institute of Opto-electronic Sciences, National Taiwan Ocean University, R.O.C.
No.2, Pei-Ning Rd., Keelung, Taiwan, R.O.C.*

^b *Institute of Atom and Molecular Sciences, Academia Sinica, R.O.C.*

ABSTRACT

Previous results showed that the non-reversible(hysteresis loop) of Bragg wave length shifting in thermal cycling of the Fiber Bragg Grating which is a high germanium doped optical fiber and high pressure hydrogen loaded was due to the diffusion out of the H₂ residue in thermal annealing. In addition, the O-H absorption peak (1.38 μ m) causes signal attenuation and stability problem in FBG applications. We demonstrated the fabrication of the D₂ loaded FBG with high stability of Bragg wave length in thermal annealing at temperature up to 250 °C. The spectrum characteristics of the D₂ loaded FBG compare to the H₂ loaded FBG is presented. In general, $\Delta \lambda_B$ of the D₂ loaded FBG is narrower than H₂ loaded, and λ_B of the D₂ loaded FBG is more stable than H₂ loaded in thermal annealing. A model base on the UV photo-induced index change in BFG core with D₂ and H₂ loaded to explain the spectrum characteristics between D₂ and H₂ loaded FBG is discussed.

Keywords: Fiber Bragg grating, deuterium loading

1. INTRODUCTION

Fiber Bragg grating has known to be the most advanced passive component for applications in fiber optic communication and sensor systems because of its low insertion loss, narrow band pass, and the flexibility of manipulating desired spectral characteristics [1-5]. FBG can be easily tailored by induced index change, grating length, chirping, and apodization, so that the desired spectral characteristics, such as filtering wavelength, reflectivity, and band-width can be achieved. In general, a FBG device is used to convert the variation of temperature or strain of the tested environment. The Bragg wavelength shifting then can be measured by interrogating, or by interferometric approach [6-9]. Thus, the performance of the fiber -optic sensing system is significantly affected by the spectrum stability of the FBG components.

Various approaches to fabricate the FBG have been demonstrated [10-19]. High pressure H₂ loading is one of the well known process to enhance the photo-sensitivity of the high germanium doped fiber by deep UV writing (248 nm). The hydrogen loading process is low cost and reproducible. Previous report showed that the hydrogen loaded FBG has an intrinsic absorption peak at 1.38 μ m by the O-H bond [20-21]. This O-H absorption might cause intrinsic problem to fiber optic communication system where a 1.3 μ m laser source is usually used. In addition, the residue of H₂ cause the drifting of the effective index change of the fiber, which in turn can affect the reflectivity and Bragg wavelength of the FBG. Although, this drift can be eliminated by cycles of post annealing, but will decrease the reflectivity of the FBG. It is suggested that the hysteresis of Bragg wavelength shifting is contribute to the diffusion out of the H₂ residue in thermal annealing.

In this report, we demonstrate the fabrication of the FBG using high pressure D₂ loading, and shows the improvement of the spectral characteristics of the FBG.

2. EXPERIMENTS

Samples of high germanium doped single mode fiber were kept in 1/4 " stainless steel (SS304) tubing pressurized at 1500 psi of H₂/D₂ for days until the saturation was reached. The concentration of H₂ in the fiber can be monitored by the

H₂O absorption peak at 1.24 μm , but the detection of the D₂ related absorption peaks is beyond the spectrum range of the optical spectrum analyzer (HP 70951B) in use. The saturation of the D₂ is estimated by the diffusion coefficient of D₂ which is $1/\sqrt{2}$ to H₂.

Figure 1 shows the FBG deep UV exposure system. A KrF excimer laser at 248 nm is used to induce the index change of the Ge-doped dispersion sifted fiber, a phase mask with 1.0780 μm grating period is used to generate the grating on the fiber core, and the HP 70951B optical spectrum analysis system with a white light out put is used to record the real time transmission of the FBG during UV exposure at 60 mJ/cm² fluence and 5 Hz pulse rate. Figure 2 shows the transmission spectrum with Bragg wavelength at 1.55 nm of the FBG with D₂ and H₂ loaded. It reveals that the absorption peak of O-H (1.38 nm) appearing beside the 1.55 nm of Bragg wavelength, but is avoided in the spectrum of D₂ loaded FBG.

3.RESULTS AND DISCUSSION

Figure 3 shows the transmission spectrum of the D₂ loaded and H₂ loaded FBG. In general, the spectrum of H₂ loaded FBG is wider than the H₂ loaded FBG, and significantly, a side lobe next to the Bragg reflection peak. In characterizing the FBG spectrum variation in thermal annealing, the FBG sample was annealed on a hot plat which was kept at a set temperature for a period of time to record the spectrum, then repeat the same process at another higher temperature up to 200 °C. Figure 4,5 are the spectrum variation of H₂ / D₂ loaded FBG in thermal annealing. It is clearly shown that the D₂ loaded FBG has better spectrum stability than H₂ loaded FBG. The Bragg reflection spectrum of the D₂ loaded FBG is almost reversible with temperature, but there is a serious hysteresis loop in the spectrum of the H₂ loaded FBG due to thermal annealing.

It is the fact that the residue of the D₂ or H₂ can vary the effective index n_{eff} of the fiber core. It is suggested that the non-reversible spectral histogram of the H₂ loaded FBG in thermal annealing might be due to the over loading of H₂, in which decrease of concentration of H₂ in fiber core can cause significant drifting of the effective index. If this is the case, it might suggest that the non-reversible variation of the H₂ loaded FBG spectrum in thermal annealing could be improved by reducing the concentration of H₂ in the fiber core to some threshold level. Also, the diffusion coefficient of D₂ or H₂ might be another factor to affect the stability of the FBG spectrum in which the diffusion of D₂ is slower because of its heavier molecular weight, and refers that spectral stability of the D₂ loaded FBG is better than H₂ loaded FBG.

4.CONCLUSIONS

We demonstrated the improvement of the FGB spectral stability by using D₂ loading. The identification of the mechanism responsible for the non-reversible spectrum variation of H₂ loaded FBG in thermal annealing, and the difference of the spectrum characteristics between H₂ loaded and D₂ loaded FBG is not clear. Further experiments to quantitatively measure the variation of the FBG spectrum characteristics parameters in thermal annealing with respect to the concentration of D₂/ H₂ in the fiber core is needed to explore the mechanism of the spectrum variation. Further exploration of the mechanism which responsible to the spectrum characteristics is important to achieve stable FBG devices in practical applications.

ACKNOWLEDGEMENT

The authors would like to thank all of the colleagues in the lab for providing their help with dedicated works, and the support from the university. We acknowledge financial support by the Asia Pacific Research Foundation and National Science Council under the grand of 89-2112-M-019-005.

REFERENCES

1. K.O. Hill, Y. Fujii, D.C. Johson, and Kawasaki, Appl. Phys, Lett, 32,647(1987)
2. M. Kawasaki, M. Yasu, and T. Edahiro, Electron. Lett.,19,583(1983)
3. Barnoski, M. K., and S. M. Jensen, Fiber waveguides: a novel technique for investigating attenuation characteristics. *Appl. Optics*, Vol. 15, 1976, p. 2112.
4. D. C. Lee, J. J. Lee & S. J. Yun, The mechanical characteristics of smart composite structures with embedded optical fiber sensors, *Composite Structures*, 32 (1995) 39 - 50.
5. Marten de Vries, Vikram Bhatia, Tiffanie D'Albarto, Vivek Arya and Richard O. Claus, Photoinduced grating-based optical fiber sensors for structural analysis and control, *Engineering Structure*, Vol. 20, No. 3, 1998, p.205 - 210.
6. H. Singh and J. S. Sirkis, Temperature and Strain Measurement by combining ILFE and Bragg Grating Optical Fiber Sensors, *Experimental Mechanics*, Vol. 37, No. 4, December 1997, p415.

7. Takamasa Suzuki, Takao Okada, Osami Sasaki, Takeo Maruyama, Real-time vibration measurement using a feedback type of laser diode interferometer with an optical fiber, *Optical Engineering*, Vol. 36, No. 9, September 1997, p2497.
8. Alan D. Kersey, Michael A. Davis, Heather J. Patrick, Michel LeBlance, K. P. Koo, Member, IEEE, C. G. Askins, M. A. Putnam, and E. Joseph Friebele, Fiber Grating Sensors, *Journal of Lightwave Technology*, Vol. 15, No. 8, August 1997, p1442.
9. A. Yariv, IEEE, *J. Quantum Electron.* QE-9,919(1973)
10. D.K.W. Lam and B.K. Garside, *Applied Optics*, Vol. 20, No.3, 440(1981)
11. Culshaw, B., *Optical Fiber Sensing and Signal Processing*. Peter Peregrinus, 1984.
12. Meltz, G., W.W. Morey, and W. H. Glenn. Formation of Bragg gratings in optical fiber by a transverse holographic method. *Optics Lett.*, Vol. 14, 1989, p. 823.
13. Hill, K. O., B. Malo, F. Bilodeau, D.C. Johnson, and J. Albert. Bragg gratings fabricated in photosensitive monomode optical fiber by UV exposure through a phase mask. *Appl. Phys. Lett.*, Vol. 62, 1993, p. 1035.
14. Morey, W. W., J. R. Dunphy and G. Meltz. Multiplexed fiber Bragg grating sensors. *Proc. Distributed and Multiplexed Fiber Optic Sensors, SPIE*, Vol. 1586, 1991, p. 216.
15. Askins, G. C., M. A. Putman, G. M. Willjams, and E. J. Friebele. Stepped-wavelength optical fiber Bragg grating arrays fabricated in line on a draw tower. *Optics Lett.*, Vol. 19, 1994, p. 147.
16. K. W. Lam and B. K. Garside, Characterization of single-mode optical fiber filters, *Applied Optics*, Vol. 20, No. 3, 1 February 1981, p440.
17. G. Meltz, W. W. Morey, and W. H. Glenn, Formation of Bragg gratings in optical fibers by a transverse holographic method, *Optical Letters*, Vol. 14, No. 15, August 1, 1989, p823.
18. Robert Fedosejevs and M. J. Brett, Direct formation of grating structures on silicon using KrF laser radiation, *Applied Optics*, Vol. 28, No.10, 15 May 1989, p 1877.
19. J. P. Spallas, A. M. Hawryluk, and D. R. Kania, Field emitter array mask patterning using laser interference lithography, *J. Vac. Sci. Technol.*, B 13 (5), Sep/Oct 1995, p1973.
20. C.L. Liou, L.A. Wang, M.C. Shih, and T.J. Chuang, "Characteristics of hydrogenated fiber Bragg gratings", *Appl. Phys. A* 64, 191(1997)
21. Gang-Chih Lin, Likarn Wang, C.C. Yang, M.C. Shih, and T.J. Chuang, "Thermal Performance of Metal-Clad Fiber Bragg Grating Sensors", *IEEE Photonics Technology Letters*, Vol. 10, No. 3, 406(1998)

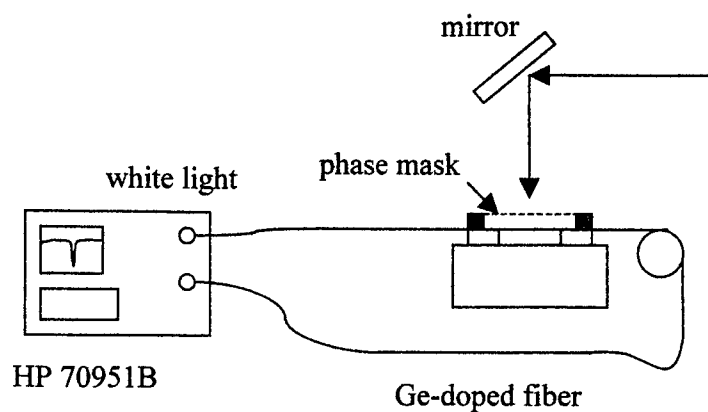


Figure 1. FBG deep UV exposure system. A KrF excimer laser at 248 nm is used to induce the index change of the Ge-doped dispersion sifted fiber, a phase mask with 1.0780 μm grating period is used to generate the grating on the fiber core, and the HP 70951B optical spectrum analysis system with a white light out put is used to record the real time transmission of the FBG during UV exposure at 60 mJ/cm^2 fluence and 5 Hz pulse rate.

Transmission spectra of the H₂ loaded FBG

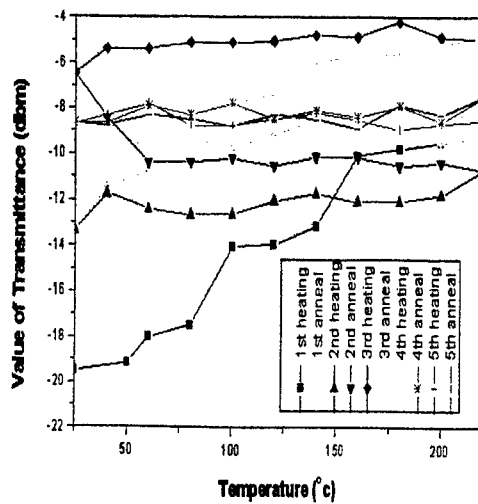
Transmission Spectra of the D2 loaded FBG

Figure 2. The transmission spectrum with Bragg wavelength at 1.55 nm of the FBG with D₂ and H₂ loaded. It reveals that the absorption peak of O-H (1.38 nm) appearing beside the 1.55 nm of Bragg wavelength(upper), but is avoided in the spectrum of D₂ loaded FBG(below).

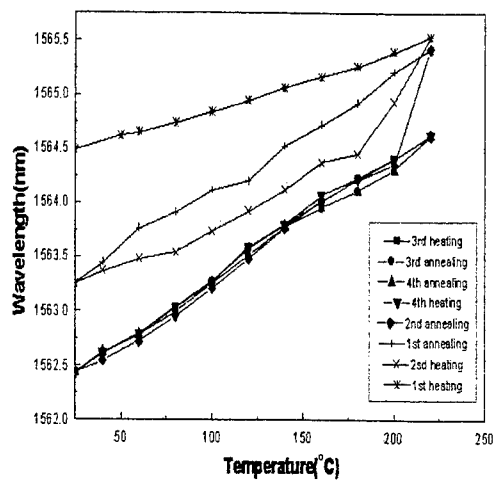
Transmission spectra of the D2 loaded FBG

Transmission spectra of the H₂ loaded FBG

Figure 3. The transmission spectrum of the D_2 loaded and H_2 loaded FBG. The spectrum of H_2 loaded FBG is wider than the D_2 loaded FBG, and significantly, a side lobe next to the Bragg reflection peak.



Hysteresis of transmission of the H₂ loaded FBG in thermal annealing



Hysteresis of wave length shifting of the H₂ loaded FBG in thermal annealing

Figure 4, The spectrum variation of H₂ loaded FBG in thermal annealing. It is clearly shown that there exists a non-reversible spectrum(hysteresis loop) variation in thermal annealing.

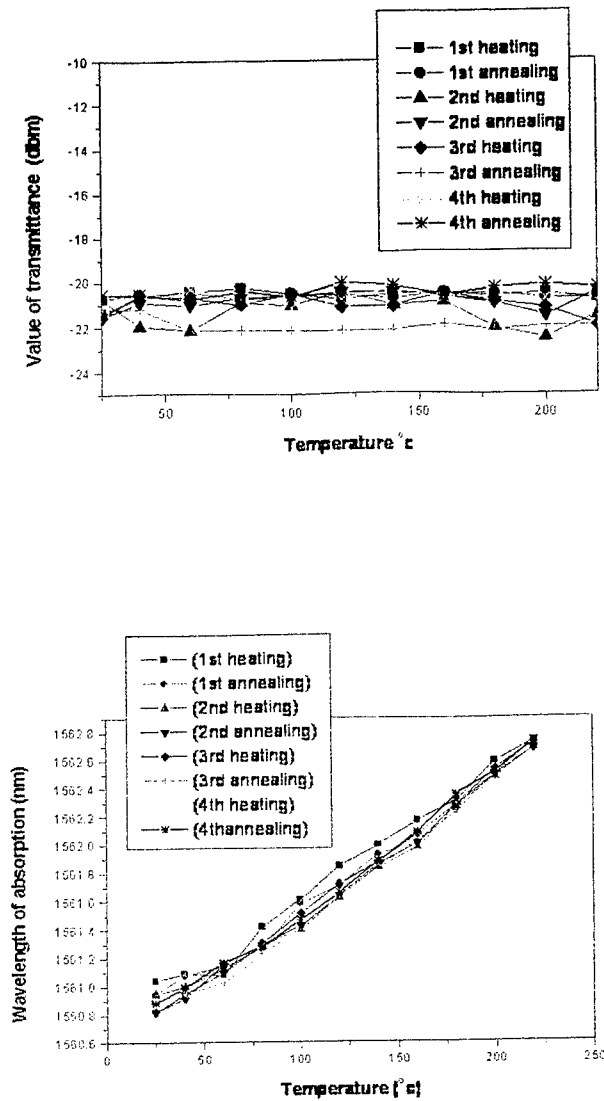


Figure 5. The spectrum variation of D_2 loaded FBG in thermal annealing. It is clearly shown that the D_2 loaded FBG has better spectrum stability than H_2 loaded FBG. The Bragg reflection spectrum of the D_2 loaded FBG is almost reversible in thermal annealing.

Temperature performance of Raman scattering in a data fiber and its application in a distributed temperature fiber-optic sensor

D. Liu*, J. Wang, S. Liu

Department of Optoelectronic Engineering,
Huazhong University of Science & Technology, Wuhan 430074, China

ABSTRACT

A wavelength-division-multiplexer (WDM) was used to extract the Raman scattering signal from a data fiber. The temperature performance of Raman scattering spectrum was studied theoretically and experimentally. On the base of this study a distributed fiber-optic temperature sensor (DFTS) system was developed. The sensing distance was 4km. The temperature accuracy and the distance resolution reached to $\pm 1^{\circ}\text{C}$ and $\pm 1\text{m}$, respectively. The system is stable and adequate for commercial usage, such as the power industry, the underground tunnel, the subway, the pipe laying, and also for the mission applications, such as the warship and the airplane.

Keywords: Fiber-optic sensor, Distributed temperature sensor, Data fiber, Raman scattering

1. INTRODUCTION

The distributed fiber-optic sensors are attracting more and more attention recently. Many sensor schemes based on a number of physical parameters, such as fiber attenuation, temperature, and strain of the optical fiber have been developed. Optical time-domain reflectometry (OTDR), is one of the powerful tools to fulfill the distributed measurement in the fiber. The spontaneous Raman scattering in optical fibers can be used to measure distributed temperature along the sensor fiber^[1-4]. Here, a laser pulse is injected into the sensing fiber and transmitted along the fiber. The backscattered Raman light due to the interaction between photons and phonons will contain information about loss and temperature along the fiber. This backscattered Raman light is detected with high temporal resolution and then transformed to a temperature distribution diagram along the fiber.

The data fiber, with a large core diameter and numerical aperture ($62.5\mu\text{m} / 0.275 \text{ NA}$), is not only an excellent communication transmission media, but also a good sensitive device in DFTS system because of its larger Raman scattering efficiency and ascendant temperature sensitivity. In this paper we describe a recently developed DFTS system using the data fiber. The detail analyses for the performance of the system is given. The design of the special wavelength-division-multiplexer is introduced. The temperature-response performance of the Raman scattering, and the influence of the system working condition on central wavelength and peak power of Stokes and anti-Stokes lights are analyzed theoretically and experimentally.

* Correspondence: Email: dmliu@mail.hust.edu.cn; Telephone/Fax: 0086-27-87543355-1

2. SPECTRUM OF THE RAMAN SCATTERING IN A DATA FIBER

The data fiber is a high Ge-doped quartz fiber to increase its numerical aperture and effective area. This kind of fiber is especially suitable to the distributed fiber-optical temperature sensors based on Raman scattering due to the high Raman scattering coefficient of the Ge molecules. The spontaneous Raman scattering in a data fiber has the following characteristics:

- 1) the intensity of the scattering is directly proportional to the induced light intensity, and in the magnitude the former is only about $10^{-8}/m \sim 10^{-10}/m$ of the latter;
- 2) the scattering light is random in the propagation direction;
- 3) the Raman frequency has a broad spectrum and a "Raman shift" corresponding to the central frequency of the induced light;
- 4) the Raman scattering has an exact relationship with the temperature.

The central wavelengths of the Stokes- and anti-Stokes spectrum of Raman scattering, λ_{as} and λ_s , could be given by the following equation:

$$\frac{1}{\lambda_{as}} = \frac{1}{\lambda_0} + \nu \quad (1)$$

$$\frac{1}{\lambda_s} = \frac{1}{\lambda_0} - \nu \quad (2)$$

in which, λ_0 is the wavelength of the input light, ν is the wave number of the Raman frequency-shift decided by the material content of the fiber. For high Ge-doped data fiber, ν is about 400cm^{-1} . If the wavelength of the input light is 805 nm, the wavelengths of the anti-Stokes and Stokes spectrum of the Raman scattering, λ_{as} and λ_s , will be 780 nm and 832 nm, respectively.

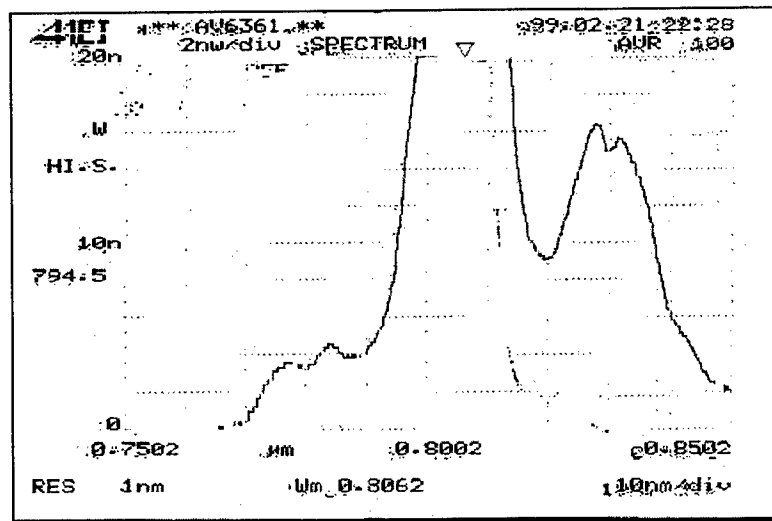


Fig.1 Back-scattering spectrum of the data fiber

Fig.1 shows the back-scattering spectrum of the data fiber. It could be seen that there exist three peaks in the back-scattering spectrum, which are Rayleigh, Stokes and anti-Stokes, respectively. The Rayleigh-peak is much larger than Stokes and Anti-Stokes peaks. The anti-Stokes light is the most sensitive to the temperature, but the smallest in the three scattering components. How to effectively extract the anti-Stokes signal is the key of the distributed temperature fiber-optic sensor.

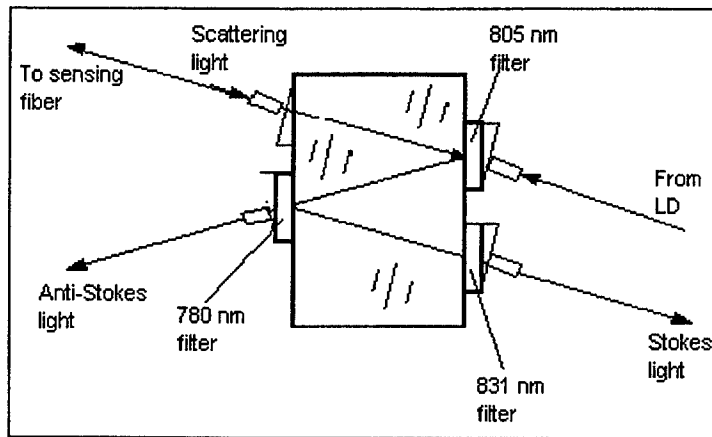


Fig. 2 Curve of ratio of anti-Stokes intensity to Stokes intensity vs. temperature

A specially designed (WDM) was used as the splitter of the three kind of scattering light. Fig. 2 shows the configuration of the WDM device. The input light from a laser diode (LD) is transmitted through a dielectric film filter of central wavelength 805nm and is coupled into the sensing fiber. The back-scattering light from the sensing fiber comes back again to the 805nm filter, in which the Stokes and anti-Stokes components are reflected and the Rayleigh component is lost. Thereafter a 780nm filter and a 831nm filter are used to extract the anti-Stoke component and the Stokes component, respectively. All the optical parts are glued to a glass block and form a compact and stable device. The filters are designed so that the Rayleigh scattering is suppressed at the maximum extent and the loss for the anti-Stokes component is smallest. Fig.3 shows the Band-transmission performance of the WDM device.

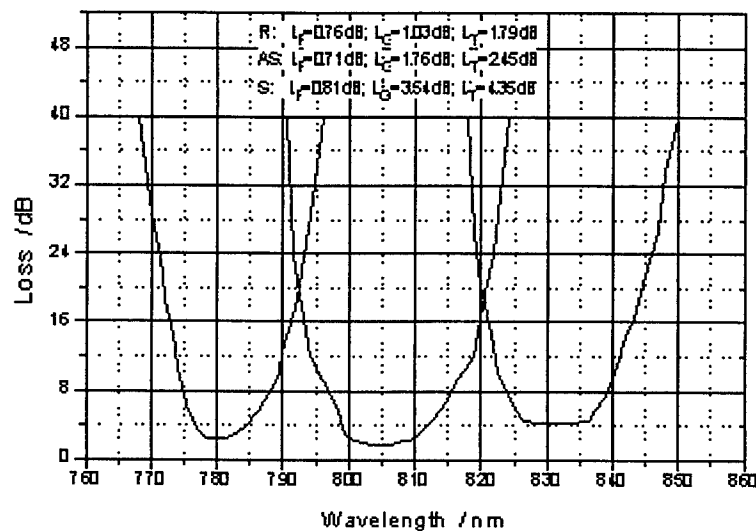


Fig.3 Band-transmission performance of the WDM device

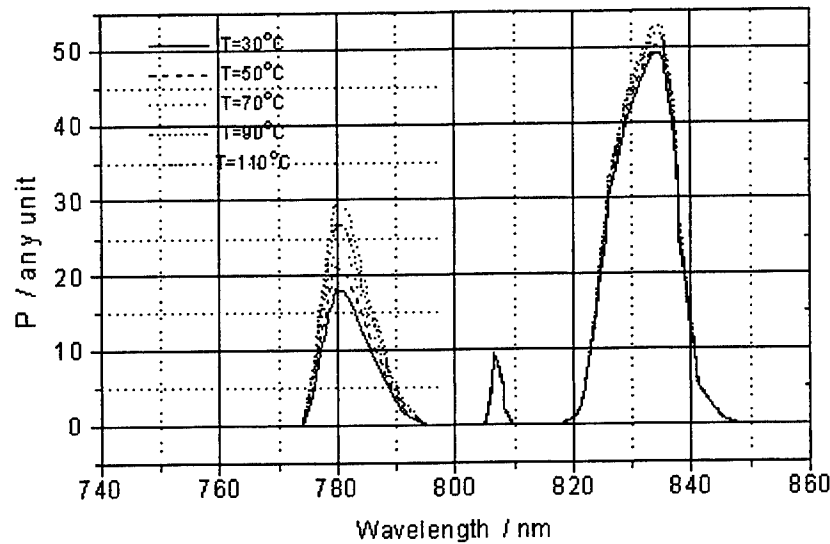


Fig. 4 Temperature response of the back-scattering spectrum of the data fiber

Fig.4 is the measured spectra back-scattering of the data fiber using the WDM under different temperatures. It could be seen that the anti-Stokes light is the most sensitive to the temperature and of excellent linear temperature-sensitive response. Rayleigh light is however almost insensitive to the temperature, which could be consider a background for the temperature sensing and should be reduced to the lowest so as to increase the sensitivity of the system.

3. EXPERIMENTAL SYSTEM

The newly developed experimental system consists of optical transmitter module, optical splitting module, sensing data fiber, optical receiver module, and signal process module, as shown in Fig.5. In the optical transmitter module, a LD is modulated by a short pulse of 30 ns and exports an optical pulse. The LD is temperature-controlled to keep stable optical performance. The light signal is sent to the optical splitting module, where the forward pump light signal is coupled to the sensing data fiber and the backward Stokes and anti-Stokes light signals from the fiber are split and exported to the optical receiver module. A specially designed wavelength division multiplexer (WDM) is used to realize the low loss splitting of the pump laser, Stokes light and anti-Stokes light. The total coupling loss is reduced successfully to 1.7 dB for anti-Stokes light, which is very helpful for increasing the signal-to noise ratio of the system. In the optical receiver module the light signals are transmitted into electrical signals and sent in to the signal process module together with a synchro-signal. The distance is calculated based on the theory of optical time domain reflectometry (OTDR). The light transmission velocity in data fiber is about 0.2m/ns, i.e. every 10 ns of the time from the injection of the optical pulse to the arrival of the back scattering light can be converted into 1m in fiber length. The ratio of anti-Stokes intensity and Stokes intensity under given temperature environment is measured and calculated, and converted into a temperature value. Accordingly the distribution of the temperature along the sensing fiber could be depicted.

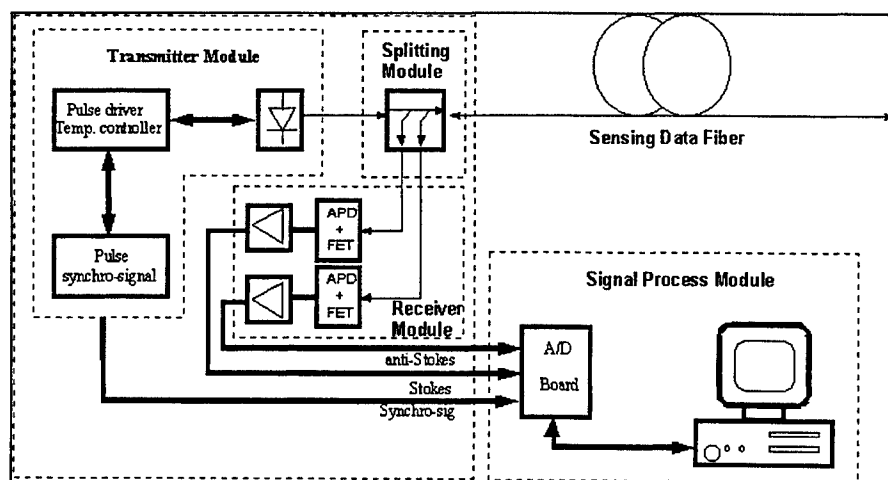


Fig. 5 Schematic of the DFTS experimental system

A practical fiber-optic distributed temperature sensing and fire-alarming system with complete functional software and excellent performances has been developed. The main functions for this system include: the access the signals of the multiple channels with 100 M sampling speed, the multiple data process, real-time temperature calibration, seeking for the abnormal points, as well as alarming the fire and storing the data.

Fig. 6 shows the measured temperature distribution. The heaves occur in the high temperature districts, which indicates that the Raman scattering intensity increases with the temperature. Table 1 lists main technological parameters of this system.

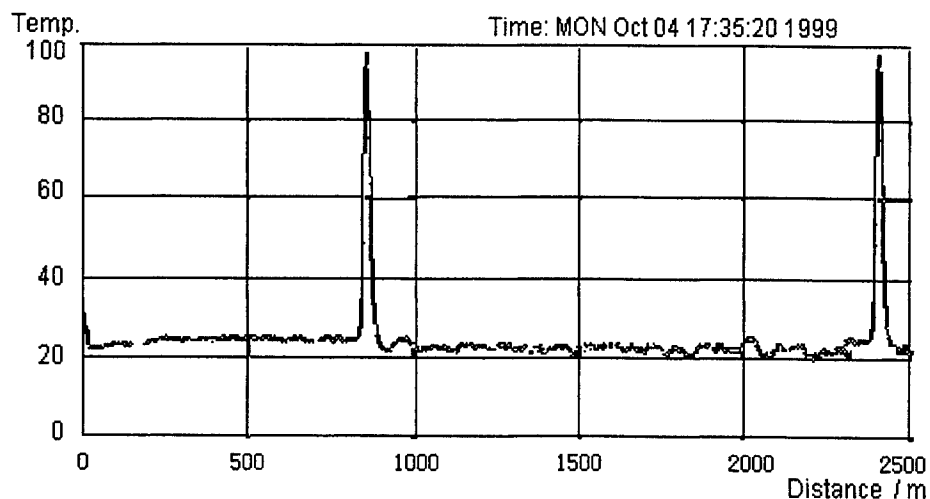


Fig. 6 Measured temperature distribution

Table 1 Specifications of the fiber distributed temperature-sensing system

Technol. Parameter	Specification
Optical fiber	62.5/125 μm GI-data fiber
Temperature accuracy	$\pm 2^\circ\text{C}$
Measured temperature range	$-40 \sim +140^\circ\text{C}$
Distance resolution	$\pm 2 \text{ m}$
Measured distance range	4 km

4. CONCLUSION

The spectra of the back-scattering of the data fiber and their temperature performance were analyzed. A WDM with excellent technological quotation was designed and fabricated and used to extract the weak temperature signal from the back-scattering of the data fiber. A perfect DFTS system based on Raman scattering has been demonstrated. The whole system is credible for long-term operation and has been applied into the fire-alarming field.

ACKNOWLEDGMENTS

Authors should be greatly appreciated the funding support from the National Foundation for Transient-Century Young Talents of Education Ministry of China and from the Nanjing Fire company (China).

REFERENCES

1. Farahani M.A., and Gogolla T., "Spontaneous Raman scattering in optical fiber with modulated probe light for distributed temperature Raman remote sensing", *Journal of Lithwave Technol. Lett.*, **17**(8), pp.1379-1391, 1999.
2. Bao, X., Webb D.J. and Jackson, D.A., "Recent progress in distributed fiber optical sensors based on Brillouin scattering", *SPIE*, **2507**, pp.175-185, 1995.
3. Wakami, T., and Tanaka, S., "1.55 microns long-span fiber-optic distributed temperature sensor", Proc. 10th Optical Fibre Sensors Conference, *SPIE*, **2360**, pp.134, 1994.
4. Boiarski A.A., Pilate G., Fink T., and Nilsson N., "Temperature measurements in power plant equipment using distributed fiber optical sensing", *IEEE Trans. On Power Delivery*, **10**(4), pp.1771-1778, 1995.

Novel Fiber Grating Sensing Technique Based on the Torsion Beam*

Weigang Zhang, Dejun Feng, Lei Ding, Ying Zhang, Xinyong Dong, Chunliu Zhao, Xiaoyi Dong

Institute of Modern Optics, Nankai University, Tianjin, 300071, China.

ABSTRACT

A novel fiber grating sensing technology based on the torsion beam is reported for the first time. The Bragg wavelength change is linear with the torsional angle and the torque. The fiber Bragg grating (FBG) is firmly mounted on the surface of the torsion beam with a determinate angle along the direction of the axes of the torsion beam. The range of the torsional angle is between -45° and $+45^\circ$. The sensing sensitivity of the torsional angle is up to 11.534 degree/nm and that of the torque is up to 0.1595 Nm/nm, respectively. The formulas have been derived theoretically and the experimental results basically accord with the theoretical ones. This technology has many advantages, such as two directional tuning, the high sensitivity, the good repetitiveness and no chirping for the torsional angle within the range from -45° to $+45^\circ$, etc. It has potential applications in the area of the fiber sensing, the fiber communication and laser technology.

Key words: Fiber Bragg grating, seansing technique, torsional beam, linear tuning.

1. INTRODUCTION

The fiber Bragg grating (FBG), which has many important advantages such as volume minuteness, compatibility with fiber system, collection frequency for wavelength and so forth, is attracting considerable subject for applications as fiber grating sensing technique in recent years¹. A number of sensors, which are based on the detection of the wavelength shift $\Delta\lambda$ and the fiber Bragg grating are used as sensing elements, including both temperature and strain (or stress), have been reported^{1,2}. The wavelength-encoded nature of the output of FBG element has many distinct advantages over direct intensity-based sensing schemes. Most importantly, as the sensed information is encoded directly into wavelength which is an absolute parameter, the output does not depend on the total light levels, losses in the connecting fibers and couplers, or source power.

In this paper, we reported a novel fiber grating sensing technology based on the torsion beam for the first time to our knowledge. The FBG is bonded to the surface of the torsion beam with a determinate angle along the direction of the axes of the torsion beam. The Bragg wavelength shift is linear to the torsional angle and the torque between -45° and $+45^\circ$. The sensing sensitivity of the torsional angle is up to 11.534 degree/nm and that of the torque is up to 0.1595 Nm/nm, respectively. This technology has many advantages such as two directional tuning, the high sensitivity, the good repetitiveness and no chirping for the torsional angle within the range from -45° to $+45^\circ$.

2. PRINCIPLE

2.1. Analyses of Torsion Beam Strain

The analytic schematics of the torsion beam strain is shown in figure 1. A FBG is mounted on the surface of the torsion beam, l is the original grating length $\overline{QN} = z_c$, L_0 and d are the length and the diameter of the torsion beam respectively, φ is the torsional angle. If the torsional strain of column beam is very small, we can consider this kind of twisting analysis to be a pure turn problem³. When the torque M_t is applied on the torsion beam, the produced stress will act on the FBG which is on the surface of the torsion beam no matter the torque M_t is along clockwise or not. Thus the torque M_t results in the change of grating period and refractive index.

*Correspondence: Email: weigang99@tjmail.com; Tel: 86-22-23509849; Fax: 86-22-23508770

In order to obtain both longer and shorter wavelengths, the FBG should be bonded to the surface of the torsion beam with a determinate angle θ along the direction of the axes of the torsion beam. In principle, when the torque M_t is along contraclockwise, grating is stretched, the grating pitch becomes longer and the Bragg reflection wavelength becomes longer. In contrast, when the torque M_t is along clockwise, the grating is compressed, the pitch becomes shorter and the Bragg reflection wavelength becomes shorter. Therefore, if the torque M_t is applied on the torsion beam, it will be possible to infer the angle displacement or the torque by detecting the Bragg wavelength shift $\Delta\lambda$ of the sensor return.

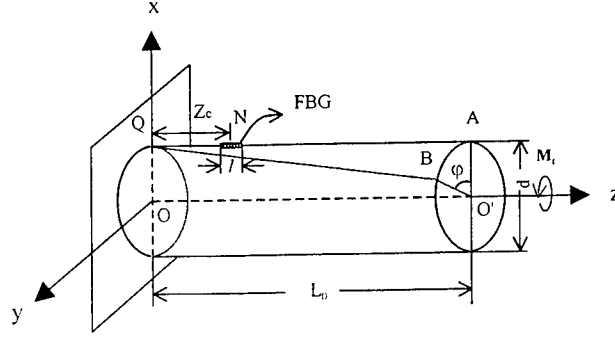


Fig.1 The analytic schematics of the torsion beam strain

From Fig. 1, the torsional strain of column beam γ can be expressed as

$$\gamma = \frac{d\varphi}{2L_0}, \quad (1)$$

the magnitude of the torque M_t is expressed by

$$M_t = GI_p \frac{\varphi}{L_0}, \quad (2)$$

where G is the modulus of the transverse elasticity of the torsion beam, and I_p is the inertia moment of cross section of the torsion beam. In our experiment, the ε of FBG due to the torque is approximately expressed by

$$\varepsilon = \frac{\Delta l}{l} \approx \frac{1}{2} \gamma \sin 2\theta, \quad (3)$$

where Δl is the change about l , θ is the angle between FBG axes and the torsion beam axes.

2.2. Principle of Torsion Beam Strain Sensing

When the temperature is stable, the Bragg wavelength shift $\Delta\lambda$ can be expressed as⁴

$$\frac{\Delta\lambda}{\lambda_0} = \eta_\varepsilon \varepsilon, \quad (4)$$

where λ_0 is the original Bragg wavelength (the center wavelength), η_ε is a constant in reference to the fiber photoelastic coefficient, fiber Poisson ratio and the effective refractive index of the fiber core. ε is the strain of FBG, it can be directly or indirectly produced by applying lateral stress or longitudinal stress in the applications. From formula above, the relationship between the angle displacement φ , the torque M_t and the FBG wavelength shift $\Delta\lambda$ can be expressed as

$$\varphi = \frac{4L_0}{\eta_e \lambda_0 d \sin 2\theta} \Delta\lambda = \kappa_\varphi \Delta\lambda, \quad \text{for } d \ll L_0 \quad (5)$$

$$M_t = \frac{4GI_p}{\eta_e \lambda_0 d \sin 2\theta} \Delta\lambda = \kappa_M \Delta\lambda, \quad \text{for } d \ll L_0 \quad (6)$$

where κ_φ and κ_M are proportional factors, the photoelastic effect is ignored.

3. EXPERIMENT

Figure 2 shows the configuration of the FBG sensing experiment based on the torsion beam. The FBG's center wavelength $\lambda_0 = 1562.48\text{nm}$, and $l = 1.2\text{cm}$, $z_c = 3.6\text{cm}$, $\theta \approx 10^\circ$. The resolution of a commercial optical spectrum analyzer (OSA) is 0.2 nm. Light from a Broadband source (BBS) is coupled via a 3dB fiber coupler into the sensor. IMG is index matching oil by which the undesirable reflection is suppressed.

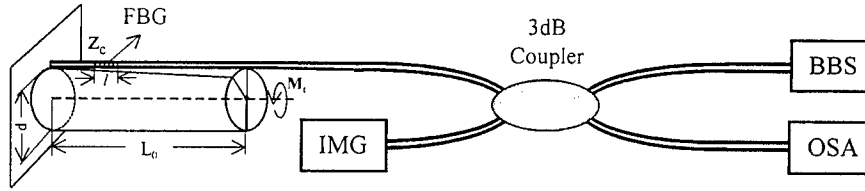


Fig.2 The configuration of the FBG sensing experiment based on the torsion beam.

Figure3 shows the shifts of the transmission intensity and the FWHM do not change in the range of 7 nm. Thus we can consider that there is no chirping within wavelength ranges above mention.

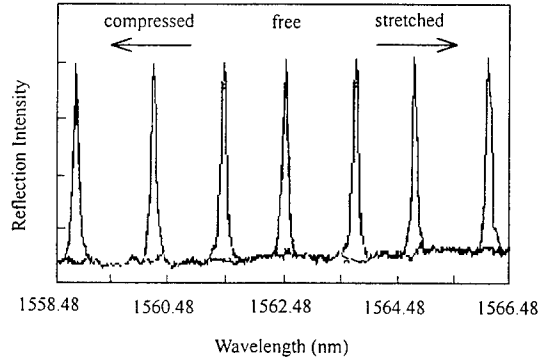


Fig.3. Bragg reflection wavelength shift as a function of intensity.

Figure4 shows the Bragg wavelength shift as a function of the torsional angle and the torque. The maximum shifts of approximately -3.4nm and 3.6nm are obtained toward shorter and longer wavelengths in our experiment, respectively. It is clear to see that the Bragg wavelength can be linearly changed with the torsional angle and the torque. The fitting straight lines are respectively: $\lambda = 0.0867 \varphi + 1562.5$ (nm/degree), $\lambda = 6.27 M_t + 1562.5$ (nm/Nm), and their linear goodness-of-fit are 0.9979. These indicate that the linearity is very good. This relationship can be rewritten as $\varphi = 11.534 \Delta\lambda$ (degree/nm), $M_t = 0.1595 \Delta\lambda$ (Nm/nm). These mean the sensing sensitivity of the torsional angle is estimated to be 11.534 degree/nm and that of the torque is to be 0.1595 Nm/nm at around 1.55 μm for single mode fiber, respectively.

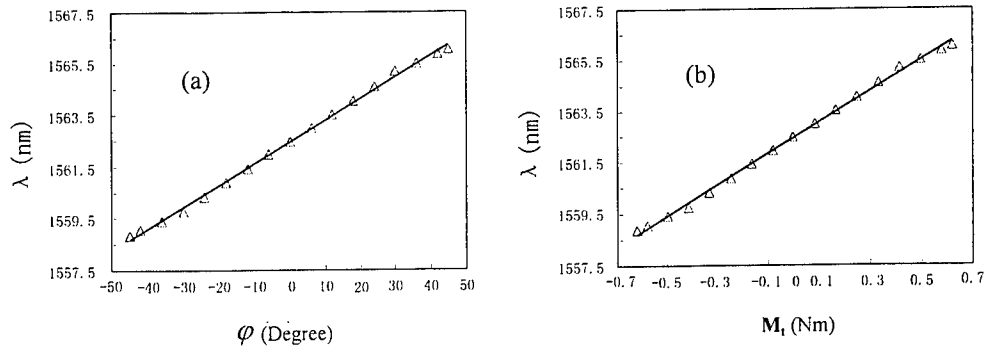


Fig.4. Bragg reflection wavelength shift $\Delta\lambda$ as a function of the torsional angle φ and the torque M_t .

With our grating sensor, adjusting beyond the wavelength shift range from -3.4 nm to +3.6 nm was possible, however, the gratings then were susceptible to chirp and to damage. These indicate that there is a certain changing range for linearly no-chirped response the torsional angle on condition that the torsional strain of torsion beam is very small.

According to the relative parameters of the formula (5) and (6), the sensing sensitivity κ_φ and κ_M can be obtained. κ_φ is 8.643 degree/nm and κ_M is 0.1159 Nm/nm for calculating theoretical values, and κ_φ is 11.534 degree/nm and κ_M is 0.1595 Nm/nm for fitting experimental values in the range between -45° and $+45^\circ$, respectively. Therefore, the revise factors χ_φ and χ_M should be introduced for application. It can be expressed as

$$\varphi = \chi_\varphi \kappa_\varphi \Delta\lambda \quad (7)$$

$$M_t = \chi_M \kappa_M \Delta\lambda \quad (8)$$

While $\chi_\varphi = 1.33$ and $\chi_M = 1.37$, the fitting experimental values are in agreement with the calculated theoretical values. If the structure in figure 2 is improved, it is possible to measure and control some parameters such as the velocity and the volume of flow, the intensity, the rigidity and stability of the tectonic elements⁵, etc.

4. CONCLUSIONS

We have designed and realized a novel fiber grating sensing technology based on the torsion beam. The Bragg wavelength shift is linear to the torsional angle and the torque and there is no-chirped between -45° and $+45^\circ$. The experimental results basically accord with theoretical analyses.

ACKNOWLEDGMENTS

This work is supported by the National Natural Science Foundation of China under Grant No. 69637050 and the Doctorial Foundation of China

REFERENCES

1. A. D. Kersey, M. A. Davis, H. J. Patrick, "Fiber grating sensors" [J]. *J. Lightwave Technology*, **15**, pp. 1442-1463, 1997.
2. G.W.Yoffe, P.A.Krug, F.Ouellette and D.A.Thorncraft, "Passive temperature-compensating package for optical fiber gratings." *Appl.Optics*, **34**, pp. 6859-6861, 1995.
3. X. F. Sun, X. S. Fang, L. T. Guan. *Material mechanics*, pp. 111-114, Higher education publishing house, Beijing, 1994.
4. Z. G. Liu, Y. B. Zhang, G. Y. Kai, X. Y. Dong, J. C. Zheng and J. A. Li. "A new method for fiber-grating linear tuning". *ACTA OPTICA SINICA*, **18**, pp. 1731-1734, 1998.
5. G. L. Wang, Z. Wan, C. D. Tao and D. X. Shao. "High precision angle displacement sensor to torsional rigidity measuring". *Journal of Transducer Technology*, **17**, pp. 42-43, 1998.

SESSION 7

Biochip and Biosensor Technology

Research and development of biochip technologies in Taiwan

S. J. Y. Ting^{*a}, A. Chiou^b

^aDepartment of Physics, Tunghai University, Taichung, Taiwan, R.O.C.

^bDepartment of Electrical Engineering, National Dong Hwa University, Hualien, Taiwan, R. O. C.

ABSTRACT

Recent advancements in several genome-sequencing projects have stimulated an enormous interest in microarray DNA chip technology, especially in biomedical sciences and pharmaceutical industries. The DNA chips facilitated the miniaturization of conventional nucleic acid hybridizations, by either robotically spotting thousands of library cDNAs or *in situ* synthesis of high-density oligonucleotides onto solid supports. These innovations have found a wide range of applications in molecular biology, especially in studying gene expression and discovering new genes from the global view of genomic analysis. The research and development of this powerful tool has also received great attentions in Taiwan. In this paper, we report the current progresses of our DNA chip project, along with the current status of other biochip projects in Taiwan, such as protein chip, PCR chip, electrophoresis chip, olfactory chip, etc. The new development of biochip technologies integrates the biotechnology with the semiconductor processing, the micro-electro-mechanical, optoelectronic, and digital signal processing technologies. Most of these biochip technologies utilize optical detection methods for data acquisition and analysis. The strengths and advantages of different approaches are compared and discussed in this report.

Keywords: Biochip, genome, micro-strip, peptide nucleic acid, protein, microarray, optical detection

1. INTRODUCTION

Biochip technologies have recently received great attentions in Taiwan. There were 10 biochip-related research projects granted by the National Science Council (NSC) in the year of 1999. In the year of 2000, about 40 proposals were submitted to the NSC (besides many industry-oriented projects supported by either private or other government agencies) for the research and development (R&D) in the DNA chips, the protein chips, the micro-fluidic chips, and other biosensors. (See Table 1.) The major driving force for such a sharp rise in R&D of biochip technologies comes from the impact of genome sequencing projects.¹ The successful advancements in several international collaborations of large scale sequencing of whole genome, either of human or model organisms, have generated a tremendous amount of information, which is extremely precious (from both the scientific and the economic points of view) in biomedical science and pharmaceutical industries. A very efficient approach to utilize the unprecedented genomic information is the miniaturization of conventional biotechnology, integrated with the semiconductor processing, the micro-electro-mechanical, optoelectronic, and digital signal processing technologies. Since Taiwan has been very successful in these chip-based industries, researchers in Taiwan are motivated to take advantages of the resources and the lessons learned from these chip-based industries, and to apply them in the frontiers of the biochip technologies.

In a generic sense, any device or component incorporating biological or organic materials, either extracted from organisms or synthesized in a laboratory, on a solid substrate can be regarded as a biochip. From the practical point of view and from the analogy taken from the IC chip, the term "biochip", however, often implies some miniaturization, and the possibility of low-cost, high-throughput mass production. Some of the examples that meet the qualification stated above include the DNA chip (or the gene chip),² the protein chip,³ the PCR (polymerase chain reaction) chip,⁴ the capillary electrophoresis chip,⁵ and the biosensor chip.⁶ In this paper, we give a brief overview of the R&D status of various biochip projects in Taiwan.

2. THE DNA CHIP

2.1. Working principle

* Correspondence: Email: sjyting@mail.thu.edu.tw; Telephone: 886-4-359-0247; Fax: 886-4-359-4643

A DNA chip refers to a two-dimensional array of small reaction cells (each on the order of $100\text{ }\mu\text{m} \times 100\text{ }\mu\text{m}$) fabricated on a solid substrate. The solid substrate can be a silicon wafer, or a thin sheet of glass or plastic, or a nylon membrane. In each reaction cell, trillions of polymeric molecules of a specific sequence of single-stranded DNA are immobilized as illustrated in Fig. 1. The DNA molecules can be either short sequence of oligonucleotides (~20 to 25 bases) or longer fragments (~1,000 to 3,000 bases) of complementary DNA (cDNA).⁷ The specific sequence of oligonucleotides or fragments in each cell is pre-selected or designed based on the intended application. The known sequences of single-stranded DNA immobilized on the substrate are often called the probes. When unknown fragments of single-stranded DNA samples (often called the target) react (or hybridize) with the probes on the chip, double-stranded DNA fragments are formed where the target and the probe are complementary according to the base pairing rule (A paired with T, and G paired with C). To facilitate the analysis of the hybridized chip, the target samples are often labeled with a tag, such as a fluorescent, a dye, or an enzyme. When the targets contain more than one type of sample, each is labeled with its own distinguishable tag. Depending on the size of the array, the DNA chip described above provides a platform where the unknown targets can potentially be identified with very high speed and high throughput by matching with tens of thousands of different types of probes via hybridization in parallel. In the DNA chip using oligonucleotides as probes, the formation of the double-stranded DNA by the base-pairing rule is so specific that under favorable conditions even a single base-pair mismatch can be detected and identified.⁸

2.2. Fabrication techniques

DNA chips are often fabricated by one of the following popular techniques: (1) robotic spotting, which uses DNA fragments as probes,⁹ (2) photolithography, which utilizes the synthesized oligonucleotides as probes.¹⁰ In the first technique, all the DNA fragments to be immobilized on the substrate are pre-amplified (by polymerase chain reaction), and stored in a set of individual containers. A robotic arm with an array of tips is used to transfer the pre-amplified DNA fragments on to the solid substrate by first dipping into the containers and then touching the substrate. In the second approach, the desired sequences of oligonucleotides are synthesized in parallel, layer by layer, using photolithographic technology as illustrated in Fig. 2.¹¹ In this approach, the substrate is first pre-coated with appropriate linkers and protectors. An ultraviolet (UV) light is used to illuminate the substrate through a photolithographic mask to remove the protecting group at specific sites where one particular type of base (say A, for example) is immobilized (via proper biochemical reactions) as illustrated in Fig. 2(a). Likewise, a second mask is then used to immobilize another kind of base (T, for example) at other selected sites as in Fig. 2(b). Four photolithographic masks are thus needed to fill the first layer with all the four types of bases. Successive rounds of de-protection (via UV illumination) and immobilization (via biochemical reactions) are carried out to synthesize the desired sequences of bases at each site, spatially addressable, layer by layer, in parallel. For a sequence of N bases, the total number of photo masks required is 4N, in general. This approach is hence more suited for the synthesis of short sequences of bases. Typically, the length of oligonucleotide is limited to 25 bases or less. When the peptide nucleic acid (PNA)¹² is substituted for the oligonucleotide, the sequence of the probe can be reduced (say, from 25 bases to about 15 bases) with the same specificity in hybridization. This alternative can greatly reduce the cost of photo masks and chemicals for the syntheses, and save the processing time. Some advantages and disadvantages of the two fabrication techniques are listed in Table 2.

The DNA chip designed and currently being developed by our research group¹³ includes lines of electrodes (in the form of micro-strips) connecting arrays of reaction cells (size = $50\text{ }\mu\text{m} \times 50\text{ }\mu\text{m}$ each, center-to-center spacing = $75\text{ }\mu\text{m}$, total number of cells = 100×100) as illustrated in Fig. 3. During the reaction (or hybridization) cycle, an appropriate positive voltage can be applied to selected strip of sites to concentrate the negatively charged DNA targets to selected sites. After the hybridization, during the "wash" cycle, an appropriate negative voltage can be applied to the sites to drive away (or wash out) the mismatched DNA targets. This technique can potentially reduce the hybridization time from hours to minutes. The probes made of PNA are particularly suitable for such kind of design since the PNA molecules are neutral and therefore not affected by the micro-strip electrodes.

2.3. Signal readout from hybridized DNA chips

The next step after the hybridization process is the signal detection or readout to determine the sites where the sequence of the unknown DNA targets complement (or match) that of the probes and stick to the site via the formation of double-stranded DNA molecules. The particular choice of signal detection techniques goes hand in hand with the choice of the tag attached to the DNA target molecules. For example, if one chooses to use fluorescence signal for detection, appropriate fluorescent molecules will be used as the tags. The signal readout system will then consist of an appropriate light source for

excitation, a photo-multiplier tube or a CCD camera (with an appropriate filter) for the detection of the fluorescence emission, and a personal computer for data acquisition and post processing. A schematic simplified diagram of such a signal detection system is shown in Fig. 4. Recently, we have developed a multi-point excitation and CCD based imaging system for high-throughput fluorescence detection of biochip microarrays. Details of the development and the characterization of the system will be reported in a separate paper. Although one can, in principle, integrate either the CCD or the CMOS imager with the DNA micro-array on the same silicon wafer chip, such an approach will unavoidably increase the complexity, and hence the cost, of the fabrication.¹⁴ Unless the fabricated chips are re-usable, such an approach may not be competitive from an economic point of view. Many commercial optical readout systems have been developed in recent years.¹⁵ An alternative optical technique for signal detection is to use dye molecules as the tags and use colorimetry for signal detection and discrimination.¹⁶ Techniques, other than optical, such as radio-isotopic, electronic, or time-of-flight mass spectrometric, have also been investigated.

3. THE PROTEIN CHIP

3.1. Working principle

A protein chip typically consists of an array of spots (each on the order of 100 μm up to 1 mm in diameter) fabricated on a conducting support.¹⁷ Each spot is designed to capture specific proteins of interest from the test sample, with an affinity capture surface, by either a chemical (ionic, hydrophobic, hydrophilic) or a biochemical (antibody, receptor) mechanism depending on the intended application. When the protein sample from cell lysate, serum, or urine is dispensed onto the surface of a protein chip, proteins of interest will be captured on spots according to affinity binding. After removing unbound proteins and interfering substances, the purified proteins on each spot are examined through a laser-induced process, called matrix-assisted (or surface enhanced) laser desorption/ionization (MALDI or SELDI),³ followed by a mass analysis using time-of-flight mass spectroscopy (TOF-MS).¹⁸ The molecular weights of the sample proteins captured or components of sample proteins (epitope of an antigen) can then be rapidly determined from spot to spot. The protein chip technology can play an important role in the discovery of disease biomarkers or the diagnostics of specific disease when the associated biomarkers are already known. It is expected to have a direct impact on drug discovery. A schematic illustration of the working principle of a protein chip is shown in Fig. 5.

3.2. Development of protein chip techniques

The techniques involved in a protein chip system are much less developed in Taiwan than those of a DNA chip. The National Health Research Institute has played a major role in the promotion of the R&D of protein chips. The protein chips and the related technologies will certainly attract the attention of more scientists in Taiwan in the near future. The number of researchers working in this area is expected to increase significantly in the next few years.

4. THE PCR(POLYMERASE CHAIN REACTION) CHIP

In many applications, the DNA samples to be tested (or identified) need to be purified and amplified to increase its amount by orders of magnitude to a detectable level. The amplification of DNA samples is often accomplished by polymerase chain reaction (PCR)¹⁹ in which a minute amount of DNA molecules are repeatedly thermal cycled through a sequence of temperature stages as illustrated in Fig. 6. The amount of the DNA molecules is doubled at the end of each cycle. Each cycle consists of denaturation (the splitting of each double-stranded DNA molecule into two complementary single strands), primer annealing, and primer extension (the reconstruction of double-stranded DNA molecules from single-stranded components through the DNA polymerase and the proper reagents at the proper temperatures). The conventional PCR system can also be miniaturized and fabricated on a chip by micro-machining and microfluidic technologies.⁴ A group of researchers at the National Cheng Kung University has successfully developed a micro-PCR chip, which can rapidly amplify cDNA of Hepatitis C virus for 30 cycles in 30 minutes, compared to 5.5 hours with traditional PCR equipment.²⁰

5. THE CE(CAPILLARY ELECTROPHORESIS) CHIP

Capillary electrophoresis has been accepted as an extremely efficient technique for the separation of small sample volume in low concentration. The time scale of a complete run of capillary electrophoresis can be less than 10% of that needed for the conventional gel electrophoresis. A team at the National Cheng Kung University has successfully developed a microchip of capillary electrophoresis that can separate and identify in less than 3 minutes DNA fragments, ϕX174RF DNA digested by

the restriction enzyme *HaeIII*.²¹ The microfluidic chips were fabricated on poly(methyl methacrylate) (PMMA) substrate using two small-diameter (79 μm) wires to create a cross impression while the substrate was softened by low-temperature heating. (This CE chip can now be routinely produced using etched quartz template.²²) The schematic illustration is shown in Fig. 7. The resulting channels have a rounded shape and are 75 μm deep. The horizontal channel is 20 mm long and serves as the loading channel for the analyte; the vertical channel is 50 mm long and used as the separation channel. The electric field applied to each channel is maintained at 300 V/cm or less to prevent Joule heating. In a typical test run, DNA samples at a concentration of about 1 $\mu\text{g/ml}$ were first injected into the loading channel and the electric field was applied to the loading channel. When the peak of sample arrived at the junction of two channels, the applied electric field was switched from the loading channel to the separation channel. The detection point was 30 mm away from the junction. It took less than 3 minutes to run and identify all 11 fragments of ϕX174RF digest as illustrated in Fig. 8. The performance of such a capillary electrophoresis chip proves to be reliable and competitive to other designs.

6. THE BIOSENSOR CHIP

One of the most significant biosensor projects in Taiwan is the R&D of electronic noses (also known as the olfactory chips). An electronic nose is a device that can detect and identify specific odorant molecules. It often consists of an array of chemical sensing elements and a pattern recognition system. The mammalian olfactory uses a variety of receptors to identify odor or volatile compound. The mechanism of identification of a specific odor is not a one-to-one mapping of one specific type of odorant molecules with one corresponding type of receptors. It is the collective set of receptors (responding with varying degrees to each type of odorant molecules) combined with pattern recognition that identifies each odor. A team at the National Dong Hwa University has successfully developed the olfactory chip.²³ This research group used piezoelectric quartz crystals (which resonate at precise frequencies) coated with selective coatings (peptide derivatives of the various mammalian olfactory receptors) to adsorb species of molecules. The adsorbed molecules increase the mass of the sensor; and thus the resonance frequency of the piezoelectric quartz crystal is changed. By measuring the shift in resonance frequency, the concentration of odorant can be derived. The advantages of this approach include high selectivity, high sensitivity, and good reproducibility. An array of multi-sensors has been assembled for pattern recognition, using numerical taxonomy or artificial neural networks. The working principle of an electronic nose is illustrated in Fig. 9. This olfactory chip system has recently been developed for diagnostics of dengue fever, a disease propagated by *Aedes* mosquitoes, and is expected to be commercialized soon.

7. SUMMARY

The efforts to develop various biochip technologies are definitely growing rapidly in Taiwan. The interdisciplinary nature of these novel technologies is obvious. The fabrication of biochips requires close collaboration of scientists and engineers from different disciplines such as photolithography, micro-electro-mechanical system, microfluidic technologies, and biochemistry. The choice of the specific DNA sequences on the chips is dictated by the target applications and may involve expertise from medical, pharmaceutical, or biological sciences. The technologies associated with detection and readout system may involve optics and opto-electronics, analytical chemistry, or semiconductor device physics. The processing, visualization, interpretation, and management of data require the collaborative effort of computer scientists, mathematicians, and the end users for whom the specific chips are designed. Hopefully, high quality and efficient products of biochip technologies will soon be available in Taiwan for research and commercial applications.

ACKNOWLEDGEMENT

This project is supported in parts by the National Science Council, Taiwan, under the Research Grants NSC88-2736-L-029-001 and NSC88-2736-L-259-002.

REFERENCES

1. P. O. Brown and D. Botstein, "Exploring the new world of the genome with DNA microarrays," *Nat. Genet.* **21**, pp. 33-37, 1999.
2. G. Ramsey, "DNA chips: State-of-the-art," *Nat. Biotechnol.* **16**, PP. 40-44, 1998.
3. H. Davies, L. Lomas, and B. Austen, "Profiling of amyloid beta peptide variants using DELDI ProteinChip arrays," *Biotechniques* **27**, pp. 1258-1261, 1999.

4. A. T. Woolley, D. Hadley, P. Landre, A. J. de Mello, R. A. Mathies, and M. A. Northrup, "Functional integration of PCR amplification and capillary electrophoresis in a microfabricated DNA analysis device," *Anal. Chem.* **68**, PP. 4081-4086, 1996.
5. C. S. Effenhauser, G. J. Bruin, and A. Paulus, "Integrated chip-based capillary electrophoresis," *Electrophoresis* **18**, pp. 2203-2213, 1997.
6. A. D'Amico, C. D. Natale, A. Macagnano, F. Davide, A. Mantini, E. Tarizzo, R. Paolesse, and T. Boschi, "Technologies and tools for mimicking olfaction: status of the Rome 'Tor Vergata' electronic nose," *Biosensors & Bioelectronics* **13**, pp. 711-721, 1998.
7. C. R. Calladine and H. R. Drew, *Understanding DNA: The Molecules and How It Works*, 2nd ed. San Diego: Academic Press, 1997.
8. P. N. Gilles, D. J. Wu, C. B. Foste, P. J. Dillon, and S. J. Chanock, "Single nucleotide polymorphic discrimination by an electronic dot blot assay on semiconductor microchips," *Nat. Biotechnol.* **17**, pp. 365-370, 1999.
9. V. G. Cheung, M. Morley, F. Aguilar, A. Massimi, R. Kucherlapati, and G. Childs, "Making and reading microarrays," *Nat. Genet.* **21**, pp. 15-19, 1999.
10. G. McCall, J. Labadie, P. Brock, G. Wallraff, T. Nguyen, and W. Hinsberg, "Light-directed synthesis of high-density oligonucleotide arrays using semiconductor photoresists," *Proc. Natl. Acad. Sci. USA* **93**, pp. 13555-13560, 1996.
11. S. P. A. Fodor, J. L. Read, M. C. Pirung, L. Stryer, A. T. Lu, and D. Solas, "Light-directed spatially addressable parallel chemical synthesis," *Science* **251**, 767-773, 1991.
12. P. Wittung, P. E. Nielsen, O. Buchardt, M. Egholm, and B. Nordén, "DNA-like double helix formed by peptide nucleic acid," *Nature* **368**, pp. 561-563, 1994.
13. S.J.Y. Ting, A. Chiou, K. Peck, J.-Y. Cheng, L. Hsu, Y.-T. Huang, C.-H. Lin, and S.-F. Tsai, "Fabrication and inspection of the gene chip (in Chinese)," Proceeding of the First Cross-straight Symposium on Microsystem Technologies, Tainan, May 17-19, 2000, pp. 298-307, 2000.
14. T. Vo-Dinh, J. P. Alarie, N. Isola, D. Landis, A. L. Wintenberg, and M. N. Ericson, "DNA Biochip using a phototransistor integrated circuit," *Anal. Chem.* **71**, pp. 358-363, 1999.
15. A. Marshall and J. Hodgson, "DNA chips: An array of possibility," *Nat. Biotechnol.* **16**, pp. 27-31, 1998.
16. J. J. W. Chen, R. Wu, P. C. Yang, J. Y. Huang, Y. P. Sher, M. H. Han, W. C. Kao, P. J. Lee, T. F. Chiu, Y. W. Chu, C. W. Wu, and K. Peck, "Profiling expression patterns and isolating differentially expressed genes by cDNA microarray system colorimetry detection," *Genomics* **51**, pp. 313-324, 1998.
17. J. Ching, K. I. Voivodov, and T. W. Hutchens, "Surface chemistries enabling photoinduced uncoupling/desorption of covalently tethered biomolecules," *J. Org. Chem.* **67**, pp. 3582-3583, 1996.
18. K. C. Weiss, T. T. Yip, T. W. Hutchens, and L. F. Bisson, "Rapid Mass Spectrometry and sensitive fingerprinting of wine proteins by matrix-assisted laser desorption/ionization time-of-flight (MALDI-TOF)," *Am. J. Enol. Vitic.* **49**, pp. 231-239, 1998.
19. K. B. Mullis, F. Ferre, and R. A. Gibbs, *The polymerase chain reaction*. Boston, MA: Birkhauser, 1994.
20. Y.-C. Lin, M.-Y. Huang, K.-C. Young, T.-T. Chang, and C.-Y. Wu, "A rapid micro-PCR system for Hepatitis C virus amplification," Proceeding of the First Cross-straight Symposium on Microsystem Technologies, Tainan, May 17-19, 2000, pp. 353-359, 2000.
21. Y.-H. Chen and S.-H. Chen, "Analysis of DNA fragments by microchip electrophoresis fabricated on poly(methyl methacrylate) substrates using a wire-imprinting method," *Electrophoresis* **21**, pp. 165-170, 2000.
22. G.-B. Lee, S.-H. Chen, G.-R. Huang, R.-B. Chang, C.-H. Wu, W.-C. Sung, I.-H. Lin, "Microfluidic chips for DNA analysis," Proceeding of the First Cross-straight Symposium on Microsystem Technologies, Tainan, May 17-19, 2000, pp. 341-346, 2000.
23. T. Z. Wu, "Piezoelectric biosensor as olfactory receptor for odor detection: electronic nose," *Biosensors and Bioelectronics* **14**, pp. 9-18, 1999.

Table 1. Biochip-related projects in Taiwan.

	Number of projects	
	Year 1999 (granted by NSC)	Year 2000 (submitted to NSC)
DNA chips	9	16
Protein chips	0	7
Micro-fluidic chips	1	11
Biosensors	0	3
Total	10	37

Table 2. A comparison of some advantages and disadvantages of different techniques for DNA chip fabrication.

Techniques	Advantages	Disadvantages
Photolithography	<ul style="list-style-type: none"> • Versatile • High density • Large array size • Mass production 	<ul style="list-style-type: none"> • High up-front cost • Time-consuming
Mechanical Micro-spotting	<ul style="list-style-type: none"> • Affordable • Simple 	<ul style="list-style-type: none"> • Sample storage • Low throughput

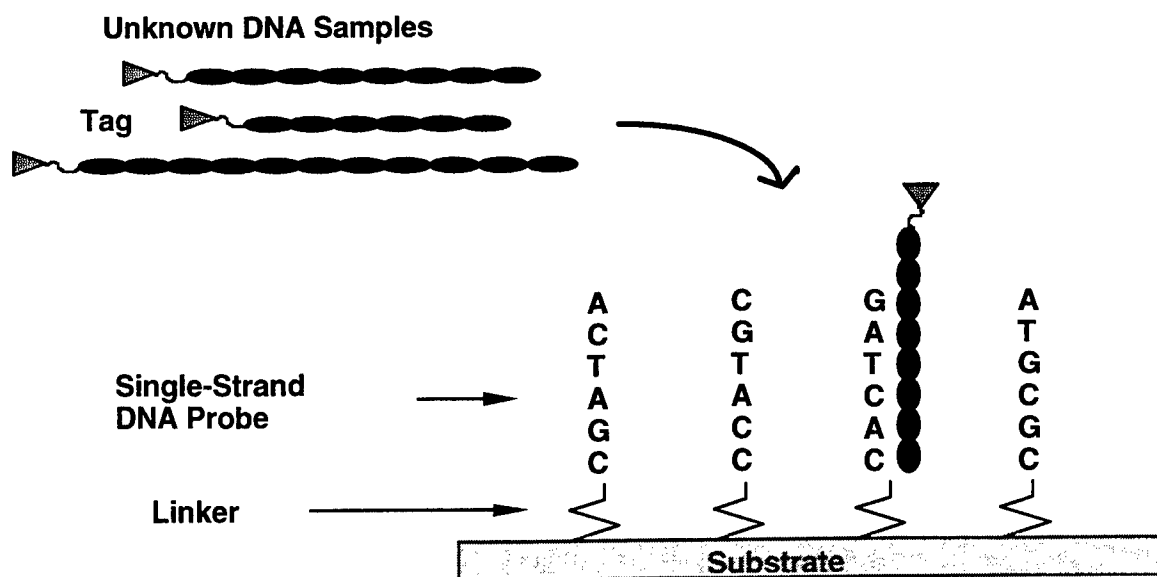


Fig. 1. A schematic illustration of the basic principle of a DNA microarray chip.

Photo-mask
Substrate



(a)



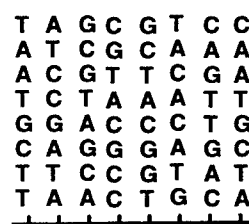
(b)



(c)



(d)



(e)

Fig. 2. *In situ* synthesis of DNA fragments (or sequence of oligonucleotides) by photolithographic technique.

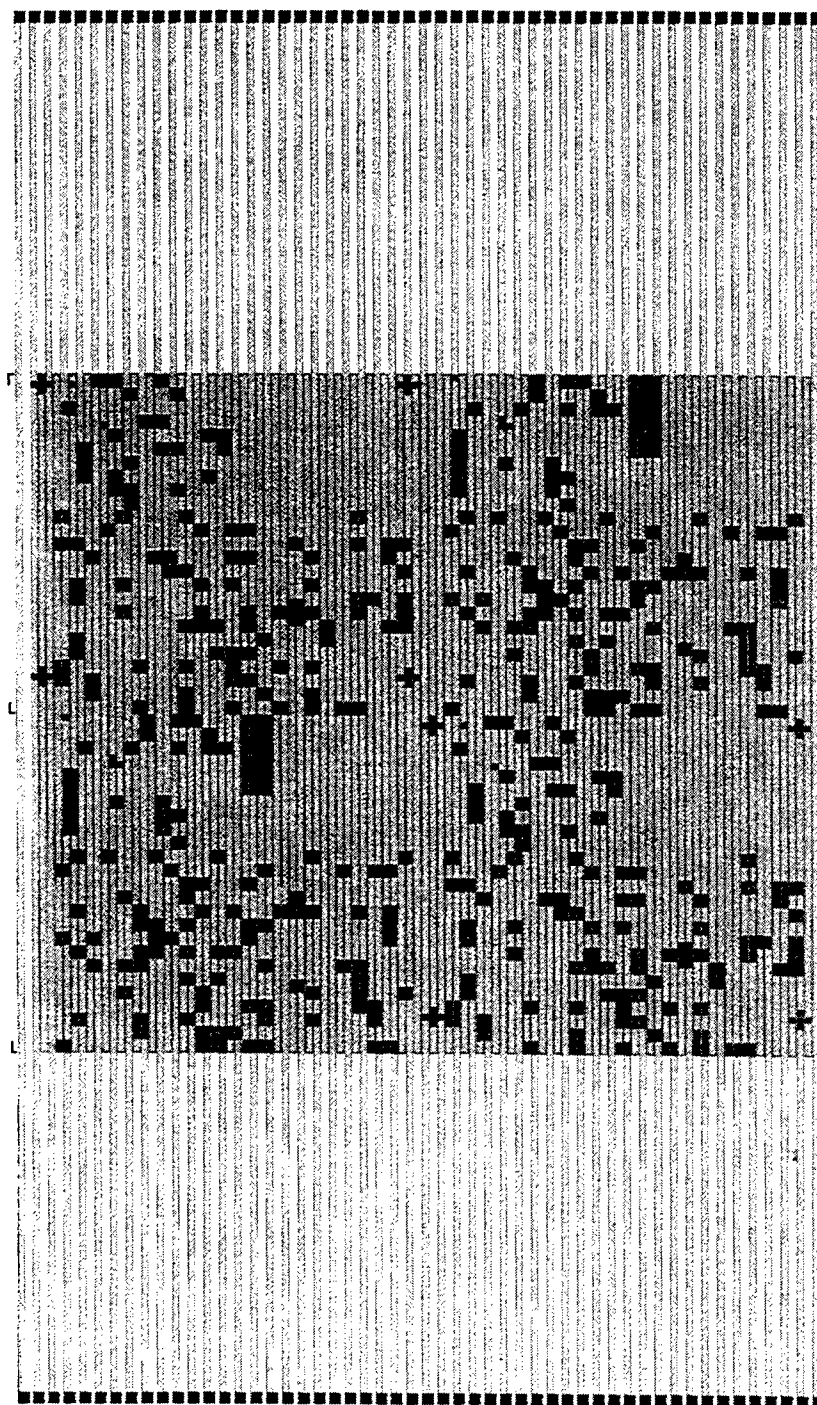


Fig. 3. A schematic illustration of a DNA chip including lines of electrodes (in the form of micro-strips) in concomitant with the array of reaction cells.

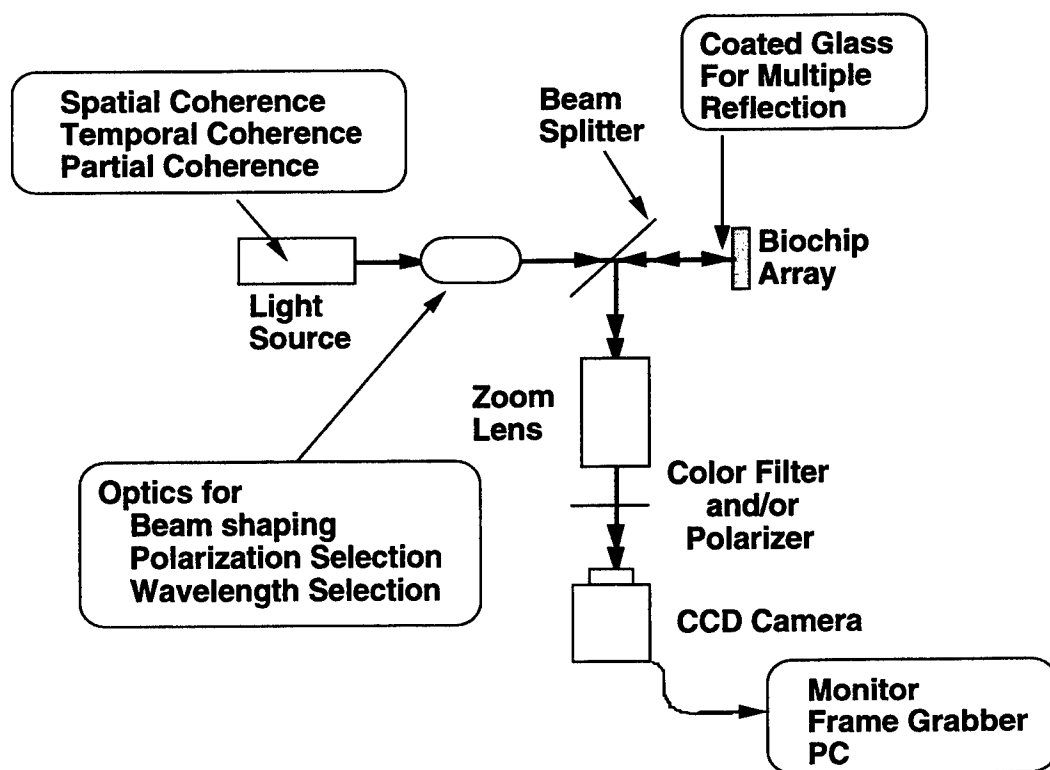


Fig. 4. A schematic illustration of a CCD-based imaging system for biochip signal detection.

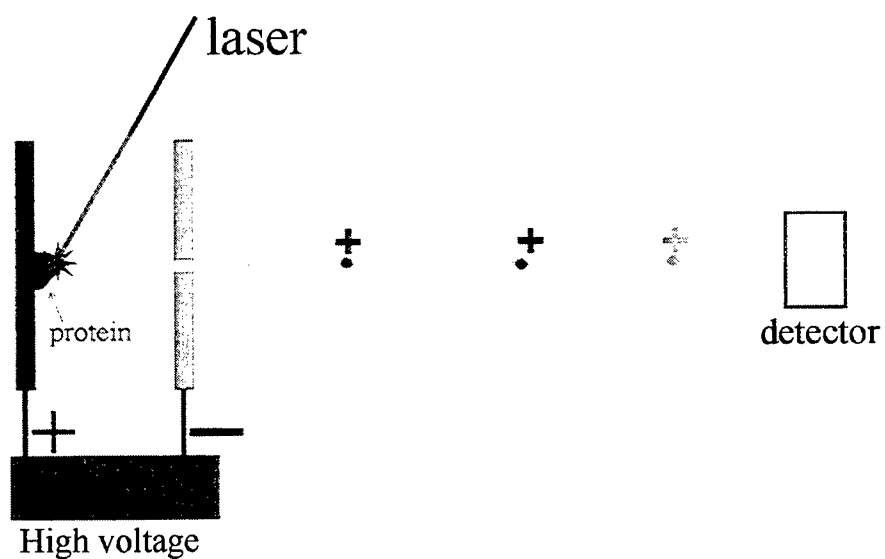


Fig. 5 A schematic illustration of the working principle of a protein chip.

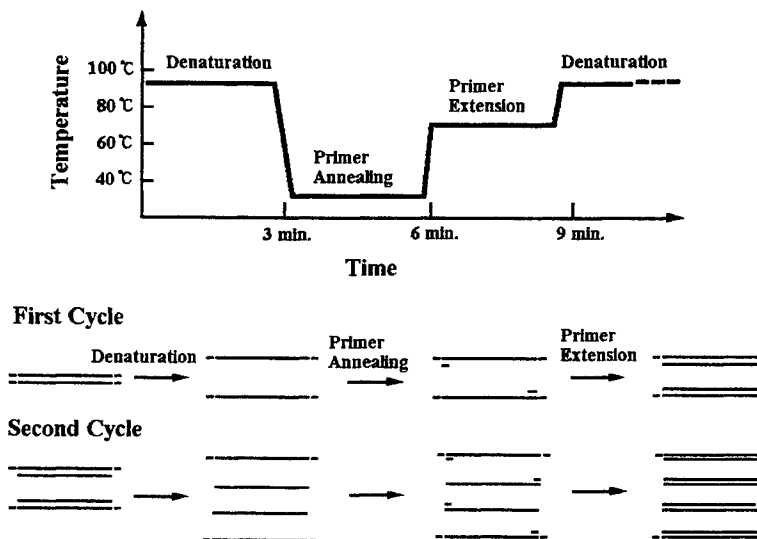


Fig. 6. Thermal cycles in polymerase chain reaction (PCR) for DNA amplification.

Unit : mm

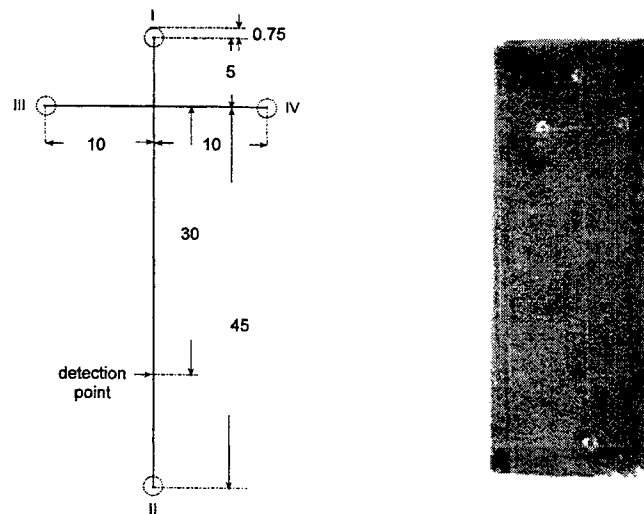


Fig. 7. A schematic illustration of a typical capillary electrophoresis chip fabricated on PMMA by a team at the National Cheng Kung University.²¹

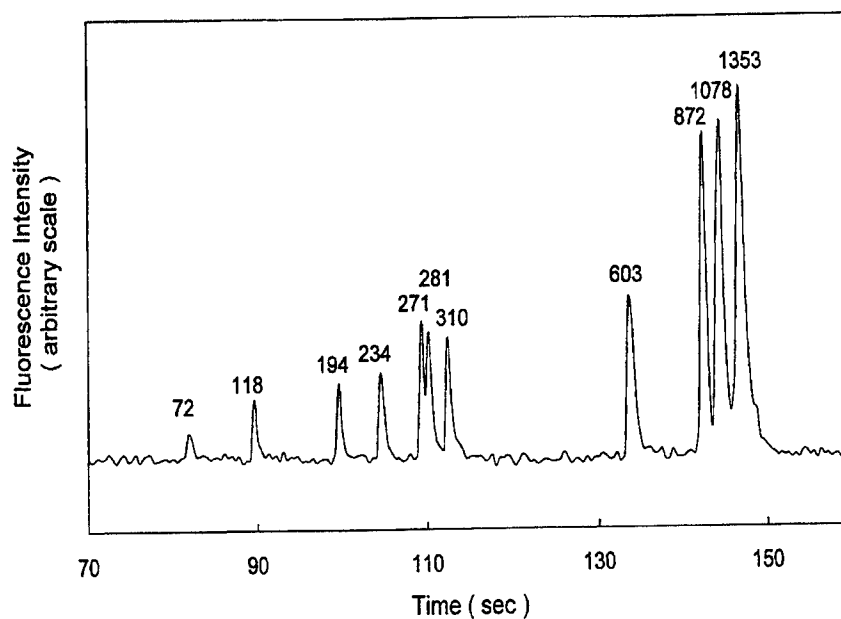


Fig. 8. Electropherogram from a capillary electrophoresis chip shows that all 11 fragments of ϕ X174RF DNA digested by the restriction enzyme *Hae*III can be identified in less than 3 minutes.²¹

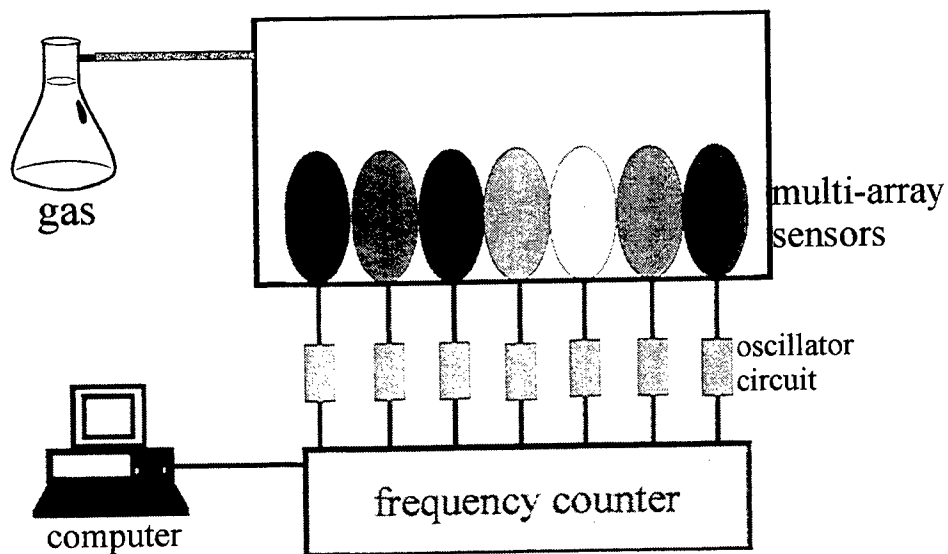


Fig. 9. A schematic illustration of the working principle of an electronic nose.²³

A novel CMOS photosensor with a gate-body tied NMOSFET structure

Youn-Jae Kook, Jae-Hun Jeong, Young-June Park, and Hong-Shick Min

School of Electrical Engineering, Seoul National University, Gwanak-gu, Seoul 151-742, Korea

Tel) + 82-2-880-7274, Fax) + 82-2-882-4658, E-mail) chipss@snu.ac.kr

ABSTRACT

A novel CMOS photosensor with a gate-body tied NMOSFET structure realized in the triple well is presented. The photocurrent is amplified by the lateral and vertical BJT action, which results in two different output photocurrents, which can be used for different applications within a pixel. The lateral action results in the drain current with higher sensitivity at low light intensity. And the vertical action results in the collector current with uniform responsivity over wider range of the light intensity. The proposed photosensor is compatible with CMOS circuits.

Keywords: Gate-body tied NMOSFET, triple well, lateral BJT, vertical BJT, photosensor

1. INTRODUCTION

There has been much interest on the miniaturization of assay for the use of detection of biological species or specific DNA sequences, which makes various experiments to be done quickly with low cost ^{1,2}. The conventional detection method is to use of fluorescence label and high performance CCD camera. But this CCD-based detection system is very expensive and relatively large compared with micro-scale assay. So, there is a strong need for an integrated detection chip compatible with the micro-scale assay. The detection chip contains photosensors such as phototransistor ³ or photodiode ⁴ fabricated with CMOS process. As the array density increases, the detection chip has complex circuits and high performance photosensors are needed. And light source is needed for fluorescence activation and but this light source itself makes the detection of emitted fluorescence light confused. So, a novel photosensor suitable for the detection of fluorescence light is greatly needed.

On the other hand, great attention has been paid to CMOS image sensor ^{5,6,7} since it has many advantages such as low power, price, and CMOS circuit compatibility compared to the conventional CCD image sensor. CCD image sensor is fabricated with the highly optimized process for charge transferring ⁵ and all the output charges are transformed to the voltage signal by a high sensitive amplifier. But CMOS image sensor is fabricated with the standard CMOS process and the output voltage (or current) of each sensor is directly accessed with a in-pixel amplifier or buffer. As a result, CMOS image sensor can be easily integrated with CMOS circuits and is useful for various applications. Widely used CCD concepts such as pixels, charge transferring and amplifiers have been developed over many years and the process has optimized to CCD and it became different with CMOS process. Consequently, simple implementation of CCD concept with CMOS process is not satisfying and a novel CMOS photosensor is needed to achieve high quality image ⁷.

The gate-body tied MOSFET structure has been recently used as a CMOS photosensor. It uses high current gain caused by the lateral BJT action ^{8,9} and useful compared to widely used n+ p-type substrate. But in the proposed photosensor ⁹, some of the injected holes are wasted by the vertical diffusion and also this can cause the latch-up. In this work, we show that the quantity of vertically injected holes can be comparable with that of laterally injected ones. And a novel photosensor is proposed. It is a gate-body tied NMOSFET in the triple well. Using this photosensor, two photocurrents are available by the lateral and vertical actions of the BJT. And it will be shown from the experiments that two currents have different characteristics. Some scaling properties of the device will be also discussed.

2. DEVICE STRUCTURE AND FABRICATION

The proposed photosensor is a gate-body tied NMOSFET realized in the triple well as shown in Fig.1. It is fabricated with 1.5 μ m CMOS process and some modifications are made to implement triple well. In this photosensor, pbody and source regions correspond to the base and emitter, respectively, of both lateral and vertical BJT's and nwell region is the collector of vertical BJT. The base widths of lateral and vertical BJT's are defined by the effective gate length ($\sim 0.67\mu$ m in this work) and difference of the junction depth between pbody and nwell ($\sim 0.80\mu$ m in this work), respectively. Photogeneration takes

place at drain-pbody junction and nwell-pbody junction. These junctions are placed at different depths from the silicon surface and have different light absorption length. So, the drain current and nwell current have different spectral responses, which may be used to distinguish the light source for fluorescence activation and emitted fluorescence light. The gate oxide thickness is 250 Å and gate material is N⁺ polysilicon. A channel implantation with boron ions was performed followed by an arsenic implantation to form the single source/drain. Gate and pbody contacts are shorted with the metal later.

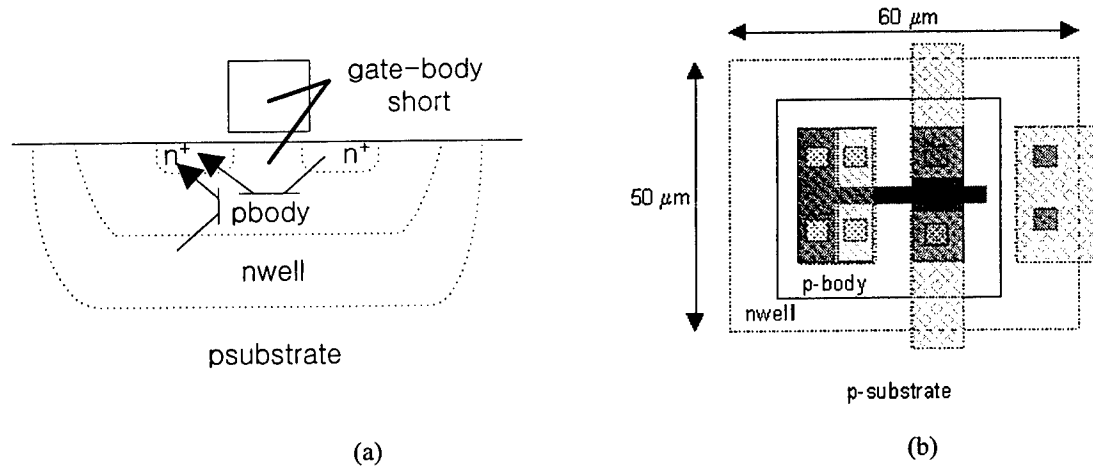


Fig.1. Structures of a proposed photosensor (a) schematic cross section (b) top view.

Fig.2 shows the simulated doping profile under the source region. Nwell is implemented with a phosphorous implantation and 20-hour drive-in at 1100°C. And the p-type body (pbody) is implemented with a boron implantation and 150-minute drive-in at 1050°C. In implementing triple well, much care is done to set the threshold voltage of PMOSFET to -0.7V.

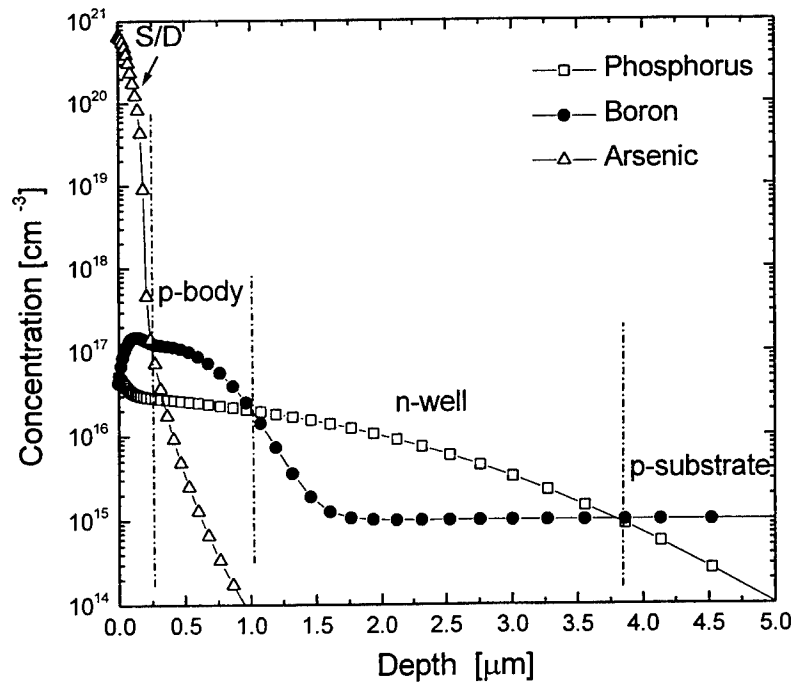


Fig.2. Doping profile under the source area

3. EXPERIMENTAL RESULT AND DISCUSSIONS

Fig. 3 shows the drain and collector(nwell) current characteristics of the fabricated device with the gate and pbody tied and floated. The peak current gains of the drain and collector currents are about 3730 and about 257, respectively. Until the surface channel is formed, the drain current is mostly composed of the diffusion of electrons injected from the source into the silicon surface. When the gate voltage reaches the threshold voltage(with the pbody voltage fixed to the gate voltage), the drain current is mostly due to the surface channel current and the contribution from the BJT action is minimal since the surface potential is nearly fixed. On the other hand, the collector current is mostly composed of the electron diffusion for all gate and pbody bias conditions. As a result, the drain current is higher than the collector current at low gate and pbody voltage but the difference becomes smaller as the voltage increases. And drain current is lower than the collector current after the channel is formed.

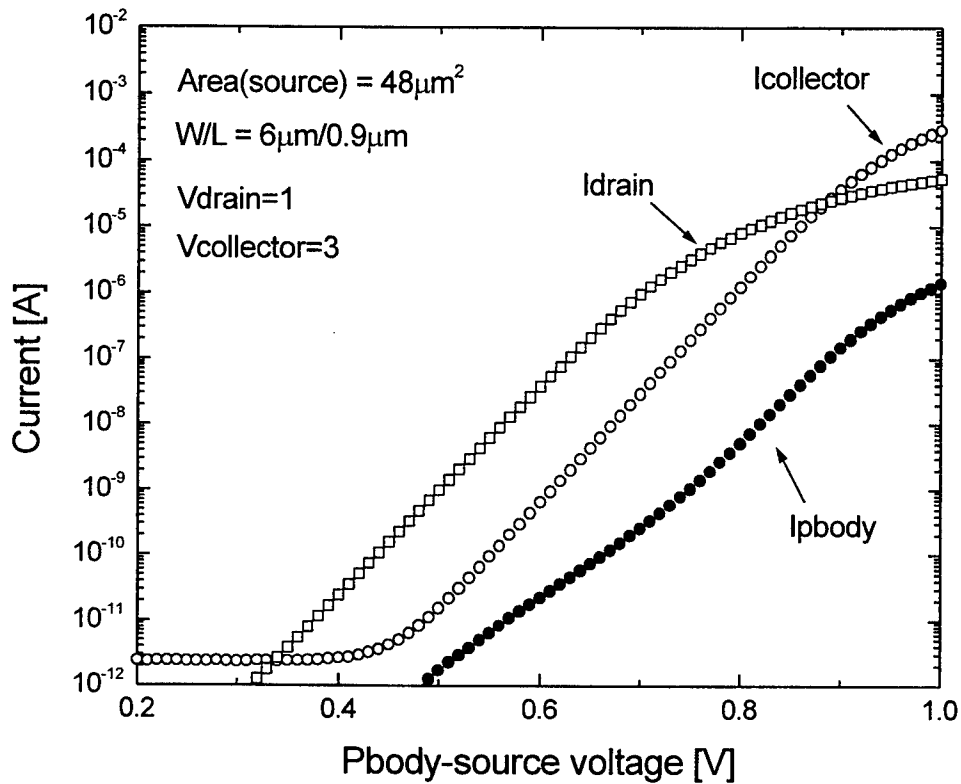


Fig. 3. Gummel plot for gate-body tied NMOSFET with W/L= $6 \mu\text{m}/0.9 \mu\text{m}$. $V_{\text{collector}}=3\text{V}$, $V_{\text{drain}}=1\text{V}$ and $V_{\text{source}}=V_{\text{psubstrate}}=0\text{V}$. Open square and circle marks are drain and collector currents, respectively. And Filled circle mark is pbody current. The inset shows the device structure.

Fig. 4 shows the measured photocurrents and photogains of the proposed photosensor. The photogain is defined to be the ratio of the collector (drain) current due to BJT action to the collector-pbody (drain-pbody) diode current. The photodiodes currents are measured for the diodes in pbody-drain and pbody-nwell junctions with the gate floated. The photogains of the collector and drain are above 1000 and 50000, respectively. Drain photocurrent is higher than the collector photocurrent at low light intensity, but the difference becomes smaller as the light intensity increases and collector photocurrent is higher at high light intensity. It is because the accumulated holes raise the pbody voltage and channel is formed. Drain photocurrent shows the much higher photogain especially low light intensity and collector photocurrent shows the more linear response over wide range of the light intensity.

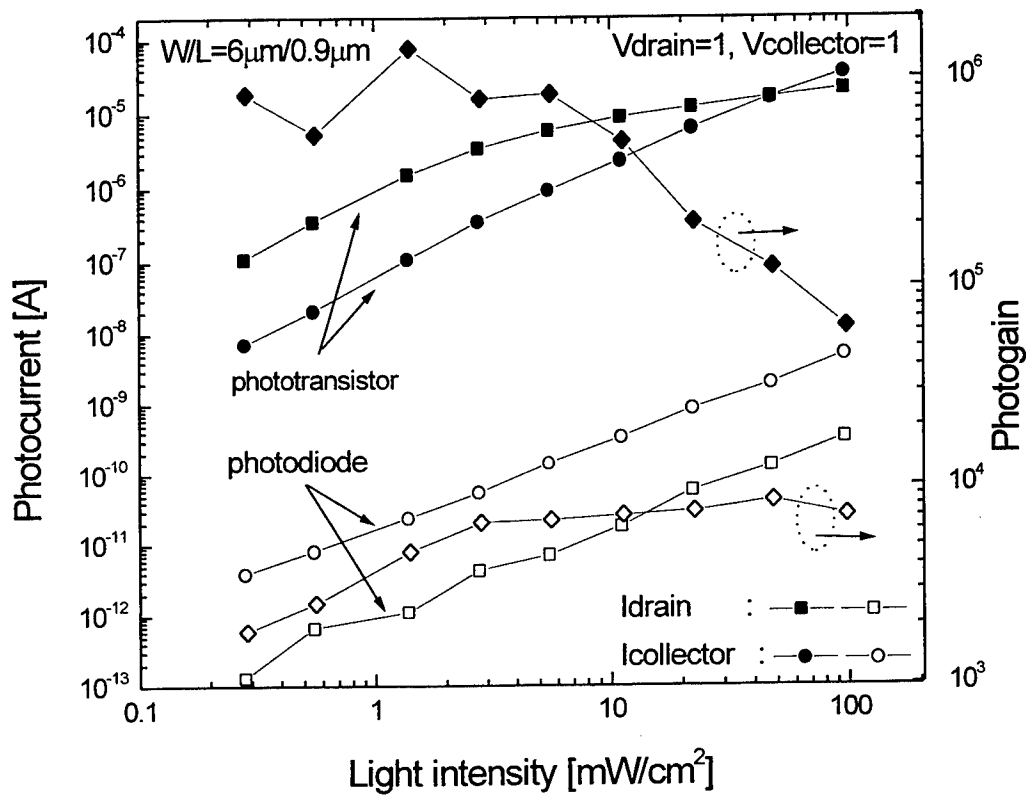


Fig. 4. Photocurrents and photogain of drain and collector with $W/L = 6\mu\text{m}/0.9\mu\text{m}$. $V_{\text{collector}} = V_{\text{drain}} = 1\text{V}$ and $V_{\text{source}} = V_{\text{substrate}} = 0\text{V}$. Filled and open marks are the currents of phototransistor and photodiode, respectively. Square and circle marks are the currents of drain and collector, respectively. Diamond marks are the photogain defined as the ratio of phototransistor current to photodiode current.

Fig. 5 shows the photocurrents measured at the drain and collector terminals with dark and light conditions as a function of drain voltage. The photocurrents show the linear or logarithmic increase with the light intensity as shown in Fig. 4 below the breakdown voltage. Drain dark current is higher than collector dark current due to the lateral BJT action, but it is lower than 10pA at room temperature. The breakdown voltage is about 2.9V in the dark condition, and it decreases to about 2.0V under the light, which is mainly due to the photogeneration induced avalanche breakdown. Between the photo-triggered breakdown and the dark breakdown voltage, the photocurrents increase rapidly by the photo-triggered avalanche, which may be used as a high sensitive photodetector at very low light intensity.

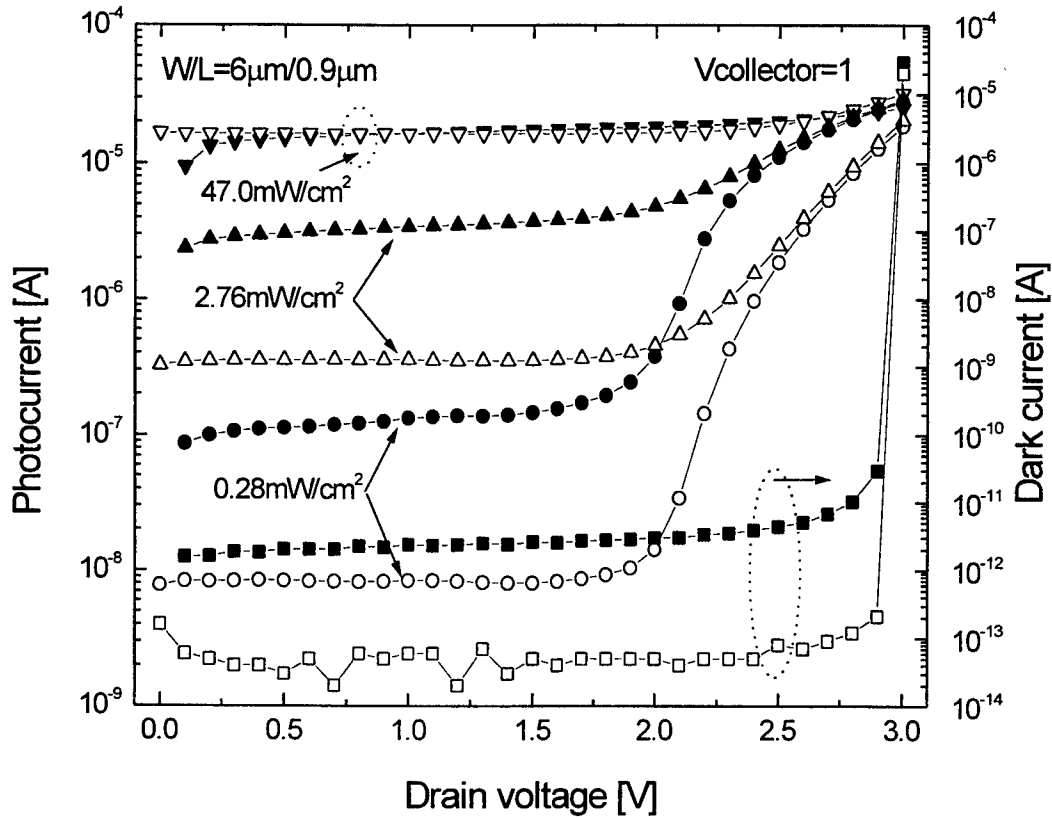


Fig. 5 Photocurrents of drain and collector versus drain voltage. $W/L=6\mu\text{m}/0.9\mu\text{m}$. $V_{\text{collector}}=1\text{V}$, and $V_{\text{source}}=V_{\text{substrate}}=0\text{V}$. Filled and open marks are drain and collector photocurrents, respectively.

In the following, some scaling properties and associated design considerations will be explained. Fig. 6 shows that the drain photocurrent, and dark current (I_d) increase as the gate length scales down while the collector photocurrent and dark current (I_c) remain constant.

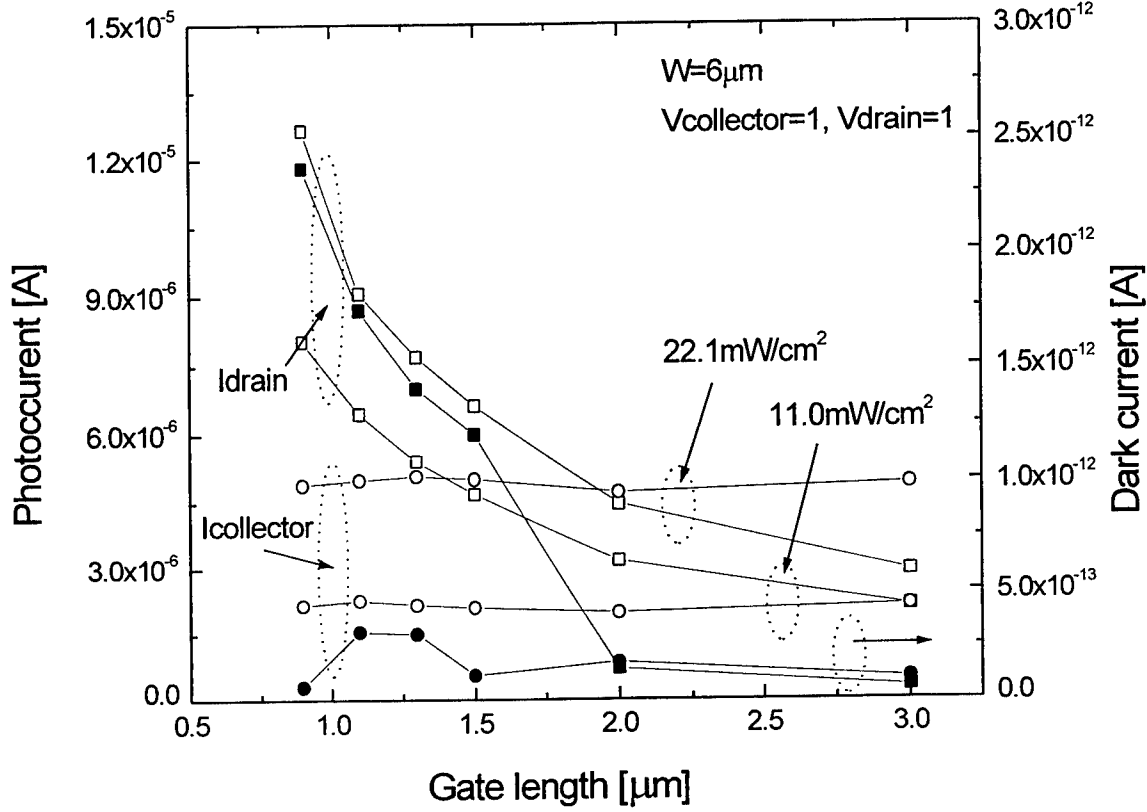


Fig. 6. Photocurrents for the various gate lengths. $W=6\mu\text{m}$. $V_{\text{collector}}=V_{\text{drain}}=1\text{V}$, and $V_{\text{source}}=V_{\text{substrate}}=0\text{V}$. Filled marks are the dark currents. Square and circle marks are the photocurrents of drain and collector, respectively.

In the pbody at steady state, the magnitude of in-flux of the generated holes and out-flux to source is same and can be expressed as,

$$q\eta\Phi A_{\text{gen}} = I_0 \exp(V_{BE} / nV_t) \quad (1)$$

where η , Φ , V_t , I_0 , A_{gen} , and n are the quantum efficiency, photon flux, and thermal voltage, saturation current and area where photogeneration occurs, and non-ideal factor, respectively. After solving (1), pbody voltage is expressed as,

$$V_{BE} = nV_t \ln(q\eta\Phi A_{\text{gen}} / I_0). \quad (2)$$

The dependency of drain and collector photocurrent on the pbody voltage can be expressed as,

$$I_c \propto I_0 \exp(V_{BE} / nV_t) = q\eta\Phi A_{\text{gen}} \quad (3)$$

$$I_{d, \text{subthreshold}} \propto W \exp(V_{BE} / nV_t) = q\eta\Phi A_{\text{gen}} W / I_0 \quad (4a)$$

$$I_{d, \text{above threshold}} \propto W (V_{BE} - V_{TH})^\alpha \quad (4b)$$

where W is gate width, V_{BE} is same V_{GS} , and I_0 is dependent on the source area. (2) and (3) show that I_c/A_{gen} is independent of the source area while (2) and (4) show that I_d/W decreases as the source area increases for a fixed A_{gen} .

Fig. 7 shows the relation of photocurrents with source area. It verifies this relation that I_c/A_{gen} is independent of the source area while $I_d/(W \cdot A_{\text{gen}})$ decreases as the source area increases.

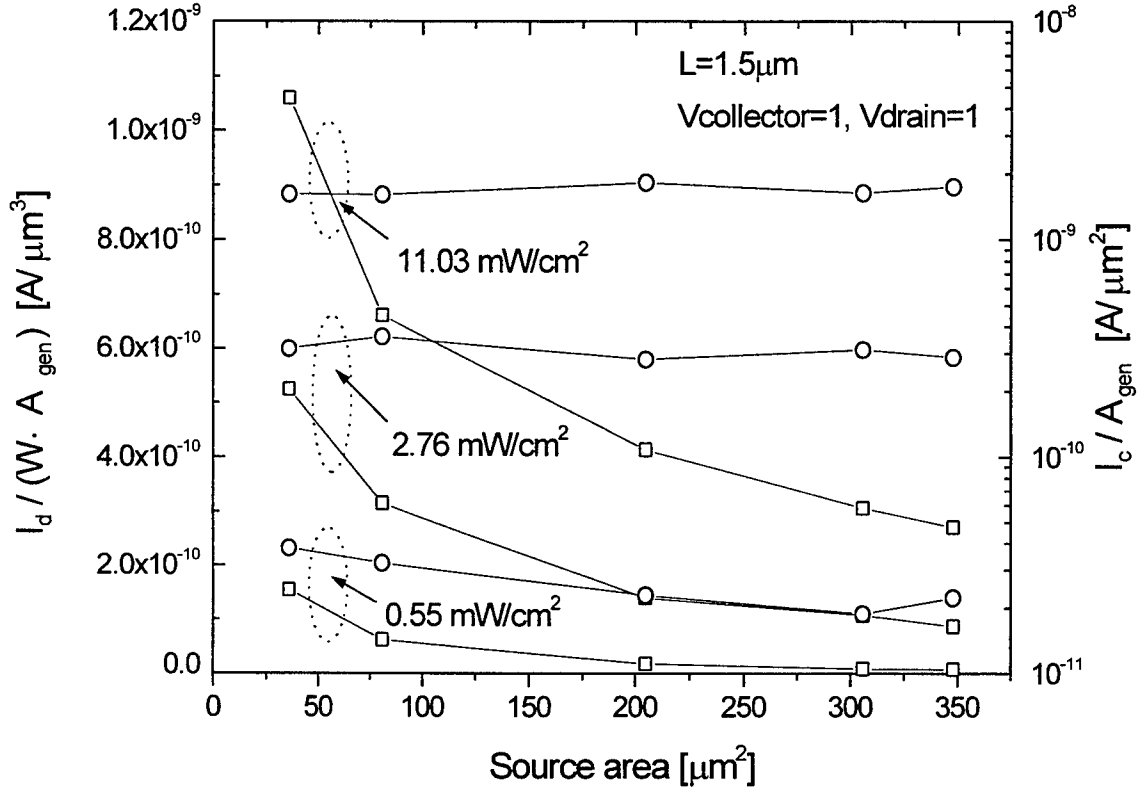


Fig. 7. Photocurrents for the various source areas. $L=1.5\mu\text{m}$. $V_{\text{collector}}=V_{\text{drain}}=1\text{V}$, and $V_{\text{source}}=V_{\text{substrate}}=0\text{V}$. Square marks are the drain photocurrents per unit gate width and unit photogeneration area. Circle marks are the collector photocurrents per unit photogeneration area.

As a result, the maximum drain photocurrent can be achieved with the ring gate structure for a given pixel size, since effectively large gate width with the small source area in the ring gate and the large drain area can be realized to obtain the high pbody voltage and large photogeneration area.

4. CONCLUSION

A novel photosensor is proposed and fabricated. Two output photocurrents are obtained through the drain and collector with different magnitudes, dark currents, and responsivities to the light intensity. The drain photocurrent has higher magnitude at

low light intensity and higher photogain, while the collector photocurrent has lower dark current, higher magnitude at high light intensity and uniform responsivity over wide range of the light intensity. And the drain photocurrent was shown to increase with the scaled gate length and source area while the collector photocurrent is independent of the gate length and source area for a fixed photogeneration area. A ring gate structure was proposed to obtain large gate width, small source area and large drain area for a given pixel size.

ACKNOWLEDGMENT

The authors appreciate the financial support of Korea Science and Engineering Foundation made in the Program Year of 1998.

REFERENCES

1. R. C. Anderson, G. J. Bogdan, Z. Barniv, T. D. Dawes, J. Winkler, and K. Roy, "Microfluidic Biochemical Analysis System," *IEEE Transducer '97*, Chicago, vol. 11, pp. 477-480, 1997
2. Kook-Nyung Lee, Jong-Uk Kim, Youn-Sik Lee, Sung-Soo Park, Byung-Gee Kim, and Yong-Kweon Kim, "Fabrication of Micro Enzyme Linked Immunosorbent Assay (ELISA) chip," *International Conference on Micro Electro Mechanical Systems*, pp. 189-193, January 17-21, 1999
3. T. Vo-Dinh, J. P. Alarie, N. Isola, D. Landis, A. L. Wintenberg, and M. N. Ericson, "DNA Biochip Using a Phototransistor Integrated Circuit," *Analytical Chemistry*, vol. 71, no. 2, pp. 358-363, 1999
4. T. Vo-Dinh, "Development of a DNA biochip : principle and applications," *Sensors and Actuators B* 51, pp. 52-59, 1998
5. E. R. Fossum, "Active Pixel Sensor: Are CCD's dinosaurs?," *Charge Coupled Devices and Optical Sensors III, Proc. SPIE*, vol. 1990, pp. 2-14, 1993
6. E. R. Fossum, "CMOS Image Sensors: Electronic Camera-On-A-Chip," *IEEE Trans. Electron Devices*, vol. 44, No. 10, pp. 1689-1698, 1997.
7. H. S. Wong, "Technology and Device Scaling Consideration for CMOS Imagers," *IEEE Trans. Electron Devices*, vol. 43, No. 12, pp. 2131-2142, 1996.
8. S. V. Vandebroek, S. S. Wong, J. C. S. Woo, and P. K. Ko, "High-gain lateral bipolar action in a MOSFET structure," *IEEE Trans. Electron Devices*, vol. 38, pp. 2487-2495, 1991.
9. W. Zhang, M. Chan, and P. K. Ko, "A Novel High-Gain CMOS Image Sensor Using Floating N-Well/Gate Tied PMOSFET," in *IEDM Tech. Dig.*, 1998, pp. 1023-1025.

Electro-optically modulated biomolecular-interaction analysis sensor

Yao Cheng^{*a}, Yi-ren Chang^b, Che-hsin Lin^a, Long Hsu^b, Minking K. Chyu^c

^aSynchrotron Radiation Research Center

#1, R&D Road VI, Science-based Industrial Park, 30077, Hsinchu, Taiwan

^bDepartment of ElectroPhysics, National Chiao-Tung University, Hsinchu, Taiwan

^cDepartment of Mechanical Engineering, University of Pittsburgh, PA 5261, USA

ABSTRACT

This paper focuses on developing the platform technology of real-time biomolecular-interaction analysis (BIA) sensor chips. A detection scheme using the electro-optically modulated surface plasmon resonance (SPR) is suggested to advance the sensor features in reducing measurement complexity and time. The SPR method of a BIA sensing system detects slight changes of refractive index due to the biomolecular interaction at the solid-liquid interface. The most sensitive interrogation method among the possible conventional schemes is to measure the SPR angle of the attenuated total reflection. The electro-optical modulation replaces the mechanism of angle measurement not only to increase the speed but also to reduce the size. Recent progress of the multilayer SPR provides an effective mean of tailoring the microchip. Several multilayer configurations have been studied in this paper to realize the electro-optical SPR sensing. Especially, the long-range mode of surface plasmon was investigated to achieve the high-resolution and high-sensitivity detection.

Keywords: Biosensor, biomolecular-interaction analysis sensor, optical sensor, surface plasmon resonance, electro-optical modulation, multilayer.

NOMENCLATURE

BIA	Biomolecular-interaction analysis	ϵ_b	Real dielectric constant the dielectric medium b
SPR	Surface plasmon resonance	d	Thickness of the metal stab
EO	Electro-optical	γ_m	Extinction coefficient of the field in the metal
ATR	Attenuated total reflection	γ_a	Extinction coefficient of the field in the dielectric a
ω	Frequency of the electromagnetic oscillation	R	Reflectivity
ω_p	Plasmon frequency of the metal	min	Minimal reflection intensity at the resonance
c	Speed of light	curv	Curvature of the reflection intensity at the resonance
k_0	Propagation constant of the incident light in vacuum	θ	Incident angle
k_{sp}	Propagation constant of the surface plasmon	θ_R	Resonance angle
k_R	Real part of k_{sp}	S_p	Sampling sensitivity
k_I	Imaginary part of k_{sp}	S_s	Steering sensitivity
ϵ_m	Complex dielectric constant of the metal	n_p	Refractive index of the sample layer
ϵ_R	Real part of ϵ_m	n_s	Refractive index of the steering electro-optical layer
ϵ_I	Imaginary part of ϵ_m	f_m	Frequency of the EO modulation
ϵ_a	Real dielectric constant the dielectric medium a		

* Correspondence: E-mail: Yao@mail.srrc.gov.tw Telephone: +886-35-780281ext 7309, Fax: +886-35-789816

1. INTRODUCTION

ATR has been used to determine the optical constants of thin film samples for more than three decades¹. Liedberg *et al*² introduced the BIA application of the SPR sensors in 1983. Instead of directly measuring the refractive index of samples by methods such as ellipsometry and reflectometry, the ATR generates an evanescent wave into the liquid phase to probe the sample interaction immobilized on the metal-liquid interface. The metal film is typically 50nm-thick Au or Ag for providing the optimum permittivities in the near IR and visible region¹. The surface plasmon, a charge density wave propagating along the interface between metal and dielectric, absorbs the energy from the incident light which would be totally reflected without the metal film. This phenomenon is also called surface plasmon resonance, providing an effective means of measuring the optical constant of flowing liquid in real time.

The SPR angle of an incident light depends on the refractive index of the probed samples at the solid-liquid interface. The detection output refers to the change of the SPR angle. The technologies of incident-angle variation and angle-dependent image detection are required to perform a high precision measurement. Instead of varying the angle, wavelength interrogation and intensity measurement are normally applied. SPR sensors based on wavelength interrogation and intensity detection are less precise than the SPR sensors applying angular interrogation^{3,4}.

In this paper, we suggest a novel scheme using the EO modulation⁵ to replace the angular detection or the wavelength variation. This is achieved by coating with nonlinear optical materials that interact with the surface plasmon. The scheme determines the SPR angle using an electrical signal that is directly readable. Canceling the angle-reading mechanism reduces the sensor size while providing the potential of array sensing as well as maintaining the precision of angular interrogation. Moreover, multiple light sources for differential measurements are one of the feasible options.

SPR sensors containing dielectric-metal-dielectric multilayer have been considered to improve the sensing sensitivity, the spectral resolution and even have the capability of detecting the sample anisotropy⁶. Recently, Toyama *et al*⁷ applied metal-dielectric-metal multilayer for higher SPR sensing stability using the difference between TM- and TE-resonance angles. A configuration of metal-dielectric-ITO, *i.e.*, indium tin oxide reported by Teng *et al*⁸ in 1990 became more or less a standard method to study the EO character of thin films. All the multilayer structures mentioned above are suitable for the application of the EO modulated SPR sensor. We present in this paper a detailed analysis of these possible configurations including some considerations from the manufacturing side.

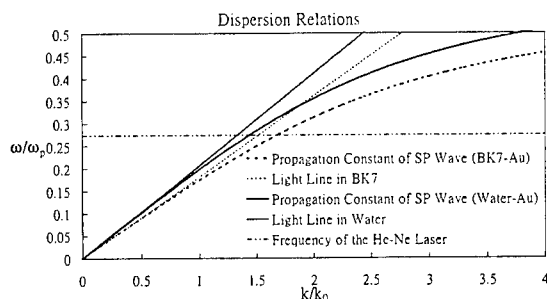


Figure 1: Dispersion relations (eq. 1) of the surface plasmons on the interface between a semi-infinite dielectric medium (BK7, $n=1.515$ or water, $n=1.33$) and a semi-infinite metal (Au, $n=0.163+i3.52$). The straight lines are the light lines in the media of BK7 glass and water, respectively. The wavelength of the He-Ne laser is 632.8nm.

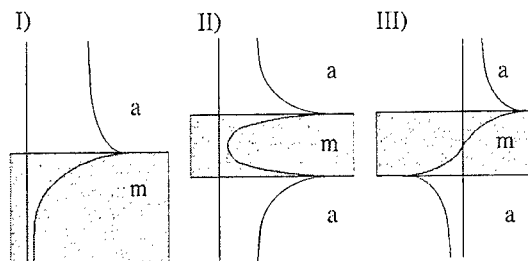


Figure 2: Distribution of the transverse magnetic field parallel to the surface on which the surface plasmon propagates. The characters m and a denote the metal and the dielectric medium, respectively. I) Plasmon fields near the interface between a semi-infinite metal and a semi-infinite dielectric medium. II) Long-range mode on a metal slab. III) Short-range mode on a metal slab.

2. SURFACE PLASMON

We consider firstly a simple interface between semi-infinite dielectric and semi-infinite metal. A charge-density oscillation associated with electromagnetic wave evanescently decaying into both media may propagate along the interface. The dispersion relation of this surface plasma wave in figure 1 is given by the equation⁹:

$$\omega = c k_{sp} \sqrt{\frac{1}{\epsilon_m} + \frac{1}{\epsilon_a}} \quad (1)$$

Considering only metals in the SPR application¹⁰, the dielectric constant ϵ_R has a large negative value, as the oscillation frequency is less than the plasma frequency. In this case, the equation (2) indicates that the propagation constant of the surface plasmon is always larger than the propagation constant of light in the associated dielectric. A finite value of ϵ_I denotes that the metal is dissipative. k_I determines the exponential decrease of the oscillation intensity. Assuming $k_R \gg k_I$ that implies $-\epsilon_R > \epsilon_a$, we have

$$k_R \approx \sqrt{\epsilon_a} k_0 \sqrt{1 + \frac{|\epsilon_a^2 + \epsilon_R \epsilon_a|}{|\epsilon_m + \epsilon_a|^2}} \quad (2)$$

and

$$k_I = \frac{1}{2} \frac{\epsilon_a^2 \epsilon_I}{k_R} \frac{k_0^2}{|\epsilon_m + \epsilon_a|^2}. \quad (3)$$

Here, we note in the equation (3) that k_I is proportional to ϵ_I . It demonstrates that the damping is due to the energy loss in the metal¹¹.

The evanescent wave decays faster in the metal than in the dielectric. These decay rates γ_m and γ_a are known as the extinction coefficients which are given by the equation

$$\gamma_m = k_0 \operatorname{Re} \left(\frac{\epsilon_m}{\sqrt{\epsilon_m + \epsilon_a}} \right) \quad (4)$$

and

$$\gamma_a = k_0 \operatorname{Re} \left(\frac{\epsilon_a}{\sqrt{\epsilon_m + \epsilon_a}} \right) \quad (5)$$

for the metal and dielectric, respectively, where the symbol of Re means the real part of the number. As ϵ_a increases, γ_m and γ_a increase too. Figure 2-I denotes this distribution of the transverse magnetic field schematically.

Secondly, we consider a metal slab of thickness d bonded on both sides by the identical medium with the dielectric constant ϵ_a .

When the thickness of metal slab is large with the condition $d\gamma_m \gg 1$, the surface plasmons propagate on each side of the interfaces with the same speed and the same damping rate. Each one of these two surface plasmons generates evanescent waves into the metal slab and into the dielectric. As the metal thickness decreases, the decoupled surface plasmons interact with each other. Consequently, the degenerate dispersion relations of the surface plasmons split into one long-range and one short-range mode^{9,11,12}.

The case that surface plasmons propagate in anti-phase⁹ is known as the long-range mode that has an identical magnetic field distribution on both metal-dielectric interfaces (fig. 2-II). In the short-range case, surface plasmons propagate in phase. The transverse magnetic field distribution are anti-symmetrical referred to central line of the metal as shown in figure 2-III.

The long-range mode has higher phase velocity and lower damping rate than the short-range mode. The damping rate of the long-range mode goes to zero with a phase velocity approaching the light speed in the dielectric ($k_R \rightarrow \sqrt{\epsilon_a} k_0$), as the metal thickness vanishes^{11,12}. Because of its long propagation distance, the mode with a symmetric magnetic field distribution is called the long-range surface-plasmon mode. As the thickness of the metal slab decreases, the decay rate in the dielectric of long-range mode proportionally decreases ($\gamma_a^2 \approx k_R^2 - \epsilon_a k_0^2$). In the case of the long probing length, the long-range mode is not useful for SPR sensing without a proper modification. The short-range mode has strong field inside the metal associated with a fast decay outside. As the film thickness decreases, the phase velocity diverges, the damping of the plasmon becomes very strong, and the evanescent waves in both sides decay very fast.

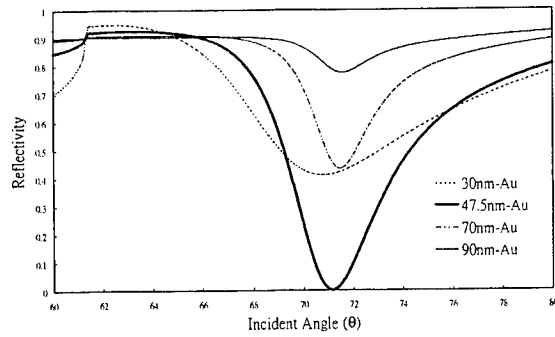


Figure 3: Reflectivity of a configuration of prism-Au-water. As the Au-film thickness decreases, the angle of minimal reflectivity increases slightly

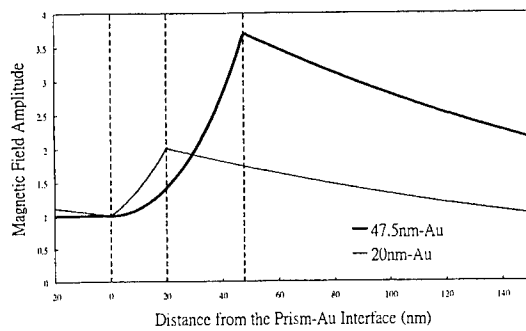


Figure 5: Intensity plot of prism-Au-water configurations. The transverse magnetic fields are normalized to 1 at the prism-Au interface. The plot starts from the BK7 at 20 nm to the interface prism-Au. The plasmons are excited on the prism-water interface where the field energy is stored to a maximal value. The thickness' of the Au-film calculated here are 20 nm and 47.5nm.

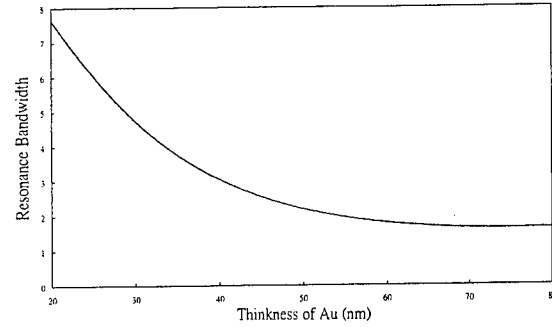


Figure 4: Resonance bandwidth (not to scale) decreases, as the Au-film thickness decreases. This curve indicates that the excited plasmon is a short-range mode.

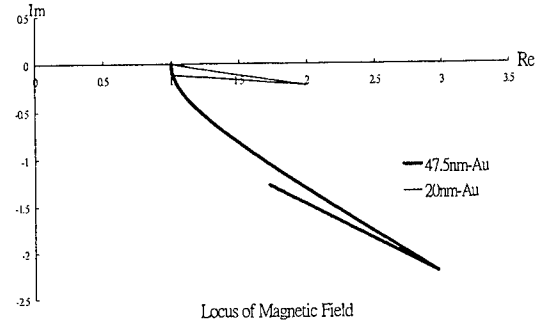


Figure 6: Locus plots of the complex field associated to Fig. 5. The complex number (1,0) presents the interface of prism-Au. The locus's move down- and rightward in the Au film and turns back to the origin point in the water. These plots demonstrate that the surface plasmons are the short-range mode whose field is almost antisymmetric for both cases of 20 nm and 47.5 nm gold.

Finally, we consider an asymmetric configuration of a metal slab bounded by semi-infinite dielectric media with different dielectric constants. They are ϵ_a and ϵ_b referred to the upper medium a and the lower medium b. Assuming $\epsilon_a > \epsilon_b$, which is commonly used for the SPR sensor in the prism coupling method also known as the Kretschmann configuration¹³. The plasmons propagate in different speeds with their own dispersion functions. As long as the slab thickness is large enough, they behave like the equation (1). As the metal thickness decreases, the interaction between the surface plasmons becomes stronger and leads to complicate solutions, especially in the case when the dielectric constants are close¹⁴. There are four kinds of possible solutions for an asymmetric configuration^{11,14}, i.e., the modes of symmetric bound (nonradiative), symmetric leaky (radiative), antisymmetric bound, and antisymmetric leaky (referred to the transverse magnetic field distribution). The nonradiative modes can be excited by the ATR method⁹.

A commonly applied configuration of the SPR sensor is the glass BK7-Au-water system with refractive indices at the He-Ne laser ($\lambda = 0.6328 \mu\text{m}$) of 1.515/ 0.163 + i3.52/ 1.33, respectively. A gold thickness of 50 nm is commonly applied. The plasmon locates at the stable working point as an antisymmetric mode described by Brurke *et al*¹¹. The damping constant k_1 is originated not only from the dissipation in the metal but also from the radiation loss into glass BK7⁹. As shown in the fig. 1, the working point of plasmon excitation is the intersection between the line of the laser frequency and the dispersion relation of the Au-water surface plasmon. The Au-BK7 plasmon is impossible to be excited by the coupling prism method, since its propagation constant is always larger than the propagation constant of the light line in BK7 (eq. 2). The propagation constant of the Au-water plasmon is less than the propagation constant of the laser light in BK7 at the working point (fig.1), therefore the reflecting wave from the plasmon back into BK7 is radiative. In this case, we observed an increasing damping associated with a decrease in gold thickness (Fig. 3,4). The resonance angle (~ 71 degree) is far from the critical angle of the BK7-water

interface (61.4 degree). The evanescent wave in the water decays relative fast. The SPR reflectivity calculated in this paper are analyzed using the complex Fresnel calculations^{15,16}.

Figure 5 illustrates the intensity of the magnetic field along the direction from the prism BK7 into the water for two configurations, *i.e.*, 47.5 nm- and 20 nm- gold film. The reflex points of the field curves indicate the charge density accumulated on the metal surface. The peaks at the gold-water interfaces denote that the surface plasmons are excited there as an active interface. The charge density across the gold film at the prism-gold interface is an image charge carrying the same sign. Figure 6 shows a phase lag between the excited plasma wave and its image due to the lower phase velocity at the image side. However, this excitation is similar to a short-range mode where the magnetic field distribution is more or less like the mode illustrated in fig. 2-II.

3. MULTILAYER STRUCTURE

There are conventionally two configurations to excite the surface plasmon by the coupling prism method, *i.e.*, the Kretschmann configuration¹³ and the Otto configuration¹⁷. It is convenient to replace the air gap in the Otto configuration by a low refractive dielectric, which leads to the multilayer structure.

One matched multilayer configuration is chosen to obtain symmetric structure, *i.e.*, prism-index matching liquid ($n=1.4564$)-Ag-fused silica ($n=1.4569$)¹⁸. A long-range surface-plasmon mode was measured on very thin silver film in this symmetric configuration¹⁸. Kessler *et al*¹⁹ extended this multilayer configuration via replacing the matching layers by Teflon. In their study, the sharp absorption bands were found for both TM and TE incident light. Salamon *et al*¹⁶ demonstrated that both the reflectivity curves of TM- and TE-waves are applicable to the BIA system. Kessler *et al*, also found the long-range surface excitation propagating on a highly lossy active layer instead of a highly conductive metal layer. The idea of a lossy active layer was originally reported by Yang *et al*²⁰. Recently, another multilayer configuration was reported by Toyama *et al*⁷ with double active metal layers. In this special multilayer configuration, The TE-resonance angle is not sensitive to the sample. On the contrast, the TM resonance angle is sensitive and tunable by changing layer thickness.

Figure 7 shows a multilayer structure of the Toyama type⁷. Two metal layers sandwich a dielectric medium that is considered to be an EO material in this paper. The EO material is highly refractive in general cases. Assuming the refractive index of a polymer EO layer is 1.63. The reflectivity curves of TM- and TE-waves have very similar behavior scanning the incident angle from 0 to 90 degree, as the thickness of the EO layer is around 400 nm. Each one performs two resonance angles. One of them is less than the critical angle and the other is greater than the critical angle. The TM-resonance in the total reflection region (fig. 8) has a bandwidth similar to the resonance in figure 3.

Assuming that the reflectivity curve at the resonance angle is proportional to

$$R \approx \min + \text{curv} \times (\theta - \theta_R)^2. \quad (6)$$

We can steer the angle by varying the refractive index of the EO layer. A general definition of the sensitivity is the reflectivity change referred to the index change at the angle where the half reflectivity occurs comparing to the resonance minimum¹⁰. We define the sampling and steering sensitivity expressed in the following equations:

$$S_p = \frac{dR}{d\theta} \frac{d\theta}{dn_p} \quad (7)$$

and

$$S_s = \frac{dR}{d\theta} \frac{d\theta}{dn_s} \quad (8)$$

with

$$\frac{dR}{d\theta} = \sqrt{2\text{curv}(1 - \min)} \quad (9)$$

that is taken at the angle of the half bandwidth¹⁰. The angle change referred to the sample index change is calculated numerically by varying the sample index slightly from the water index. The sample layer is set to be 5 nm thick attached between Au-water. The formulae of (7-9) are suitable for the feedback application of the EO modulation as described later in the section 4. These definitions of sensitivities do not include the feature of the apparatus such as the diffraction effects associated with the finite width of the laser beam^{10,18}. In the following calculations, we try to avoid the very sharp resonance whose bandwidth is less than 0.05 degree¹⁸.

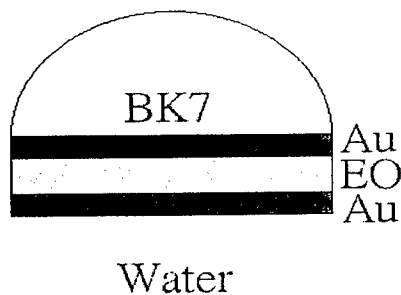


Figure 7: Multilayer structure of coupling prism method using two identical gold-films to sandwich the EO layer. The BIA layer should be attached to the gold-water interface. The calculations apply the He-Ne laser with the wavelength of 632.8 nm.

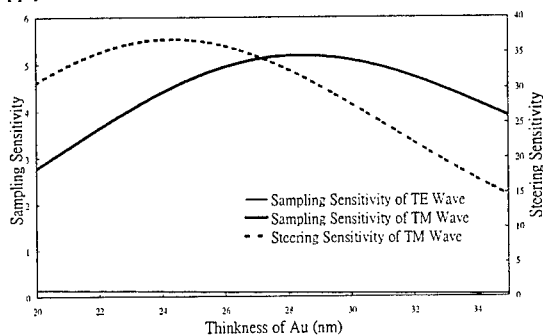


Figure 9: Sampling sensitivities and steering sensitivity of the TE- and TM-resonance illustrated as functions of the gold thickness. The sampling sensitivity of TE-resonance is very low, as shown here. Its associated steering sensitivity is not illustrated. The thickness of the EO layer used in this calculation was 400 nm.

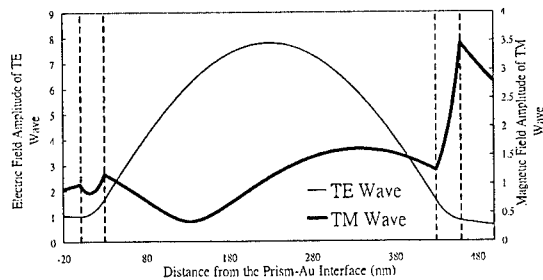


Figure 11: Transverse field distributions of the TE- and the TM-resonance. Two gold films locate at the sections of 0-30 nm and 430-460 nm. The excited plasmon locates at the gold-water interface at 460 nm. The field distributions in the EO layer are symmetric and antisymmetric referred to the TE- and TM-resonance. The plot starts from the BK7 at 20 nm to the interface.

Figure 9 and figure 10 illustrate the functional parameters of the multilayer SPR sensor shown in figure 7. The sampling sensitivity of the TE-resonance is very low as described in Toyama's configuration⁷. In this case, we can apply a differential measurement between the resonance angles of the TM- and the TE-wave. Figure 9 shows that the TM-sampling and TM-steering sensitivities have different maximal values, as the gold thickness increases. The TM-steering sensitivity is low

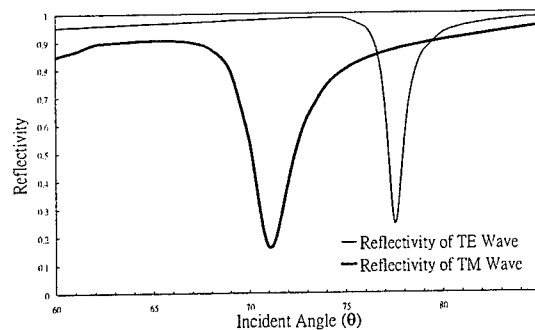


Figure 8: Reflection curves of the TE- and TM-resonance. Both resonance have angles greater than the critical angle of prism-water. The calculated configuration is 30nm Au-400 nm EO-30nm Au.

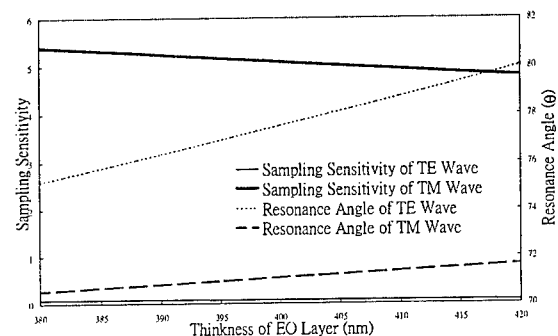


Figure 10: Sampling sensitivities and resonance angles of the TE- and TM-resonance illustrated as functions of the EO thickness. The thickness of gold-films calculated here is 30 nm. As the EO thickness increases, the resonance angles increase, but the sampling sensitivities decrease.

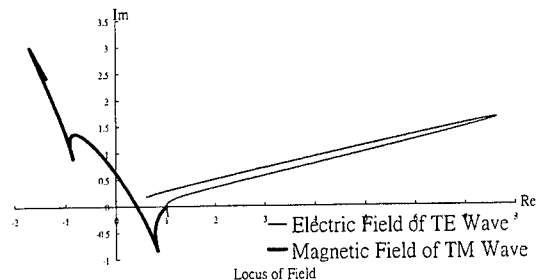


Figure 12: Locus plots of the complex transverse fields of the TE- and TM-resonance associated to their field plots of Fig. 11. The deflections of TM locus denote the charge density accumulation at the metal-dielectric interfaces. The plasmon has a symmetrical field distribution in the first gold film but antisymmetrical in the second gold film referred to each metal center.

compared to the TE-steering sensitivity due to the TM-phase change in the EO layer. The TE steering sensitivity is very high because of the in-phase high-field distribution in the EO layer (fig. 11). We found that the field drop at the second gold film causes a low TE-sampling sensitivity. The TE-steering sensitivity is not shown in Fig. 9 due to its low sampling sensitivity. The probing depth is directly related to the resonance angle (fig. 10). One chooses large resonance angle for the short probing depth and vice versa. An optimal choice of these parameters depends on the applications. The TM-sampling sensitivity decreases due to the field reduction at the water interface, as the EO thickness increases. The surface plasmon on the Au-water interface is excited and characterized by a peak of the transverse field (fig. 11). High field is preferred for a high sampling sensitivity. The associated locus plot in figure 12 demonstrates that the TM-phase changes sign in the EO layer. We found that the magnetic fields are symmetric in the upper gold film but antisymmetric in the lower gold film. Note that the charge densities are symmetric between the gold films across the EO layer. We like to remind the readers again that all field calculations are normalized to the prism-gold interface with the complex number (1,0).

According to the description in section 2, we find significant long-range plasmon coupling through the three interfaces on which plasmon excitations perform similar dispersion relations, as the dielectric constant of the EO layer approaches the water index. The magnetic field distributions in the second gold film become symmetric (fig. 13 and 14). The resonance bandwidths are smaller and resonance fields are higher, if we compare these results with the cases of figures 9 ~12. However, the probing evanescent waves become long extended. Note that plasmons on different interfaces are excited in the configurations with EO indices changing from 1.4 to 1.33.

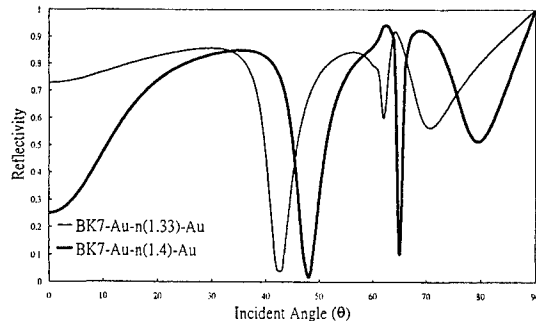


Figure 13: Reflectivity curves of the TM-wave configured with the refractive index of the EO layer to be 1.33 (water) and 1.4. The resonance angles are close to the critical angle (61 degrees) of prism-water. The parameters used in this calculation are 25 nm AU - 600 nm EO layer - 25 nm Au.

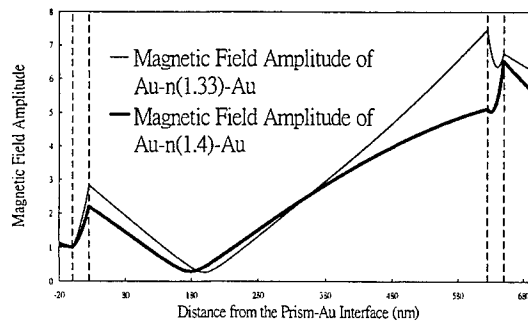


Figure 14: Magnetic field of TM-wave associated to the sharp resonance near the critical angle in Fig. 13. Note that the plasmons at different interface were excited. Note that the second gold film has a symmetric field distribution. The plot starts from the BK7 at 20 nm to the interface.

In this paragraph, we describe the TM-resonance shown in figure 15 with a typical gold thickness of 50 nm. As the EO layer (index=1.63) is less than 20 nm, the reflectivity curve has the same behavior as the configuration discussed in figure 3. This mode is not interesting due to its low sampling sensitivity. As the EO thickness increases to 280 nm, a sharp resonance appears. The TM-resonance angle increases from the critical angle of 61 degrees to 90 degrees as the EO thickness increases from 280 nm to 530 nm. On the other hand, the TE-resonance firstly appears at 130 nm with an angle close to the critical angle. The TE-resonance disappears around 380 nm characterized by its angle passing 90 degrees. The resonance angles of both TM- and TE-waves move periodically, as the EO thickness increases. One can choose the EO thickness to obtain either one resonance between TM- and TE-waves or both resonance (fig. 16). The resonance angles are tunable by the EO thickness. Both types of resonance are sensitive from the viewpoint of the BIA system. The TE-resonance performs very high sensitivities in steering as well as in sampling (fig. 17), since the fields are high and in-phase in the EO layer (fig. 19). The TE-sensitivities decrease due to less energy transferred into the resonant waveguide of the EO layer, as the thickness of the gold film increases (fig. 17). On the contrast, the TM sensitivities increase due to the growth of plasmon excitation (same behavior as fig. 5), as the thickness of the gold film increases (fig. 17). The coupling prism excitation of this mode is difficult to interpret, because the plasmon should have a propagation constant greater than that of the light line in BK7 due mainly to the higher EO index ($1.63/EO > 1.515/BK7$). Consequently, the ATR method can not excite the plasmon. However, the EO layer is finite and works like a waveguide coupling the field from low-index side of sample to metal by a standing wave. This leads to the coupled plasmon-waveguide resonance excitation⁶. The field and locus plots in figure 19 and 20 indicate two different types of TE- and TM-resonance in the EO layer. One performs symmetric field-distribution and the other performs antisymmetric field-distribution referred to central line of the EO layer.

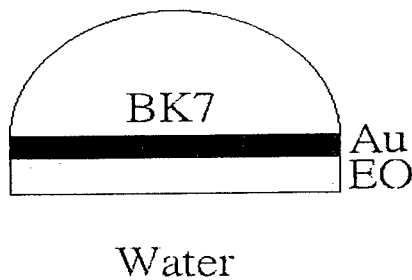


Figure 15: Multilayer structure of coupling prism method using an EO layer. The BIA layer should be attached to the EO-water interface. The calculations apply the He-Ne laser with the wavelength of 632.8 nm.

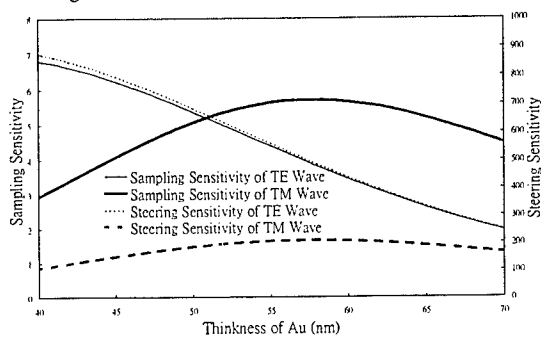


Figure 17: Sampling sensitivities and steering sensitivities of TE- and TM-resonance illustrated as functions of the gold thickness. Both the sampling and steering sensitivities of the TE-resonance are very high compared to those sensitivities of the TM resonance. The thickness of the EO layer used in this calculation is 350 nm.

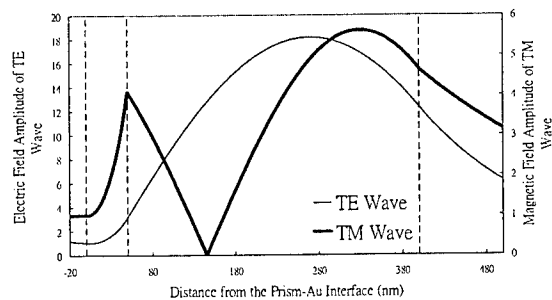


Figure 19: Transverse field distributions of the TE- and the TM-resonance. The thickness of the gold film and the EO layer used in the calculation are 50 nm, 350 nm, respectively. The plasmon excited locates at the gold-EO interface. The field distributions in the EO layer are symmetric and antisymmetric referred to the TE- and TM-resonance, respectively.

According to the calculation of Zervas¹⁴, we can find the long-range surface-plasmon, as the EO index approaches the index of BK7. Figure 21 illustrates this result to be a long-range mode. The resonance is very sharp that indicates that the propagation distance is very long. Figure 22 illustrates the associated field distribution. For such a high field at the interface, several papers^{21,22,23} considered nonlinear effects of the material. It should be carefully studied, especially in our case.

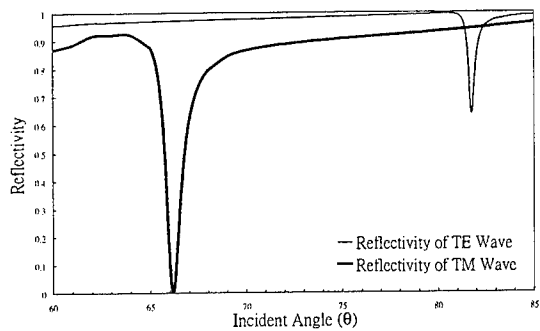


Figure 16: Reflection curves of the TE- and TM-resonance. Both the resonance angles are greater than the critical angle of prism-water. The configuration calculated here is BK7-50 nm Au-350 nm EO-water.

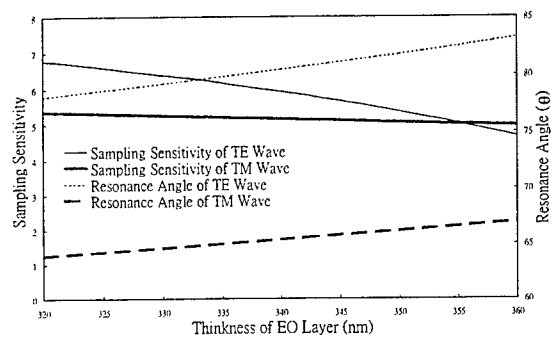


Figure 18: Sampling sensitivities and resonance angles of the TE- and TM-resonance illustrated as functions of the thickness of the EO layer. The thickness of the gold film used in the calculations is 50 nm. As the EO thickness increases, the resonance angles increase, but the sampling sensitivities decrease.

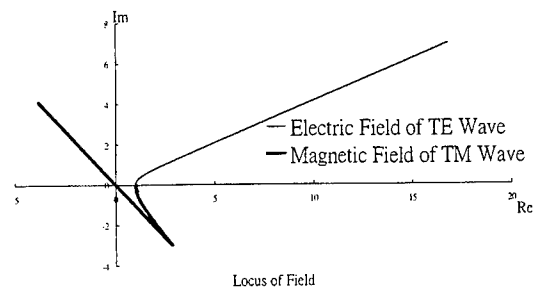


Figure 20: Locus plots of the complex transverse fields of the TE- and TM-resonance associated to the field plots in Fig.19. The deflections of TM locus denote the charge density accumulation at the metal-dielectric interfaces. The plot starts from the BK7 at 20 nm to the interface.

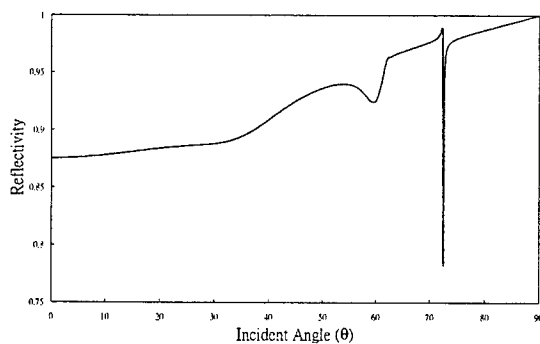


Figure 21: Reflectivity curves of the TM-wave configured in the same geometry shown in Fig. 19 but with a EO index to be 1.5 close to the index of the prism.

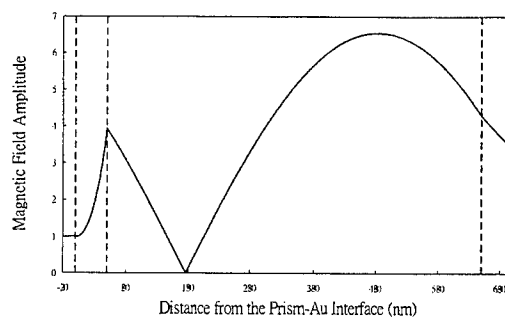


Figure 22: Magnetic field associated to the sharp TM-resonance in Fig. 21. The configuration is BK7-50 nm Au-600 nm EO-water. The plot starts from the BK7 at 20 nm to the interface.

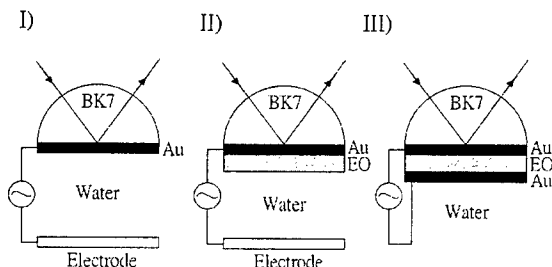


Figure 23: Three possible configuration of EO modulation. Figures I and II have an electrode in the water. The BIA sample is considered to coat on the metal-water interface.

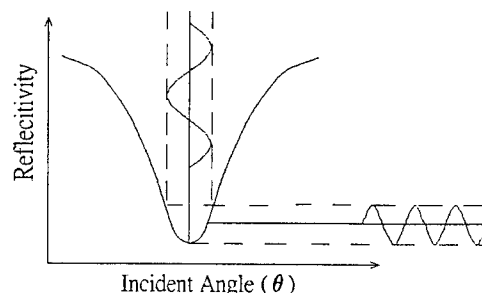


Figure 24: Using the electric signal to modulate the EO layer. The second harmonic results in the reflectivity, as the incident angle match the resonance angle.

4. ELECTRO-OPTIC MODULATION

Loulergue *et al.*²⁴ investigated in 1988 how a static electrical field affects a Langmuir-Blodgett film (single molecular layer, thickness 2.5nm – 3nm) of an azo dye. In this study, the dye layer has been deposited on an Ag film and also measured its reflectivity has been measured versus applied field. An angle change of 3 degrees for an applied field of 9 volts has been reported. A simple EO-modulation scheme is considered using water as the EO material (figure 23-I). The charge density in the double layer induced by the current flow at the metal-water interface attributes to the modulation of the SPR sensing²⁵. This scheme has the drawbacks that the modulation response is not linear and slow. Furthermore, the electric current is large and passes through the BIA sample.

Figure 21-II sketches the improved scheme to replace the double layer by the EO layer. Recent progress in the EO polymers^{26,27} provides the fabrication capability of integrated optic devices that is suitable for the SPR array sensing. Although the modulation speed of polymer can be driven up to the GHz range, this scheme should stay in the low frequency region to avoid current flow in the water.

The third scheme of figure 21-III avoids all drawbacks of the previous two. The modulation field appears only between the gold films. The film thickness is not too thin to fabricate. Even the upper gold layer can be replaced by silver that provides a further improvement of sensitivities without worrying about the degradation⁷.

Assuming that a sinusoid electric field of frequency f_m applies on the EO layer and the incident angle of light is at the resonance angle. Figure 24 shows that the photo detector will generate a second harmonic signal. As long as the incident angle matches the resonance angle, there is no signal of the f_m modulation frequency. We consider a feedback loop to cancel the modulation frequency using a dc bias voltage between the electrodes. The dc bias is directly readable with a high response speed. There is no electrode in the water. Therefore, an integrated circuit with this biochip can drive the modulation speed up to multi-GHz range. A high S/N ratio and a very fast feedback loop with high gain can be obtained. It is possible to realize the array and the differential sensing on the chip.

5. DISCUSSION

An ideal design of the SPR sensor using EO modulation described in this paper should have the following features:

1. High sensitivity to probe the BIA sample,
2. Capability of array sensing with single incident light,
3. Capability of multiple wavelength of the incident light,
4. Differential measurement to increase the precision,
5. High real-time detecting speed,
6. High S/N ratio for the high resolution sensing,
7. Tunable probing depth,
8. Large dynamic range of EO modulation,
9. Stable working point with large manufacturing tolerance,
10. Small size and easy to fabricate.

We discussed the physics of the surface-plasmon excitation in section 2. Two major configurations of figures 23-II and 23-III were considered realizing the features mentioned above. The configuration of metal-dielectric-ITO reported by Teng *et al*⁸ is less favorable because of its low dynamic range of the EO steering. The EO layer should be placed as close as possible to the plasmon surface where the field is high. A long-range surface-plasmon with tunable resonance angle is preferred due to its high resolution and high field concentration. However, a very sharp bandwidth might not increase the resolution due to the divergence of the laser light. But, the strong resonance field certainly leads to the required features in the aspects of large modulation dynamic range and high sampling sensitivity. We choose a polymer as EO material because of its low refractive index. The index of EO polymer is unfortunately higher than the index of prism. Although we can choose the high refractive prism in our application, it is not favorable due to its high price and low popularity. In this paper, we found a long-range mode that is usually not considered to be possible but occurred only in a strong coupling configuration.

The configuration of figure 23-II has the advantages of high sampling sensitivity, large dynamic range and possibility of stereo detection. However, the electrode in the water will inhibit the modulation speed. The nonlinear modulation of the double layer will cause further problems. The polymer might also degrade due to ac charging in the water solution.

The optimal choice of a EO configuration seems to be figure 23-III so far. The detecting speed is high, the metal layer is not too thin, and almost all the required features listed above are satisfied. We are sure that there is still plenty of room to improve this configuration.

6. CONCLUSION

We suggested a novel detection schemes to replace the mechanism of the angular measurements or wavelengths variation using an EO coating on the plasmon active interface to perform EO modulation. This method determines the SPR angle using an electrical signal that is directly readable. Canceling the angle-reading mechanism reduces the sensor size while providing potential of array sensing as well as maintaining the precision of angular interrogation. Moreover, multiple light sources for array and differential measurements are one of the feasible options.

ACKNOWLEDGEMENT

The National Health Research Institutes supported this work within the National Science and Technology Program of Pharmaceuticals and Biotechnology. Grants number is NSC-89-2323-213-001. The authors thank Miss M.-F. Tsai for the search of references.

REFERENCES

1. G. J. Sprokel and J. D. Swalen, "The Attenuated Total Reflection Method", chapter 4, *Handbook of Optical Constants of Solids II*, Edited by E. D. Palik, Academic Press, INC., 1991.
2. B. Liedberg, C. Nylander, I. Lundström, "Surface plasmons resonance for gas detection and biosensing", *Sensors and Actuators* **4**, pp. 299-304, 1983.
3. J. Homola, S.S. Yee, G. Gauglitz, "Surface plasmon resonance sensors: review", *Sensors and Actuators* **B54**, pp. 3-15, 1999.
4. J. Homola, I. Koudela, S.S. Yee, "Surface plasmon resonance sensors based on diffraction gratings and prism couplers: sensitivity comparison", *Sensors and Actuators* **B54**, pp. 16-24, 1999.
5. B. E. A. Saleh, M. C. Teich, "Electro-optics", Chapter 18, *Fundamentals of photonics*, John Wiley & Sons, 1991.

6. Z. Salamon, H. A. Macleod, and G. Tollin, "Coupled plasmon-waveguide resonators: A new spectroscopic tool for probing proteolipid film structure and properties", *Biophys. J.* **73**, pp. 2791-2797, 1997.
7. S. Toyama, N. Doumae, R. Usami, K. Horikoshi, and Y. Ikariyama, "Ag-SiO₂-Au Thin film for the stabilization of the signal of SPR-based immunosensor" *Transducer '99*, Sendai, Japan, pp. 1344-1346, 1999.
8. C. C. Teng and H. T. Man, "Simple reflection technique for measuring the electro-optic coefficient of poled polymers", *Appl. Phys. Lett.* **56** (18), pp. 1734-1736, 1990.
9. H. Raether, "Surface plasma oscillations and their applications", *Phys. Thin Films*, **9**, pp. 145-261, 1977.
10. H. E. de Bruijn, R. P. H. Kooyman, and J. Greve, "Choice of metal and wavelength for surface-plasmon resonance sensors: some considerations", *Applied Optics*, **31**(4), pp. 440-442, 1992.
11. J. J. Burk and G. I. Stergeman, T. Tamir, "Surface-polariton-like waves guided by thin, lossy metal films", *Phys. Rev. B*, **33**, pp. 5186-5201, 1986.
12. D. Sarid, "Long-range surface-plasma wave on very thin metal films", *Phys. Rev. Lett.* **47**, pp. 1927-1930, 1981.
13. E. Kretschmann, H. Raether, "Radiative decay of non-radiative surface plasmon excited by light", *Z. Naturforsch.* **23A**, pp. 2135-2136, 1968.
14. M. N. Zervas, "Surface plasmon-polariton waves guided by thin metal film", *Opt. Lett.* **16**(10), pp. 720-722, 1991.
15. W. N. Hansen, "Electric fields produced by propagation of plane coherent electromagnetic radiation in a stratified medium", *J. Opt. Soc. Am.* **58**, pp. 380-390, 1968.
16. H. A. Macleod, *Thin-film optical filter*, Ch. 2, Adam Hilger Ltd, Bristol, 1986.
17. A. Otto, "Excitation of surface plasma waves in silver by the method of frustrated total reflection", *Z. Physik* **216**, pp. 398-410, 1968.
18. J. C. Quail, J. G. Rako, and H. J. Simon, "Long-range surface-plasmon modes in silver and aluminum films", *Opt. Lett.* **8**(7), pp. 377-379, 1983.
19. M. A. Kessler, E. A. H. Hall, "Multilayered structure exhibiting long-range surface exciton resonance", *Thin Solid Films*, **272**, pp. 161-169, 1996.
20. F. Yang, J. R. Sambles, and G. W. Bradberry, "Long-range coupled surface exciton polaritons", *Phys. Rev. Lett.* **64**, pp. 559-562, 1990.
21. D. Sarid, R. T. Deck, and J. J. Fasano, "Enhanced nonlinearity of the propagation constant of a long-range surface plasma wave", *J. Opt. Soc. Am.*, **72**(10), pp. 1345-1347, 1982.
22. R. T. Deck, D. Sarid, "Enhancement of second-harmonic generation by coupling to long-range surface plasmons", *J. Opt. Soc. Am.*, **72**(12), pp. 1613-1617, 1982.
23. G. I. Stergeman and J. J. Burk, D. G. Hall, "Nonlinear optics of long-range surface plasmons", *Appl. Phys. Lett.*, **41**(10), pp. 906-908, 1982.
24. J. C. Loulergue, M. Dumont, Y. Levy, P. Robin, J. P. Pocholle and M. Papuchon, *Thin Solid Films* **160**, 399, 1988.
25. Badia, S. Arnold, V. Scheumann, M. Zizlsperger, J. Mack, G. Jung W. Knoll, "Probing the electrochemical deposition and/or desorption of self-assembled and electropolymerizable organic thin films by surface plasmon spectroscopy and atomic force microscopy", *Sensors and Actuators B* **54**, pp. 145-165, 1999.
26. J. G. Grote, "Design and fabrication of nonlinear optic polymer integrated optic devices", chapter 16, *Electrical and optical polymer systems*, MARCEL DEKKER, INC., New York, 1998.
27. L. R. Dalton, "Polymers for electro-optic modulator waveguides", chapter 19, *Electrical and optical polymer systems*, MARCEL DEKKER, INC., New York, 1998.

In Vivo, noninvasive glucose monitoring with optical heterodyne polarimetry in a range of 50 mg/dl ~ 100 mg/dl

Wei-Hsiung Wang, Chien-Yuan Han, Pei-Chin Tu and Chien Chou
Institute of Radiological Science, and Department of Medical Radiation Technology, National
Yang-Ming University, Peitou, Taipei, 112 Taiwan, R. O. C.

ABSTRACT

An amplitude sensitive optical heterodyne polarimeter was setup in order to monitor noninvasively the aqueous glucose concentration in rabbit's eye. A range of the blood glucose from 35 mg/dl to 135mg/dl was measured *in vivo* by biological glucose assay (BGA), while the optical rotation of the aqueous glucose was measured by a polarimeter simultaneously. The experimental results showed the consistence between these two independent measurements. There was no time delay between the blood glucose and the aqueous glucose when the blood glucose was descending after the insulin was injected. It was in contract to a 10 minutes time delay when the blood glucose was ascending. The detection sensitivity of the polarimeter was 4 mg/dl in the measurement.

Key words : heterodyne, polarimeter, glucose, noninvasive

1. INTRODUCTION

Different techniques have been used to monitor glucose concentrations noninvasively¹⁻⁵. The reduced scattering coefficient of the tissue, which shows a correlation with the glucose concentration^{3,5}. However, the experimental result of measuring μ'_s *in vivo* showed a 73% confidence level in noninvasive glucose monitoring by the diabetic volunteers. Physiological interference such as temperature change, blood flow, and tissue heterogenetics can degrade the performance of the detection. The polarimeter in the photometric technique used a Faraday modulator to generate the polarization modulation of the incident laser beam before the test sample^{2,3}. A Faraday rotator and an analyzer were used to null the rotation of the polarization vector due to the glucose sample and then to sense the optical rotation angle in terms of the dc voltage applied to the Faraday compensator. The sensitivity of that method showed a 10-mg/dl detection sensitivity of the glucose concentration in the double distilled water and the cell culture medium with a 1-cm-wide optical path. The aqueous humor in the eye is the window for measuring the blood glucose that relies on the measurement of the optical rotation angle of the aqueous glucose (see Fig. 1). The measurement is based

on the result of a high correlation between the blood glucose and the aqueous glucose according to the observations made by March *et al*⁶ and the fact that the optical rotation angle of the glucose is linear proportional to its concentration. The aqueous protein, which is also an optical active substance, has a very low concentration (0.013g/100ml) in the aqueous humor owing to the diffusion filtering processing across the semi-permeable membrane. The optical rotation caused by the other substances in the aqueous humor can be ignored^{6,7}. The measurement of the concentration of the optical active medium is related to the optical rotation angle θ_m by

$$[\alpha]_{\lambda,PH}^T = \frac{\theta_m}{CL} \quad (1)$$

where $[\alpha]_{\lambda,PH}^T$ is the specific rotation of a molecule in the medium^{2,4}, C is the concentration, and L is the optical path length of the test medium. Chou *et al*⁴ proposed a different technique based on an optical heterodyne polarimeter in which a Zeeman laser in conjunction with a Glan-Thompson analyzer was used. The glucose concentrations can be measured in terms of the optical rotation of a linear polarized light in the aqueous humor by measuring the amplitude of the heterodyne signal. Blood glucose in the range of 100-200 mg/dl of New Zealand white rabbits have been measured in terms of the optical rotation after the rabbit was anesthetized. The result was consistent with the blood glucose by biological glucose assay (BGA). However, a 30 minutes time delay⁽⁴⁾ between the blood glucose and the aqueous glucose was observed. It was caused by the blood glucose diffusing slowly into the aqueous humor through a semi-permeable membrane⁷. In this paper, a range of low concentrations of the blood glucose (35-135 mg/dl) of healthy New Zealand white rabbits were measured *in vivo* by BGA. Meanwhile, the optical rotation of the aqueous glucose was monitored by the polarimeter simultaneously. The experiment showed the consistence between these two independent measurements. There was no time delay between the blood glucose and the aqueous glucose after the insulin was injected when the blood glucose was descending. It was in contrast to a 10 minutes time delay that the glucose was ascending 45 minutes after the insulin was injected.

2. PRINCIPLE

An amplitude-sensitive optical heterodyne polarimeter was set up as shown in Fig. 2. A Zeeman laser that consists of two orthogonal linearly polarized states with different temporal frequencies and one Glan-Thompson analyzer was used. The optical heterodyne signal was generated when the laser beam was passing through a Glan-Thompson analyzer at a fixed azimuth angle. The laser was incident on the optical active medium, the aqueous humor, that rotates the P and S states by angle θ_m simultaneously (see Fig. 3). When the laser beam passed the analyzer, where the azimuth angle of the analyzer was set at θ_s , the output intensity is

$$I_s = a_1 a_2 \sin 2(\theta_s + \theta_m) \cos(\Delta\omega t) \quad (2)$$

where a_1 and a_2 are the amplitudes with respect to the two eigenmodes from the laser. If $|0^\circ < \theta_s + \theta_m < 5^\circ|$,

then Eq. (2) can be expressed as

$$I_s \equiv 2a_1 a_2 (\theta_s + \theta_m) \cos(\Delta\omega t) \quad (3)$$

If we assume that $I_0 = 2a_1 a_2 \theta_s \cos(\Delta\omega t)$ when the zero concentration of the glucose is tested, the difference intensity of the non-zero concentration is $|\Delta I| = |I_s - I_0| = 2a_1 a_2 \theta_m$. It means that the variation of the optical rotation angle equals to $2a_1 a_2 \theta_m$. The detection sensitivity of the optical rotational angle is then amplified by a factor $2a_1 a_2$.

3. EXPERIMENTAL SETUP AND DISCUSSION

Figure 2 shows the configuration of the experimental setup in which an HP5519 Zeeman laser was used. The laser beam consisted of two eigenmodes with different temporal frequencies in 1mW output power. The frequency difference between the two orthogonal polarized waves, the P and the S waves, was 2.6 MHz. The output wavelength of the Zeeman laser was 632.8 nm. A Glan-Thompson analyzer was adopted in this experiment to generate the 2.6-MHz heterodyne signal. Two healthy New Zealand white rabbits were tested successfully. Their weights ranged from 3.0 to 4.0 kg. At the beginning, Changzine and Imalgene were injected into a rabbit (I. M.) to anesthetize the rabbit. A blood sample from the artery of the rabbit ear was then measured by BGA every 2 minutes. A 0.65 I.U/kg Humulin (Humulin R, Lilly, USA) was then injected into the artery right after the first sampling of the blood sample. Then, the aqueous glucose was monitored. The blood glucose were checked every 2 minutes in order to follow the rapid response of the blood glucose⁷. Two independent measurements were matched under the same time base as shown in Fig. 4(a). The magnitude of the aqueous glucose has been scaled linearly by fitting the data points in the descending curve of the blood glucose after Humulin was injected. From the experimental results, we can see that there is not any time delay when the blood glucose was descending. In contrast, once the blood glucose started to ascend, the aqueous glucose followed the blood glucose 10 minutes time delay as shown in Fig. 4(a). The delay time was caused the blood glucose slowly penetrated the semi-permeable membrane from the artery into the aqueous humor⁸. Figure 4(b) shows the same response of the aqueous glucose of the second rabbit after the Humulin was injected. Similar response between the blood glucose and the aqueous glucose was observed in Fig. 4(a) and Fig. 4(b). Therefore, the proposed glucose monitoring system successfully monitored the blood glucose through the aqueous glucose in a range of 35~135 mg/dl without any time delay.

A Zeeman laser in conjunction with a Glan-Thompson analyzer to form an optical heterodyne polarimeter is able to measure the aqueous glucose from 35 mg/dl to 220 mg/dl⁴. A time delay between the blood glucose and the aqueous glucose depends on the situation of the ascending or descending of the blood glucose. The detection sensitivity as well as the linearity of the measurement proves that this method is able to monitor the blood glucose *in vivo*, noninvasively and accurately. The signal fluctuation of the polarimeter can be suppressed by keeping the eyeball steady during the measurement or using a pulse laser to measure the aqueous glucose.

In conclusion, When the equilibrium between the aqueous glucose and the blood glucose is maintained. The aqueous glucose equals to the blood glucose. There is no delay time between the blood and the aqueous glucose to be considered. This proposed method has been proved to be effective in achieving the goal of monitoring the blood glucose in vivo and noninvasively.

ACKNOWLEDGEMENTS

The authors are grateful to L. C. Peng, C. W. Lyu for offering help in the experiment. L. C. Jan's assistance in preparing the manuscript is also appreciated.

REFERENCES

1. B. Rabinovitch, W. F. March and R. L. Adams, "Noninvasive glucose monitoring of the aqueous humor of the eye: Part I, Measurement of very small optical rotations" *Diabetes Care* **5** pp. 254-258, 1982.
2. G. L. Cote and B. D. Cameron, "Noninvasive polarimetric measurement of glucose in cell culture media" *J. Biomed. Opt.* **2** pp. 275-281, 1997.
3. J. T. Bruulsema, J. E. Hayward, T. J. Farrell, M. S. Patterson, L. Henemaun, M. Berger, T. Koschiusky, J. Snadahl-Christiansen, H. Orskov, M. Essenpreis, G. Schmelzeisin-Redeker, and D. Bocker, "Correlation between blood glucose concentration in diabetics and noninvasive measured tissue optical scattering coefficient" *Opt. Lett.* **22** pp. 190-192, 1997.
4. C. Chou, C. Y. Han, W. C. Kao, Y. C. Huang, C. M. Feng and J. C. Shyu, "Noninvasive glucose monitoring in vivo with an optical heterodyne polarimeter" *Appl. Opt.* **37** pp. 3553-3557, 1998.
5. M. Kohl, M. Cope, M. Essenpris and D. Bocker, "Influence of glucose concentration of light scattering in tissue-simulating phantoms" *Opt. Lett.* **19** pp. 2170-2172, 1994.
6. B. Rabinovitch, W. F. March and R. L. Adams, "Noninvasive glucose monitoring of the aqueous humor of the eye: Part I, Measurement of very small optical rotations" *Diabetes Care* **5** pp. 254-258, 1982.
7. H. Lodish, D. Baltimore, A. Berk, S. L. Ziprsky, P. Matsadaira and J. Darnell, *Molecular Cell Biology*, W. H. Freeman Co. New York pp. 905-912, 1995.
8. R. L. Stamper *Aqueous humor: secretion and dynamics in physiology of the Humor Eye and Visual System*, R. E. Records, ed, Harper & Row, Hagerstown, Md., pp. 156-182, 1979.

* Correspondence: E-mail: cchou@ym.edu.tw ,Tel: (02) 28267061 ,Fax: (02) 28251310

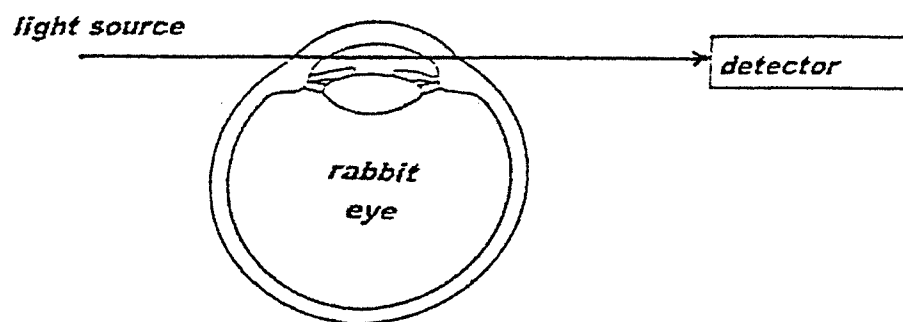


Fig. 1

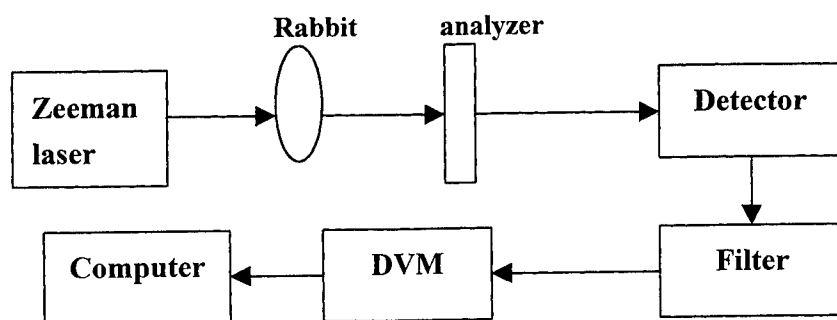


Fig2.

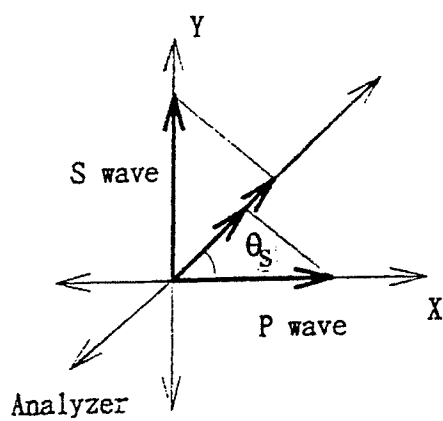


Fig3.(a)

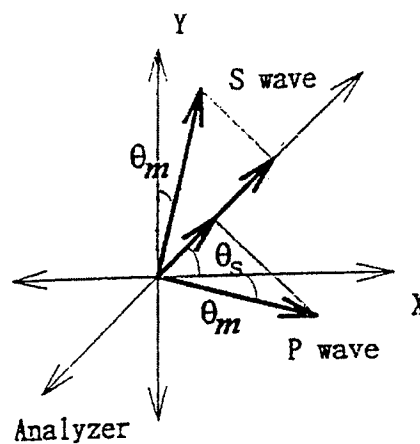


Fig3.(b)

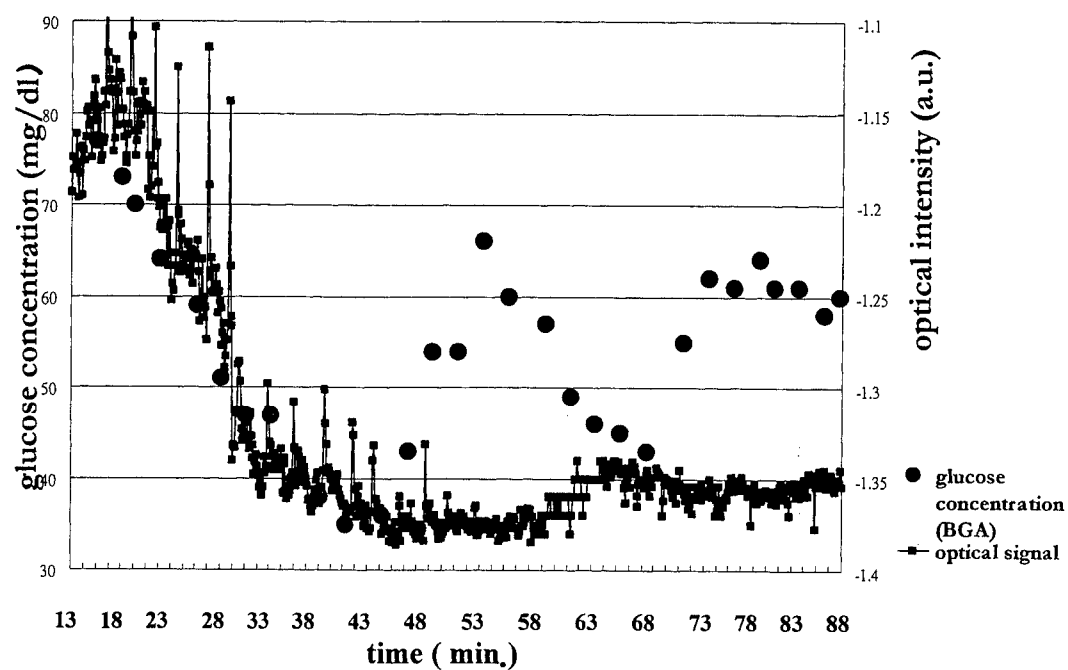


Fig.4(a)

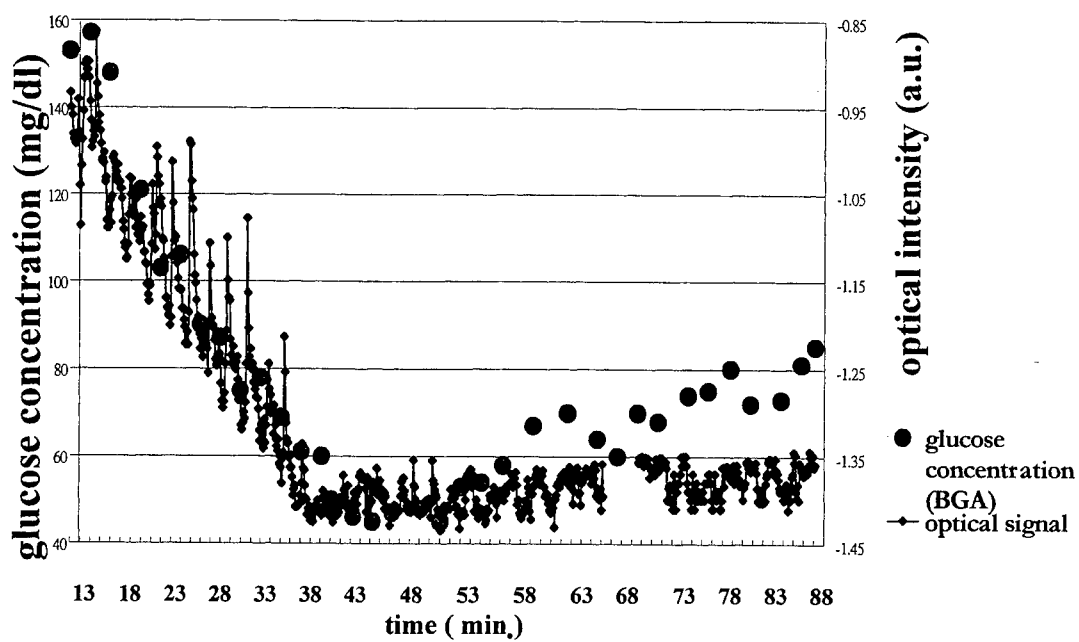


Fig.4(b)

Design and development of laser Doppler velocimetry based on DSP technique for blood flow measurement

Yuan-Hsiang Lin, Yan-Yu Chen, Yuan Ho, Yi-Lin Li, and Gwo-Jen Jan*

Department of Electrical Engineering, National Taiwan University

ABSTRACT

A graphic user interface and real-time laser Doppler velocimeter (LDV) based on the digital signal processor (DSP) had been designed and developed. The hardware setup included the Michelson interferometer optics, photo-detector, current to voltage converter, AC amplifier and filtering circuits, as well as a DSP module. The software system on DSP module was also developed to access data and to perform the moment weighting algorithms. In addition, the processed data was transmitted to the personal computer and advanced analysis could be achieved. The velocity measurement using developed LDV device was calibrated by a mirror mounted on a linear vibrator. The outcomes presented high linearity and good accuracy. In vitro experiment employing this LDV system was also carried out. The results showed that the developed LDV instrument offered a flexible tool to investigate the blood flow of microcirculation system.

Keywords: Laser Doppler, Blood flow, Digital Signal Processor (DSP)

1. INTRODUCTION

In recent years, scientists have devoted to investigating how the circulation diseases influence microvascular flow¹. Some relations were found and early-stage detection of these diseases can be achieved by continuous monitoring of microcirculation. Among various measuring techniques, laser Doppler velocimetry (LDV) has been adopted most widely. Since first introduced by M.D. Stern² in 1975, LDV is now well established and extensively used in skin perfusion measurements. Other applications to monitor choroidal flow³, renal arterioles⁴ and microcirculation in gums were also developed. Because the technique is non-invasive and highly spatial sensitive, so far it can hardly be replaced by any other methods in physiology measurement.

However, though LDV provides such advantages, there are still some problems to be solved⁵. Since the scattering mechanism is too complicated to be determined in tissue⁶, various algorithms^{7,8} are developed to obtain indicators for fluid velocity. Applying different algorithms, the results may somewhat differ. In addition, the processing bandwidth⁹ is also involved. Adopting low cut-off frequency may lead to under-estimation of velocity while using high cut-off frequency limits the frequency resolution. Besides, the computed result is closely related to the penetration depth¹⁰, which is decided by the laser used¹¹. With different penetration depths, different volumes are sampled; and it's hard to say which interprets the fluid velocity better. More than that, absolute in vivo calibrations of LDV systems are difficult to achieve due to the large variation in cutaneous structure¹².

Therefore, in this study we developed a digital signal processor (DSP) based LDV system and a simplified physical model was also implemented for the in vitro experiment. By applying the DSP framework, we evaluated the linearity of different algorithms, and determined a linear indicator for the fluid velocity.

2. THEORY AND COMPUTATION ALGORITHMS

When a photon is scattered by a moving particle, the light frequency is slightly shifted. The Doppler frequency-shift Δf is given by¹³

$$\Delta f = (|\mathbf{k}|v/\pi) \sin^{1/2} \theta \cos \alpha \quad (1)$$

where \mathbf{k} is the incoming wave vector ($\mathbf{k} = 2\pi/\lambda$, λ is the wavelength), v is the velocity of the moving particle, θ is the scattering angle, and α is the angle between $\Delta \mathbf{k}$ and \mathbf{v} .

Applying Doppler effect on skin perfusion measurement, the situation becomes much more difficult due to the complicated scattering mechanism in tissue. The intensity modulation of the detected signal shows an approximately exponential decay in the spectra. Bonner and Nossal's¹⁴ results showed that the first (weighted) moment $\langle \omega \rangle$ of the spectral power density $S(\omega)$ of the detector signal is linearly proportional to the average velocity $\langle v \rangle$ of all moving particles in the optical sampling volume. The first weighted moment (FWM) is expressed as

$$\langle v \rangle \sim \langle \omega \rangle = M_1 / M_0, \text{ with } M_n \equiv \int_{-\infty}^{\infty} \omega^n S(\omega) d\omega. \quad (2)$$

The numerator M_1 is the first moment of the spectral power density $S(\omega)$. It is assumed to be proportional to the blood flow rate in the optical sampling volume. The denominator M_0 is proportional to the total amount of Doppler-shifted light.

The second weighted moment (SWM) is expressed as

$$\langle v^2 \rangle \sim \langle \omega^2 \rangle = M_2 / M_0 = \frac{\int_{-\infty}^{\infty} \omega^2 S(\omega) d\omega}{\int_{-\infty}^{\infty} S(\omega) d\omega}. \quad (3)$$

Square root of $\langle v^2 \rangle$ represents the RMS value of blood velocity, and can be regarded as another representative of the blood velocity.

After the calculation of the first and second weighted moments, the results can be derived, in the unit of frequency (Hz) instead of velocity (m/s). The calculated value is proportional to the blood velocity, and a conversion factor should be added to compute the fluid velocity. However, the conversion factor varies between individuals and even between different sites on an individual. Thus we adopted an linear indicator to represent the fluid velocity instead of the absolute value.

3. INSTRUMENTATION

3.1. Hardware Setup

The block diagram of the LDV hardware system is shown in Fig. 1. It includes an optical system, analog signal conditioning circuits, a DSP module and a graphic user interface (GUI). The optical system contains a 5mW laser diode (650nm) and/or He-Ne laser (632.8nm), a test object, and an optical detector. It detects the optical heterodyne and converts the signal into electrical domain. In analog module, the preamplifier initially amplifies the weak signal and transforms photocurrent to voltage (gain is 200 V/mA). The AC amplifier further amplifies the AC signal and the gain is depending on the light intensity (max. gain is 200). The total bandwidth of the analog module is 50kHz.

The DSP module consists of a 16 bit, 200 kHz sampling rate ADC for A/D conversion, a 32k-byte EEPROM for program storage, high speed SRAMs up to 128k-word for DSP data buffer, and a TMS320C31 DSP as well as an ADS7843 touch-screen controller. In this module, a 2048-points Fast Fourier Transform (FFT) is performed on DSP. The sampling

rate is 200kHz and the frequency resolution is 97.7Hz. According to equation (1), in simulation experiment ($\lambda=632.8\text{nm}$) the maximal measurable velocity is 15.82mm/s and velocity resolution is 30.9 $\mu\text{m/s}$ in this system that are depended on θ and α . The GUI consists of a 240 \times 128 dots graphic LCD and a touch screen panel. The touch screen allows a user to enter a command simply by touching a location on the panel. The two devices together make the user interface more friendly and easy to use. In the other hand, the DSP can transfer the results to PC in real-time through RS-232 interface, and data analysis and storage can be further achieved. It has flexibility to modify the computing algorithm of velocity of DSP through the control panel of PC.

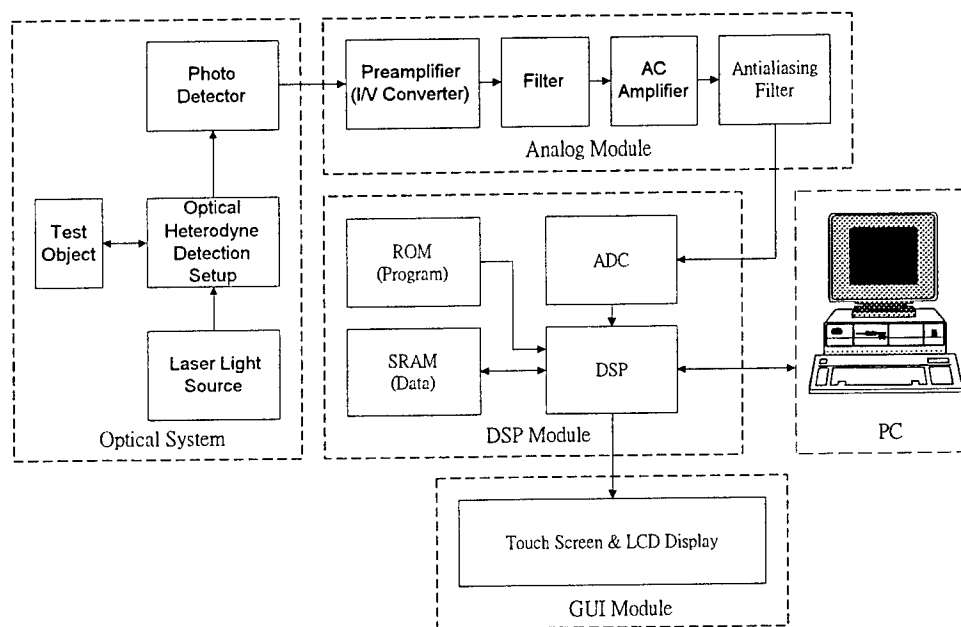


Fig. 1 The block diagram of the LDV hardware system

3.2. Software Development

The main flowchart of our program is shown in Fig. 2. After power on, program starts at initializing all control registers of DSP and LCD. Then program goes into the major loop, which makes the DSP wait for sample data to fill an input buffer, perform FFT on the data to obtain the power spectrum, calculate blood velocity based on the spectrum, then display it and carry out any user input. For the requirement of real-time processing, all source codes were written in C3x assembly language instead of other high-level languages.

The FFT used in the program is a 2048-point, decimation in time algorithm. Powered by the bit-reverse addressing mode and parallel instructions of the C3x DSP, the FFT can be calculated in a very short period of time. With a sampling rate of 200kHz, the frequency resolution df is

$$df = \frac{200k}{2048} = 97.7\text{Hz} . \quad (4)$$

Sampling of signal goes continuously, and every 5μsec DSP will receive a new sample data from ADC. To prevent new data from mixing with data that are currently under processing, a three buffer rotating technique is used. Input buffer accumulates new data coming from ADC. The data in FFT buffer are those currently under processing (FFT or calculation of blood velocity), and output buffer stores previously processed data, which is used for the spectrum display.

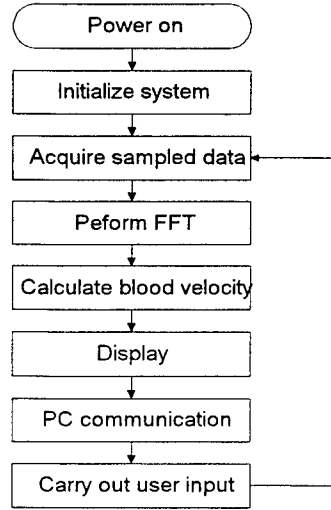


Fig. 2 The flowchart of the main program

When sample data fills the input buffer, a buffer rotating occurs. The input buffer becomes FFT buffer so that its contents are ready for FFT calculation. FFT buffer becomes output buffer and the spectrum stored in it will be displayed immediately. Output buffer becomes input buffer and will start accepting new sample data.

The calculation of blood velocity involves three algorithms –FWM, SWM, and the peak value of the frequency (PVF) methods. PVF was devised by us and is simply the selection of the frequency that has maximum power in the power spectrum. Since the power spectrum stored in memory is actually in discrete form, the integration of equation (2) must be approximated by the following summation:

$$FWM = \frac{\sum_{n=n1}^{n2} n df \cdot S[n]}{\sum_{n=n1}^{n2} S[n]} \quad (5)$$

Where df is the same as in equation (4) and $S[n]$ is the power spectrum after FFT calculation. It is obvious that frequencies lower than $n1 \cdot df$ and those higher than $n2 \cdot df$ will be excluded from the calculation of blood velocity. Thus by choosing the value of $n1$ and $n2$, a thresholding mechanism is easily implemented, with $n1 \cdot df$ and $n2 \cdot df$ being the lower and upper threshold. Proper use of this thresholding mechanism can eliminate unwanted frequency components like high frequency noises or the large DC component in the signal spectrum.

Similarly the calculation of SWM uses the following summation form instead of the integration form in equation (3).

$$SWM = Sqrt \left(\frac{\sum_{n=1}^{n2} (ndf)^2 \cdot S[n]}{\sum_{n=1}^{n2} S[n]} \right) \quad (6)$$

The PVF algorithm was implemented using a simple compare-and-update algorithm for finding the frequency that has largest power in the signal spectrum.

4. EXPERIMENTS

4.1. Simulation Experiment

FWM, SWM, and PVF methods are designed to calculate the velocity of a moving object. The simulation experiment is to check the computation of the algorithms and to calibrate the LDV device. The experimental setup is shown in Fig. 3. A 632.8nm He-Ne laser provides a light beam which pass through the beam splitter (50:50) and splits into two. One beam hits the moving mirror and is Doppler frequency shifted. The other hits a stationary mirror and keeps its frequency non-shifted. The reflected beams are collected by an optical fiber and picked up by a detector.

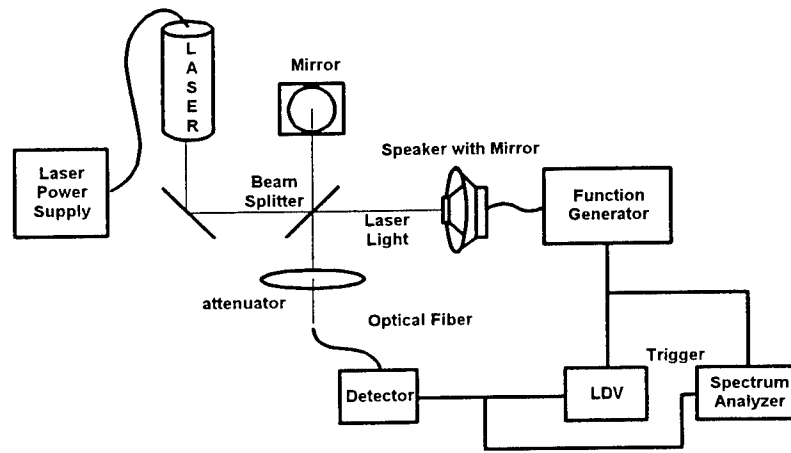


Fig. 3 The block diagram of measurement system setup for simulation experiment

The moving mirror is mounted on the front surface of a speaker center. A function generator outputs a triangular wave to the speaker and vibrates the mirror. In the forward and backward motion of the speaker, the mirror on its center would have a constant velocity. The relationship between applied voltage and speaker displacement has been measured. The linear relationship from the experiment measurement is shown in Fig. 4.

For the forward motion, the speaker kept pushing the mirror forward in velocity v , which can be calculated from frequency and peak-to-peak voltage of the triangular wave. For convenience the backward motion is neglected. The trigger signal from the function generator is connected to the LDV, which could be set to trigger mode so that it functioned only for the forward motion of the speaker, be sure the measured velocity is constant. If the shifted frequency hasn't been triggered, the

peak would vibration in the spectrum. This function also could be used to investigate the sequence relation of ECG signal and the blood flow in microcirculation.

Applying Doppler frequency shift equation (1) we get

$$\Delta f(kHz) = 3.161 \times v(mm/s) \quad (7)$$

where Δf is Doppler frequency shift, v is Mirror velocity.

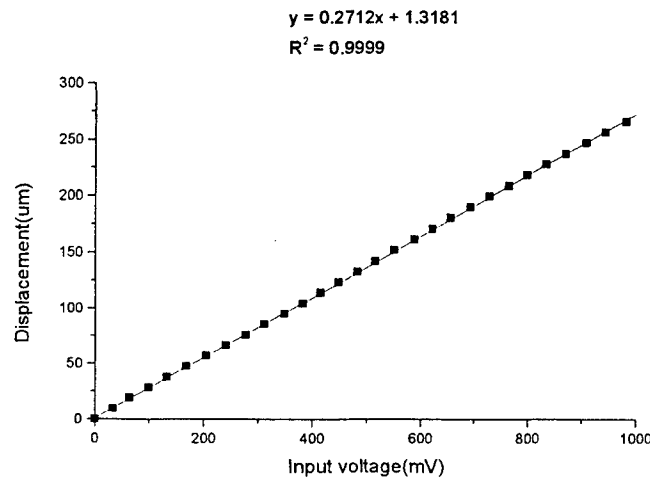


Fig. 4 Displacement calibration curve of a vibrating mirror

Note that this conversion factor between frequency and velocity is valid only in this simulation, and cannot be applied to any other situations. By changing the peak-to-peak voltage of the triangular wave, the velocity of the mirror changed as well. For each velocity the outputs of the three algorithms (FWM, SWM, and PVF) were recorded. The results are discussed in the following section.

4.2. In Vitro Experiment

In order to evaluate our system, we developed a simplified close-loop model, in which the linearity of various algorithms can be tested. The schematic diagram of the setup is shown in Fig. 5. In this model, micro-spheres were added into the water to serve as scattering particles (mass concentration = 0.1 %), and a DC motor with a precise controller was also employed to pump the solution. The photo-detector of the LDV picked up the light signals scattered either by the moving particles or the static tube. The Doppler shifted and non-shifted parts of the scattered beams heterodyned at the photodiode and produced corresponding photocurrent. After being amplified, the analog signals were translated into digital signals and a FFT processing was performed. Deriving this information in the frequency domain, we applied different algorithms to search for a linear transformation between the frequency spectrum and the fluid velocity. The processed data were transmitted to the PC, and advanced analysis could be taken.

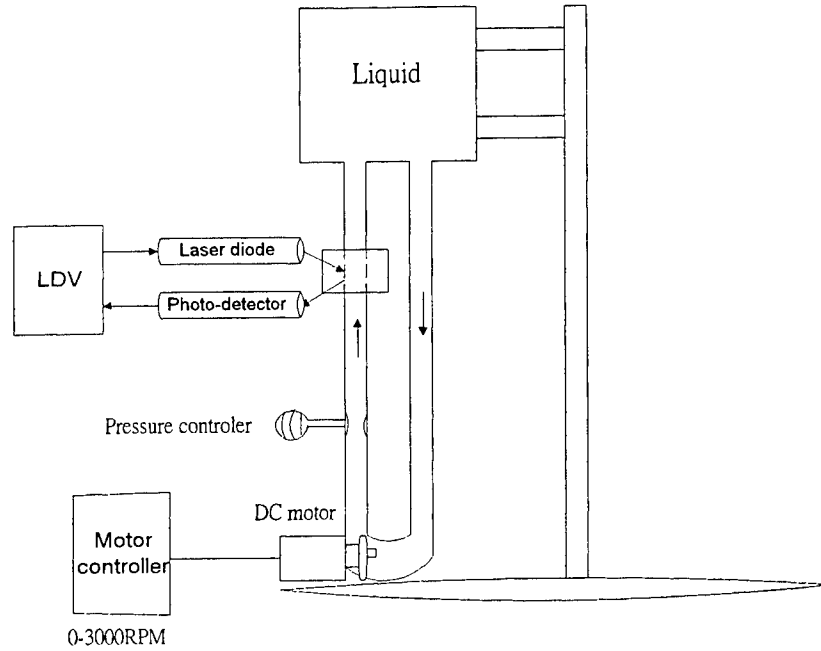


Fig. 5 Experimental setup for in vitro measurement

5. RESULTS AND DISCUSSION

5.1. Simulation Experiment

The design value of the mirror velocity can be calculated from the displacement measurement and vibrating period. The measured values using the FWM, SWM algorithms and PVF method are originally in terms of frequency unit (Hz) and are converted to the unit of velocity (mm/s) using equation (7). The comparison between designed value and measured value was displayed in Fig. 6 (A), (B), and (C). As the figure shows, all three algorithms gave values lower than the design value. This is because the actual mirror velocity is lower than the design value. Since speaker displacement versus applied voltage is calibrated under DC condition, when an AC signal is applied to the speaker, the speaker will exhibit a frequency response and its displacement will tend to be smaller than in DC. Therefore the real mirror velocity is smaller than the designed value and should be very close to the measured values in Fig. 6. If the frequency of AC bias is decreased, the difference be reduced.

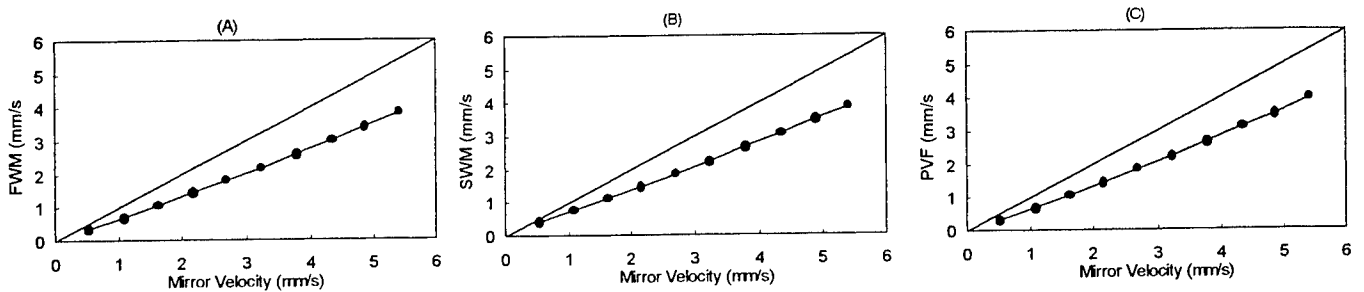


Fig. 6 Measured velocity versus mirror velocity for the (A) FWM (B) SWM algorithm and (C) PVF method

However, due to the indetermination of the conversion factor described in section 2, the important parameter is not the absolute value of an algorithm's output. It is the linearity with which algorithm responses to the simulator's velocity, that is, how straight the curves in Fig. 6 are. Table 1 shows the coefficient of determination R^2 of the four sets of data. R^2 is an indication of linearity of a set of data, with $R^2 = 1$ means perfectly linear and $R^2 = 0$ means totally unrelated. It can be observed from Table 1 that all three algorithms yield very good linearity with the mirror velocity.

Table 1 Coefficient of determination	
Algorithm	Coefficient of Determination R^2
First Weighted Moment	0.9991
Second Weighted Moment	0.9988
Peak Value Frequency	0.9991

5.2. In Vitro Experiment

The bandwidth is cut-off on 800Hz and line width is 1Hz in our experiment setup. Three groups of spectral response corresponding to different rotation rates are shown in Fig. 7. With an increase in fluid velocity, the fractions of the Fourier components are reduced at low frequencies and increase at high frequencies.

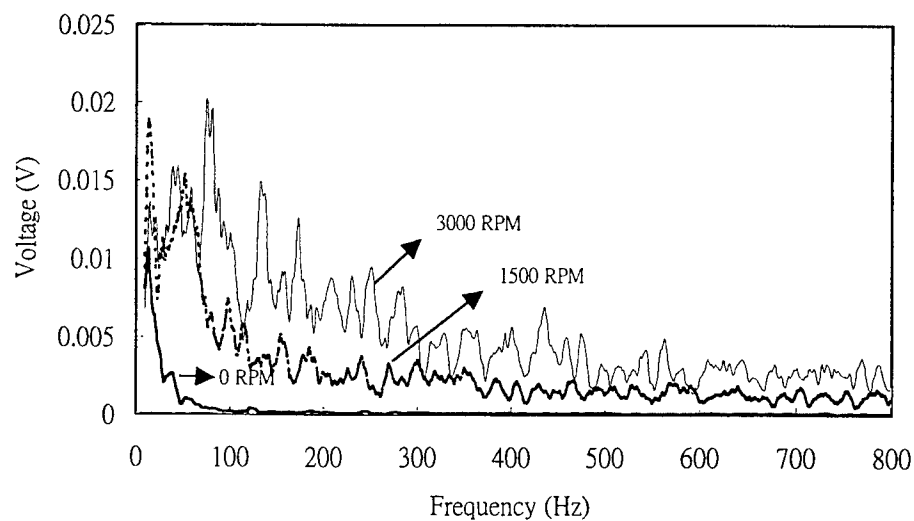


Fig. 7 Three groups of spectra corresponding to different velocities processed by moving average (10 periods)

Fig. 8 shows the computed velocities versus the DC motor's rotation rate. For each rotation rate, 20 samples were taken and averaged. According to the highly correlated relation between the rotation rates and the computed values employing FWM algorithm ($R^2=0.9922$), the derived value might be a reliable indicator to evaluate the relative fluid velocity. An indicator applying SWM is also provided. Though quite linear at high velocity measurement, it seemed to deviate at low velocity.

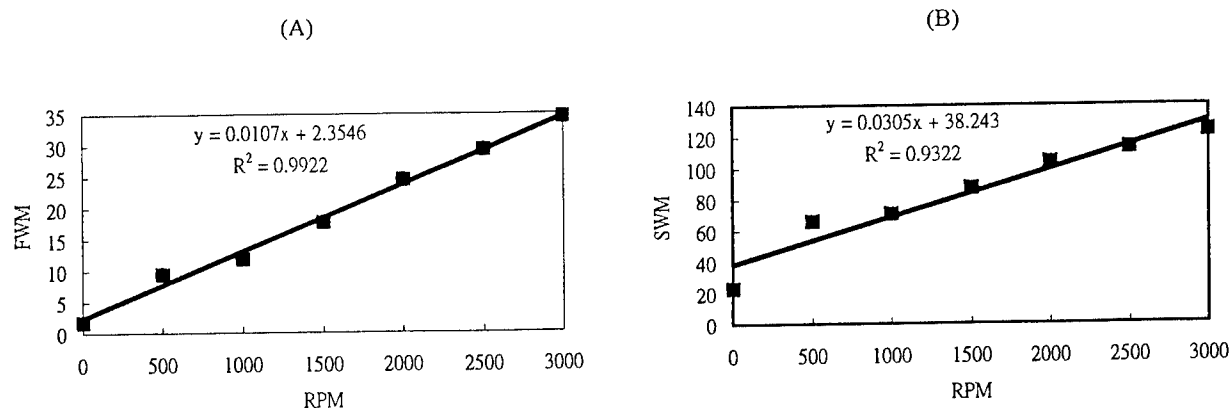


Fig. 8 (A) Relationship between FWM (in arbitrary unit), (B) SWM (in arbitrary unit) and Rotation Per Minute (RPM) of DC motor

6. CONCLUSIONS

We have developed a portable, real-time, and turn-key LDV system based on DSP techniques. Two most frequently used algorithms are adopted to test their linearity. Our outcome showed that both algorithms provide good indicators for fluid velocity measurement, and FWM seems to be a little better than SWM. Since different designs of simulation model and probe may also influence the corresponding results, more experiments should be taken to further evaluate the algorithms.

Now the in vivo experiment is taken on a cow. After installing a left ventricular assistant device on the cow, we use the LDV system to monitor its microvasculature. Information collected is used to evaluate the target's recovery, and helps the doctors to adjust the process of surgery.

ACKNOWLEDGMENTS

The research is supported by the National Science Council (Taiwan) under grant contract no. NSC 89-2213-E-002 -055.

REFERENCES

1. T. W., D. J. Haumschild, D.W. Winsor, Y. Wang, and T. N. Luong, "Clinical application of laser Doppler flowmetry for measurement of cutaneous circulation in health and disease", *The J. Vascu. Disea.* **38**, pp. 727-736, 1987.
2. M.D. Stern, "In vivo evaluation of micro circulation by coherent light scattering", *Nature* **254**, pp. 56-58, 1975.
3. Martial H. Geiser, Ulrich Diermann, and Charles E. Riva, "Compact laser Doppler choroidal flowmeter", *J.Biom. Opt.* **4**, pp. 459-464, 1999.
4. G. Smedley, K. P. Yip, A. Wagner, S. Dubovitsky, and D. J. Marsh, "A laser Doppler instrument for in vivo measurements of blood flow in single renal arterioles", *IEEE Trans. On Biomed. and Eng.* **40**, pp. 290-297, 1993.
5. A. N. Obeid, N. J. Barnett, G. Dougherty, and G. Ward, "A critical review of laser Doppler flowmetry", *J. Med. Eng. & Technol.* **14**, pp. 178-181, 1990.

6. S. R. Arridge, M. Cope, and D. T. Delpy, "The theoretical basis for the determination of optical pathlengths in tissue: temporal and frequency analysis", *Phy. Med. Biol.* **37**, pp. 1531-1560, 1992.
7. L. Duteil, J. C. Bernengo, and W. Schalla, "A double wavelength laser Doppler system to investigate skin microcirculation", *IEEE Trans. On Biomed. and Eng.* **32**, pp. 439-445, 1985.
8. M. D. Stern, D. L. Lappe, P. D. Bowen, J. E. Chimosky, G.A. Holloway, JR., H.R. Keiser, and R. L. Bowman, "Continuous measurement of tissue blood flow by laser-Doppler spectroscopy", *Am. J. Physiol.* **232**(4), H441-H448, 1977.
9. A. N. Obeid, "In vitro comparison of different signal processing algorithms used in laser Doppler Flowmetry", *Med.&Biol. Eng. & Comput.* **31**, pp. 43-52, 1993.
10. A. N. Obeid, D. M. Boggett, N. J. Barnett, G. Dougherty, and P. Rolfe, "Depth discrimination in laser Doppler skin blood flow measurement using different lasers", *Med. & Biol. Eng. & Comput.* **26**, pp. 415-419, 1988.
11. M. H. Koelink, F. F. M. de Mul, J. Gereve, R. Graaff, A. C. M. Dassel, and J.G. Aarnoudse, "Laser Doppler blood flowmetry using two wavelengths: Monte Carlo simulations and measurements", *Appl. Optics* **33**, pp. 3549-3558, 1994.
12. M. J. C. Van Gerert, S. L. Jacques, H. J. C. M. Sterenborg, and W. M. Star, "Skin optics", *IEEE Trans. On Biomed. Eng.* **36**, pp. 1146-1154, 1989.
13. F. F. M. de Mul, M. H. Koelink, M. L. Kok, P. J. Harmsma, J. Gereve, R. Graaff, and J.G. Aarnoudse, "Laser Doppler velocimetry and Monte Carlo simulation on models for blood perfusion in tissue", *Appl. Optics* **34**, pp. 6595-6611, 1995.
14. R. Bonner, and R. Nossal, "Model for laser Doppler measurements of blood flow in tissue", *Appl. Optics* **20**, pp. 2077-2107, 1981.

*Correspondence : Email: gjian@cc.ee.ntu.edu.tw; Telephone: (02)23635251-421(o)
 Fax:(02)23671909; Taipei 10617, Taiwan

SESSION 8

Optical Manipulation

Particle-trapped near-field scanning optical microscopy: scattering and depolarization

Min Gu

Centre for Micro-Photonics
School of Biophysical Sciences and Electrical Engineering
Swinburne University of Technology
PO Box 218 Hawthorn 3122
Victoria, Australia
Email: mgu@swin.edu.au

ABSTRACT

Particle-trapped near-field scanning optical microscopy utilises a laser-trapped dielectric or metallic particle as a near-field scatterer to probe the high spatial frequency information from a sample. Scattering and depolarization by a trapped particle in an evanescent wave are two important issues in such an imaging system. These two issues are addressed in this paper. The strength of scattered evanescent waves was measured for particles of different sizes (0.1 μm to 2 μm in diameter) and different materials (polystyrene, gold and silver). It has been found that the signal strength of scattered evanescent waves increases appreciably with the size of a particle. As a result, image contrast is improved significantly with laser-trapped metallic particles of large size. It has also been found that the depolarization of scattered evanescent waves under s polarised illumination is stronger than that under p polarized beam illumination, and that image contrast of the evanescent wave interference pattern can be improved by a factor of 3 with a parallel analyser under s polarized beam illumination. This result suggests that less depolarized scattered evanescent photons carry more information of an object and should be utilised for the imaging in particle-trapped near-field scanning optical microscopy.

Key words: laser trapping laser scanning imaging, near-field microscopy, Mie scattering, biophotonics.

1. INTRODUCTION

Particle-trapped near-field scanning optical microscopy utilises a laser-trapped dielectric or metallic particle as a near-field scatterer to probe the high spatial frequency information from a sample [1]. Compared with other types of probes used in near-field microscopy, a probe produced by a trapped particle has a number of advantages including high resolution (which is mainly determined by the contacting part of a laser-trapped particle), improved image contrast (which can be controlled by the scattering properties of a trapped particle), high signal-to-noise ratio (which results from the use of a high numerical aperture objective), and optically remote control (which allows the imaging system suitable for biological imaging). The use of a trapped metallic particle [2-4] can enhance transverse trapping force, leading to high scanning speed in near-field imaging. In addition, scattering efficiency can be enhanced using a trapped metallic particle due to high reflection and surface plasmon excitation, which results in high contrast and high signal-to-noise ratio in near-field imaging.

The rapid development of particle-trapped near-field scanning optical microscopy requires comprehensive understanding of scattered evanescent waves with particles. Scattering and depolarization of evanescent waves by a trapped particle are two important issues in such an imaging system. The strength of scattered evanescent waves was measured for particles of different sizes (0.1 μm to 2 μm in diameter) and different materials (polystyrene, gold and silver) [5, 6]. It has been found that the signal strength of scattered evanescent waves increases appreciably with the size of a particle. As a result, image contrast is improved significantly with laser-trapped metallic particles of large sizes. The effect of depolarisation of scattered evanescent waves plays a significant role in particle-trapped near-field microscopy. It has been found that the depolarization of scattered evanescent waves under s polarized illumination is stronger than that under p polarized beam illumination, and that image contrast of the evanescent wave interference pattern can be improved by a factor of 3 with a parallel analyser

under s polarized beam illumination [7]. This result suggests that less depolarized scattered evanescent photons carry more information of an object and should be utilised for the imaging in particle-trapped near-field scanning optical microscopy. The effect of scattering and depolarization on near-field imaging with a laser-trapped particle is discussed in this paper. The detail of the experimental setup has been explained in our previous papers [5-7].

2. EFFECT OF SCATTERING

Because the strength of scattered signal by a trapped gold particle is increased significantly [5], image contrast should be improved accordingly. This feature has been demonstrated by imaging the evanescent wave interference pattern [5]. In Fig. 1, images of the surface ($\lambda/4$) of a BK7 prism are shown. The incident laser for producing evanescent waves (He-Ne laser) was p polarized. In the case of using a confocal scanning microscope (Olympus: FluoView), no clear detail of the surface structure was observed (Fig. 1a), while it can be observed using a trapped particle (Figs. 1b and 1c). The contrast of the imaged structure is enhanced when a trapped gold particle was employed, as expected.

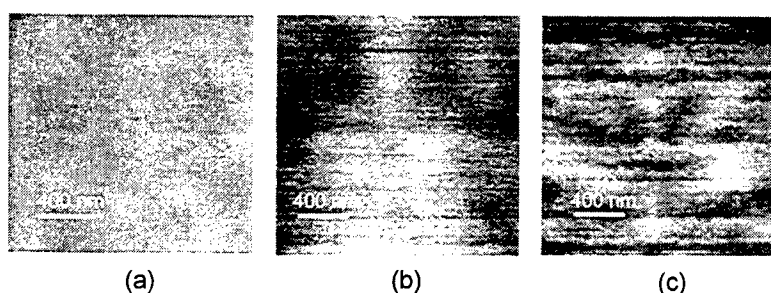


Fig.1 Images of the surface of a BK7 prism with a laser trapped particle of diameter 100 nm: (a) confocal image; (b) dielectric particle; (c) gold particle.

3. EFFECT OF DEPOLARIZATION

As has been pointed before, less depolarized photons scattered by a trapped particle carry more information of an object under inspection [7]. Therefore, it is very important to understand the dependence of the degree of polarization of the scattered signal. Fig. 2 shows the degree of polarization of the scattered evanescent wave by a dielectric particle as a function of the particle size [6]. The degree of polarization increases with the particle size, as may be expected from Mie scattering theory [8]. However, for a particle larger than 500 nm, the degree of polarization under p polarized illumination is higher than that under s polarized illumination; otherwise the situation is reversed.

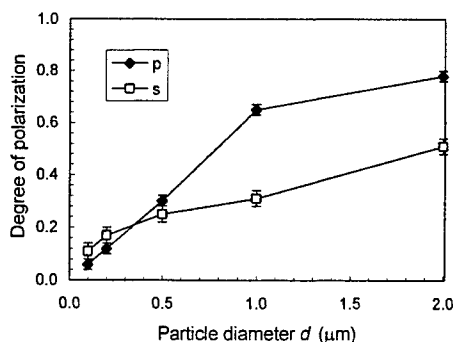


Fig. 2 Degree of polarization for a dielectric particle.

In Fig. 3, the measured dependence of the degree of polarization on the particle size for a trapped gold particle is depicted. Clearly, it is different from Fig. 2 in that the degree of polarization for a gold particle decreases with the particle size in particular for p polarized illumination. This phenomenon is not expected from Mie scattering theory [8]. It may be related to surface plasmon excitation associated with a small metallic particle, which enhances the evanescent wave near the trapped metallic particle [9].

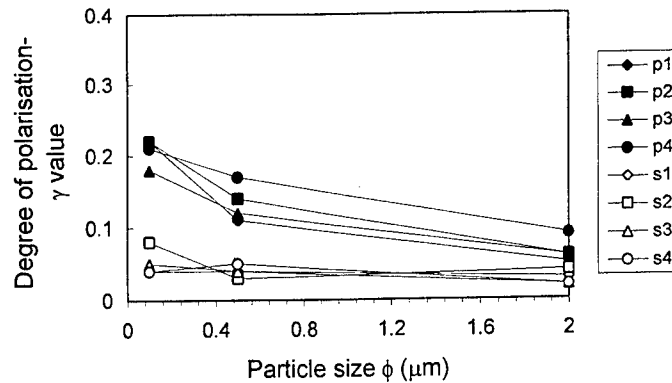


Fig. 3 Degree of polarization for a gold particle. p1, p2, p3, and p4 correspond to p polarized illumination at 4 different incident angles of the He-Ne laser. s1, s2, s3, and s4 correspond to s polarized illumination at 4 different incident angles of the He-Ne laser.

4. CONCLUSION

We have demonstrated in Fig. 1 that the enhanced signal leads to the improvement in image contrast in particular when a gold particle is used. It can be concluded from Figs. 2 and 3 that it is advantageous to use a small gold particle illuminated by a p polarized evanescent wave because scattered evanescent photons are less depolarized compared with the use of an s polarized beam. In the latter case, polarization gating [7] is needed to remove those highly depolarized photons. Further theoretical work based on the multiple-multipole method is needed to understand the different behaviour of the degree of polarization between dielectric (Fig. 2) and metallic (Fig. 3) particles.

ACKNOWLEDGEMENTS

The author thanks the Australian Research Council for its support. Special thanks are given to Mr. Puchun Ke who conducted the detailed experimental work on this topic at Victoria University.

REFERENCES

- [1] S. Kawata, Y. Inouye and T. Sugiura, *Jpn. J. Appl. Phys.* **33**, (1994), L1725.
- [2] P. Ke and Min Gu, *Appl. Opt.*, **38** (1999), 160.
- [3] P. Ke and Min Gu, *J. Modern Optics*, **45** (1998), 2159.
- [4] Min Gu, P. C Ke, and X. Gan, *Rev. Sci. Instrum.*, **68** (1997), 3666.
- [5] Min Gu and P. Ke, *Opt. Lett.*, **24** (1999), 74.
- [6] P. Ke and Min Gu, *Opt. Commun.*, **171** (1999), 205.
- [7] Min Gu and P. Ke, *Appl. Phys. Lett.*, **75** (1999), 175.
- [8] M. Born and E. Wolf, *Principles of Optics*, (Pergaman, New York, 1980).
- [9] B.J. Messinger, K. U. von Raben, R. K. Chang, and P. W. Barber, *Phys. Rev. B*, **24** (1981), 649.

Applications of optical tweezers and an integrated force measurement module for biomedical research

Jin-Wu Tsai¹, Bing-Yao Liao², Chun-Cheng Huang³, Wen-Liang Hwang², Da-Wei Wang²,
Arthur E. Chiou³, and Chi-Hung Lin^{1*}

¹Institute of Microbiology and Immunology, National Yang-Ming University, Taipei, Taiwan, ROC

²Institute of Information Science, Academia Sinica, Nankang, Taipei, Taiwan, ROC

³Institute of Electrical Engineering, National Dong Hwa University, Shoufeng, Hualien, Taiwan, ROC

ABSTRACT

Optical tweezers are useful for manipulating biological samples and measuring biological forces. In the present study, we have integrated a forward scatter analysis (FORSA) module into the "single-beam gradient force optical tweezers". The entire set-up was then incorporated onto an inverted microscope. In the FORSA module, a Helium-Neon probing laser was spotted (at a slightly out-of-focus way) onto the object being trapped by the infrared laser-based tweezers and generated a diffraction pattern. Images of the diffraction pattern were captured by a charge-coupled device (CCD), and digitized and processed by a computer. We demonstrated that tracking the "amplified" diffraction pattern was much more precise to determine the movement of the object within the trap than analyzing the minute motion of the object itself. Displacement of the object could then be translated into the force being applied by the tweezers. Also, using an algorithm developed in the lab, we were able to follow the movement of the scattering pattern at a temporal resolution close to video rate. We have used this system to investigate the binding force associated with cell-cell interactions and molecular interactions. In these studies, a cell was carefully positioned to make contact with another cell or a microparticle coated with proteins of interest by optical tweezers in a well-controlled manner. During these events, we noted a progressive increase of cell adhesion at the immediate early period (i.e., a few minutes after initial contact) of cell-cell interactions. Also, binding of a disintegrin, rhodostomin, and its mutant to the counterpart integrin on the cell surface could be assessed with great convenience and accuracy. Our results demonstrated that addition of the forward scatter analysis module to conventional optical tweezers provides an effective and convenient way for monitoring biological activities *in situ* and measuring changes of biological forces with precision.

Keywords: forward scattering, optical tweezers, adhesion, integrin, disintegrin

1. INTRODUCTION

Forces are involved in proper functioning of tissues and cells, in the processes ranging from muscle contraction (Huxley et al., 1969), morphogenesis during embryonic development (for review, see Schwarzbauer, 1997), vesicular transport across the cell, and alignment of chromosomes at metaphase plate and subsequent segregation (for review, see Warner et al.). In all these biological activities, forces must be adjusted to proper levels at the right time and the right subcellular loci. At molecular level, it was also clear that proteins such as molecular motors and polymerases could respond to changes in mechanical forces by altering their enzymatic functions (for review, see Khan et al., 1997). Forces associated with these biological events are typically very small, ranging from pico-Newtons (pN) to tens of pN, posing difficulties for quantification and close monitoring of their dynamic changes over time.

Traditionally, forces associated with cell activities were measured mainly by mechanical methods such as attaching fine needles or compliant probes to the motile component of the cell. Spring constants derived from these experiments were then used to calculate the magnitude of forces involved. However, data obtained from such approaches were sometimes varied and the experimental procedures were often time-consuming and/or invasive. Recent technical advances, primarily on atomic force microscopy (for review, see Lal and John, 1994) and laser tweezers (Ashkin et al, 1986), had made possible measuring biological forces at single-cell or molecular level (for review, see Mehta et al., 1999), in a more convenient and consistent way.

* Correspondence: Email: linch@ym.edu.tw; Telephone: 886-2-2826-7219; Fax: 886-2-2821-2880

Microscopic objects, including biological materials, could be remotely manipulated with tightly focused beams of infrared laser light (Ashkin et al, 1987). After focusing by high numerical aperture (N.A.) objectives, light pressure and optical gradient forces of optical tweezers could be used to hold, and therefore move sub-micrometer sized objects, even in the interior of the cells (Ashkin et al, 1990). Using such conventional "single-beam gradient radiation pressure laser traps", we were able to initiate interactions between living cells with accuracy and measure non-invasively an intracellular kinetic activity, called cortical F-actin flow, at a local lamella region in real time (Lin and Forscher, 1995). In addition to micromanipulation, optical tweezers could also be employed to biological force measurement (for review, see Ghislain et al, 1994). Typically, optical tweezers with a working wavelength in the optical window of biological material (700-1100 nm) could exert pN forces. The object trapped in optical tweezers might be viewed as being held in three-dimensional space by elastic springs. By calibrating the displacement with a known force applied to the trapped object, one could obtain the spring constants, and then derive the actual force being applied from these constants in the experiments. However, the range of motion within the trap was usually little (at sub-micron range), making displacement analysis and quantification of the trapped object a very difficult task.

Recent progress in video and digital image processing had made possible measurement of nanometer displacement under a microscope (Gelles et al., 1988; for reviews, see Khan and Sheetz, 1997 and Mehta et al., 1999). By amplifying the contrast of light microscopic images, Sheetz and his colleagues successfully observed in real time the diffraction images of cell structures 10 times smaller than the Raleigh resolution limit of 0.2 μm (Schnapp et al., 1988). In this paper, we have applied the forward-scattered light and used the diffraction images to extract information about motion of the object trapped in the tweezers at sub-nanometer level. This technique enabled us to characterize the immediate early events of cell-cell and molecular interactions with better precision in real time. The integration of a convenient force measurement module to optical tweezers holds great promise to extend the use of the tool, not only for noninvasive micromanipulation but also for mechanical assessment in cell biological studies.

2. EXPERIMENTAL CONFIGURATION

2.1. Optical tweezers

The experimental configuration is shown in Fig. 1. Essentially, a research-grade inverted light microscope was equipped with a single-beam gradient force optical trap (optical tweezers) and a force measurement module based on forward scatter analysis (FORSA). A 100mW CW single-mode diode laser at $830\pm 10\text{nm}$ was used as the trapping beam. The laser beam was collimated and circularized with a collimating lens and a pair of anamorphic prisms, and further expanded by a pair of lens to fill the back aperture of the objective. The lens L1 was mounted on a 3-dimension translation stage for lateral and axial position control of the trap in the specimen plane. The trapping beam was then directed to the objective via a dichroic mirror that reflected near infrared but passed UV/visible light. With careful choice of focal lengths of L1 and L2, lateral translation of L1 was equivalent to angular rotation of the laser beam at the back aperture of the objective, thus preventing power decrease when moving the trap. For trapping polystyrene beads ranging from 1 to 10 micrometer and cells, oil-immersion 100X (NA = 1.25) and 40X (NA = 1.0) objectives, respectively, were employed to bring the laser beam to a diffraction limited focus and produce gradient of light intensity serving as a stable 3-D trap.

For high-resolution position measurement of the bead, a beam from a 15mW Helium-Neon (He-Ne) laser was coupled to the light path of the tweezers serving as the probe. The probing beam was focused by the objective and directed to the same position but on a lower plane of the trapping area. A condenser of NA = 0.7 that originally functioned on the microscope to condense incoherent illumination collected the scattered light transmitted through the sample. When a microsphere was trapped, it acted as a microlens to refract the probing light and produced a high contrast light spot. This pattern was subsequently monitored by a charge-coupled device (CCD) after blocking the trapping beam through an IR filter. The signals were captured and digitized in video rate by an image capture card and analyzed by the program discussed later to find the center of the diffraction spot. We used an advanced fast tracking algorithm that was able to operate during frame capturing, so frame-by-frame analysis could be done on line (i.e., at video rate) with high accuracy.

The microscope system included a fully functional inverted microscope capable of bright field, phase contrast, differential interference contrast (DIC), and fluorescence imaging. Bright field and DIC images were detected by a CCD camera and fluorescence images by a silicon intensified target (SIT) camera. Data was recorded in videotapes or as digital files in the computer.

2.2. Tracking diffraction patterns in real time and force calibration

To measure the stiffness of the optical tweezers, a viscous force was generated by oscillatory motion of the specimen by a DC motor-driven stage at constant velocity. The tracking program tracked the diffraction pattern that reflected the bead position in the trap. Moving beads attached to a coverslip then determined the relationship between the diffraction pattern and bead position.

2.3. Cell Culture

A human embryo kidney cell line HEK-293T and a Chinese hamster ovary (CHO) cell line expressing integrin $\alpha_{\text{IIb}}\beta_3$, a gift from Dr. Yoshikazu Takada of the Scripps Research Institute, were used for cell-cell and rhodostomin-integrin interactions, respectively. Cells were grown in Dulbecco's modified Eagle medium (DMEM) supplemented with 10% fetal bovine serum, 0.1 mM non-essential amino acids, 2 mM L-glutamine, and 50 μ M gentamycin. HEK-293T and CHO cells were incubated in 8% and 5% CO₂, respectively, at 37 °C. Cells were removed from tissue culture dishes by brief treatment with trypsin-EDTA, and plated onto glass coverslips coated with 0.2mg/ml 70kD poly-L-lysine for 1 hr at 37 °C.

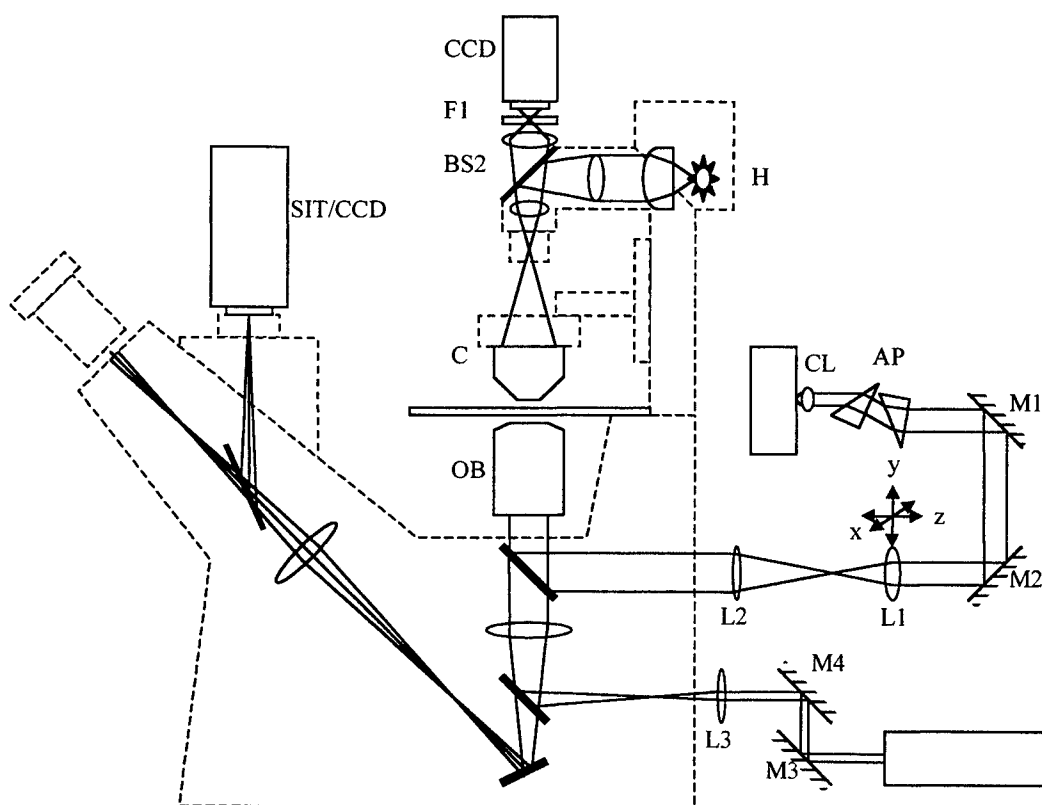


Fig. 1 A schematic illustration of the experimental configuration. The set-up consists of optical tweezers and a force measurement module incorporated into an inverted microscope. A diode laser and a Helium-Neon laser serve as a trapping and a probing beam, respectively. Optics include collimating lens CL and anamorphic prisms AP for collimating and circularizing the trapping beam; mirrors M1, M2, M3, and M4 for beam steering; lenses L1, L2, L3, and L4 for beam expansion and movement. A short-pass dichroic mirror DM1 and a beam splitter BS1 direct the beam to the objective OB and transmit the incoherent illumination to the imaging system. For collection and detection of the scattered light from the probing beam, the condenser C of the microscope is used for light collecting, followed by an IR filter F1 to block the trapping beam. The incoherent illumination for bright field and DIC imaging of the sample includes a halogen lamp H steered by a beam splitter BS2 and condensed by the condenser C, providing Kohler illumination in the specimen field. The fluorescence light path from the epi-fluorescence port is not shown for clarification.

2.4. GST-Rhodostomin Constructs and Protein Purification

The various rhodostomin constructs were kind gifts from Dr. S.J. Lo, Institute of Microbiology & Immunology, National Yang-Ming University, Taipei, Taiwan. Rhodostomin expression plasmids (pGST-RHO(RGD) and pGST-RHO(RGE)) were generated as previously described (Chang et al., 1999). Mutations were made by insertion alanine to amino acid position 48, 52 or 53 (Fig. 5). Synthesis of the GST-fusion proteins was induced in *Escherchia coli* JM109 by adding 0.1M isopropyl-1-thio- β -D-galactopyranoside (IPTG) to the culture medium. Protein in the bacterial lysate was purified by binding to glutathione sepharose 4B and eluted with 10mM reduced glutathione in 50 mM Tris-HCl, pH 8.0.

2.5. Bead Coating

The bead coating utilized physical hydrophobic adsorption. Polystyrene beads were incubated with 0.1 mg/ml of proteins of interest in phosphate buffered saline (PBS) for 1.5 hrs at room temperature and subsequently back coated with 2% bovine serum albumin (BSA) in PBS. The coated beads were kept in 4°C for use in no more than 1 week.

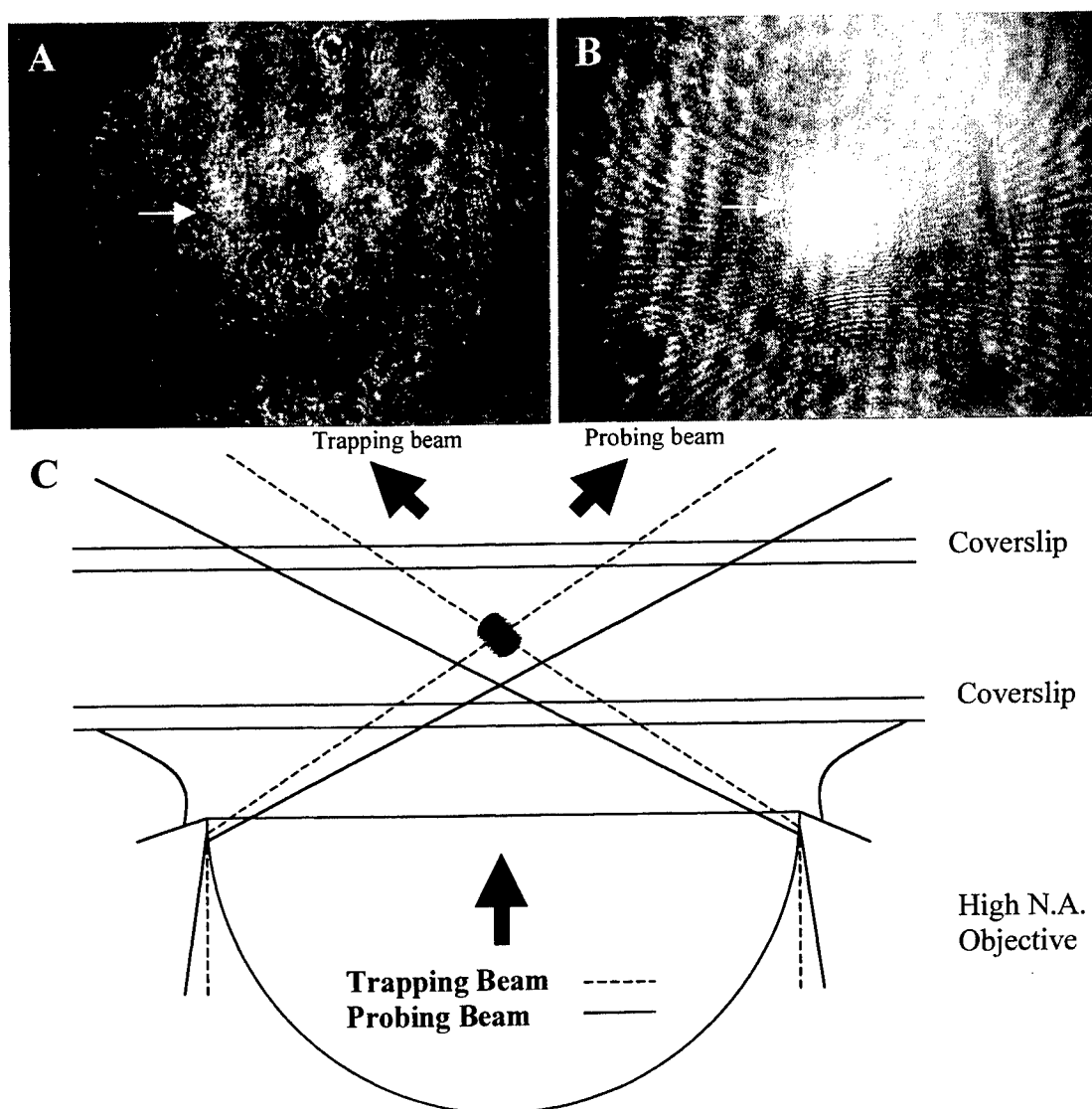


Fig. 2. Improving the image quality of diffraction patterns by addition of a probing Ne-Ne laser. (A) The probing beam was focused at a slightly lower plane than the trapping beam. Diffraction patterns of the trapped bead (arrows) generated by either the trapping (B) or probing (C) beam capture from the conjugated aperture planes of the microscope.

3. EXPERIMENTAL RESULTS

3.1. The image quality of scattering patterns was improved by the probing laser

Within the FORSA module (see Materials and Methods and Fig. 1), the probing He-Ne laser (*solid lines*, Fig. 2C) was directed into the light path of the optical tweezers (*dashed lines*, Fig. 2C). The probing beam was focused at a slightly lower plane than the trapping beam and generated a highly contrasted circular scattering pattern of the trapped bead (*arrow*, Fig. 2B) at the conjugated aperture plane of the microscope. Note the trapping beam also formed a ring-shaped scattering pattern (*arrow*, Fig. 2A), but the contrast was very low. In other words, the integrated probing beam dramatically improved the image quality of the scattering pattern and made possible precise tracking of the object movement within the tweezers (see below).

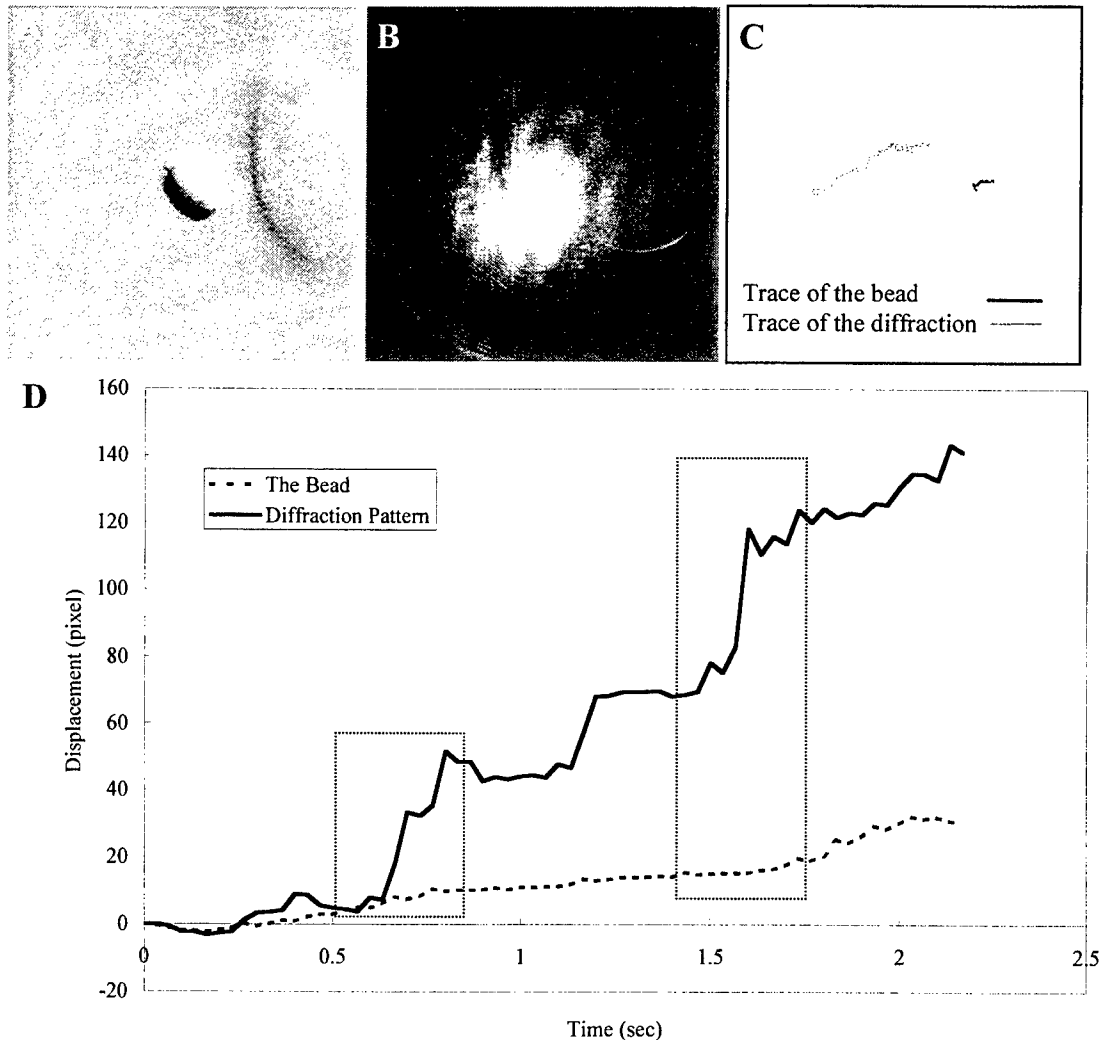


Fig. 3. The displacement of the trapped bead was amplified, and therefore could be better quantified, by following the movement of the diffraction spots. A $7.75\mu\text{m}$ bead coated with poly-L-lysine was put in contact with a NIH-3T3 cell for 30 sec. The cell was then pulled away from the bead trapped in the tweezers by moving the DC motor-driven microscope stage rightward. The bead (A) and its diffraction pattern (B) generated by the probing beam were simultaneously recorded by two CCD cameras; and their displacement traces (*black line*: bead; *gray line*: diffraction spot) were recorded in real time (C). (D) Detailed analysis of the displacement over time revealed two phases of impulsive advance (*arrows and arrowheads*) that were readily resolved by following the diffraction pattern (*gray trace*), but were hardly visible by monitoring the bead movement (*black trace*).

3.2. Tracing the trapped object with better accuracy and in real time

We then analyzed both the spatial and temporal resolution of the FORSA module. As shown in Fig. 3A, a 7.75 μm polystyrene bead coated with poly-L-lysine made contact with a NIH-3T3 cell for 30 sec and was then pulled away from the cell by moving the DC motor-driven stage rightward at a constant velocity of ~ 1 micron/sec. There was a membrane tether (not shown at this focal plane) linking the bead and the cell surface as previously described (Dai and Sheetz, 1995; for review, see Sheetz and Dai, 1997). The DIC image of the bead (Fig. 3A) and the diffraction pattern at the aperture plane (Fig. 3B) were separately monitored by two different CCD cameras simultaneously, and digitized and analyzed using a program developed in the lab (see Materials and Methods). Note this program enabled us to trace the displacement of the bead and the diffraction spot at a temporal resolution close to video rate (30 frame per second).

As shown in Fig. 3C, the motion of the bead within the tweezers (*black trace*) was greatly amplified by forward scatter analysis (*gray trace*). The displacements of both the bead and the diffraction spot were plotted as a function of time (Fig. 3D). Note detailed analysis of the diffraction trace revealed two obvious impulsive movements which could hardly be identified by following the bead motion (*dashed rectangles*). These two steps of abrupt advance might actually reflect the discontinuous stage motion driven by the DC-motor.

Using fluid flow assay, we estimated that the maximal force our experimental configuration could exert was ~ 12 pN on a 7.75- μm polystyrene bead, and the stiffness was ~ 3.8 pN/ μm (data not shown). Since trapping force exerted on the bead was directly proportional to the displacement of the bead in the tweezers, the FORSA module that gave a more sensitive measure of bead motion should provide a more accurate way for biological force measurement.

3.3. Applications in cell-cell interactions

We then employed optical tweezers to monitor the adhesion force during immediate early period (within just a few minutes) of cell-cell interactions. A HEK-293T cell was manipulated to make contact with another cell already attached to the

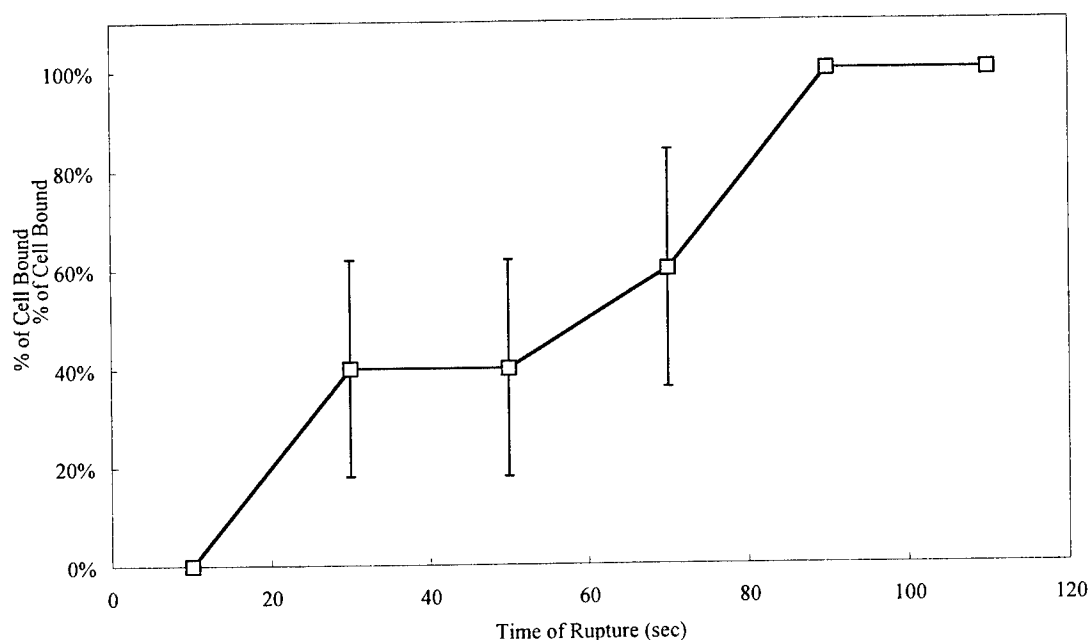


Fig. 4. Adhesion analysis on HEK-293T cells. A HEK-293T cell in the medium was put in contact with another cell tightly attached to the substrate for a period of time (time of rupture) before being pulled apart by optical tweezers exerting approximately 10 pN force. At least 25 pairs of interacting cells were tested in each condition. From this, the percentage of cell pairs that resisted the separation procedure was calculated. Mean \pm SE were shown.

substrate. The interacting cells were held for various periods of time (termed rupture of time, Fig. 4), and then pulled apart by a maximal force exerted by the optical tweezers (approximately 12 pN). At least 25 pairs of cells were tested in each condition. The percentages of cell pairs that resisted the pulling and remained adhered were plotted as a function of rupture of time (from 10 to 110 sec). As shown in Fig. 4, we found a progressive increase of cell adhesion, about 50% of the cell pairs were tightly adhered one minute after the contact and in two minutes none of the cell pairs could be pulled apart by ~12 pN force.

3.4. Applications in integrin-disintegrin interactions

In another set of experiments, we have used optical tweezers to analyze the binding between disintegrin and integrin proteins. To facilitate the force measurement, we placed a kind of disintegrins, the snake venom rhodostomin, and its mutants each containing single amino acid insertion at the peptide position of 48th, 52nd or 53rd amino acid, on 7.75 μ m polystyrene beads. These uni-sized beads provided a uniform pulling force for assessing the binding between integrin and disintegrin proteins. Beads coated with different rhodostomin constructs were held, and then interacted with CHO cells expressing the receptor integrin $\alpha_{IIb}\beta_3$ for different periods of time (rupture of time) before being pulled away with maximal trapping force. At least 20 beads were tested in each condition. As shown in Fig. 5, the percentage of beads that resisted pulling, i.e., remained bound to the cells, were plotted as a function of rupture of time (from 0 to 90 sec). Note beads coated with wild-type rhodostomin, containing the RGD sequence at position 49-51 (RGD), exerted the strongest binding to the

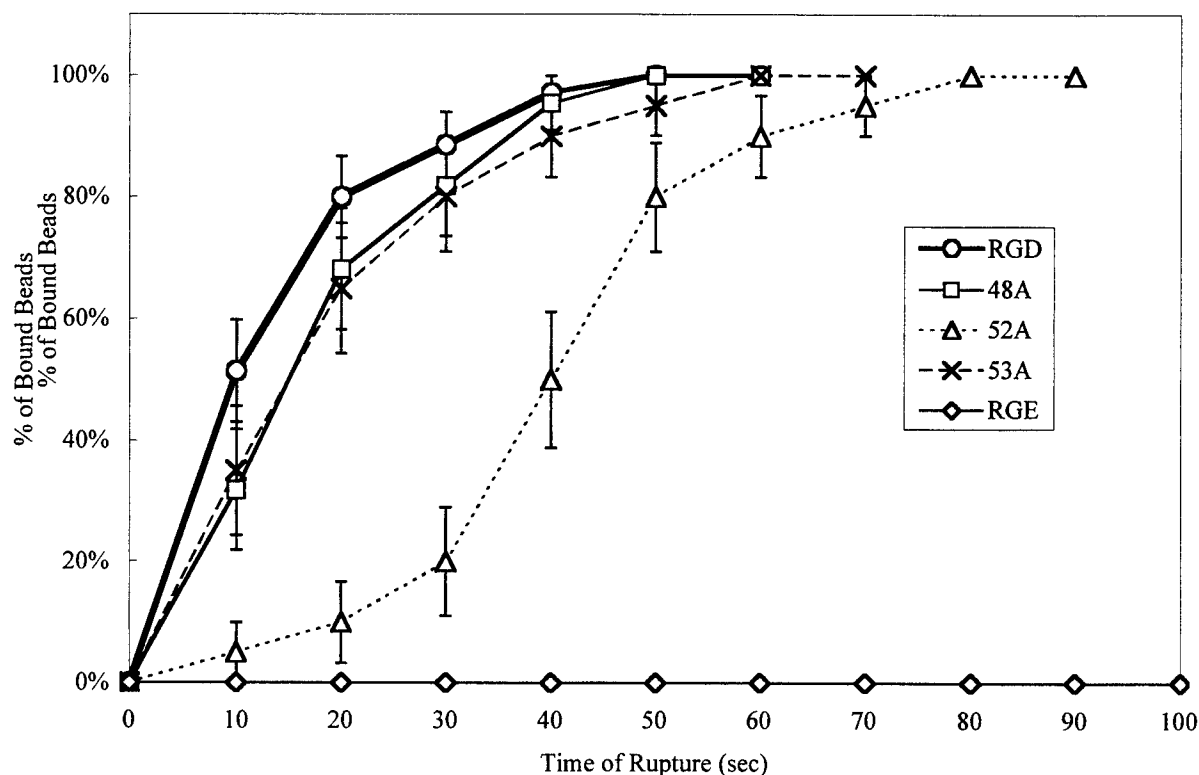


Fig. 5 Interactions between beads coated with different recombinant rhodostomin proteins and CHO cells steadily expressing integrin $\alpha_{IIb}\beta_3$. Beads were positioned and held to the cell surface for different periods of time (time of rupture) before being pulled away with optical tweezers exerting ~12 pN force. The proportion of beads that remained attached to the cell were then calculated (Mean \pm SE, $n = 20-30$ beads). Note beads coated with wild-type rhodostomin, containing the RGD sequence at position 49-51, exerted the strongest binding to the cell. Within 10 sec after initial contact, more than 50% of the beads resisted the separation procedure. An insertion of alanine at the position of 48th or 53rd amino acid (48A and 53A, respectively) slightly decreases the binding affinity whereas addition at the 52nd amino acid drastically decreased the binding and hence increased the time of rupture. Replacing the RGD sequence motif of the rhodostomin with the RGE sequence essentially abolishes the binding between rhodostomin and integrin; no significant binding was found even after 5 min of interactions.

cell. Within 10 sec after initial contact, more than 50% of the beads became tightly associated with the cell. Insertions of alanine at the 48th or 53rd amino acid (48A and 53A, respectively) only slightly affected the binding affinity whereas addition at the 52nd amino acid of rhodostomin (52A) significantly reduced the binding of the mutated rhodostomin to integrin $\alpha_{IIb}\beta_3$. These findings were in good agreement with biochemical results and/or cell-attachment experiments performed on different rhodostomin-coated substrates (data not shown, but see Chang et al., 1999). Also consistent with previous investigations (Chang et al., 1997, 1998, 1999), replacing RGD sequence motif of rhodostomin with RGE (RGE) essentially abolished the binding between the integrin and disintegrin protein.

4. SUMMARY AND CONCLUSION

In the present study, we have constructed a functional module that could be easily integrated into conventional optical tweezers (Fig. 1). Since the entire design was based on forward scattered light analysis, this system was dubbed the FORSA module. Several improvements were achieved by the addition of an auxiliary off-focus probing beam to the system. These include: (1) The contrast of diffraction patterns from the trapped object was greatly enhanced compared to the contrast generated by the trapping beam (Fig. 2). The better image quality obtained significantly increased the accuracy for displacement analysis. (2) The motion of the object within the tweezers, indicative of the force being applied, could be effectively amplified by analyzing the diffraction pattern (Fig. 3) which combined with (3) the fast tracking algorithm that monitored the central maximum of the scattered light at a temporal resolution close to video rate, made possible a new way of measuring biological forces with improved accuracy and in real time.

Although forward scatter analysis was successfully applied to optical tweezers for trapping and force measurement, the relationship between the extent of "off-focusing" of the probing beam and the size of bead being trapped have not yet been determined. It was clear from our experiences that the focusing position of the probing beam significantly influenced the quality of diffraction patterns. Also important is the numerical aperture (NA) of the objectives used for trapping and probing since the unscattered background is proportional to NA. Using beads of smaller sizes, for example requires a decrease in the NA of the objectives to optimize the contrast because increased unscattered light are produced by smaller beads.

The addition of a probing beam provided not only better contrast but also extra flexibility for incorporating different illumination methodologies. For example, we have applied an annular aperture to this system; the resulting donut-shaped probing beam appeared to greatly decrease the background of unscattered light and, as a result, enhanced signal to noise ratio (S/N ratio) of the system (Tsai et al., manuscript in preparation). Other kinds of modulation of the probing laser were also under investigation aiming to improve the S/N ratio and the sensitivity/accuracy for displacement analysis.

Using the FORSA algorithm developed in our lab, we were able to follow the movement of the diffraction spot "on-line" or close to video rate (~33 ms). Current temporal resolution was actually limited by our detection system, the CCD camera and NTSC analog format, which could be further improved to up to sub-nanosecond level by using a quadral photodiode for detection.

Two experimental biological systems were tested for optical tweezers applications. In cell adhesion experiments, we were able to monitor and resolve the progressive adhesion between cells held by optical tweezers (Fig. 4). This tool provided us with a unique way to make measurements on individually selected cells and within a very precise window of time (for example, the first few seconds after cell-cell or molecular contact), which is very difficult to analyze using other methodologies. Similar advantages could be extended to experiments addressing molecular interactions (Fig. 5). Different binding affinity between molecules containing single amino acid change could be readily identified and quantified by our system. More importantly, using micron-sized beads as probes also makes possible the measurement of receptor density on the cell surface during various physiological and pathological conditions (Tsai, Yi et al., manuscript in preparation). We believe that the new tool described in this report would help tremendously in on-line monitoring and/or analysis of biological activities *in situ*, such as initial events of cell-cell and ligand-receptor interactions, which might occur within seconds and are difficult to study using traditional biochemical assays. The FORSA system represents an intuitive and easy-to-install solution for trapping as well as force measurement with higher accuracy and convenience than direct visualization of the trapped objects themselves.

ACKNOWLEDGEMENTS

The authors gratefully acknowledge Dr. Pei-Hsi Tsao of National Taiwan University and Dr. Szecheng J. Lo of National Yang-Ming University for the inspiration and valuable comments, and Dr. Yoshikazu Takada of the Scripps Research Institute for providing the cell lines. Also thanks to Chih-Pei Chang and Yong-Shyang Yi for providing the wonderful rhodostomin system. Special thanks to Weber Chen for his superior technical assistance. The works were supported by grants from Frontier Medical Genomic Program, and Program for Promoting Academic Excellency, and National Science Council, NSC89-2318-B-010-002-M51 awarded to CHL.

REFERENCES

1. Ashkin, A., Dziedzic, J. M., Bjorkholm, J. E., and Chu, S., "Observation of a single-beam gradient force optical trap for dielectric particles," *Optics Lett.* **11**, pp. 288-290, 1986.
2. Ashkin, A., Dziedzic, J. M. and Yamane, T., "Optical trapping and manipulation of single cells using infrared laser beams" *Nature* **330**, pp. 769-771, 1987.
3. Ashkin, A., Schutze, K., Dziedzic, J. M., Euteneuer, U., and Schliwa M., "Force generation of organelle transport measured in vivo by an infrared laser trap," *Nature* **348**, pp. 346-348, 1990.
4. Chang H. H., Tsai W. J., and Lo S. J., "Glutathione S-transferase-rhodostomin fusion protein inhibits platelet aggregation and induces platelet shape change," *Toxicon*. **35**(2), pp. 195-204, 1997.
5. Chang H. H. and Lo S. J., "Full-spreading platelets induced by the recombinant rhodostomin are via binding to integrins and correlated with FAK phosphorylation," *Toxicon*. **36**(8), pp. 1087-99, 1998.
6. Chang H. H., Lin C. H., and Lo S. J., "Recombinant rhodostomin substrates induce transformation and active calcium oscillation in human platelets," *Experimental Cell Research* **250**(2), pp. 387-400, 1999.
7. Dai, J. and Sheetz, M. P., "Mechanical properties of neuronal growth cone membranes studied by tether formation with laser optical tweezers," *Biophys. J.* **68**, pp. 988-996, 1995.
8. Dai, J. and Sheetz, M. P., "Axon membrane flows from the growth cone to the cell body," *Cell* **83**, pp. 593-901, 1995.
9. Gelles J., Schnapp B. J., and Sheetz, M.P., "Tracking kinesin-driven movements with nanometre-scale precision," *Nature*. **331**(6155), pp. 450-453, 1988.
10. Ghismain, L. P., Switz, N. A., and Webb, W. W., "Measurement of small forces using an optical trap," *Rev. Sci. Instr.* **65**, pp. 2762-2768, 1994.
11. Huxley, H. E., "The mechanism of muscular contraction," *Science* **164**, pp. 1356-1366, 1969.
12. Khan, S., and Sheetz, M. P., "Force effects on biochemical kinetics," *Annual Review of Biochemistry* **66**, pp. 785-805, 1997.
13. Lal, R. and John. S., "A. Biological applications of atomic force microscopy," *Am. J. Physiol.* **266** (*Cell Physiol.* **35**), pp. C1-1-221, 1994.
14. Lin, C. H. and Forscher, P., "Growth cone advance is inversely proportional to retrograde F-actin flow," *Neuron* **14**, pp. 763-771, 1995.
15. Mehta, A. D., Rief, M., Spudich, J. A., Smith, D. A., and Simmons, R. M., "Single-molecule biomechanics with optical methods," *Science*. **283**(5408), pp. 1689-95, 1999.
16. Schnapp, B. J., Gelles, J., Sheetz, M. P., "Nanometer-scale measurements using video light microscopy," *Cell Motility & the Cytoskeleton*. **10**(1-2), pp. 47-53, 1988.
17. Schwarzbauer, J. E., "Cell migration: may the force be with you," *Current Biology*. **7**(5), pp. R292-4, 1997.
18. Sheetz, M. P. and Dai, J., "Modulation of membrane dynamics and cell motility by membrane tension," *Trends Cell Biol.* **6**, pp. 85-89, 1996.
19. Warner, F. D. and McIntosh, J. R. (eds) in *Cell Movement* Vol. 2 Liss, New York, 1989.
20. Yin, H., Wang, M. D., Svoboda, K., Landick, R., Block, S. M., Gelles, J., "Transcription against an applied force," *Science* **270**, pp. 1653-1657.

Quantitative comparison of single-beam gradient-force optical traps and dual-beam optical traps

Z. H. Huang, D. S. Mehta, H. C. Huang, C. F. Wang, and A. Chiou*
Department of Electrical Engineering, National Dong Hwa University,
1, Sec.2, Da Hsueh Rd. Shou-feng, Hualien, Taiwan, R.O.C.

ABSTRACT

In this paper, we compare the performance of the single beam gradient-force trap (SBGFT) and the counter propagating dual-beam trap (CPDBT) quantitatively in terms of three performance parameters, namely, the transverse trapping efficiency, the width of the stable trapping zone, and the axial stiffness. Ray-Optics Model (for optical trapping of Mie particles) was used to obtain the numerical results. In the SBGFT, the particle is trapped in the vicinity of the focal spot of a strongly focused (N.A. ~ 0.65 to 1.3) laser beam by gradient forces in both the transverse and the axial directions. In the CPDBT, with the two counter-propagating beams often mildly focused (N.A. < 0.6), the particle is confined transversely by the transverse gradient forces of the two beams, and stabilized axially by balancing the scattering forces from the two beams. Depending on the separation between the two beam waists, there can be more than one stable trapping zones in the CPDBT. Qualitatively, one obvious key advantage of SBGFT is that it is very simple to implement. In contrast, the CPDBT requires precise alignment of the two beams. The latter, however, allows longer working distance and offers more degrees of freedom. The theoretical values of the aforementioned performance parameters for the CPDBT vary over a wide range because they depend on the distance between two beam waists. This extra degree of freedom in the CPDBT allows us to trade off one performance parameter against the others. We have also measured these performance parameters experimentally to verify the general trend predicted by the theoretical model.

Keywords: Single-beam gradient force trap (SBGFT), counter-propagating dual-beam trap (CPDBT), transverse trapping efficiency, axial stiffness, stable trapping zone.

*Correspondence: E-mail: aechiou@mail.ndhu.edu.tw; Tel: 886-38-662-500, Fax: 886-38-662-300.

1. INTRODUCTION

Optical trapping and manipulation of micro-particles using the radiation pressure of counter-propagating laser beams was first discovered by Ashkin in 1970¹. In 1986 Ashkin et al² demonstrated the optical trapping of dielectric particles using a single beam gradient force trap (or the so-called "optical tweezers"). Since then both experimental configurations, i.e., the single-beam gradient-force trap (SBGFT) and the counter-propagating dual-beam trap (CPDBT) have been applied for many applications in the field of biological and biomedical sciences³⁻⁷, as well as in physics⁸⁻²⁰. Optical traps are often characterized by the trapping force (or the trapping efficiency) in the transverse and the axial directions, and the size of the stable trapping zone. In this paper, we compare the performance of the SBGFT and the CPDBT quantitatively in terms of three performance parameters, namely, the transverse trapping efficiency, the width of the stable trapping zone, and the axial stiffness. Theoretical results were obtained for both configurations using the Ray-Optics model. The experimental results for maximum transverse trapping efficiency of the CPDBT are compared with the corresponding theoretical results and a fair agreement was found. In the following section the Ray-Optics model (for optical trapping of Mie particles) is introduced. In Section 3, numerical results for maximum transverse trapping efficiency (Q_{tr}), the width of axial trapping zone, and the axial stiffness for SBGFT and CPDBT are compared. Description of the experimental technique for CPDBT and comparison of experimental results with the corresponding numerical results are presented in Section 4. Our main results are summarized in Section 5.

2. THEORETICAL ANALYSIS BY RAY-OPTICS MODEL

The Ray-Optics Model for predicting the forces acting on a particle in an optical trap was first proposed by Ashkin in 1992²¹. This model is applicable when the particle size is much larger than the wavelength of the trapping light. According to this model, reflection and refraction of light at the surface of the particle give rise to two types of forces on the particle. Reflection gives rise to scattering force, or radiation pressure, which is proportional to the optical intensity and points in the direction of propagation of the light beam. Refraction gives rise to a gradient force due to an optical intensity gradient and points towards the direction of increased intensity. Figure 1(a) shows the scattering and the gradient forces exerted by a Gaussian beam on a spherical particle (for the case where the refractive index of the particle is higher than that of the surrounding medium), along with the contribution of force components from two constituent pencils of ray (Ray A and Ray B). Figure 1(b) represents the geometry for calculating the force due to the scattering of a single incident ray of power P by a dielectric sphere. The total force acting on the particle is given by the following expression²¹

$$F_{tot} = F_s + iF_g$$

$$= \frac{nP}{c} [1 + R \cos 2\theta] + i \frac{nP}{c} R \sin 2\theta - \frac{nP}{c} T^2 \sum_{n=0}^{\infty} R^n e^{i(a+nb)} \quad (1)$$

where the scattering force F_s and the gradient force F_g acting on the particle are given by

$$F_s = \frac{nP}{c} \left\{ 1 + R \cos 2\theta - \frac{T^2 [\cos(2\theta - 2\theta_r) + R \cos 2\theta]}{1 + R^2 + 2R \cos 2\theta_r} \right\} \quad (2)$$

$$F_g = \frac{nP}{c} \left\{ R \sin 2\theta - \frac{T^2 [\sin(2\theta - 2\theta_r) + R \sin 2\theta]}{1 + R^2 + 2R \cos 2\theta_r} \right\} \quad (3)$$

In equations (2) and (3), n is the refractive index of the surrounding medium, P is the laser beam power, c is the speed of light, R is the reflectance of light at the surface of the particle, T is the transmittance of light, θ is the angle of incidence, and θ_r is the angle of refraction. The total force on the sphere (Fig. 1(b)) is the sum of the contributions due to the reflected ray of power PR and infinite number of emergent refracted rays of successively decreasing power PT^2 , PT^2R , ..., PT^2R^n , ...²¹. The total scattering force F_s , the gradient force F_g , and the absolute magnitude of the total force $F_{mag} = (F_s^2 + F_g^2)^{1/2}$ can be calculated as function of the angle of incidence θ using equations (1) and (2), and the corresponding trapping efficiencies Q_s , Q_g , and $Q_{mag} = (Q_s^2 + Q_g^2)^{1/2}$ can be calculated using the following expression²¹

$$F=Q(nP/c) \quad (4)$$

where Q represents the optical trapping efficiency and the quantity (nP/c) is the incident momentum per second of a ray of power P in a medium of refractive index n . The trapping force can be measured by balancing against a dragging force in a viscous fluid, and by using Stokes Law, $F_D=6\pi\eta rv$, where F_D is the dragging force, $\eta = 0.001025\text{Ns/m}^2$ is the viscosity of water, r is the radius of the sphere, and v is the critical velocity, which is defined as the velocity at which the sphere escapes from the optical trap due to the viscous drag.

3. NUMERICAL RESULTS

In this section the numerical results for aforementioned parameters are presented for both configurations. The parameters used in the calculations are, laser beam power, (10mW for SBGFT, and 5mW each for CPDBT), wavelength of the laser ($\lambda=532\text{nm}$), particle size ($15\mu\text{m}$), and surrounding refractive index ($n=1.33$). The total scattering force (F_s) and total gradient force (F_g) were computed using Eqs. (2) & (3) and the total trapping force on the micro-sphere was computed using Eq. (1). The transverse trapping efficiency (Q_{tr}) was evaluated from equation (4) using these data. The results are presented in the following sub-section.

3.1 Transverse trapping efficiency

The maximum transverse trapping efficiencies were calculated for SBGFT using objectives with NA varying from 1.25 to 0.65, and as a function of beam waist separation d , for CPDBT using a low numerical aperture objective ($NA=0.40$). The theoretical results are shown in Fig. 2. From this figure we see that the maximum transverse trapping efficiency (Q_{tr}) of CPDBT, at the beam waist separation $d=0$, is higher than that of the SBGFT and that Q_{tr} of CPDBT covers a wide range of values as compare to Q_{tr} of SBGFT. It can also be seen that the transverse trapping efficiency of the dielectric particle decreases on increasing the value of NA of the trapping objective in the case of SBGFT. Experimentally, we have also observed that the axial trapping force of the SBGFT is, in general, greater than that of the CPDBT. In the case of CPDBT a shorter beam waist separation, d , and a larger relative refractive index result in a stronger transverse confinement of the particle¹⁵.

3.2 The axial trapping zone width

Figure 3 shows the results of the calculations of axial trapping zone width for CPDBT and SBGFT. In the CPDBT, the particle is confined transversely to the common beam axis by the transverse gradient forces of two weakly focussed laser beams. The particle is stabilized axially at a location where the scattering forces of two beams balance each other and also at the two beam waists. Therefore the CPDBT has a larger trapping zone width than SBGFT. Besides, the trapping position along the axis of the beams can be easily adjusted, in the case of CPDBT, by changing the relative intensity of the two laser beams. On the other hand, in the SBGFT, the beam is strongly focussed to a diffraction-limited spot by a high-numerical aperture objective and a strong three-dimensional gradient-force trap is created in the vicinity of the focus point and hence has only one stable trapping zone. It can also be seen from the Fig.3 that the width of axial trapping zone decreases on increasing the value of NA of the objective in the case of single-beam trap. The trapping zone width is, for example, about $13\mu\text{m}$ in a single beam trap (with $NA=1.25$, laser power = 10mW, and particle size = $15\mu\text{m}$).

3.3 The axial stiffness

In a stable 3D-optical trap, the axial stiffness is an important parameter that dictates the resolution of the optical trap as a force-transducer for the measurement of force (typically on the order of pico-Newton). For small displacements from the center of the optical trap, the restoring force is proportional to displacement, i.e. the optical tweezers act like a linear spring obeying Hook's law. There are various methods to determine axial stiffness, such as the escape force method, the drag force method, and the equi-partition method¹³. We used drag force method to measure the axial stiffness for CPDBT and SBGFT. By applying a known viscous drag force, F , and measuring the displacement produced from the trap center, z , the axial stiffness can be determined by $F=\alpha z$; where α is the axial stiffness. The axial stiffness depends on various experimental parameters. We calculate the axial stiffness as a function of beam waist separation d , in the case of CPDBT, and for the values of NA (of the objective) varying from 0.65 to 1.25 in the case of SBGFT. Our results indicated that the SBGFT often provides a higher axial stiffness than the CPDBT.

The theoretical results of the axial stiffness for both cases are depicted in Fig.4. In the case of SBGFT, the axial stiffness increases on increasing the NA of the objective.

4. EXPERIMENTAL SETUP AND RESULTS FOR CPDBT

Figure 5 illustrates the basic experimental set-up for the CPDBT. A Nd:YAG laser (with a frequency doubler) of wavelength 532nm was used to generate the trapping beams. The laser light was expanded and collimated using a spatial filter and a beam expander (SF/BE) to a spot size of 1cm diameter. A set of half-wave ($\lambda/2$) plate and a polarizer was used for controlling the laser power and the polarization of the trapping beam. A relay lens of focal length 250mm was used to control the focus position of the trapping light. The expanded laser beam was divided by the polarizing beam splitter (PBS) and further directed by two beam splitters (BS) in counter-propagating directions along a common optical axis (as shown in Fig.5). Two microscope objectives (NA=0.45 each) were used to focus the counter propagating beams on the sample from the opposition directions. A glass capillary tube (with a square inner cross-section of 0.2 mm x 0.2 mm) filled with Polystyrene spheres of size 15 μ m in water was put in the focal point of the two counter propagating beams. The sample tube was mounted on a x-y-z motorized translation stage of 10 μ m/s velocity resolution, and 0.5 μ m position resolution. The laser beam power for trapping was 5mW each. A polarizer and a polarizing beam splitter (PBS) was used for changing the power ratio of two beams. An incoherent light source was used to illuminate the sample particles for imaging on a TV monitor using a CCD camera. The experimental arrangement on the right side of Fig. 5 shows the side view of the sample cell and the associated optics for observing the trapped particle from the top. Fig. 6 shows the image of a particle trapped by the CPDBT inside the capillary.

We measured the transverse trapping force by dragging the tube (with a particle trapped in the beam) in the direction parallel to the tube axis using the motorized translation stage. The drag force (or the equivalent trapping force) was calculated from the measured escape velocity and the Stokes law. The experimental results were compared with the theoretical results obtained from the Ray-Optics Model. Figure 7 shows a comparison of the experimental data (points in Fig.7) and the theoretical results (solid line in Fig. 7) for the maximum transverse trapping efficiency (Q_{tr})_{max} for the CPDBT. Although the general trend of the experimental results follows the theoretical curve, the detail differs. For example, the experimental values of Q_{tr} peak at beam waist separation $d = 14.2\mu$ m, while the corresponding theoretical values peak at beam waist separation $d = 0$, and distributed symmetrically around $d = 0$. The asymmetry (and the discrepancy) in the experimental values of Q_{tr} is probably due to the imperfection in the alignment. Moreover, the theoretical results for Q_{tr} were calculated particle trapped in the π_M -plane shown in Fig.2, whereas in actual practice, the particle may not be stabilized exactly in the π_M -plane; hence, the discrepancy may also be attributed to this factor.

5. SUMMARY

A theoretical analysis has been presented for CPDBT and SBGFT in terms of three performance parameters, namely, the transverse trapping efficiency, the width of the stable trapping zone, and the axial stiffness. Ray-Optics Model (for optical trapping of Mie particles) was used to obtain the theoretical results. The theoretical results for SBGFT and CPDBT are summarized in table I.

Table I Quantitative comparison of transverse trapping efficiency, axial trapping zone width, and axial stiffness for SBGFT and CPDBT.

	SBGFT				CPDBT
NA	1.25	0.95	0.85	0.65	0.4
Transverse Trapping Efficiency (Q_{tr})	0.281	0.375	0.392	0.415	From 0 - 0.431
Axial Trapping Zone Width (μ m)	13	18	19	26	From 0 - 86
Axial Stiffness (pN/ μ m)	0.5	0.385	0.285	0.140	From 0 - 0.314

Each of the two experimental configurations has its own merit. The values of the three performance parameters for the CPDBT vary over a wide range because they depend on the separation between the two beam waists. This extra degree of freedom in the CPDBT allows us to trade off one performance parameter against the others. We have also measured experimentally the maximum transverse trapping efficiency (Q_{tr})_{max} in the case of CPDBT and compared with the corresponding theoretical results. The experimental data follow the general trend predicted by the theory.

ACKNOWLEDGEMENT

This project is supported by the National Science Council, Taiwan, under the Research Grant #NSC87-2112-M-259-002.

REFERENCES

1. A. Ashkin, "Acceleration and trapping of particles by radiation pressure", *Phys. Rev. Lett.* **24**, pp. 156-159 1970.
2. A. Ashkin, J. Dziedzic, J. Bjorkholm, S. Chu, "Observation of a single-beam gradient force optical trap for dielectric particles", *Opt. Lett.* **11**, pp. 288-290, 1986.
3. S. Sato, H. Inaba, "Optical trapping and manipulation of microscopic particles and biological cells by laser beams", *Opt. Quant. Electron.*, **28**, pp. 1-16, 1996.
4. A. Ashkin, J. M. Dziedzic, and T. Yamane, "Optical trapping and manipulation of single cells using infrared laser beams", *Nature* **330**, pp. 769-771, 1987.
5. K. Svoboda, S. M. Block, "Biological applications of optical forces", *Annu. Rev. Biophys. Biomol. Struct.* **23**, pp.247-285, 1994.
6. J. T. Finer, R. M. Simmons, and J. A. Spudich, "Single myosin molecule mechanics: piconewton forces and nanometer steps", *Nature* **368**, pp. 113-119, 1994.
7. C. M. Coppin, J. T. Finer, J. A. Spudich, and R. D. Vale, "Detection of sub-8-nm movements of kinesin by high-resolution optical-trap microscopy", *Proc. Natl. Acad. Sci. U.S.A.* **93**, pp. 1913-1917, 1996.
8. L. Malmqvist, and H. M. Hertz, "Trapped particle optical microscopy", *Opt. Comm.* **94**, pp.19-24, 1992.
9. L. Ghislain, W. Webb, "Scanning-force microscope based on an optical trap", *Opt. Lett.* **18**, pp.1678-1681, 1993.
10. S. Kawata, Y. Inouye, and T. Suguira, "Near-field scanning optical microscope with a laser trapped probe", *Jpn. J. Appl. Phys.* **33**, pp. L1725-L1727, 1994.
11. L. Malmqvist, M. Hertz, "Two-color trapped-particle optical microscopy", *Opt. Lett.* **19**, pp. 853-855, 1994.
12. M. E. J. Friese, H. Robinsztein-Dunlop, N. R. Heckenberg, and E. W. Dearden, "Determination of the force constant of a single beam gradient force trap by measurement of backscattered light", *Appl. Opt.* **35**, pp.7112-7116, 1996.
13. K. Visscher, S. P. Gross, and S. M. Block, "Construction of multiple-beam optical traps with nanometer resolution position sensing", *IEEE J. of Selected Topics in Quant. Electr.* **2**, Pp. 1066-1076, 1996.
14. T. Suguira, T. Okada, Y. Inouye, O. Nakamura, S. Kawata, "Gold-bead scanning near-field optical microscope with laser force position control", *Opt. Lett.* **22**, pp.1663-1665, 1997.
15. E. Sidick, S. D. Collins, and A. Knoesen, "Trapping forces in a multiple-beam fiber-optic trap", *Appl. Opt.* **36**, pp. 6423-6433, 1997.
16. E. Fallman, and O. Axner, "Design for fully steerable dual-trap optical tweezers", *Appl. Opt.* **36**, pp. 2107-2113, 1997.
17. M. Gu, P. C. Ke, "Image enhancement in near-field scanning optical microscopy with laser trapped metallic particles", *Opt. Lett.* **24**, pp. 74-76, 1999.
18. P. C. Ke, and M. Gu, "Characterization of trapping force on metallic Mie particles", *Appl. Opt.* **38**, pp.160-167, 1999.
19. M. E. J. Friese, A. G. Truscott, H. Rubinsztein-Dunlop, N. R. Heckenberg, "Three-dimensional imaging with optical tweezers", *Appl. Opt.* **38**, pp. 6597-6603, 1999.
20. P. Zema'nek, A. Jonas, L. Sramek, M. Liska, "Optical trapping of nanoparticles and microparticles by a Gaussian standing wave", *Opt. Lett.* **24**, pp. 1448-1450, 1999.
21. A. Ashkin, "Forces of a single-beam gradient laser trap on a dielectric sphere in the ray optics regime", *Biophys. J.* **61**, pp. 569-582, 1992.

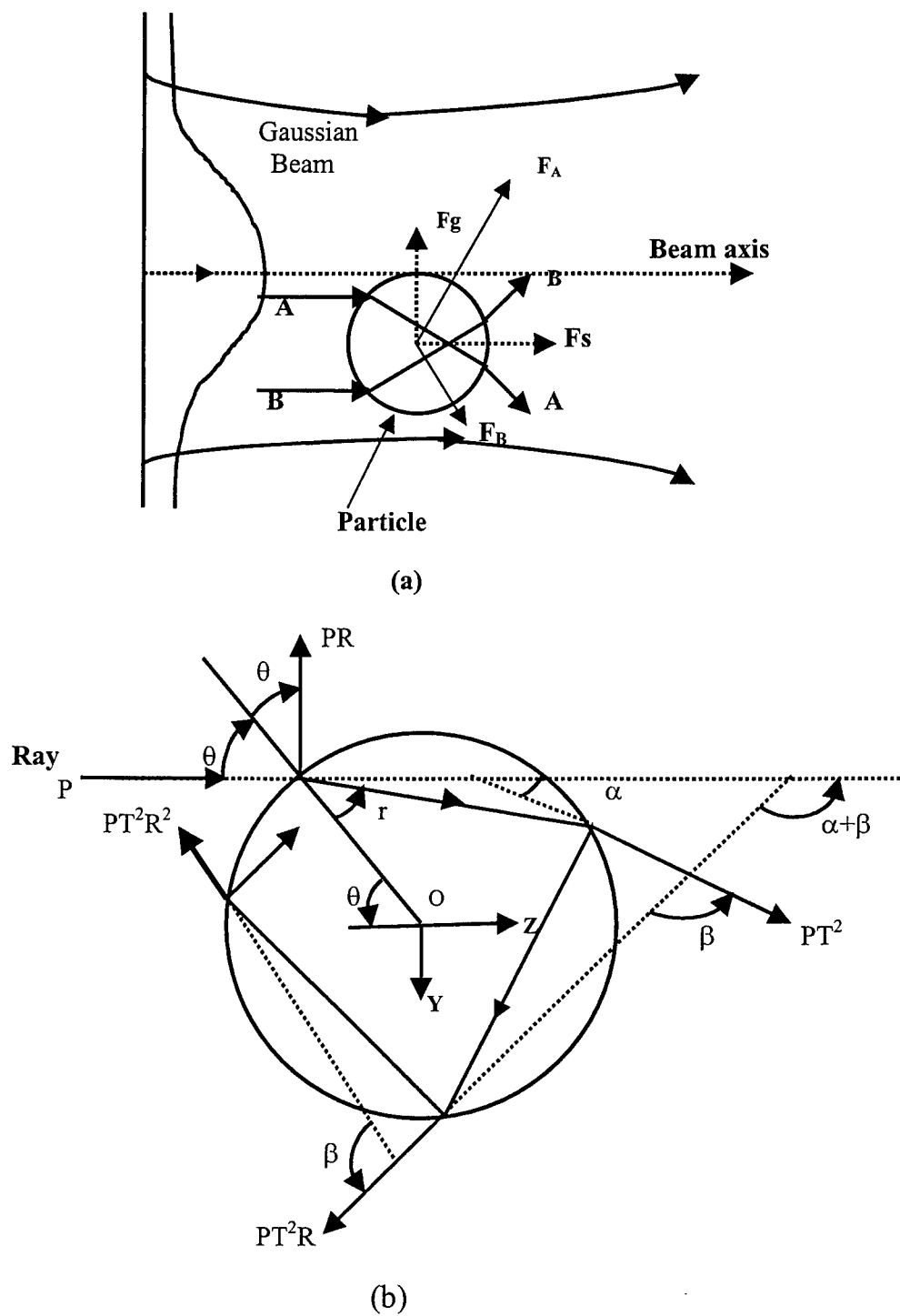


Fig. 1 (a) Geometry of Gaussian beam giving rise to the gradient force F_g and the scattering force F_s . (b) Geometry for calculating the force due to the scattering of a single incident ray of power P by a dielectric sphere.

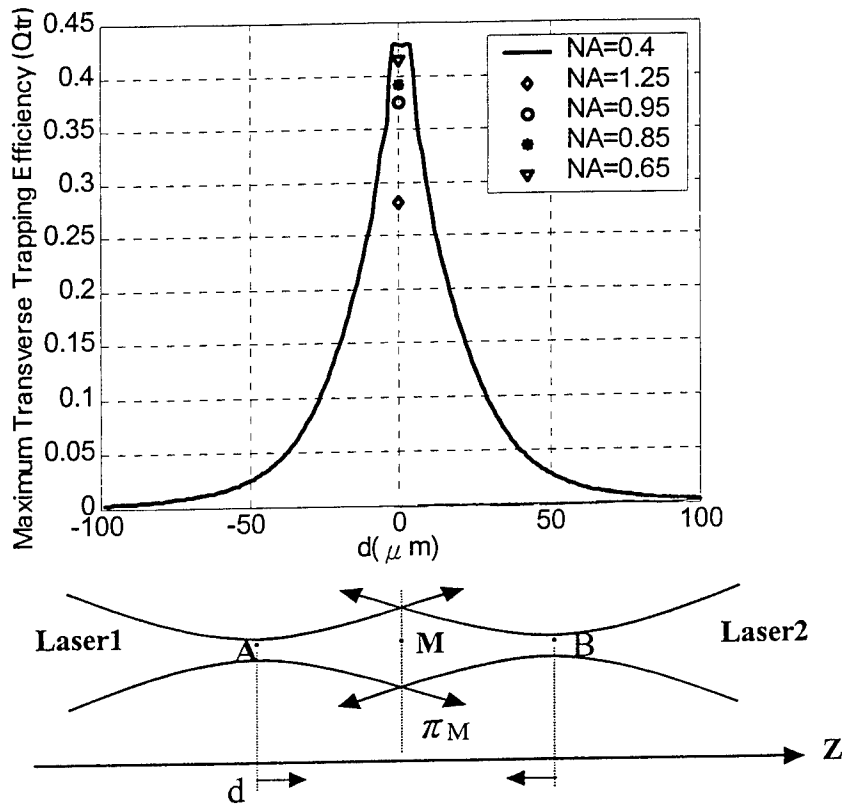


Fig. 2 Distribution of maximum transverse trapping efficiency (Q_{tr}) for CPDBT (solid line) as a function of the beam waist separation, and for SGBFT (dots) with various NAs.

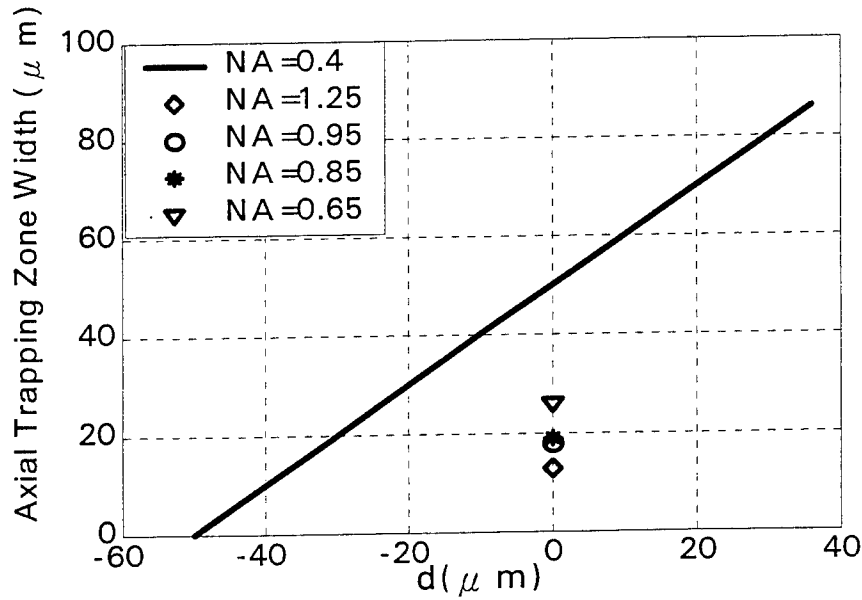


Fig. 3 Comparison of axial trapping zone width of CPDBT and SGBFT with respect to beam waist separation distance, d .

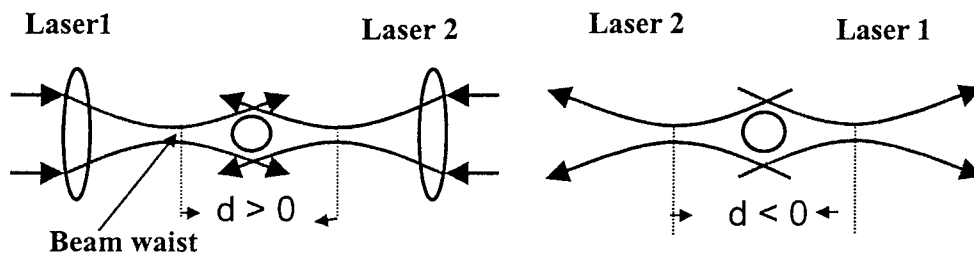
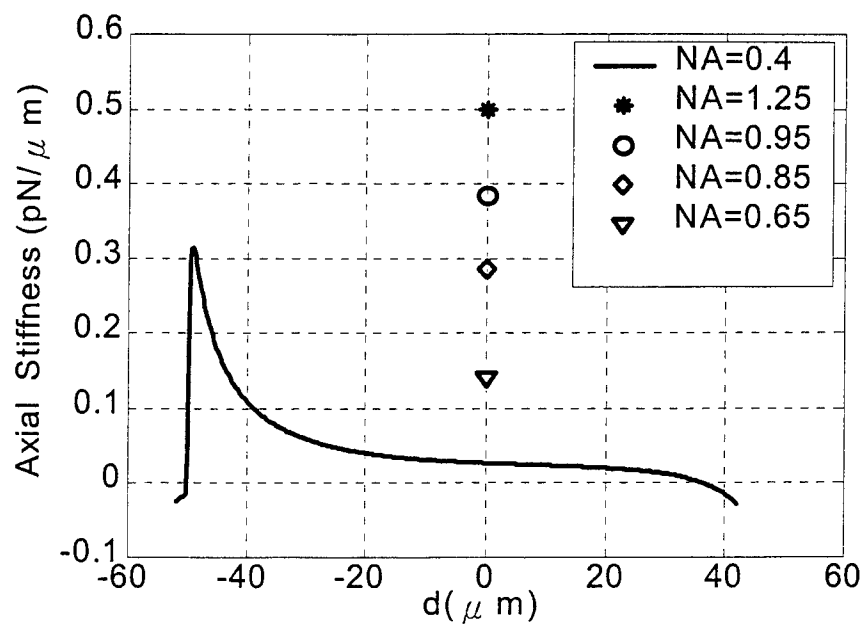


Fig. 4 Axial stiffness as a function of axial trapping position d for CPDBT (Solid line) and for SGBFT (symbols).

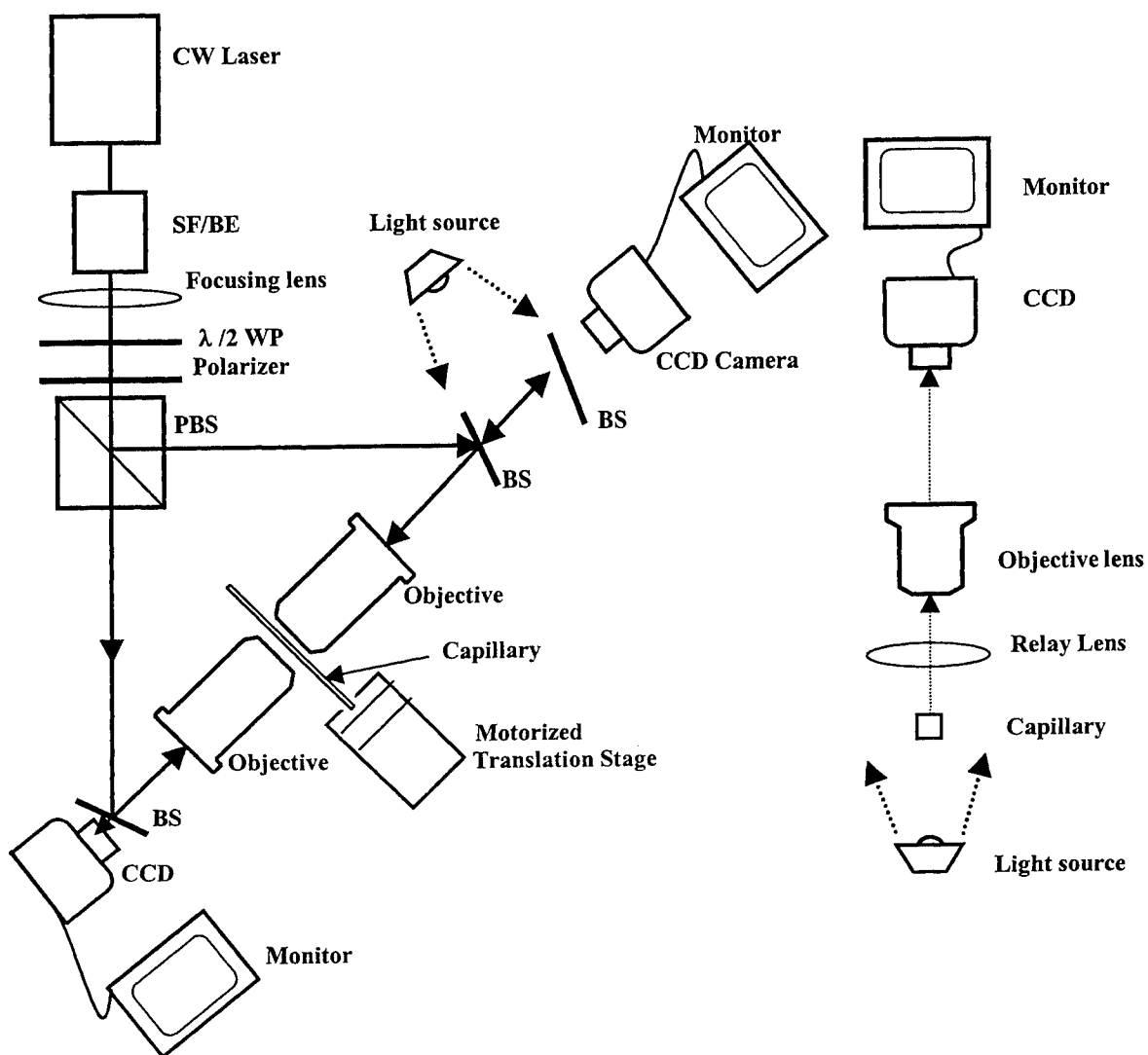


Fig. 5 Arrangement of the experimental setup for counter propagating dual beam trap (CPBDT).

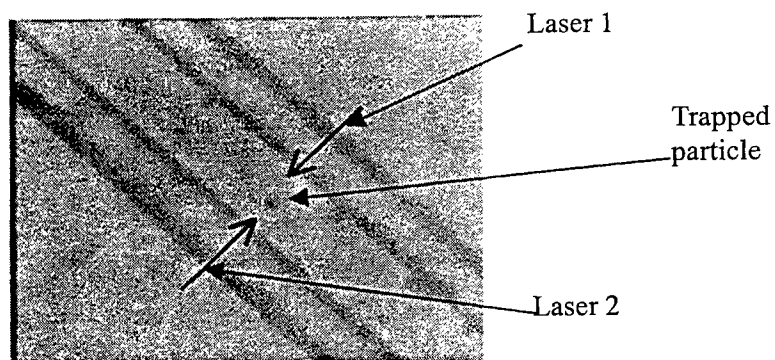


Fig. 6 Image of the trapped particle recorded by CCD camera under the bright field illumination.

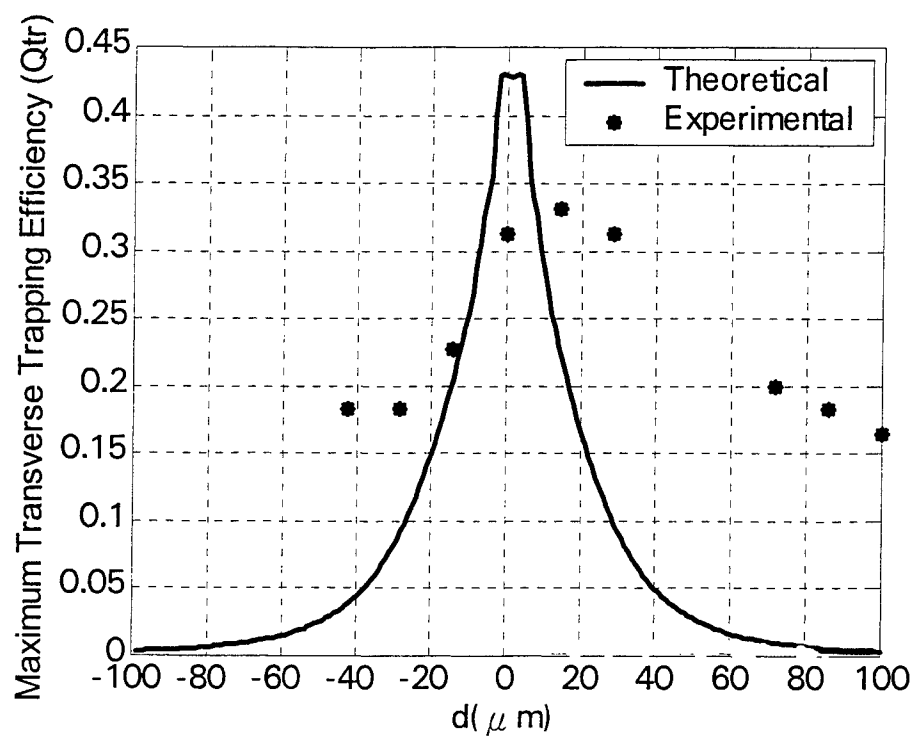


Fig. 7 Comparison of the experimental results with the theoretical results for transverse trapping efficiency for CPDBT.

Automation of an Optical Tweezers

Tseng-Ming Hsieh^a, Bo-Jui Chang^b, Long Hsu^{b*}

^a Institute of Electro-Optics , National Chiao-Tung University

^b Department of Electrophysics , National Chiao-Tung University

ABSTRACT

Optical tweezers is a newly developed instrument, which makes possible the manipulation of micro-optical particles under a microscope¹. In this paper, we present the automation of an optical tweezers which consists of a modified optical tweezers, equipped with two motorized actuators to deflect a 1W argon laser beam, and a computer control system including a joystick. The trapping of a single bead and a group of *lactoacidofilus* was shown, separately. With the aid of the joystick and two auxiliary cursors superimposed on the real-time image of a trapped bead, we demonstrated the simple and convenient operation of the automated optical tweezers. By steering the joystick and then pressing a button on it, we assign a new location for the trapped bead to move to. The increment of the motion, $0.04\mu m$ for a 20X objective, is negligible. With a fast computer for image processing, the manipulation of the trapped bead is smooth and accurate.

The automation of the optical tweezers is also programmable. This technique may be applied to accelerate the DNA hybridization in a gene chip². The combination of the modified optical tweezers with the computer control system provides a tool for precise manipulation of micro particles in many scientific fields.

Keywords: optical tweezers, DNA hybridization, gene chip

* Correspondence : E-mail: c2654@ms19.hinet.net, Telephone: +886-3-5712121 ext 56165, Fax: +886-3-5725230

1. INTRODUCTION

Optical tweezers is a powerful tool to manipulate a small particle by radiation force without physical contact. Since *Ashkin*³⁻⁵ first demonstrated the trapping and acceleration of particles by radiation pressure in 1970, the single-beam optical tweezers has been used in a variety of applications, especially in the fields of molecular biology and biotechnology. Substantially, an optical tweezers generates a piconewton restoring force due to radiation pressure and works like a spring over a range of a few hundreds of microns in diameter. It is, therefore, suitable for the manipulation of micrometer-sized particles and various biological objects such as viruses, bacteria, cells, and chromosomes⁶. In the last decade, the optical tweezers has been further utilized to measure the forces generated by a single myosin⁷ and a single kinesin⁸ separately. The smaller the object^{9,10} is, the stricter the requirement on the precise control of the optical tweezers becomes. Therefore, it is desired to have an automated optical tweezers.

The automated optical tweezers developed in this work consists of an optical system and a computer control system. It is capable of trapping and manipulating a single bead or a group of *lactocacidophilus*, separately. By steering a joystick and then pressing a button on it, we assign a new location for the trapped bead to move to. With a fast computer for image processing, the manipulation of the trapped bead is smooth, accurate, and programmable. We automatized this optical tweezers by deflecting the laser beam with two motorized actuators, which is controlled by the computer control system.

In this paper, we report the automation of an optical tweezers and the operation of the automated optical tweezers. This technique can be readily applied to the fields of biotech and biomedicine for precise manipulation and programmable control of small biological objects.

2. MODEL

Figure 1 shows the basic setup of an optical tweezers¹¹, which simply consists of a lens and a laser. The trapping force generated by the optical tweezers results from the interaction between the photons of the laser beam and the small object to be trapped. The mechanism of the trapping force is illustrated in Fig. 1, using a simple model of geometric ray optics¹². Consider a spherical and transparent bead, which is placed behind the focus of a lens. The lens focuses a collimated and normally incident laser beam. As the diverging beam passes through the bead, each ray refracts twice. The double-refraction of the ray changes the propagating direction and the photons' momenta of the ray¹³. The rate of change of the photons' momenta is indeed the force exerted by the bead to deflect the ray. According to *Newton's* third law of motion, an equal and opposite reaction force acts on the bead as well. The sum of the two reaction forces, arising from the pair of symmetrically diverging rays as drawn in Fig. 1, points toward the focus of the lens. To be more general, the net reaction force due to refraction always pulls the bead back to the point where the laser beam converges.

It can be shown that the converging point is an equilibrium position where the trapping force vanishes. Consequently, shifting the converging point leads the movement of the bead. The manipulation of the trapped object is performed simply

by tilting a 45° reflection mirror to deflect the incident angle of the collimated laser beam with respect to the lens. Traditionally, two 80-pitch fine screws are manually adjusted to tilt the mirror in a manual optical tweezers. In the automation of an optical tweezers in this work, we use two motorized actuators to tilt the mirror, which is controlled by a computer.

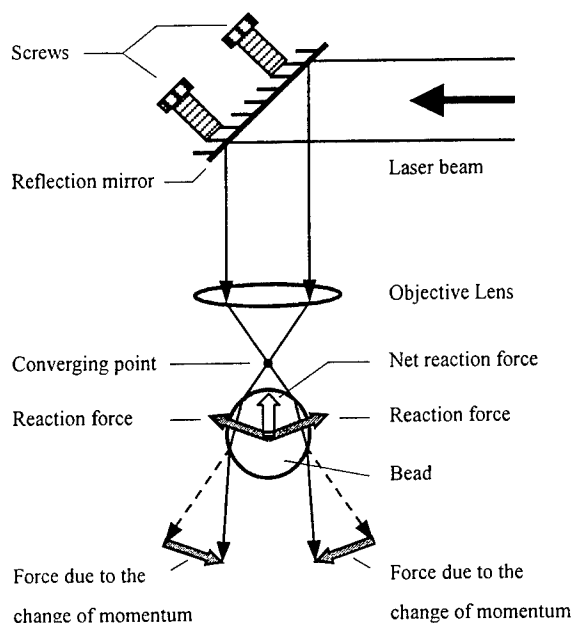


Fig. 1 The basic setup of an optical tweezers

3. SETUP

The automated optical tweezers system developed in this work can be classified into two sub-systems: namely, an optical system, including a modified optical tweezers and a monitoring and recording system, and a computer control system. Figure 2 shows the configuration of the automated optical tweezers and experimental setup.

3.1 OPTICAL SYSTEM

The optical system consists of a continuous-wave argon laser (LEXEL, 3500), a shutter, a periscope, two motorized actuators (Newport, 860A-1) and a motion controller (Newport, 860-C2), a beam expander, a dichroic mirror (CVI, AR1-1025-45-UNP), a 100X objective (Nikon, MSB01901, 100X/1.25, Oil) or a 20X objective (Nikon, MSB00201, 20X/0.40), a glass slide holder mounted on a XYZ stage, a condenser (Nikon, Abbe 1.25), a 300W halogen lamp, a filter (Newport, 10D20DM.5), a CCD camera, a monitor, and a VCR recorder.

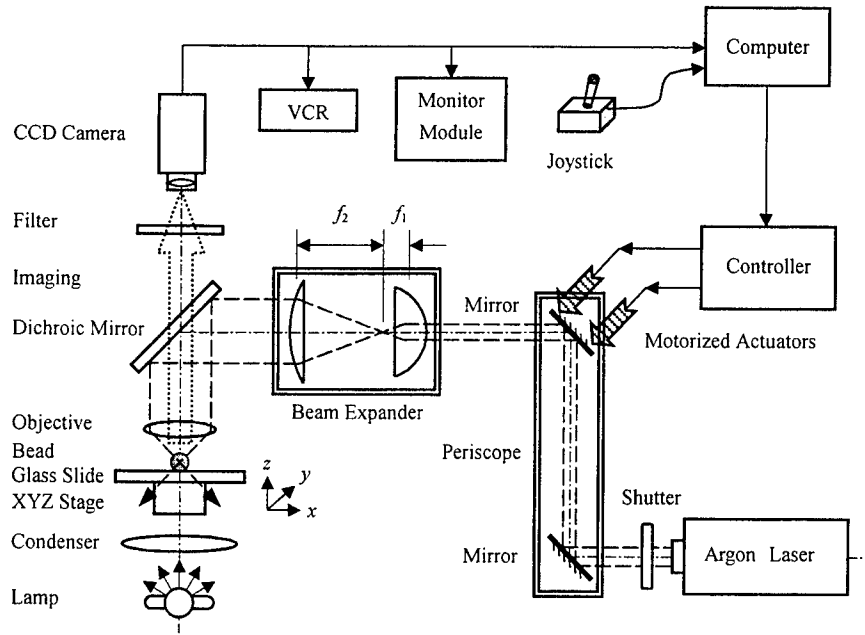


Fig. 2 The configuration of the automated optical tweezers and experimental setup

The argon laser is the light source for trapping. It outputs a laser beam up to $10W$ at two wavelengths of $488nm$ and $514nm$ with a beam waist of $3mm$ in diameter. Although harmful to most living objects due to high absorption, these two wavelengths are harmless to the beads ($10\mu m \sim 100\mu m$ -diameter spheres) and visible for demonstration. After passing through the shutter, the laser beam is raised by the periscope, a pair of two 45° reflection mirrors. Then, the laser beam is expanded by the beam expander, a pair of plano-convex lenses of focal lengths of $f_1 = 38.1mm$ (Newport, KPX079 AR.14) and $f_2 = 75.6mm$ (Newport, KPX088 AR.14), separately. Spaced the sum of their focal lengths apart, $f_1 + f_2$, these two lenses expand the beam from $3mm$ to $6mm$ in diameter so as to fill it in the entrance aperture of the objective. By adjusting the XYZ stage, we can move one of the beads, immersed in a drop of water upon the glass slide, to the focus of the beam. Thus, this bead is trapped. From now on, we shift the trapped bead by deflecting the laser beam without adjusting the XYZ stage. As shown in Fig. 2, this is achieved by tilting the top 45° reflection mirror of the periscope with the two motorized actuators. For reference, the actuator has an incremental motion capability to $\Delta l = 0.2\mu m$, giving an angular sensitivity to $\Delta \theta \cong 1 \times 10^{-5} rad.$ ($= 2arcsec$) in tilting a gimbal mount. The motion controller of the actuator provides a variable speed $v_{actuator}$ ranging from $50\mu m/sec$ to $250\mu m/sec$. It can be shown that the corresponding increment ΔL and travelling speed v_{trap} of the trapped bead on the glass slide are given by, respectively,

$$\Delta L(M) = \frac{160}{M} \frac{f_1}{f_2} \Delta \theta \quad (1)$$

and

$$v_{trap}(M) \cong \frac{v_{actuator}}{\Delta \ell} \Delta L(M), \quad (2)$$

where M is the magnification of the objective. Consequently, the increments ΔL are $0.04\mu m$ and $0.008\mu m$ for the 20X ($M = 20$) objective and the 100X ($M = 100$) objective, respectively. The traveling speed v_{trap} of the trapped bead may vary from $10\mu m/sec$ to $50\mu m/sec$ for the 20X objective and from $2\mu m/sec$ to $10\mu m/sec$ for the 100X objective. Because these increments ΔL are beyond the resolution of the microscope, the motion of the trap is expected to be smooth and accurate.

The monitoring and recording system is necessary during manipulating the trapped bead. It is coupled to the optical tweezers via the dichroic mirror between the beam expander and the objective. The dichroic mirror has a high reflectance of $R \geq 99\%$ for $488nm \leq \lambda \leq 515nm$ and a high transmittance otherwise. It reflects the expanded argon laser beam to the objective while transmits to the CCD camera most of the illumination light, $\lambda < 488nm$ and $\lambda > 515nm$, emitted from the halogen lamp. The illumination light is first converged by the condenser and then scattered by the beads and its surroundings. The image of the sample is formed by the objective and projected onto the CCD camera. The video signal from the CCD camera is then connected to a monitor for observation and a VCR for recording. To avoid the undesired argon light back scattered from the sample to the camera, we insert the additional filter (Newport, 10D20DM.5, $R \geq 99\%$ for $488nm \leq \lambda \leq 515nm$) in front of the CCD camera. This results in an image with a reddish background and a bright spot, as will be shown in Fig. 3 and Fig. 4 in section 4. At this stage, the optical tweezers is semi-automatic; we need to push the buttons on the motion controller to start and stop the actuators.

3.2 COMPUTER CONTROL SYSTEM

In order to control the actuators automatically, we further setup a computer control system to regulate the motion controller. This computer control system consists of a personal computer (Pentium II 333MHz CPU, 64Mb SDRAM), an image acquisition board (National Instruments, IMAQ PCI-1408, variable scan rate 5 to 20 MHz), a graphical programming language (National Instruments, LabVIEW 5.0), a PC compatible joystick, and an analog-to-digital (A/D) converter card (National Instruments, Lab-PC+).

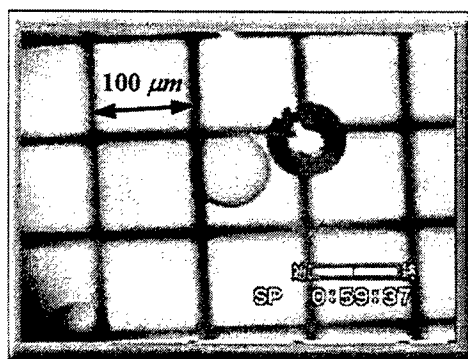
Firstly, we send the video signal of the sample image from the CCD camera to the personal computer via the image acquisition board. With a scanning rate up to 20 MHz and a typical size of 640×480 pixels for each frame, this image acquisition board transfers up to 30 monochromatic frames per second for real-time monitoring. Using LabVIEW5.0 for image acquisition, image processing, A/D data acquisition, and data analysis, we can easily locate the brightest spot in the image and display its coordinates on the computer screen.

Secondly, we use a PC compatible joystick to assign a destination for the trap to move to. This destination signal is sent, via the A/D converter card, to the computer and displayed on the screen as a striking crossed cursor. The distance between the cursor and the brightest spot is then calculated and converted into a voltage signal.

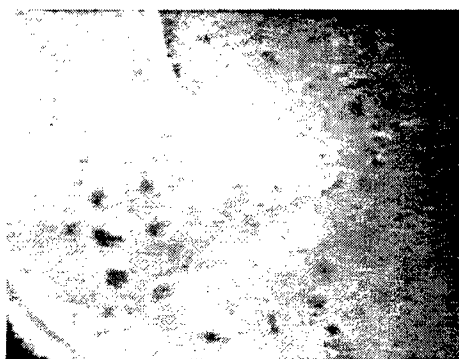
Lastly, this voltage signal is output, via the A/D converter card, to the motion controller to drive the actuators and deflect the angle of the laser beam. As a result, the trapped object will be moved to the new position and comes to a fully stop. Alternatively, a series of pre-assigned positions can be programmed into the computer in advance, which results in an automatic operation of the optical tweezers.

4. RESULTS AND DISCUSSION

Figure 3 shows two typical pictures of a trapped bead and a group of trapped *lactoacidophilus*, separately. The image of the beads and trap was formed by the 20X objective (Nikon, MSB00201, 20X/0.40). The brightest spot in the picture indicates the center of the trap produced by the argon laser with an output power of 1W, whereas all the other bright but smaller spots are noises due to reflection. The dark bead which is out of focus tightly occupies the center of the trap, leaving the bright bead aside. It can be seen that the diameter of the beads is approximately $75\mu\text{m}$, which is calibrated with respect to the $100\mu\text{m} \times 100\mu\text{m}$ grids coated on the slide (Nakamura, A05-1220 OM-500N). Similarly, the image of the *lactoacidophilus* was formed by the 100X objective (Nikon, MSB01901, 100X/1.25, Oil). However, the argon laser was operated at a lower output power of 0.1W. This is because the *lactoacidophilus*, only a few microns in length, is much smaller than the bead. Moreover, it is so small that a group of *lactoacidophilus* can be trapped at a time.



(a) Beads



(b) *Lactoacidophilus*

Fig. 3 The images of (a) a trapped bead and (b) a group of trapped *lactoacidophilus*

Figure 4 illustrates the operation of the automated optical tweezers developed in this work. We used the 20X objective to have a relatively large field of view for the smaller beads to travel within. Note that there are two auxiliary

crossed cursors superimposed on top of the image: namely, a target cursor and a joystick cursor. The target cursor is automatically fixed over the trapped bead at the brightest spot. The joystick cursor is free to move with the steering of the joystick until we push a stop button on the stick. Once the moving joystick cursor is fixed at a new location, the trapped bead along with its target cursor starts to shift toward this destination. The numerical values of the coordinates of the two cursors are real-time processed by the computer and displayed on the screen. Accordingly, the two motorized actuators are independently driven by the motion controller to tilt the 45° reflection mirror, which is controlled by the computer. The spindle of each actuator is controlled to travel at a speed varying from up to $250\mu\text{m/sec}$ to $50\mu\text{m/sec}$, depending on the instantaneous distance between the two cursors. We observed that the target cursor and the trapped bead always followed the joystick cursor straightly. The trapped bead moved faster for longer separation between the two cursors and slower for shorter separation between the two cursors, and stopped at the assigned location. Programmably, it could be steered around, too.

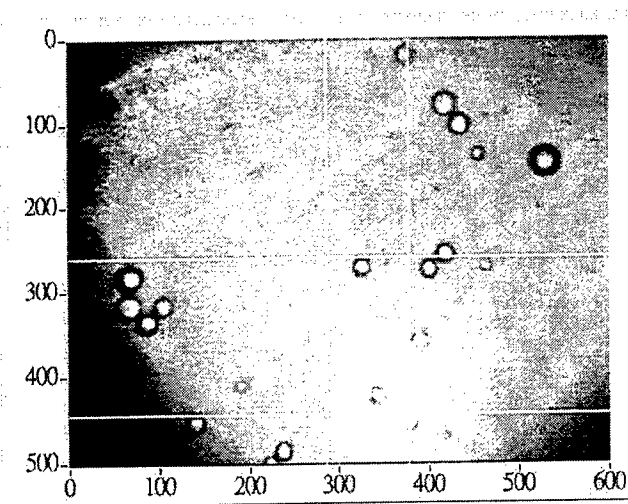


Fig. 4 The superposition of the image of a trapped bead and the two auxiliary cursors

Unfortunately, we also observed the bead pausing. Once in a while, the traveling bead encountered a very short pause and the real-time image on the computer screen was suspended simultaneously. Consequently, the observed travelling speed of the trapped bead was slower than the predicted according to Eq. (2). Nevertheless, we have improved this problem by deleting the sub-program for the real-time image display from the LabVIEW 5.0 main program. The manipulation of the trapped bead was smooth again, which was confirmed from another monitor and from the recording of the VCR. Therefore, we believe that the pause problem is due to insufficient computer speed. Using a fast computer with an efficient central processing unit (CPU) to enhance the image processing and real-time monitoring will solve this problem.

5. CONCLUSION

We automatized an optical tweezers for a precise and convenient manipulation of micrometer-sized objects. The operation of the automated optical tweezers, consisting of a modified optical tweezers, a monitoring and recording system, and a computer control system, is manual and programmable. In short, we used two motorized actuators to deflect the laser beam and manipulate the trapped objects, while using the computer control system along with a joystick to control the actuators. We showed the trapping of a single bead and a group of *lactoacidophilus*, separately, by this optical tweezers using an argon laser. With the aid of a joystick and two auxiliary cursors superimposed on the real-time image of the trapped bead, we also demonstrated the operation of the automated optical tweezers. The increments for the bead to shift at a time, $0.04\mu\text{m}$ for the 20X objective and $0.008\mu\text{m}$ for the 100X objective, are beyond the resolution of the microscope and thus negligible. The manipulation of the bead was fairly smooth and accurate except for some occasional pauses due to insufficient computer speed. We believe that the pause problem can be easily solved with a fast computer.

The automated optical tweezers is designed to meet the future demand for manipulating smaller and smaller objects¹⁴, especially in the fields of molecular biology and biotechnology¹⁵. This technique may be applied to accelerate the DNA hybridization in a DNA chip in our future work. The combination of a traditional optical tweezers with our computer control system also provides a tool for accurate manipulation of micro particles in many scientific fields.

6. ACKNOWLEDGMENTS

This paper was a result of significant input from many individuals of our laboratory. Much intellectual support from my dear friends also helped the development of the experiment. We particularly wish to thank the National Science Council for supporting this work in the Electro-Optics program. Grants number is NSC 89-2215-E-009-011.

7. REFERENCE

1. R. C. Gauthier, "Optical trapping: a tool to assist optical machining," *Optics & Laser Technology*, **29**(7), pp. 389-399, 1997.
2. M. J. O'Donnell-Maloney, C. L. Smith, and C. C. Cantor, "The development of microfabricated arrays for DNA sequencing and analysis," *Trends Biotech.*, **14**, pp. 401-407, 1996.
3. A. Ashkin, "Acceleration and trapping of particles by radiation pressure," *Phys. Rev. Lett.*, **24**, pp. 156-169, 1970.
4. A. Ashkin, "Optical levitation by radiation pressure," *Appl. Phys. Lett.*, **19**, pp. 283-285, 1971.
5. A. Ashkin, "Applications of laser radiation pressure," *Science*, **210**, pp. 1081-1088, 1980.
6. W. H. Wright, G. J. Sonek, Y. Tadir, and M. W. Berns, "Laser trapping in cell biology," *IEEE Journal of Quantum Electronics*, **26**(12), pp. 2148-2157, 1990.

7. J. T. Finer, R. M. Simmons, and J. A. Spudich, "Single myosin molecule mechanics: piconewton forces and nanometer steps," *Nature*, **368**, pp.113-119, 1994.
8. C. M. Coppin, D. W. Pierce, L. Hsu, and R. D. Vale, "The load dependence of kinesin's mechanical cycle," *Proc. Natl. Acad. Sci., USA*, **94**, pp. 8539-8544, 1997.
9. F. Julicher, and R. Bruinsma, "Motion of RNA polymerase along DNA : a stochastic model," *Biophysical Journal*, **74**, pp. 1169-1185, 1998.
10. M. D. Wand, M. J. Schnitzer, H. Yin, R. Landick, J. Gelles, and S. M. Block, "Force and velocity measured for single molecules of RNA polymerase," *Science*, **282**, pp. 902-907, 1998.
11. Michael P. Sheetz, "Methods in Cell Biology," *Laser Tweezers in Cell Biology*, **55**, pp.1-41, 1998.
12. W. H. Wright, G. J. Sonek, and M. W. Berns, "Parametric study of the forces on micro spheres held by optical tweezers," *Appl. Opt.*, **33**, pp. 1735-1748, 1994.
13. Y. Harada, and T. Asakura, "Radiation forces on a dielectric sphere in the Rayleigh scattering regime," *Opt. Comm.*, **124**, pp. 529-541, 1996.
14. E. Higurashi, H. Ukita, H. Tanaka, O. Ohgushi, "Optically induced rotation of anisotropic micro-objects fabricated by surface micro machining," *Appl.Phys. Lett.* **64**, pp. 25, 1994.
15. S. M. Block, inJ. K. Foskett, and S. Grinstein, "Noninvasive Technology in Cell Biology," New York: Wiley-Liss. *Mod. Rev. Cell Biol.* **9**, pp. 375-402, 1990.

Application of phase contrast microscopy to the study of marine micro-biota

Ming Chang Shih^a, Chang Ten Lian^a, and J. S. Hwang^b

^aInstitute of Opto-electronic Sciences, National Taiwan Ocean University

^bInstitute of Marine Biology, National Taiwan Ocean University

ABSTRACT

We present the observation of the activity of artemia, one of the popular marine micro-biota species, in free space by the application of Fourier optics imaging technique. The Fourier optic imaging system is consisted by a collimated laser beam source, a Fourier spatial filter, an non-coherent IR source, and a CCD imaging system. By recording the images of Artemia's motion in real life, we are able to study the fundamental patterns of artemia motion mechanism, and the response of the motion pattern to the variation of its environment. Characteristic patterns of artemia's motion, such as linear motion, spiral motion, and mating collision are observed. It is shown that the increasing of the environment temperature driving the motion of artemia's moving faster and more frequently, and still saves alive even at the environment temperature up to 38 C.

Keywords: Artemia, brine shrimp, Fourier optics imaging

1.1. Introduction

The life form of micro-biota is closely linked with the oceanic life. Algae and bacteria are primary food producer, and micro-biota are their predators. Micro-biota in turn is preyed by fishes, thus the status of micro-biota's living is known as an indicator of the marine life. It is important for us to know what the environmental perturbation and pollution might cause damage to the micro-biota living system, and the threatening to the ecological status of marine life. Since, most of the micro-biota is transparent, low contrast relative to their environment, and microscopically small; range in size from tens of micrometers to few millimeters, thus causing challenge in observing their living behavior in free space. J.R. Strickler, and J. S. Hwang had developed a Fourier optic imaging system which used a spatial filter to observe a phase object in long working distance(1-5), and showed that Fourier imaging technique is an effective approach to study the life motion of the tiny, transparent marine objects.

In this paper, we present the application of Fourier transform imaging system to study the activity of the Artemia in free space. Artemia known as the brine shrimp is in the phylum Arthropoda, class Crustacea. Artemia are zooplankton like Copepods and Daphnia, which are the primitive food source for the early stages of many fish and crustacean larvae (6). Since artemia is easily produced in the lab, and its response to the variation of environmental factors, such as temperature, light illumination, PH value and oxygen contain in the water can be repeatedly controlled in the experiments, artemia is an ideal sample of studying the micro-biota in marine life. In addition, the Fourier transform images is able to reveal more detailed features of artemia behavior in real life than by conventional imaging technique,

1.2. Experimental setup

The schematics of the Fourier optic system is shown in Fig 1, a collimated laser beam of plane-wave and uniform intensity is illuminating the objects S_0 which is optically transparent. The diffracted light from the object then pass through a Fourier transform lens L_1 , and is focused on the spatial filter. An high pass spatial frequency filter and the lens L_2 are used to inversely Fourier transform the diffracted pattern of the observed object and to image by the CCD.

The artemia life cycle begin by the hatching of dormant cysts, which are encased embryos that are metabolically inactive. The cysts can remain dormant for many years as long as they are kept dry and oxygen free. When the cysts are placed back into salt water they are re-hydrated and resume their development. The conditions for hatching artemia is :25 degrees C, salinity - 5 ppt (1.030 density), heavy continuous aeration, light - 2000 lux constant illumination, pH around 8. Good circulation is essential to keep the cysts in suspension. After 15 to 20 hours cyst bursts and the embryo leaves the shell. For the first few hours, the embryo hangs beneath the cyst shell, still enclosed in a hatching membrane. This is called the Umbrella stage, during this stage the nauplius completes its development and emerges as a free swimming nauplii.

Approximately 12 hours after hatch they molt into the second larval stage and they start filter feeding on articles of various

microalgae, bacteria, and detritus. The nauplii will grow and progress through 15 molts before reaching adulthood in at least a week. Since artemia are non-selective filter feeders, a wide range of food can be used, such as bread yeast, wheat flour, soybean powder, fish meal, and egg yolk.

For the observation of artemia motion in real life, we filter the adult artemia in valuable numbers out from the cysts in the hatching container, then put into the observation vessel which has the dimension of 12cmx5cmx15cm and is made by glass. The Fourier optic system is aligned with the collimated laser beam at 660 nm first, after a clear Fourier transform image is achieved, we cut off the incident of the alignment laser beam, and using an IR non-coherent light source to illuminate the objects in the vessel. In order to eliminate the imaging noise due to the diffraction caused by micro-alga or sediment in the water, instead of using a coherent laser source for illumination, we introduce an IR non-coherent collimated light source illuminating aside the vessel. Figure 2 shows the improvement of the Fourier transform image quality by using the IR non-coherent light source.

1.3. Results & Discussion

We study the motion patterns of artemia by the Fourier transform images recorded by the CCD and the PC based digital image acquisition system. Figure 3 shows a series of images of the continuous motion of the artemia. The pictures show that the basic driving mechanism of artemia forward motion is by swimming of the pair of its antennae which is also the sensing element to the variation of the environment. Figure 4 shows the most commonly seen spiral tracing of artemia motion, and shows that the direction of artemia's tail, named as postmaxillar region, is along its spiral trace, and that is the evidence of proving that the tail of artemia has the function of controlling its direction of motion, and the balancing of the body in swimming.

Since that mating behavior is important not only to the generation of artemia ecology of life but other marine species as well. Figure 5 shows the mating behavior of adult artemia. The mating collision time is measured by the recording time between the CCD images, and is estimated about the mill-seconds order. The observation shows that the probability of success second encounter is smaller than 2%. Since not all of the encountering are mating collision, certain ration of encountering are escaping that provides the evidence of the behavior of selection the mating partner.

Temperature is the key factor of effecting the marine life physically or mechanically. In our experiments of observing the response of artemia motion patterns by locally heating of its environment using high power IR irradiation. The temperature of the sea water can be heated from 18 °C to 38 °C at a temperature ramping of 0.5 C/minute. The results shows that there is not significant changes of the fundamental patterns of artemia's motion. However, it is found that the speed of motion does increase with the increasing of the temperature of its environment. In principle, the higher the temperature, the smaller the viscosity of the sea water is, and thus might cause artemia moving faster in the laminar flow. It might suggest that the effect of temperature to artemia motion behavior is mostly due to the change of mechanical property of the sea water. The artemia survives even at the environment temperature up to 38 C. This revealed that the artemia has wide tolerance to the variation of the temperature.

It is known that the pair of the antennae of artemia are important elements of sensing the perturbation of its environment. Marine biologists are interested of knowing the answer of how long is the limited distance of artemia's perception. Since the limitation of artemia perception might be closely related with its ecological domain size, and the interaction between the artemia. From the observation of artemia encountering, it is shown that the perception distance is about two to three times the length of artemia body.

1.4. Conclusion

As a conclusions, we shows the improvement of the Fourier transform microscopy technique by using a non-coherent IR source, and the application of this system in observing the behavior of artemia in real life. The Fundamental mechanism of the artemia's driving motion has been concluded as the swimming mechanism in a laminar flow, and the pair of antenna are the swimming arms. The mating encountering time is estimated in the order of mini-seconds, and the selectivity of mating partner has been observed. It is suggested that the effect of temperature to artemia is due to the change of the mechanical property, the reasonable answer might be the change of viscosity to effect the motion of artemia mechanically. Although, a 532 nm laser beam has been used to study the visual response of artemia to the illumination condition of the environment, particularly the spectrum response, there is no conclusion due to the lack of observation data, and further study is needed to conclude the facts.

ACKNOWLEDGEMENTS

The authors would like to thank professor J. R. Strickler, or his generous help to improve the optical system, and graduate student of professor J. S. Hwang for the help in hatching the artemia cysts. We acknowledge financial support by the Asia Pacific Research Foundation and National Science Council.

REFERENCES

1. Trager G. C., Hwang J. -S., and Strickler J. R. (1990). Barnacle suspension-feeding in variable flow. *Marine Biology*. Vol.105: 117-127.
2. Hwang J. -S., Turner J. T., Costello J. H., Coughlin D. J., and Strickler J. R. (1993). A cinematographic comparison of behavior by the calanoid copepod *Centropages hamatus*: Tethered versus free-swimming animals. *Journal of Experimental Marine Biology and Ecology*. Vol. 167: 277-288.
3. Hwang J. -S., Costello J. H., and Strickler J. R. (1994). Copepod grazing in a turbulent flow: elevated foraging behavior and habituation of escape responses. *Journal of Plankton Research*. Vol.16(5): 421-431.
4. Strickler J. R., and Hwang J. -S. (1998). Matched spatial filters in long working distance microscopy of phase objects. In Wu J. -L., Hwang P. -P., Wong G., Kim H., Cheng P. -C. (eds.) *Focus on Multidimensional Microscopy*. World Scientific Publishing Co., Singapore (In press). (Chapter in the textbook).
5. Bardach, J.E., J.H. Ryther and W.O. McLarney. 1972. *Aquaculture: the farming and husbandry of freshwater and marine organisms*. Wiley Interscience, New York, 868 pp.
6. Robert A. Browne, Patrick Sorgeloos, Clive N. A. Trotman, *Artemia Biology*, CRC press, p.166, 1991.

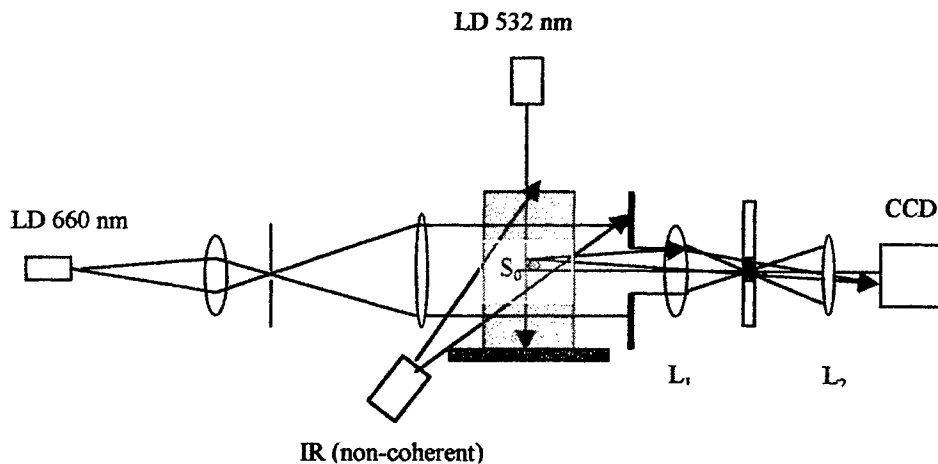


Fig 1. The schematics of the Fourier optic system as shown, a collimated laser beam of plane-wave and uniform intensity is illuminating the objects S_0 which is optically transparent. The diffracted light from the object then pass through a Fourier transform lens L_1 , and is focused on the spatial filter. An high pass spatial filter and the lens L_2 are used to inversely Fourier transform the diffracted pattern of the observed object and to image by the CCD.

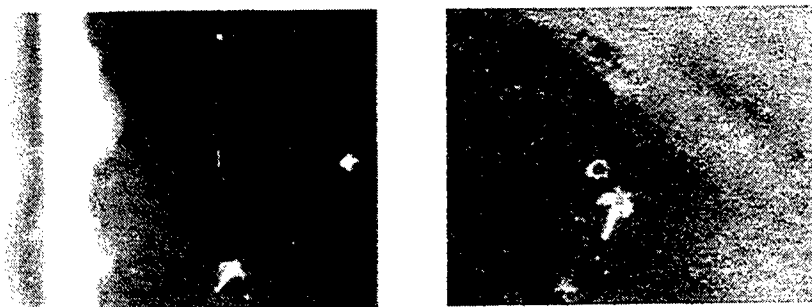


Figure 2. Left hand side is the Fourier transform image by using non-coherent IR light source, and the right hand side is taken by the coherent laser source. It shows the improvement of the Fourier transform image quality by using the IR non-coherent light source.



Figure 3 shows a series of images of the continuous motion of the artemia . It shows that the basic driving mechanism of artemia forward motion is by swimming of the pair of its antennae.

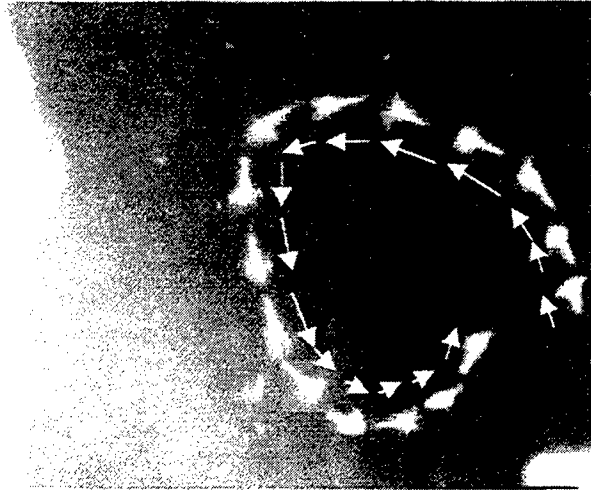


Figure 4. The most commonly seen spiral tracing of artemia motion. The artemia's tail, named as postmaxillar region, is to control its direction, and the balance in swimming .

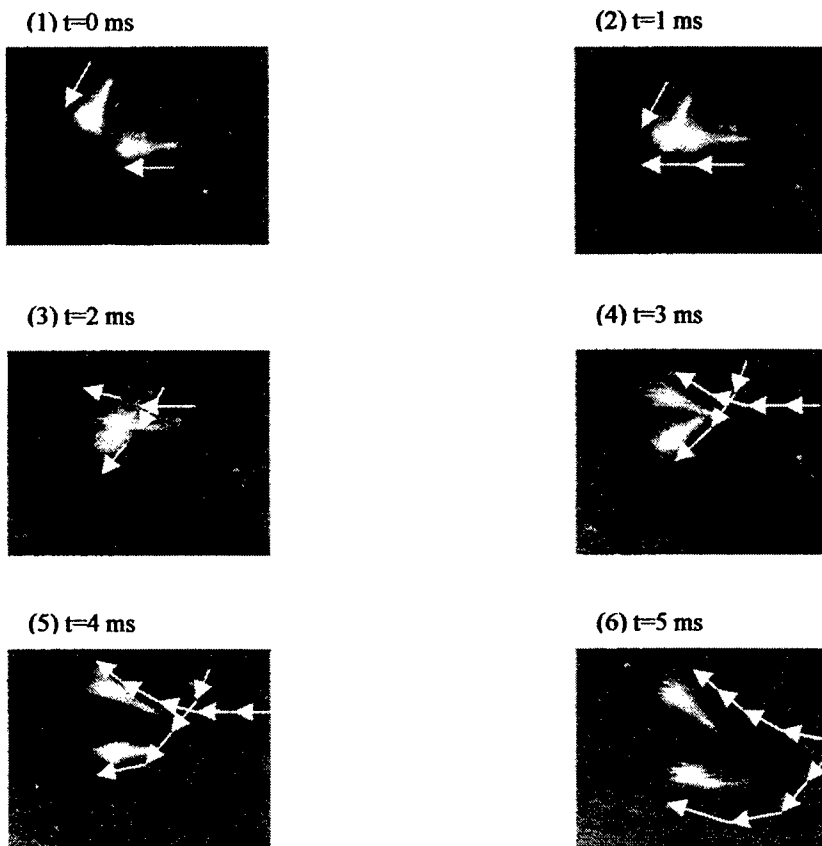


Figure 5. The series of photos show the mating behavior of adult artemia. The mating collision time is estimated about the order of mill-second..

Poster Session

Characteristics of acoustic wave propagation in dermis for the diagnosis of the superficial tissue damage in radiation therapy

Chung-Wei Lyu^a, Hsian-Jenn Wang^{*b}, Lee-Cheng Peng^a and Chien Chou^a

^aInstitute of Radiological Science and Department of Medical Radiation Technology National Yang-Ming University, Peitou, Taipei, Taiwan 112, R.O.C

^bDepartment of Medical Care and public health, Medical Bureau, Ministry of National Defense, Taipei, Taiwan 100, R.O.C.

ABSTRACT

Measurement of tissue radiation damage quantitatively in radiation therapy is very important to optimize the therapeutic treatment. Ionized radiation induces homogenization of the extracellular matrix which is synthesized by fibroblast and the randomization of the orientation of the collagen fibers in dermis. If the dermis is exposed by ionized radiation, a thermal acoustic shear wave which propagates in dermis becomes harmonic wave; Otherwise, an inharmonic wave is expected because of inhomogeneous and the anisotropic properties of dermis. A polarized optical heterodyne interferometer was setup in order to measure the transverse displacement of the shear wave in order to analyze the propagation mode of the shear wave in dermis. The detection sensitivity of the displacement was 1nm and the dynamic range was 300 nm in this arrangement. The lowest dose that can be detected by the exposure of 4 MeV radiation on porcine dermis was 1 cGy.

Keywords : Dermis, interferometer, heterodyne, collagen, fibroblast, shear wave, displacement

1. INTRODUCTION

In the area of dermatology, different techniques to measure the change of linear and circular birefringence caused by the thermal damages are studied extensively^(1,2). However, the most attractive technique recently developed was the polarization sensitive optical coherence tomography(OCT). It can be used to sense birefringence image caused by the thermal damages tomographically^(3,4). The thermal denaturation of collagen which is from α -helix to a random-coil conformation that is accompanied by a loss of birefringence⁽²⁾. In loose connective tissue like dermis is highly cellular and contains numerous fibroblasts which synthesize much of the extra-cellular matrix and collagen fibers. However, at least 40°C of temperature is required to result thermal denaturation of dermis^(2,4). In contrast, the ionized radiation induces the denaturation of collagen fibers and the extra-cellular matrix in dermis is examined in this paper⁽⁵⁻⁷⁾. According to the percentage depth dose of 4 MeV photon radiation, the radiation dose is built up in dermis⁽⁷⁾ which contains abundant collagen fibers and fibroblasts⁽⁵⁾. The orientation of collagen fibers is then randomized their orientation by the exposure of radiation. Meanwhile, the extra-cellular matrix is enforced lost the structure and becomes homogeneous^(5,6) as well. For a living tissue, if the dose of the exposure does not induced a permanent damage, the dermis is able to repair itself the and recovers the dermis back to inhomogeneous

and anisotropic as it was before the exposure. A thermal acoustic wave which propagates in dermis then becomes inharmonic from the harmonic sinusoidal wave which propagates in a isotropic and homogeneous medium. In a bulk isotropic material, there are thermal acoustic shear wave and longitudinal wave propagating in the medium⁽⁸⁾. However, the shear wave displaced in X direction is in the direction perpendicular to the propagation in Z-axis while the longitudinal wave displaced in Z direction is in the direction parallel to Z-axis. Because dermis is so sensitive to the ionization radiation that induces dermis homogeneously and isotropically. Therefore, a harmonic thermal acoustic shear wave is expected propagation in dermis at room temperature. A polarized optical heterodyne interferometer which measures the transverse displacement of the shear wave is setup in order to analyzer the harmonic mode of the shear wave. Then, a highly sensitive biological ionization radiation sensor is demonstrated.

2. PRINCIPLE

There are a thermal acoustic longitudinal wave and a two shear waves propagating in the bulk of isotropic and homogeneous material when the material reaches the thermodynamic equilibrium with its surroundings⁽⁸⁾. The speed of propagation of the longitudinal wave is faster than shear wave⁽⁸⁾. The equation of the thermal acoustic longitudinal wave can be expressed

$$\frac{\partial \bar{\mu}_l}{\partial t^2} - v_l^2 \nabla^2 \bar{\mu}_l = 0 \quad (1)$$

and the thermal acoustic shear wave is

$$\frac{\partial \bar{\mu}_s}{\partial t^2} - v_s^2 \nabla^2 \bar{\mu}_s = 0 \quad (2)$$

where v_l and v_s are the propagation speed of the longitudinal wave and the shear wave respectively. $\bar{\mu}_l$ and $\bar{\mu}_s$ are the displacements with respect to the longitudinal wave and the shear wave. It is because the exposure of the ionized radiation induces extra-cellular matrix and the collagen fibers in dermis homogeneously and isotropically. Therefore, a polarized optical heterodyne interferometer is setup in order to analyze the propagation mode of the thermal acoustic shear wave in dermis⁽⁹⁾. A beam splitter (BS1) divides the laser beam into a reference beam and a signal beam. According to theory, a linear polarized light can be separated into two orthogonal linear polarized waves. P wave and S wave, which propagate in the Mach-Zehnder interferometer simultaneously. There are two acoustic-optic modulators---AOM1 and AOM2---in the interferometer where P wave and the S wave are simultaneously modulated. A polarized beam splitter (PBS1) divides the signal beam into P_1 wave and S_1 wave which are driven by AOM1 at frequency ω_s . P_1 wave is incident onto the test sample T. While the S_1 wave is onto the reference mirror R. Both P_1 wave and S_1 wave are reflected back to the interferometer. Similarly, P_2 wave and S_2 wave which are driven by AOM2 at frequency ω_r propagate in the reference beam. The P_1 and P_2 waves are separated from S_1 and S_2 waves by PBS2 and are detected and heterodyned at D_p and D_s respectively. The intensities of the heterodyned P wave (P_1+P_2) and S wave (S_1+S_2) are

$$\begin{aligned} I_p(\Delta\omega t) &= \left| A_{p_1} \exp[i(\omega_s t + \phi_{p_1})] + A_{p_2} \exp[i(\omega_r t + \phi_{p_2})] \right|^2 \\ &= I_{p_1} + I_{p_2} + 2(I_{p_1} I_{p_2})^{1/2} \cdot \cos(\Delta\omega t + \Delta\phi_p) \end{aligned} \quad (3)$$

$$\begin{aligned}
I_s(\Delta\omega t) &= \left| A_{s_1} \exp(i(\omega_s t + \phi_{s_1})) + A_{s_2} \exp(i(\omega_r t + \phi_{s_2})) \right|^2 \\
&= I_{s_1} + I_{s_2} + 2(I_{s_1} I_{s_2})^{1/2} \cdot \cos(\Delta\omega t + \Delta\phi_s)
\end{aligned} \tag{4}$$

where $\Delta\omega = \omega_s - \omega_r$ is the beat frequency of the signal beam and the reference beam. $\Delta\phi_p = \phi_{p_1} - \phi_{p_2}$ and $\Delta\phi_s = \phi_{s_1} - \phi_{s_2}$ are the phases difference of the heterodyne P wave and S wave respectively. A lock-in amplifier is chosen to measure the phase difference $\Delta\phi = \Delta\phi_p - \Delta\phi_s = \phi_{p_1} - \phi_{s_1}$ and the amplitude at the same time. Besides, the measurement of the amplitude ratio of the heterodyne P wave and S waves, which is $(\frac{I_{p_1} I_{p_2}}{I_{s_1} I_{s_2}})^{1/2}$ enables us to monitor the degradation of the heterodyned efficiency in real time. A phase difference $\Delta\phi$ between the heterodyned P wave and S wave relates to the relative displacement Δh between the test surface T and the reference mirror R. The relation is $\Delta\phi = \frac{4\pi}{\lambda} \Delta h$. λ is the wavelength of the laser source. When a thermal acoustic shear wave is propagating in dermis at room temperature. A transverse displacement of the shear wave can be monitored in real time by the interferometer. Then a propagation mode of the thermal acoustic shear wave is analyzed following the variation of the transverse displacement versus time. Therefore a highly sensitive biological ionized radiation sensor in terms of the propagation mode analysis of the thermal shear wave is introduced.

3.Experimental Setup

A shown in Fig.1, a linearly polarized frequency stabilized He-Ne laser (Spectra Physics, Model 117A) in conjunction with a $\frac{\lambda}{2}$ wave plate and an optical isolator were used in the configuration. A laser beam which was divided into two equal amplitude by a beam splitter (BS1) was incident on the Mach-Zehnder interferometer. Two modulators--AOM1 and AOM2--were driven at frequencies of $\omega_r = 80.0000$ MHz and $\omega_s = 80.0377$ MHz, respectively. A beat frequency of 33.7-kHz of the heterodyned P and S waves was generated by the detector D_p and D_s respectively. To obtain a better signal-to-noise ratio, a bandpass filter with the central frequency at 33.7 kHz was required behind each detector. The stability of the phase and the amplitude of the interferometer were $\pm 0.2^\circ/\text{hr}$ and $\pm 0.3\%/\text{hr}$ in the experiment. It corresponded to 1 nm resolution in transverse displacement. The dynamic range of the displacement was 300 nm. A 40X objective (N.A.=0.65) was used to focus the P_1 wave onto the sample which was a 5×8 cm porcine dermis of 0.3 mm in thickness⁽¹⁰⁾. The lateral resolution was 0.6 μm . Before radiation exposure an irregular inharmonic thermal acoustic shear wave was observed in the experiment as shown in Fig2.. A 5nm variation of the transverse displacement was measured. Figure 3(a), shows the transverse displacement of a harmonics shear acoustic wave in porcine dermis of 1cGy dose by 4MeV photon exposure using Varian 2100C LINAC. Fig.3(b) shows the displacement response of the shear wave 30 minutes later. The result confirms the repair ability of the living porcine dermis that an irregular inharmonic wave propagated in the porcine dermis. The displacement of the thermal acoustic shear wave was an order of 30 nm in the measurement. After a 10Gy radiation dose of 4MeV photon radiation exposure on the porcine dermis. Fig.4(a) presents the response of harmonic shear wave as we expected. However, a

analysis of the displacement of the shear wave 24 hrs later, Fig.4(b) shows the some response of the shear wave of the porcine dermis that was unable to repair itself biologically. Therefore, a ionized radiation sensitive biological sensor is introduced. A polarized optical heterodyne interferometer was used to sense the propagation mode of the thermal shear wave in porcine dermis is demonstrated experimentally. The lowest dose of the exposure was 1cGy that strengthens the detection sensitivity of ionized radiation in comparison with the method in radiation biology⁽⁶⁾.

ACKNOWLEDGMENT

The authors are indebted to The Cancer Center, Taipei Veterans General Hospital for providing the facility of Varian 2100C LINAC 4 MeV photon radiation. L.C.Jan for her assistance of preparing the manuscript is also appreciated.

REFERENCES

- (1) S. Thomsen, J.A. Pearce and W.F.Cheong " Changes in Birefringence as Makers of Thermal Damage in Tissues" *IEEE Tran.Biomed.Eng.* **36**, pp.1174-1179, 1989
- (2) D.J.Maitland and J.T.Walsh, Jr., " Quantitative Measurement of linear birefringence during Heating of Native Collagen" *Laser Surg.Med.* **20**, pp.310-318, 1997
- (3) J.F.deBoer, T.E. Milner, M.J.C. VanGemert and J.S.Nelson." Two-dimensional Birefringence Imaging in Biological Tissues by Polarization Sensitive Optical Coherence Tomography" *Opt.Lett.*, **22**, pp.934-936, 1997.
- (4) K.Schoenenberger, B.W.Colston,Jr., D.J.Maitland, L.B.Dasilva, and M.J.Everett "Mapping of Birefringence and Thermal Damage in Tissue by Use of Polarization Sensitive Optical Coherence Tomography" *Appl.Opt.*, **37**, pp.6026-6036, 1998
- (5) H.Lodish, D.Baltimore, A Berk. S.L.Zipursky . P.Matsudaira and J.Darnell."Molecular Cell Biology" (W.H.Freeman and Co. New York) , pp.1123-1136,1995
- (6) E.J.Hall " Radiobiology for the Radiologist" 4th ed.(J.B.Lippincott co.philadelphia) pp1-13, 1994
- (7) H.E.Johns and J.R.Cunningham."The physics of Radiology" 4th ed.(Charles C Thomas:springfield). pp.349-351, 1983
- (8) V. M.Ristic," Principles of acoustic devices" (Wiley: New York). pp.44-46. 1983
- (9) C.Chou, J.C.Shyu, Y.C.Huang, and C.K.Yuan. " Common-path optical heterodyne profilometer : a configuration" *Appl. Optics.* **37(19)**, pp4137-4142, 1998.
- (10) H.J.Wang,, T.M.Chen, . and T.Y.Cheng.. "Use of a porcine dermis template to enhance widely expanded mesh autologous split-thickness skin graft growth: preliminary report" *The Journal of Trauma: Injury, Infection, and Critical Care.* **142(2)**, pp.177-182, 1997

Correspondence: Email:cchou@ym.edu.tw; Telephone: 886-2-28267061; Fax: 886-2-28251310

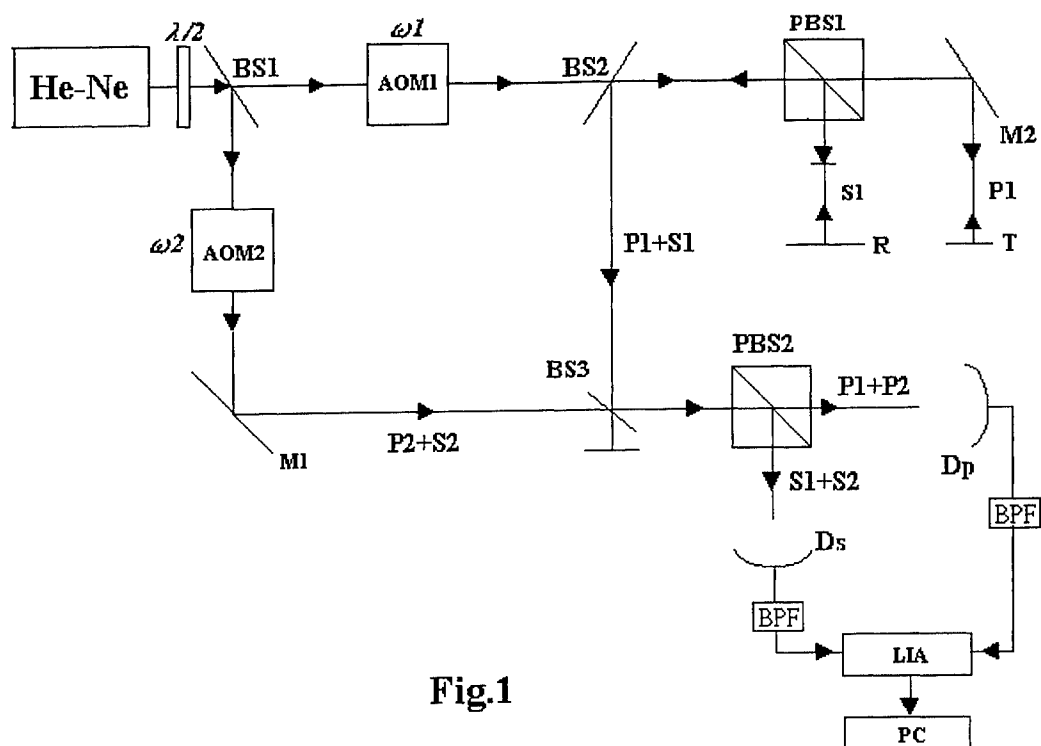


Fig.1

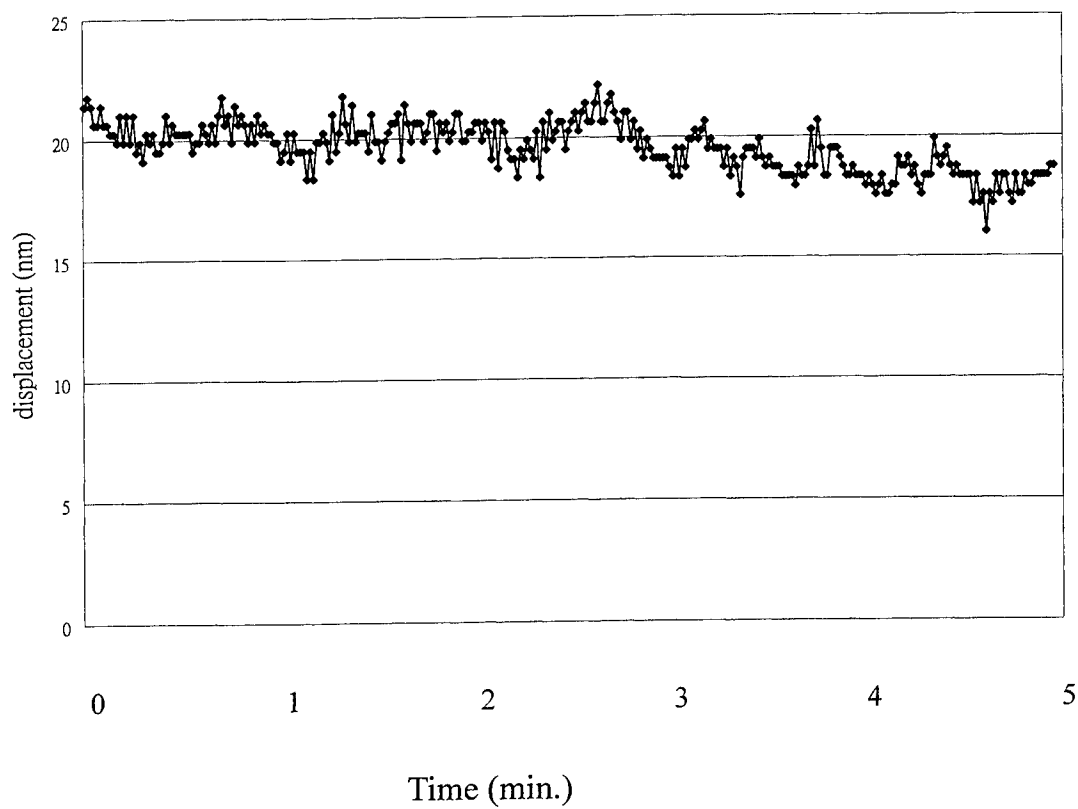


Fig.2

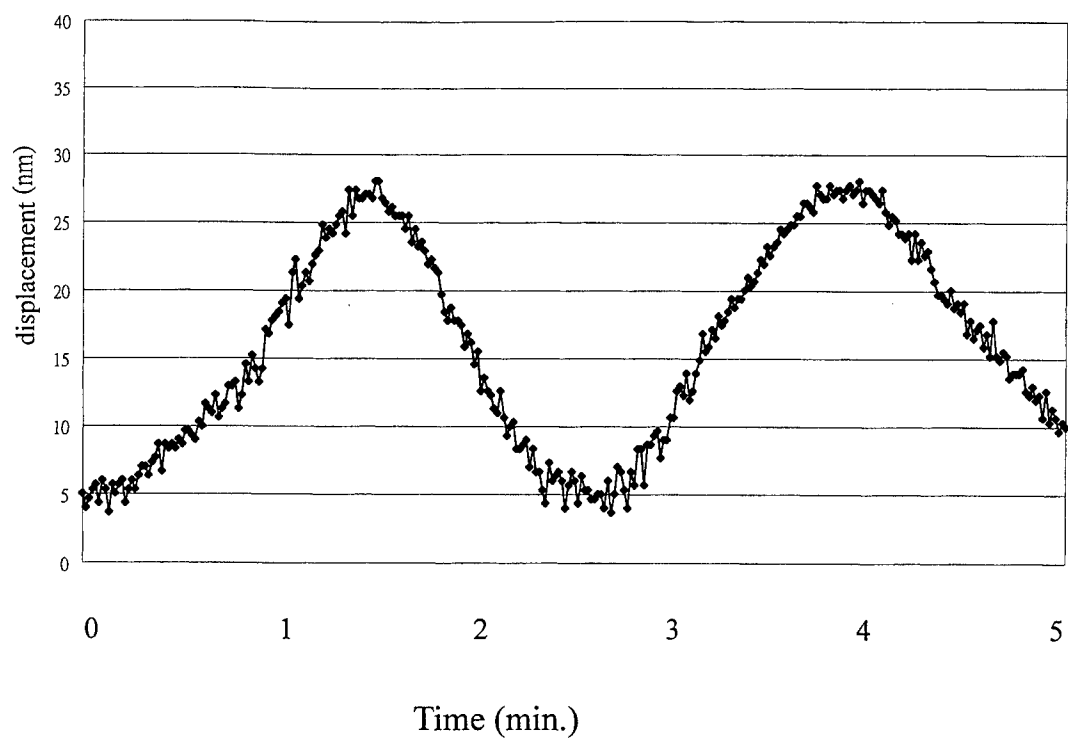


Fig.3 (a)

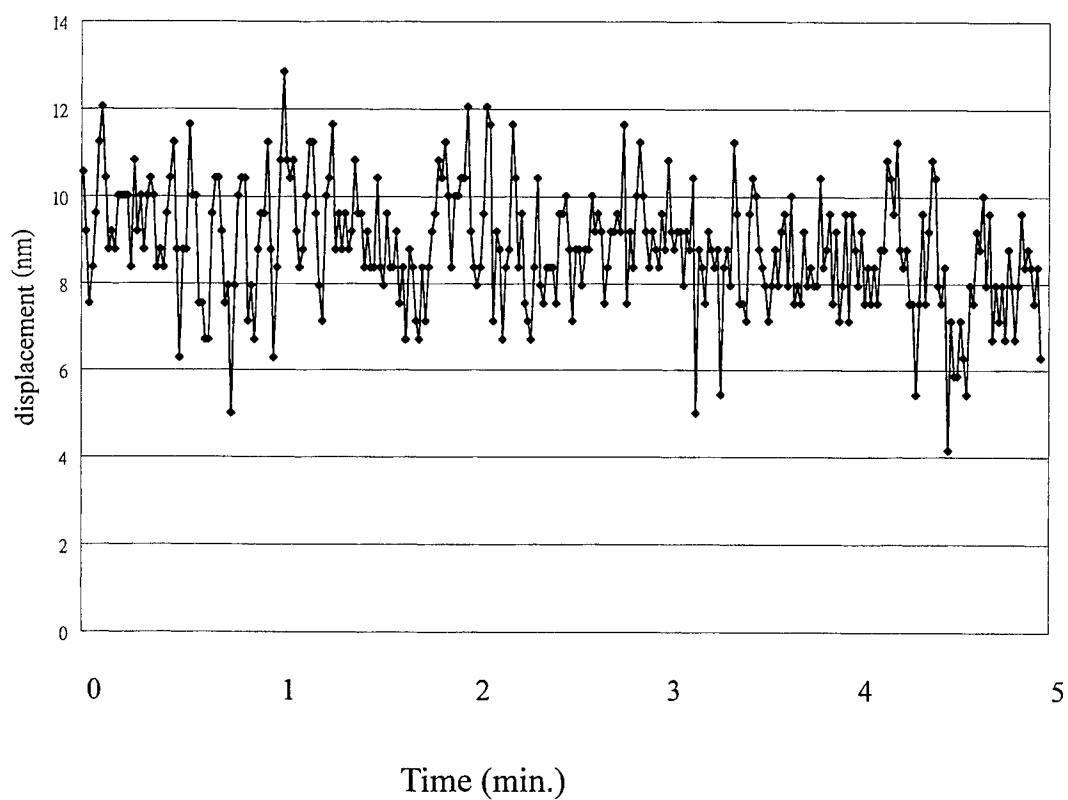


Fig.3 (b)

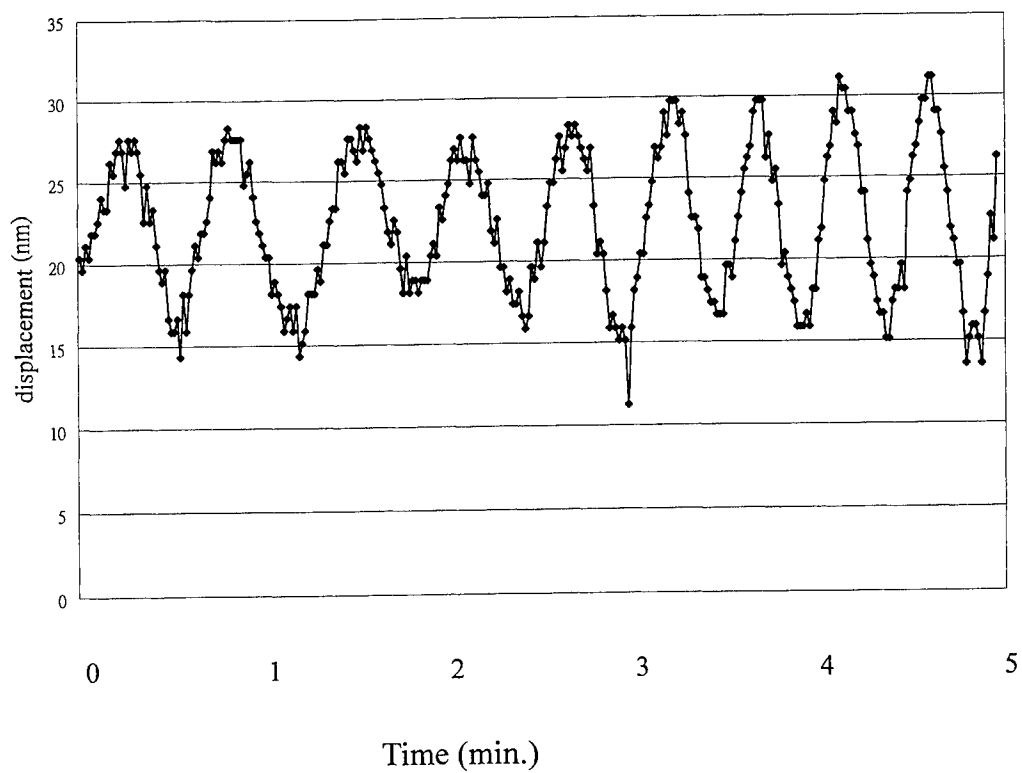


Fig.4 (a)

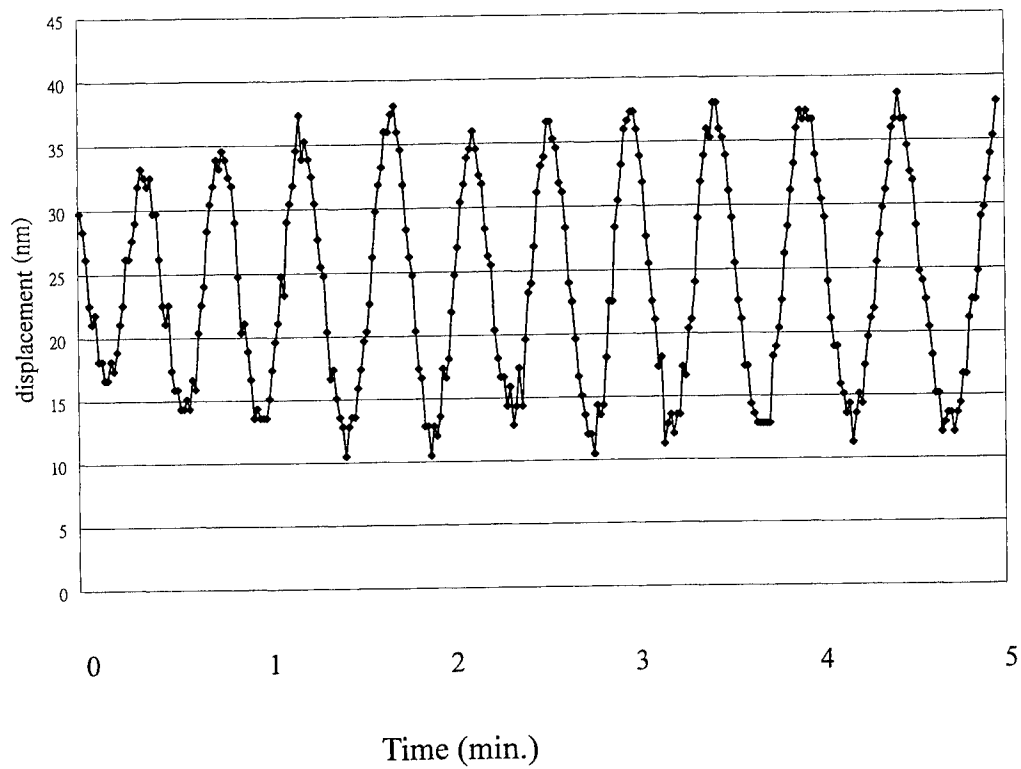


Fig.4 (b)

An analysis system for PET detector

Hong-Chih Liu, Hsing-Ching Liang

Institute of Nuclear Energy Research, P. O. Box 3-4, Lung-Tan,
Taiwan, Republic of China

ABSTRACT

The ASR-PET detector is designed by coupling a 7×8 array of BGO scintillation crystals to a PSPMT (Position Sensitive Photo-Multiplier Tube). Reflectors between the crystals confine the light from a gamma ray interaction and control the distribution of light to the PSPMT. The output signals of the PSPMT are used to identify the crystal of scintillation and the energy being released from the gamma ray interaction.

The subject of this study is to generate a LUT (Lookup Table) from the position response distribution of the block detector and to analyze the PHS (Pulse Height Spectrum) of each crystal. By combining the image-processing and neural network data fitting techniques, this system gives a flexible, user-friendly and powerful approach to perform the analysis with satisfactory accuracy.

Keywords: PET, Block detector.

1. INTRODUCTION

In most PET system, BGO block detectors¹⁻⁶ are used to detect coincident 511Kev gamma rays resulting from positron annihilations. In the ASR-PET (designed by the Institute of Nuclear Energy Research, Taiwan, Republic of China), each BGO block detector module consists of a 7×8 BGO array coupled to the compact PSPMT (Position Sensitive Photo-Multiplier Tube). Reflectors between the crystals confine the light from a gamma ray interaction and control the distribution of light to the PSPMT. The PSPMT output signals are decoded into transaxial (x) and axial (y) position information. The summation of the PSPMT output signals is transformed into energy information.

The subject of this study is to generate a LUT (Lookup Table) from the position response distribution of the block detector and to analyze the PHS (Pulse Height Spectrum) of each crystal. The ASR-PET block detector and data acquisition system is briefly described in section 2, while the detail of LUT and PHA algorithms are presented in section 3 and 4. A conclusion is given in section 5.

2. THE ASR-PET BLOCK DETECTORS AND DATA ACQUISITION SYSTEM

The ASR-PET block detector module consists of a 7×8 BGO array coupled to the compact PSPMT (Hamamatsu R5900-00-C8) as shown in Figure 1. The dimensions of each BGO crystal are 2.6 mm in width, 2.6 mm in height and 25 mm in depth. Crystals are painted with reflection material and closely packed. Reflectors between the crystals confine the light from a gamma ray interaction and control the distribution of light to the PSPMT. The PSPMT has metal channel dynodes and 8 cross plate anodes (4 for X dimension and 4 for Y dimension). These anodes output signals can be used to determine the location of the scintillation event. The total summation of these anode signals can also provide information of the energy of the scintillation event.

The hardware used for data acquisition is shown in Figure 2. The signals from 8 anodes of PSPMT are independently amplified through preamplifiers (LeCroy 612AM Fast Preamplifier) and offset-compensated by Fan-in/Fan-out modules (LeCroy 428F Linear Fan-in/Fan-out). The sum of these eight PMT signals is filtered (ORTEC 474 Timing Filter Amplifier), threshold (LeCroy 4608C Discriminator) and gated (LeCroy 222 Gate Generator) before it can be sent to trigger the ADC module. A delay device is inserted between each output of the preamplifier and the input of the charge integrating ADC to compensate the timing delay introduced by the trigger module. The digitized signals captured by the ADC (LeCroy 4300 Fast Encoding/Readout ADC) are recorded and further processed by LUT and PHS analysis programs.

3. LUT GENERATION ALGORITHM AND RESULTS

The LUT generation program is developed under Borland C++ Builder. In Figure 3, flow diagram of the LUT generation algorithm is shown. The LUT generation algorithm use the PSPMT anode signals to identify the crystal of scintillation. For each gamma ray interaction, the measured position value (X_m, Y_m) from these signals are calculated by:

$$X_m = \frac{3X_1 + X_2 - X_3 - 3X_4}{X_1 + X_2 + X_3 + X_4}$$

$$Y_m = \frac{3Y_1 + Y_2 - Y_3 - 3Y_4}{Y_1 + Y_2 + Y_3 + Y_4}$$

where X_1, X_2, X_3, X_4 and Y_1, Y_2, Y_3, Y_4 are the amplified anodes signals captured by the ADCs. The relationship between the measured position and the true position is nonlinear in both X and Y positions. The LUT generation algorithm is designed to identify the crystal of interaction corresponding to a given (X_m, Y_m) pairs.

Figure 4(a) shows the intermediate output of the LUT generation algorithm. A 256×256 position response distribution is obtained from the flood source (Na^{22}) measurement. There is a distinct peak in the distribution for each crystal in the position response distribution. The lookup table is generated for each detector from its flood source response such that every possible (X_m, Y_m) pair will be assigned to one crystal and no detected events are thrown away. The region of each crystal occupied is assumed to have a boundary of four-sided polygons³, since it is easy to generate and flexible to bound the 56 crystal position peaks. Figure 4(c) shows the 2-D position response distribution after smoothing and energy threshold. Figure 4(d) gives the LUT boundaries overlaid on the original position response distribution.

Large peak-to-valley ratios are desirable for block detectors. Large ratios mean the peaks are well separated and thus identification the crystals of interaction are correct for a large fraction of the events. Figure 5(a) shows two areas (each with 10 pixels wide on a 256×256 image) marked across BGO crystal array and their relative position profiles are shown in Figure 5(b). Even after averaging across 10 pixels, the separations between the peaks are still acceptable. Figure 5(c) and (d) shows the results of two thin lines (each with 2 pixels wide on a 256×256 image) drawn across BGO crystal arrays and their profiles.

4. PHS ANALYSIS ALGORITHM AND RESULTS

Figure 6 shows the coarse energy spectrum of an ASR-PET block detector being exposed to the Na^{22} flood source. The poor energy spectrum may results from the gain variation within the PSPMT and the inconsistent physical contact between the crystal and the PSPMT surface.

In order to overcome the problem of non-uniformity of energy resolution and gamma ray detection efficiency of each BGO crystal, the PHS algorithm is designed to analysis the energy spectrum of each individual BGO crystal. PHS analysis algorithm first calculate the (X_m, Y_m) for each event collected, it then determine which crystal the interaction occurred in, using the LUT generated earlier, and histogram the energy of the every event into one of 56 arrays. In this manner an energy spectrum can be obtained for each crystal. Figure 7 shows the energy spectra of each BGO crystal being exposed to Na^{22} flood source. Using the 56 energy spectra, PHS analysis algorithm approximates gaussian function on each energy peak by artificial neural network data fitting technique. Figure 8 displays results of several BGO crystal energy spectra being approximated by gaussian functions.

In order to observe the 511 keV photopeak detection efficiency of each BGO crystal, PHS analysis algorithm estimates the relative detection efficiency by comparison the area of gaussian function approximation of each 511 keV photopeak. Figure 9 shows the distribution of the number of 511 keV photopeak detected in each crystal of an ASR-PET detector. The counts of the left row are about 20% less than the counts of the central row. These loss counts are believed to be due to the insufficient effective area of the PSPMT surface.

5. SUMMARY

The prime motivation for this study is to conduct a comprehensive and quantitative evaluation of the performance of the BGO block detectors. The LUT algorithm creates the look-up table of each BGO block detectors based on the image-

processing technique. Using the artificial neural network data fitting technique, the PHS analysis algorithm provides a means of observing the 511 keV photopeak detection efficiency. More work will be needed to extend the proposed algorithm to analysis other types of PET detector.

REFERENCES

1. M.E. Casey and R. Nutt, "A multicrystal two dimensional BGO detector system for positron emission tomography", IEEE Trans Nucl Sci, Volume 33, 1986.
2. M. Dahlbom and E.J. Hoffman, "An evaluation of a two-dimensional array detector for high resolution PET", IEEE Trans Med Imaging, Volume 7, 1988.
3. J.G. Rogers, A. J. Taylor, M. F. Rahimi, R. Nutt, M. Andreaco and C.W. Williams, "An improved multicrystal 2-D BGO detector for PET", IEEE Trans Nucl Sci, Volume 39, 1992.
4. M.P. Tornai, G. Germano and E.J. Hoffman, "Positioning and energy response of PET block detectors with different light sharing schemes", IEEE Trans Nucl Sci, Volume 41, 1994.
5. M. Watanabe, T. Omura, H. Kyushima, Y. Hasegawa and T. Yamashita, "A compact position-sensitive detector for PET", IEEE Trans Nucl Sci, Volume 42, 1995.
6. M. Watanabe, H. Okada, K. Shimizu, T. Omura, E. Yoshikawa, T. Kosugi, S. Mori and T. Yamashita, "A high resolution animal PET scanner using compact PSPMT detectors", IEEE Trans Nucl Sci, Volume 43, 1996.

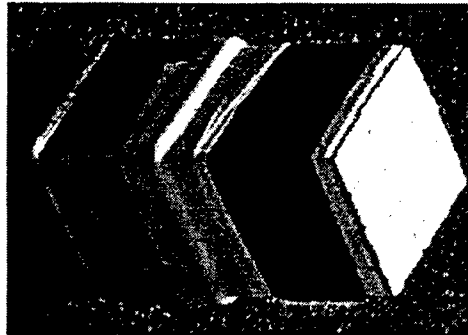


Figure 1. ASR-PET block detector.

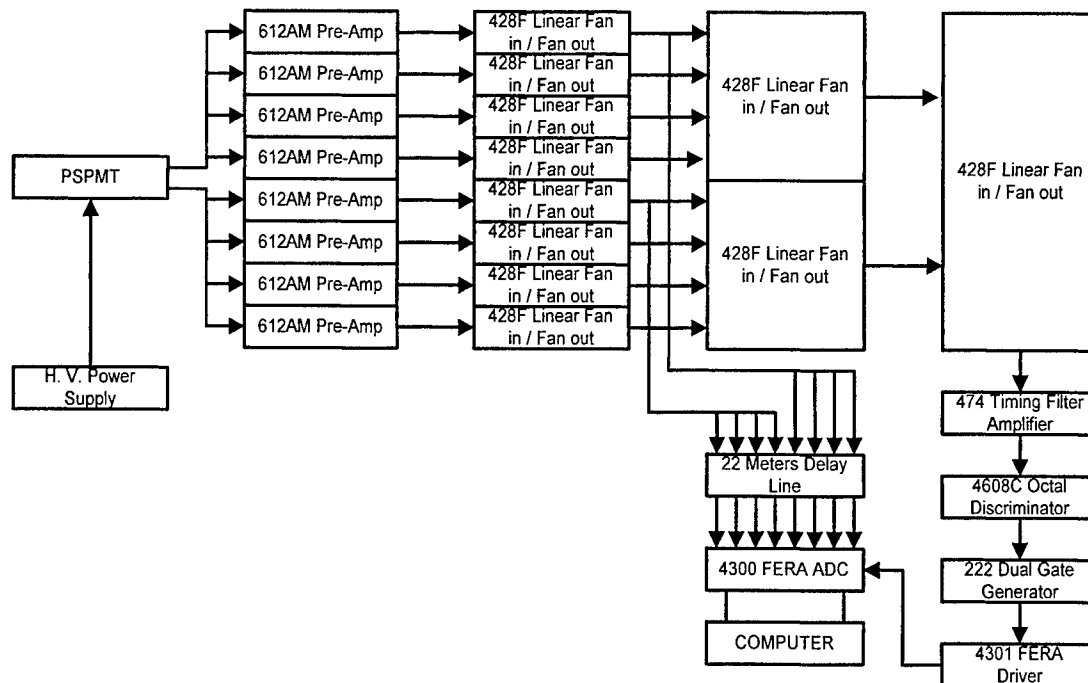


Figure 2. CAMAC modules used for data acquisition.

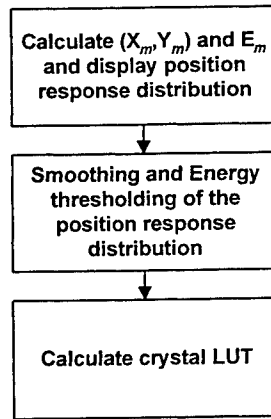


Figure 3. Flow diagram of the LUT generation algorithm

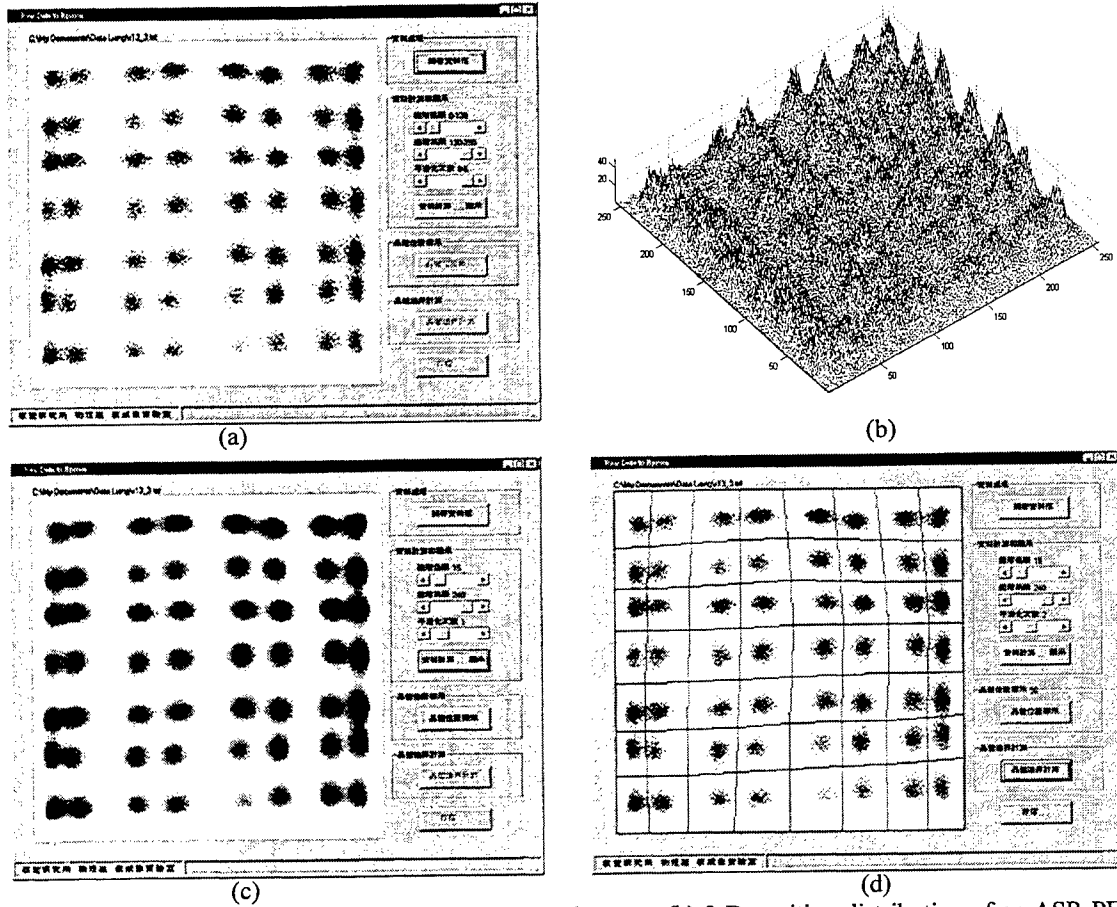


Figure 4. (a) 2-D position distribution of an ASR-PET block detector. (b) 3-D position distribution of an ASR-PET block detector. (c) 2-D position distribution after smoothing and energy thresholding. (d) 2-D position distribution with LUT overlaid.

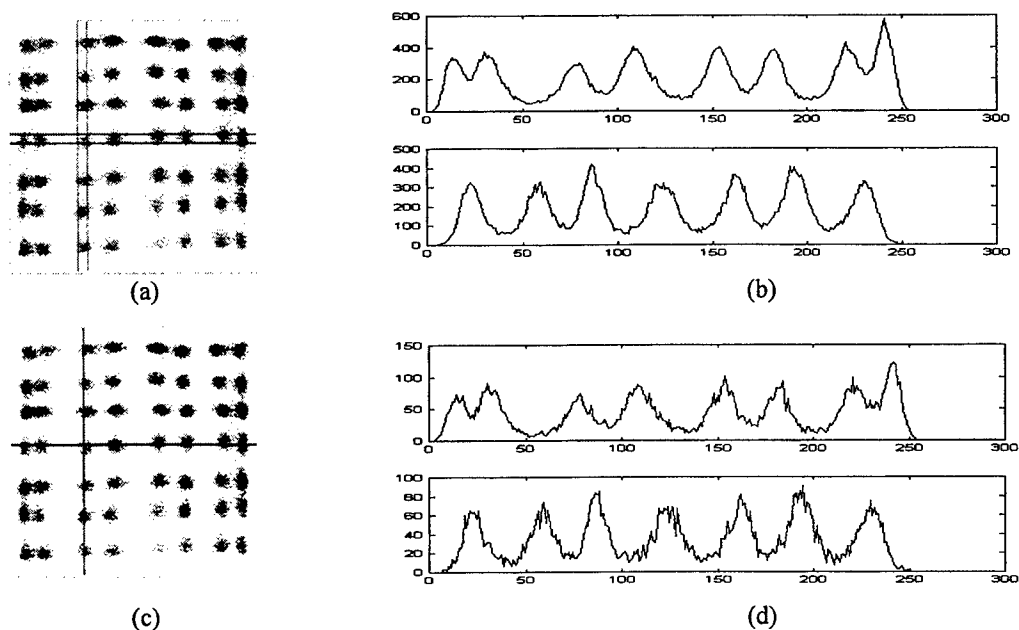


Figure 5. (a) 2-D position distribution with two thick areas overlaid (b) Result profiles of (a). (See text for details.) (c) 2-D position distribution with two thin lines overlaid (d) Result profiles of (c).

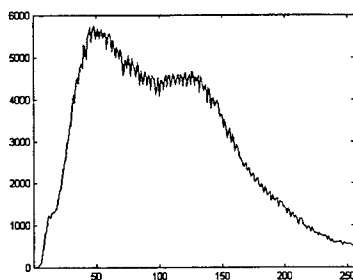


Figure 6. Coarse energy spectrum of an ASR-PET block detector being exposed to the Na^{22} flood source.

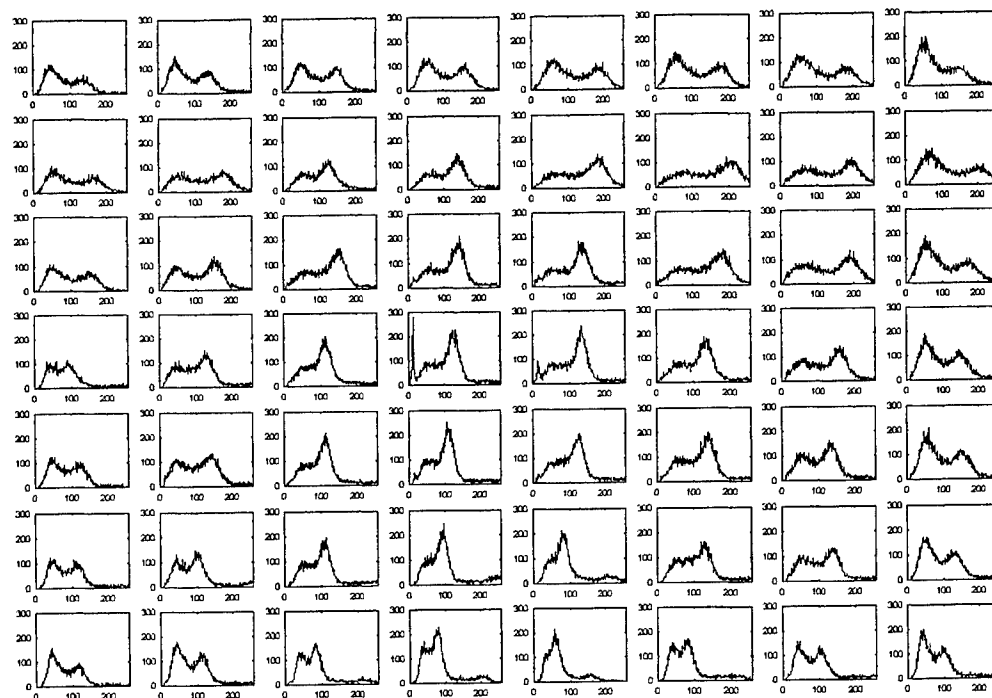


Figure 7. Pulse height spectra (PHS) of each BGO crystal exposed to Na^{22} flood source.

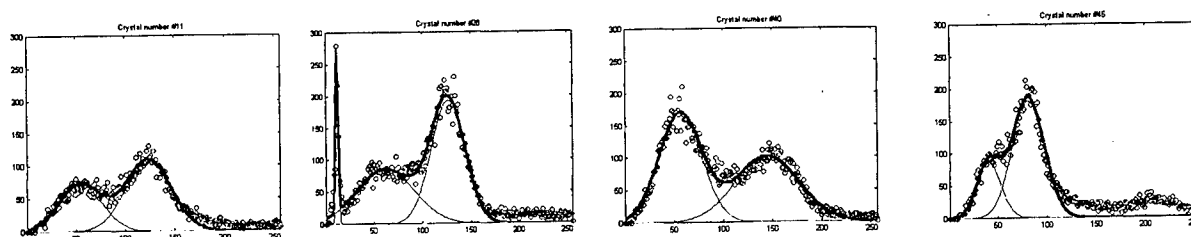


Figure 8. Examples of the individual BGO crystal energy spectra (denoted by small circles) and their approximation of gaussian functions (denoted by solid lines).

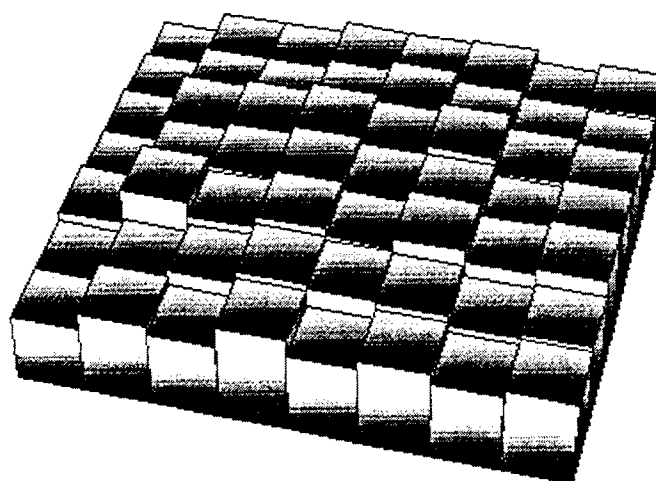


Figure 9. Relative 511 keV detection efficiency across the detector.

Detection of Objects Hidden in Highly Scattering Media Using Time-Gated Imaging Methods

L. Wang, X. Liang, P. A. Galland, P. P. Ho#, and R. R. Alfano
Institute for Ultrafast Spectroscopy and Lasers
New York State Center for Advanced Technology at CUNY
Departments of Physics and Electrical Engineering
The City College the City University of New York, New York, NY 10031

ABSTRACT

Non-linear ultrafast amplification optical gate has been used to detect back-scattered images of objects hidden in diluted Intralipid solutions.

Key words: amplification gate, time gating, polarized gate, optical Kerr gate

1. INTRODUCTION

To directly detect objects hidden in highly scattering media, the diffusive component of light needs to be sorted out¹⁻¹¹ from early arrived ballistic and snake photons. In the transmission imaging approach, early light imaging techniques such as optical Kerr gate (OKG), streak camera, second harmonic generation cross-correlation gate, and polarization gate have been employed. The back-scattered early light imaging has one major difference from the transmission approach. In the transmission approach, the earliest photons arrive at the detector always carry the direct information of the hidden object embedded in the turbid medium. However, in the back-scattered approach, the first arrival photons will be directly the back-scattered photons from the host material. The later arriving ballistic back-scattered photons from the hidden object will be mixed with other photons (including ballistic, snake, and diffusive) from the host medium. Additional gating mechanism is needed to separate the light scattered back from host medium surrounding the object. In this paper, a $\chi^{(2)}$ nonlinear optical based gated (NLOG) is applied to acquire time resolved back-scattered images. In comparison to our previous results using an OKG based imaging system, back-scattered imaging using parametric amplification based NLOG has greatly improved the sensitivity and signal to noise ratio of the image.

2. PRINCIPLE

The principle governing the implementation of the NLOG is based on the second order nonlinear optical coefficient $\chi^{(2)}$ from materials such as: KTP (KTiOPO₄), BBO, etc. under the phase matching condition. A time-gated amplified signal can be obtained through this NLOG process. Optical parametric amplification gate has previously been used in transmission configuration¹². The output of the amplified signal, I_s , at frequency ω_s , can be expressed as: $I_1 + I_2 = I_s + I_{\text{residue}}$. Where the energy conservation $\omega_2 - \omega_1 = \omega_s$ and the momentum conservation $K_2 - K_1 = K_s$ hold. The amplification factor can be expressed as: $I_s(L) = I_1(0) [\sinh GL/2]^2$ and the gain coefficient, $G = 2 \chi^{(2)} \{I_2(0) [\mu \omega_1 \omega_2] / [\epsilon n_1 n_2]\}^{0.5}$, where I_1 is the input signal intensity at frequency ω_1 , I_2 is the gating pulse intensity at frequency ω_2 , I_{residue} is the residue energy from the input I_1 and I_2 after the NLOG, L is the interaction length, and $\chi^{(2)}$ is the second order nonlinearity. The amplification gain of the output at ω_s is attributed from the loss of the intense gating pulse at ω_2 . An off-axis type II phase matched NLOG is generally used where the polarization of the amplified signal ω_s is perpendicular to the input. The improvement of the S/N from an NLOG can be estimated using an example from the gain equation of $I_s(L) \sim I_1(0) \exp[GL]$. Given $G = 0.5 \text{ mm}^{-1}$ and $L = 10 \text{ mm}$, the output signal gain factor after a NLOG is: $I_s(L=10 \text{ mm})/I_1(0) = \exp[10 \times 0.5] \sim 143$.

Correspondence: E-mail: ho@engr.ccny.cuny.edu; Telephone: 212-650-6808; Fax: 212-650-5530

3. METHOD

The schematic diagram of the back-scattered NLOG imaging system is shown in fig.1. A mode-locked YAG laser system which emitted a 40-ps 1064-nm pulse was used as the illumination beam and its second harmonic at 532-nm was used as the gating pulse in NLOG. A 20-mm long phase-matched cut KTP crystal was used as the $\chi^{(2)}$ gain medium. A pair of crossed polarizers was added into an scattered signal $I_1(t)$ at ω_1 (1064nm) before and after the NLOG crystal. Without the gating pulse ω_2 (532nm), the polarization of the input signal (1064-nm) remained unchanged and the 1064-nm beam would be blocked by the second polarizer (Analyzer). With the gating pulse ω_2 on, a portion of the input scattered profile of ω_1 was selected and amplified within the gating pulse duration. The polarization of the amplified output signal was perpendicular to that of the input signal. In this manner, by synchronizing and gradually delaying the gating pulse $I_2(t)$ at ω_2 relative to the input signal $I_1(t)$, the scattered signal intensity profile as a function of different part of $I_1(t)$ could be selectively sliced and the most of the diffusive part could be rejected simultaneously.

The time-sliced output NLOG signal ω_s (1064nm) was amplified and then passed through the analyzer. Following that, a narrow band filter centered at ω_s was used to select the NLOG signal at 1064nm. The sample used in the back-scattered imaging was a positive USAF Resolution Power Test Target (RPTT) immersed in the middle of a $5.5 \times 5.5 \times 10\text{cm}^3$ (L x W x H) cell filled with a 2.2% diluted Intralipid solution.

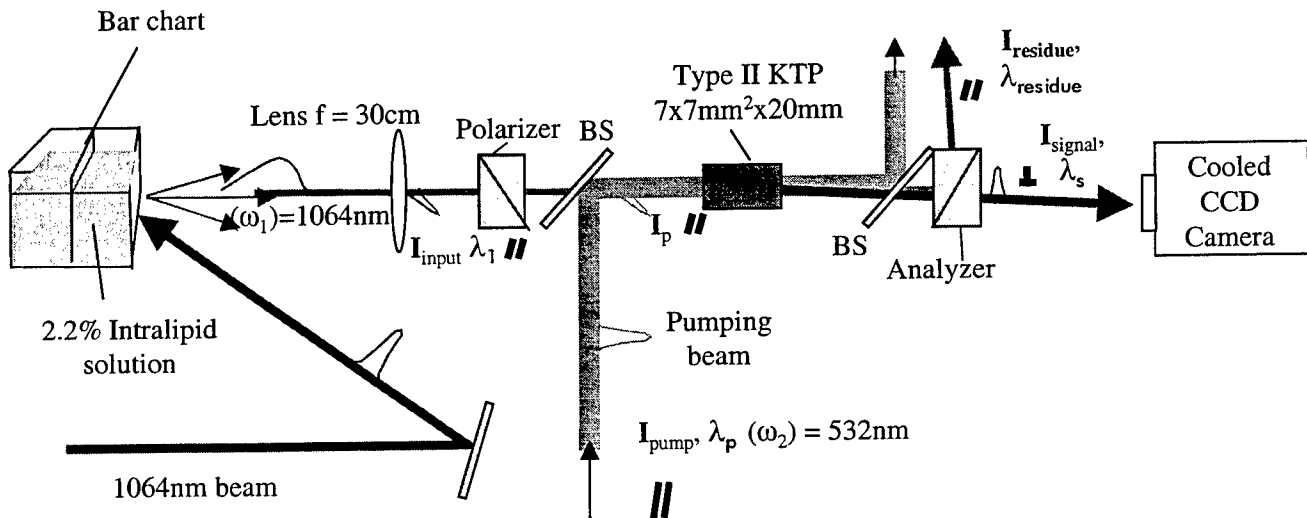


Fig. 1 Experimental setup of a back-scattered imaging system using a $\chi^{(2)}$ NLOG. BS: beam splitter 532 nm reflection /1064 nm transmission. I_{pump} , $\lambda_p = 532\text{nm}$, pulse width 40ps, pumping beam, frequency 10Hz, power density $\sim 15\text{mJ}/(\sim 0.4\text{cm}^2)$ (cross section area at the input of the KTP). I_{signal} , $\lambda_s = 1064\text{nm}$, amplified input signal component without any background; I_{residue} , $\lambda_{\text{residue}} = 1064\text{nm}$, signal component with the background present. The amplification factor is ~ 100 . Calcite polarizer and analyzer are set perpendicularly and parallel from each other respectively to obtain amplified signal component, I_{signal} , (shown in Fig.2) and amplified residue component I_{residue} .

4. RESULTS

Three pictures from the reflection bars of the RPTT under various conditions of the back-scattered imaging from samples using NLOG are displayed in fig. 2. An NLOG image is shown in fig.2a when the RPTT was immersed in a clear water cell. This measurement represents a reference to calibrate the gain factor of the imaging system. By taking the ratio of the images with and without the gating pulse, the absolute gain factor of the NLOG gate was found to be > 100 times at the delay time = 0 and was \sim five times at a time delay of 34-ps. In an image from the RPTT immersed in the diluted Intralipid solution cell was obtained when the gating pulse was off. No image was detected as seen in fig.2b. This picture represented the system minimum background level using a pair of crossed polarizers. An image of RPTT immersed in a 2.2% diluted Intralipid solution was displayed in figure 2c when the gating pulse was on at $t = 0$ ps. This image signal was greatly amplified and the background noise was low. Beside the improved sensitivity of ~ 100 times, the improved in S/N may also attributed to the change in polarization of the input signal where most of the background was removed.

Using an OKG for a similar back-scattered optical imaging, the reflection test bars can only be imaged through a 3cm long 2% diluted Intralipid solution. The measured image contrast values were ~ 0.80 and 0.65 , respectively, in a 5-cm long 2.2% Intralipid

cell using this NLOG and in a 3-cm long 2% Intralipid cell using OKG. The measured scattering length (l_s) of a 2.2% diluted Intralipid solution at 1060-nm was ~ 2.1 mm [ref. 1]. An effective S/N improvement $> 5 \times 10^4 = \exp(-3/0.23) / \exp(-5/0.209)$ was achieved using the NLOG. The larger S/N gain is attributed to the lower background noise from the signal beam.

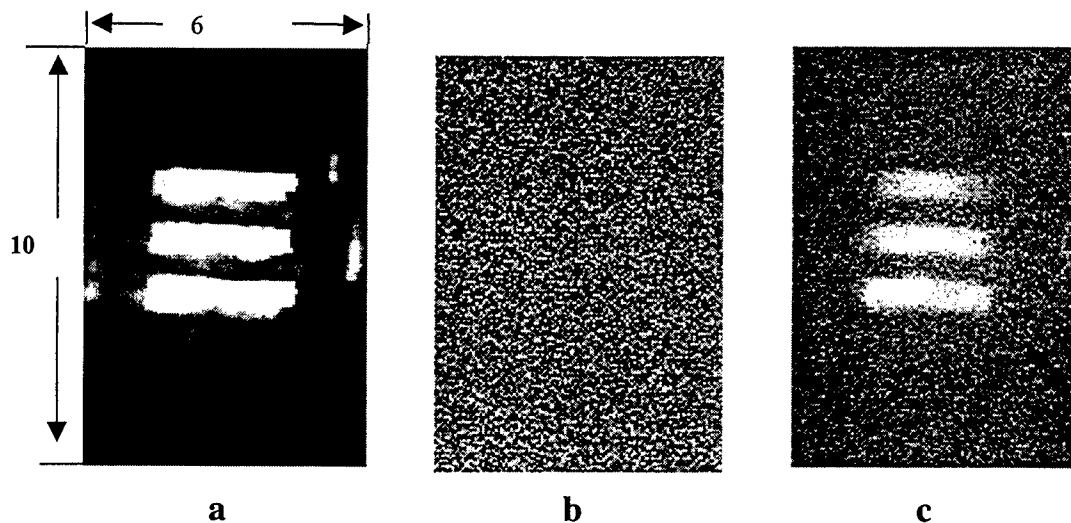


Fig.2. Experimental results from back-scattered from Intralipid using NLOG imaging system. These are images from a section of the reflection bars of an USAF RPTT (1 line pairs/mm) in the middle of a $5.5 \times 5.5 \times 10$ cm³ plastic cell. The terms: I_s , I_p , I_{residue} are intensity and the subscripts, residue signal, p-pump which provides energy to the input signal; s-signal input signal without the background noise amplified and with a change in polarization from x to y. The measured contrast values are 0.99 and 0.80 for a, and c respectively, and $I_p \perp I_s$.

- (a) Sample cell filled with clear water
- (b) Sample cell filled with 2.2% diluted Intralipid (No gating pulse)
- (c) Sample cell filled with 2.2% Intralipid

ACKNOWLEDGEMENT

This work is supported in part by a grant from NASA/FAR and NASA/IRA.

REFERENCES

1. "True scattering coefficients of turbid media", L. Wang, X. Liang, P. Ho, R. Alfano, *Optics Letters*, **20** 913-5 (1995)
2. "2D Kerr-Fourier imaging of translucent phantoms in thick turbid media", X. Liang, L. Wang, P. Ho, R. Alfano, *Applied Optics*, **34** 3463-7 (1995)
3. "Fourier spatial filter acts as a temporal gate for light propagating through a turbid media", Q. Wang, L. Wang, X. Liang, P. Ho, R. Alfano, *Optics Letters*, **20** 1498-1500 (1995)
4. "Comparison of nonlinear effects of linearly and circularly polarized picosecond pulses propagating in optical fibers", J. Chen, Q. Liu, P. Ho, R. Alfano, *Journal of Optical Society of America*, **B12** (1995)
5. "Time-resolved transillumination for medical diagnosis", S. Anderson-Engels, R. Berg, S. Svanberg, and O. Jarlman, *Opt. Lett.* **15**, 1178-1180 (1990)
6. "Femtosecond transillumination optical coherence tomography", M. Hee, D. Huang, E. Swanson, J. Fujimoto, *Opt. Lett.*, **18** 950-952, (1993)
7. "Photon Migration and Imaging in Random Media and Tissues", B. Chance, R. Alfano, ed. *SPIE 1888*, 1993.
8. "Ultrahigh speed photography of picosecond light pulses and echoes", M. A. Duguay and A. T. Mattick, *Opt. Lett.*, **10**, 2162-2170 (1971)
9. "Time-resolved imaging of translucent droplets in highly scattering media", R. Alfano, X. Liang, L. Wang, P. Ho, *Science*, **264** 1913-1915 (1994)
10. "Snake light tomography", P. Ho, L. Wang, X. Liang, P. Galland, L. Kalpaxis, R. R. Alfano *Optics and Photonics*, pp23-27, Oct. (1193)

11. "Three-dimensional temporal image reconstruction of an object hidden in highly scattering media by time-gated optical tomography", L. Kalpaxis, L. Wang, P. Galland, X. Liang, P. Ho, R. Alfano, Opt. Lett., 18 1691-3 (1993)
12. "Imaging in diffusive media with ultrafast degenerate optical parametric amplification", J. Watson, P. Georges, T. Lepine, B. Alonzi, A. Brun, Opt. Lett., 20 231-3 (1995)

Tightly Bending Loss Measurement for 1.3 μm and 1.55 μm Broadband Wavelength Division Multiplexing Fiber Sensor Systems

Shyh-Lin Tsao* and Wen-Ming Cheng
Department of Electrical Engineering
Yuan Ze University
Chung-Li, Taiwan, R. O. C.

ABSTRACT

A tightly bending loss technique is developed for application in biomedical WDM fiber sensors. In this paper, we present the measurement and comparison of bending sensor in 1.3 μm and 1.55 μm wavelength region, respectively. A two - wavelength measurement setup is built for bending loss testing. Various wrapping method and turns are invested for studying the bending loss for broadband biomedical sensing system. We found that as the bending loss increases, the oblique angle of wrapping become large. These research results is helpful for multi-channel multi-array fiber optic biomedical sensor systems.

Keywords : Biomedical sensor, Fiber Sensor, Bending Loss, Wavelength Division Multiplexing

1. INTRODUCTION

Biomedical fiber-optical sensors attract a lot of attentions in last ten years¹⁻². Bending fiber-optic sensors are simple and cost effective. The fiber-optic bending sensors can be applied to measure many physical quantities, such as voltage, strain, temperature, pressure, etc³⁻¹¹. With the wavelength division multiplexing techniques intensively grew up¹², multichannel high-speed WDM distributed fiber-optic bending sensor become an important issue¹³⁻¹⁴. Such WDM fiber bending sensors can be applied in biomedical sensor systems.

In this paper, the bending fiber sensor we developed are using the Walsin- Fujikura single mode fiber (Spec No. : NWF-98F101, SM.10 / 125.04.UV)¹⁵ which is commonly used in Taiwan. Three wrapping schemes: normal wrapping, overlap

*Correspondence : E-mail : jimmy@saturn.yzu.edu.tw, Telephone : 886-3-4638800-424, Fax : 886-3-4639355

wrapping and cross wrapping are considered. The tightly bending losses are measured with the three wrapping schemes with bending radius 1 mm to 25 mm. The bending losses are different in 1.3 μm and 1.5 μm with various wrapping schemes and bending radii. We also analyze the bending loss with various wrapping turns. In broadband WDM fiber biomedical bending sensor system, it is important to determinate the wavelength responses in different wavelength channels. The experimental results can be used for clarifying the relationship between the maximum number of bending loss sensor and the operation wavelength band.

Owing to bending and unsuitable wrapping structure will induce tension in process of the fiber manufacture and construction, the optical transmission signal will experience the extra radiation losses and be attenuated. Although several bending loss measurement standard have been developed^{16,17}, only a few papers discuss about wrapping in various structure, turns and wavelength have been reported¹⁸⁻¹⁹. This work is important for future achieving wide-band WDM biomedical fiber sensors systems, including manufacturing, constructing and cabling process. In the following, we will concentrate on bending loss mechanism, and the bending loss characteristics in various wavelength windows. The following sections show the experimental setup and results.

2.DESRIPTION OF EXPERIMENTAL ARRANGEMENT

The schematic diagram of the experimental apparatus consist of two laser sources operating at 1.3 μm and 1.55 μm wavelength, the fiber is wrapped around a mandrel with various diameters R, the end is a power meter for reading the power losses, as shown in Fig .1. The schematic diagram of the wrapping style is considered three schemes: normal wrapping, cross wrapping and overlap wrapping as shown in Fig .2.

3.EXPERIMENTAL RESULTS

3.1 The relation of bending losses v. s. bending radius

Some Walsin-Fujikura single mode fibers (SM.10 /12504UV) are used for the following experiments. Their mode field diameter is $9.3 \pm 0.5 \mu\text{m}$ at 1310 nm, cladding diameter is $125 \pm 1.0 \mu\text{m}$ and outer coating diameter is $245 \pm 10 \mu\text{m}$. Their typical refractive index difference value is 0.36 % , and intrinsic attenuation value is 0.35 dB / km at 1.3 μm wavelength and 0.22 dB / km at 1.55 μm wavelength. The bending losses versus the bending radii are shown in Fig .3. The bending losses with radii from 1mm to 10 mm are measured at 1.3 μm and 1.55 μm wavelength windows. The bending losses are larger at 1.55 μm than at 1.3 μm wavelength. When the fiber is bent smaller than radius of 10 mm, the bending loss will increase from 0 dB to 70 dB rapidly at 1.55 μm and bending loss will increase from 0.5 dB to 2.5 dB at 1.3 μm . Obviously, the smaller bending radius will induce the bigger bending loss. Especially, the bending loss is obviously become higher with radius $R < 3 \text{ mm}$ at 1.55 μm .

3.2 The relation of bending loss v. s. wrapping scheme

The fiber is wrapped around a mandrel of 25 mm diameter in this subsection. The power losses versus 1 to 20 turns with three wrapping schemes: normal, overlap and cross wrapping at 1.3 μm are shown in Fig .4. Obviously, the bending loss is a function of loop turns with various wrapping. The bending loss belongs to the cross wrapping comparing with the overlap wrapping and the normal wrapping schemes show large variation with respect to wrapping turns. Therefore, how the fiber was wrapped is important for fiber bending sensor design. The most sensitive scheme is cross wrapping bending fiber sensor. The same phenomenon happen at 1.55 μm wavelength, but losses is much higher. As shown in Fig .5, we find that the bending loss sensitivity of the wrapping scheme at 1.55 μm wavelength is higher than at 1.3 μm wavelength, so the sensitive wavelength band is 1.55 μm for WDM optical bending fiber biomedical sensor system.

3.3 The relation of bending loss v.s. wrapping oblique angle

The fiber was wrapped with oblique angle θ from 0° to 60° experimentally . As shown in Fig .6 and Fig .7, the bending loss is a function of oblique angle, the fitting bending loss functions can be written as :

$$L_{1.3\mu\text{m}}(\theta) = 0.0064 \theta^2 - 0.2144 \theta + 0.6467 , \quad (1)$$

$$L_{1.55\mu\text{m}}(\theta) = 0.0218 \theta^2 - 0.4354 \theta + 1.1514 , \quad (2)$$

For comparison, the experimental and theoretical curves shown in Fig .6 and Fig .7 show the difference between the 1.3 μm and 1.55 μm . The bigger the wrapping oblique angle, the bigger the losses in both wavelength. The bending losses are still greater at 1.55 μm than at 1.3 μm wavelength. Especially, the laser operating at 1.55 μm wavelength for WDM optical fiber biomedical sensor system show promising sensitivity with respect to the oblique angle. The oblique angle of wrapping is demonstrate as an important parameter for WDM optical bending fiber biomedical sensor system in the first time.

3.4 The relation of bending loss v. s. wrapping interval

The fiber was wrapped 5 turns with interval from 1 mm to 5 mm. In Fig .8 and Fig .9, the bending loss is a function of wrapping interval, the fitting functions can be represented as:

$$L_{1.3\mu\text{m}}(D) = - 0.0046D^2 - 0.219D + 0.3907 , \quad (3)$$

$$L_{1.55\mu\text{m}}(D) = - 0.0568D^2 - 0.1766D + 7.2921 , \quad (4)$$

Comparing the experimental and theoretical curves shown in Fig.8 and Fig.9, the theoretical fitting curve is well matched the experimental data. The bigger the wrapping interval, the smaller the losses we found. The bending loss sensitivity of wrapping interval at 1.55 μm wavelength is still higher at 1.55 μm than at 1.3 μm wavelength. So the better light source is 1.55 μm wavelength for WDM optical fiber sensor system. The interval of wrapping is also an important parameter considered for WDM fiber biomedical sensor network.

4.CONCLUSION

In summary, before achieving a broadband WDM fiber-optical bending biomedical sensor networks, we measured the

bending losses in 1.3 μm and 1.5 μm band with various bending radius, wrapping schemes, and turns. Based on those experimental results, we built up some simple theoretical models for describing the design rules. In the future, the models can be applied to develop a WDM fiber biomedical sensor system as shown in Fig.10. This work is very helpful for future broadband WDM fiber biomedical sensor network. Because the transceiver in 1.3 μm and 1.55 μm band are cost effective for applying in fiber communication systems, we believe using 1.3 μm and 1.55 μm light for broadband WDM distribution fiber biomedical sensor systems is possible in the future.

5.ACKNOWLEDGE

This work was supported in part by the communication business unit of the Walsin - Lihwa Corporation. The authors would like to thank Technology Director Ping-Ching Lin of Walsin-Lihwa Corporation for valuable experimental components and equipment supports.

REFERENCE

1. J. J. Magera and B. P. McCann, "Silica-core fibers for medical diagnosis and therapy", *proc. Of optical Fibers in Medicine VII*, 1649, pp. 2-7, 1992.
2. L. A. Tempelman, J. P. Golden, G. P. Anderson, F. S. Ligler, "Use of cyanine dyes with evanescent wave fiber optic biomedical applications", *Proc. of Chemical, Biomedical, and Environmental Fiber Sensors VI*, 2293, pp.139,148.
3. P. Dinev, "Fiber - optic voltage sensor using an optical lever", *IEEE proceedings Optoelectronics*, **144**, pp. 253 - 255, 1997.
4. A. Todoroki, T. Hotanaka, H. Kobavashi, H. Nakamura, Y. Shimamura, "Strain measurement by curved optical fiber sensor", *Transactions of the Japan Society of Mechanical Engineers, Part C*, **62**, pp. 3710 - 3714, 1997.
5. A. Golbazi, "Prebiased microbending optical sensor", *proceeding of SPIE*, **2839**, pp.426 - 433, 1996.
6. C. K. Asawa, S. K. Yao, R. C. Streans, N. L. Mota, and J. W. Downs, "High sensitivity strain sensor for measuring structural distortion", *Electron Lett.*, **18**, pp. 362-364, 1982.
7. J. W. Berthold, "Historical review of fiber-optic sensors", *J. Lightwave Technol.*, **13**, pp. 1193-1199, 1995.
8. S. Tomita, H. Tachino, and N. Kasahara, "Water sensor with optical fibre", *J. Lightwave Technol.*, **8**, pp. 1892-1832, 1990.
9. T. Yoshino, M. Nara, and K. Kurosawa, "Remote and multi-point fiber sensors using optical time domain reflectometry", *Proceedings of 13th congress of the International Commission for Optics, Sapporo*, pp. 324 - 325, 1984.
10. D. Varshneya, W. L. Ghering, and J. W. Berthold, "High-temperature fibre-optic microbend sensor", *Proceedings of 3rd Optical fiber sensors conference, San Diego*, pp.140, 1985.
11. J. N. Fields, and J. H. Cole, "Fiber microbend acoustic sensor", *Appl. Opt.*, **19**, pp. 3236 - 3267, 1980.
12. C. D. Chen, I. Kim, D. Mizura, T. V. Nguyen, K. Ogawa, R. E. Tench, L. D. Tzeng, P. D. Yeates, "1.2 Tbit /s (30ch \times

- 40Gbit/s) WDM transmission over 85 Km fiber “, *Electronic Letters*, **34**, pp.1002 – 1004,1998.
13. T.E. Clark et al., ” Overview of multiplexing techniques for all-fiber interferometric sensor arrays “. *Proc. SPIE-Int. Soc. Opt. Eng.* **718**, pp. 80 – 91, 1986.
 14. E. Udd and J. P. Theriault , “ Fiber-optic microbending sensors sensitive over different bands of wavelength of light.” *U.S. Pat.* **5, 118, 931**, 1992.
 15. Walsin - Fujikura single mode optical fiber (SM.10 / 125.04UV) SPECIFICATION, Spec. No. : NWF – 98 F 101, Issue Date : Feb.25,1998.
 16. P. D. Lazay, A. D. Person, ” Developments in single-mode fiber design, materials, and performance at Bell Laboratories “ . *IEEE Trans. MTT-30*, pp. 350-356, 1982.
 17. A. O Garg, C. K. Eoll, ” Experimental characterization of bend and microbend losses in single-mode finer fibers “. *Wire & Cable Sympos . Proceed 1986*, P.P. 406-414, 1986.
 18. T. Yoshino, K. Inoue, Y. Kobayashi, “ Spiral fibre microbend sensors “, *IEE Proc.-Optoelectron.*, **144**, 1997.
 19. T. Yoshino, K. Inoue, Y. Kobayshi, and Y. Takahashi, “Spring coil fiber microbend sensor with well – defined characteristics ” , *Proceedings of 11th Optical fiber sensors conference, Sapporo*, pp. 264 – 267 , 1996 .

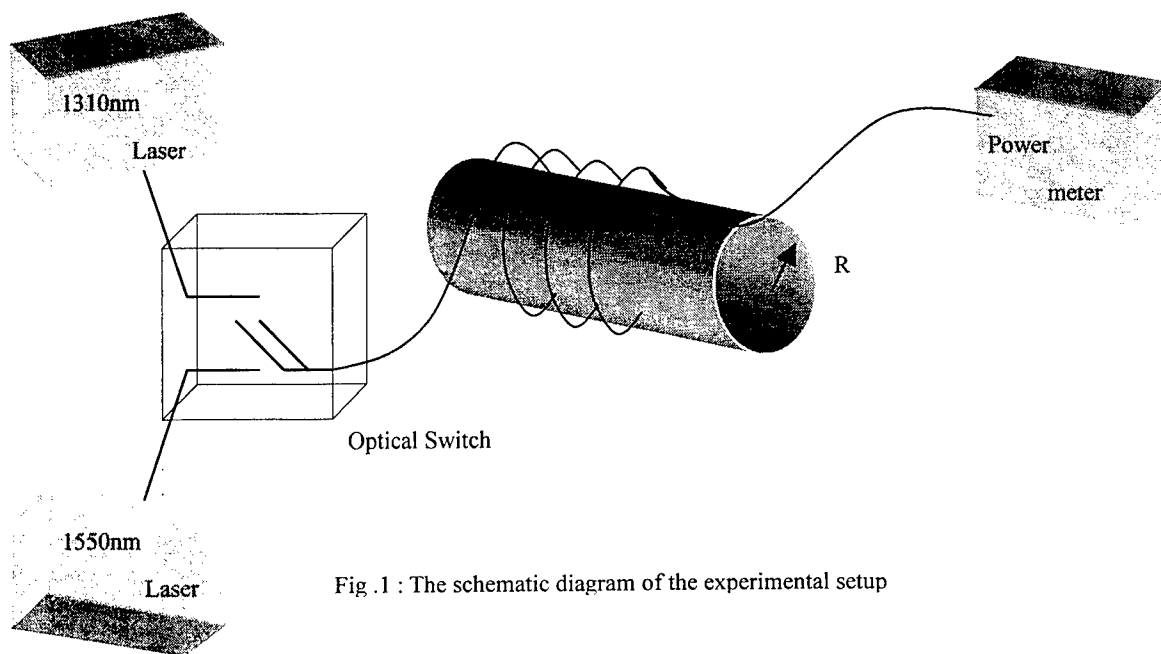
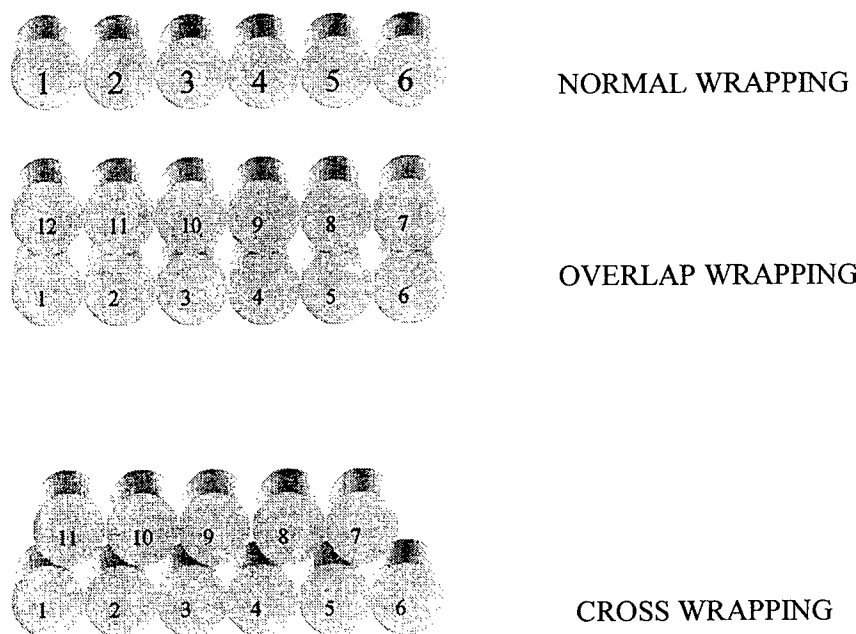


Fig .1 : The schematic diagram of the experimental setup



F i g .2 : The schematic diagram of various wrapping structure

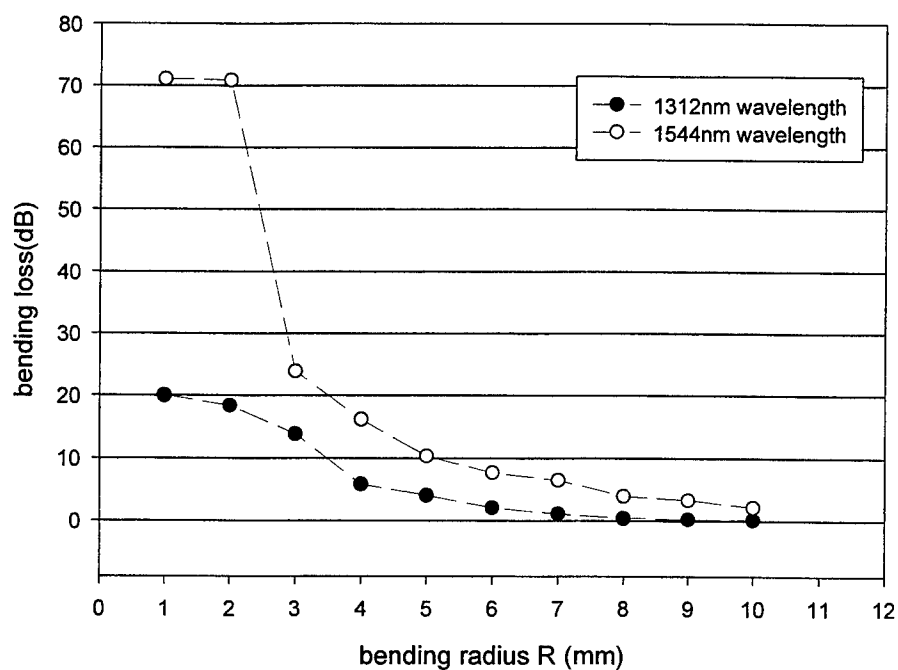


Fig . 3 : The bending loss v.s. bending radii

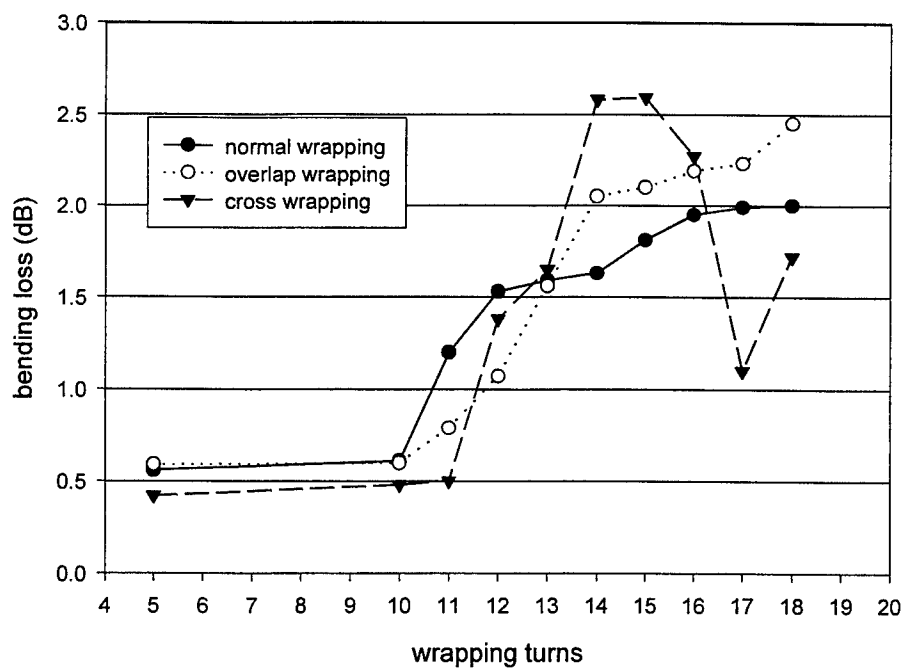


Fig . 4 : The bending loss v.s. wrapping turns at 1312 nm

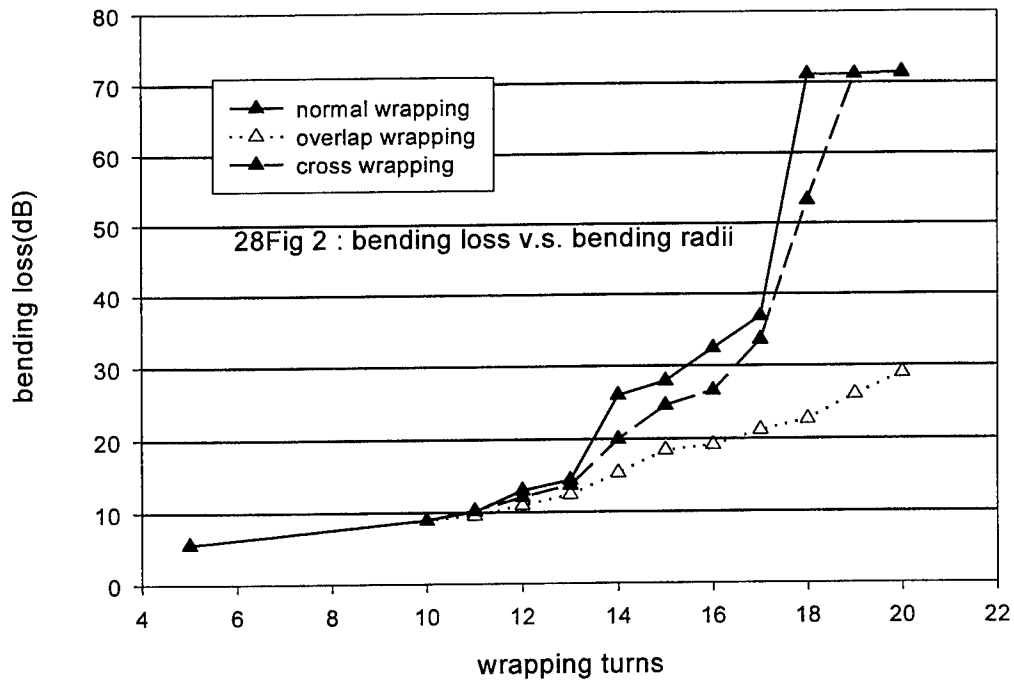


Fig . 5 : The bending loss v.s. wrapping turns at 1544nm

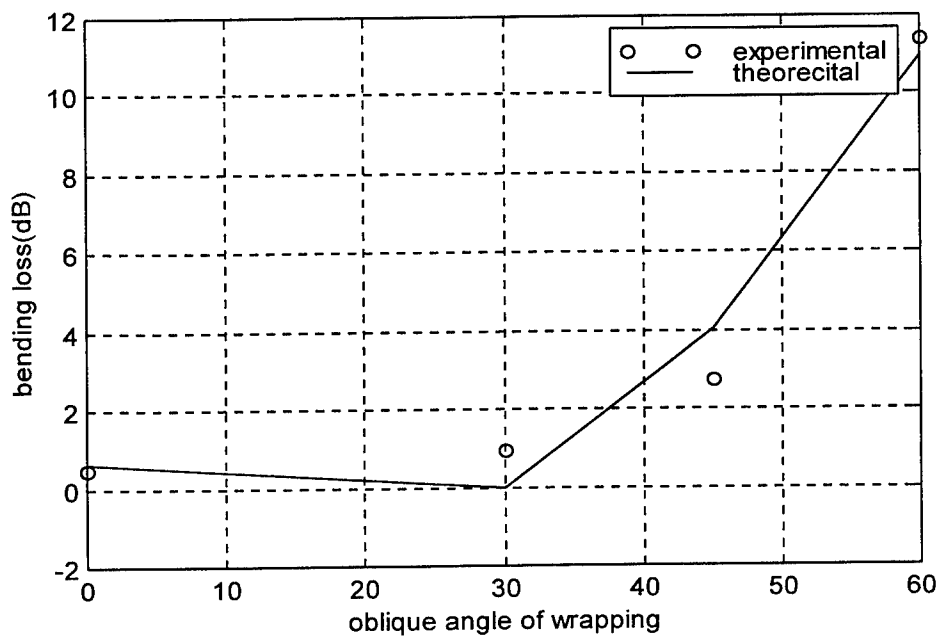


Fig .6 : The bending loss v.s. oblique angle of wrapping at 1.3 μm wavelength

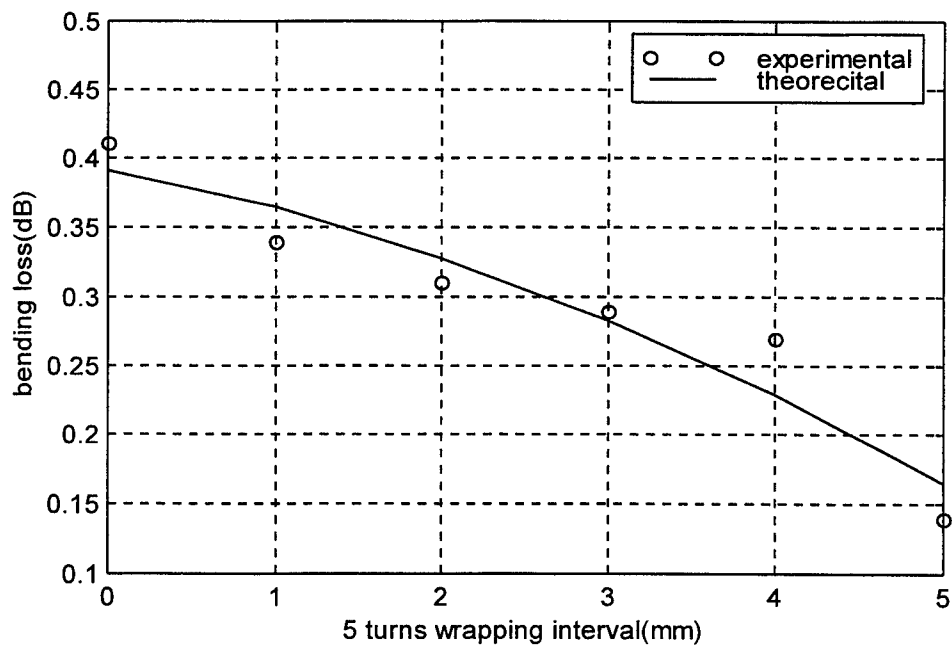


Fig. 7 The bending loss v. s oblique angle of wrapping at 1.55μm wavelength

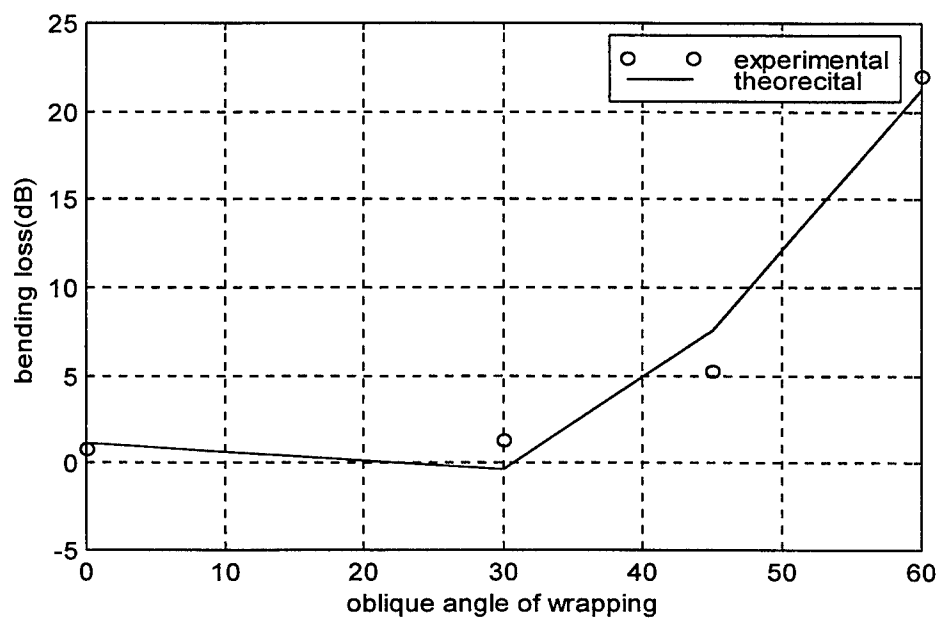


Fig. 8: The bending loss v.s. wrapping interval at 1.3 μm wavelength

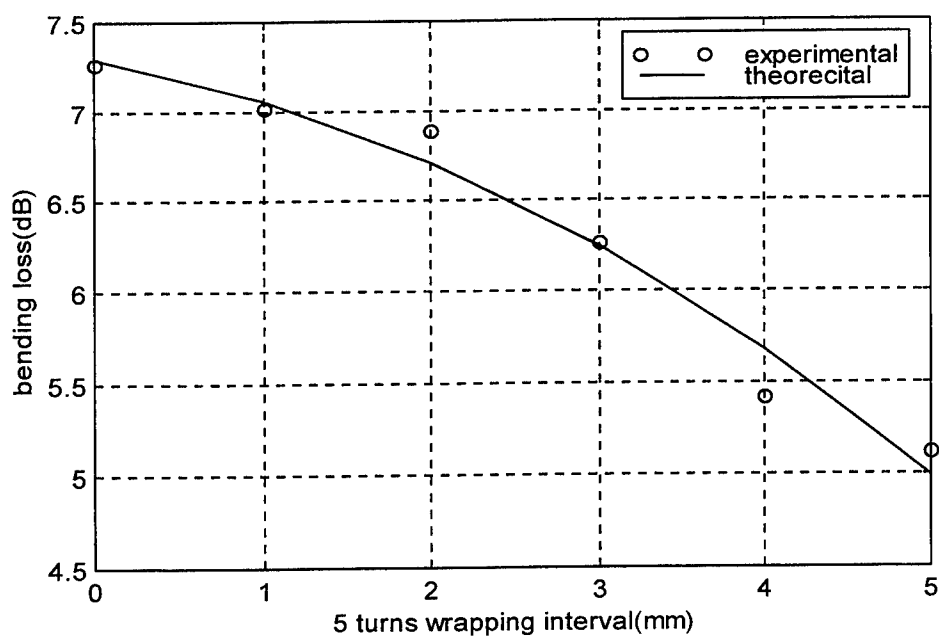


Fig .9 : The bending loss v.s. wrapping interval at 1.55 μm wavelength

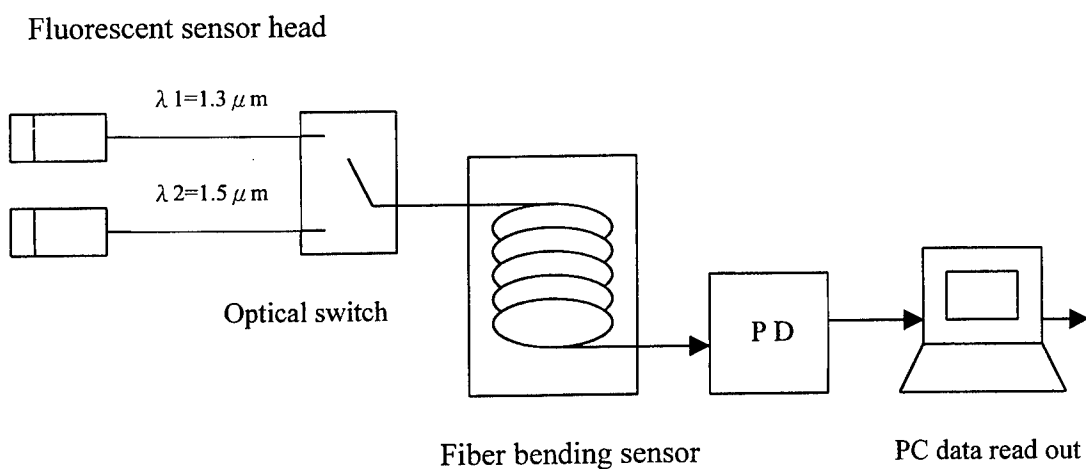


Fig.10 : Schematic diagram of a WDM bending sensor

Experimental study on fiber Bragg grating electric current sensor

Dejun Feng*, Guiyun Kai, Lei Ding, Heliang Liu, Xiaoyi Dong

Institute of Modern Optics, Nankai University, Tianjin 300071, China

ABSTRACT

A new electric current sensor based on fiber Bragg grating tuned by giant magnetostrictive material rod is demonstrated in this paper. A fiber Bragg grating is firmly clung on a giant magnetostrictive rod that is put into the central part of a solenoid. The Bragg wavelength of the fiber grating will shift when the uniform magnetic field in the solenoid changes. The rod will have elastic lengthening along the direction of the magnetic field. The grating resonant wavelength of fiber grating will shift as consequence of the rod lengthening. The relationship between the electric current and the wavelength shift is basically linear. The wavelength range of linear tuning is about 0.9nm. The tuning sensitivity is about 0.001nm/mA.

Keywords: Giant magnetostrictive material, Fiber grating, Solenoid, Electric current sensor

1. INTRODUCTION

Fiber Bragg grating (FBG) sensor technology has become one of the most progressing sensing topics of this decade in the field of optical fiber sensor technology as FBG sensors are capable of measuring a wide range of parameters^{1,2}. The main reason for this is because FBG sensors have a number of distinguished advantages over other implementations of fiber-optic sensors, in particular absolute measurement, potential low-cost, flexibility, and unique wavelength-multiplexing capacity. Hence, FBG sensors are of great importance in civil, industrial and military fields.

Faraday effect is used for electric current sensing for conventional current sensors while Kerr effect or Pockels effect is used for voltage sensors³. Optical fiber sensors exploiting Faraday effect have been intensively studied. However, the practical application of optical fiber sensors cannot meet our need for problems associated with induced linear birefringence, temperature and vibration have limited the application of them. Several alternative methods have been set up in experiment to measure electric current and voltage, for example, a hybrid system that consists of a conventional current transformer and a piezoelectric element and an interferometric wavelength-shift detection method. FBGs are ideal for use in electrical power industry due to the immunity to electro-magnetic interference. A new electric current sensor based on fiber Bragg grating tuned by giant magnetostrictive material rod is demonstrated in this paper.

2. PRINCIPLE

The Bragg wavelength λ_B of the FBG is given by

$$\lambda_B = 2n_{eff} \Lambda, \quad (1)$$

where Λ is the fringe spacing of the FBG and n_{eff} is the effective refractive index.

* Correspondence: Email: feng_dj@263.net or feng_dj@freemail.online.tj.cn; Telephone: 86 22 23509479; Fax: 86 22 23508770

Both the refractive index and spacing, therefore Bragg wavelength are depended on temperature and strain. Assuming the temperature is unvarying, the strain-to-wavelength relation is given by

$$\frac{\Delta\lambda_B}{\lambda_B} = (1 - p_e)\epsilon_{ax}, \quad (2)$$

where p_e is the effective photoelastic coefficient. ϵ_{ax} is the strain along the grating's axis direction. The effective photoelastic coefficient can be expressed as

$$p_e = \frac{n_{core}^2}{2} [p_{12} - \mu(p_{11} + p_{12})], \quad (3)$$

where p_{11} and p_{12} are the photoelastic coefficients of the strain tensor, μ is the Poisson ratio and n_{core} is refractive index of the fiber core. For SiO_2 fiber, $n_{core} = 1.46$, $p_{11} = 0.12$, $p_{12} = 0.27$, $\mu = 0.16$, so $p_e \approx 0.22$. According to equation (2), the Bragg wavelength can shift under an axial strain. The giant magnetostrictive material is a special kind of alloy of TbDy(FeM)_2 system composition and a magnetostrictive rod of dimensions $5 \times 50\text{mm}$ is used in experiment as magnetic field transducer. When a magnetic field is applied to it, the magnetic domains in the magnetostictive material tend to align along the field direction and, as a result of the magnetoelastic coupling, the material suffers an elastic lengthening in the direction of the magnetic field⁴. Assuming a FBG is hold on a giant magnetostrictive rod which is placed into the central part of a multi-layer solenoid, the Bragg wavelength of the fiber grating will shift when the uniform magnetic field in the solenoid changes because the strain of the giant magnetostrictive rod will transfer to the FBG.

3. EXPERIMENTAL RESULTS AND DISCUSSION

Fig.1 is the diagram schematic of FBG sensing head. The FBG approximately 11mm in length is used in experiment, which is fabricated in Germanium-doped silica fiber by ourselves using a KrF excimer laser emitting at 248nm and a phase mask. The fiber Bragg grating with 96% peak reflectivity at 1549.02nm and 0.22nm bandwidth is used in this preliminary experiment. Fig.2 shows the experiment setup for current measurement of the sensor. Light from a broadband light source (BBS) is launched into the sensing head, the transmission light is monitored by a commercial optical spectrum analyzer (Advantest Q8383). The application of mechanical prestress will result in significance modification of its performance. The prestress will reduce the sensitivity to the magnetic field but gives a more linear response. The solenoid has about 2000 circles and the length of this solenoid is 120mm. Put the sensing head in the central part of a multi-layer solenoid and the magnitude of magnetic field is uniform in the central part. The magnitude of uniform magnetic field determined by the scope of the electric current in wax cloth windings. No mechanical prestress is applied in order to achieve maximum sensitivity to magnetic field. The relationship between the electric current and the wavelength shift is shown in Fig.3 (the dots is experimental results, the line is the fitted line).

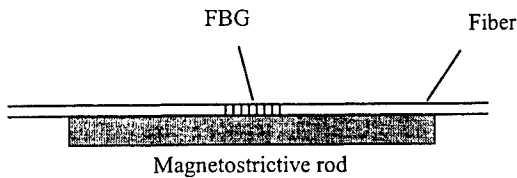


Fig.1 FBG sensing head

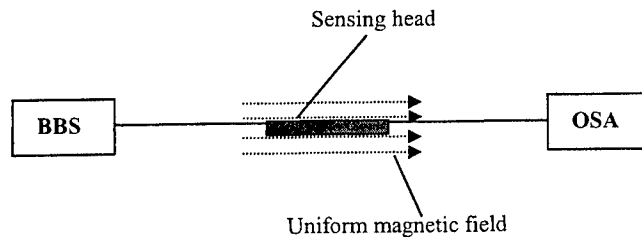


Fig.2 Schematic diagram of experimental setup for current effect measurement

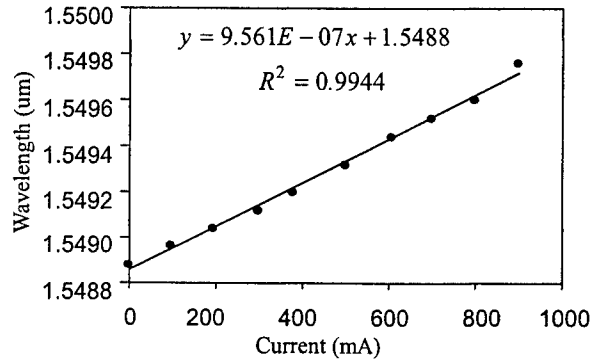


Fig.3 The relationship between the bragg wavelength of FBG and current

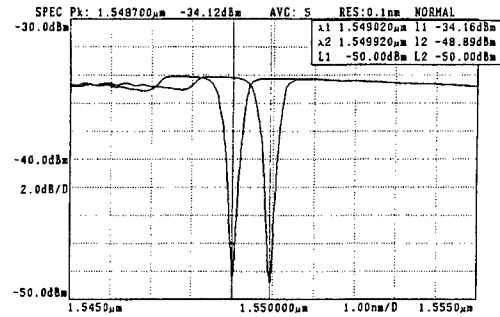


Fig. 4 The spectra of FBG at different currents

It is easy to see that the relationship between the current and the Bragg wavelength shift of FBG is basically linear ($R^2=0.9944$) in measuring range and the Bragg wavelength range of linear tuning of 0.9nm is achieved. The tuning sensitivity is about 0.001nm/mA. In preliminary experiment, we observe that Hysteresis will affect the measuring results if we go on increasing the current (more than 1A), so the measuring range of this current sensor not more than 900mA. When the current exceeds the linear operating range of the magnetostrictive material, the nonlinear behavior will appear due to the saturation of the alloy. The FBG suffers no chirp in the tuning process as it is illustrated in Fig. 4.

Temperature effect must be considered if the measuring time is long. The heat created by the solenoid will accumulate and it will affect the Bragg wavelength. In experiment, we use an adiabatic pipe to protect the sensing head from heat. How to eliminate the Hysteresis and temperature effect and extend the measuring range are important questions to be resolved in our farther study.

4. CONCLUSION

A new electric current sensor based on fiber Bragg grating tuned by giant magnetostrictive material rod is proposed. The relationship between the electric current and the wavelength shift is basically linear by the regression coefficient of $R=0.945$. This device has many characteristics, such as simple structure, high sensitivity, and good linearity. It is promising to be used into in-process industrial measurement and biological sensing. It also offers a potential alternative to promote the application of optoelectronic technology for improving human health, safety and environmental protection.

ACKNOWLEDGMENTS

The authors are grateful to the "National 863 Research Project" for its fund support.

REFERENCES

1. Alan D. Kersey, Michael A. Davis, *et al.*, "Fiber Grating Sensors." *J. Lightwave Technol.* **15**, pp. 1442-1463, 1997.
2. Yun-Jiang Rao, "Recent progress in in-fiber Bragg grating sensors:applications," *SPIE*, **3555**, pp. 429-441, 1998.
3. Yang Zhi, Li Changsheng, *et al.*, "A novel multi-function optical fiber sensing system for simultaneous measurement of current and voltage," *SPIE*, **3555**, pp. 57-62, 1998.
4. J. L. Cruz, A. Diez, *et al.*, "Fiber Bragg gratings tuned and chirped using magnetic fields," *Electron. Lett.*, **33**, pp. 235-236, 1997.

Characteristics Analysis of SOI Waveguide Michelson Interferometers for Developing Biomedical Fiber Temperature Sensing Head

Shyh-Lin Tsao* and Shin-Ge Lee
Department of Electrical Engineering
Yuan Ze University
Chung-Li, Taiwan, R.O.C

ABSTRACT

A new silicon-on-insulator (SOI) waveguide Michelson interferometer with Bragg reflective gratings as a biomedical temperature sensing array head is presented in this paper. The waveguide Bragg reflective gratings work as mirrors for adjusting the transfer function of the Michelson interferometer sensor. We will show the comparison of the temperature sensing accuracies of the fiber Bragg grating and SOI waveguide Michelson interferometers in biomedical applications. The grating length and perturbation period of waveguide Bragg grating in SOI waveguide Michelson interferometer will increase as temperature rises, that is, the thermal effects of the reflective Bragg gratings are considered in our analysis. According to the numerical analysis of power reflective spectra of waveguide Michelson interferometers, the temperature sensing of waveguide SOI Michelson interferometer can improve at least 20 times than traditional fiber Bragg grating temperature sensor. Moreover, the SOI waveguide interferometer sensor we designed presents high sensitivity than pure single waveguide Bragg grating sensor and fiber Bragg grating sensor by adjusting the length of the two interferometric arms. The full width of half maximum (FWHM) of the frequency responses of passband of SOI waveguide Michelson interferometer can be designed smaller than fiber and waveguide Bragg grating sensors for sensitivity improvement.

Key words: Biomedical waveguide sensor, silicon-on-insulator, Michelson interferometer, waveguide, temperature sensor

1. INTRODUCTION

Because of the fiber Bragg gratings (FBGs) have many advantages such as high sensitivity, and biocompatibility provide excellent reliability for physiological temperature sensing, we have studied them for measuring temperature in the field of biomedical applications¹. Fiber-optic temperature sensors have been widely studied²⁻⁴. Those fiber-optic sensors have many advantages, such as low volume and light weight, electromagnetic immunity and low cost. That is, to cooperate accurate fiber-optic temperature sensors with fiber-optic biomedical sensors is very desirable. Therefore, highly accurate

* Correspondence: E-mail: jimmy@saturn.yzu.edu.tw, Telephone: 886-3-4638800-424, Fax: 886-3-4639355

fiber-optic temperature sensors are valuable in the trend of developing all fiber-optic physiological sensors. Moreover, some advanced fiber optical sensors using optical fiber interferometer structures have also been discussed and developed because of their high sensitivity in measurement of vibration, surface roughness, and chromatic dispersion, etc⁵⁻⁹. Recently, the integrated optical devices have shown outstanding performance as the tremendous promising developments of silicon-on-insulator (SOI) integrated electrical circuits¹⁰⁻¹¹. Especially, the application of integrated optical periodic dielectric waveguide gratings in optical sensing have been widely studied¹²⁻¹⁴.

In this paper, we designed a new SOI waveguide Michelson interferometer sensor for developing biomedical fiber temperature sensing head. The application scheme we proposed is shown in Fig. 1. The optical SOI waveguide Michelson interferometer sensor we designed are used for replacing fiber Michelson interferometer sensors for reducing the sensor size. This paper is organized as follows: Section 2 describe the mathematical formulations of our designed integrated optical waveguide Michelson interferometer sensor in temperature sensing. The numerical results of SOI waveguide Michelson interferometer sensor for temperature sensing are exhibited in Section 3. We also give the conclusions of our designed optical devices in final section.

2. MATHEMATICAL FORMULATIONS OF OPTICAL SOI WAVEGUIDE MICHELSON INTERFEROMETER SENSORS

In this section, we describe the mathematical formulations of the SOI optical waveguide Michelson interferometer sensors. The schematic structures of our designed SOI waveguide Michelson interferometer and single SOI waveguide Bragg grating sensor on UNIBOND SOI wafer are shown in Fig. 2 and Fig. 3, respectively. The UNIBOND SOI wafer is designed with 1.5 μm thick silicon surface layers and 0.4 μm buried-oxide layer on silicon substrate. Considering the SOI waveguide coupler of Michelson interferometer sensor shown in Fig. 2, each arm has a length, l_i ($i = 1$ to 4) and two SOI waveguide grating with reflection coefficient r is designed in the ends of two output arms. The light is launched at any arm and reflected and interfered in our designed Michelson interferometric cavity to achieve narrow optical passband spectra for increasing sensor sensitivity.

The scattering matrix method¹⁵ is used for deriving the reflected optical fields from output ports of the SOI waveguide Michelson interferometer and are derived as following terms:

$$E_{r1} = \frac{re^{-i\beta l_1}}{(1-K)} [Ke^{-2i\beta l_3} + (1-K)e^{-2i\beta l_4}] E_{in} \quad (1)$$

$$E_{r2} = \left[\frac{i\sqrt{K}}{K + \sqrt{1-K}} r(e^{-2i\beta l_3} + e^{-2i\beta l_4}) e^{-i\beta(l_1+l_2)} \right] E_{in} \quad (2)$$

$$E_{r3} = [i\sqrt{K}(1-r)^2 e^{-i\beta(l_1+l_4)}] E_{in} \quad (3)$$

$$E_{r_4} = [\sqrt{1-K}(1-r)e^{-i\beta(l_1+l_4)}]E_{in} \quad (4)$$

where E_{in} is the initial input optical field, K is the coupling constant of the SOI waveguide coupler, β is the propagating constant, $l_{i(i=1, 2, 3, 4)}$ is the length of each arm, r is defined as the reflected power ratio of SOI waveguide Bragg grating with amorphous silicon cover and is derived in the following. In this paper, we will show the improvement of the accuracy with replacing the fiber Bragg gratings by SOI waveguide Michelson interferometer sensors. The author can determine the variance of temperature by designing and analyzing the reflecting power spectra of waveguide devices. A periodic sinusoidal index corrugation is distributed along the direction of this waveguide device. We may derive the reflected power of single SOI waveguide Bragg grating sensor with amorphous silicon cover based on the coupled-mode equations¹⁶ as

$$r = \frac{\left(\frac{\pi \Delta n f}{c}\right)^2 \sinh^2 \left[\sqrt{\left(\frac{\pi \Delta n f}{c}\right)^2 - \left(\frac{2\pi f}{c} - \frac{\pi}{\Lambda}\right)^2} L \right]}{\sqrt{\left(\frac{\pi \Delta n f}{c}\right)^2 - \left(\frac{2\pi f}{c} - \frac{\pi}{\Lambda}\right)^2} \cosh^2 \left[\sqrt{\left(\frac{\pi \Delta n f}{c}\right)^2 - \left(\frac{2\pi f}{c} - \frac{\pi}{\Lambda}\right)^2} L \right] + \left(\frac{2\pi f}{c} - \frac{\pi}{\Lambda}\right)^2 \sinh^2 \left[\sqrt{\left(\frac{\pi \Delta n f}{c}\right)^2 - \left(\frac{2\pi f}{c} - \frac{\pi}{\Lambda}\right)^2} L \right]} \quad (5)$$

where L is the length of Bragg grating, Δn is the grating index perturbation, c is the light speed in free space, f is the optical frequency, n is the refractive index and Λ is the period of the waveguide Bragg grating. From Eq. (5), we know that the maximum power reflection only occurs on the phase matching condition. When we considered the variance of temperature ΔT of SOI wafer under monitoring biomedical signals, the central optical frequency of the reflecting spectrum will drift as f_R as¹⁷

$$f_R = \frac{c}{[1 + (E + T_0)\Delta T]2n\Lambda} \quad (6)$$

where E and T_0 are the thermal expansion coefficient and the thermo-optic coefficient of the SOI waveguide Bragg grating, respectively. The parameters for analyzing the reflective spectra of SOI waveguide sensor and fiber sensor are listed in Table I¹⁸. The length L and period Λ of waveguide Bragg grating will increase as temperature rises, that is, the thermal effects are considered in our analysis.

3. NUMERICAL RESULTS OF SOI WAVEGUIDE MICHELSON INTERFEROMETER SENSORS FOR TEMPERATURE SENSING

Through a serial analysis and derivations of the work formulations mentioned above, Fig. 4 shows the numerical results of the reflected spectra of FBG and SOI Michelson interferometer sensor with the temperature variation 10°C. The numerical results of the reflected spectra of SOI waveguide grating sensor and SOI Michelson interferometer sensor with the temperature variation 10°C is shown in Fig. 5. The SOI Michelson interferometer sensor is designed with $K=0.5$, $l_1=l_2=3$ mm, $l_3=4$ mm, $l_4=4.068$ mm, $L=0.1$ mm, and $\Lambda=0.2215$ μ m. The SOI grating sensor with $L=0.1$ mm and $\Lambda=0.2215$ μ m, the same parameters for comparing with SOI Michelson interferometer sensor. The fiber Bragg grating sensor is designed with $L=5$ mm and $\Lambda=0.5166$ μ m for achieving the same reflected spectrum as SOI grating sensor. In Fig. 4 and Fig. 5, the FBG sensors and SOI waveguide Bragg grating sensors were compared with SOI waveguide Michelson

interferometer sensors, assume all of the devices have the same initial center wavelength of the reflection spectrum at 1.55 μm . Especially, the FBG sensor and SOI grating sensor are designed with almost the same reflection spectra at initial setting temperature as a solid line in Fig. 4 and Fig. 5 with the 10°C temperature variation, the reflecting spectra shifting show the SOI grating has much better response. Attaching the same SOI waveguide grating on the ends of a 2 x 2 optimal SOI coupler, the reflecting spectra coming from the output port 2 of the designed SOI Michelson interferometer sensor show a narrow bandwidth. Therefore, a SOI waveguide Michelson interferometer sensor has higher sensing resolution for biomedical applications.

4. CONCLUSION

According to the numerical analysis of the power reflective spectra of waveguide Michelson interferometers mentioned above, the temperature sensing of waveguide SOI Michelson interferometer for developing biomedical fiber temperature sensing head can improve at least 20 times than fiber Bragg grating temperature sensor. Moreover, the SOI waveguide interferometer sensor we designed presents high sensitivity than pure single waveguide Bragg grating sensor. The full width at half maximum (FWHM) of the frequency responses of passband of SOI waveguide Michelson interferometer can be designed smaller than fiber Bragg grating sensors for sensitivity improvement. Owing to excellent characteristics of smaller FWHM and high finesse in temperature sensing for biomedical signal monitoring, the waveguide SOI Michelson interferometer we designed may replace the traditional fiber Bragg grating sensors system for biomedical applications.

ACKNOWLEDGMENT

This work was supported in part by National Science Council of Republic of China under contract no. NSC 89-2215-E-155-002 and NDL-89-C-017. The authors would like to thank Peng-Chun Peng and Ming-Chun Chen for valuable discussions and simulation supports.

REFERENCE

1. S. -L. Tsao, and J. Wu, "Highly accurate temperature sensor using two fiber Bragg grating gratings," *IEEE J. of Selected Optics in Quantum Electronics*, **2**, pp. 894-897, 1996.
2. A. M. Vengasarkar, C. Michie, L. Jankovic, B. Culshaw, R. O. Claus, and C. Senior, "Fiber-optic dual-technique sensor for simultaneous measurement of strain and temperature," *J. Lightwave Technol.*, **12**, pp. 170-177, 1994.
3. X. Bao, D. J. Webb, and D. A. Jakson, "Combined distributed temperature and strain sensor based on Brillouin loss in an optical fiber," *Opt. Lett.*, **19**, 1994.
4. O. Shenfeld and A. Katzir, "Infrared fiberoptic temperature control of the heating process in a microwave oven," *IEEE Trans. Microwave Theory Tech.*, **42**, pp. 901-903, 1994.
5. D. P. Hand, T. A. Carolan, J. S. Barton, and J. D. C. Jones, "Extrinsic Michelson interferometric fiber optic sensor with bend intensive downlead," *Opt. Commun.*, **97**, pp. 295-300, 1993.
6. D. P. Hand, T. A. Carolan, J. S. Barton, and J. D. C. Jones, "Profile measurement of typically rough surfaces by

- fiber-optic ineterferometry," *Opt. Lett.*, **18**, pp. 1361-1363, 1993.
7. W. Jin, D. Uttamchandani, and B. Culshaw, "Direct readout of dynamic phase changes in a fiber-optic homodyne inetrferometer," *Appl. Opt.*, **31**, pp. 7253-258, 1992.
 8. J. A. Ferrari, E. M. Frins, and W. Dultz, "Optical fiber vibration sensor using (pancharatnam) phase step interferometry," *IEEE J. of Lightwave Tech.*, **15**, no. 6, pp. 968-971, 1997.
 9. L. Thrvenaz, J. P. Pellaux, and J. P. V. D. Weid, "All-fiber interferometer for chromatic dispersion measurements," *IEEE J. of Lightwave Tech.*, **6**, no. 1, pp. 1-7, 1997.
 10. H. Shimano, N. Sakashita, F. Okuda, T. Oashi, Y. Yamaguchi, T. Eimori, M. Inuishi, K. Arimoto, S. Maegawa, Y. Inoue, S. Konwri, K. Kyuma, "1V 46ns 16MB SOI-DRAM with body control technigue", *IEEE Journal of Solid- State Cirauits*, **33**, pp. 1712-1720, 1997.
 11. Y.-H. Koh, Pq.-R. Oh, J.-W. Lee, J.-W. Yang, W.-C. Lee, C.-K. Park, J.-B. Park, Y.-C. Heo, K.-M. Rho, B.-C. Lee, M.-J. Chung, M. Huh, H.S. Kim, K.-S. Choi, W.-L. Lee, "1 giga bit SOI DRAM with fully bulk compatible process and body contacted SOI MOSFET structure" *Proceedings of the 1997 International Electron Device Meeting*, pp. 579-582, 1997.
 12. S. F. Helfert, and Reinhold Pregla, "Efficient analysis of periodic structures", *IEEE J. of Lightwave Technology*, **16**, pp. 1694-1702, 1998.
 13. S. M. Melle, K. Liu, and R. M. Meaures, "A passive wavelength demoudulation system for guided-wave Bragg grating sensors," *IEEE Photonic Technology Letters*, **4**, no.5, pp. 516-518, 1992.
 14. T. S. Larsen, S. Bouwstra, and O. Leistiko, "Opto-mechanical accelerometer based on strain sensing by a Bragg grating in a planar waveguide," *The 8th International Conference on Solid State Sensors and Actuators, and Eurosensors, Sweden*, 405-C12, June pp. 25-29, 1995.
 15. F. Scanchez, "Matrix algebra for all-fiber optical resonators", *IEEE J. of Lightwave Technology*, **9**, pp. 838-844, 1991.
 16. A. Yariv and P. Yeh, "Optical waves in crystals", *New York: Wiley*, 1984, Chapter 6.
 17. M. G. Xu, L. Reekie, Y. T. Chow, and J. P. Dakin, "Optical in fiber grating high pressure sensor", *Electron. Lett.*, **29**, pp. 398-399, 1993.
 18. G. Cocorullo and I. Rendina, "Thermo-optical modulation of a 1.5 μ m in silicon etalon", *Electron. Lett.*, **28**, pp. 83, 1992.

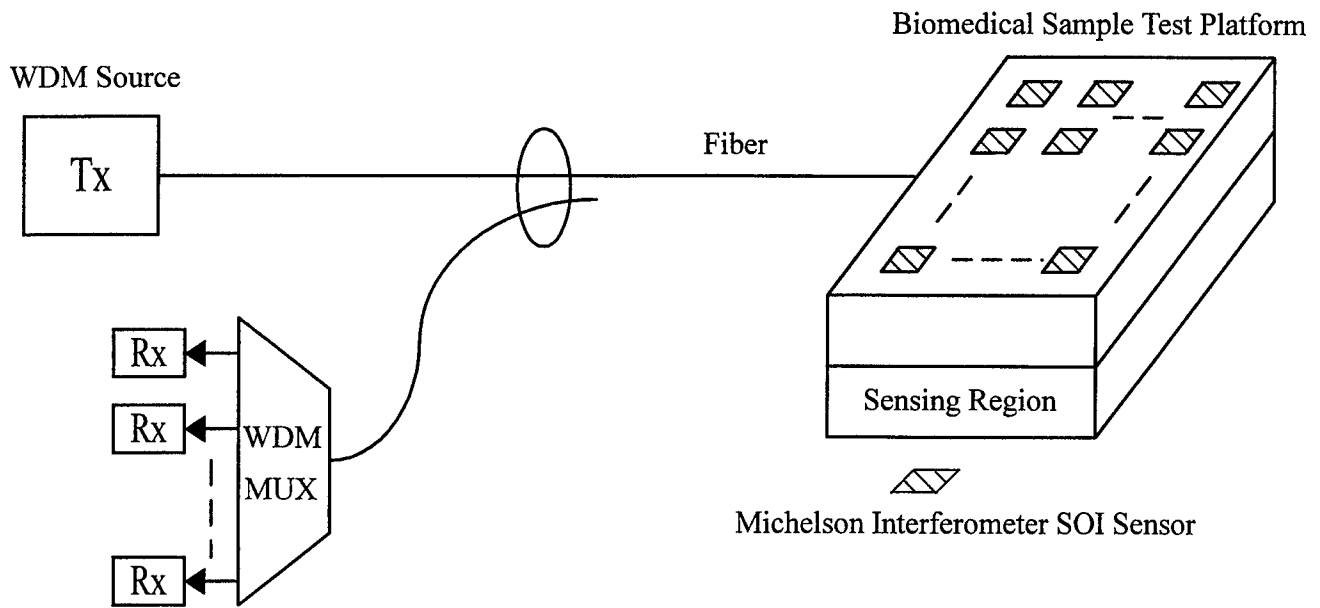


Fig. 1 The design of a SOI waveguide Michelson interferometer for developing biomedical fiber temperature sensing head

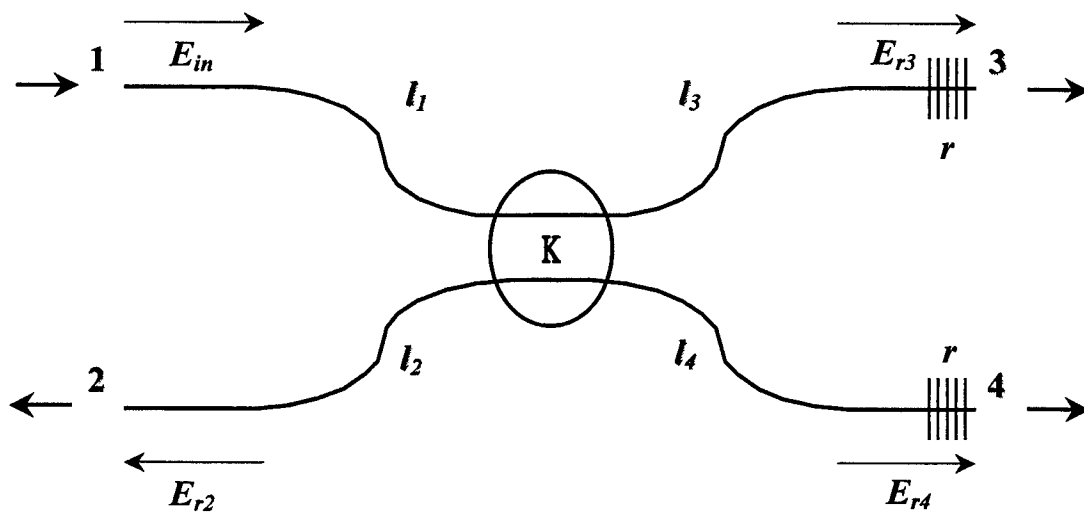


Fig. 2 The schematic diagram of a SOI waveguide Michelson interferometer sensor

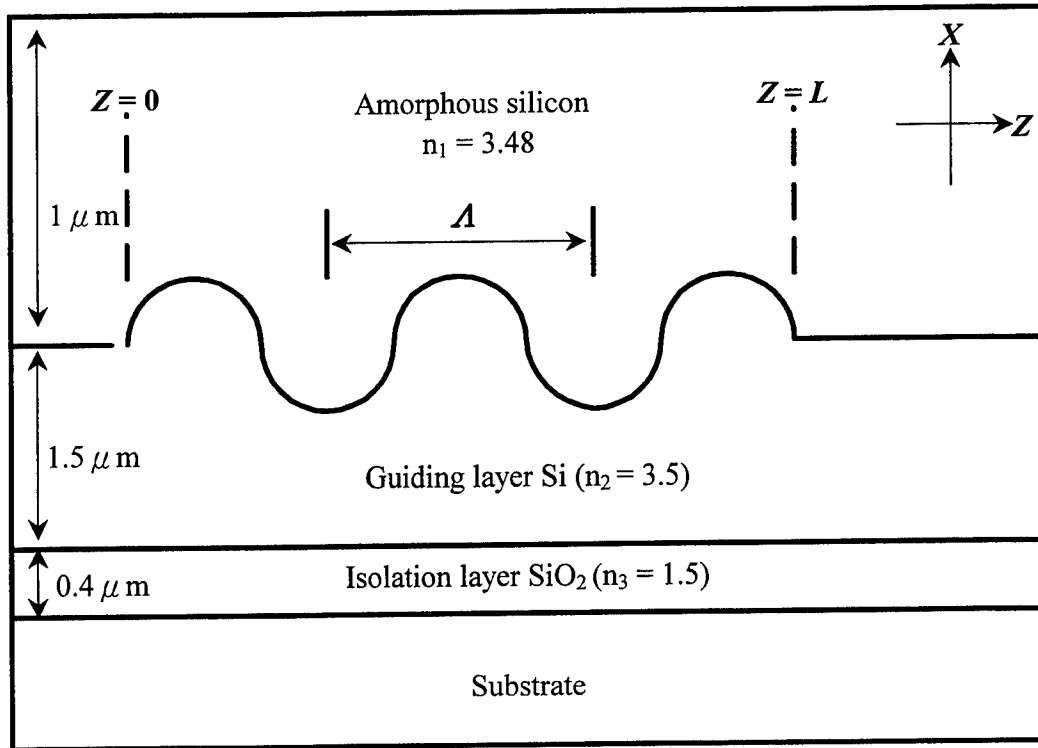


Fig. 3 The schematic diagram of a sinusoidal-index SOI Bragg grating waveguide with amorphous silicon cover sensor

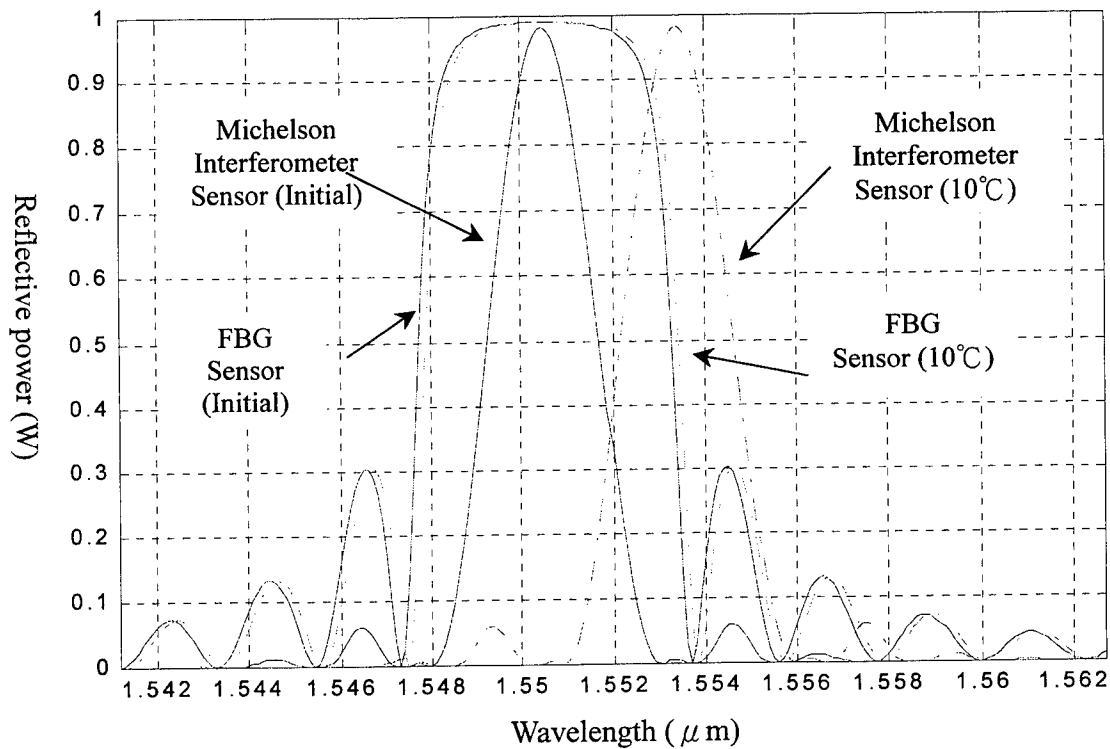


Fig. 4 The comparison of the reflected spectra from FBG and SOI Michelson interferometer sensor with temperature 10°C offset from the initial temperature

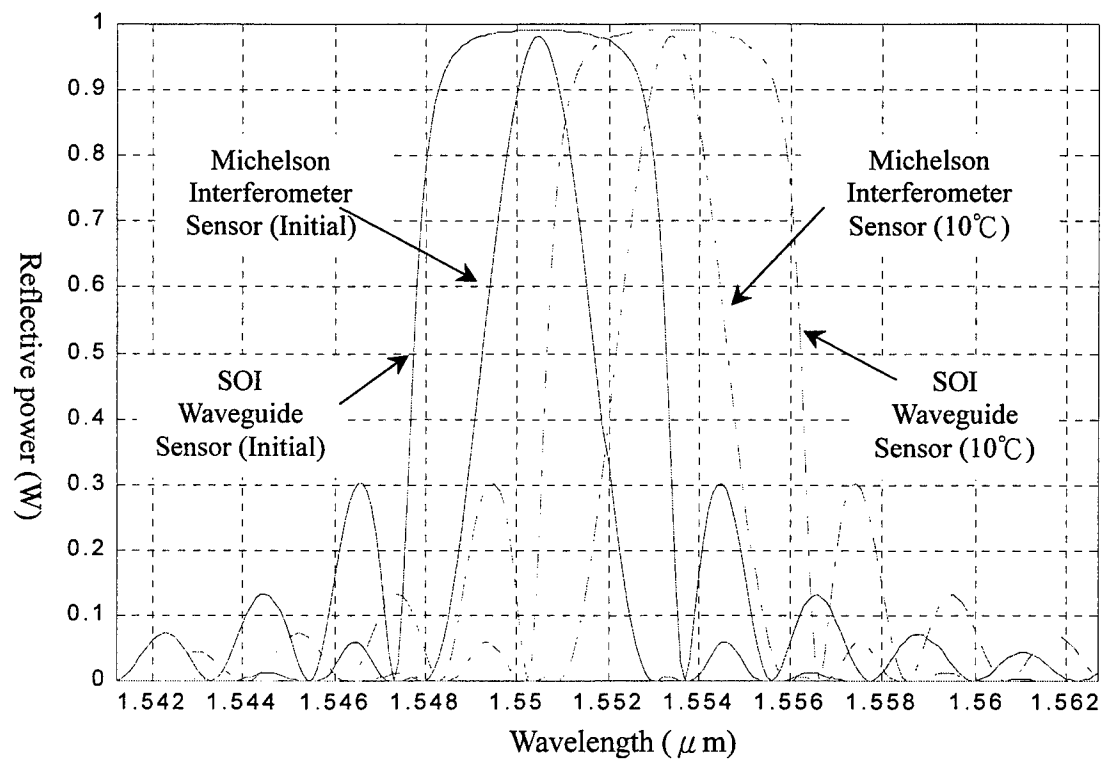


Fig. 5 The comparison of the reflected spectra from SOI waveguide grating sensor and SOI Michelson interferometer sensor with temperature 10°C offset from the initial temperature

Parameters	Thermal Expansion coef. (E)	Thermal-Optical coef. (T ₀)
SOI Wavaeguide Grating	2.6x10 ⁻⁶ /°C	1.86x10 ⁻⁴ /°C
Fiber Bragg Grating	1.1x10 ⁻⁶ /°C	8.6x10 ⁻⁶ /°C

Table I Some thermo-optical parameters of fiber Bragg grating and SOI waveguide Bragg grating used in this study

Implementation of A 1280nm-1380nm Light Source for Reflective Spectrum Measurement of Biomedical Fiber Sensors

Shyh-Lin Tsao* and Shien-Cheng Chiou

Department of Electrical Engineering

Yuan Ze University

Chung-Li, Taiwan, R.O.C

ABSTRACT

In this paper, we present a new broadband light source covers 1280-1380nm region for application in a wavelength-division multiplexing biomedical fiber-optic Bragg grating spectra reflective sensors. We cascade two optical amplifiers for achieving the 100nm broadband light source. The cascaded two optical amplifiers are praseodymium fluoride fiber amplifier (PDFA) and multiple quantum well optical semiconductor amplifier (MQW-SOA), respectively. The optimal driving current of MQW-SOA and the optimal pumping power of PDFA are experimentally searched. We find the bandwidth can reach 100nm from 1280nm to 1380nm with driving current 50mA and pumping power 885mW of MQW-SOA and PDFA, respectively.

Keywords: Biomedical sensor light source, Broadband light source, Fiber sensing, Reflective Spectrum, Optical amplifier

1. INTRODUCTION

Fiber-optic biomedical sensors have been developed over last ten years¹⁻³. The fiber-optic *in vivo* monitoring sensors present multi-functions. Such as PH value, pressure of O₂ and CO₂ detection. Those *in vivo* biomedical sensors need fiber-optic temperature sensors for preventing thermocouple embedded sensor contamination of blood. We reported a highly accurate temperature sensor using two fiber Bragg gratings(FBGs)⁴ which can replace thermocouple sensor combined with the fiber-optic biomedical sensors. These FBGs sensors usually are applied in the medical apparatus by analyzing the of optical reflective spectrum⁵⁻⁶. Besides, optical amplifiers with the feature of broadband have the great advantage of micro- sensors for biomedical applications. The schematic diagram of the biomedical sensor system with using broadband light source we proposed is shown in Fig.1. Therefore, the intensity and spectrum range of the broadband light source is very important. In anticipation of this need, many researches have focused on the broadband and the flat gain bandwidth optical amplifier broadband light source achievement in last several years for 1.55 μ m region. Novel host materials have further broadened the optical spectral width, which can be completed with material improvement⁷⁻⁹. Moreover, increasing of the optical amplifier bandwidth has been proposed through cascading different optical amplifiers technologies, such as EDFA series with the Thulium-doped fiber amplifier (TDFA)¹⁰ or the Raman amplifier¹¹ for 1.55 μ m region. Some promising research results of cascaded broadband optical amplifier and light source were reported¹²⁻¹⁵.

Correspondence: E-mail:jimmy@saturn.yzu.edu.tw, Telephone: 886-3-4638800-424, Fax: 886-3-4639355

In this paper, we demonstrate a 1.3 μ m broadband light source which can be applied in wavelength-division multiplexing (WDM) biomedical fiber sensor system. We use the optical spectrum analyzer to show our experimental results which include the characteristics of WDM coupler, spontaneous emission spectra of PDFA with various pumping powers, spontaneous emission spectra of MQW-SOA with injecting current at 20°C. Finally, a new broadband light source including cascaded two optical amplifiers including PDFA and MQW-SOA is presented.

2. DESCRIPTION AND EXPERIMENTAL RESULTS

The schematic diagram of our proposed 1.3 μ m broadband light source is shown in Fig.2. This optical light source include two optical amplifiers : one is PDFA, the other is MQW-SOA. We present the experimental study results in the following subsections.

2.1 . Measurement of WDM coupler

In this section, we use optical spectrum analyzer to measure the transmission spectra of optical WDM coupler for combining the pump light and signal light. First, we use a white light source as input singal source and let this singal source go through the optical WDM coupler. The experimental setup is shown in Fig.3. The measured spectrum of white light source is shown in Fig.4 at first. Then, the transmission band of the optical WDM coupler at pigtail 1 is shown in Fig.5. Similarly, we measure the output pigtail 2 for the signal passband spectra shown in Fig.6. We found this optical WDM coupler can be used for combining the Nd :YLF pump light working at 1047nm and the signal light working at 1300nm.

2.2 . Experimental results of PDFA

The components of the PDFA include a praseodymium-dope fluoride fiber (PDFF), a 2 \times 2 optical WDM coupler (1047nm/1300nm) and a high power laser pumping source (1047nm). The PDFA use a high power-pumping source to achieve the population inversion. This optical WDM coupler can mix the 1047nm light coming from Nd :YLF laser and 1300nm light signal into the PDFF as a forward pumping scheme. Then, we use an optical spectrum analyzer to measure the amplified spontaneous emission spectra. The experimental setup is shown in Fig.7. With tuning the pumping power emitted from Nd :YLF laser form 0.1W to 0.8W, the amplified spontaneous emission spectra of PDFA of port 1 is shown in Fig.8. The relationship between the amplified spontaneous emission of PDFA peak output power versus the input pumping laser is shown in Fig.9. The experimental result of light coming from port 2 is shown in Fig.10 which represents the amplified spontaneous emission spectra with various pumping powers. Fig.11 shows the peak power of amplified spontaneous emission is almost linearly increased as the pumping laser power increased. When the pumping power of PDFA is provided higher than 0.885W, the lasing phenomenon may be happen because of light reflections at both fiber faces. Therefore, we know exactly how the pumping power affect the output spectrum.

2.3 . Experimental results of MQW-SOA

The basic components of the MQW-SOA include a diode of optical semiconductor amplifier, a circuit of bias current source and a circuit of temperature control. The MQW-SOA we implemented can be temperature controlled. The gain of the multiple quantum well optical semiconductor amplifier can be adjusted by the driving current. The amplified spontaneous emission spectra of the MQW-SOA is measured at first. The temperature of MQW-SOA is stabilized at 20°C during spectra measurement. The experimental setup is shown in Fig.12 with tuning the injecting current of MQW-SOA from 10mA to 60mA, the amplified spontaneous emission spectra of MQW-SOA of port 1 is shown in Fig.13. Similarly, the relationship between the amplification of spontaneous emission of MQW-SOA peak power versus the driving current is shown in Fig.14. The experimental result of port 2 is shown in Fig.15. The relationship between the ASE spectrum at pigtail 2 and the driving current is shown in Fig.16. When the injecting current of the MQW-SOA is provided higher than 70mA, the lasing phenomenon may be happen because of light reflections at fiber facets. So, the injecting current tuning can vary the output spectrum distribution.

2.4 Experimental results of the cascaded amplifier

After we understand the performance of the PDFA and MQW-SOA presented in section 2.2 and section 2.3, we cascade two optical amplifiers as a broadband optical light source shown in Fig.2. The bandwidth of broadband optical amplifier of light amplification is combined with the two amplified bands of PDFA and MQW-SOA. We find the bandwidth can reach 100nm from 1280nm to 1380nm with driving current 50mA of MQW-SOA and pumping power 885mW of PDFA and MQW-SOA, respectively. The spectrum of a PDFA and a MQW-SOA compared with the spectrum of a cascade broadband optical amplifier is shown in Fig.17. Finally, the results show light spectrum can be used between 1280nm and 1380nm region.

3. CONCLUSION

In summary, we have designed a broadband light source with cascading a PDFA and a MQW-SOA. The basic idea and implementation of a broadband optical amplifier covers 1280nm-1380nm is presented. The amplified spontaneous emission spectra of the cascaded PDFA and MQW-SOA are measured for optical parameters searching. The conspicuous performance of this broadband optical amplifier at wavelength 1.3 μ m band can be applied for WDM biomedical fiber sensor systems as shown in Fig.1. Moreover, the range of bandwidth and gain can be tuned by injecting current of MQW-SOA and pumping power of PDFA. This 1.3 μ m broadband light source is very useful for multi-channel broadband WDM fiber biomedical sensor systems.

ACKNOWLEDGMENT

This work was supported in part by National Science Council of Republic of China under contract no. NSC 89-2215-E-155-003.

REFERENCE

1. R. A. Lieberman, M. T. Wlodarczyk, "Chemical, Biochemical and Environmental Fiber Sensors", *Proceeding of SPIE*, **1172**, 1989.
2. D. R. Hansmann, F. P. Milanovich, G. G. Vurek, D. R. Walt, "Fiber Optic Medical and Fluorescence Sensors and Applications", *Proceeding of SPIE*, **1648**, 1992.
3. R. A. Lieberman, "Chemical, Biochemical and Environmental Fiber Sensors II", *Proceeding of SPIE*, **2293**, 1989.
4. Shyh-Lin Tsao, Jingshown Wu, "High accurate temperature sensor using two fiber Bragg gratings", *IEEE Journal of Selected Topics in Quantum Electronics*, **2**, pp.894-897, 1996.
5. O. Tohyama, M. Kohashi, M. Sugihara, H. Itoh, "A fiber-optic pressure micosensor for biomedical application", *Sensors and Actuators (A)*, pp.150-154, 1998.
6. Allen Moradian, Gerhard J. Mohr, Michael Linnhoff, Marc Fehlmann, "Continuous optical monitoring of aqueous amines in transflectance mode", *Sensors and Actuators (B)*, pp.154-161, 2000.
7. H. Ono, M. Yamada, T. Kanamori, Y. Ohishi, "1.58 μ m band fluoride-band Er³⁺-doped fiber amplifier for WDM transmission systems", *Electronics Letters*, **33**, pp.1471-1472, 1997.
8. A. Mori, Y. Ohishi, S. Sudo, "Erbium-doped tellurite glass fiber laser and amplifier", *Electronics Letters*, **33**, pp.863-864, 1997.
9. L. Goldberg, D. Mehuys, D.C. Hall, "3.3W CW diffraction limited broad area semiconductor amplifier", *Electronics Letters*, **28**, pp. 1082-1084, 1992.
10. T. Komukai, T. Yamamoto, T. Sugawa, Y. Miyajima, "Correction to upconversion pumped Thulium-Doped Fluoride Fiber Amplifier and Laser Operating at 1.4", *IEEE Quantum Electronics*, **32**, pp.173, 1996.
11. Hiroji Masuda, Shingo Kawai, Ken-Ichi Suzuki, Kazuo Aida, "1.65/spl mu/m band fiber Raman amplifier pumped by wavelength-tunable amplified spontaneous emission light source", *Electronics Letters*, **34**, pp. 2339-2340, 1998.
12. H. Masuda, S. Kawai, K.-I. Suzuki, K. Aida, "Wideband, gain-flattened, erbium-doped fiber amplifiers with 3dB bandwidths of > 50nm", *Electronics Letters*, **33**, pp.1070-1072, 1997.
13. A. Mori, K. Kobayashi, M. Yamada, T. Kanamori, K. Oikawa, Y. Nishida, Y. Ohishi, "Low noise broadband tellurite-based Er³⁺-doped fiber amplifiers", *Electronics Letters*, **34**, pp.887-888, 1998.
14. J. Kani, M. Jinno, "Wideband and flat-gain optical amplification from 1460 to 1510nm by serial combination of a thulium-doped fluoride fiber amplifier and fiber Raman amplifier", *Electronics Letters*, **35**, pp.1004-1006, 1999.
15. F. Koyama, "Tapered Semiconductor Optical Amplifiers for Broad-Band and High-power Operations", *Proceeding of ECOC*, **3**, pp.177-180, 1996.

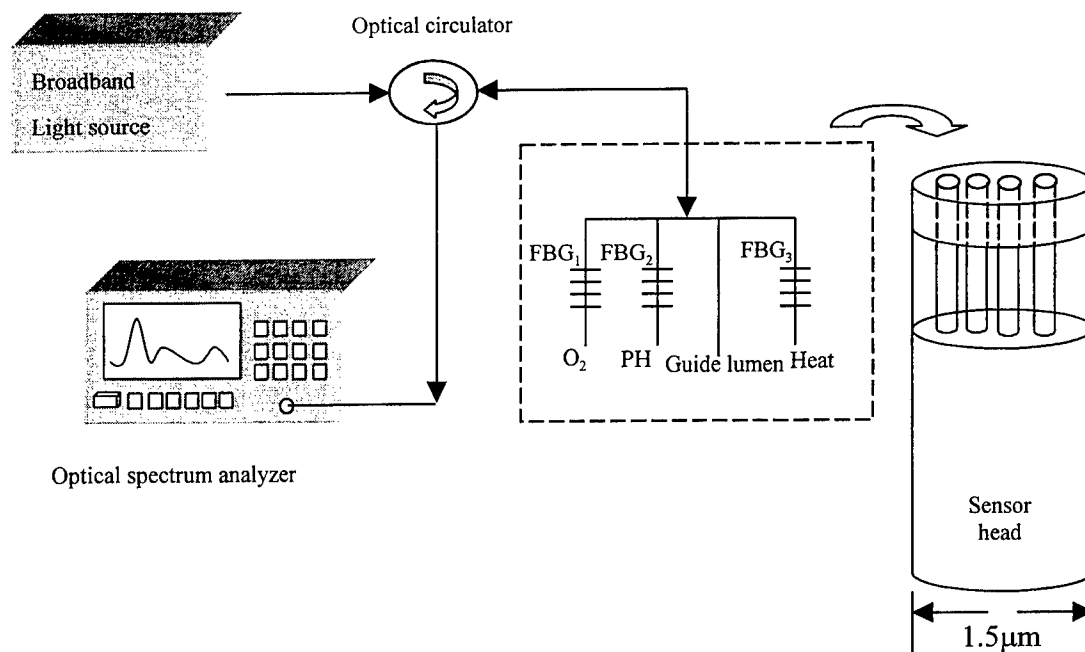


Fig.1 Schematic diagram our proposed in vivo biomedical sensor system with using a broadband light source 1280nm-1380nm

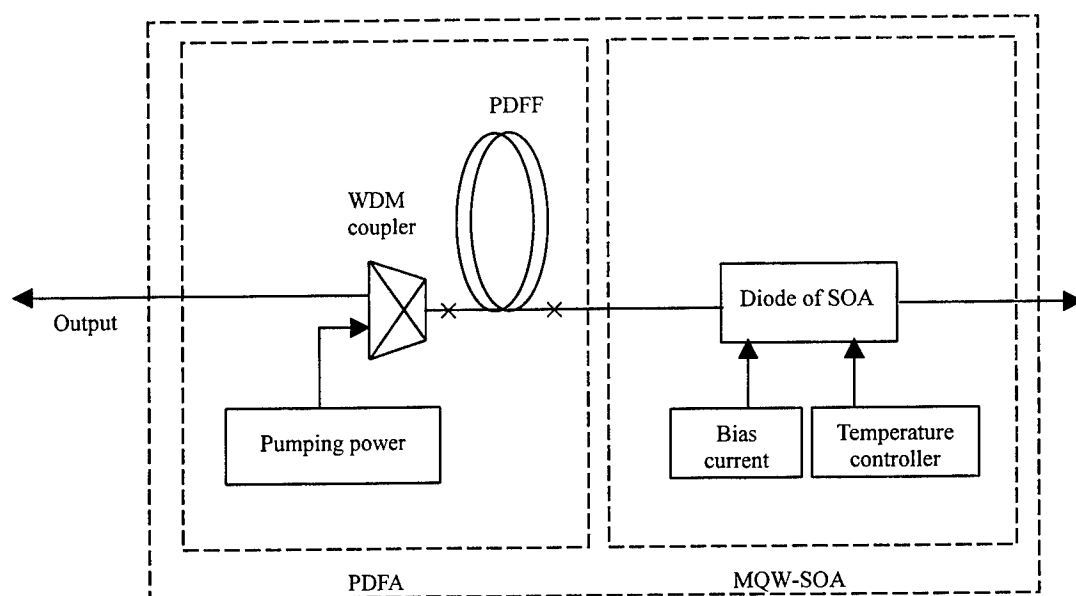


Fig.2 The schematic diagram of the proposed $1.3\mu\text{m}$ broadband optical amplifier and light source

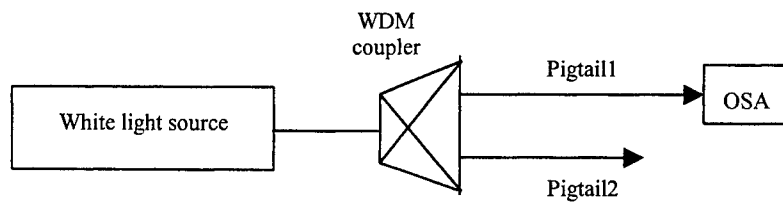


Fig.3 The experimental setup of measure the transmission spectra of WDM coupler

OSA: Optical Spectrum Analyzer

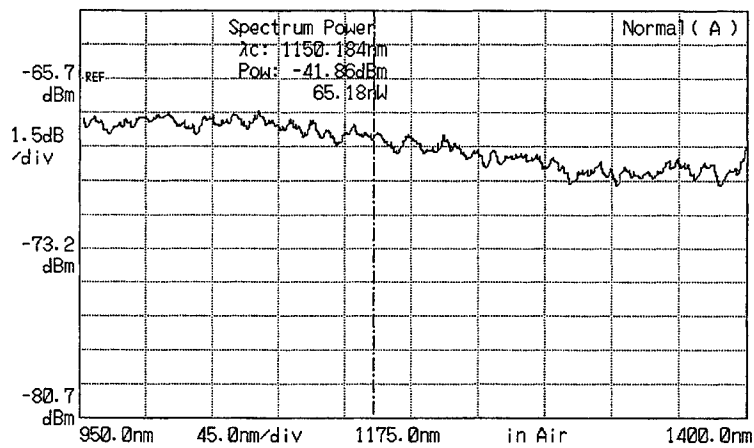


Fig.4 The measured spectrum of white light source

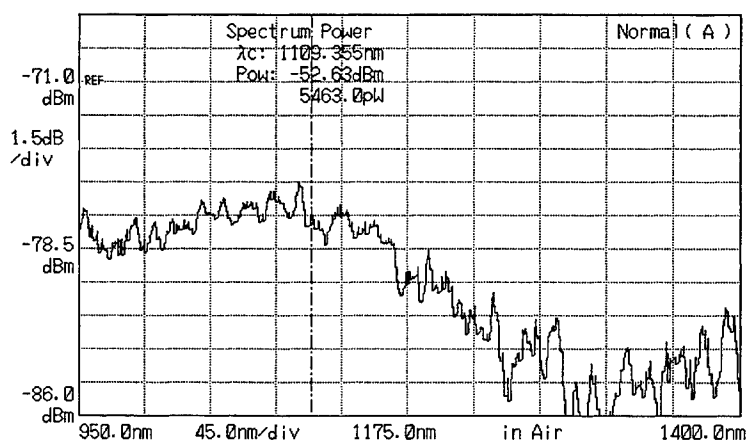


Fig.5 The transmission spectrum of WDM coupler measured at pigtail 1

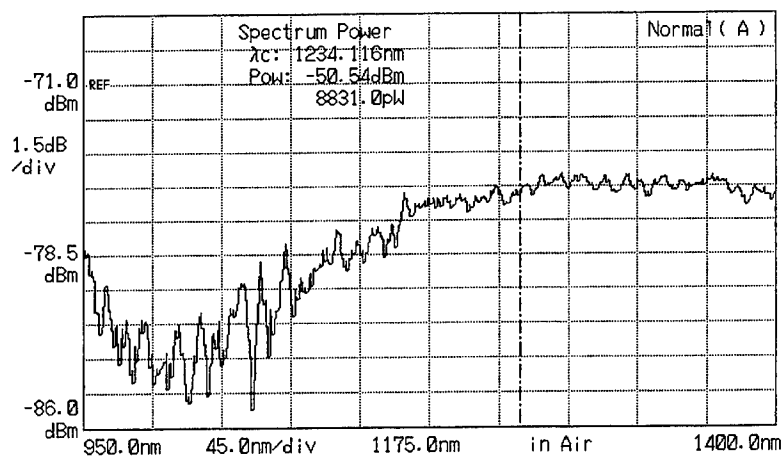


Fig.6 The transmission spectrum of WDM coupler measured at pigtail 2

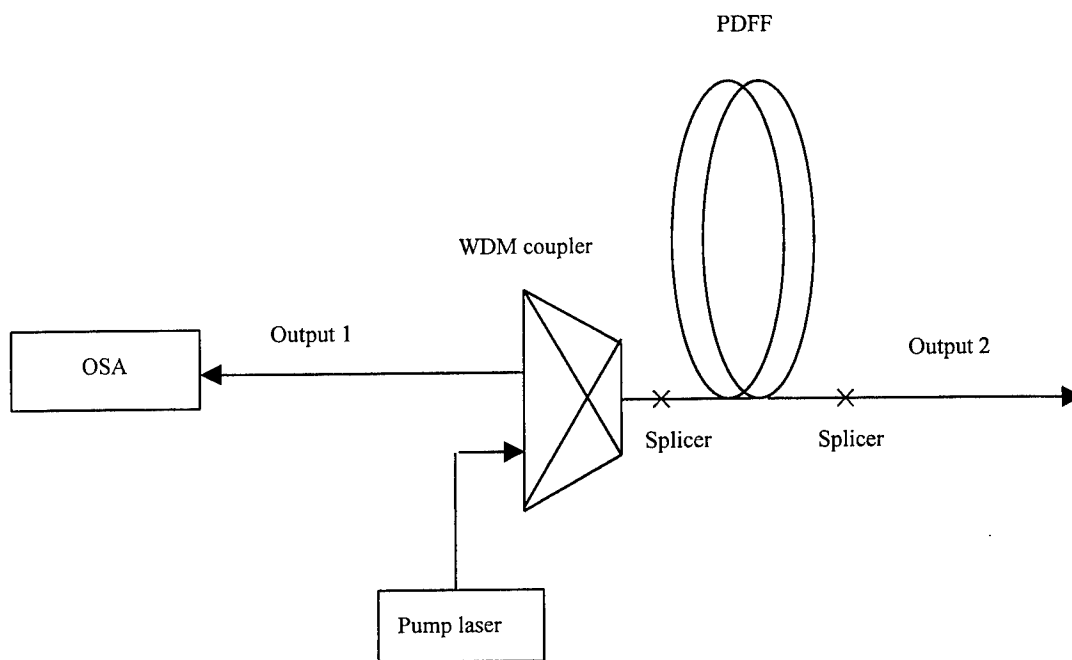


Fig.7 The experimental setup of measurement of the ASE spectrum of PDFA

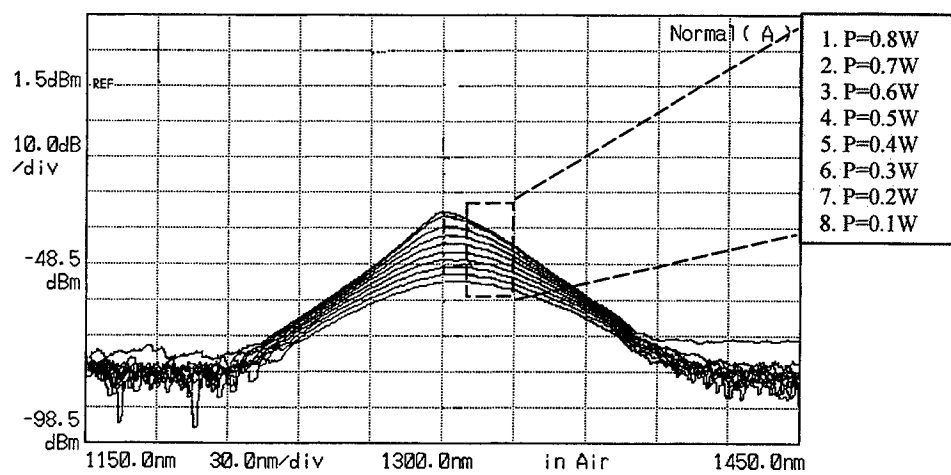


Fig.8 The ASE spectrum of praseodymium fluoride fiber amplifier at port 1

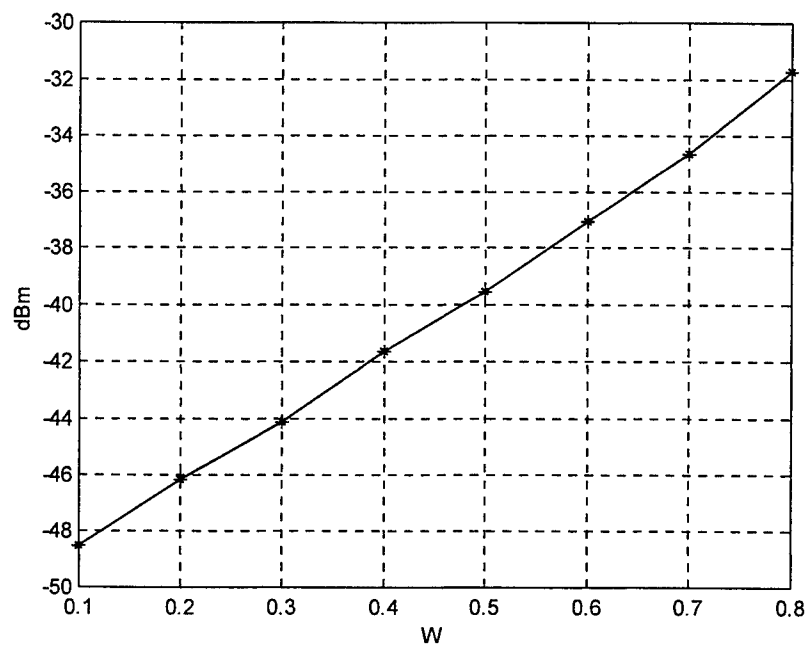


Fig.9 The output of ASE peak power at port 1 of PDFFA versus the input pumping laser power

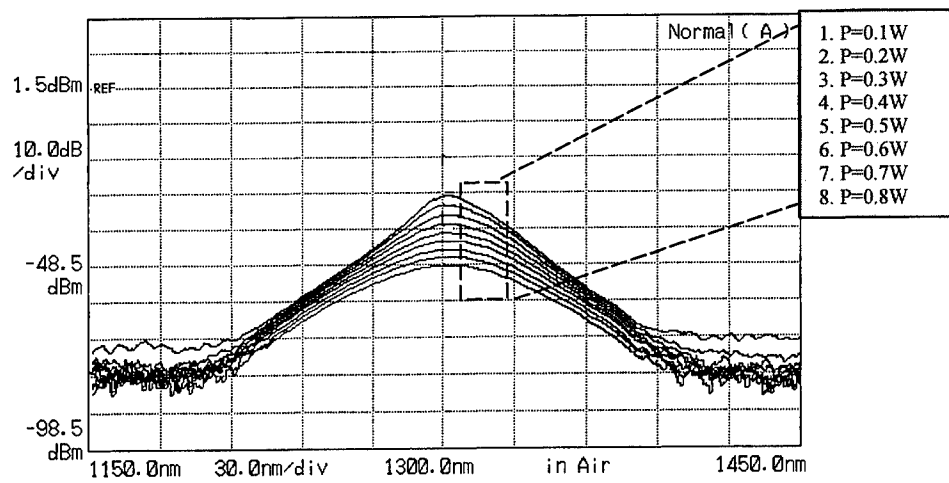


Fig.10 The ASE spectrum of PDFA at port 2

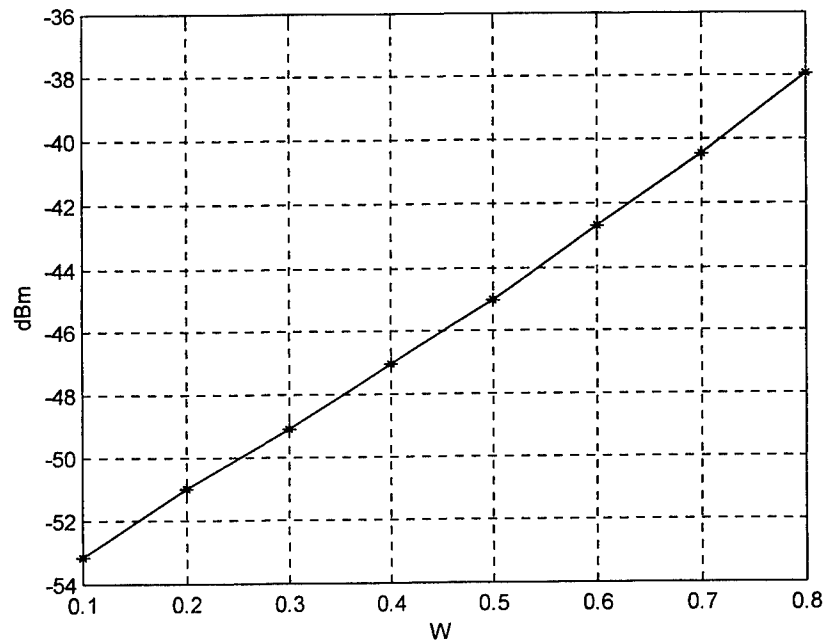


Fig.11 The relationship of PDFA peak power ASE spectrum at port 2 versus the input pumping laser power

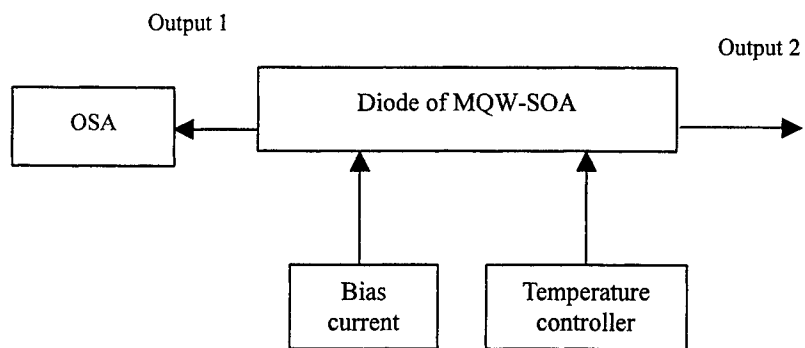


Fig.12 The experimental setup of measurement of the ASE spectrum of MQW-SOA

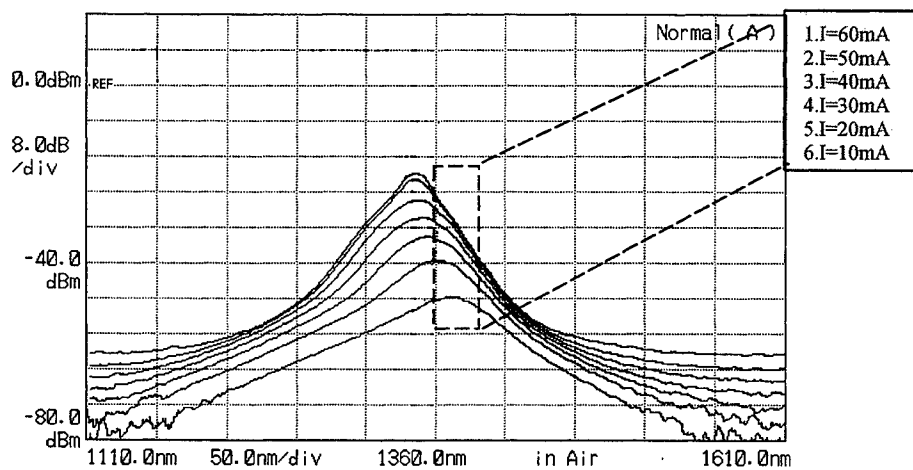


Fig.13 The ASE spectrum of MQW-SOA at port 1

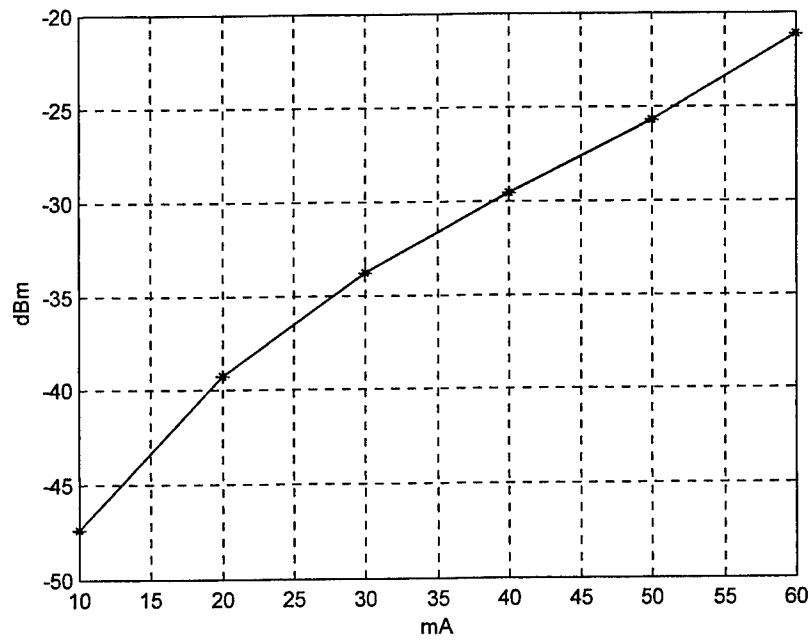


Fig.14 The relationship of MQW-SOA ASE spectrum peak power at port 1 versus the injection current

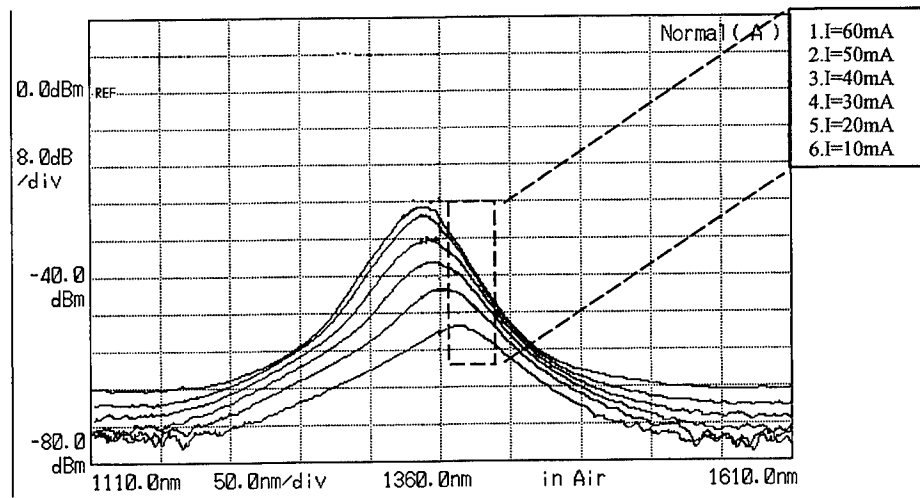


Fig.15 The ASE spectrum of MQW-SOA at port 2

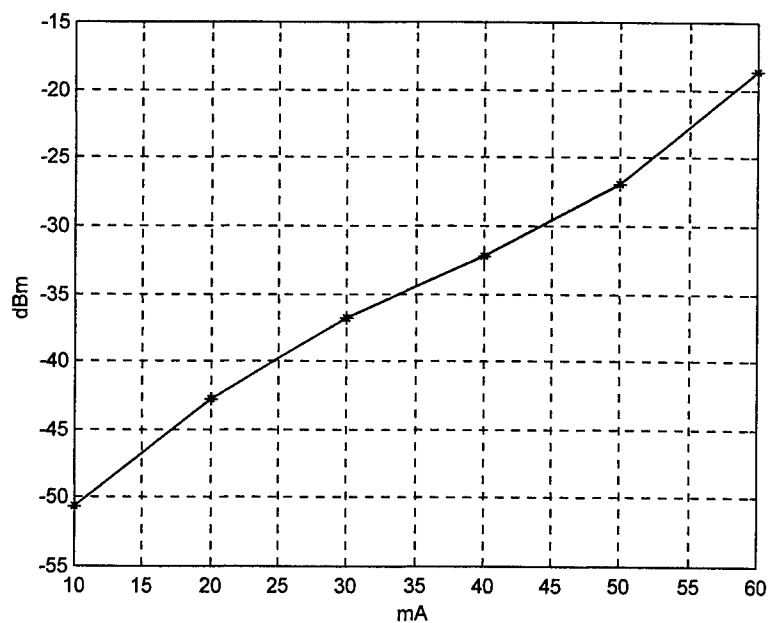


Fig.16 The relationship of MQW-SOA ASE spectrum peak power at port 2 versus the injection current

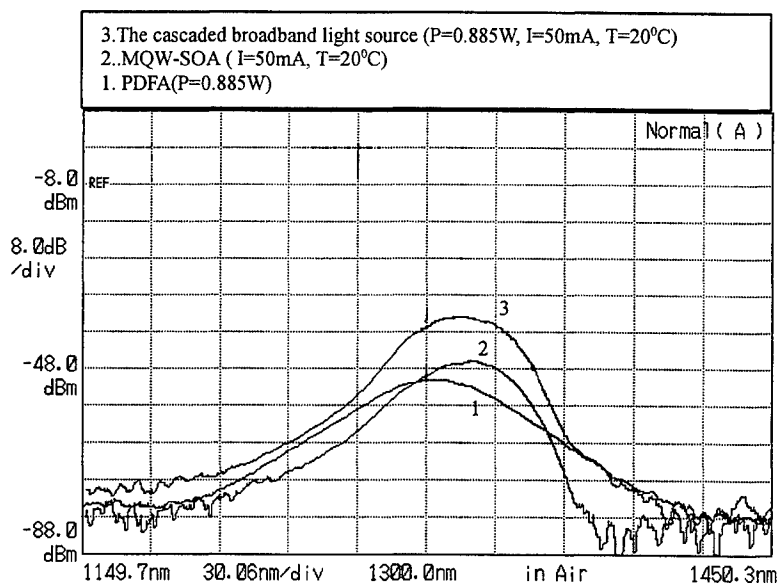


Fig.17 The spectrum of a PDFA and a MQW-SOA compare with the spectrum of a cascade broadband optical light source

Electro-optical measurement of highly intense electric field with high frequency

Xiaojun Zeng , Haiqing Chen *

Dept. Of Optoelectronics Eng., Huazhong University of Science and Technology
Wuhan (430074), Hubei , China

ABSTRACT

The transient electric field of highly intense electromagnetic pulse (EMP) will seriously damage the military and civil installations, so it is significantly important to measure such electric field of EMP with high frequency. This paper describes a fiber-optic sensor for measuring highly intense electric field with high frequency. The sensor consists of a probe of electrooptic(EO) crystal, optic fiber, polarizer, photodetector, processing circuits and single-chip microprocessor. According to Pockels effect, the polarized light will be modulated by the electric field to be measured when it penetrates the EO crystal. Then, its polarized direction will vary following the variation of electric field. The change of polarized direction is converted to the variation of light intensity by polarizer. In order to gain good performance, it is important to choose suitable crystal carefully. The interrelated optical axes of the components are adjusted on the basis of the theoretical analysis and calculations. A special temperature compensating method is used to decrease the temperature effect. At the meantime, the low noise circuit is used. The testing results show that the linearity is 0.2%, the error of the measurement is approximately 0.5% and the risetime is less than 4ns.

Keyword: EMC, fiber-optic sensor, highly intense electric field, temperature compensation

1. INTRODUCTION

Mankind throws emphasis more and more on electromagnetic pollution, now. Electromagnetic compatibility(EMC) is requested for various electronic devices^[1]. The transient electric field of highly intense electromagnetic pulse will seriously damage the military and civil installations, even do harm to the health of living things. So it is significantly important to measure such electric field of EMP with high frequency. In traditional, the devices (such as static voltage meter, specialized probe, etc) applied to measure electric field are all made of electrical active substance, which will cause induced electric field easily. The perturbation of induced electric field will interfere with the testing electric field, which limits the validity and resolution of measurement. Especially, when there are lots of space charges, induction and inflow of space charges will result in serious errors and dangerousness. Furthermore, traditional instrument with big volume is very inconvenient in practical application. Fiber-optic electric field sensor has superior performances that have not in the traditional instruments, such as small volume, good insulativity, high corrosion resistance, not disturbing electric field to be measured, large range of measurement, etc^[2,3]. The electric field sensor using an optical modulator makes possible accurate measurement without disturbing the electromagnetic field to be measured and is expected to have application in EMC measurement. With the advancement of new principle of measurement, various fiber-optic electric field and voltage sensors are developed.

2.THEORY

1893, Pockels, German physical scientist, discovered that refractive rates of some transparent optic medium vary with the electric field load-on its two ends. It is Pockels effect or linear electrooptic effect. According to Pockels effect, the polarized light coming from polarizer P_1 will be modulated by the electric field to be measured when it penetrates the Pockels crystal, and its polarized direction will vary following the change of the electric field. In other words, a phasic difference is generated between ordinary light and extraordinary light. When the beam go through polarizer P_2 , the variation of phase is converted to the change of the light intensity by the polarizer P_2 , so the electric signal coming from photodetector contains the characteristic of the electric field to be measured. Fig. 1 shows the method of Pockels effect.

* Correspondence: Email: hqchen@mail.hust.edu.cn

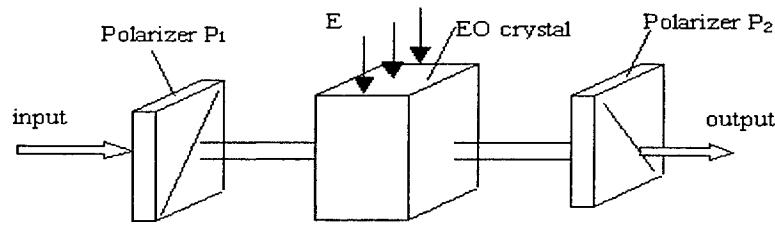


Fig. 1 the method of Pockels effect

The phasic difference $\Delta\varphi$ due to the electric field to be measured can be given as

$$\Delta\varphi = 2\pi n^3 \gamma_e l E / \lambda \quad (1)$$

Where

n ----- the refractive rates of crystal

λ ----- wave length of the light

γ_e ----- effective EO coefficient

l ----- the length of EO crystal

E ----- the intensity of electric field to be measured

2.1 Selection of EO crystal

Only piezoelectricity crystals without symcenter maybe have electrooptic effect, because the EO coefficient γ_e is a three-order tensor. The crystals with good electrooptic and steadily physical properties are very little. Diagram (I) displays some typical EO crystals that are applied usually in electric field sensor.

For the measurement based on the method of polarized light, anything disturbing the polarized status of the polarized beam should be avoided to guarantee the precision of the sensor, such as natural birefringence, natural rotary polarization, strain and stress, etc. Because natural rotary polarization and birefringence (which are usually temperature dependent) all will cause additional phase retardation, the crystals without natural birefringence and rotary polarization is best EO crystal. According to these rules, $Bi_4Ge_3O_{12}$ (BGO) is suitable, which belongs to cubic crystal class $\bar{4}3m$. When there is not electric field, BGO, the isotropic crystal, is a ideal sensitive crystal to voltage or electric field.

crystal	class	EO coefficient $\lambda = 0.63\mu m \quad (10^{-10} cm/v)$	n	ϵ	pyroelectricity	Optical rotation
L_iNbO_3	T_d	$\gamma_{13}^T = 10, \quad \gamma_{33}^T = 32.2$ $\gamma_{51}^T = 32, \quad \gamma_{22}^T = 6.7$	$n_o = 2.286$ $n_e = 2.220$	$\epsilon_1^T = 84.6$ $\epsilon_2^s = 28.6$	Y	N
$Bi_4Ge_3O_{12}$	Cube $\bar{4}3$	$\gamma_{41}^T = 0.95$	$n_o = 2.11$	16	N	N
$Bi_{12}SiO_{12}$	Cube $\bar{4}3$	$\gamma_{41}^T = 4.35$	$n_o = 2.45$		N	Y

Diagram (I), Optical parameters of three typical EO crystals

If the electric field E is along the direction $\langle 110 \rangle$, the angle between the direction of the electric field E and new axis x' or y' of refractive rates is 45° , and z' is orthometric with x' and y' (see fig. 2). New refractive rates are given by ^[3,4]

$$n_{x'} = n + \frac{1}{2} n^3 \gamma_{41} E$$

$$n'_y = n - \frac{1}{2} n^3 \gamma_{41} E \quad (2)$$

$$n'_z = n$$

Then, the phasic difference is

$$\Delta\phi = \frac{2\pi}{\lambda} (n'_x - n'_y) l = \frac{2\pi}{\lambda} n^3 \gamma_{41} E \quad (3)$$

2.2 Method of interference measurement

The method of interference measurement is usually applied to measure phasic variation, because it is very difficult to measure the phasic variation accurately. In order to obtain optimally output of the beam, it is necessary to calculate the angle between the polarized direction of beam and the optical axis of polarizer and the angle between the optical axis of polarizer P_1 and the optical axis of polarizer P_2 . Fig.3 shows the relation of P_1, P_2, x_1 and x_2 . P_1 and P_2 are the optical axis of polarizer, x_1 and x_2 are the polarized direction of two beams in crystal, and ϕ is the angle between P_1 and x_1 . After the light go through polarizer P_1 , the beam reaching crystal is linear polarized light and its amplitude is E_0 . The light whose polarized direction parallel to the optical axis of polarizer can go through the polarizer, so the amplitude A_1 and A_2 of input beam in the direction of x_1 and x_2 can be expressed as

$$A_1 = E_0 \cos \phi \quad (4)$$

$$A_2 = E_0 \sin \phi$$

A phase difference is generated between A_1 and A_2 by the birefringence caused by the electric field to be measured, when the beams penetrate the EO crystal. At the end of output, the constituents of A_1 and A_2 along the optical axis of polarizer P_2 can be written as

$$A'_1 = E_0 \cos \phi \cos(\phi - \alpha) \quad (5)$$

$$A'_2 = E_0 \sin \phi \sin(\phi - \alpha)$$

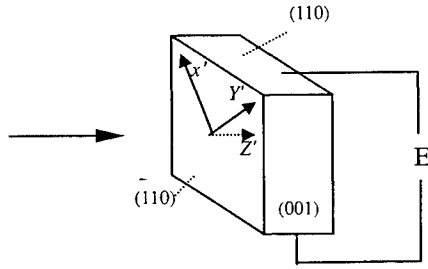


Fig. 2 new optic axes of the BGO

According to the theory of light interference, beam A'_1 and beam A'_2 will interfere with each other. The intensity of output light can be given by

$$I = I_1 + I_2 + 2\sqrt{I_1 I_2} \cos \Delta\phi$$

with

$$I_1 = E_0^2 \cos^2 \phi \cos^2(\phi - \alpha) \quad I_2 = E_0^2 \sin^2 \phi \sin^2(\phi - \alpha)$$

Then,

$$I = I_0 [\cos^2 \alpha - \sin 2\phi \sin 2(\phi - \alpha) \sin^2 \frac{\Delta\phi}{2}] \quad (7)$$

The input and output polarizers are either crossed or parallel to each other in the fiber-optic sensor. For convenience, from now on, the polarizers are referred to as crossed polarizers when they are crossed and as parallel polarizers when they are parallel.

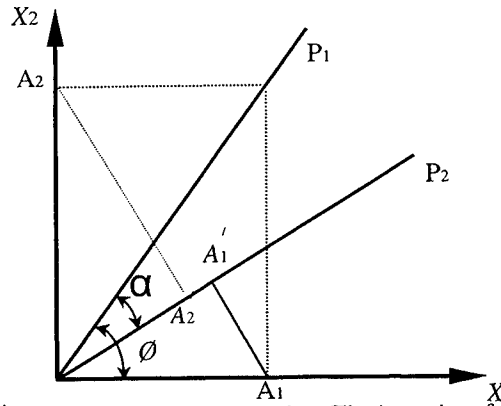


Fig. 3 Method of interference measurement

For crossed polarizers ($\alpha = \pi/2$), the intensity of output light can be described simply as

$$I = I_0 \sin^2 2\phi \sin^2 \frac{\Delta\phi}{2} \quad (8)$$

with $I = E_0^2$

The expression shows us that the intensity of output beam is due to the angle between the optical axis of polarizer and the polarized direction of the polarization along direction x_1 and x_2 . In order to make the effect of $\Delta\phi$ maximal in the intensity of output, ϕ is evaluated as $\pi/4$. Hence, if turning the crystal and making the angle ϕ is $\pi/4$, we can obtain the maximum intensity of output light. And the intensity of the output light is

$$I = I_0 \sin^2 (\Delta\phi/2) \quad (9)$$

2.3 Optic bias

By the expression (9), the intensity variation of output beam due to $\Delta\phi$ is nonlinear, which make it difficult to measure the electric field accurately (see fig.5). Distinctly, the quiescent operating point is $\Delta\phi = 0 \text{ rad}$, and its linear rate is very bad in the region of measurement. If we shift the quiescent operating point from 0 rad to $\pi/2 \text{ rad}$, the output due to phase difference is linear approximately in a very large range of measurement. A quarterwave plate being placed between the input polarizer and output polarizer is applied to make a $\pi/2$ phase shift fixedly between ordinary light and extraordinary light. Then, the intensity of output beam is expressed as

$$\begin{aligned} I &= I_0 \sin^2 (\Delta\phi/2 + \pi/4) \\ &= \frac{I_0}{2} (1 + \sin \Delta\phi) \\ &= \frac{I_0}{2} (1 + \Delta\phi) = \frac{I_0}{2} (1 + \Gamma_m) \end{aligned} \quad (10)$$

due to $\Delta\phi \ll 1$, where $\Gamma_m = 2\pi m_0^3 \gamma_e E l / \lambda_0$.

If $\Gamma_m < 0.24$, the response of the sensor is linear approximately due to the E and the nonlinear error is less than 1%. In order to decrease the measurement errors, the modulation index Γ_m can be much less than 0.24, but little the modulation index Γ_m will bring about a small range of measurement. When the electric field change from 5 kv/m to 500 Kv/m , the nonlinear error is less than 0.2% by experimental results. The sensor with a quarterwave can be seen in fig. 4.

3. TEMPERATURE COMPENSATION

The best temperature stability of an optical fiber sensor using bulk crystals reported so far is $\sim 1\%$ over a temperature range of 80°C . Even if a crystal is properly chosen and well prepared for sensor applications, the bulk crystals might have temperature dependent strain birefringences that are generated during its annealing process, temperature sensitive stress birefringence induced by mechanical pressure, or other types of randomly varying birefringence, all of which may exist simultaneously^[6]. The $\text{Bi}_4\text{Ge}_3\text{O}_{12}$ of class $\bar{4}3m$ often exhibit unwanted birefringences due to strain, stress or precipitates, whose magnitudes significantly vary with environmental changes such as temperature and pressure, even though it possesses neither natural birefringence (which is usually temperature dependent) nor optical activity (which often quenches the linear electrooptic effect). Therefore, it is necessary to find a method that can eliminate the effects of such birefringences on the stability of the fiber-optic sensor to build a sensor that is stable with respect to environment

Once upon a time, Kyung S. Lee developed a good method of temperature to decrease the effects of such birefringences^[5]. The input and output polarizers are either crossed or parallel to each other in the fiber-optic sensor. If the slow axis of the linear birefringence induced by the electrooptic effect and the slow (or fast) axis of a quarterwave plate are in the plane normal to the direction of a propagating beam and are oriented at 45° with respect to the input polarizer, the power transfer functions of crossed polarizers and parallel polarizers are given by, respectively (see fig. 4)

$$\frac{p_{\parallel}}{p_i} = \frac{1}{2} [1 - (\delta_{0l} + \sum_{n=1}^N \delta_{nl} \sin 2\theta_n)] \quad (11)$$

$$\frac{p_{\perp}}{p_i} = \frac{1}{2} [1 + (\delta_{0l} + \sum_{n=1}^N \delta_{nl} \sin 2\theta_n)] \quad (12)$$

with $\delta_{ol} = 2\pi m_0^3 \gamma_{41} El / \lambda_0$ (for cubic crystal class $\bar{4}3m$) and $\delta_{nl} = k_0 n_0 l \Delta \varepsilon_{nl} / \lambda_0$, respectively, and here δ_{nl} is the phase retardation due to the n th linear birefringence, θ_n is the angle between the x axis and the slow axis of the n th linear birefringence. First, two terms on the right-hand sides of Equations (11) and (12) represent the well-known power transfer function of a typical electrooptic voltage sensor in the absence of unwanted birefringences, and the third term is the perturbation term due to unwanted birefringences present in the electrooptic crystal. Hence, if there are N unwanted linear birefringence with slow axis having azimuth angles $\theta_i (\theta_i \neq I \times \pi/2; I = 0, 1, 2, \dots)$ in the plane transverse to the direction of wave propagation, N linear birefringences will individually contribute to the intensity transmission of the sensor. However, if the unwanted birefringences remain constant over the environmental changes, the output signal of the sensor remains stable. On the other hand, if the unwanted birefringences vary with the environmental changes, the sensor becomes unstable. For ac voltage sensor, detecting ac signal is in fact identical to measuring the modulation index Γ_m . By equations (11) and (12), the modulation index $\Gamma_{m\parallel}$ of the beam after the parallel polarizers is given by

$$\Gamma_{m\parallel}(T, P) = \frac{\Gamma_m}{1 - \sum_{n=1}^N \delta_{nl}(T, P) \sin 2\theta_n} \quad (13)$$

and the modulation index $\Gamma_{m\perp}$ of the beam after the crossed polarizers is given by

$$\Gamma_{m\perp}(T, P) = \frac{\Gamma_m}{1 + \sum_{n=1}^N \delta_{nl}(T, P) \sin 2\theta_n} \quad (14)$$

where $\Gamma_m = 2\pi m_0^3 \gamma_{41} El / \lambda_0$ (for cubic crystal class $\bar{4}3m$) (15)

Here $\delta_{nl}(T, P)$ is the phase retardation due to the unwanted birefringence and is a function of temperature T and pressure P . Γ_m is the modulation index of the sensor without unwanted birefringences and is assumed to be constant over the temperature variation, because Γ_m is usually much less temperature dependent than $\delta_{nl}(T, P)$. Two equations can be expanded in a Taylor series, a series of powers of $\sum \delta_{nl}(T, P) \sin 2\theta_n$. Adding these expressions together, we can obtain

$$\Gamma_{m\parallel}(T, P) + \Gamma_{m\perp}(T, P) = 2\Gamma_m(1 + A^2 + A^4 + \dots) \cong \Gamma_m \quad (16)$$

for small $A [= \sum \delta_{nl}(T, P) \sin 2\theta_n]$. Therefore, averaging $\Gamma_{m\parallel}$ and $\Gamma_{m\perp}$ results in eliminating the birefringences term A and gives rise to the modulation index Γ_m . This tells us that $\Gamma_{m\parallel}$ and $\Gamma_{m\perp}$ should be simultaneously measured and added together to remove the effect of the unwanted linear birefringences.

By the method of temperature compensation, we can modify the design of the fiber-optic sensor to eliminate unwanted linear birefringences. If the output polarizer is replaced by a Wollaston prism or one polarizing beam splitter, the crossed polarizers and parallel polarizers are existing simultaneously in the same system. The polarized beam coming from crystal will split into two beams, the beam coming from crossed polarizers and the beam coming from parallel polarizers, when it reach at the Wollaston prism. Using for the beams, we can eliminate the perturbations caused by temperature variation.

4. DESIGN OF THE SYSTEM

Considering the linear rate and temperature compensation, we design a practical sensor. Fig. 4 shows the structure of the sensor system.

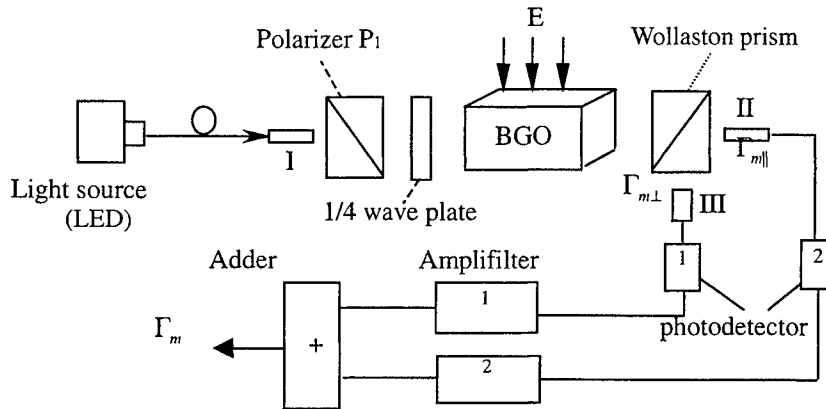


Fig. 4 the practical system with temperature compensation

I, II, III ----- coupled fiber

The sensing head consists of an input polarizer, a quarterwave plate, electrooptical crystal, Wollaston prism (WP) and two detectors. Light from LED is initially linearly polarized by the input polarizer. Then the quarterwave plate changes the linear polarization to circular polarization. Because of the electrooptical crystal effect induced by the modulating electric field applied to the crystal, the circularly polarized light is changed to elliptically polarized light. The elliptically polarized light splits into two orthogonal linearly polarized beams. The reflected and transmitted signals from WP are equivalent to the signals transmitted from the crossed polarizers and from the parallel polarizers, respectively. Signals reflected and signals transmitted from the WP are detected by photodetector 1 and 2, respectively, and are processed by electronics and a computer until the output yields $(\Gamma_{m\parallel} + \Gamma_{m\perp})/2$.

In order to decrease interference of noise, we use some low noise devices. Photodetector 1 and 2 all are PIN photodiode that is low noise. Electric signals from photodetectors are amplified by OPA-128 (which is made by B-B Corporation and has very low null shift). The use of these low noise devices will ensure that the precision of the sensor is very fine.

5. EXPERIMENTAL RESULTS

By experimental results, the relative error of the sensor is less than 0.2%, when the measurement range changes from 5kv/m to 50kv/m. Fig. 6 shows the variation of the measurement due to the variation of electric field.

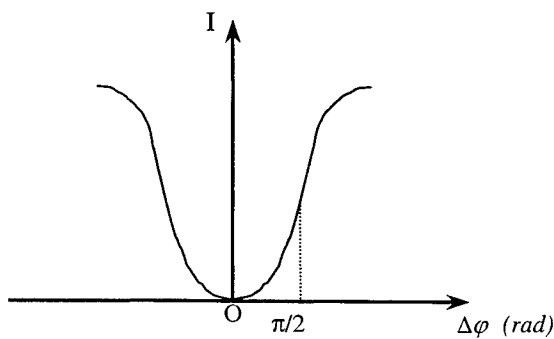


Fig. 5 the diagram of bias point

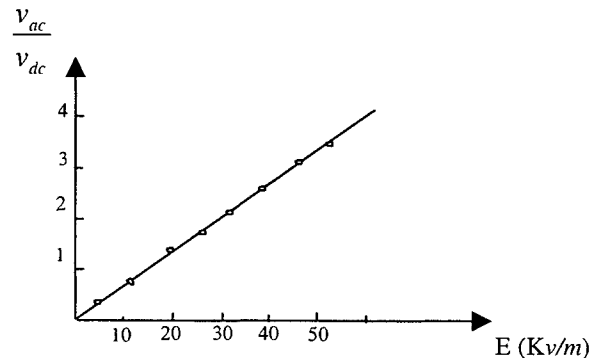


Fig.6 Variation of v_{ac}/v_{dc} due to E

The stability is very good in the laboratory in a long time. The measurement range is from 500v/m to 500kv/m with 0.5% error. And the frequency response covers a wide range from 50Hz to 300MHz, which means that the risetime is less than 4ns.

REFERENCES

1. A.J.Schwab , *Elektromagnetische Verträglichkeit Springer-Verlag*, in German, 1991.
2. H.J.M.Hulshof et al: *SPIE*, 1987: 778 266-269
3. Gao Xicai, et al.: The Collection of Papers, 1986 Harbin, *China-Japan International Scientific Symposium on Sensor*, pp. 75--85
4. Kamada. Osamu, Kakishita K. , Electro-optical effect of $Bi_4Ge_3O_{12}$ crystals for optic voltage sensors. *Jpn. J. Appl. Phys.* V. 32 , Part 1, No. 9B
5. Lee K S. New compensation for bulk optical sensors with multiple birefringence, *Applied Optics*, 1989,28
6. K.S.Lee and G.W.Day, □The effect of the Temperature and Pressure Dependent Birefringence on a voltage Sensor and , the Elimination of its Effect on a Voltage sensor Using a Bulk-Type Bismuth Germanate: Experiment,□to be submitted for publication.

Channel-switching add/drop multiplexer with tunable fiber Bragg grating based on the cantilever beam

Dejun Feng*, Heliang Liu, Weigang Zhang, Chunfeng Ge, Guiyun Kai, Xiaoyi Dong
Institute of Modern Optics, Nankai University, Tianjin 300071, P.R.China

ABSTRACT

A channel-switching add/drop multiplexer with tunable fiber grating tuned by cantilever beam is proposed and experimentally demonstrated. The device consists of two 3dB couplers and a fiber Bragg grating with 99% peak reflectivity at 1557.86nm and a 0.2nm bandwidth. The grating is firmly clung on an organic glass cantilever beam and we can continuously tune the reflectivity wavelength through tuning the cantilever beam manually. The no-chirped linearly tuning range is about 6.1nm, which may permit 7 channels with channel spacing of 0.8nm (100GHz) to insert or drop signal. A broadband light source and a 4-wavelength all fiber laser are used to test its capability in experiment. The adjacent channel isolation is not less than 23dB. The device shows good performance, but suffers from a high insertion loss.

Keywords: Optical add/drop multiplexer, fiber Bragg grating, linearly tuning, cantilever beam.

1. INTRODUCTION

Optical fiber gratings have perfect spectral characteristics for multiplexing and demultiplexing in a wavelength division multiplexing system (WDM), since they are inherently low loss, spectrally extremely selective, and potentially low cost¹. The ability to add and drop wavelengths from WDM is a key function. Accomplishing this task optically, rather than electrically, is an exciting challenge for photonics lightwave system developers. Optical add/drop multiplexers (OADM), in the simplest of terms, add and drop wavelengths at intermediate points in a communication networks.

There has been a large amount of work recently on the construction of OADM using fiber Bragg grating and strongly coupled fiber coupler^{2,3}. Up to now, many schemes have been put forward. Classified by the operation principle, these optical add/drop multiplexer can basically be categorized into two types, namely, interference type⁴⁻⁶ and non-interference type⁷⁻¹¹. For example, all-fiber Mach-Zehnder interferometer is an interferometric type OADM which has been researched deeply². In order to show proper performance, these devices have to be fine tuned and maintained throughout the device lifetime, which is not desirable. Moreover, the two gratings have to be identical and their path lengths to the couplers must match. This cause many difficulties in the fabrication of these devices. Recently, a few new scheme of OADM based on wavelength grating router, optical switches and arrayed grating waveguide are also been proposed¹²⁻¹⁷, however, these devices is very expensive and not easy to fabricate. A tunable add/drop filter, giving access to all frequency components of the WDM signals is needed to provide flexibility in DWDM ring architecture and several ways have been put forward. In this paper, a channel-switching add/drop multiplexer with tunable fiber grating tuned by cantilever beam is proposed and experimentally demonstrated. The tuning principle of fiber Bragg grating is a mechanic tuning method which is very easy to realize.

*Correspondence: Email: feng_dj@263.net or feng_dj@freemail.online.tj.cn; Telephone: 86 22 23509479; Fax: 86 22 23508770

2. THE CONFIGURATION and OPERATION PRINCIPLE OF OADM

Fig.1 shows a schematic diagram of the proposed channel-switching OADM device. The OADM is composed of two 3dB couplers and a tunable fiber Bragg grating. These two remnant ports of the two 3dB couplers are disposed to diminish the reflection light which will give rise to the decline of its capability. The basic principle of it is as follows: a stream of several wavelength (for example, $\lambda_1, \lambda_2, \lambda_3, \lambda_4$) signals are launched into the input port of the OADM. Assuming the tunable fiber Bragg grating resonant wavelength is λ_2 , light at wavelength λ_2 will be reflected by the fiber Bragg grating and emerge in the drop port. The remaining light ($\lambda_1, \lambda_3, \lambda_4$) not dropped by the fiber Bragg grating will pass through and emerge in the output port together with the light added through the add port.

Fig.2 shows the configuration of cantilever beam tuning unit. The fiber Bragg grating is photoimprinted with KrF excimer laser and the phase mask technology. The fiber Bragg grating is firmly stuck on a cantilever beam that is made of organic glass with epoxy resin. Through tuning the cantilever beam with the precision adjuster, we can tune the resonant wavelength of fiber Bragg grating consecutively. The no-chirped linearly tuning range of fiber Bragg grating is about 6.1nm in our experiment, which may permit 7 channels with channel spacing of 0.8nm (100GHz) to insert or drop.

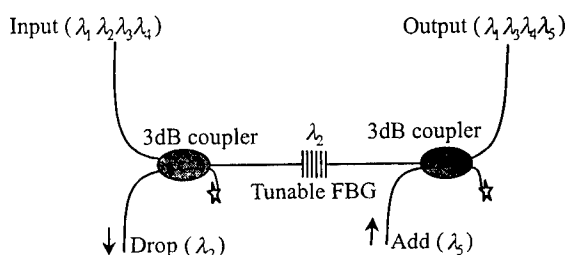


Fig.1 Schematic diagram of channel switching OADM

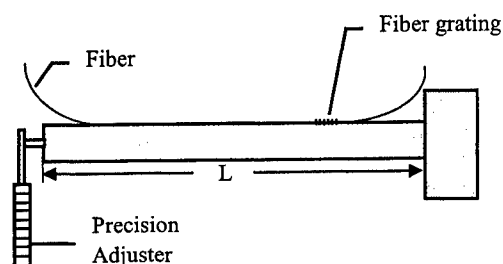


Fig.2 The configuration of fiber Bragg grating tuning unit

3. EXPERIMENTAL RESULTS and DISCUSSION

3.1. The experimental results using the broadband light source as the input signals

A FBG with 99% peak reflectivity at 1557.86nm and a 0.2nm bandwidth is used in this experiment. We use a broadband light source made by ourselves as the input signals to test the capability of OADM. The OADM is linked with optical isolator at both sides in order to diminish the reflective light before it is used in the experiment. The spectral response of the device is shown in Fig.3, which is measured by a commercial Optical Spectrum Analyzer (Advantest Q8383) with a resolution 0.1nm. The output signals of the broadband light source are launched into the input port, the power transferred to the drop port, add port and output port is shown in Fig 3, (b), (c), (d), respectively. Fig.3 (a) is Power spectrum of the broadband light source. Please note that all the curves are not corrected by the reference curve. In experiment, we also find that the groove in add port spectrum will be bigger if we do not dispose the remnant port of couplers or we do not use an isolator at the output port. From the add port spectrum, it is easy to see that the OADM has very good unidirectional and isolation. We can use 3dB coupler to demultiplex the input multiple signals and utilize the fiber Bragg grating to select corresponding wavelength to drop. In the following part, we will test the capacity of this device.

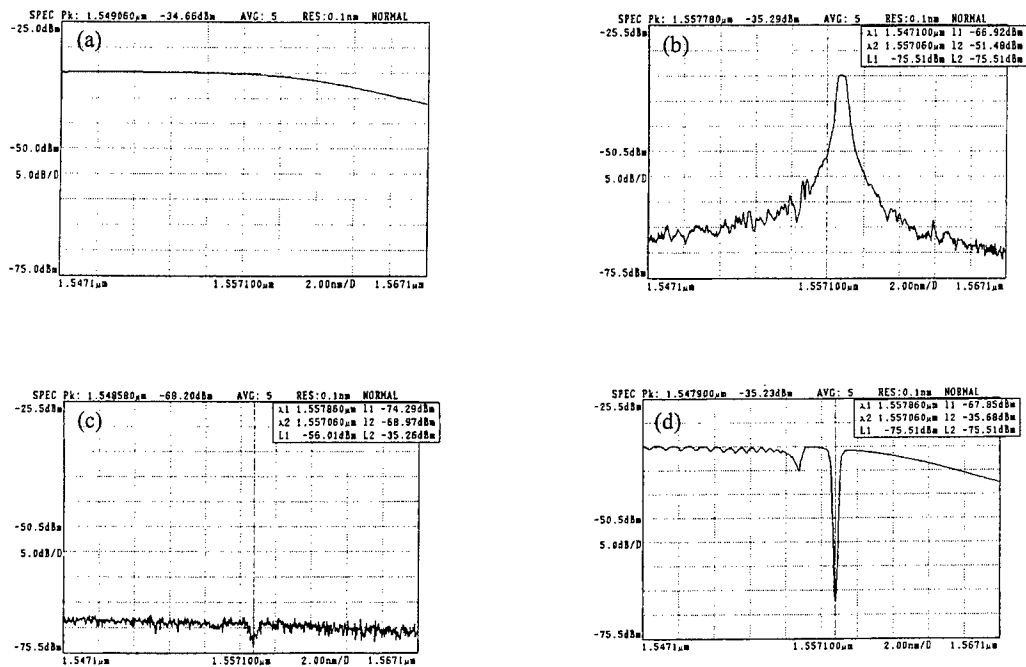


Fig.3 (a) Power spectrum of broadband light source. (b) Power spectrum of the Drop port. (c) Power spectrum of the add port. (d) Power spectrum of the output port.

3.2. The experimental results using a 4-wavelength all fiber laser as the input signals

To investigate the feasibility of this OADM, one set of four channel signals created by a 4-wavelength all fiber laser with 0.8 nm channel spacing in the 1555 nm band are used as signal source. The spectrum of 4-wavelength all fiber laser is shown in fig.4 and the wavelengths are 1555.8 nm, 1556.6 nm, 1557.4, 1558.2 nm, respectively. We have accomplished a 100 km, 4 × 2.5 GHz WDM transmission experiment. In this experiment, we use the OADM to drop relevant signal that has been transferred 100 km. Fig.5 (a), (b) are the signal spectra dropped when the fiber Bragg grating is tuned to 1555.84 nm, 1557.4 nm, respectively. The three small spectral components contaminating the dropped signal are due to the crosstalk. The interchannel isolation in fig.5 (a) is about 29 dB and 23 dB in fig.5 (b). This OADM can demultiplex other channel signals by tuning the fiber Bragg grating using the cantilever beam method.

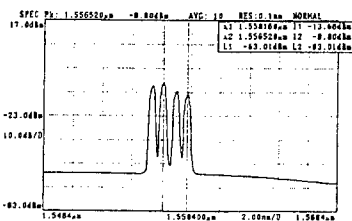


Fig.4 4-wavelength all fiber laser

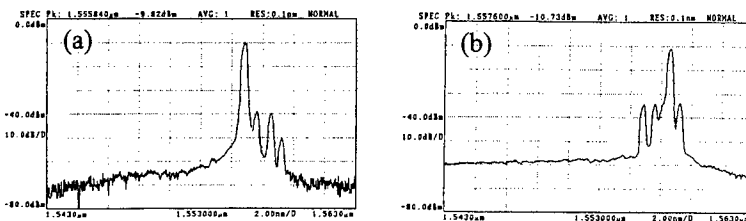


Fig.5 (a) The dropped signal at 1555.84 nm. (b) The dropped signal at 1557.4 nm

The crosstalk level of the OADM shows that the OADM can basically meet the practical need of WDM ring network. Further reduction in the crosstalk level for upgrading the system performance is possible by improving the fiber Bragg

grating reflectivity. Over two months we observed no decline in the devices performance. Due to using two 3dB optical couplers, so the transmission loss is very high. This is its main disadvantage. The loss of signals can be counteracted by EDFA. in fact, we use two EDFA in our transmission system to magnify these signals. If we use the optical circulators instead of the 3dB optical couplers, the performance of the OADM will improve.

4. CONCLUSION

In summary, a simple structure, linear tuning, high channel isolation, low channel crosstalk, low cost scheme of OADM is proposed. It performs perfect with a channel wavelength selectivity. Its high insertion loss will restrict the improvement of system performance, however, it provide us with one low cost, precision tuning, reliable choice. The low cost makes it very attractive in WDM optical networks. OADM makes the WDM optical networks flexible and it allows people to add or drop signals they need at the node expediently.

ACKNOWLEDGMENTS

The authors are grateful to the "National 863 Research Project" for its fund support.

REFERENCES

- 1 G. Meltz, W. W. Morey, and W. H. Glenn, "Formation of Bragg gratings in optical fibers by a transverse holographic method," *Opt. Lett.*, **14**, pp. 823-825, 1989.
- 2 F. Bilodeau, D C. Johnson, S. Theriault, B. Malo, J. Albert, and K.O. Hill, "An all-fiber dense-wavelength-division multiplexer/demultiplexer using photoimprinted Bragg gratings," *IEEE Photon. Technol. Lett.*, **7**, pp. 388-390, 1995.
- 3 J. L. Archambault, P. St. J. Russell, S. Bachelos, P. Hua, and L. Reekie, "Grating-frustrated coupler: A novel channel-dropping filter in single-mode optical fiber," *Opt. Lett.*, **19**, 180-182, 1994.
- 4 Bethuys S, Lablonde L, Rivoallan L, *et al.*, "Optical add/drop multiplexer based on UV-written Bragg gratings in twincore fiber Mach-Zehnder interferometer," *Electron Lett*, **34**, pp. 1250-1252, 1998.
- 5 Bakhti F, Sansonetti P, Sinet C, *et al.*, "Optical add/drop multiplexer based on UV-written Bragg grating in a fused 100% coupler," *Electron Lett*, **33**, pp. 803-804, 1997.
- 6 Ortega B, Dong L, Reekie L., "All-fiber optical add-drop multiplexer based on a selective fused coupler and a single fiber Bragg grating," *Appl Opt*, **37**, pp. 7712-7717, 1998.
- 7 Se Yoon, Sang Bae lee, Seo Won Kwon, *et.al.*, "Channel-switching active add/drop multiplexer with tunable gratings," *Electron Lett*, **34**, pp. 104-105, 1998.
- 8 Kim S Y, Lee S B, Chung J, *et al.*, "Highly stable optical add/drop multiplexer using polarization beam splitters and fiber Bragg gratings," *IEEE Photon Technol Lett*, **9** pp. 1119-1121, 1997.
- 9 Archambault J L, Russell P St J, Barcelos S, *et al.*, "Grating frustrated coupler: a novel channel-dropping filter in single-mode optical fiber," *Opt Lett*, **19** pp.180-182, 1994.
- 10 Ortega B, Dong L., "Selective fused couplers consisting of a mismatched twin-core fiber and a standard optical fiber," *J Lightwave Technol*, **17** pp. 123-128, 1999.
- 11 Okayama H, Ozeki Y, Kunii T., "Dynamic wavelength selective add/drop node comprising tunable gratings," *Electron Lett*, **33** pp. 881-882, 1997.
- 12 B. Glance, "Wavelength-tunable add/drop optical filter," *IEEE Photon Technol Lett*, **8**, pp. 245-247, 1996.
- 13 G. Nykolak, M. R. X. De Barros, *et. al.*, "All-fiber active add-drop wavelength router," *IEEE Photon Technol Lett*, **9**,

pp. 605-606, 1997.

- 14 Okayama H, Ozeki Y, Kunii T. *et. al*, "Dynamic wavelength selective add/drop node comprising tunable gratings and optical awitches," *Electron Lett*, **33** pp. 403-404, 1997.
- 15 Shien-kuei Liaw, Keang-Po Ho and Sien Chi, "Multichannel add/drop and cross-connect using fiber Bragg grating and optical switches," *Electron Lett*, **34(16)**, pp. 1601-1603, 1998.
- 16 K. Okamoto, K. Takiguchi, Y. Ohmori, "16-channel optical add/drop multiplexer using silica-based arrayed-waveguide gratigs," *Electron Lett*, **31(9)**, pp. 723-724, 1995.
- 17 W. D. Zhong, S. Dods, J. P. R. Lacey, R. S. Tucker, "Reconfigurable multichannel add-drop multiplexer with improved performance," *Electron Lett*, **32(16)**, pp. 1477-1478, 1996.

A novel Interferometer for Measuring Small Distance

Wu zhaoxia^{*a}, Li zhiquan^{*b}, Tong kai^a, Qiang xifu^b

^aYanshan University, Qinghuangdao 066004, CHN

^bHarbin institute of technology, Harbin 150002, CHN

ABSTRACT

A novel wavelength scanning optical fiber dual-interferometer for measuring small distance has been developed in this paper. A wavelength-scanning source is used to simultaneously illuminate two Fabry-Perot (F-P) cavities. One is as the sensing cavity, the other is as the reference cavity. If the length of the reference cavity is pre-calibrated and maintain constant, and the scanning wavelength is taken as an inter-converter to compare the gap length of the sensing cavity with the reference cavity length, using the frequency spectrum separator, absolute measurement can be obtained.

Key words Wavelength-scanning , Optical fiber interferometer , Absolute distance measurement

1. INTRODUCTION

F-P interferometer is applied to analyze the spectrum with narrow rang and simple spectrum. But since 1980's many researches have indicate that F-P interferometer for measuring has many advantage compared with other interferometers^{[1]-[5]}. A.Kersey was first to demonstrate the use of optical fiber F-P interferometer (FPI)^[1] for measuring small distance in 1983. Due to its unique characters of simple structure and single-end operation, and has common characters of fiber sensors, the FPI has been extensively utilized in various practical applications since then. In 1991 K.Murphy suggested a bi-directional fringe counting FPI system^[2]. This FPI system may improve the dynamic character in perturbation environment, but it still has a differential technique. In order to realize the absolute measurement for small distance, a novel wavelength scanning optical dual-interferometer has been developed in this paper. A wavelength-scanning source is used to simultaneously illuminate two F-P cavities: One is as the sensing cavity, the other is as the reference cavity. If the length of the reference cavity is pre-calibrated and maintain constant, and the scanning wavelength is taken as inter-converter to compare the gap length of the sensing cavity with the reference cavity length, absolute measurement for the sensing cavity length can be obtained.

2. WAVELENGTH SCANNING OPTICAL FIBER F-P INTERFEROMETER (FPI)

2.1 The Decision of Harmonic Cavity Length

In the standard FPI, the two beams which reflected from the two fiber ends in FPI are interfered each other and the signal received from the detector can be expressed as (1) and (2):

$$I_{(\lambda,L)} = I_{0(\lambda)} \cos(\phi_s + \phi_0) \quad (1)$$

$$\phi_s = 2KL = (4\pi Ln) / \lambda \quad (2)$$

Where λ is the wavelength , L is the harmonic cavity's length, $I_{(\lambda,L)}$ is the intensith received at the detector (this intersity is the function of λ and L), $I_{0(\lambda)}$ is the spectrum intensity of the source , ϕ_s is the phase difference between the two beams that was introduced by L and λ , ϕ_0 is the initial phase, n is the

refractive index in F-P cavity and $K = 2\pi / \lambda$.

If the wavelength is scanned from λ_1 to λ_2 while the cavity length remains constant, the phase change can be obtained.

$$\Delta\phi_s = \int_{\lambda_1}^{\lambda_2} d\phi_s = 4\pi L \int_{\lambda_1}^{\lambda_2} (-n / \lambda^2) d\lambda = 4\pi L \Delta(n\lambda) / (\lambda_1 \lambda_2) - 4\pi L_n \Delta\lambda / \lambda_1 \lambda_2 \quad (3)$$

The harmonic cavity length L can be decided from Equation (3), which is valid for the accuracy required by most applications.

2.2 Wavelength Scanning Optical Fiber Dual Interferometer(DFPI)

The experimental configuration of the DFPI is shown in fig.1. Two FPIs are connected to the output ports of couplers C_2 and C_3 respectively. Each FPI is constructed with two carefully prepared fiber ends inserted in

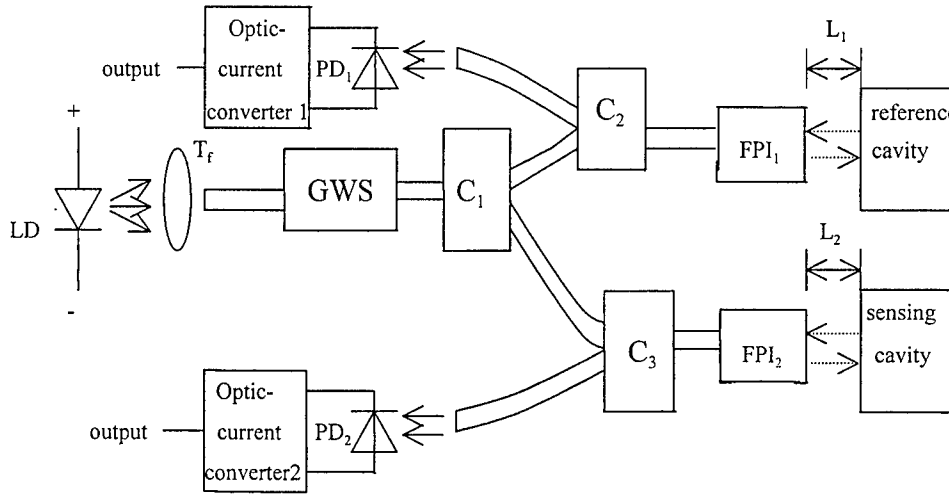


Figure 1. Experimental setup of DFPI

the silica fiber in the sensing FPI₂ is epoxied to the hollow tube end to provide accurate distance for the experiments and for the self-calibration of the reference cavity length. For the reference FPI₁, the input and output were epoxied to the hollow tube to construct a stable cavity. The Fresnel reflections from the fiber/air interface and from the air/fiber interface in each FPI are interfered. The light from the tunable LD-grating-scanner is split into two beams in coupler C_1 to illuminate FPI₁ and FPI₂ through C_2 and C_3 respectively. The structure of LD grating-wavelength-scanner (GWS) is shown in fig.2. The light source is a 1300nm edge-emitting LD. As dispersion element the diffraction grating G is mounted on the shaft of scanner. Thus the GWS is constituted. The broad spectrum light from the LD is collimated in lens T_1 and diffracted by the grating. Part of the refracted light is collected into the coupler C_1 by the second lens T_2 . When a triangle driving current is applied to the GWS, it rotates the grating and the wavelength launched into the coupler C_1 is correspondingly scanned.

According to equation (1)~(3), each FPI can produces a group of fringes when the wavelength is scanned from λ_1 to λ_2 . Using subscript 1 and 2 to denote the reference and sensing FPIs, the phase changes of these two independent FPIs can be obtained from Equation (3).

$$\Delta\phi_{s_1} / \Delta\phi_{s_2} = L_1 / L_2 \quad (4)$$

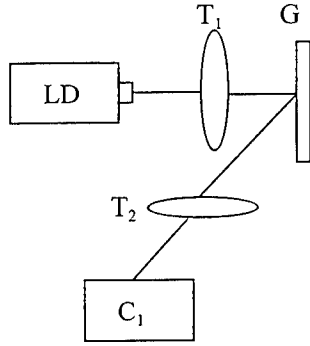


Figure 2. Grating wavelength scanner

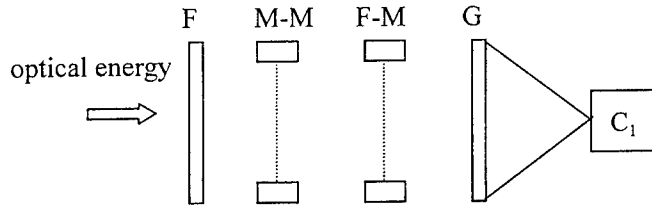


Figure 3. Frequency spectrum separator

Equation (4) indicates that the measurement of sensing cavity length L_2 relative to reference length L_1 is independent of other factors. This means we don't need the light source to be tuned accurately nor repeatedly. The only requirement for the wavelength scanning is smoothness. This is much easier to achieve.

In practice the phase information can be obtained from an analysis of the corresponding interference fringes. The fringe number produced during one optical tuning cycle in each cavity can be expressed as^{[2]-[3]}:

$$m_i = \Delta\phi_{s_i} / 2\pi = \varepsilon_i + f_{i,1} + f_{i,2} \quad (5)$$

Where m_i is the number of the fringes ($i=1$ for the reference cavity and $i=2$ for the sensing cavity). ε_i is the integer of m_i . $f_{i,1}$ and $f_{i,2}$ are the fraction before the first fringe peak and the fraction after the last peak respectively. The absolute gap length L_2 of the sensing FPI is:

$$L_2 = L_1 m_2 / m_1 = L_1 (\varepsilon_2 + f_{2,1} + f_{2,2}) / (\varepsilon_1 + f_{1,1} + f_{1,2}) \quad (6)$$

Equation (6) indicates that $\Delta\phi_{s_1}$ and $\Delta\phi_{s_2}$ are medium values. The measurement of L_2 is decided by the number of fringes. We can obtain a high measuring precision by adjust L_1 .

3. THE IMPLEMENT OF SYSTEM CHARACTER

The theory and method of optical scanning interferometer for measuring small distance has been concrete indicated in the conferences. But how to improve the characters of measuring system hasn't been satisfactory solved^[4]. The problem of wavelength rang from λ_1 to λ_2 is solved by using frequency spectrum separator. This method can improve the character of system effectively.

In fig.3 the optical energy should pass a preposition wave filter F to separate suitable frequency spectrum rang before it enters GWS. This rang is decided by standard detecting plate which is composed with moving mirror (M-M) and fixing mirror (F-M). In order to avoid hot noise, F, M-M, and F-M are sealed in a vacuum bottle. The function of standard detecting plate is act as multi-band filter. A lower resolution frequency is operated when scanning begin. The spectrum's resolution is improved when M-M is moved to a property distance, and the higher frequency part in the spectrum can be resolved. This distance is decided by the expecting resolution. M-M must parallel to F-M exactly when M-M is moving. The output of scanning interferometer can be described as:

$$N_i = \frac{A_0 \Omega_i}{4\pi} Q_c T_{0i} \int_{T_f} (\nu, t) B_{atmos}(\nu) d\nu \quad (7)$$

The transmission coefficient of standard detecting plate can be described with array as ^[5]:

$$T_e(\nu, t) = \frac{1-R}{1+R} \left\{ 1 + 2 \sum_{n=1}^{\infty} R^n \nu_n \cos[4\pi N \mu t \nu \cos(\theta)] \right\} \quad (8)$$

In equation (7) and (8), ν is optical wavelength, N_i is the transmission energy which is obtained from the coupler. A_o is the hole's area of M-M. Ω_i is the stereoscopic angle facing with the couple. Q_c is the coupling efficiency of the coupler C_1 . T_o is the transmission coefficient except standard plate and filter. T_f is the filter's transmission coefficient. R is the reflection coefficient of the standard plate. n is the exponential function being related to internal reflection of cavity. D_n is the coupling function (when $D_n=1.0$ the state is ideal coupling state). μt is the distance between the two plates. θ is the beam angle when optic is passing the two plates. N is the numbers of optical wave in the cavity. We can obtain a small dimensional angle when radiation beams are passing these plates. If the brightness $B_{atmos}(\nu)$ is given, the radiation can be measurement by these plates. So the spectrum rang from λ_1 to λ_2 can be decided by the filter and the standard detecting plates.

4. EXPERIMENTAL RESULTS

The experimental results from optical scanning DFPI are shown in fig.4. The operation wavelength is

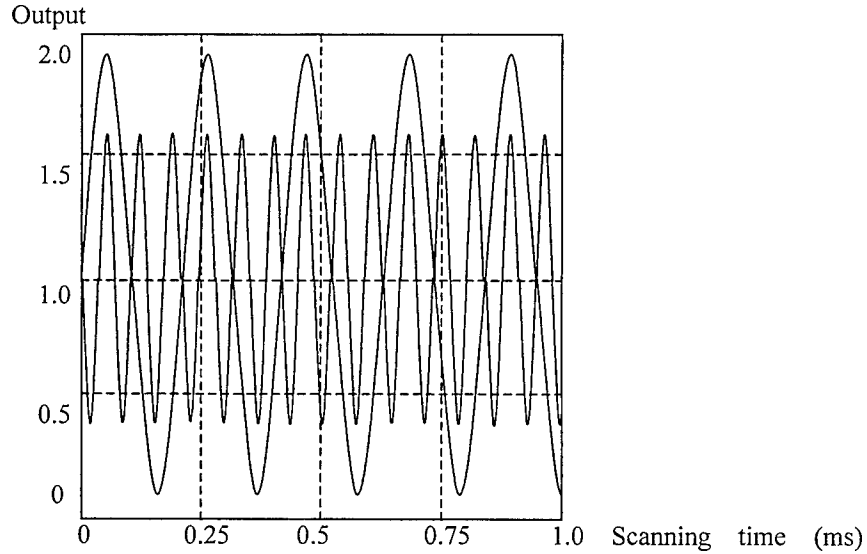


Figure 4. The experimental results

1300nm. The upper trace is the fringes of reference cavity; the lower one is the fringes of sensing cavity. The linear scanning rang is about 40nm. The reference cavity length is 0.2mm. It's seen that the amplitude of output will decrease when sensing cavity length increased. The reference cavity and sensing cavity length are 0.20 mm and 0.65mm respectively. From the fig4, We know that the two group of fringe numbers are 4.745 and 15.383. So we can obtain that the sensing cavity length is 0.6498mm from calculation. The relative error is 0.03%. The measurement accuracy is $0.2 \mu m$. The resolution is $0.03 \mu m$.

5.CONCLUSION

In this paper using DFPI, the absolute measurement is realized. But the demands on the source, such as stability of frequency, repetition of scanning, stability of source power are reduced. The experimental results show that the accuracy of $0.2\ \mu\text{m}$ and resolution of $0.03\ \mu\text{m}$ are achieved, in the rang of 0~3mm. This technique can be easily applied in the absolute measurement of pressure, strain and so on.

REFERENCE

1. A.D. Kersey, D.A.Jackson and M.Corko, Opt.Comm., V.45,P.71 (1983) ;
2. K.A. Murphy, M.F.Gunther, A.M.Vengsarkar and R.O.Claus, Opt.Lett.,V.16,P.273(1991)
3. T.Li, A.Wang, K.Murphy and R.Claus, Opt, Lett., V.20,P.785~787(1995)
4. F.Maystre and R.Dandliker, Polarimetric fiber optical with high sensitivity using a Fabry-Perot structure, APPLIED OPTICS, Vol.28, NO.11,1995-2000(1989).
5. D.Wang, Y.Ning, A.Palmer, K.Grattan and K.Weir, IEEE Photonics Tech.Lett.,V.6,P855(1994)

Grating angular displacement transducer using a Fabry-Perot structure

Li zhiquan^{*a}, Qiang xifu^a, Wu zhaoxia^{*b}, Fan lina^b

^aHarbin institute of technology, Harbin 150001 CHN

^bYanshan University, Qinghuangdao 066004, CHN

ABSTRACT

A novel grating angular displacement transducer using a multiplex Fabry-Perot interference technology has been developed. The Fabry-Perot interferometer (FPI) has been traditionally used to examine either small spectral ranges or relatively simple spectra. Recently, however, the studies have shown that the FPI can be competitive with the Michelson interferometer over extended spectral ranges. A relatively new FPI is described based on two gratings.

Keywords: Angular-movement transducer, Fabry-Perot Interferometer, Grating, Transducers

1. INTRODUCTION

The interferometer based on the Fabry-Perot interference technology has been used historically at high resolution either to examine an elementary spectrum, containing only a few lines or to examine a small spectral region that has been isolated by a filter of other dispersive device^{[1]-[6]}. When larger spectral regions or complex high-resolution spectra are required, the instrument of choice has been the Michelson interferometer or the Fourier transform spectrometer (FTS). However, recent studies^{[1]-[4]} have challenged this choice. These authors pointed out correctly that the inversion of a Fabry-Perot interferometer (FPI) is competitive with a Michelson interferometer over an extended spectral range. Yet in one of these studies there has been some limitation that is related to the application technique and the theory. In this paper, we have first reviewed the method of grating measuring angular displacement, and then introduced the grating angular displacement transducer using a Fabry-Perot structure.

2. PRINCIPLE AND STRUCTURE

2.1 Transducer Using Grating

National Engineering Laboratory (NEL.1966) developed a measuring system that uses an optical grating with shaft encoders^[5]. The accuracy of the complete system is determined by the highly accurate optical grating.

The system is unique in the method used to relate the encoder and grating signals. The system was used interpolation of the grating pitch described above to increase the resolution of the shaft encoder and provide some sensing logic.

Fig.1(a) shows a relationship between the grating division and the encoder resolution which indicates that a

precise mechanical relationship is required between the encoder and the grating if ambiguity is to be avoided at the transition points of the encoder.

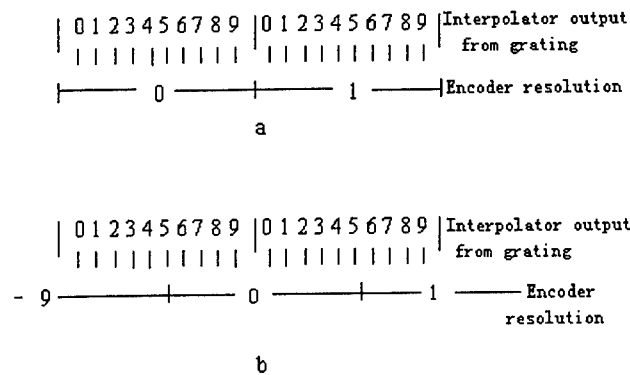


Fig.1 grating and encoder relationship

This requirement is avoided in the NEL system by modifying the relationship to that shown in Fig.1(b). The encoder track and the grating division needed now only have an accuracy up to $\pm 1/2$ for a division of the grating, providing this tolerance is not exceeded over the whole length of the grating. The encoder is interrogated only during the transition of the interpolator output from 0 to 9 or from 9 to 0, i.e. at each grating division. Other, coarser tracks of the encoder can be interrogated in a similar manner.

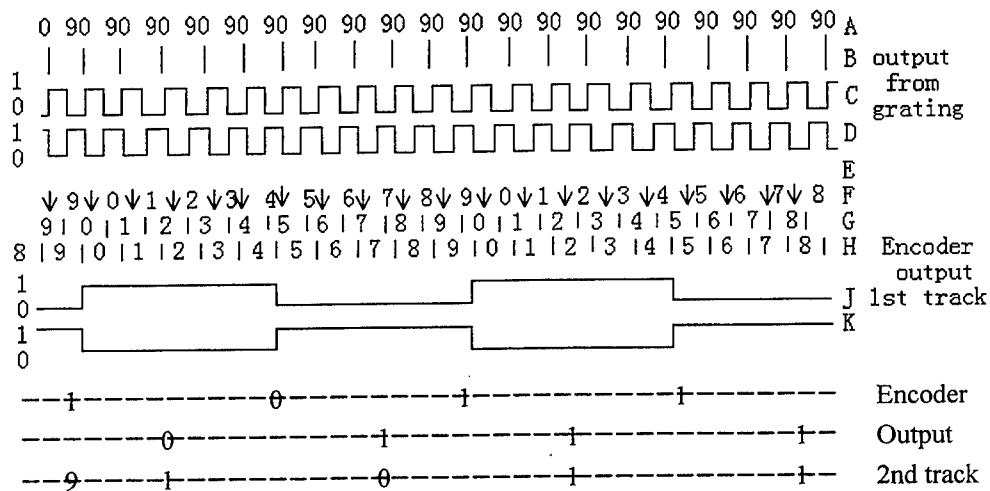
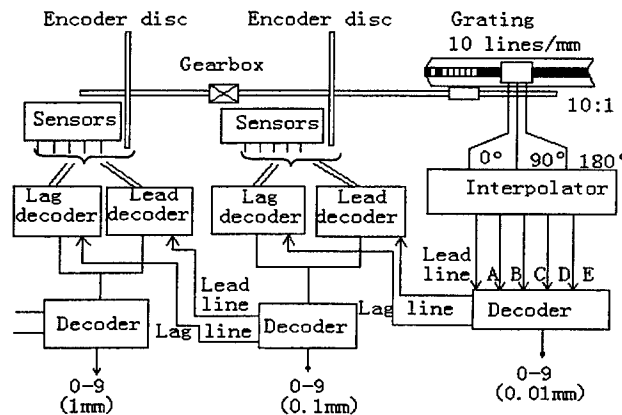


Fig.2 Interrogation of grating-encoder combination

The system described by Russell is detailed in Fig.2. The upper four rows are the output and the derived outputs from the grating. Row A represents the cycle of output from the grating divisions, e.g. each cycle representing 0.1 mm for a 10 lines/mm grating. Row B represents the ten subdivisions generated by the interpolator, each

The method shown is for a decade readout, but, for purely digital readout, the interpolator output can be decoded to provide the required digital code and the shaft encoder output can be left in a digital code. The lag/lead signals are generated with respect to the main grating divisions which are the same as the least significant bits on the shaft encoder.



Where the fixed grating transmission[2] can be expressed as the series

$$T_{ei}(\lambda, t) = [(I - R)/(I + R)] \left\{ I + 2 \sum_{n=1}^{\infty} R^n D_n \cos[4\pi n \mu t \lambda \cos(Q)] \right\} \quad (2)$$

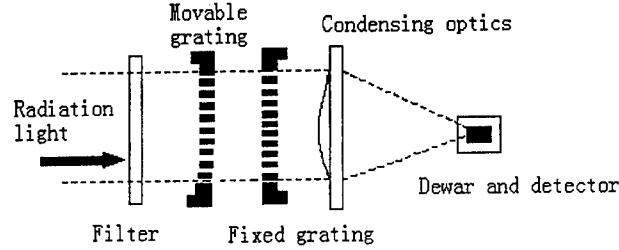


Fig4 Optical elements of the FPI

In Eqs.(1)and (2), A_0 is the area of the seam of the gratings; Ω_i is the solid angle subtended by the detector; Q_e is the quantum efficiency of the detector; T_{oi} is the system transmission coefficient for all elements except the fixed grating and filter; T_f is the system transmission of the filter; R is fixed grating reflecting; n is an index related to the number of reflections within the two grating cavities; D_n is the defect function (which is 1.0 for a perfect instrument); t is the distance between the grating; μ is the index of refraction; θ is angle of movable grating moving; λ is wavelength; $B_{atmos}(\lambda)$ is the brightness per unit wave number of the radiation. Such as Fig.5, the analysis can be simplified if the fixed grating is oriented at normal to the path of the incident radiation.i.e.,

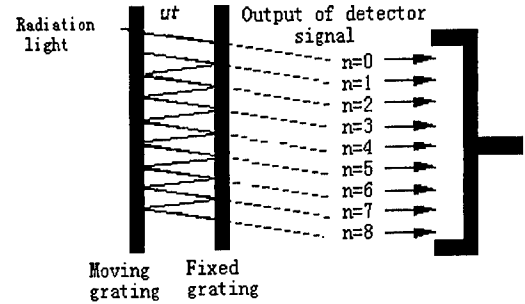


Fig.5 The signal of FPI modulation

$$N_i = f(\theta) \quad (3)$$

Then,

$$\theta = N_i^{-1} \quad (4)$$

where N_i^{-1} is the inverse function.

3.RESULTS

The results obtained by passing a computer-generated spectrum through the above FPI transform equations show that this analytical technique can be useful for the high accuracy angular displacement measuring. In our simulations, we found that it is relatively easy to limit the instrumental broadening and to resolve small spectral features, while the required grating motion remains quite short compared with that of a FTS(Fourier Transform spectrometer).For test purposes, we chose to examine a simulated spectrum from the region near 21.88 cm^{-1} . This region of the spectrum contains a nearly random distribution of several strong ozone lines.

Fig.6 is a comparison of the individual harmonic terms from a 20 cm scan^[1]. One can see that the higher-harmonic

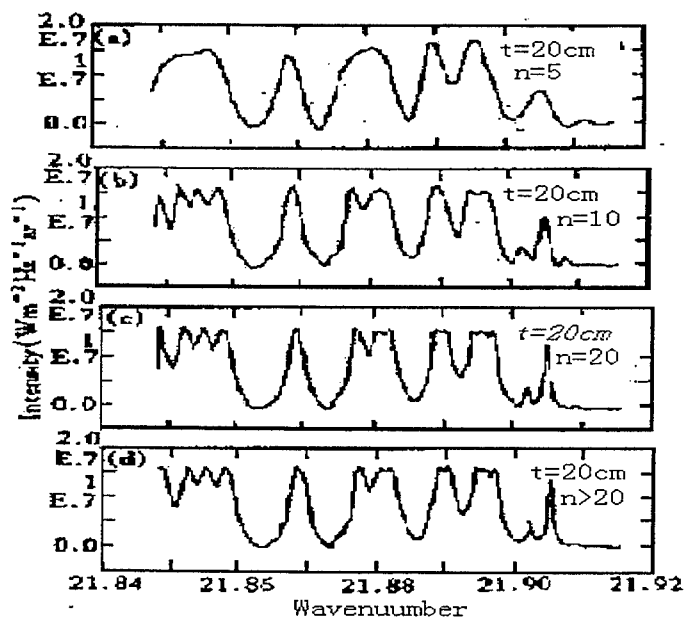


Fig.6 The output of the transducer

terms, e.g., $n = 20$, are much less broader than that of the lower harmonics, such as $n = 5$. The higher-harmonic terms of the FPI are equivalent to a longer scan distance for a Michelson interferometer: the 20th harmonic of a 20cm FPI scan has an equivalent Michelson path length of 4 m. One should note that the data in these figures have been normalized to permit comparison; in practice the signal from the higher harmonics is weaker than that from the lower harmonics as the result of reflective losses. Consequently, the higher harmonics must be weighted with the lower harmonics in such a way as to produce a spectrum with little broadening but with enough signal that the minor features can be resolved.

4. CONCLUSION

In this paper we have illustrated a new analysis technique for the FPI. It was shown previously that a FPI can be used as a Michelson interferometer by changing the separation between the gratings by examining the first harmonic, using Fourier Transform spectroscopy. It has also been shown that, with FPI, the necessary scan distance is a factor of 10 less than needed by a Michelson interferometer to achieve the same spectral resolution. Angular displacement is normal problem. But, after we confine it with FPI, a novel instrument has been developed.

REFERENCES

1. Paul B. Hays and Hilaiy E. Snell, Multiples Fabry-perot interferometer, APPLIED OPTICS, Vol. 30, No. 22, August 1991, (3108-3113).
2. Claude belleville and Gaetan Duplain White-light interferometric multimode fiber-optic strain sensor, OPTICS LETTERS/Vol. 18, No. 1/January 1, 1993 (78-80).
3. Stephen T. West and Chib-Lin Chen, APPLIED OPTICS/Vol. 28, No. 19/1 October 1989, (4206-4209).
4. Chia-Chen Chang and Jim Sirkis Multiplexed Optical Fiber Sensors Using a Single Fabry-Perot Resonator for Phase Modulation, JOURNAL OF LIGHTWAVE TECHNOLOG. VOL. 14, NO. 7, JULY 1996, (1653-1663).
5. Anatoli A. Chtcherbakov and Pavel V. Bulkin Long dual-cavity fiber optic Fabry-Perot strain

- sensor with rugate mirrors, *Optical Engineering*, Vol, 35 No. 4, April 1996 (1059-1063).
6. T. W. Kao and H. F. Tayler High-sensitivity intrinsic fiber-optic Fabry-Perot pressure sensor, April 15, 1996/Vol. 21, No. 8/OPTICS LETTERS.
 7. S. F. Masri, M. S. Agbabian, A. M. Abdel-Ghaffar, M. Higazy, R. O. Claus, and M. J. deVries, Experimental study of embedded fiber-optic strain gauges in concrete structures, *Journal of Engineering mechanics*, 1994. Vol. 20, No. 8 (1696-1717).
 8. Murphy, K., Fogg, B. R., and Vengsarkar, A. M., Spatially weighted vibration sensors using tapered two-mode optical fibers, *J. Lightwave Technol.*, Vol. 10, No. 11 (1680-1687).
 9. Y. J. Rao, P. J. Henderson, N. E. Fisher and D. A. Jackson, Wavelength division multiplexed in-fibre Bragg grating Fabry-Perot sensor system for quasi-distributed current measurement, *Appl. Opt. Div. Conf.*, Brighton, 16-19 March 1998.
 10. Kersey A D, Berkoff T A and More W W, Multiplexed fibre Bragg grating strain-sensor system with a fibre Fabry-Perot wavelength filter, *Opt. Lett.* 18 (1370-1372) 1993.

Numerical analysis of near-field optical trapping using tapered fiber probe

Guoping Zhang*, Zhongru Zhu, Yanping Li, Ge Xia, and Qi Lin

Department of Physics, Central China Normal University, Wuhan, 430079, China

ABSTRACT

A new scheme for optical trapping is presented in this paper. The method is based on a tapered fiber probe with a tip diameter less than a light wavelength. A three-dimension gradient optical field is formed within the optical near field of the fiber probe, and a particle approaching the fiber probe tip will be trapped. The evanescent electromagnetic field in the vicinity of the fiber tip is calculated by the multiple multipole method (MMP). The intensity distributions and the trapping potential of the near fields of the tip versus the longitudinal and transverse distances from the tip are analyzed respectively. The trapping force is obtained for a dielectric particle. The numerical calculating results show the availability of this method.

Key words: optical trap, near-field optics, fiber probe, scanning near-field optical microscope

1. INTRODUCTION

Optical trapping by a single-beam gradient force trap was proposed by Ashkin *et al.* for the first time.^[1] Since then, this method has been developed as an optical tweezers technology, and extensively used for manipulation of various submicron-size dielectric particles and biological structures (such as viruses, bacteria and yeast cells).^[2,3] However, conventional optical tweezers, based on the gradient field near the focus of a laser beam, have a diffraction-limited trapping volume.

Scanning near-field optical microscopy (SNOM), developed recently from the combination of the scanning probe technology with the optical microscopy, offers an optical image technology with an ultra-high resolution beyond the diffraction limit.^[4-6] The resolution capability of the SNOM system is determined by the transmission property of the fiber probe, such as the output photon flux density from the probe and the tip size of the probe. Nowadays its longitudinal and transversal resolutions have reached 0.1nm and 7nm respectively.

In this paper, a novel high-resolution optical trapping scheme is presented by a tapered fiber probe used for SNOM. Because the tip diameter of the fiber probe is smaller than a light wavelength, the near field close to the tip mainly consists of evanescent components which decay rapidly with distance from the tip.^[7-9] Thus a three-dimension gradient optical field is formed within the optical near field of the fiber probe. When one particle approaches the fiber probe tip, it will be trapped by a three-dimension optical trap, which is produced from the action of the three-dimension optical gradient force. As this type of optical trapping appears within the optical near field of the fiber probe tip, it is called as the near-field optical trap.

* Correspondence: Email: gpzhang@phy.ccnu.edu.cn

2. TAPERED FIBER PROBE

Tapered fiber probes used for the scanning near-field optical microscopy are generally fabricated by local melting and pulling single-mode optical fibers.^[10,11] An about 2-meter-length single-mode fiber stripped off a short section of jacket in its middle part is heated locally by a beam of CO₂ laser, simultaneously an external pulling force is applied on two ends of the fiber. When it is broken, a tapered fiber probe is obtained. Appropriate choosing the laser intensity, the heating length and time, and the pulling force strength can be used to yield fiber probes with various tip sizes and taper shapes. The tip diameters of the fiber probes used for the SNOM system are required less than an optical wavelength, e.g., tens to hundreds of nanometers for the visible light. Figure 1 gives schematic diagrams of the conical-taper and the parabolic-taper fiber probes.

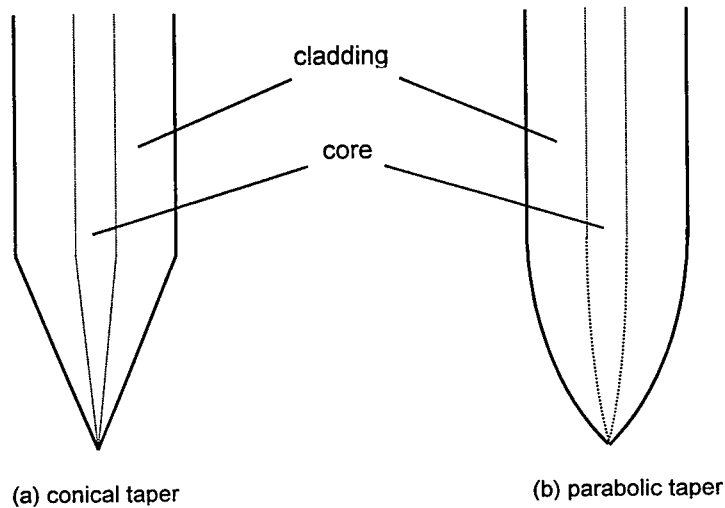


Fig.1. Schematic diagram of tapered fiber probes with (a) a conical taper and (b) a parabolic taper. The areas within the dash lines stand for the fiber core, and those between the solid lines and the dash lines for the fiber cladding.

Both the diameters of the cladding and the core of the tapered fiber probe decrease gradually along the taper, and they are usually assumed to maintain their initial ratio. The modes in the beginning of the fiber taper exhibit first the core-guided modes, and they contract slightly. After propagating a certain distance along the taper, the core-guided modes spread into the cladding, and gradually couple to the cladding-guided modes, for which the boundary condition becomes the cladding/air boundary.

The waveguide structure of the tapered fiber is changed with a different taper shape, thus results in different transmission property. It is shown by the local modal analysis that, the mode field is first the core-guided mode and contracts slightly along the taper, then spreads into the cladding and gradually couples to the cladding-guided modes. When the tip size of the tapered fiber is less than an optical wavelength, the evanescent wave becomes the major part of the optical near field from the tapered fiber. Meanwhile, due to the tip scattering, the evanescent wave is mostly concentrated at the axial direction, and the lateral optical field decreases gradually. So optical field gradients are formed near the tip of the

tapered fiber probe.

The transmission properties and the electromagnetic field distributions are different for the conical and parabolic tapered fiber probes.^[9] Generally, the parabolic tapered probe has a transmission efficiency of almost one order of magnitude higher than the conical one. The electromagnetic near-field distributions of these two probes are more focused while their taper angles increase.

3. THEORY

A laser beam is coupled into the single-mode fiber from the end opposite to the tip. In order to solve Maxwell's equations in the specific geometry of the tip of the tapered fiber probe and its environment, we employ the multiple multipole method (MMP) which recently has been applied to study near-field optical phenomena.^[12,13] The MMP method expands the solutions on multipolar eigenfunctions. The vector multipolar eigenfunctions $\mathbf{F}_n(\mathbf{r}, \omega)$ for the eigenvalue q_n satisfy the vector wave equation:

$$-\nabla \times \nabla \times \mathbf{F}_n(\mathbf{r}, \omega) + q_n^2 \mathbf{F}_n(\mathbf{r}, \omega) = 0. \quad (1)$$

In terms of scalar fields, the scalar multipolar eigenfunctions $\phi_n(\mathbf{r}, \omega)$ for the eigenvalues q_n satisfy the scalar Helmholtz equation:

$$\nabla^2 \phi_n(\mathbf{r}, \omega) + q_n^2 \phi_n(\mathbf{r}, \omega) = 0, \quad (2)$$

where

$$\int \phi_n^*(\mathbf{r}, \omega) \phi_{n'}(\mathbf{r}, \omega) d\mathbf{r} = \delta_{n,n'} \quad (3)$$

These eigenfunctions form an orthonormal basis set in the Hilbert space. The simplest solution is obtained in Cartesian coordinates:

$$\phi_n(\mathbf{r}, \omega) = \frac{1}{\sqrt{8\pi^3}} \exp\{j\mathbf{k} \cdot \mathbf{r}\}, \quad (4)$$

where \mathbf{k} is the wave vector. The multipolar wave functions are formulated in the spherical coordinates:

$$\phi_n(\mathbf{r}, \omega) = \phi_{\sigma,l,m,q_n}(\mathbf{r}, \omega) = P_l^m(\cos\theta) z_l(q_n r) \begin{Bmatrix} \cos m\varphi \\ \sin m\varphi \end{Bmatrix}, \quad (5)$$

where $P_l^m(\cos\theta)$ represents for the associated Legendre polynomials and $z_l(q_n r)$ for the spherical Bessel functions. The index σ distinguishes between the even and odd functions. In the cylindrical coordinates, the multipolar wave functions are characterized as

$$\phi_n(\mathbf{r}, \omega) = \phi_{\sigma,m,q_n}(\mathbf{r}, \omega) = B_m(\kappa \rho) \exp\{jq_n z\} \begin{Bmatrix} \cos m\varphi \\ \sin m\varphi \end{Bmatrix}, \quad (6)$$

where the B_m are Bessel functions, $\kappa = \sqrt{q_{n,x}^2 + q_{n,y}^2}$ and $\rho = \sqrt{x^2 + y^2}$.

Three sets of vector eigenfunctions can be built by applying the gradient operator to the scalar functions:

$$\mathbf{L}_n(\mathbf{r}, \omega) = C \nabla \phi_n(\mathbf{r}, \omega), \quad (7)$$

$$\mathbf{M}_n(\mathbf{r}, \omega) = C \nabla \times \phi_n(\mathbf{r}, \omega) \mathbf{S}, \quad (8)$$

$$\mathbf{N}_n(\mathbf{r}, \omega) = \frac{C}{k} \nabla \times \nabla \times \phi_n(\mathbf{r}, \omega) \mathbf{S}, \quad (9)$$

where C is a normalization factor which relies on the coordinates system, and \mathbf{S} is a constant vector of unit length, sometimes called "Poynting vector".

Because of the property of the Poynting vector and the orthonormalization of the scalar eigenfunctions, the above three sets $\mathbf{L}_n(\mathbf{r}, \omega)$, $\mathbf{M}_n(\mathbf{r}, \omega)$ and $\mathbf{N}_n(\mathbf{r}, \omega)$ are mutually orthogonal in the Hilbert sense. The following relationship can be easily proved valid for an infinite homogeneous system:

$$\sum_n [\mathbf{L}_n(\mathbf{r}, \omega) \cdot \mathbf{L}_n^*(\mathbf{r}', \omega) + \mathbf{M}_n(\mathbf{r}, \omega) \cdot \mathbf{M}_n^*(\mathbf{r}', \omega) + \mathbf{N}_n(\mathbf{r}, \omega) \cdot \mathbf{N}_n^*(\mathbf{r}', \omega)] = \delta(\mathbf{r} - \mathbf{r}'). \quad (10)$$

The longitudinal eigenfunctions $\mathbf{L}_n(\mathbf{r}, \omega)$ have no physical meaning for our discussion. Therefore, after dividing the space in subdomains where the refractive index is constant, the MMP method performs the expansion of the electric field in each subdomain only on the sets of transverse eigenfunctions $\mathbf{M}_n(\mathbf{r}, \omega)$ and $\mathbf{N}_n(\mathbf{r}, \omega)$:

$$\mathbf{E}^P(\mathbf{r}, \omega) = \sum_n [a_n^P \mathbf{M}_n(\mathbf{r}, \omega) + b_n^P \mathbf{N}_n(\mathbf{r}, \omega)]. \quad (11)$$

The unknown coefficients a_n and b_n are then determined from the electromagnetic boundary conditions on the interfaces between adjacent subdomains by a least-squares minimization.

The multipolar functions used in the basis set of the multiple multipole method are so short range that only their close neighborhood is affected. Thus the method is better suited to account for localized geometries than the expansion in plane waves.

While the electric field distribution near the tip is determined, the gradient force for a Rayleigh particle can be easily calculated as

$$\mathbf{F} = \frac{\alpha}{2} \nabla E^2, \quad (12)$$

where α is the polarizability of the particle. The particle tends to move to the higher intensity region where its induced dipole has lower potential energy. To overcome the limitation of Rayleigh approximation, a rigorous treatment of the trapping force can be performed by applying the conservation law for momentum.

The gradient force can be expressed by the Maxwell's stress tensor \mathbf{T} as

$$\mathbf{F} = \int_{\partial V} \langle \mathbf{T} \cdot \mathbf{n} \rangle dS, \quad (13)$$

where $\langle \dots \rangle$ stands for the time average, ∂V denotes a surface enclosing the particle, \mathbf{n} is the outwardly directed normal unit vector, and

$$\mathbf{T} = \varepsilon_0 \varepsilon \mathbf{E} \mathbf{E} + \mu_0 \mu \mathbf{H} \mathbf{H} - \frac{1}{2} (\varepsilon_0 \varepsilon E^2 + \mu_0 \mu H^2) \mathbf{I}. \quad (14)$$

Where, \mathbf{I} stands for the unit dyad and ϵ, μ are the dielectric constant and magnetic permeability of the surrounding medium, respectively. For a particle in the vicinity of the tip, the magnetic contribution to the force is found approximately two orders of magnitude lower than the electric one.

The trapping potential U of a particle located at \mathbf{r}_0 is then given by

$$U(\mathbf{r}_0) = - \int_{\infty}^{\mathbf{r}_0} \mathbf{F}(\mathbf{r}) \cdot d\mathbf{r} . \quad (15)$$

4. RESULTS AND DISCUSSIONS

The following parameters of the single-mode fiber are chosen in our calculation. The refractive indices of the core and cladding are $n_1=1.4544$ and $n_2=1.45$, respectively. The diameters of the core and cladding are respectively $2a=8\mu\text{m}$ and $2b=125\mu\text{m}$. The wavelength of the illuminating light is $\lambda=632.8\text{nm}$ (He-Ne laser). The fiber taper is assumed to be linear with an 100nm -tip size.

Figure 2 shows the contours of the near field distribution in the vicinity of the tip of the fiber probe with a conical taper. The near field close to the tip is mainly of evanescent components which are mostly concentrated at the axial direction. The field is rotationally symmetric in the vicinity of the tip, and attenuate rapidly with distance from the tip. So a three dimensional gradient optical field is formed near the tip of the tapered fiber probe. The field is rotationally symmetric in the vicinity of the tip since the fiber probe has a rotationally symmetric geometry.

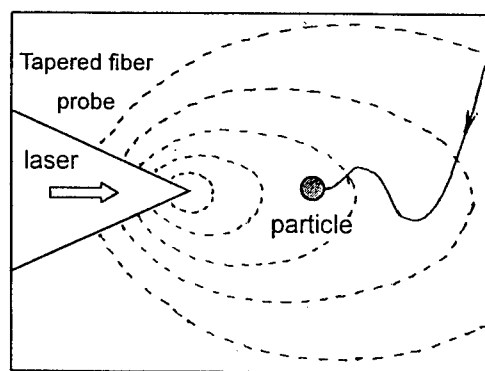


Fig.2. Contours of the near field of tapered fiber probe. The single-mode fiber is specified as $n_1=1.4544$, $n_2=1.45$, $2a=8\mu\text{m}$, and $2b=125\mu\text{m}$. The illuminating wavelength is $\lambda=632.8\text{nm}$ (He-Ne laser). When a particle approaches the vicinity of the fiber tip, it will be trapped by the gradient force of the near field of the fiber probe.

Figures 3 and 4 give the intensity distributions of the near fields out of the tip as functions of the longitudinal and transverse distances (z and x , respectively) from the tip, respectively. Since the optical near field in the vicinity of the tip is evanescent, the field amplitude reduces dramatically with the distance from the tip, and shows almost rotationally symmetric in the vicinity of the tip.

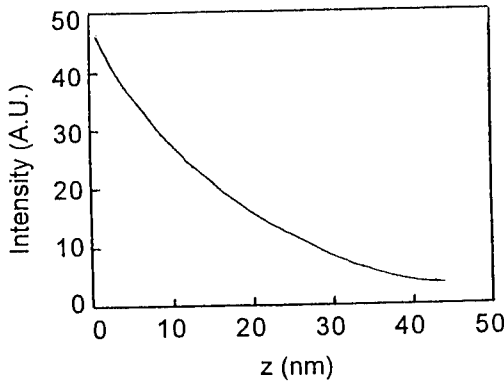


Fig.3. Intensity distribution of the near field of the tip along the longitudinal direction z . The illuminating wavelength is $\lambda = 632.8\text{nm}$ (He-Ne laser). The tip diameter of the fiber probe is assumed as 100nm .

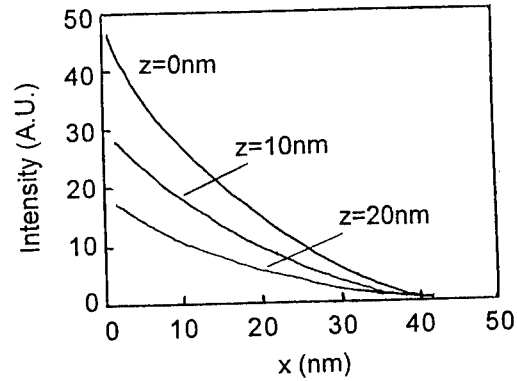


Fig.4. Intensity distribution of the near field of the tip along the transverse direction x with different longitudinal distances ($z=0, 10\text{nm}$ and 20nm , respectively). The field is rotationally symmetric in the vicinity of the tip.

In our calculation, the interaction of the tip and a nanometric particle close to the tip is not counted. However, the field distributions will be distorted around a dielectric particle. A rigorous treatment of the gradient field and the trapping force may be performed by applying the conservation law for momentum.^[14]

When a particle (of diameter $d=10\text{nm}$) approaches the fiber tip, the trapping force and the potential energy can be calculated from the above equations (12) to (15). Figures 5 and 6 show cross sections of the trapping potential along the axial (z) and lateral (x) directions from the tip, respectively. Since the trapping potential is almost rotationally symmetric, we only show the results for the (x, z) plane.

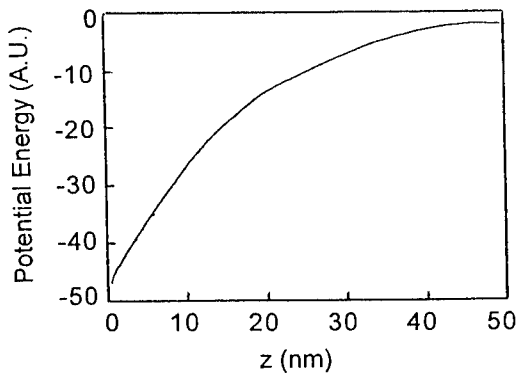


Fig.5. Normalized trapping potential energy of a particle (of diameter $d=10\text{nm}$) as the function of the longitudinal distance z from the tip.

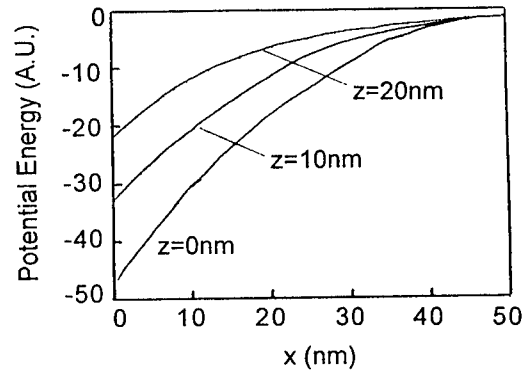


Fig.6. Normalized trapping potential energy of a particle ($d=10\text{nm}$) as the function of the transverse distance x from the tip, with different longitudinal distances ($z=0, 10\text{nm}$ and 20nm , respectively).

The trapping potential is sensitively dependent upon the size, shape and dielectric constant of the trapping particle, as well as the size and refractive index of the fiber tip. Generally, the trapping force is inversely proportional to the tip size, and a sharper tip is required for trapping smaller particles.

The trap force may be affected by the wavelength of the incident light. The particle can be trapped and approach the probe for one wavelength, however, it is also possible to be repelled and escape from the probe for another wavelength. By the wavelength-dependent optical force, one can trap, move, and deposit the particle on a desired position on a nanometer scale.

5. CONCLUSIONS

A method performing near-field optical trapping by a tapered fiber probe has been presented in this paper. Since the fiber probe has a nanometer-scaled resolution, the near-field optical trap is better suited to trap smaller particles. The multiple multipole method is employed to calculate the near field in the vicinity of the fiber tip and obtain the trapping force for a dielectric particle. The calculation results indicate the feasibility of the method.

Compared with the optical trap by a highly focused laser beam, the near-field optical trap using a tapered fiber probe exhibits the following advantages: (1) the optical trapping system is simplified without focusing objective lenses; (2) the fiber is conveniently coupled with a laser diode acted as the illuminating source, so that high a coupling efficiency is easily obtained; (3) the highly confined evanescent fields significantly reduce the trapping volume; (4) the large field gradients result in a large trapping force; and (5) the trapped particles can be moved precisely and freely when the fiber probe is mounted on the three dimensional scanning set-up of the SNOM system.

The experiment of the near-field optical trapping is in progress, and the experimental results will be reported in another article in the near future.

ACKNOWLEDGMENTS

We are very grateful to Prof. Hai Ming and Dr. Ming Bai of University of Science and Technology of China for many helpful discussions. This research is supported financially by Central China Normal University.

REFERENCES

1. Ashkin, J. M. Dziedzic, J. E. Bjorkholm and S. Chu, "Observation of a single-beam gradient force optical trap for dielectric particles," *Opt. Lett.*, 1986, **11**, pp.288-290
2. W. H. Wright, G. J. Sonek, Y. Tadir and M. W. Berns, "Laser trapping in cell biology," *IEEE J. Quantum Electron.*, 1990, **26**, pp.2148-2157
3. K. Taguchi, H. Ueno, T. Hiramatsu and M. Ikeda, "Optical trapping of dielectric particle and biological cell using optical fibre," *Elect. Lett.*, 1997, **33**(5), pp.413-414
4. Zhang Guoping, Ming Hai, Chen Xiaogang, Yang Bao, Xie Jianping, "Experiment Researches on Active Fiber Probe for Scanning Near-field Optical Microscopy," *Chinese J. of Lasers*, 1997, **B6**, pp.513-517
5. E. Betzig, and J. K. Trautman, "Near-field optics: microscopy, spectroscopy, and surface modification beyond the

- diffraction limit," *Science*, 1992, **257**, pp.189-195
6. H. Heinzelmann, and D. W. Pohl, "Scanning near-field optical microscopy," *Appl. Phys. A*, 1994, **59**, pp.89-101
 7. W. Jhe, "Photon scanning tunneling microscope and optical nanotechnology," *AAPPS Bulletin*, 1995, **5**(1&2), pp.12-14
 8. Zhang Guoping, Ming Hai, Chen Xiaogang, Wu Yunxia, Xie Jianping, "Transmission properties of two kinds of fiber probes in scanning near-field optical microscope," *Acta Optica Sinica*, 1998, **18**(7), pp.886-889
 9. Zhang Guoping, Ming Hai, Chen Xiaogang, Wu Yunxia, Xie Jianping, "Effect of the Taper Shape upon Transmission Efficiency of Fiber Probes for Scanning Near-field Optical Microscopy," *Chinese J. of Lasers*, 1998, **B7**, pp.357-362
 10. G. A. Valaskovic, M. Holton and G. H. Morrison, "Parameter control, characterization, and optimization in the fabrication of optical fiber near-field probes," *Appl. Opt.*, 1995, **34**, pp.1215-1228
 11. Zhang Guoping, Ming Hai, Chen Xiaogang, Yang Bao, Xie Jianping, "Research and development of active fiber probe for scanning near-field optical microscope," *Semiconductor Optoelectronics*, 1997, **18**, pp.250-252
 12. Ch. Hafner, *The Generalized Multiple Multipole Technique for Computational Electromagnetics*, Artech, Boston, 1990
 13. Lukas Novotny, Randy X. Bian and X. Sunney Xie, "Theory of nanometric optical tweezers," *Physical Review Letters*, 1997, **79**(4), pp.645-648
 14. J. A. Stratton, *Electromagnetic Theory*, McGraw_Hill, New York, 1941

Author Index

- Alfano, Robert R., 8, 71, 140, 261
 Blankschstein, D., 105
 Budansky, Y., 140
 Celmer, Edward J., 71
 Chang, Bo-Jui, 232
 Chang, Yi-ren, 181
 Chen, Haiqing, 298
 Chen, Jian-cheng, 87, 100
 Chen, Rang-Wu, 100
 Chen, Yan-Yu, 198
 Cheng, Ping-chin, 87, 92, 100, 119, 134
 Cheng, Wen-Ming, 265
 Cheng, Yao, 181
 Chiou, Arthur E. T., 162, 213, 222
 Chiou, Shien-Cheng, 286
 Chou, Chien, 192, 248
 Chuang, Tung J., 144
 Chyu, Minking K., 181
 Dieckmann, William, 40
 Ding, Lei, 157, 275
 Dong, Chen Yuan, 105
 Dong, Xiaoyi, 157, 275, 305
 Dong, Xinyong, 157
 Fan, Lina, 315
 Feng, Dejun, 157, 275, 305
 Galland, Pierre A., 261
 Gauderon, Regis, 115
 Ge, Chunfeng, 305
 Gkanatsios, Nikolaos A., 40
 Grable, Richard J., 40
 Gu, Min, 210
 Hamaoka, Takafumi, 48
 Han, Chien-Yuan, 192
 Hiruma, Teruo, 2
 Ho, Ping-Pei, 8, 71, 261
 Ho, Yuan, 198
 Hsieh, Tseng-Ming, 232
 Hsu, L., 105
 Hsu, Long, 181, 232
 Huang, Chun-Cheng, 213
 Huang, H. C., 222
 Huang, Mao-Kuo, 87, 92, 100, 119
 Huang, Sheng-Lung, 92, 119
 Huang, Z. H., 222
 Hwang, C. S., 241
 Hwang, Wen-Liang, 213
 Iwata, Makoto, 24
 Jan, Gwo-Jen, 198
 Jeong, Jae-Hun, 173
 Johnson, Iain, 87
 Kai, Guiyun, 275, 305
 Kao, Fu-Jen, 87, 92, 100, 119, 134
 Kaplan, Peter D., 105
 Katsumura, Toshihito, 48
 Katz, Alvin, 140
 Kiang, Yean-Woei, 14
 Kohata, Daisuke, 48
 Koizumi, Hideaki, 24
 Kook, Youn-Jae, 173
 Kourakos, Alexander, 61
 Koutcher, Jason A., 71
 Kudo, Nobuki, 48, 76
 Langer, R., 105
 Lee, Chau-Hwang, 125
 Lee, Ming-Kwei, 92
 Lee, Shin-Ge, 278
 Li, Yanping, 321
 Li, Yi-Lin, 198
 Li, Zhiquan, 310, 315
 Lian, Chang Ten, 241
 Liang, Hsing-Ching, 255
 Liang, Xiang, 261
 Liao, Bing-Yao, 213
 Lichty, Wemara, 34
 Lin, Bai-Ling, 87, 100, 134
 Lin, Che-hsin, 181
 Lin, Chi-Hung, 213
 Lin, Chii-Wann, 14
 Lin, Ling, 76
 Lin, Qi, 321
 Lin, Wan-Jen, 125
 Lin, Yuan-Hsiang, 198
 Liu, Deming, 151
 Liu, Heliang, 275, 305
 Liu, Hong-Chih, 255
 Liu, S., 151
 Liu, Tzu-Ming, 87, 100
 Lukins, Philip B., 115
 Lyu, Chung-Wei, 248
 Maki, Atsushi, 24
 Mehta, D. S., 222
 Min, Hong-Shick, 173
 Niwayama, Masatsugu, 48, 76
 Olivier, Patrick, 40
 Park, Young-June, 173
 Peng, Li-Cheng, 248
 Ponder, Steven L., 40
 Poon, Ting-Chung, 61
 Qiang, Xifu, 310, 315
 Roy, Maitreyee, 57
 Sakatania, Kaoru, 34
 Shao, Jun, 48, 76
 Sheppard, Colin J. R., 57, 115
 Shih, Ming Chang, 144, 241

So, Peter T. C., 105
 Sun, Chia-Wei, 14
 Sun, Chi-Kuang, 87, 92, 100, 134
 Svahn, Peter, 57
 Tang, Gui Chen, 140
 Tanikawa, Yukari, 24
 Ting, Solomon J. Y., 162
 Tong, Kai, 310
 Tsai, Jin-Wu, 213
 Tsao, Shyh-Lin, 265, 278, 286
 Tu, Pei-Chin, 192
 Wake, Robert H., 40
 Wang, C. F., 222
 Wang, C. C., 144
 Wang, Chih-Yu, 14
 Wang, Da-Wei, 213
 Wang, Hsian-Jenn 248
 Wang, J. M., 151
 Wang, Jyhyng, 125
 Wang, Le Ming, 261
 Wang, Wei-Hsiung, 192
 Wang, Yi-min, 87, 100
 Wang, Yung-Shun, 87, 92, 100, 119
 Watanabe, Eiju, 24
 Wu, Zhaoxia, 310, 315
 Xia, Ge, 321
 Xie, Yuxiao, 34
 Yamada, Yukio, 24
 Yamamoto, Katsuyuki, 48, 76
 Yamamoto, Tsuyoshi, 24
 Yamashita, Yuichi, 24
 Yang, Chih Chung, 14
 Yang, Yuanlong, 71
 Yoshizawa, Hiroshi, 24
 Yu, B., 105
 Yu, C. T., 144
 Zeng, Xiangjun, 298
 Zeng, Yueping, 40
 Zhang, Guoping, 321
 Zhang, Weigang, 157, 305
 Zhang, Ying, 157
 Zhao, Chunliu, 157
 Zhu, Zhongru, 321
 Zou, Huangcong, 34